Contribution de la pétrologie expérimentale sur les processus de formation de roches et de minéralisation de granites du Jurassique en Chine du Sud

Fangfang Huang

ÉCOLE DOCTORALE

ENERGIE, MATERIAUX, SCIENCES DE LA TERRE ET DE L'UNIVERS

Institut des Sciences de la Terre d'Orléans

School of Earth Sciences and Engineering, Nanjing University

THÈSE EN COTUTELLE INTERNATIONALE présentée par:

Fangfang HUANG

Soutenue le: **29 Octobre, 2018**

Pour obtenir le grade de:

Docteur de l'Université d'Orléans et de l'Université de Nanjing

Discipline/ Spécialité: Sciences de la Terre et de l'Univers

Contribution de la pétrologie expérimentale sur les processus de formation de roches et de minéralisation de granites du Jurassique en Chine du Sud

THÈSE dirigée par:

Rucheng WANG	Professeur, Université de Nanjing
Bruno SCAILLET	Professeur, Université d'Orléans
Yan CHEN	Professeur, Université d'Orléans
Lei XIE	Professeur associée, Université de Nanjing

RAPPORTEURS :

Robert L. LINNEN	Professeur University of Western Ontario, Canada
Xiaolin XIONG	Research Professor, Institute of Geochemistry Chinese Academy of Sciences, China (GIG-CAS)

JURY *(y reporter tous les membres de jury présents à la soutenance)* **:**

Zhenmin JIN	Professeur, China University of Geoscience
Meifu ZHOU	Professeur, University of Hong Kong
Xiaolin XIONG	Research Professor, GIG-CAS
Rucheng WANG	Professeur, Université de Nanjing
Bruno SCAILLET	Professeur, Université d'Orléans
Yan CHEN	Professeur, Université d'Orléans

“昨夜西风凋碧树，独上高楼，望尽天涯路”。

——晏殊（北宋 991—1055）《蝶恋花》

“Last night the west wind withered the green trees;

climbing the tower alone, I gaze at the road stretching to the horizon”. [1]

——YAN Shu (Northern Song Dynasty 991—1055)《Butterflies in Love with Flowers》

“衣带渐宽终不悔，为伊消得人憔悴”。

——柳永（北宋 984—1053）《蝶恋花》

“I have no regrets as my girdle grows too spacious for my waist;

with everlasting love for you I pine”. [2]

——LIU Yong (Northern Song Dynasty 984—1053)《Butterflies in Love with Flowers》

“众里寻他千百度，蓦然回首，那人却在，灯火阑珊处”。

——辛弃疾（南宋 1140—1207）《青玉案·元夕》

“But in the crowd once and again;

I look for her in vain;

when all at once I turn my head;

I find her there where lantern light is dimly shed”.[3]

——XIN Qiji (Southern Song Dynasty 1140—1207)《The Lantern Festival Night - to the tune of Green Jade Tabl

Summarized by WANG Guowei (1877-1927) in book of *Renjian Cihua* 人间词话 (Poetic Remarks in the HumanWorld).Translated by [1, 2] Ching-I Tu; [3] Yuanchong Xu, Ming Xu

Acknowledgements

Firstly, I would like to extend my sincerest gratitude to my supervisors and all the people who helped me during my PhD studies and my life. Four years of study in Nanjing University and three years of study in Unisversité d'Orléans are meaningful in my life.

When I entered in the School of Earth Sciences and Engineering, Nanjing University as a master student, it is my honor to study under the supervision of Professor Rucheng Wang. He not only teaches me how to do the research but also teaches me the truth in life. Besides, I am particularly grateful for the opportunity of studying in France which supported by Professor Rucheng Wang. Thanks a lot for his careful cultivation and help to me.

Four years ago, it was my first time to go aboard for study. I am glad that I can under the cooperation supervision of Professor Bruno Scaillet from the Unisversité d'Orléans (ISTO) for my experimental petrology study. I appreciate his patience in teaching me the technique of the internally heated pressure vessel and his immense knowledge of experimental petrology.

What is more, I would like to express my sincere gratitude to all of my co-supervisors who help me do my research during my study: Professor Yan Chen, for his teaching, professional guidance in my study and kindly help in my life. Associate professor Lei Xie, for her careful teaching and inspiration to me. Professor Michel Faure, for his field observation teaching and the tectonic guidance. Professor Bo Wang, for his help in the field and the communication between Orleans and Nanjing.

Sincere thanks also to the members of our research group. Dr. Saskia Erdmann who had many discussions with me and helped me in manuscript writing and polishing. I also like to thank Dr. Hongsheng LIU, who made many efforts in organizing fieldwork and shared the ideas in terms of the AMS experiments with me. Also many thanks for

their kindly help in my life when I was studying in France.

Besides, I would also like to thank to other teachers and engineers for their help when I studied in France and China. Professor Jinchu Zhu, for his fieldwork guidance and providing us the precious samples. Professor Wenlan Zhang, for her technical support of EPMA, who teach me lot of knowledge of microprobe. Professor Michel Pichavant, for his nice suggestions and discussion when I was puzzled in doing my experiments. Dr. Remi Champallier and Dr. Juan Andujar, for their careful instruction in using the IHPV, Dr. Ida Di Carlo for her nice training in EMP analysis, Mrs Patricia Benoist for her nice help in SEM, Mr. Sylvain Janiec for his high quality thin sections preparation. Dr. Stephane Scaillet and Mr. Florian Duval for their Ar-Ar dating guidance. Associate professor Huan Hu for her help in La-ICP-Ms measurement, professor Aicheng Zhang for his nice discussions with me, associate professor Xudong Che and Dr. Rongqing Zhang for their help in collecting the samples in the field.

I am grateful that I can have so many colleagues and friends when I study in Nanjing University and the Université d'Orléans (ISTO). Many thanks for their help and company during my study. This is a long list. Our mineral group: Lubin Wang, Rong Yin, Chengxiang Li, Bin Wu, Xiangyu Zhu, Zeying Zhu, Di Zhang, Runlina Pang, Lu Xiang, Yunqiao Lu, Rong Liu, Wendi Chen, Ennong Tian, Zhengjun Wang, Haoran Dou, Chen Liu, Zhaoyu Yang, Ying Liu, Xuejiao Li, Xiangyuan Tao. My roommates: Juan Li, Chunyu Ni, Fajun Sun, Bingjie Wang. Other nice classmates, colleagues and friends who help me a lot: Yan Xia, Lei Liu, Youlian Li, Xin Zhu, Chaolei Yan, Ting Fang, Di Wang, Jianqiang Liu, Jiaolong Zhao, Wenjing Xu, Ying Bai, Xudong Huang, Fengfeng Zhang, Xin Chen, Kai Zhao. And equally thanks to those friends and teachers who I met in ISTO this big famliy: Alex (thanks for the summer barbecue and the cycling trip), Ali (thanks for sharing the office and small cookies with me), Aneta, Anne-Aziliz (thanks for the talk in French with me), Arnaud, Clement, David, Emanuela, Fabrice, Gaëtan (thanks for becoming our driver and the discussions), Giada, Giulia, Hugues, Leïla (thank you so much for inviting me to your family for a special Christmas in

French way), Malcolm (thanks for discussion about the linear fit method), Mickaël (thanks for the discussion and encouragement in EGU), Morgane, Nolween, Pierreangelo (thanks for sharing the experiment ideas with me), Valentin, Vincent, Weiwei&Wenjing (thanks a lot for your help), Yves, Zineb. Besides, many thanks for the supports and help from Mrs. Wang Shujun, Tang Xiaoqian, Zhang Xiaoqing in Nanjing University and Marie-Noëlle Pailhès (thanks for your nice help) at ISTO.

In addition, the financial supports from the program of China Scholarships Council, the National Basic Research Program of China, the Open Fund of State Key Laboratory for Mineral Deposits Research of Nanjing University and the Centre National de la Recherche Scientifique of France are also truly acknowledged.

Finally, I would like to thank my family. Without the supports from my parents, I can't finish my study. Thanks for all their unceasing love, care, and encouragements in my life.

Voilà, c'est fini!

Abstract

As a natural laboratory, the huge amounts of Mesozoic granite distributing in South China provided a unique opportunity to unravel the Mesozoic crust formation and evolution in southern China as well as for guiding mining exploration efforts in this area. The studies of mineralogy, petrology, geochemistry and geochronology had been carried out in South China for many decades, however, the conditions for the formation of these Mesozoic granites remain controversial. In this thesis, based on the systematically study of whole-rock geochemistry, geochronology, petrography, mineralogy, we use internally heated pressure vessel to explore the phase equilibrium of the granite from South China and successfully set up the phase diagrams. In terms of experimental petrology, our experimental results provided the first quantitative framework for the understanding of the petrogenesis of Mesozoic granites in South China.

With 520 km^2 out crop area, the Qitianling pluton is representative metaluminous (amphibole-bearing) Mesozoic granites in the central part of the Nanling Range in SE China, which is associated with world-class tin mineralization. It consisted of three main phases: phase-1, porphyritic, medium- to coarse-grained amphibole-biotite-rich monzonitic granite; phase-2, medium-grained biotite±amphibole-bearing granite; phase-3, fine-grained, biotite-bearing granite. The geochemical data show that Qitianling pluton is metaluminous, and belongs to aluminous A-type granites (A2 post-orogenic subtype) with high Ga/Al ratio and high contents of HFSE (Zr, Nb, Ce, Y) and REE. Harker and REE spider diagrams show that the Qitianling pluton display well organised fractionation trends. Radiometric data show that the emplacement of Qitianling pluton occurred during Jurassic times. We have found crystallization ages (Zircon U-Pb age) for Qitianling pluton ranging between 149.5±4.8 Ma to 162±2 Ma being coincident with previous constraints (146±5 Ma to 163±3 Ma). The Ar-Ar dating of Qitianling granite shows that the amphibole and biotite record ages ranging from 151

Ma to 155 Ma which represent the cooling age of Qitianling. Located in the central part of the pluton, sample SC-52 acquired the ages from zircon (U-Pb system at 157.5±1.4 Ma), amphibole (Ar-Ar system at 153.4±0.4 Ma) and biotite (Ar-Ar system at 152.6±0.8 Ma) which give a cooling rate of 80°C / Ma for the cooling process of Qitianling pluton.

We have experimentally established the phase relationships for the Qitianling granite. Three representative amphibole-bearing, metaluminous granitic samples were chosen for constraining crystallization conditions of the Qitianling pluton. Crystallization experiments were performed at 100-700 MPa, albeit mainly at 200 MPa or 300 MPa, at an fO_2 of ~NNO-1.3 (1.3 log unit below the Ni-NiO buffer) or ~NNO+2.4, at 660°C to 900°C, and at variable melt water contents (~3-8 wt%). Amphibole stability field and barometry both show that the pressure of magma emplacement was around 300-350 MPa. Amphibole and biotite Fe/Mg ratios further suggest that magmatic fO_2 was around NNO-1±0.5 near solidus, while Fe-Ti oxides record an fO_2 increase up to NNO+1 below solidus. Amphibole crystallization is restricted to near H_2O-saturation conditions, requiring at least 5.5 wt% H_2Omelt at 200 MPa, or 6-8 wt % at $\geqslant$ 300 MPa. Amphibole occurrence in K_2O-rich metaluminous silicic magmas thus indicates water contents significantly higher than the canonical value of 4 wt%. The experimental liquid line of descent obtained at 200-300 MPa mimic the geochemical trend expressed by the pluton suggesting that fractionation in the upper crustal reservoir could happen.

Based on the phase equilibria of intermediate-acid igneous rocks, combining the composition of rock forming minerals (Amp and Bt) and bulk rock composition, we proposed an empirical oxygen barometer. The database of our oxygen fugacity modeling including Qitianling granite, Santa Maria dacite, Pinatubo dacite, Jamon granite, Lyngdal granodiorite which cover a SiO_2 content of bulk rock ranging from 60 wt% to 71 wt%. All the required parameters are temperature, pressure, whole rock composition:

$$\triangle NNO = -0.00254 \times T(^{\circ}C) - 13.9602 \times Fe\#_{Amp} + 0.00143 \times P(MPa) + 6.2809 \times Fe\#_{Amp} \times Fe\#_{w} + 0.2803 \times wTiO_2 - 2.1 \times w(Al_2O_3/SiO_2) + 0.2768 \times w(Na_2O/K_2O) + 5.9663 \quad (1)$$

$$\triangle NNO = -0.0004 \times T(^{\circ}C) - 0.0004 \times Fe\#_{Bt} + 8.3772 \times Fe\#_{Bt} \times Fe\#_{w} + 0.0027 \times P(MPa) + 2.4082 \quad (2)$$

These equations allow to calculate magmatic fO_2 to within 1 log unit: the retrieved values most likely correspond to conditions during the late crystallization stage of the magma, owing to the easiness of re-equilibration of the used minerals. Application of our oxygen barometer to three Jurassic plutons (Jiuyishan, Huashan and Guposhan pluton) in South China demonstrates that the oxygen fugacity of those three plutons suggest a relative reduced redox environment, similar to that inferred for Qitianling granite.

Besides, a highly evolved, composite ongonite-topazite with Nb-Ta- and Sn-bearing ore minerals dike was also involved into our study. The crystallization of Nb-Ta- and Sn-bearing ore minerals was strongly controlled by the separation of the aluminosilicate and hydrosaline melt phases, which both are rich in F. Exsolution of the two melt phases and their efficient segregation into core and rim zones of the dike may have been driven by dike propagation/widening subsequent to the initial dike emplacement. The different content of F and other volatile components in two different melts may cause the early Nb-Ta mineralization in ongonite and later Sn mineralization in topazite.

The experimental constraints on the emplacement conditions of Jurassic Qitainling granite gave several clues for better understanding the tin mineralization. The experiment of solubility of SnO_2 suggested that low oxygen fugacity can be a significant constrain on the Sn incorporation in a granitic melt. Qitianling magma was emplaced at relative low oxygen fugacities (NNO-1±0.5), hence providing a beneficial environment for incorporating the Sn in the melt, at least during the early stages of its

production/crystallisation. Besides, High liquidus temperature of magma plays an important role on extracting ore elements, especially in thoes anatectic melts, thus also allows high concentration of tin being reached in the silicate melt during the different geological process. Lastly, water rich magmas dissolve other volatiles such as chlorine, fluorine, boron and phosphorus which will be also helpful in capturing and transiting the ore elements such as Sn. Based on the low oxygen fugacity, high temperature and rich in melt water content, we deduced that Qitianling magma system is beneficial for the tin mineralization. What is more, high melt content in the Qitianling magma system may raise the question: Where is the water come from? Assume that there was no excess and extraneous water from the source or the country rocks, then the hydrous minerals such as amphibole and biotite bearing rocks could be a possibility of source rock of Qitianling pluton which can produce high content of water after the dehydration melting.

Key words: South China; Jurassic granite; experimental petrology; phase equilibrium; emplacement conditions; temperature; pressure; oxygen fugacity; melt water content; cooling rate; amphibole; biotite; oxybarometer; Sn-Nb-Ta mineralization.

Table of Contents

Chapter 1 Introduction

1.1 Research background

1.1.1 The research advance of the petrogenesis of Mesozoic granitoids in South China

In the southeastern part of China, the wide distribution and long duration of the late Mesozoic magmatism presents a unique opportunity in the world, offering a natural laboratory to study the magma genesis, their emplacement mechanisms, the geodynamic role on magma emplacement and related lithospheric evolution, and the relationships between magmatism and mineralization. Among these hot debated scientific questions, numerous Chinese and international research teams are working on the petrogenesis of Mesozoic granitoids and related volcanic rocks in South China for many years (Xu et. al., 1963; Jahn et al., 1976; Wang et. al., 1984; Mo, 1985; Zhou and Li, 2000; Sun and Zhou, 2002; Wang, 2004; Zhou et. al., 2006; Hsieh et. al., 2008; Gao et. al., 2017). Different scientists hold different opinions on the petrogenesis of Mesozoic granitoids in South China. Zhou et al., (2006) summarized the current accepted views: (1) lithosphere extension and asthenosphere upwelling; (2) mantle plume activities; (3) rifts in coastal areas of east China; (4) Rifting and lithosphere delamination in east Asia; (5) Paleo-Pacific Plate subduction beneath East Asia; (6) Extension-induced deep crustal melting and underplating of mantle-derived basaltic melts (Li, 2000; Li et al., 2001; Xie et al., 1996; Xie et al., 2001;Gilder et al., 1991; Zhu et al., 1997; Cai et al., 2002; Jahn et al., 1976, 1990; Guo et al., 1980; Charvet et al., 1994; Lapierre et al., 1997; Zhou and Li, 2000; Niu, 2005. However, in order to find out the consensus on the petrogenesis of Mesozoic granitoids in South China, the study on the emplacement conditions of Mesozoic granites is a key likely to give important

information and detailed evidence.

1.1.2 Emplacement conditions of Mesozoic granites in South China

Starting in the 1990's, geoscientists have made important efforts and obtained remarkable scientific achievements in both geochemistry and geochronology fields of Mesozoic granites in South China. As for the emplacement conditions, generally, most of the studies of emplacement condition of granite from south China are based on the different thermometers, barometers and oxygen barometers. For example, Zhao et al. (2005) used different thermometers and barometers to calculate the temperature and pressure of the representative Mesozoic metallogenetic A-type granite – Qitianling ganite and concluded that the forming temperature and pressure should be 750-820℃ and 3.6±0.9 kbar, respectively. Similar conclusion also came from Zr-in-titanite thermometer from Xie et al. (2010), which indicated a range in temperature of 721-780℃.As for the redox condition, information from biotite suggests that the oxygen fugacity of the Qitianling granite is between the Ni-NiO (NNO) and the Fe2O3- Fe3O4 (MH) buffers (Zhao et al., 2005). This redox state is consistent with the biotite calculated results that inferred for other Mesozoic metallogenetic granites in South China such as Huashan and Guposhan (Wang et al., 2013).

1.1.3 The experimental petrology for granite

Although the different thermometers, barometers and oxygen barometers can give some indirectly indications of the crystallization conditions, some of the estimation of the temperature, pressure or redox state may be overestimated or underestimated due to the accuracy of the method or the re-equilibrium of the minerals which can't record the crystallization composition. Therefore, the experimental petrology method of the phase equilibrium will provide more direct and accurate constrain on the magma system. In the early stage of the development of experimental petrology, many phase equilibrium

studies were carried out using the synthetic materials or simple binary and ternary systems (Tuttle and Bowen, 1958; Whitney, 1972, 1975; Luth, 1976). Along with the development of the technique, such as the application of internally heated pressure vessels technique that took traditional petrology one step further. Based on this technique, phase equilibria studies were widely developed in the felsic magma system. i.e. Scaillet, (1995) successfully set up the phase diagrams of the leucogranite of Himalayan at 4 kbar, under moderately reducing conditions (FMQ -0.5), for varying melt water content, and in the temperature range of 663-803°C. Besides, the phase equilibria in the peralkline rhyolite system were also constrained by the same experimental petrology method (Scaillet and Macdonald, 2001; 2003). The phase diagrams of A-type granite were first established by Clemens et al. (1986) for the metaluminous Watergums granite from southeastern Australia. The experimental works of Dall'Agnol et al. (1999), Bogaerts et al. (2003) and Klimm et al. (2003, 2008) have subsequently constrained emplacement conditions for other metaluminous A-type granites. These studies have shown that the precursor magmas of such granites have relatively high temperatures during emplacement in upper crust (>800°C) with melt water contents up to 6.5 wt% (Dall'Agnol et al., 1999), and variable redox conditions (from NNO to NNO+1). In addition, the phase equilibrium experiments of Klimm et al. (2003, 2008) also explored the relationships between different compositions of Wangrah Suite A-type granites. Their results show that crystal fractionation can explain the geochemical trends expressed by the Wangrah pluton. What is more, the experimental petrology can also be applied into exploring the ore-forming processes in granitic magma system. i.e. Linnen et al. (1995, 1996) also explored the SnO_2 solubility in haplogranitic melt under broadly similar experimental conditions, finding that tin diffusivity was dependent on both fO_2 and melt composition. Hence, according to the previous experimental studies, we believe that using the experimental petrology method can help us better understanding the petrogenesis of Mesozoic granitoids and their associated mineralization in South China.

1.2 Key problems

What are the temperature-pressure conditions of magma emplacement in upper crust, and what are the relationships among tectonics (geodynamics) - magmatism - mineralization? These are still the most hotly debated questions among the geologists in the world. However, various fundamental questions remain unanswered and the better understanding of emplacement condition of Mesozoic granites still remains an important task. In this thesis, besides the traditional petrology, mineralogy, geochemistry, geochronology, the experimental petrology technique (e.g. internally heated pressure vessels) will be applied for the study of the Mesozoic metallogenetic granites in Southern China which has never been utilized for this area before, in order to simulate and constrain the emplacement conditions and evolution of magma (pressure, temperature, volatile contents, redox state). Meanwhile, the information from the experimental petrology simulations can help us have a better understanding on the relationship existing between magmatism and mineralization.

The main objectives of this research are to determine the emplacement conditions (P, T, fO_2, H_2O in melt) of representative Mesozoic granites using the experimental petrology approach. Building up the phase equilibria diagram of representative granites in South China will supplement more basic knowledge of Mesozoic magmatic events. Economically significant W, Sn, U, Nb-Ta, and REE mineralizations are genetically associated with these granites in South China. Therefore, we also aim to explore the relationship between emplacement conditions and mineralization. Here in this thesis, using the same experimental approach we mentioned above, we chose the Jurassic metallogenetic Qitianling granite in southern China for our case study. We set up the phase diagram of Qitianling granite, and find out its possible emplacement conditions which provide some more clues for understanding the later mineralization.

1.3 Workload of the study

All the study was supervised by both professors from Nanjing University and University of Orleans. The main workload which is consists of the work in the field and laboratory is listed in Table 1.

work type	work content	number	unit
Field work	Field observation	105	day
		42	pluton
		5	profile
	Sample collection	188	sample
Sample preparing	Starting materials	3	sample
	Thin section	230	piece
	Au capsule	200	piece
	Epoxy mount	18	piece
	Zircon selection	18	sample
	Biotite selection	12	sample
	Amphibole selection	3	sample
Experiments and analysis	Crystallization and melting experiment	20/ >8600	run/ hour
	Thin section observation	230	piece
	Bulk rock major element analysis	46	sample
	Bulk rock trace element analysis	46	sample
	Minerals phases EMP analysis	>5000	analysis
	CL image of zircon	190	photo
	BSD image of natrural and experimental minerals	>1000	photo
	U-Pb zircon dating	18	sample
	^{40}Ar-^{39}Ar biotite and Ampibole dating	15	sample

Table 1 Workroad of this study.

After the literature investigation on the Mesozoic metallogenetic granites in South China, we recognized the significance to conduct detailed fieldwork in Hunan, Guangdong, Guangxi, Jiangxi and Fujian provinces. Field observations and sample collection is the first step. The observation of the contact between the granites body and their country rock can give a rough reference for the choice of the conditions in later

experimental petrology experiments.

Laboratory studies include samples preparing (thin sections making; rock sample crushing; rock sample powder grinding; mineral separating and picking; samples mounting), crystallization experiments using internally heated pressure vessel (IHPV), major element determination by wet-chemical analyses, trace element measurement by Inductively Coupled Plasma Mass Spectroscopy (ICP-MS), major composition analyzing of natural and experimental mineral phases by electron microprobe (EMP), trace element (including U-Pb isotope) analyzing of mineral by Laser ablation inductively coupled plasma mass spectrometry (La-ICP-MS), ^{40}Ar-^{39}Ar isotope determination by Noble Gas Mass Spectrometry, zircon cathodoluminescence (CL) and mineral phases imaging by Scanning Electron Microscopy (SEM). All these methods are described in details in Chapter 3.

1.4 Main achievements and innovations

Based on the systematically experiments of our study, the following findings can be concluded:

The Ar-Ar dating of Bt and Amp of Qitianling granite gave the age ranging from 151 Ma- 155 Ma which is consistent with the U-Pb zircon age (150 Ma- 162 Ma) representing the slowly cooling history of Qitianling pluton.

Located in the central part of the pluton, sample SC-52 acquired the ages from zircon (U-Pb system at 157.5±1.4 Ma), amphibole (Ar-Ar system at 153.4±0.4 Ma) and biotite (Ar-Ar system at 152.6±0.8 Ma) which give a cooling rate of 80°C / Ma for the cooling process of Qitianling pluton.

We built up the phase diagrams of representative Jurassic A-type metaluminous potassium rich Qitianling granite. The high content of potassium has an effect on the

stability of biotite which indirectly influences the stability of amphibole.

The Qitianling granite have a relatively high liquids temperature (>900 ℃).

The A-type Qitianling granite was cooling down in a water rich (>5.5 wt% or even up to ~7 wt%) environment.

Phase equilibrium relationships and compositions of minerals such as amphibole suggest a pressure of crystallization at 300MPa-350MPa.

Fe/(Fe+Mg) ratio of experimental amphibole and biotite suggest the oxygen fugacity of Qitianling granite is relatively reduced (~NNO-1±0.5), which is beneficially for concentrating Ore elements such as tin.

Using the Fe/(Fe+Mg) ratio of amphibole and biotite and the bulk rock composition, we set up two empirical oxygen barometers.

The application of our empirical oxygen barometers showed that the adjacent Jurassic plutons (Jiuyishan, Huashan, Guposhan) have a relatively reduced (<NNO) redox state.

Chapter 2 General geological background of the South China Block

2.1 General tectonic background in South China

The current South China Block (SCB) is surrounded by four major tectonic units, i.e. the North China Craton in the north, Tibet plateau in the west, the Indo-China Block in the southwest and the Pacific plate in the east-southeast part (Fig. 2.1a; Zheng et al., 2013. Faure et al., 2017; Li et al., 2017). These units were gradually collided with the South China Block since Paleozoic epoch to late Cretaceous. However, previous geochronological studies on the sutures, which separate the South China Block from the surrounding units (Fig. 2.1a), show that these sutures are mainly closed at the Triassic time and some of them re-activated by subsequent tectonic events (Mattauer et al. 1985; Faure et al.,1999, 2014; Hacker et al., 2004; Lepvrier et al.,2004; Yan et al., 2011)

The South China block is amalgamated by the Yangtze block in the north and the Cathaysia block in the south during Neoproterozoic epoch. These two blocks are separated by a > 100km wide and ~1500km long Jiangnan orogen, which cross Guangxi, Guizhou, Hunan, Jiangxi, Anhui and Zhejiang provinces (Fig. 2.1b; Wang et al., 2004; Shu et al., 2012). Within the Jiangnan orogen region, previous geochronological studies on the syn-collisional granitoids and the detrial zircon dating of the conglomerate show that the time of collision is between 1.0 Ga to 0.8 Ga (Shu et al., 1996; Li et al., 1994, 2007b, 2009; Wang et al., 2006, 2007b; Ye et al., 2007). In the eastern part of the Jiangnan orogen region, the discovering of Neoproterozoic ophiolite along the Shaoxing–Jiangshan–Pingxiang fault has demonstrated the boundary between the Yangtze and the Cathaysia block (Shu et al., 1994, 2006, 2011; Li et al., 2009). While for the western part, the boundary remains uncertain due to the lack of reliable

evidences. Therefore, different opinions were proposed by geologists: 1) Anhua-Luocheng fault; 2) Chenzhou-linwu fault; 3) Hangzhou-Zhuguangshan- Huashan (Qinhang belt) (Charvet,1996; Hong et al., 1998; Wang et al., 2007b; Zhao and Guo,

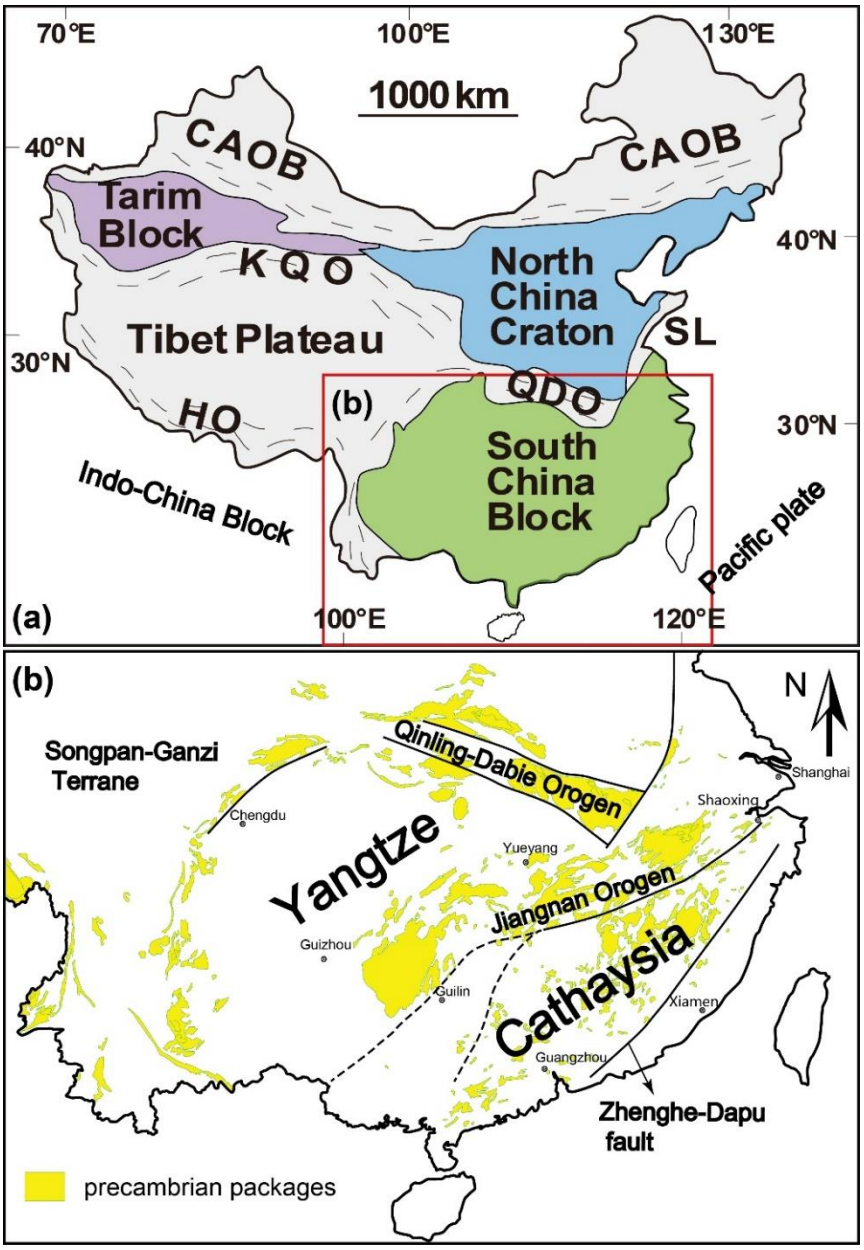

Fig. 2.1 (a) Sketch map showing major tectonic units in China. Abbreviations: CAOB: Central Asia Orogenic Belt; HO: Himalaya Orogen; KQO: Kunlun Qiangtang Orogen; QDO: Qinling-Dabie Orogen; SL: Sulu belt. (b) Geological map showing distribution of Precambrian rocks (including metamorphosed volcanic- sedimentary basement and granites) in the South China Block and the possible boundry of Yangtze and Cathaysia blocks (Modified after Dong et al., 1986; Li et al., 2003; Yu et al., 2009; Faure et al., 2009; Shu, 2012).

2012; Charvet et al., 2013).

The Yangtze Block possess the Archean TTGs series as it basement and characterized by the Neoproterozoic magmatism around the margin of the block (Fig. 2.1b; Qiu et al., 2000; Gao et al., 2011). However, the Cathaysia Block is considered as an accreted block with Paleoproterozoic basement, which supported by the Paleoproterozoic gneissic granitoids (~1830- ~1890 Ma) or amphibolite (1766 Ma) developed in southwestern Zhejiang Province and northwestern Fujiang Province (southeastern China) (Li, 1997; Yu et al., 2009; Li and Li, 2007b). Moreover, the Precambrian strata are randomly and widely developed inside of the Cathaysia Block and previous detrital zircon dating and isotope studies show different affinity (Xu et al., 2005; Yu et al., 2007, 2009, 2010, 2012).

2.2 General magmatism in south China

2.2.1 Neoproterozoic magmatism series

In Southern China, the distribution of Neoproterozoic magmatism is less (Fig. 2.1b; Fig. 2.2). Since the uniform South China Block was formed at the Neoproterozoic epoch, the following rifting related Neoproterozoic granitoids and volcanic rocks revealed by previous displayed the major magmatism events in Precambrian. Consequently, the widely distributed volcanic sediments in the Jiangnan orogeny and late Neoproterozoic granitoids (~770 Ma), which intruded in the syn-collisional early Neoproterozoic peraluminous granitoids (Xu and Zhou, 1992; Wang et al., 2013) were revealed. Moreover, the rifting related Neoproterozoic volcanic rocks also reported inside of the Cathaysia Block (Li et al., 2002; Wang et al., 2008).

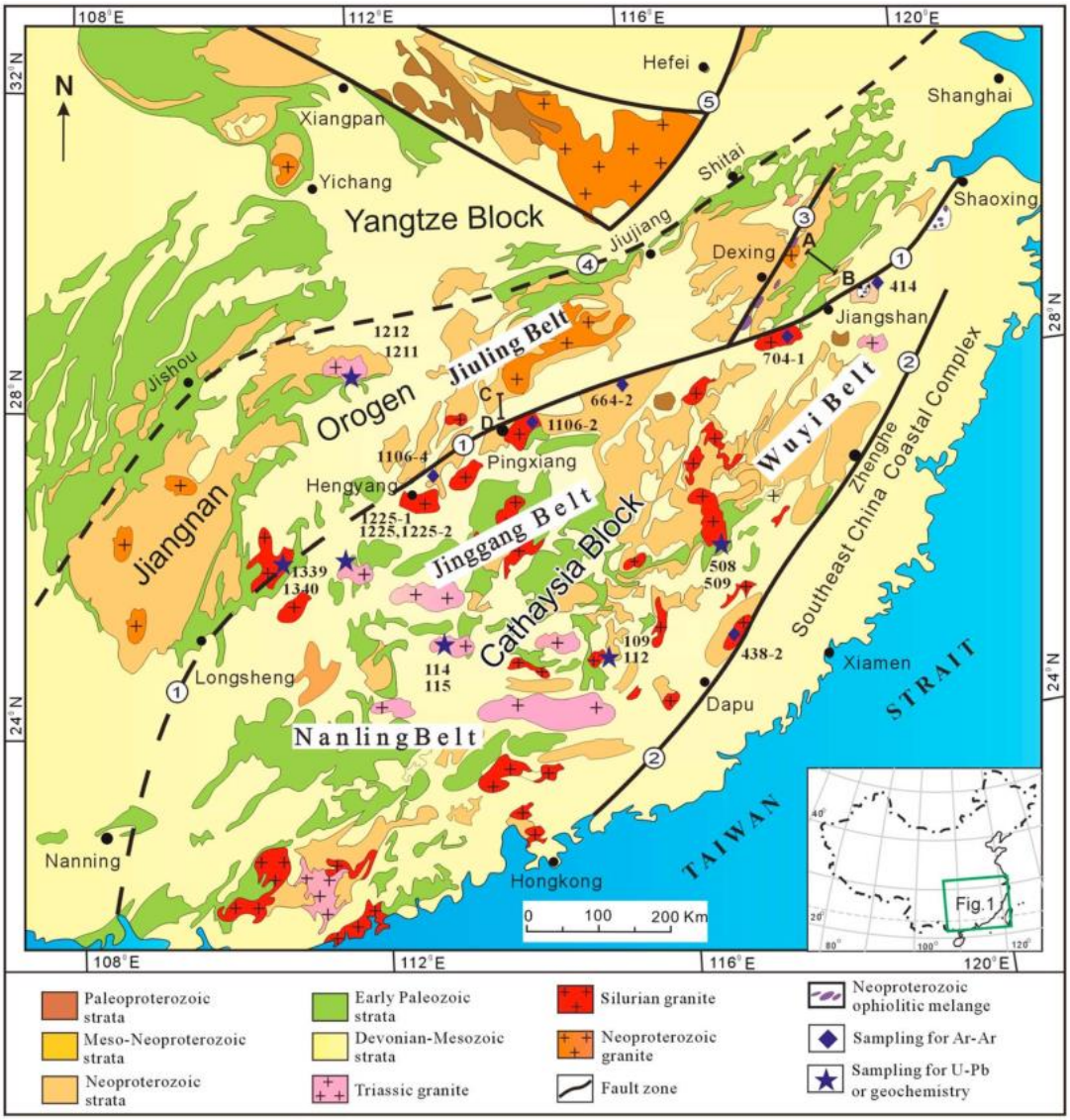

Fig. 2.2 Geological sketch map of the South China. ①: Shaoxing-Pingxiang boundary fault zone between Yangtze and Cathaysia Blocks; ②: Zhenghe-Dapu boundary fault zone between the Cathaysia basement and the SE-China Coastal Complex; ③: Northeast Jiangxi Neoproterozoic ophiolitic zone; ④: Jiujiang-Shitai buried fault zone of the northern boundary of the Jiangnan Belt; and ⑤: Tanlu sinistral strike-slip fault zone (cited from Shu et al., 2015).

2.2.2 Paleozoic magmatism series

The distribution of Paleozoic granitoids (mainly between 360 Ma and 540 Ma) in the South China Block has an outcrop area around 22000 km^2 (Sun, 2006). Those early Paleozoic granites are distributed near the boundary of the Hunan, Jiangxi, Guangxi

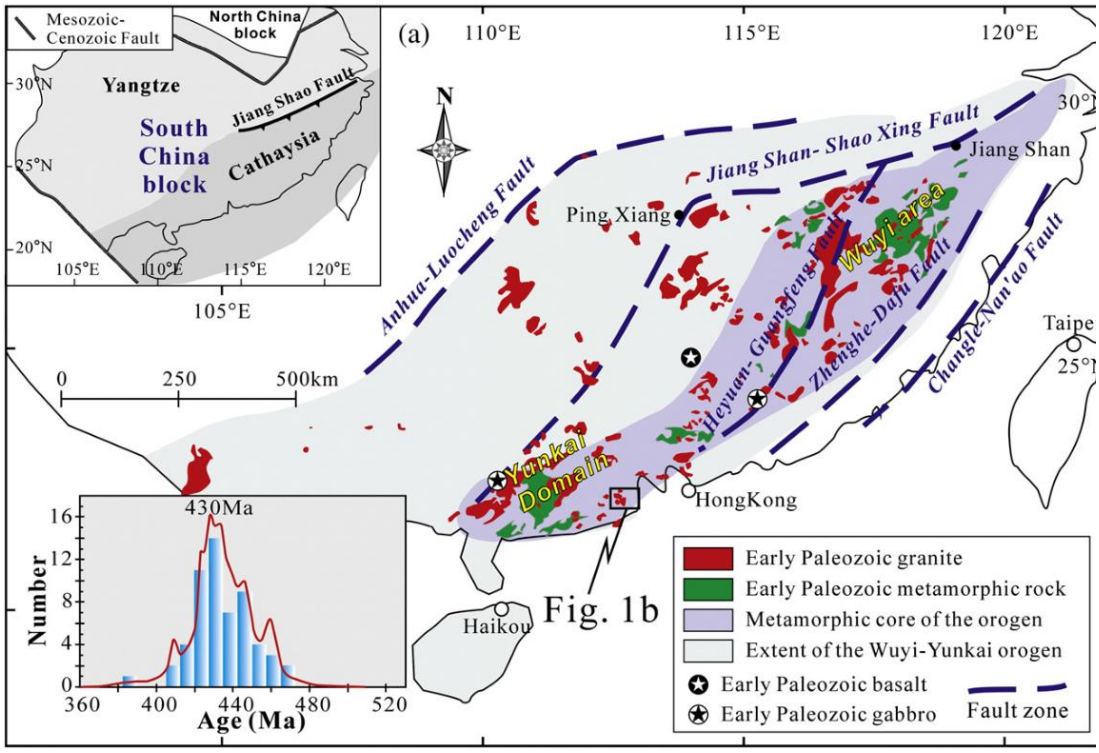

Fig. 2.3 Distribution of early Paleozoic granitoid rocks of the eastern South China Block. (Cited from Huang et al., 2013)

and Guangdong provinces, being dominantly concentrated in the Yunkai and Wuyi areas. Representative plutons with age peaks between 400 Ma and 460 Ma are Miaoershan-Yuechengling, Ninghua, WeiPu, Guangping, Shidong, Haiyangshan, Penggongmiao–Wanyangshan–Zhuguangshan plutons etc. (Fig. 2.2). Most of them are granite and granodiorite or minor tonalite with gneissic structure. More than half of those granitoids are classified as S-type granite containing sillimanite, cordierite, muscovite, garnet or tourmaline (Wang et al., 2007b), but contemporaneous minor I-type and A-type granite are also present (Feng et al., 2014; Guan et al., 2013; Huang et al., 2013; Cai et al., 2016). This sugggests that early Paleozoic granitoids are related to an intracontinental orogenesis (Charvet et al., 1996; Shu et al., 2006; Chen et al., 2010; Li et al., 2010). Based on geochemistry and Sr-Nd-Hf isotopic results, the proterozoic metapelite and meta-igneous rocks are interpreted as the source of these early Paleozoic S-type granites (Li et al., 2010; Zhang et al., 2011; Peng et al., 2015; Zhong et al., 2016).

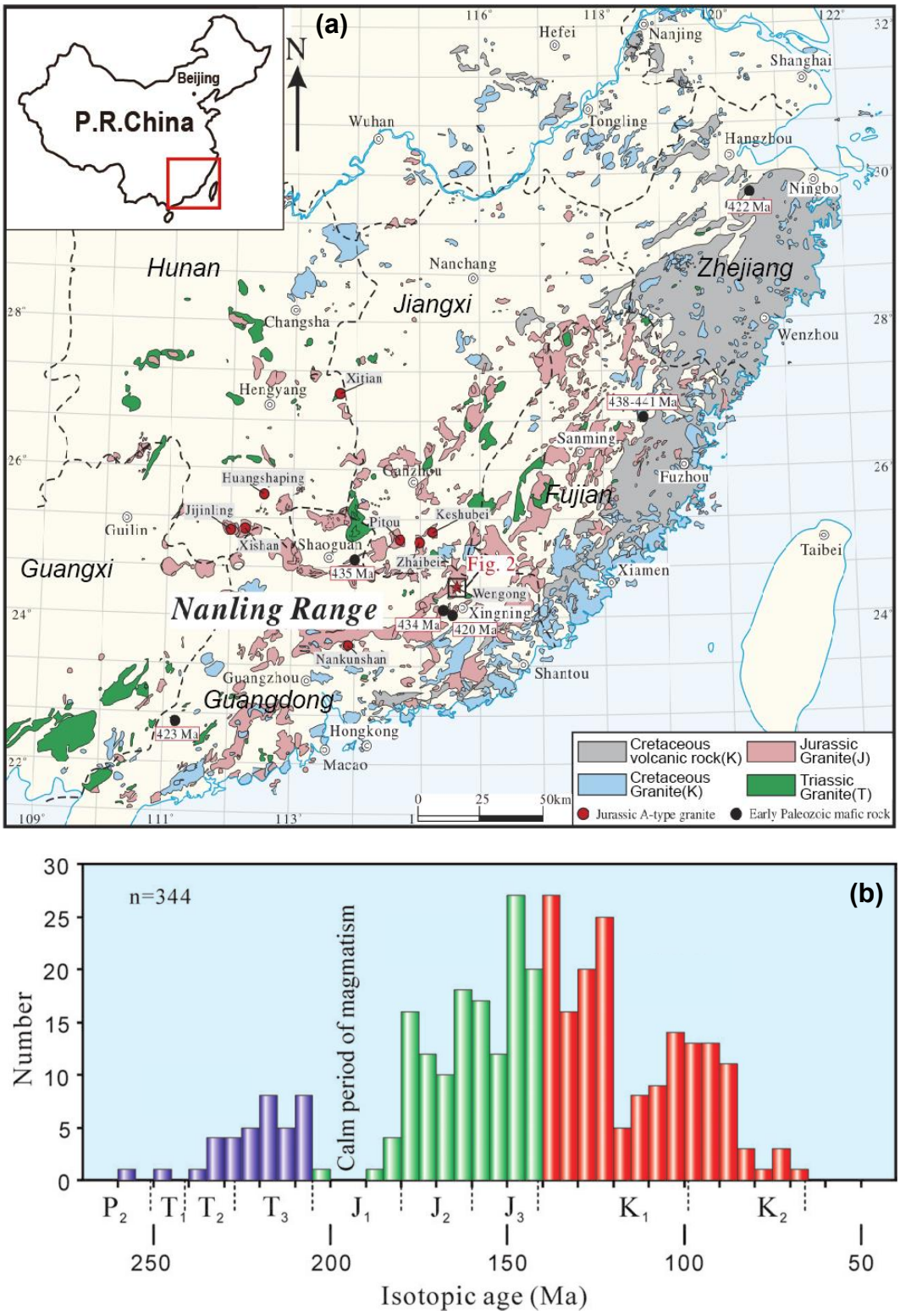

Fig. 2.4 Distribution of major Mesozoic magmatism in South China (a)(cited from Gan et al., 2017).; (b) isotopic age histogram of Mesozoic granites-volcanic rocks in South China (cited from Zhou, 2006).

2.2.3 Mesozoic magmatism

Mesozoic (~66-251 Ma) granitic rocks (sensu lato) make up a large proportion (~60 %) of the exposed crust in south China, with an overall exposure of ~135,000 km^2 (Fig. 2.4. e.g. Zhou et al., 2006).

Triassic (~201-252 Ma) granitoids have ~14300 km^2 outcrop area in South China while the Late Triassic (~205-234 Ma) plutonic rocks representing up to more than 90 vol % proportion (Zhou et al., 2006). The Triassic granitoids are mainly distributed in Hunan, Guangdong, Guangxi, Jiangxi, Fujian and Hainan provinces. Representative plutons include Baimashang, Dayishan, Yuechengling, Miaoershan, Guidong, Darongshan, Longyuanba etc. Those granitoids are biotite-granite, monzonitic granite and granodiorite (Wang et al., 2013 and references therein). Geochemical data show that more than 60 vol % of these granitoids have ACNK values >1.1 hence are defined as peraluminous granites with muscovite, garnet and tourmaline phases (Sun et al., 2003). In contrast, calc-alkalic magmatism is volumetrically minor and only found locally (Sun et al., 2011). Gneissic or mylonitic structures can be observed in the early Triassic granitoids which suggests that the magmas were broadly syn-collisional. The collision between Indochina Block and South China Block occurred between 258 Ma to 243 Ma which is older than the age of dominant Late Triassic plutonic rocks (Carter et al., 2001). Subsequent to the crust thickening, high pressure caused the partial melting of the lower crust via the dehydration melting of hydrous minerals e.g. amphibole and mica in lower crust. In contrast, Sun et al, (2003) suggested that the Triassic magmatism results from decompression melting during late to post collision to extension.

Early Jurassic (~200-180 Ma) granitoids are rarely observed in South China which is considered as a magmatic lull. However, starting from ~180Ma, magmatic events became active. The exposed area of Jurassic (~142-180 Ma) granitoids is as large as

62700 km^2 and comprises ~50% of the exposed Mesozoic intrusions in south China. They are found throughout Guangxi, Guangdong, Hunan, Jiangxi and Fujian provinces and parallel to the coastline (Fig. 2.4). In contrast to Triassic granites, many Jurassic granitoids (cluster at ~155 Ma) are metaluminous with ACNK<1.1, which is more than coeval prealuminous granitoids in south China. They dominant variety is characterised by a biotite±amphibole mineralogy, many A-type and I-type granites being defined. In addition, coeval volcanic rocks (~170-180 Ma) including basalts and rhyolites in bimodal packages, are also found (Chen et al., 2002; He et al., 2010). Those volcanic rocks are spatially associated to plutonic rocks and are commonly explained as being related to a rift mechanism during the Tethyan tectonic phase.

Cretaceous magmatism (67-142 Ma) is famous for the voluminous granitoids and volcanic rocks with an overall outcrop area of ~139920 km^2 (Zhou et al., 2006). They are mainly distributed near the coast (Guangdong, Fujian, Zhejing, Anhui provinces) in south China and the exposed area of volcanic rocks is twice as much as that of coeveal granitoids (Fig. 2.4) (Zhou et al. 2006). Cretaceous granitoids are mostly high-K I-type and A-type granites which were emplaced at 136 -146 Ma, 122-129 Ma, 101-109 Ma and 87-97 Ma, respectively, or four main episodes (Li, 2000). The volcanic rocks were erupted mainly during the time intervals of 124-135 Ma and 88-97 Ma. Most of them are rhyolites, dacites, andesites and basalts (Li, 2000; Chen and Jahn, 1998). The age of Cretaceous granitoids and associated volcanic rocks becomes younger coastward. Combining with the geochemical investigations, the Cretaceous magmatism is explained as the result of the subduction of Paleo-Pacific plate below the South China Block with an episodic slab rollback (Zhou and Li, 2000; Li and Li, 2007).

2.3 Metallogeny associated with Mesozoic magmatism in south China

South China block is not only famous for its huge amount of magmatism but also for its various and large associated ore-deposits which makes it an ideal natural

laboratory for exploring the formation and the evolution of continental lithosphere and related resources. The main mineralizations in South China include W, Sn, Nb, Ta, Ag, Au, Mo, Cu, Pb, Zn and U deposits. Most of them are associated with Jurassic and Cretaceous magmatism (80Ma-180 Ma). (Fig. 2.5; Mao et al., 2004, 2011). Four metallogenic regions have been identified according to their distribution and deposit types (Fig. 2.5; Mao et al., 2013).

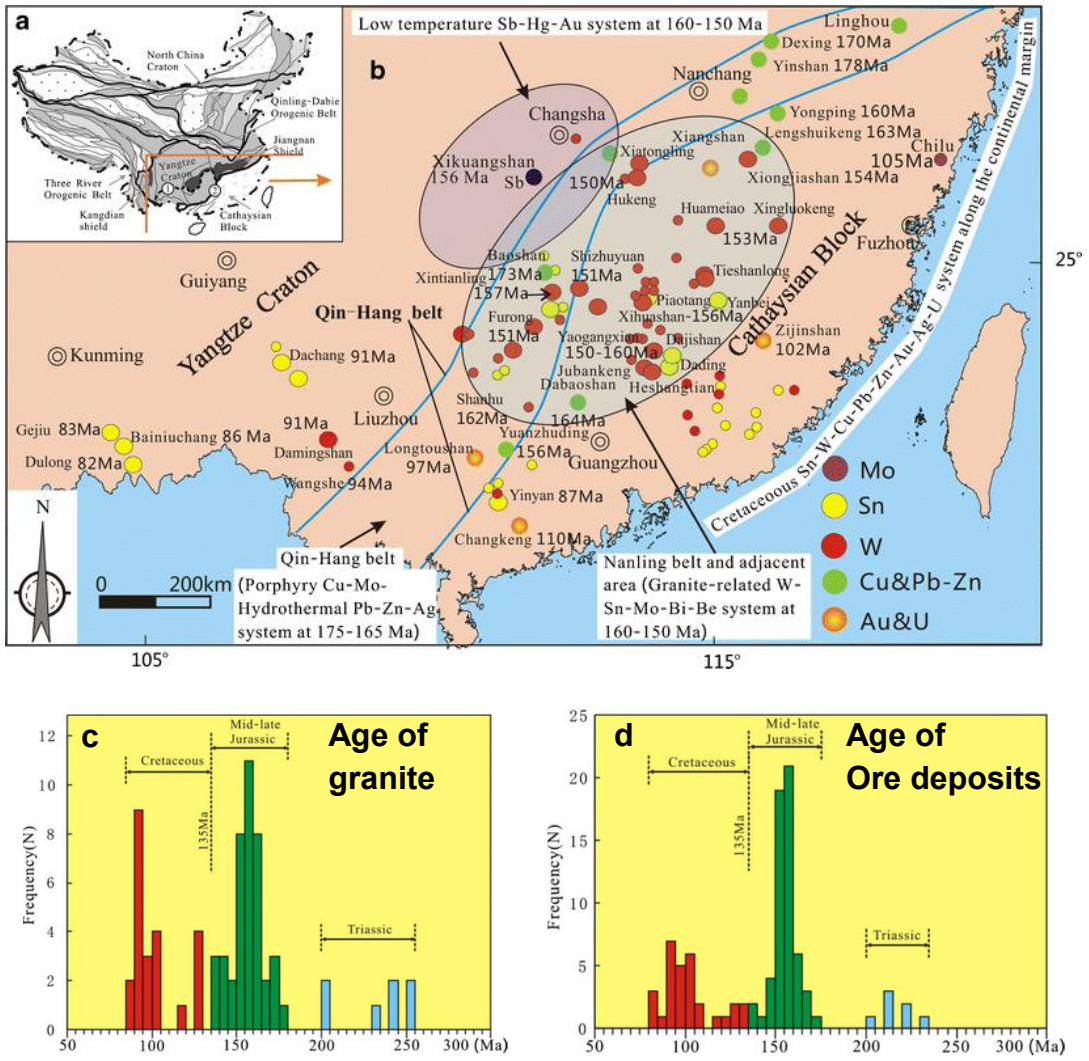

Fig. 2.5 Distribution of major Mesozoic ore deposits in South China (a), (b) and the comparison of age between ganites(c) and related ore deposits(d). (Cited from Mao et al., 2013)

1) Qin-Hang belt (Fig. 2.5a). It is located betweenthe Yangtze and Cathaysia Blocks and the Qinzhou-Hangzhou Neoproterozoic suture. Qin-Hang belt is famous for its Cu-Mo-Pb-Zn-Ag deposits, including porphyry (Cu) and hydrothermal vein-types

(Pb-Zn-Ag). Within this belt, the main mineralization age is between 165 and 175 Ma. Representative ore deposit are: Dexing porphyry (Cu-Au-Mo), Linghou hydrothermal vein (Cu), Shuikoushan hydrothermal (Pb-Zn), Tongshanling porphyry-skarn (Cu) etc (Lu et al., 2005; Tang et al., 2015; Huang et al., 2017).

2) Nanling belt and adjacent area (Fig. 2.5a). This region is on the east side of Qin-Hang belt and overlaps with the middle part of Qin-Hang belt. It hosts large amounts of W-Sn-Nb-Ta-Mo-Bi-Be deposits which are associated with the contemporaneous metaluminous granites: deposits include granite related type, skarn type, quartz ± chlorite vein type and greisen type. Differing from the Qin-Hang belt, the mineralization age of Nanling belt is younger, ranging from 150 to 160 Ma. Representative ore deposits are: Qianlishan-Shizhuyuan (W-Sn-Mo-Bi), Huangshaping (Pb-Zn-Sn-Mo), Qitianling-Furong (Sn) and Xintianling (W), Xianghualing (Sn-Nb-Ta-Be), Yaogangxian (W), Piaotang (W) and Dajishan (W) (Mao et al. 1996; Lu et al. 2003; Zhao et al. 2005; Wang et al., 2007; Yao et al. 2007; Zhang et al., 2007; Bai et al., 2013; Huang et al., 2015; Zhang et al. 20015; Huang et al. 2017).

3) Northwestern Nanling belt (Fig. 2.5a). This metallogenic area is predominantly located in the Southern part of Jiangnan Orogen. The mineralization age is between 130 and 155 Ma, which is younger than the Nanling belt. Mainly, Sb deposits within this region genetically belongs to epithermal (lower temperature hydrothermal fluid) type. Representative ore deposits are: Xikuangshan (Sb), Banxi (Sb), Longshan (Sb) and Woxi (Sb-Au) (Peng et al., 2001; Peng et al., 2004; Pang et al., 2011).

4) Coast marginal belt (Fig. 2.5a). Spatially, this metallogenic belt stretches from the coast of northeast part of Fujian province to the southwest part of Guangxi province. The ore-forming types includes porphyry hydrothermal Cu-Au-Ag deposits, polymetallic Sn deposits and hydrothermal U deposits. Their mineralization ages varied from ~80 Ma to 120 Ma. Representative ore deposits are: Luoboling porphyry (Cu-Mo), Zijinshan (Cu-Au), Xiazhuang (U), Xiangshan (U), Dulong (Sn-Zn) polymetallic, Gejiu

polymetallic (Sn) (So et al., 1998; Deng et al., 2003; Liu et al., 2007; Hu et al., 2009; Zhong et al., 2014).

2.4 Representative Jurassic plutons in Nanling area, South China

Nanling Range area is located in south of South China block covering a geographic area of ~200,000 km^2 (110.0–116.5°E, 23.5–26.5°N, Fig. 2.6). It is popularly known as the constitution of five mountains, i.e. Yuechengling, Doupangling, Mengzhuling, Qitianling, Dayuling, which cross Hunan, Guangxi, Guangdong, Jiangxi and Fujian provinces. The Nanling Range includes various granites and sedimentary basins which have experienced a complex geological evolution. Many of which are Jurassic granites and they are host to various W, Sn, Nb, Ta and U mineralizations. Here we introduce several representative Jurassic plutons in Nanling Range (Fig. 2.6).

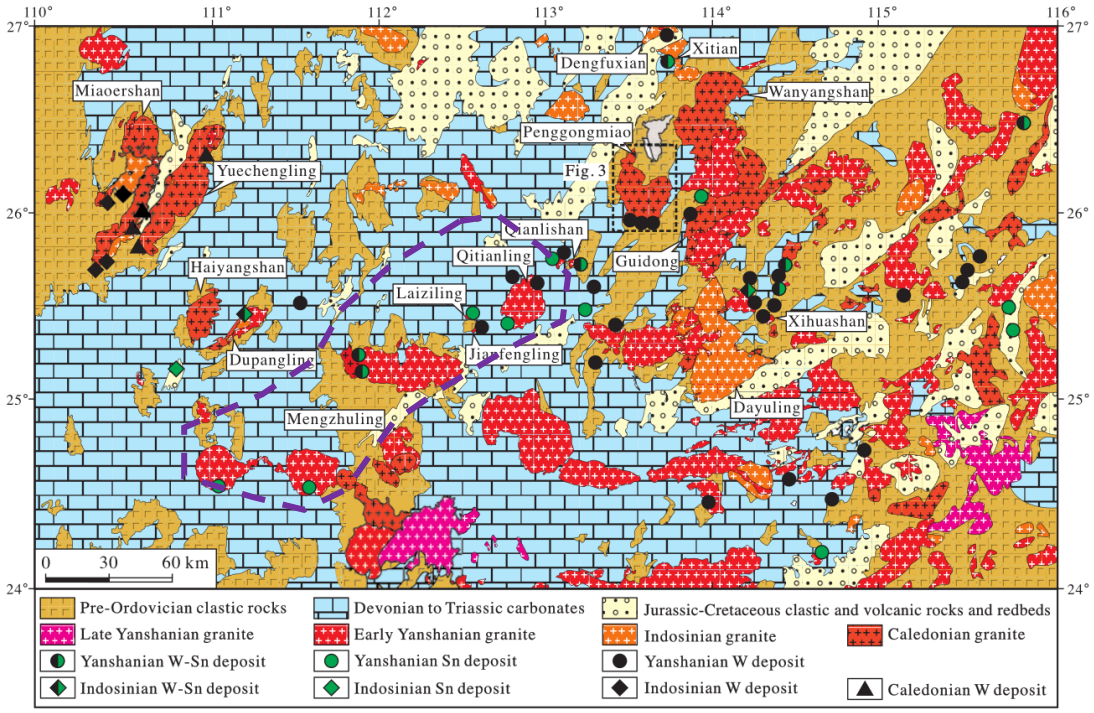

Fig. 2.6 Geologic map of the Nanling Range showing the distribution of granites and associated tungsten/tin deposits (cited from Yuan et al., 2018). Note: Late Yanshanian (140-66 Ma)≈Cretaceous; Early Yanshanian (180-142 Ma)≈Jurassic; Indosinian (251-205 Ma)≈ Triassic ; Caledonian (600-405 Ma)≈ Cambrian-Ordovician-Silurian-early Devoniain (Zhou et al., 2006).

2.4.1 Qitianling pluton

The Jurassic (~147-162 Ma) Qitianling granite, South Hunan province in China, is representative of metaluminous (amphibole-bearing) Mesozoic A-type granites outcropping in the central part of the Nanling Range in SE China (Fig. 1a, b; Zhu et al., 2009). The Qitianling pluton crops out over ~520 km^2, being intruded within Carboniferous to Triassic carbonates and sandstones, lying close to the NNE–SSW-

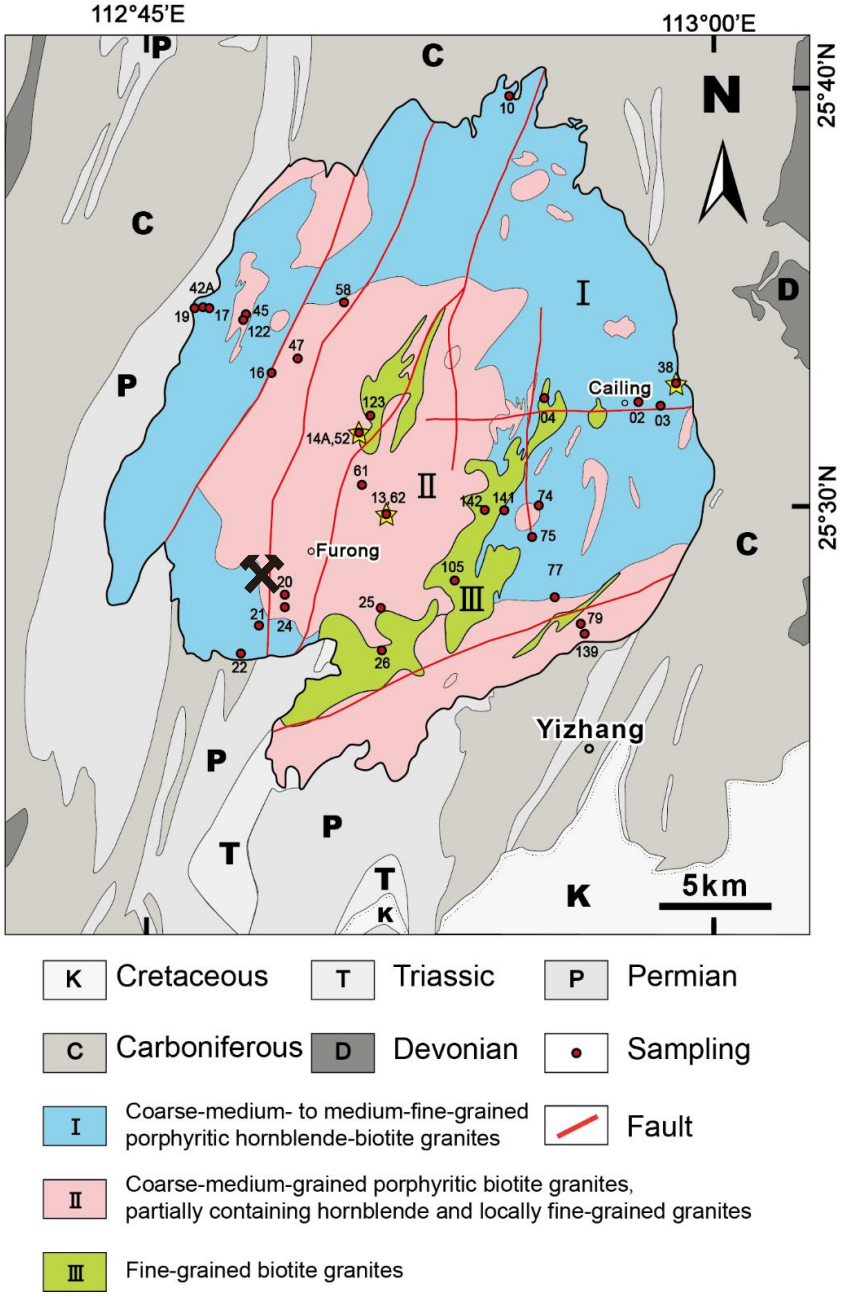

Fig. 2.7 Geologic map of Qitianling pluton. ⚒ represent the Sn(-W) ore deposit district.

trending Chenzhou–Linwu crustal fault (Fig. 2.1; Wang et al., 2003). Exposed contacts between the Qitianling granite and its country rocks are sharp with narrow metamorphic aureoles (typically <30 metres wide), whose lithology varies from biotite-muscovite hornfels (in the east), to garnet-bearing skarns (in the northeast), to marbles (in the southwest).

Three main rock types (phases) have been distinguished for the Qitianling pluton (Zhu et al., 2009): (1) a discontinuous outer boarder of porphyritic, medium- to coarse-grained amphibole-biotite-rich monzonitic granite (phase-1, ~45% of the exposure) where the mafic black enclaves were also often observed; (2) a medium-grained biotite±amphibole-bearing granite (phase-2), which mostly forms the central part and the southern margin of the pluton (~40% of the exposure); and (3) a fine-grained, biotite-bearing granite (phase-3), which is locally exposed in the central and southern parts of the pluton (~15% of the exposure) (Fig. 2.7).

The granite hosts the world-class Furong Sn deposit with the estimation of Tin reserve up to 600,000 tons (Huang et al., 2001; Li et al., 2007a) and is therefore of particular interest in assessing the influence of the granite-ores magmatism on the mineralization relationships. The Furong Sn deposit district is located in the southwest of Qitianling pluton and the ore body occurs as veins and lenses along NE-SW-trending fault zone and crush zone in the phase-2 granite. Three main tin-belts were discovered in the district from west to east: 1) Bailashui–Anyuan tin belt; 2) Heishanli–Maziping tin belt; 3) Shanmenkou–Goutouling tin belt (Huang et al., 2001; Mao et al., 2004). The main metallogenic types in Furong Sn deposits are skarn-type (representative No.19 and No.52 ore veins), greisen-type (representative No.3 and No.54 ore veins) and chloritization alteration granite-type (representative No.10 ore vien). Among approximately 50 orebodies within the Furong district, No.19 vein is the largest one with Sn reserve up to ~270,000 tons and it has thus attracted many economy geologists. Recently, Yuan et al. (2011) used in-situ LA–MC–ICP–MS and ID-TIMS U–Pb dating

on cassiterite from No.19 vein and acquired tin mineralization ages at 159.9±1.9 Ma and 158.2±0.4 Ma, respectively. These mineralization ages are very close to the granite

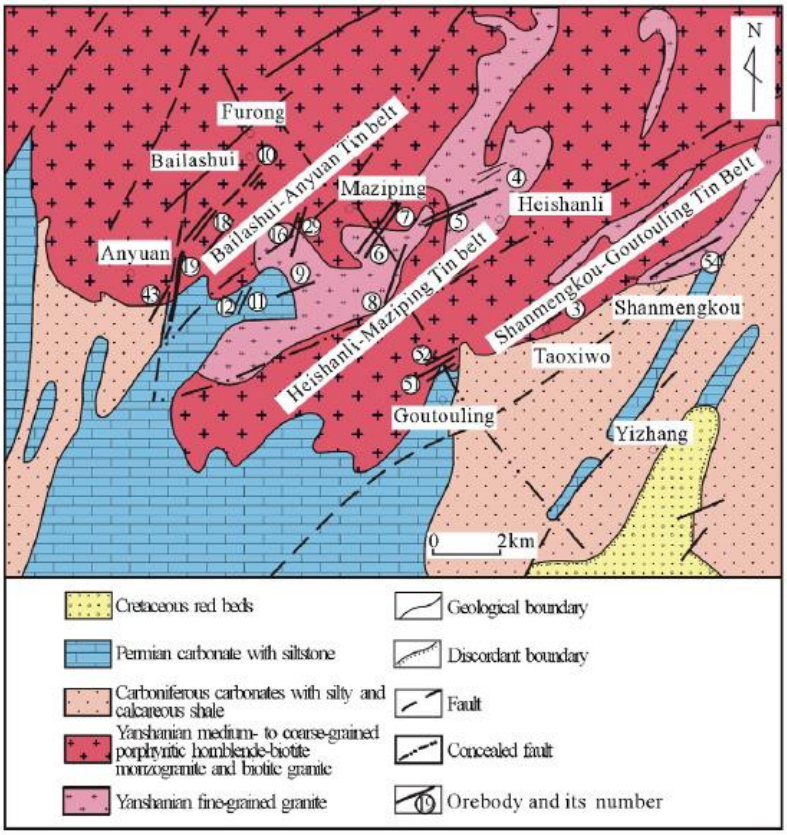

Fig. 2.8 Geological map of the Furong tin deposit and distribution of orebodies (cited from Yuan et al., 2011).

age which demonstrates the close relationship between the magmatism and the tin mineralization (Fig. 2.8).

2.4.2 Jiuyishan pluton

Jiuyishan pluton is located near the boundary of Hunan and Guangdong provinces, southwest of Qitianling pluton (Fig. 2.9). The total outcrop area of Jiuyishan pluton complex is ~1,200 km^2 and it is composed of Xuehuading pluton, Jinjiling pluton (including Pangxiemu pluton), Shaziling pluton and Xishang volcanic-intrusive complex. The plutons intruded into the country rocks include Sinian silicalite sandstone and slate, Cambrian sandstone and shale, Devonian sandstone and carbonatite with

local thermal metamorphism (Fig. 2.9; Fu, 2004).

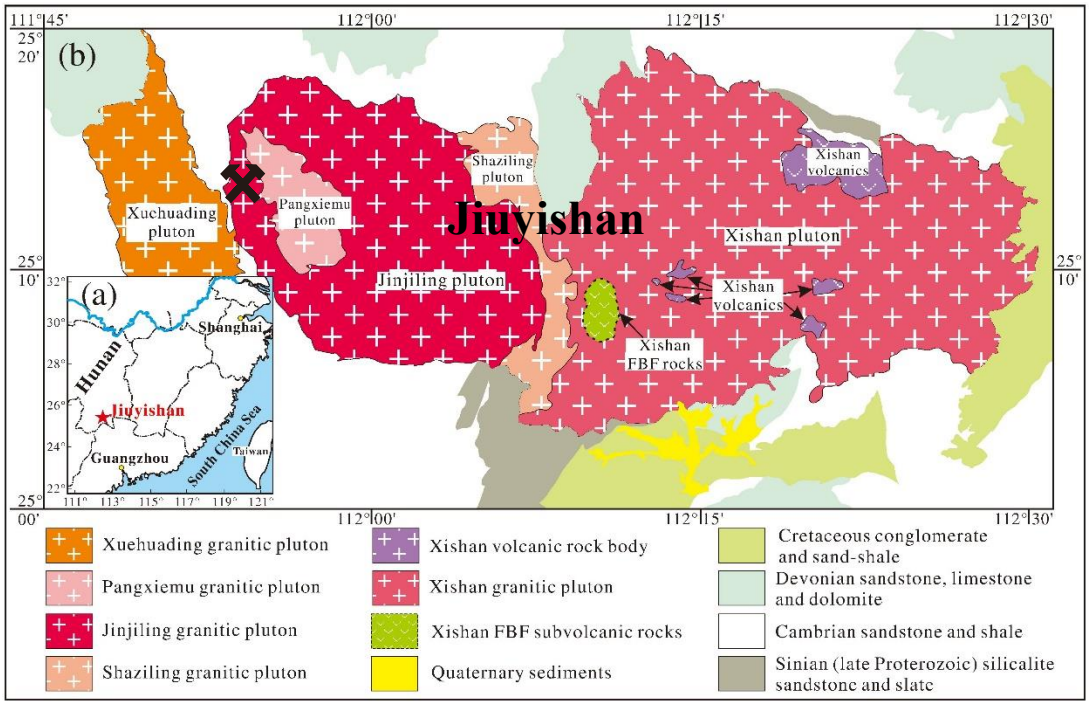

Fig. 2.9 Geological map of the Jiuyishan pluton. ⚒ represent the Sn(-W) ore deposit district. (cited from Guo et al., 2016)

From west to east of Jiuyishan pluton complex is made of: 1) the Xuehuading pluton. It has an outcrop area of 130 km^2 with a dominant medium- to fine-grained amphibole-biotite-rich monzonitic granite. SHRIMP Zircon U-Pb dating has given an age of 432±21 Ma; 2) the Jinjiling pluton (390 km^2) is mainly a medium- to coarse-grained biotite monzonitic granite with a Zircon U-Pb age of 156 ±2 Ma. Pangxiemu pluton is intruded within the Jinjiling pluton and consists of medium- to fine-grained two-micas or biotite monzonitic granite. Da'ao W-Sn deposit district is located in the western part of the Jinjiling pluton and near the Panxiemu pluton which contains greisen-type and quartz vein -type Sn deposit; 3) the Shaziling pluton (65 km^2) has a SHRIMP Zircon U-Pb age of 157 ± 1 Ma. The lithologies are medium- grained amphibole-biotite monzonitic granite and minor granodiorite; 4) the Xishang volcanic-intrusive complex (705 km^2) consists mainly of porphyritic fine-grained biotite monzonitic granite, microfine-grained porphyritic subvocanic rocks and porphyritic

dacite or rhyolite. It is worth noting that fayalite and ferrosilite were observed in those subvolcanic rocks. Zircon U-Pb dating gives an age for the Xishang volcanic-intrusive complex of 156 ±2 Ma (Fu et al., 2004; Huang et al., 2011).

2.4.3 Huashan pluton and Guposhan pluton

The Huashan and Guposhan plutons are about 50km southweast of the Jiuyishan pluton (lat. 24º30' to 24º46' N; long. 110º56' to 111º47' E; Fig. 2.10; Wang et al., 2013). They intrude into the Devonian limestones and sandy shales, Carboniferous limestones and Cambrian-Ordovician low-grade metamorphic rocks, all with sharp intrusive contacts. In the contact zone, marble or hornfels can be observed locally. Huashan pluton is on the west of Guposhan pluton. Its exposed area is approximately 500 km^2. The dominant lithologies are medium- to coarse-grained amphibole-biotite monzonitic granite and medium- to coarse-grained biotite granite which constitute the major phases of the batholith. Minor fine-grained granite occurs in the central part. Tong'an quartz monzonite and Niumiao diorite are in the west and southeast part of the main pluton body, respectively. The U-Pb zircon ages of the coarse-grained biotite granite, diorite and monzonite are 162±1, 163±4 and 160±4 Ma, respectively (Zhu et al. 2006). Accessory minerals of Huashan granite are zircon, apatite, magnetite, ilmenite and titanite. The tin mineralization types associated with the biotite granite and fine-grained granite near the central part are placers, greisens, and quartz veins (Wang et al.,2012).

Guposhan pluton occurs east of Huashan pluton with an approximately 700 km^2 exposed area. Four principle lithology associations are identified: 1) Medium- to coarse-grained amphibole-biotite monzonitic Lisong granite unit (phase-1), is located in the center part of the pluton with locally some mafic enclaves exposed. The Lisong granite is surrounded by the 2) medium- to coarse-grained biotite granite (phase-2) while in its outer parts are 3) medium- to fine-grained biotite granite (phase-3) and 4) fine-grained granite (phase-4). U–Pb zircon ages of those three types of rocks are 162±3

Ma, 163±4 Ma, Ma,151±6 Ma, respectively (Zhu et al., 2006). The tin deposits type in Guposhan pluton are mainly located near the boundary between the country rocks and granite with the ore districts: Xinlu (in the south), Lantoushan (in the southwest) and Keda (in the west) Sn deposits.

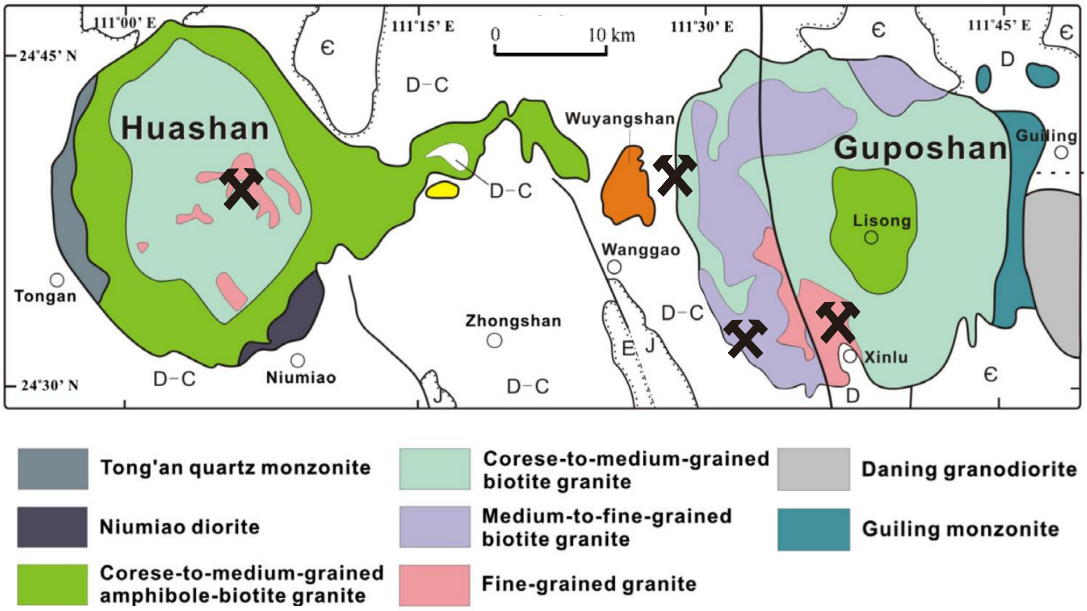

Fig. 2.10 Geologic map of Huashan and Guposhan pluton. ⚒ represent the Sn(-W) ore deposit district (cited from Wang et al., 2013).

Chapter 3 Experimental procedure and analytical method

3.1 Material pretreatment

About 130 fresh rock samples were chosen for our study. All samples were first cleaned by water and crushed into small fragments by hammer. Those rock fragments (around 5cm×3cm×3cm) were selected for preparing the thin sections and other rock fragments were collected for preparing the bulk rock powder and minerals separation. Small fragments of rock samples were further ground until to around 3~5mm and cleaned by water or ethanol again. Those rock fragments were separated into two parts. One is for whole rock chemistry studies and the other part is for amphibole, biotite and zircon selection. An agate ball mill was used for grinding the first part of rocks fragments into 200 mesh grain size for whole rock chemistry analysis. While the second part of rocks fragments were grinded into 60 mesh. Amphibole and biotite were extracted using gravity separation and firstly handpicked under a binocular stereomicroscope. All selected amphibole and biotite grains were washed in an ultrasonic bath and then cleaned by deionized water for several times. The residual materials were collected for magnetic and gravity separation. After then zircon was separated by handpick under the binocular stereomicroscope. Zircon grains were mounted in the epoxy disk and polished for further analysis.

3.2 Whole rock chemistry studies

3.2.1 Major elements

Whole-rock major-element compositions of the samples were measured using wet-chemical analysis at the Analysis Center of the No. 230 Research Institute of the China National Nuclear Corporation (CNNC), Changsha, China. The following procedures

were employed for determining various oxide contents: polyethylene oxide gravimetric methods for SiO_2; ethylene diamine tetra-acetic acid titration for Al_2O_3; the potassium dichromate volumetric method for Fe_2O_3; ethylene glycol tetra-acetic acid complexometric titration for CaO and MgO; hydrogen peroxide solution spectrophotometry for TiO_2; phosphomolybdenum blue spectrophotometry for P_2O_5; flame atomic absorption spectrophotometry for MnO_2; flame photometry for K_2O and Na_2O; and the potassium dichromate volumetric method for FeO. The ion selective electrode technique was used for determining F. The procedures are described in the Chinese National standard protocol GB/T 14506 (3-14) -2010. All errors are less than 5%.

3.2.2 Trace elements

The analyses of trace and rare-earth elements were conducted with a Thermo X7 ICP-MS at the State Key Laboratory of Ore Deposit Geochemistry, Institute of Geochemistry, Chinese Academy of Science, Guiyang, China. For detailed information on the methods, see Qi et al. (2000). Standards include OU-6, AMH-1 and GBPG-1. Precisions for most elements were typically better than 10 % RSD (relative standard deviation).

3.3 Mineral chemistry studies

3.3.1 Scanning electron microscope (BSE)

Imaging backscattered electron (BSE) images and phase characterization were performed using two scanning electron microscopes: a Zeiss SUPRA 55 Field Emission scanning electron microscope (FE-SEM) at the State Key Laboratory for Mineral Deposits Research of Nanjing University, China, and a Zeiss Merlin Compact scanning electron microscope at the ISTO (Institute des Sciences de la Terre d'Orléans), France.

Working distance were 8.7mm and 10 mm, respectively, with an acceleration voltage at 15kv.

3.3.2 Electron microprobe (EMP)

Quantitative analyses of the minerals and glasses were obtained by two electron microprobes. The analyses were carried out on polished thin sections and epoxy resin disk using a JEOL JXA-8100M electron microprobe (EMP) at the State Key Laboratory for Mineral Deposits Research of Nanjing University, China and a CAMECA SX-Five electron microprobe (EMP) at the Institute des Sciences de la Terre d'Orléans, France. The analyses of the natural mineral assemblages and all experimental run products were performed at a 15 kV accelerating voltage, at either 20 nA (China) or 6 nA (France) beam currents, and at a nominal beam diameter of 1 μm for minerals and a 10 μm beam diameter for glasses. Natural minerals (albite, andradite, fayalite, orthoclase, apatite, hornblende, topaz, scheelite and vanadite), synthetic metals (Nb, Ta and Sc metals) and compounds (UO_2, SnO_2, $MnTiO_3$, MgO, Fe_2O_3 and Al_2O_3) were used as standards. For silicates and glasses, peak counting times were 10 s for all major elements except Sn and W (30 s). As for oxides, peak counting times were 10 s for Sn, 30 s for Ta and Nb, and 20 s for all other major elements. Repeat analyses were performed on selected run products and natural minerals to ensure that the microprobe analyses on the two instruments yielded equivalent results within accepted uncertainties of the method.

For our experimental run products, four hydrous rhyolite glass standards (Scaillet and Evans 1999) were also analysed in each session to correct for alkali migration under the electron beam and to calculate the glass H_2O content of the unknowns (using the corrected by-difference method, following Scaillet and Evans 1999). In addition to the glass (melt) H_2O contents calculated on the basis of the EMP analyses, nominal melt H_2O contents were also calculated using VolatileCalc (Newman and Lowenstern 2002), using a rhyolite composition, and the XH_2O values of the individual charges. Melt H_2O

contents calculated with both methods generally agree within ±1 wt % (see detail in Chapter 5), but values calculated on the basis of EMP analyses are scattered owing to analytical errors (in particular in crystal-rich charges). For consistency, we therefore refer to the values calculated using VolatileCalc in text and figures.

The results of our experimental run products showed that most crystals were large enough for analysis, but crystals in some low-temperature, low-H_2O charges were too small for uncontaminated EMP analyses (e.g. biotite and oxides). Possible contamination of mineral analyses by matrix glass and/or neighbouring minerals was evaluated on the basis of analytical totals (sum of wt % oxides) and on the basis of the calculated stochiometry. For some charges no uncontaminated compositions could be determined, despite considerable effort (e.g. charges 01, 02, and 03). Phase proportions were calculated by mass balance, whenever possible, and they are summarized in Chapter 5. We note that for most of the run products, the residuals of the mass balance calculations ($\sum r^2$) are low (<0.1). For these charges, we estimate that the calculated phase abundances have uncertainties of ±3 wt%. In cases with higher residuals, which reflect some analytical problems, we consider uncertainties of ±5-10 wt %.

3.3.3 Zircon and amphibole trace elememt and Zircon U-Pb geochronology

Mounted zircon grains were firstly photographed under the microscope for the transmission light and reflected light images to acquire the inclusion information. After that, zircon grains were imaged using cathodoluminescence (CL) under Zeiss SUPRA 55 Field Emission scanning electron microscope (FE-SEM) to determine their internal crystallization structures.

Zircon U-Pb dating and trace elements were analyzed using an Agilent 7500a ICP–MS instrument equipped with a New Wave UP-213nm laser-ablation system at the State Key Laboratory for Mineral Deposits Research of Nanjing University, China. Zircon standard GEMOC GJ-1(608.5±1.5Ma Jackson et al. 2004), Mud Tank (732±5 Ma Black

and Gulson, 1978) and glass standard NIST- SRM 610 (Pearce et a1., 1997) were chosen for the analysis as the external standards and quality control. Element setting included ^{29}Si, ^{31}P, ^{49}Ti, ^{88}Sr, ^{89}Y, ^{90}Zr, ^{93}Nb, ^{137}Ba, ^{139}La, ^{140}Ce, ^{141}Pr, ^{146}Nd, ^{147}Sm, ^{153}Eu, ^{157}Gd, ^{159}Tb, ^{163}Dy, ^{165}Ho, ^{166}Er, ^{169}Tm, ^{172}Yb, ^{175}Lu, ^{178}Hf, ^{181}Ta, ^{206} Pb, ^{207} Pb, ^{208}Pb, ^{232}Th, ^{238}U which ^{29}Si was used as an internal standard for zircon. The analyses were performed using a 5 Hz repetition rate and a 35 μm diameter beam size. Each run included 12 sample analyses following by 2 GJ-1 analyses, 2 NIST- SRM 610 analyses and 1 Mud Tank analyse. Raw data reduction were calculated using GLITTER (ver 4.0) (Griffin et al., 2008). Microsoft Excel program ComPbCorr#3_15G (Andersen, 2002) was used for the common Pb correction at the end.

In situ analyses of amphibole trace elements were accomplished using an Agilent Technologies 7700x ICP-MS instrument equipped with a eledyne Cetac Technologies Analyte Excite laser-ablation system at Nanjing FocuMS Contract Testing Co. Ltd. Element setting included ^{7}Li, ^{9}Be, ^{11}B, ^{23}Na, ^{24}Mg ^{27}Al ^{29}Si, ^{31}P, ^{39}K, ^{42}Ca, ^{45}Sc, ^{47}Ti, ^{51}V, ^{53}Cr, ^{55}Mn, ^{57}Fe,^{59}Co, ^{60}Ni, ^{65}Cu, ^{66}Zn, ^{69}Ga, ^{72}Ge, ^{85}Rb, ^{88}Sr, ^{89}Y, ^{90}Zr, ^{93}Nb, ^{95}Mo, ^{107}Ag, ^{111}Cd, ^{115}In, ^{118}Sn, ^{121}Sb, ^{133}Cs, ^{137}Ba, ^{139}La, ^{140}Ce, ^{141}Pr, ^{146}Nd, ^{147}Sm, ^{153}Eu, ^{157}Gd, ^{159}Tb, ^{163}Dy, ^{165}Ho,^{166}Er, ^{169}Tm, ^{172}Yb, ^{175}Lu, ^{178}Hf, ^{181}Ta, ^{182}W, ^{205}Tl, ^{208}Pb, ^{209}Bi, ^{232}Th, ^{238}U, which ^{29}Si was used as an internal standard for amphibole. The analyses were performed using a 7 Hz repetition rate and a 20-40 μm diameter beam size. Other analytical procedures in details see Gao et al., 2013. Standard glass NIST-SRM 610 and GSE-1G (Pearce et a1., 1997) and USGS-Basalt standard BIR-1G, BHVO-2G, BCR-2G (Gladney et al., 1988) were chosen for the analysis as the external standards and Chinese Geological Standard Glasses CGSG-1 standard were treated as quality control (Hu et al., 2011). Each run included 10 sample analyses following by 1 NIST- SRM 610 analyse. Raw data reduction were performed off-line by ICPMSDataCal software using 100%-normalization strategy without applying internal standard (Liu et al, 2008).

3.3.4 Amphibole and biotite ^{40}Ar-^{39}Ar geochronology

Amphibole and biotite grains were extracted by gently crushing the samples and hand-picking the coarsest fraction produced. They were firstly imaged using a high-resolution (×20 to ×60) binocular microscope to screen out suspect(altered or broken) specimens. All grain sizes were between 0.25-1.00 mm. After weighing using a high-precision (± 0.001 mg) micro-balance, the individual samples were wrapped in aluminium foil and coaxially stacked in an irradiation package about 2.5 cm long along with sanidine standard FCS (28.02 ± 0.28 Ma, Renne et al., 1998) interleaved every 4 to 5 level position. The batch was irradiated for 10 h in CLICIT (Corvallis irradiation center, OSU, USA).

$^{40}Ar/^{39}Ar$ geochronology of amphibole and biotite was conducted by Helix SFT™ Split Flight Tube Noble Gas Mass Spectrometry combining continuous-wave CO_2 (10.6 μm) lasers with very-low background extraction systems at the $^{40}Ar/^{39}Ar$ Lab housed at ISTO, Orléans, France. After about 100 days of post-irradiation cooling, the single grains of amphibole and biotite were loaded into a differentially-pumped sample holder connected to the ultra-high vacuum extraction and purification system and baked out at 200 °C for 48 h. The amphibole and biotite grains were individually step-heated with a nominal step increase of 0.5 % of the total output laser power until total fusion (single-grain analysis). Each measurement included one blank every consecutive sample extraction step. Purification prior to expansion into the MS consisted in 6 min static exposure to a cold trap (-127 °C) and two hot (250 °C) GP-50 St-101 SAES® getters, followed by static MS peak-hopping of the five argon isotopes plus ^{35}Cl (blank: 5 peak-hopping cycles; unknown: 10 cycles). Raw blanks for each isotope were fitted using a 3rd to 4th-order polynomial across the daily session, and each assigned a respective error corresponding to the empirical mean average deviation from the best fit trend. Typical blank values were $5{\cdot}10^{-1}$, $7{\cdot}10^{-3}$, $2{\cdot}10^{-3}$, $2{\cdot}10^{-2}$, $7{\cdot}10^{-3}$ fA at m/e = 40, 39, 38, 37, 36, respectively. Corrections applied include (1) static blanks, (2) mass-bias and isobaric

interferences, (3) post-irradiation ^{39}Ar, ^{37}Ar, and ^{36}Cl decay, (4) neutron-flux gradient and monitoring, and (5) K, Ca, and Cl isotopic interferences following Scaillet (2000). Ages were calculated using isotopic constants listed in McDougall and Harrison (1999). TGA refers to total-gas ages calculated by summing all volumes of gaz (i.e., Ar beam intensity) extracted for each isotope till fusion with an error derived by quadratic error propagation of all individual error terms involved in the age calculation. This corresponds to a formal K-Ar age. WMA are weighted-mean ages calculated by pooling and inverse-variance weighing the $^{40}Ar^*/^{39}Ar$ ratios included in the mean, with a final error corresponding to the maximum-likelihood estimate (MLE) of the error of the mean ($^{40}Ar^*$ = radiogenic ^{40}Ar). WMA errors basically differ from TGA errors by the effect of the $1/\sqrt{N}$ error-reduction rule typical of pooled MLE. PA are plateau ages calculated as the WMA, but for which the empirical MSWD score (MSWD = Mean Square Weighted Deviation) fall in the fiducial interval for the corresponding degrees of freedom according to CHI-2 statistics.

3.4 Experimental petrology: Phase equilibrium experiments

3.4.1 Starting materials preparation

Three representative samples of the two main Qitianling rock types (one phase-1 and two phase-2 samples), were chosen as raw starting materials. To prepare the dry glass starting materials, powders of the bulk rocks were individually melted twice for three hours in air at atmospheric pressure (with grinding in between) in a Pt crucible at 1400°C and then quenched in water (Fig. 3.1a). The resulting dry glasses were ground to <20 μm, which we used as the experimental starting material (Fig. 3.1b). Analyses of several glass chips by electron microprobe (EMP) showed them to be homogeneous, with compositions similar to whole rock analyses indicating that elemental loss during fusion was negligible (see Chapter 5, Appendix table 8).

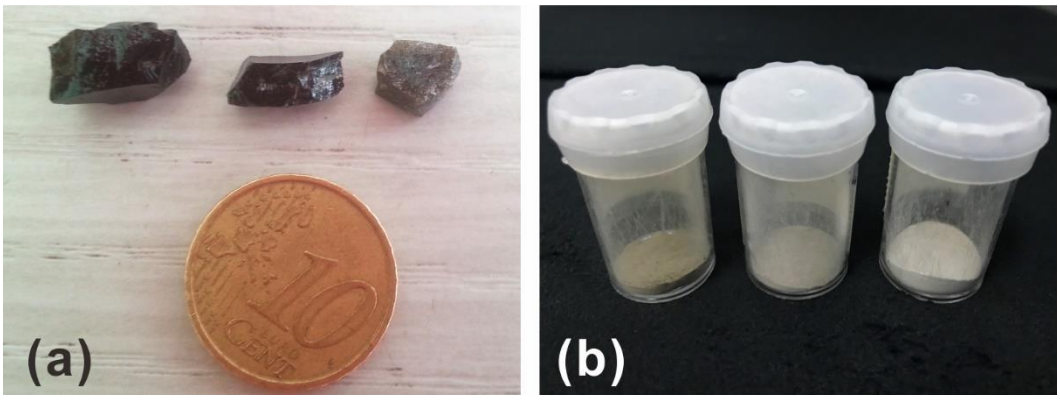

Fig. 3.1 (a) Experimental starting material: dry glasses; (b) the powder of dry glass

3.4.2 Capsules preparation

To prepare the experimental charges, deionized water was first loaded into Au capsules (2.5/2.9 mm inner/outer diameter, ~1.5 cm long). To vary XH_2O [mol% $H_2O/(H_2O+CO_2)$], silver oxalate ($Ag_2C_2O_4$) was then added in various amounts (keeping H_2O+CO_2 at ~3 mg), followed by loading of ~30 mg of the dry starting glass powders for crystallization experiments or the bulk rock powder for melting experiments (Fig. 3.2). All the Au capsules were then welded shut and checked for leaks by weighing. The capsules were put into an oven at 120 °C for several (>2) hours to ensure homogeneous fluid distribution and they were then weighed again to check for capsule integrity.

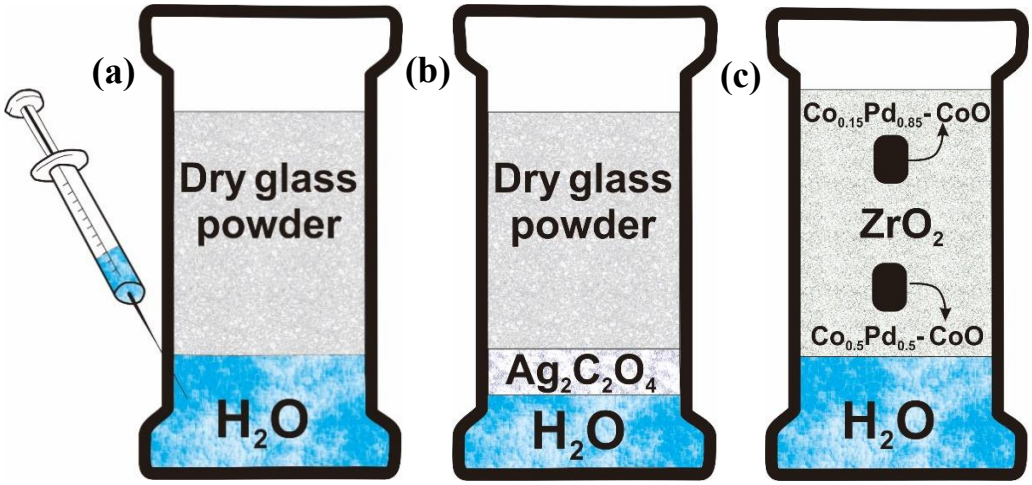

Fig. 3.2 (a) Water saturated capsule with only H_2O as valotile; (b) water under saturated capsule with H_2O and CO_2 as valotiles;(c) the sensor.

According to Boldyrev (2002), silver oxalate can decompose at around 140°C and yield metallic silver and carbon dioxide:

$$Ag_2C_2O_4\ (s) = 2Ag\ (s) + 2CO_2\ (g)$$

To monitor fO_2 during the experiments, solid Co-Pd-O and Ni-Pd-O sensors were prepared following the technique of Taylor et al. (1992) and Pownceby and O'Neill (1994), except for our most oxidized series of experiments, which were buffered at the intrinsic fH_2 of the pressure vessel (i.e. at ~NNO+3; cf. Dall'Agnol et al. 1999). Similar capsules parepation as before, pure water (~45mg) was firstly loaded into the gold capsule. Then ZrO_2 powder was using for separating two alloy-oxide mixture of pellets with the gold capsule in order to avoid the reaction between the pellets and the gold capsule. Take the solid Co-Pd-O sensor as an example: two pellets consist of different proportion of alloy and oxide mixtures of $Co_{0.5}$-$Pd_{0.5}$-CoO and $Co_{0.15}$-$Pd_{0.85}$-CoO (Fig. 3.2c). During the experiments, the two different compositions of the CoPd [XCo=Co/(Co+Pd) in mole)] alloy at certain redox state condition will reach to a similar composition. The calibration expression of the solid Co-Pd-O is:

$$\log fO_{2(Co,Pd)} = -2\log X_{Co} - 1/(2.3025RT) <(491649 - 508.527T + 122.6909T - 0.0251872T^2) + \{2(1- X_{Co})^2 - [9.76T + 16445(4X_{Co} - 1)]\}> \quad (1)$$

Where the X_{Co} value can be mearsured by microprobe, which help to calculate the fO_2 of the sensor.

In the closed experimental system, the hydrogen fugacity of all the charges of samples and sensor at one run are equal. Therefore, we have:

$$fH_2^{(sample)} = fH_2^{(sensor)} \quad (2)$$

The determination of $fH_2^{(sensor)}$ was according to the following equations:

$$H_2 + 1/2O_2 \rightleftharpoons H_2O \quad (3)$$

$$Kw = \frac{fH_2O}{fH_2 * (fO_2)^{1/2}} \quad (4)$$

$$\log fH_2 = \log fH_2O - \log Kw - 1/2 \log fO_2 \quad (5)$$

The Kw is the equilibrium constant of pure water which also is the function of the temperature. The fH_2O of pure water were acquired from the tables of the experiments of Burnham et al. (1969). Since the hydrogen fugacity of the sensor can be acquired from equation (3), (4) and (5), according to the same equations, we can calculate the oxygen fugacity of each charge of our samples.

3.4.3 Internally heated pressure vessel

All 19 experiments were performed in internally heated pressure vessels (IHPV) using a Kanthal furnace. Up to 23 capsules, including the sensor, were loaded at once. Experiments at reducing conditions (~NNO-1.3) were pressurized by a mixture of Ar-H_2 gas (Scaillet et al., 1992). Oxidizing runs were performed using pure Ar gas as the pressure medium. Temperature was then increased and final pressure reached. Temperature was monitored with two S-type thermocouples bracketing the sample holder, with an error of ±5°C; pressure was monitored with a transducer calibrated against a Heise Bourdon gauge, with an overall uncertainty of ±0.2 MPa. All experiments were terminated by switching off the power supply, which decreased temperature to <100 °C within ≤5 minutes. After the experiments, all capsules were checked for weight changes. Fragments of the run products recovered from each charge were embedded in epoxy and polished for backscattered electron imaging and electron microprobe analysis.

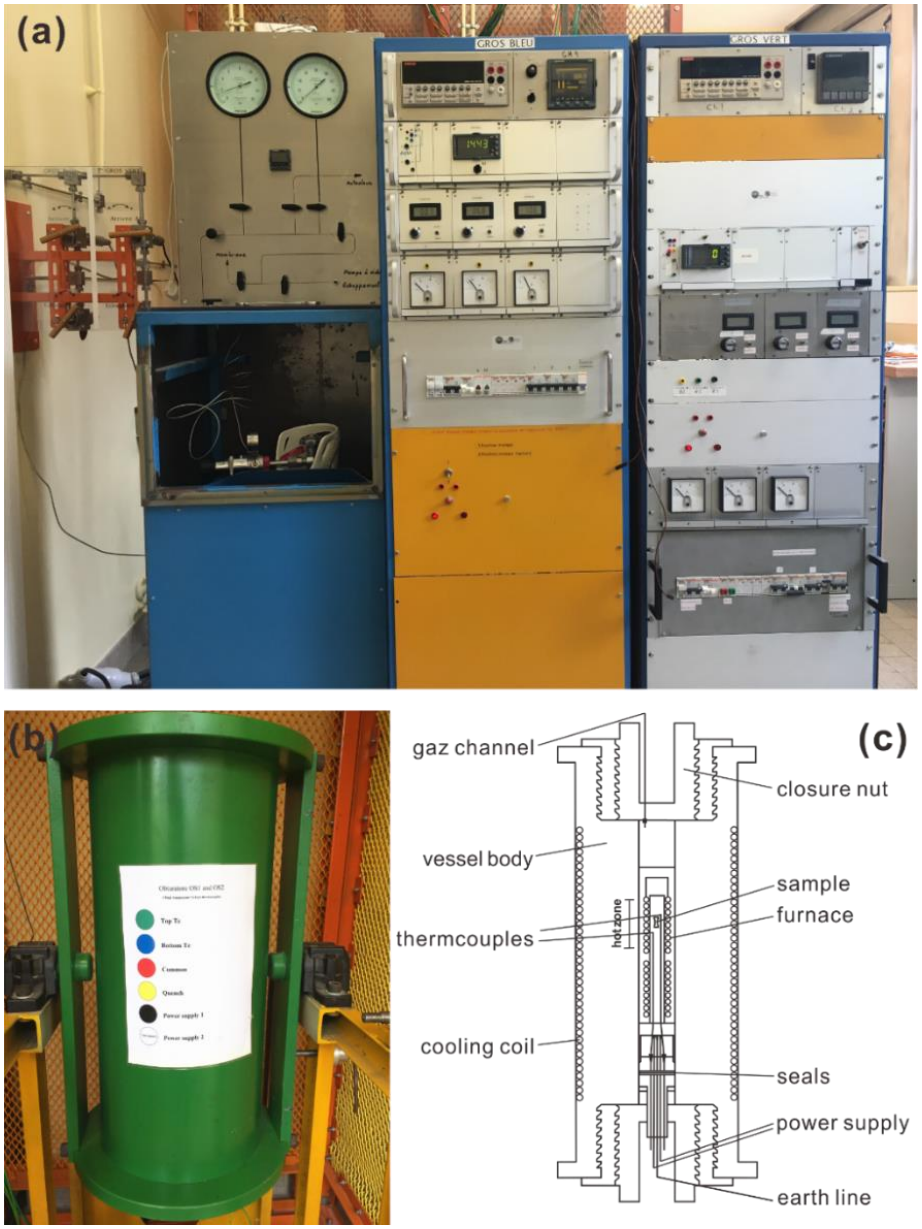

Fig. 3.3 (a) Internally heated pressure vessel monitors; (b) Internally heated pressure vessel (Gros vert); (c) Schematic cross section of the IHPV modified after Berndt et al., 2002.

Chapter 4 Petrology, geochemistry and geochronology of Jurassic Qitianling granite

4.1 Petrography and mineralogy

Three main rock-types have been distinguished in Qitianling pluton.

(1) A porphyritic, medium- to coarse-grained amphibole-biotite-rich monzonitic granite (phase-1) (Fig. 4.1a). It contains plagioclase (~30%), K-feldspar (~30%), quartz (~25%), amphibole (~5%), biotite (~8%), and accessory minerals including magnetite, ilmenite, apatite, zircon, and titanite. The main phenocrysts are the K-feldspar, followed by plagioclase, most of which are zoned (Fig. 4.1g, h). Tabular phenocrysts of K-feldspar can reach up to 5 cm in length, some of them having small inclusions of biotite and amphibole in a ring-like display. Matrix minerals include amphibole, biotite, plagioclase, K-feldspar and quartz. Basically, amphibole and biotite are euhedral to subhedral, and have sharp contacts with each other, although biotite is occasionally included in amphibole. This suggests that amphibole and biotite co-crystallized. Both minerals contain magnetite, ilmenite, apatite and zircon inclusions, biotite having more inclusions than amphibole (Fig. 4.1b, c, d, e, f).

(2) A medium-grained biotite±amphibole-bearing granite (phase-2) (Fig. 4.2a); it has plagioclase (~30%), K-feldspar (~35%), quartz (~25%), biotite (~7%), locally with amphibole (<3%), and contains the same accessory minerals than phase-1. Mafic minerals are euhedral to subhedral, having slightly smaller sizes compared to those in Phase-1(Fig. 4.2 b, c, d).

(3) A fine-grained, biotite-bearing granite (phase-3) (Fig. 4.2e). Normally, it is light pink or light grey. Dark-coloured minerals occur in lesser amounts compared to

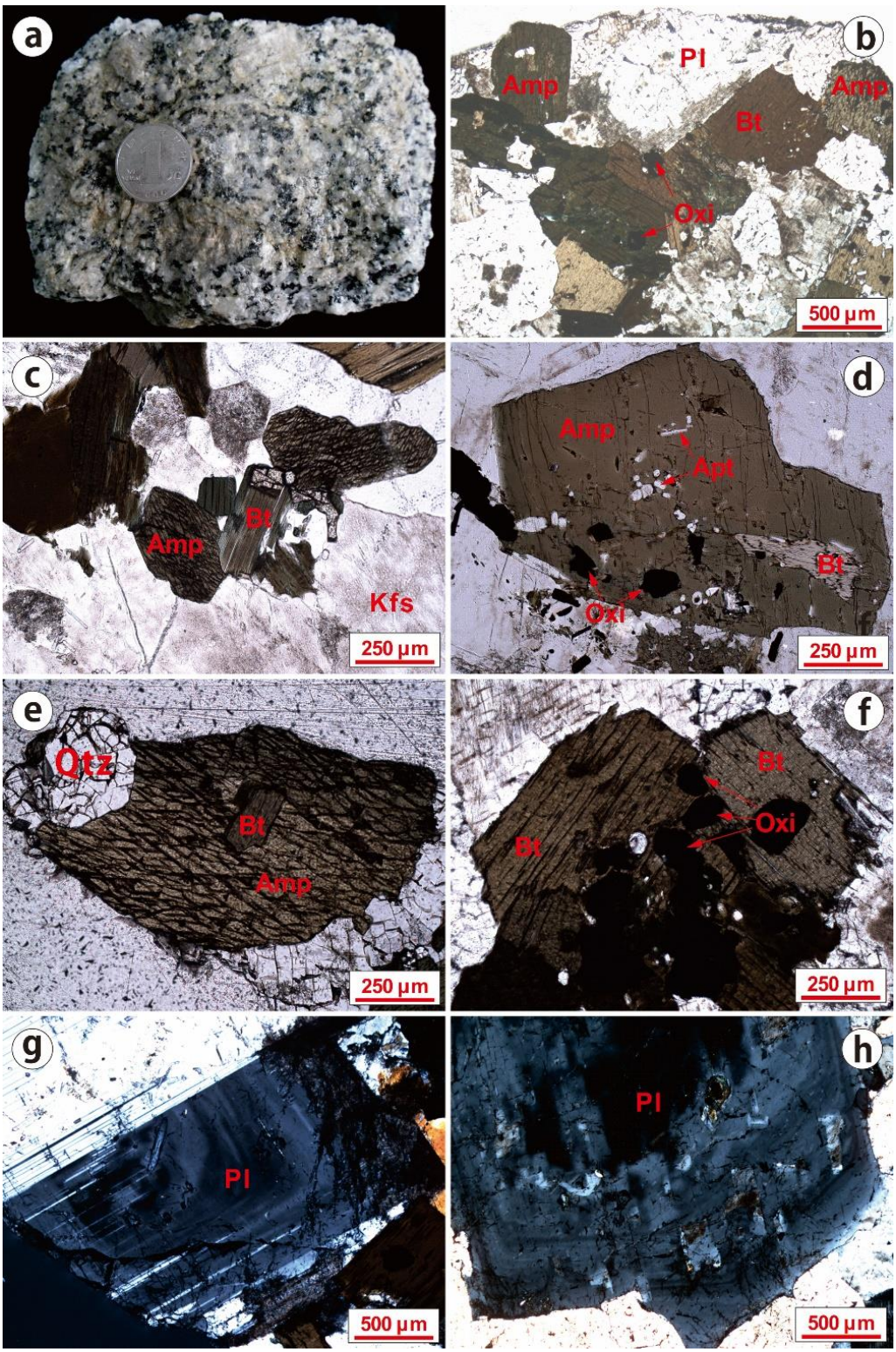

Fig. 4.1 Photographs and thin section photomicrographs of phase-1 from Qitianling pluton. (a) Hand specimen of Phase-1, Porphyritic, medium- to coarse-grained amphibole-biotite-rich monzonitic granite. (b) to (c) Sharp contact between amphibole and biotite. (d) to (f) Different inclusions in euhedral to subhedral amphibole and biotite. (g) and (h) Zoning plagioclase. Abbreviations: Amp, amphibole; Bt, biotite; Pl, plagioclase; Oxi, oxides; Kfs, K-feldspar; Qtz, quartz; Apt, apatite.

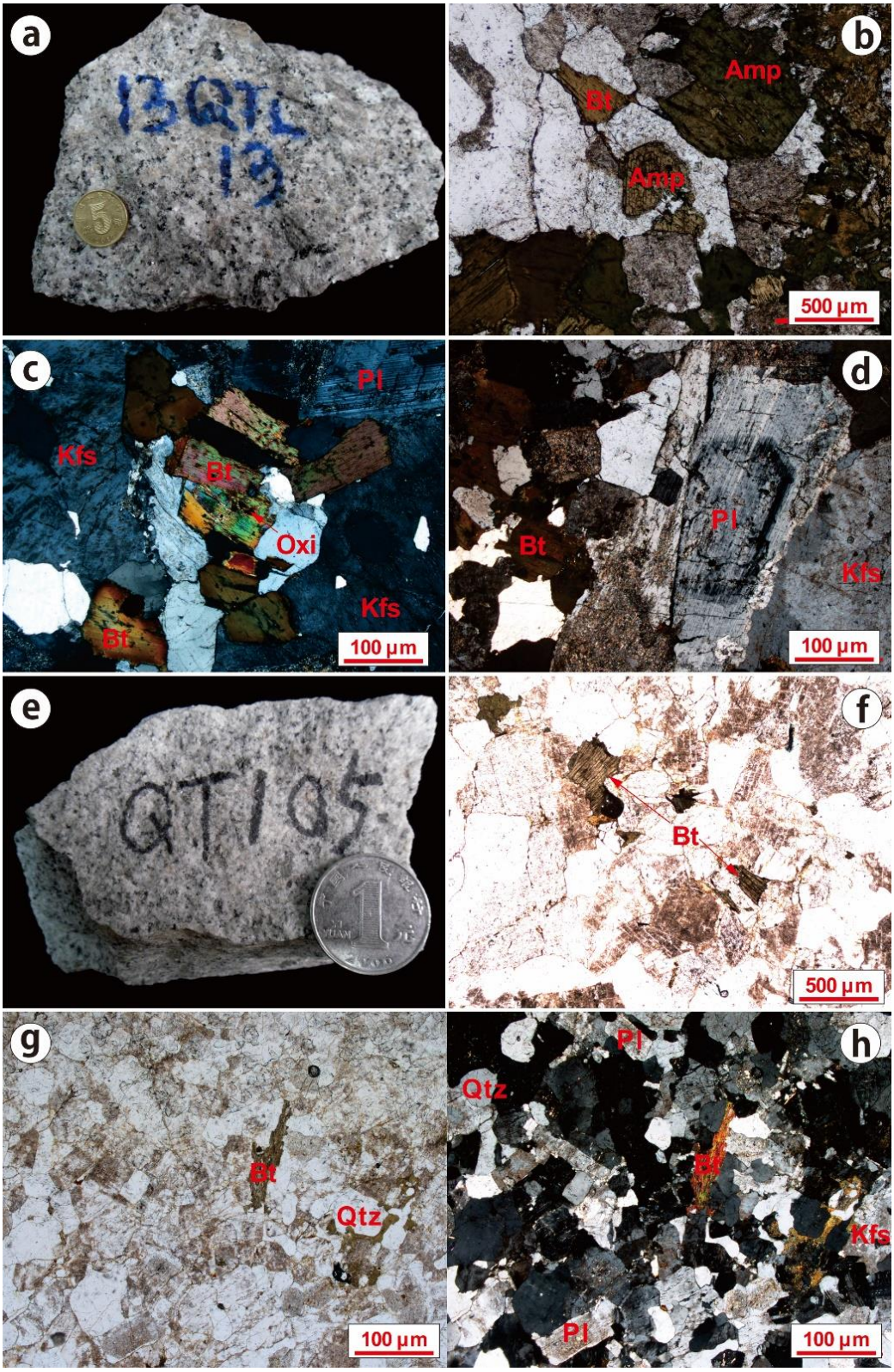

Fig. 4.2 Photographs and thin section photomicrographs of phase-2 and phase-3 from Qitianling pluton. Phase-2, medium-grained biotite±amphibole bearing granite (3) Phase-3, fine-grained, biotite-bearing granite. Abbreviations: Amp, amphibole; Bt, biotite; Pl, plagioclase; Oxi, oxides; Kfs, K-feldspar; Qtz, quartz; Apt, apatite.

other phases. It contains plagioclase (~30%), K-feldspar (~35%), quartz (~30%), <5% biotite, with lower contents of magnetite, ilmenite, apatite, zircon, and titanite relative to phases 1 and 2 (Fig. 4.2 f, g, h).

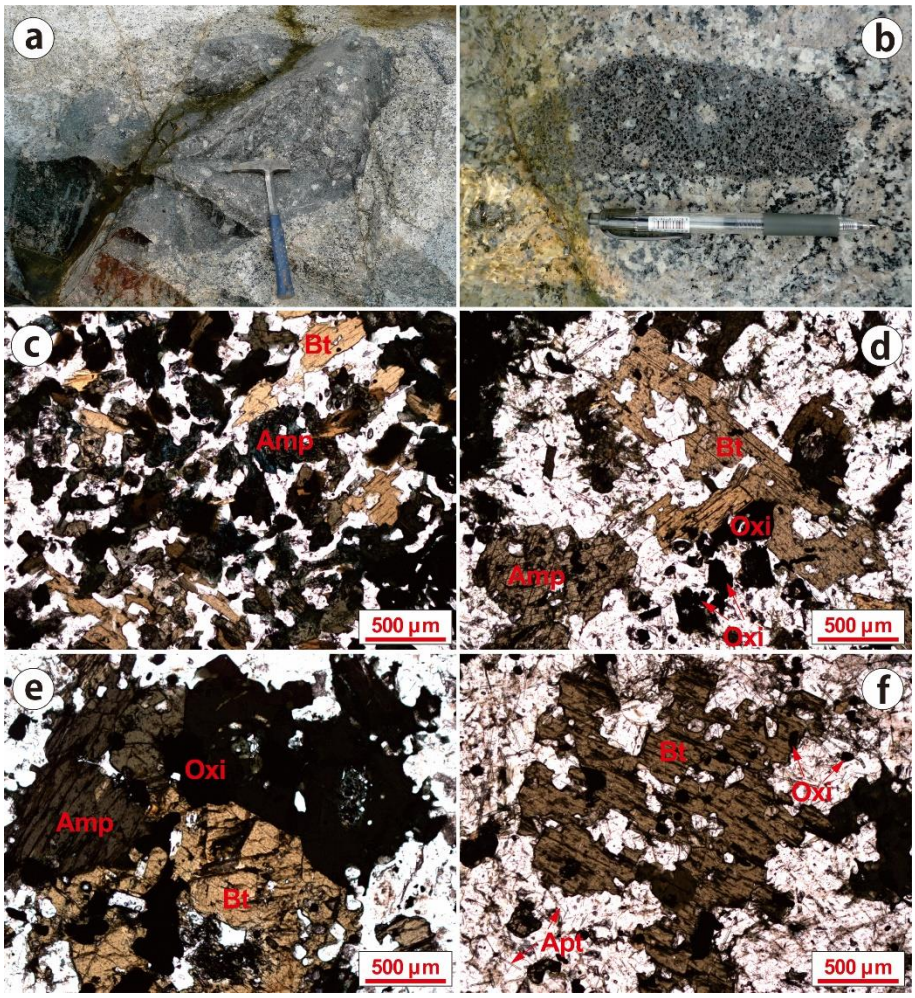

Fig. 4.3 Photographs and thin section photomicrographs of Qitianling mafic enclave. (a) and (b) Mafic enclave in the outcrop within the Phase-1 granite. (c) to (f) Mineral assemblages and textures of mafic enclaves. Abbreviations: Amp, amphibole; Bt, biotite; Oxi, oxides; Apt, apatite.

Along the margins of the pluton, black mafic enclaves were observed in phase-1 (samples 38, 42A and 21). The enclaves have elliptic shapes with sizes ranging from several centimeters to almost 1 meter. K-feldspar or plagioclase phenocrysts (1-3 centimeters in length) similar to those in phase-1 are often observed in the enclaves (Fig. 4.3 a, b). Some of those phenocrysts may even cut across enclave and host granite

interface. Enclaves in phase-1 display a magmatic-equant texture. They contain amphibole, biotite, plagioclase, K-feldspar and quartz: the proportion of mafic minerals reaches up to 30 vol %. Most of the mafic minerals in enclaves have a rounded shape or display resorption textures (Fig. 4.3 c, d, e, f).

From the observed inclusion relationships, the crystallization order of the phase I amphibole-bearing granite is as follows: Magnetite and ilmenite crystallized first followed by apatite and then biotite, amphibole, and plagioclase, the last phases to crystallise being K-feldspar and quartz.

4.2 Whole rock geochemistry

4.2.1 Major elements

The bulk rock major and trace elements compositions of Qitianling granite and associated enclaves are listed in Appendix Table 1. Qitianling granite has a rather wide range of SiO_2 content, from ~65 to ~77 wt.%, with an alkali content ($Na_2O + K_2O$) between 6.9 and 9.6 wt%. In the SiO2 *vs*. ($Na_2O + K_2O$) diagram, Qitianling granites plot in the field of Quartz Monzonite, Granodiorite and Granite, while mafic enclaves plot mostly in the Monzonite field (Fig. 4.4 (a)). Both mafic enclaves and Qitianling granites have a rather low alumina saturation index (A/CNK value is 1 on average for Qitianling granite and 0.84 for mafic enclave) which indicates that Qitianling pluton is metaluminous (Fig. 4.4 (b)).

Apart from the mafic enclaves, phase-1 is the most mafic granite phase in Qitianling pluton. Representative bulk rock compositions from phase-1 show that SiO_2 ranges mostly between ~65 and ~68 wt.%, while other oxides vary as follows: Al_2O_3: 13.4-14.6 wt.%; FeO_{tot} :4.5-5.7 wt.%; MgO : 0.8-1.4 wt.%; CaO : 1.7-3.3 wt.%; Na_2O : 2.9-3.3 wt.%; K_2O : 3.9-4.8 wt.%; TiO_2: 0.7-1 wt.%. The A/CNK value is on

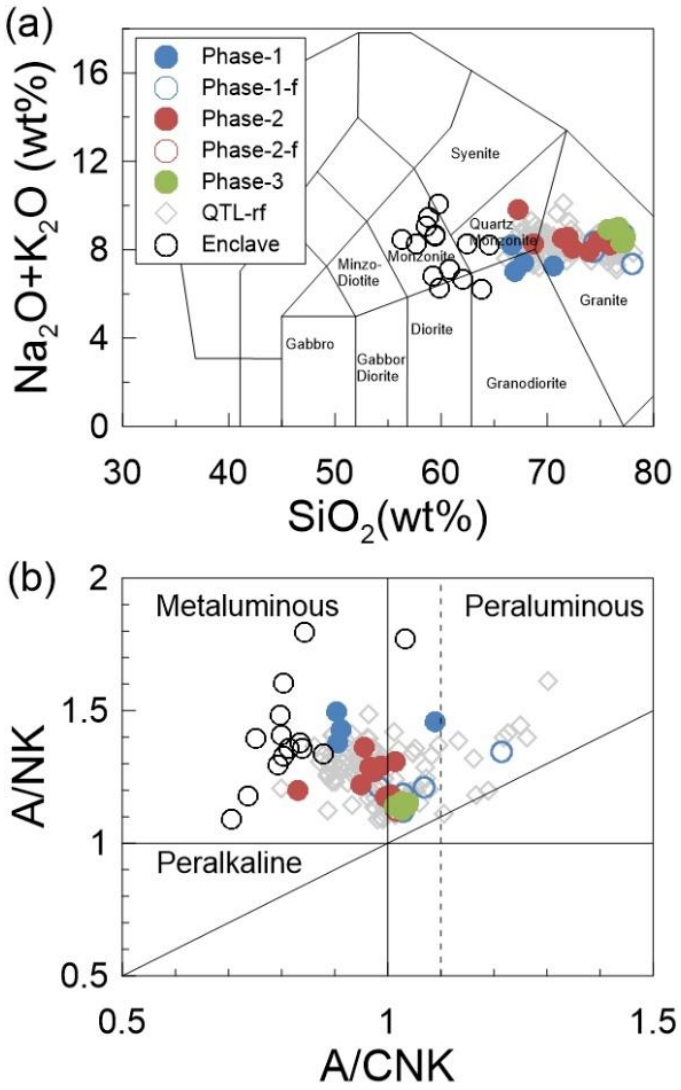

Fig. 4.4 (a) SiO_2 *vs.* (K_2O+Na_2O) (after Le Bas et al., 1986; Le Maitre, 1989) and (b) A/NK [molar ratio Al_2O_3/ (Na_2O+K_2O)] *vs.* A/CNK [molar ratio Al_2O_3/ ($CaO + Na_2O+K_2O$)] diagram of Qitianling granite and mafic enclaves. Solid circles stand for the major phases of Qitianling pluton; Blue circles stand for phase-1; Red circles stand for phase-2; Green circles stand for phase-3; Unfilled blue circles are the fined-grained samples collected from phase-1; Unfilled red circles are the fined-grained samples from phase-2; Unfilled dark circles are stand for the mafic enclave; Unfilled grey diamonds are bulk rock composition of Qitianling granite from the literature (Zhao et al., 2012; Zhu et al., 2005; Li et al., 2005; Zhu et al., 2008; Deng et al., 2005; Bai et al., 2005; Li et al., 2010; Zhu et al., 2003; Xie et al., 2010; Liu et al., 2003; Wang et al., 2004; Fu et al., 2006; Hu et al., 2004).

average 0.95. Fine-grained granites collected in areas where coarse grained phase-1 predominates tend to be more felsic with higher content of SiO_2 (up to ~78 wt.%). For phase-2, the bulk rock composition is slightly more evolved with higher content of SiO_2

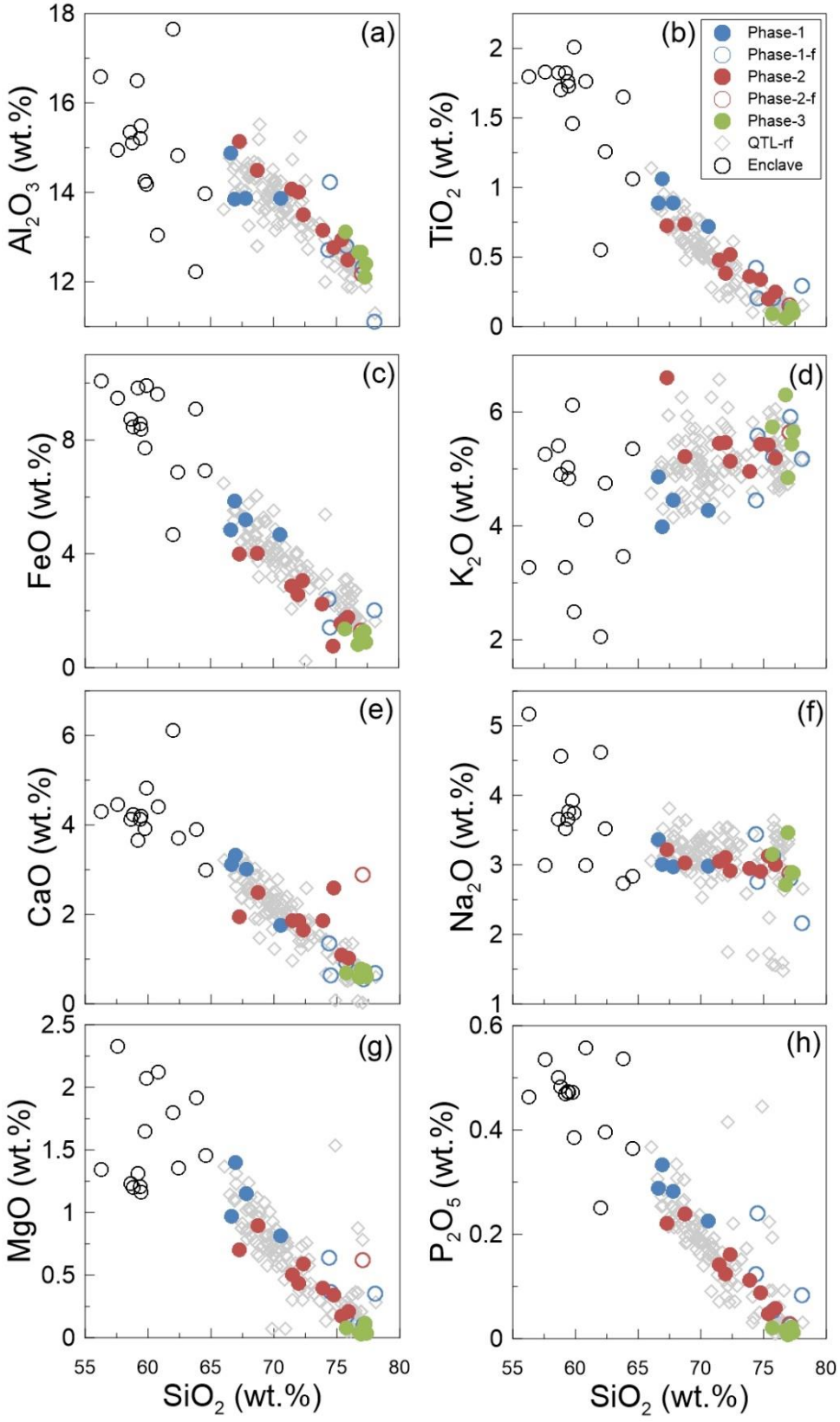

Fig. 4.5 Harker diagram of Qitianling granite and mafic enclaves. The Symbols in fig.4.5 are as in Fig. 4.4.

(~68- ~76 wt.%), K_2O (4.9-5.6 wt.%) and lower Al_2O_3 (12.0-14.4 wt.%), FeO_{tot} (1.3-

4.0 wt.%), MgO (0.1-0.9 wt.%), CaO (1.0-2.5 wt.%) and TiO_2 (0.2-0.7 wt.%) contents. A/CNK value is on average 0.99. Phase-3 has the most felsic composition with SiO_2 content up to 77 wt.% and the lowest contents of Al_2O_3 (11.9-12.8 wt.%), FeO_{tot} (0.8-1.3 wt.%), MgO (0.03-0.1 wt.%), CaO (0.6-0.8 wt.%) and TiO_2 (0.06-0.10 wt.%). A/CNK value of phase-3 is on average 1.03. Compared to granites, mafic enclaves have obviously a lower SiO_2 content spanning a range from ~56 up to ~64 wt.% (Zhao et al., 2012; Zhu et al., 2003). The contents of oxides are: Al_2O_3: 12.0-17.6 wt.%; FeO_{tot} : 4.6-10.0 wt.%; MgO : 1.2-2.3 wt.%; CaO : 3.0-4.7 wt.%; Na_2O : 2.7-5.1 wt.%; K_2O : 2.0-6.1 wt.%; TiO_2: 0.6-2.0 wt.%, with a rather low A/CNK value (on average 0.82).

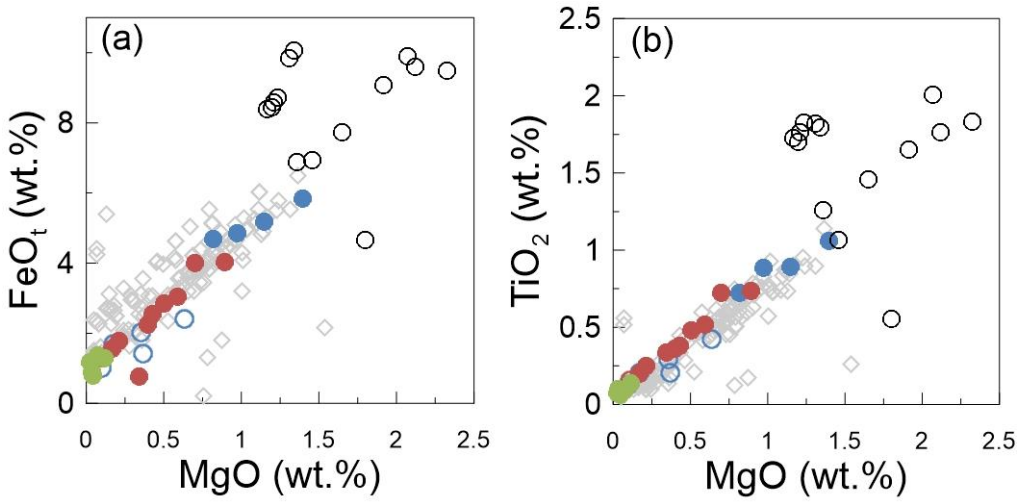

Fig. 4.6 Bulk rock MgO *vs* FeO_t and MgO *vs* TiO_2 diagram of Qitianling granites and mafic enclaves. Symbols are as in Fig. 4.4.

The representative compositions from each phase, including the mafic enclaves, define a continuous evolution trend in Harker plots (Fig. 4.5). Generally, from mafic enclaves to phase-3, as SiO_2 content increases, K_2O increases while Al_2O_3, FeO_{tot}, MgO, CaO, TiO_2, P_2O_5 decrease systematically. The FeO_{tot} - MgO and TiO_2 - MgO diagrams (Fig. 4.6) also show strong linear trends. From the most felsic phase to mafic enclaves, FeO_{tot} and TiO_2 increase as MgO increases. The compositions of the fine-grained granites collected inside phase-1 or phase-2 predominant zones are shown as unfilled colored circles, broadly falling on the general trend defined by the main phases.

4.2.2 Trace elements

The analyses results show that Rb, Th, Zr, and Y trace elements are enriched in the Qitianling granite, while Sr, Ba, P, and Ti are relatively depleted. Temperatures estimated by zircon saturation thermometry (Watson and Harrison, 1984) yield values around 800°C for all terms (~ 796°C for mafic enclaves, and ~830°C, ~808°C and ~785°C, on average, for phase-1,2,3, respectively). The contents of Sr, Sc, Co decrease systematically as SiO_2 content increases. The Nb/Ta and Zr/Hf ratios of the granite also decrease from phase-1 to phase-3 (Fig. 4.7).

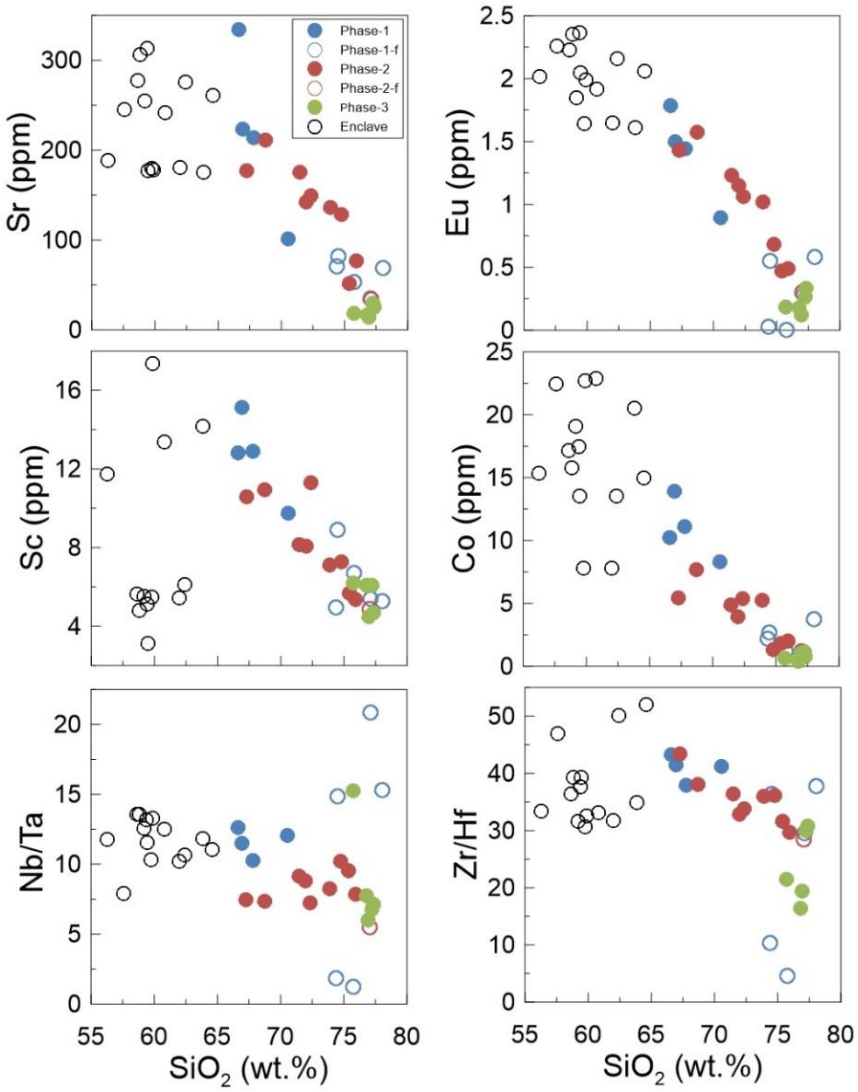

Fig. 4.7 Bulk rock compositions plot in SiO_2 *vs* Sr, Eu, Sc, Co, Nb/Ta, Zr/Hf diagrams of Qitianling granites and mafic enclaves.

Qitianling pluton is rich in rare earth elements with a ΣREE value of ~305 ppm on average. In chondrite-normalized REE variation diagrams, Qitianling granites and mafic enclaves show strong Eu negative anomalies ($\delta Eu = 2Eu_N/(Sm_N + Gd_N)$) and an enrichment in Light Rare Earth Element (LREE) relative to Heavy Rare Earth Element (HREE) resulting in high values of $(La/Yb)_N$ ratios (21.3 on average), the variation patterns of HREE being flatter than those of LREE (Fig. 4.8). The $10000*(Ga/Al)_N$ ratios (3.2 on average) are also relatively high. From mafic to felsic compositions, δEu increases significantly which indicates that the degree of plagioclase fractionation increases: the δEu ranges of mafic enclaves and Qitianling granites (phases-1,2,3) are 0.25-0.67, 0.31-0.57, 0.22-0.57 and 0.03-0.2, respectively.

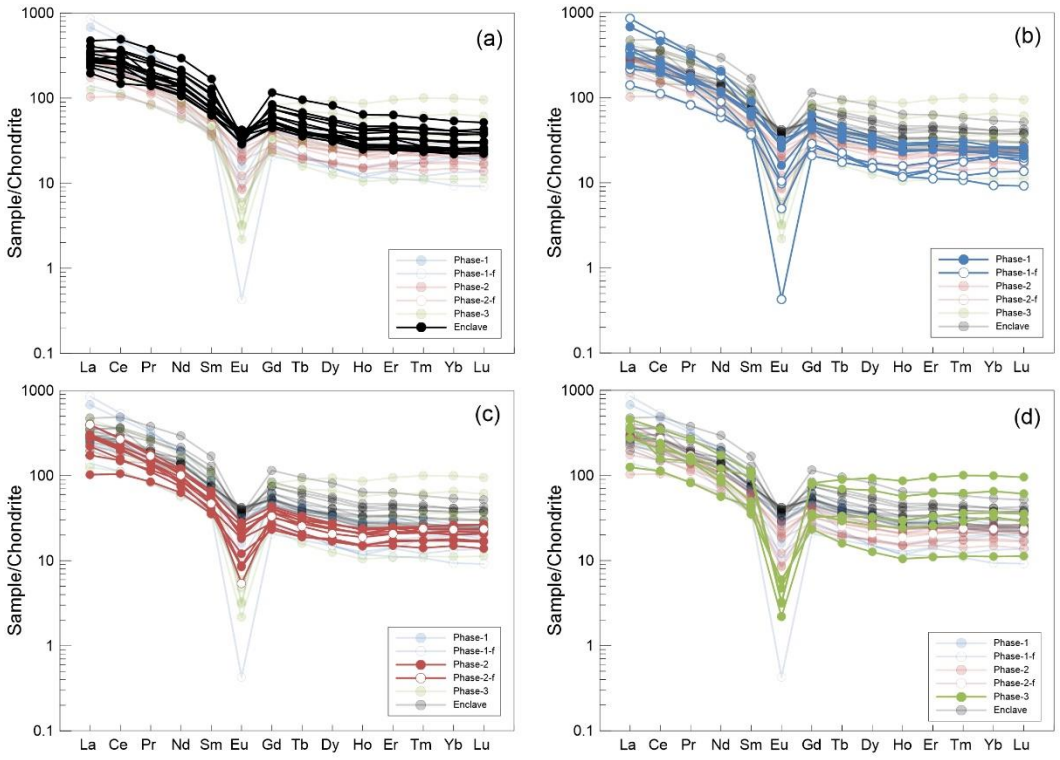

Fig. 4.8 Bulk rock chondrite-normalized REE diagrams of Qitianling granites (b, phase-1; c, phase-2; d, phase-3) and mafic enclaves (a). The sample QTL-10 is not shown in this diagram because of its low content of REE.

4.3 Mineral chemistry

4.3.1 Amphibole

Representative amphibole compositions and structural formulae are shown in Appendix table 2. Amphiboles from phase-1, phase-2 and mafic enclaves are all similar, with CaO (on average) 10.8 wt.%, 10.6 wt.% and 10.9 wt.%; Na_2O: 1.9 wt.%, 1.9 wt.% and 1.86 wt.%; K_2O: 1.2 wt.%, 1.3 wt.% and 1.2 wt.%, respectively. Structural formulae calculated on the basis of 23 oxygens indicate that all amphiboles have $(Ca+Na)_B>1.00$, $(Ca)_B>1.50$ $(Na+K)_A>0.5$ being thus calcic amphiboles (Leake et al., 1997). Amphiboles are relatively rich in Fe, with FeO contents of phase-1, phase-2 and mafic enclaves of, 20.9-25.9 wt.%, 20.8-28.5 wt.% and 22.5-24.6 wt.%, respectively. The $Mg/(Mg+Fe^{2+})$ ratios are all lower than 0.5. Therefore, most of the amphibole from Qitiangling pluton are ferro-edenite some being close to ferro-pargasite or hastingsite. Fe/(Mg+Fe) are 0.56-0.76 for phase-1, 0.59-0.80 for phase-2 and 0.63-0.69 for mafic

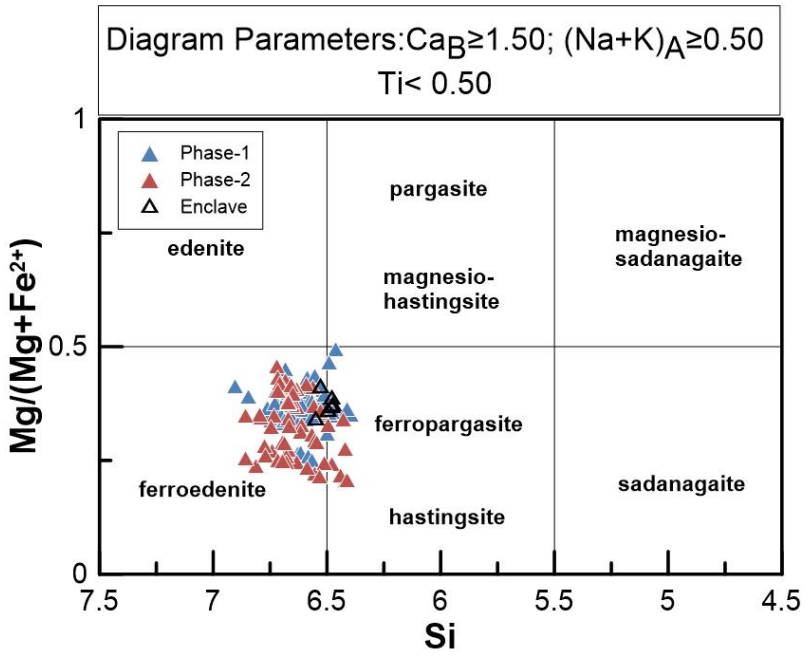

Fig. 4.9 Composition of amphiboles from the Qitianling granites and enclaves (after Leake et al., 1997). The data of amphibole in enclaves are from Zhao et al., 2012.

enclaves (Fig. 4.9).

Trace element concentrations of amphibole from phase-1 show they are rich in Sc (116 ppm on average), V (275 ppm on average), Y (372 ppm on average), Zr (92 ppm on average), Nb (75 ppm on average) and HREE (La 162 ppm, Ce 550 ppm, Pr 83 ppm, Nd 381 ppm, Sm 95 ppm, Gd 83 ppm on average, respectively). In the primitive mantle normalized trace element diagram, amphiboles display negative anomalies in Ba and Sr (Fig. 4.10a). As for chondrite normalized REE patterns of amphibole from phase-1, they have distinct depletion in Eu. Normalised HREE contents are higher than LREE, with concave patterns (Fig. 4.10b).

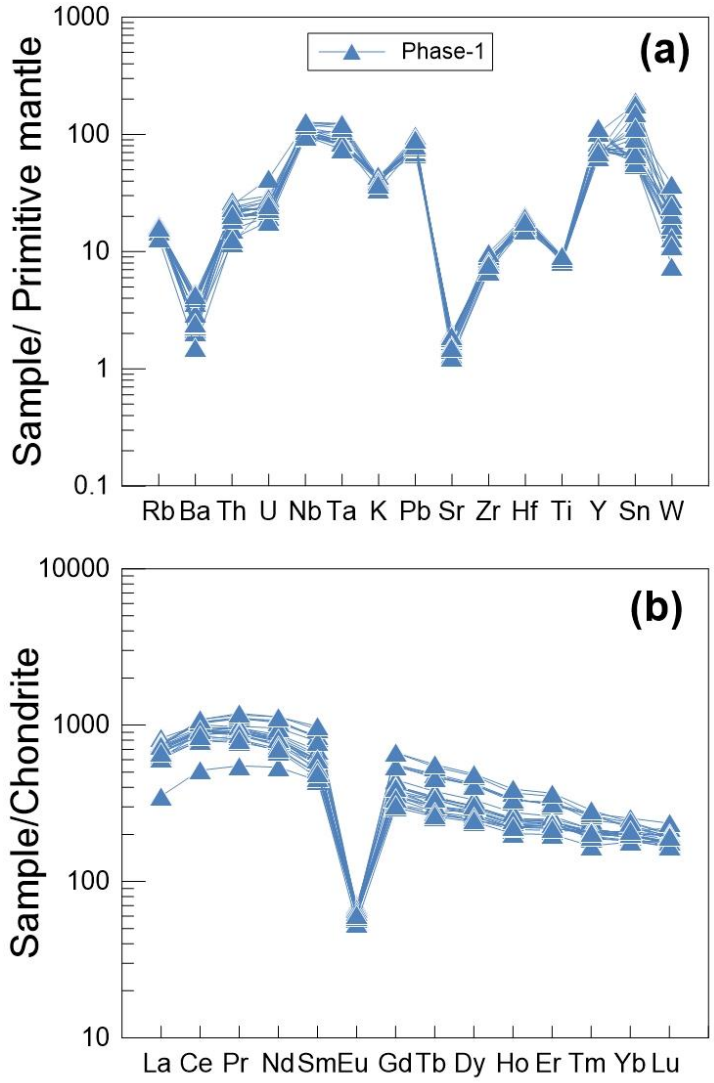

Fig. 4.10 Primitive mantle-normalized trace element diagram (a) and Chondrite-normalized REE diagrams of amphibole from Qitianling granite (Phase-1) (b).

4.3.2 Plagioclase

Representative plagioclase compositions are listed in Appendix table 3. Plagioclases from Qitianling pluton have An values ranging from ~2 to ~48. Zoned plagioclases are common in phase-1 and phase-2. In the feldspar classification diagram, most plagioclase are oligoclase or andesine while minor albite can be observed in phase-2 (Fig. 4.11).

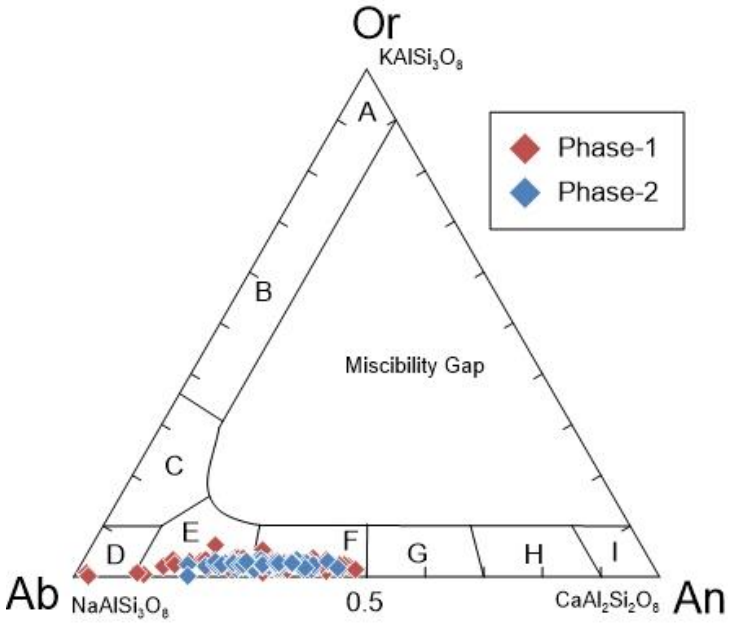

Fig. 4.11 Composition of plagioclases from the Qitianling granites. A: Orthoclase; B: Sanidine; C: Anorthoclase; D: Albite; E: Oligioclase ; F: Andesite; G: Labradorite; H: Bytownite; I: Anorthite.

4.3.3 Biotite

Representative biotite compositions are listed in Appendix table 4. As for amphibole, biotites are rich in Fe. In phase-1 and phase-2, FeO contents are 26.4-27.4 wt.% and 26.3-30.9wt.%, while MgO varies from 7.1-7.9 wt% to 5.6-7.6 wt.%, respectively. In phase-3, the FeO and MgO contents are 27.4-29.2 wt.% and 5.6-7.6 wt.%. The Fe/(Fe+Mg) ratio increases from phase-1 to phase-3 (0.67, 0.70, 0.85). The TiO_2 content of biotite from phase-1 and phase-2 are similar, varying from ~3.5 to ~4.7

while biotite from phase-3 has lower TiO_2, ~2.7 wt.% (Fig. 4.12).

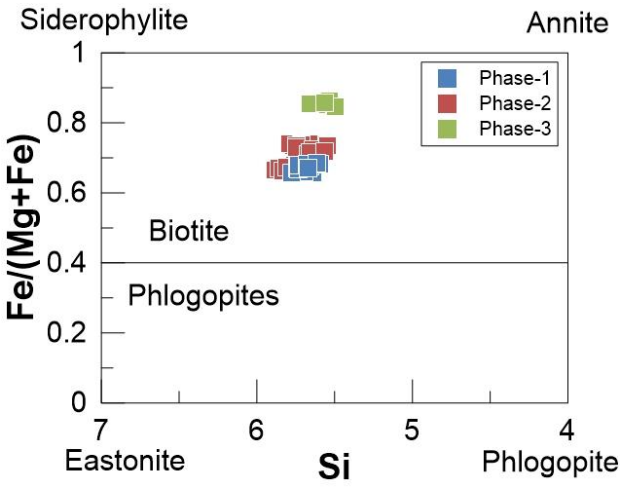

Fig. 4.12 Composition of biotite from the Qitianling granites.

4.3.4 Titanite

Titanite in Qitianling pluton is a common accessory mineral. Usually, it occurs interstitially as euhedral to subhedral crystals.It is rich in Fe (Fe_2O_3 2.3 wt.% on average) and Al (Al_2O_3 3.4 wt.% on average). Structural formulas, calculated on a 3 cations basis, show that Ti and Al+ Fe^{3+} display a substitution relationship (Fig. 4.13a). In a Al *vs* Fe^{3+} (apfu) diagram (Fig. 4.13b), titanite plots between the Al= $Fe^{3+}$and Al= $3Fe^{3+}$ trends which suggests that most of the studied titanites are close to the magmatic field consistent with the results of Aleinikoff et al. (2012). (See in Appendix table 5)

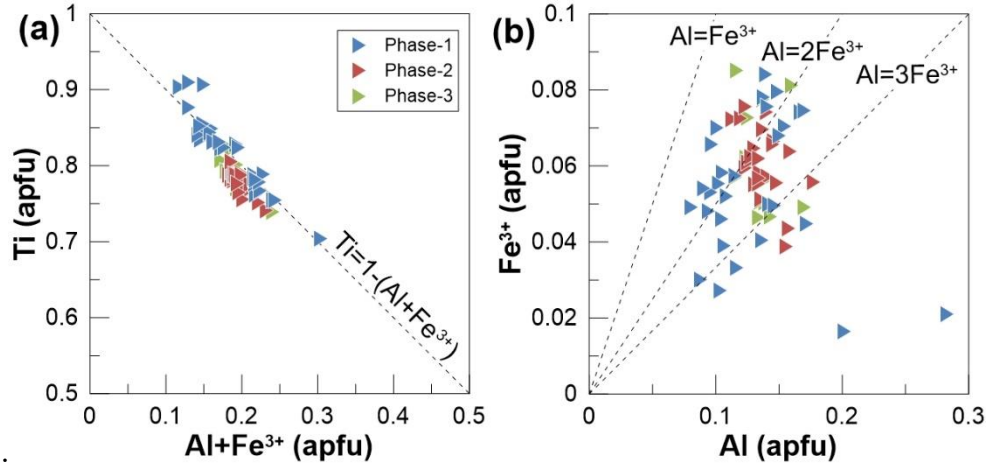

Fig. 4.13 Plot of Al *vs* Fe^{3+} (apfu) and Al+Fe^{3+} *vs* Ti (apfu) of titanite from the Qitianling granites.

4.4 Zircon U-Pb and Amphibole-biotite ^{40}Ar-^{39}Ar geochronology

4.4.1 Geochronology of Zircon

4.4.1.1 Zircon U-Pb geochronology

Zircon ($ZrSiO_4$) is a very common accessory mineral in igneous rocks especially in granitoids. It belongs to the tetragonal mineral group (*$I4_1/amd$* space group). The crystal structure of zircon can be explained as a combination of SiO_4 tetrahedra and ZrO_8 dodecahedra. Parallel to the c axis, ZrO_8 dodecahedra share edge with SiO_4 tetrahedra. Along the direction of the b axis, ZrO_8 dodecahedra share edge with each other as a zigzag chain. ZrO_8 dodecahedra can be regarded as two ZrO_4 tetrahedras with different bond length, 0.227nm (shared edge with SiO_4 tetrahedra) and 0.213nm (shared corners with SiO4 tetrahedra) (Nyman et al. 1984; Finch and Hanchar, 2003). This special structure plays an important role in favouring the incorporation of elements such as P, Hf, U, Th, Y and REEs which make zircon a potent geochronometer (Robinson et al., 1971; Hoskin and Schaltegger, 2003).

Eighteen samples were chosen for U-Pb dating for Qitianling pluton. The sample locations are shown in Fig. 2.7 and Appendix table 6. According to the geological map, we collected 6 samples (QTL-10, QTL-21B, SC14-42A, SC14-74, SC14-75 and SC14-141) in phase-1. Sample QTL-10 is a fine grained biotite granite, and was collected in the northern part of Qitianling, close to the Xintianling tungsten mine. Samples QTL-21B and SC14-42A are located in the western and southwestern margin parts of the pluton, where mafic enclaves can be observed. The rock types are coarse-medium grained biotite granite and coarse-medium grained amphibole-biotite granite. Samples SC14-74, SC14-75 and SC14-141 were collected in the southeastern part of Qitianling pluton. Sample SC14-141 is a medium-fine grained biotite granite collected near the

boundary of phase-1 and phase-3. Samples SC14-74 and SC14-75 are medium-fine grained biotite granite and coarse grained biotite granite, respectively.

10 samples were collected from phase-2 (QTL-25, SC14-45, SC14-47, SC14-52, SC14-58, SC14-61, SC14-62, SC14-77, SC14-79, SC14-139). Among those samples, QTL-25(in the south, a medium grained biotite-bearing granite), SC14-52(in the center, a coarse-medium grained amphibole-biotite granite), are close to the boundary of phase-1 and phase-3 whereas SC14-58 (in the north, a coarse-medium grained amphibole biotite granite) and SC14-77 (in the southeast, a coarse-medium grained biotite granite) are close to the boundary between phase-1 and phase-2. Sample SC14-45, a medium-fine grained biotite granite and SC14-47, a medium grained biotite granite, are from the northwestern part of the pluton whereas sample SC14-61, a medium-fine grained biotite granite and SC14-62, a coarse-medium grained amphibole biotite granite, are from the central part of the pluton. Sample SC14-79, a fine grained biotite granite, and SC14-139, a medium-fine grained biotite granite, are collected from the margin of the southeastern part of the pluton.

In phase-3, only 2 samples were collected (QTL-04, SC14-142). Sample QTL-04 is a fine-grained biotite granite which was collected in the eastern part of the pluton. Sample SC14-142 is close to the central part and is a medium-fine grained biotite granite. The detail of sample location is given in the Appendix table 6.

Most of the zircon crystals have an euhedral crystal morphology with tetragonal prism shape, a length >100 μm and a length-width ratio varying from 1:2 to 1:4. Almost all zircons are transparent to colourless or slightly light brown. Some of them contain apatite, and Fe-Ti oxides as inclusions. The cathodoluminescence (CL) images show clear oscillatory zoning which demonstrates that those zircons are magmatic (Fig. 4.14). A few inherited zircon cores were observed in this study. The zircons which are free of inclusions were chosen for the analyses meanwhile the cracks were also avoided during the analysis. The zircon U-Pb age results are shown in Appendix table 6.

(1) QTL04: Fine grained biotite granite (25°32'36"N; 112°55'22"E)

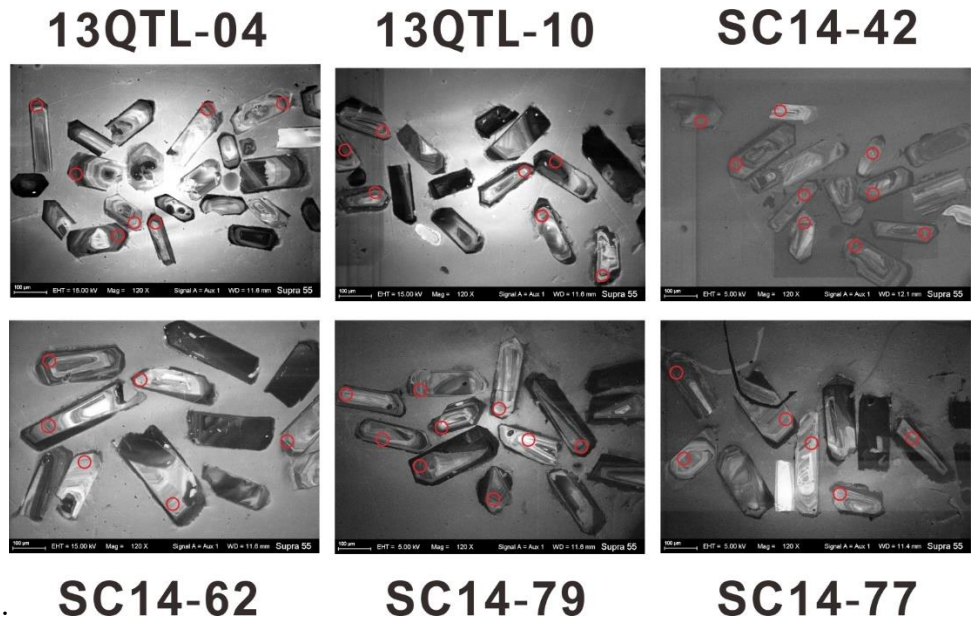

Fig. 4.14 The cathodoluminescence (CL) images of zircons extracted from Qitianling pluton.

16 analyses were acquired from sample QTL04. Th/U ratios vary from 0.46-0.83. The $^{206}Pb/^{238}U$ age is between 153±3 and 159±4 with a Concordia average age of 155.9±1.6 Ma (MSWD =0.17).

(2) QTL10: Fine grained biotite granite (25°39'49"N; 112°54'46"E)

14 analyses were acquired from sample QTL10. Th/U ratio ratios vary from 0.24-0.74. The $^{206}Pb/^{238}U$ age is between 145±4 and 158±4 with a Concordia average age

of 152.9±2.6 Ma (MSWD =1.2).

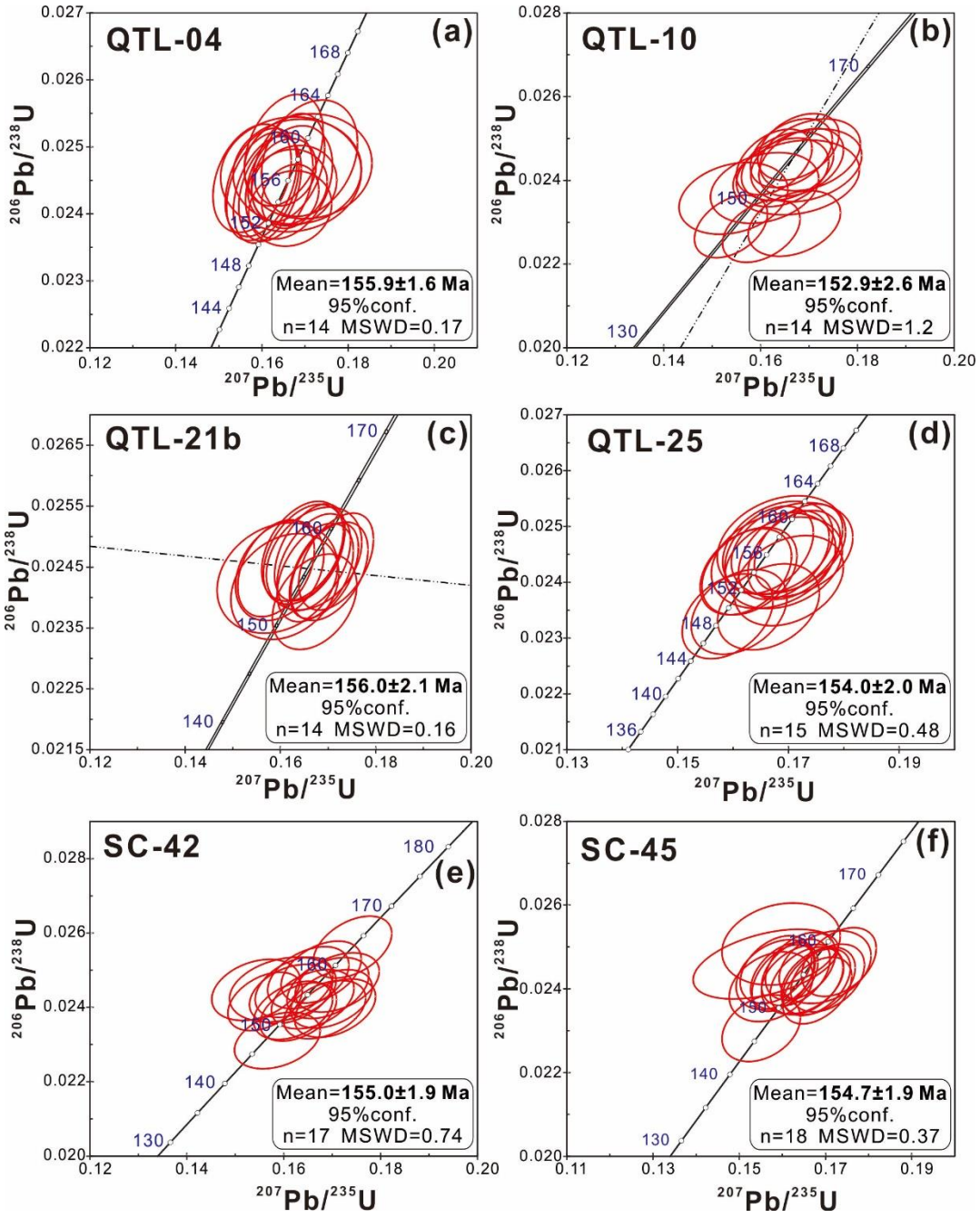

Fig. 4.15 Zircon U-Pb Concordia diagrams showing the geochronological results for the Qitianling granites. Concordia ages are shown on the bottom right.

(3) QTL21B: Coarse-medium grained biotite granite (25°27'09'N; 112°47'59"E)

14 analyses were acquired from sample QTL21B. Th/U ratios vary from 0.39-0.69. The $^{206}Pb/^{238}U$ age is between 152±4 and 158±4 with a Concordia average age of 156 ±2.1 Ma (MSWD =0.16).

(4) QTL25: Medium grained biotite granite (25°27'27"N; 112°51'20"E)

15 analyses were acquired from sample QTL25. Th/U ratios vary from 0.39-0.68. The $^{206}Pb/^{238}U$ age is between 153±3 and 159±4 with a Concordia average age of 154 ±2 Ma (MSWD =0.48).

(5) SC1442A: Coarse-medium grained amphibole biotite granite (25°34'46"N; 112°46'33"E)

17 analyses were acquired from sample SC1442. Th/U ratios vary from 0.49-0.82. The $^{206}Pb/^{238}U$ age is between 147±4 and 163±4 with a Concordia average age of 155 ±1.9 Ma (MSWD =0.74).

(6) SC1445: Medium-fine grained biotite granite (25°34'36"N; 112°47'38"E)

18 analyses were acquired from sample SC1445. Th/U ratios vary from 0.46-0.83. The $^{206}Pb/^{238}U$ age is between 147±3 and 160±5 with a Concordia average age of 155.7±1.9 Ma (MSWD =0.37)

(7) SC1447: Medium grained biotite granite (25°33'31"N; 112°49'02"E)

20 analyses were acquired from sample SC1447. Th/U ratios vary from 0.46-0.83. The $^{206}Pb/^{238}U$ age is between 153±3 and 157±3 with a Concordia average age of 154.5±1.3 Ma (MSWD =0.14).

(8) SC1452: Coarse-medium grained amphibole biotite granite (25°31'46"N; 112°50'39"E)

19 analyses were acquired from sample SC1452. Th/U ratios vary from 0.46-0.83. The $^{206}Pb/^{238}U$ age is between 153±3 and 161±3 with a Concordia average age of 157.4±1.4 Ma (MSWD =0.46)

(9) SC1458: Coarse-medium grained amphibole biotite granite (25°34'59"N; 112°50'14"E)

18 analyses were acquired from sample SC1458. Th/U ratios vary from 0.46-0.83. The $^{206}Pb/^{238}U$ age is between 152±3 and 164±4 with a Concordia average age of

157.2±1.4 Ma (MSWD =1.05)

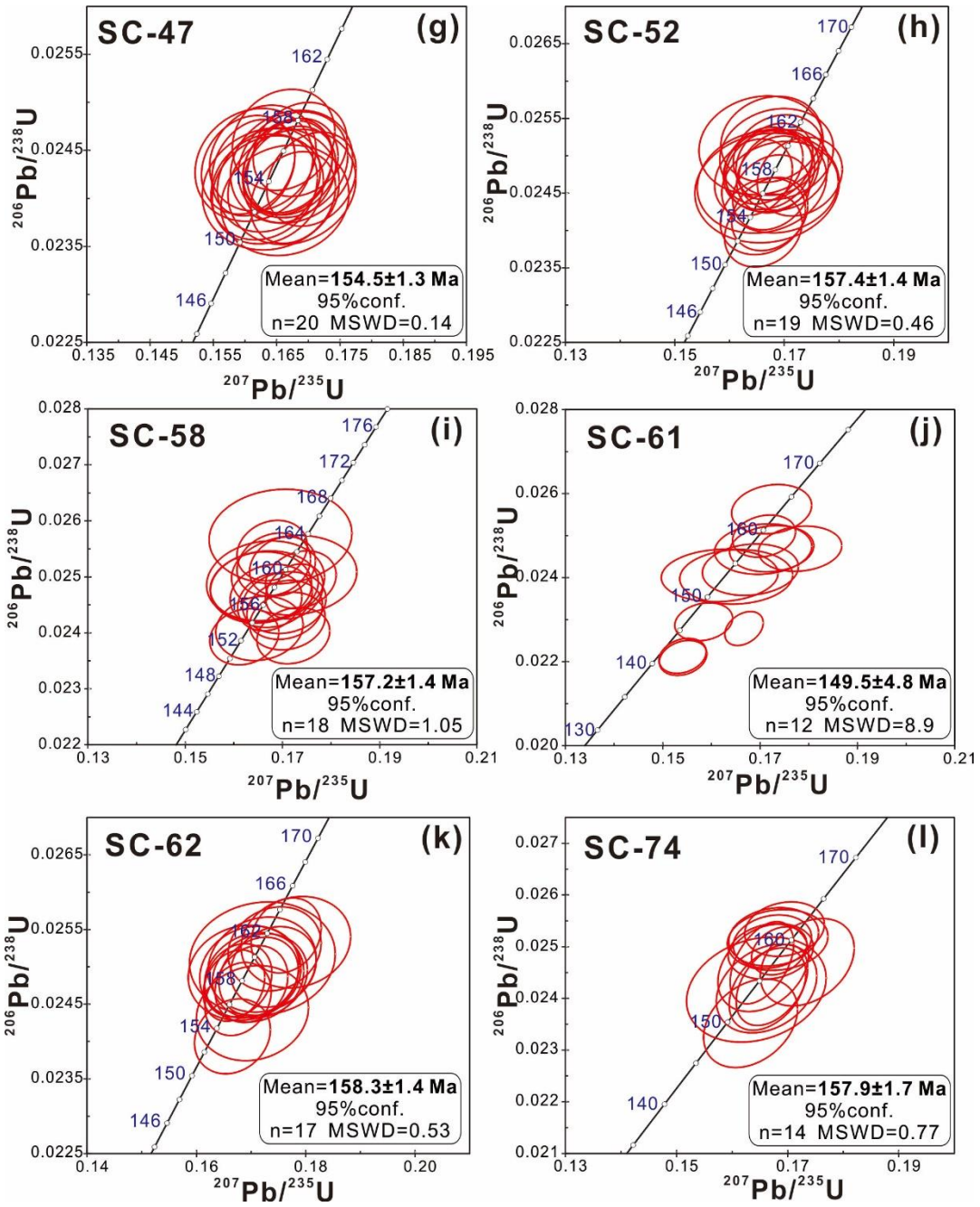

Fig. 4.15 Zircon U-Pb Concordia diagrams showing the geochronological results for the Qitianling granites. Concordia ages are shown on the bottom right.

(10) SC1461: Medium-fine grained biotite granite (25°30'30"N; 112°50'42"E)

12 analyses were acquired from sample SC1461. Th/U ratios vary from 0.46-0.83. The $^{206}Pb/^{238}U$ age is between 141±2 and 159±3 with a Concordia average age of 159.5±4.8 Ma (MSWD =8.9).

(11) SC1462: Coarse-medium grained amphibole biotite granite (25°29'55"N; 112°51'21"E)

17 analyses were acquired from sample SC1462. Th/U ratios vary from 0.46-0.83. The $^{206}Pb/^{238}U$ age is between 153±3 and 162±3 with a Concordia average age of 158.3±1.4 Ma (MSWD =0.53).

(12) SC1474: Medium-fine grained biotite granite (25°29'54"N; 112°55'15"E)

14 analyses were acquired from sample SC1474. Th/U ratios vary from 0.46-0.83. The $^{206}Pb/^{238}U$ age is between 150±4 and 161±3 with a Concordia average age of 157.9±1.7 Ma (MSWD =0.77).

(13) SC1475: Coarse grained biotite granite (25°29'17"N; 112°55'12"E)

16 analyses were acquired from sample SC1475. Th/U ratios vary from 0.46-0.83. The $^{206}Pb/^{238}U$ age is between 146±4 and 158±5 with a Concordia average age of 154 ±2 Ma (MSWD =0.71).

(14) SC1477: Coarse-medium grained biotite granite (25°28'11"N; 112°55'48"E)

22 analyses were acquired from sample SC1477. Th/U ratios vary from 0.46-0.83. The $^{206}Pb/^{238}U$ age is between 147±4 and 160±4 with a Concordia average age of 154.7±1.7 Ma (MSWD =0.64).

(15) SC1479: Fine grained biotite granite (25°27'12"N; 112°56'31"E)

17 analyses were acquired from sample SC1479. Th/U ratios vary from 0.46-0.83. The $^{206}Pb/^{238}U$ age is between 153±4 and 158±4 with a Concordia average age of 156 ±2 Ma (MSWD =0.15).

(16) SC14139: Medium-fine grained biotite granite (25°26'57"N; 112°56'35"E)

21 analyses were acquired from sample SC14139. Th/U ratios vary from 0.46-0.83. The $^{206}Pb/^{238}U$ age is between 150±4 and 162±4 with a Concordia average age of 156.4±1.8 Ma (MSWD =0.62).

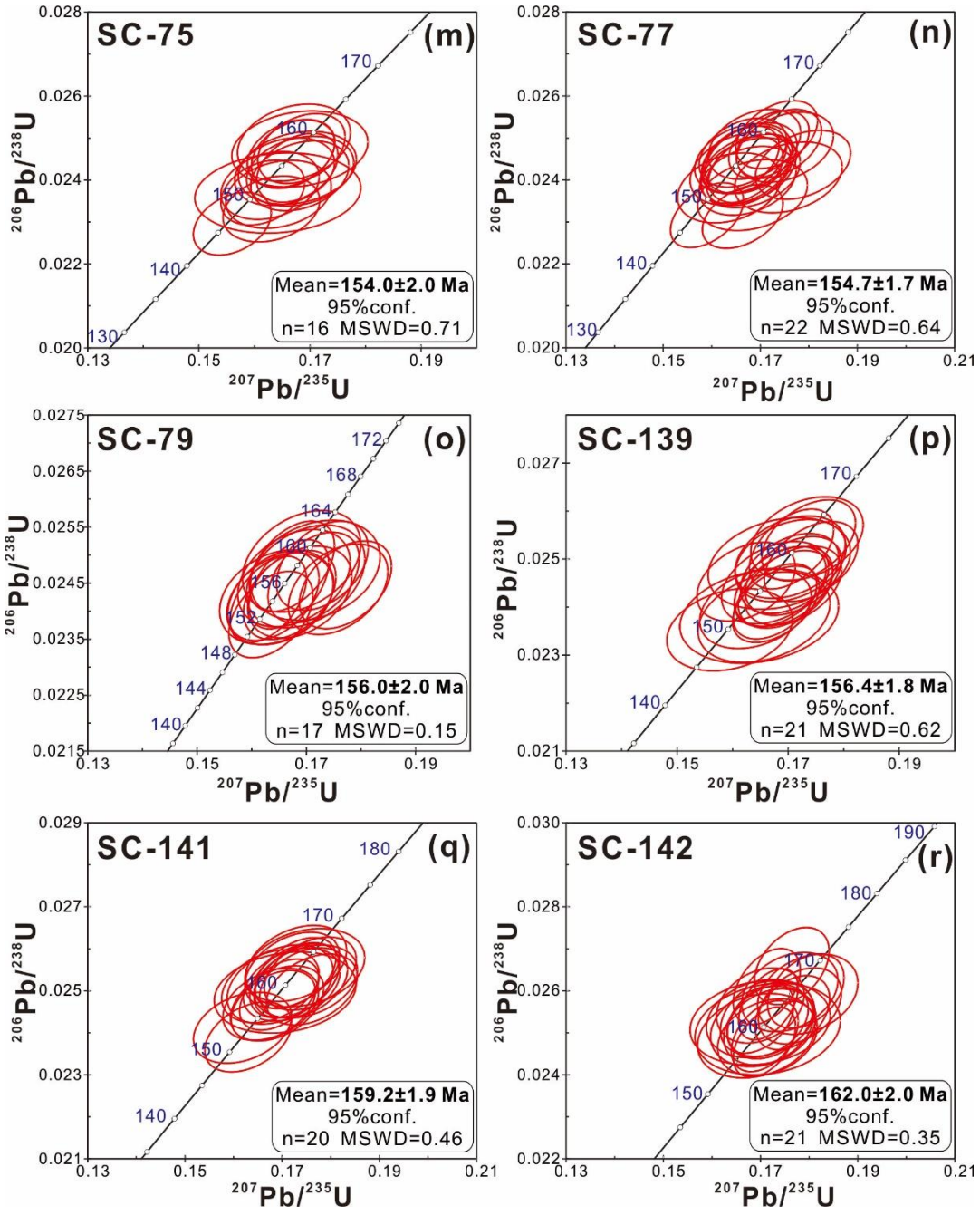

Fig. 4.15 Zircon U-Pb Concordia diagrams showing the geochronological results for the Qitianling granites. Concordia ages are shown on the bottom right.

(17)SC14141: Medium-fine grained biotite granite (25°29'54"N; 112°54'26"E)

20 analyses were acquired from sample SC14141. Th/U ratios vary from 0.46-0.83. The $^{206}Pb/^{238}U$ age is between 152±4 and 163±5 with a Concordia average age of 159.2±1.9 Ma (MSWD =0.46).

(18)SC14142: Medium-fine grained biotite granite (25°29'54"N; 112°53'58"E)

21 analyses were acquired from sample SC14142. Th/U ratios vary from 0.46-0.83. The $^{206}Pb/^{238}U$ age is between 158±4 and 169±5 with a Concordia average age of 162 ±2 Ma (MSWD =0.35).

4.4.1.2 Trace elements geochemistry of zircon

Zircons from Qitianling are rich in Th (238 ppm on average) and U (712 ppm on average) with a Th/U ratio 0.37 on average. Zr/Hf ratios vary between ~35 and ~41. As

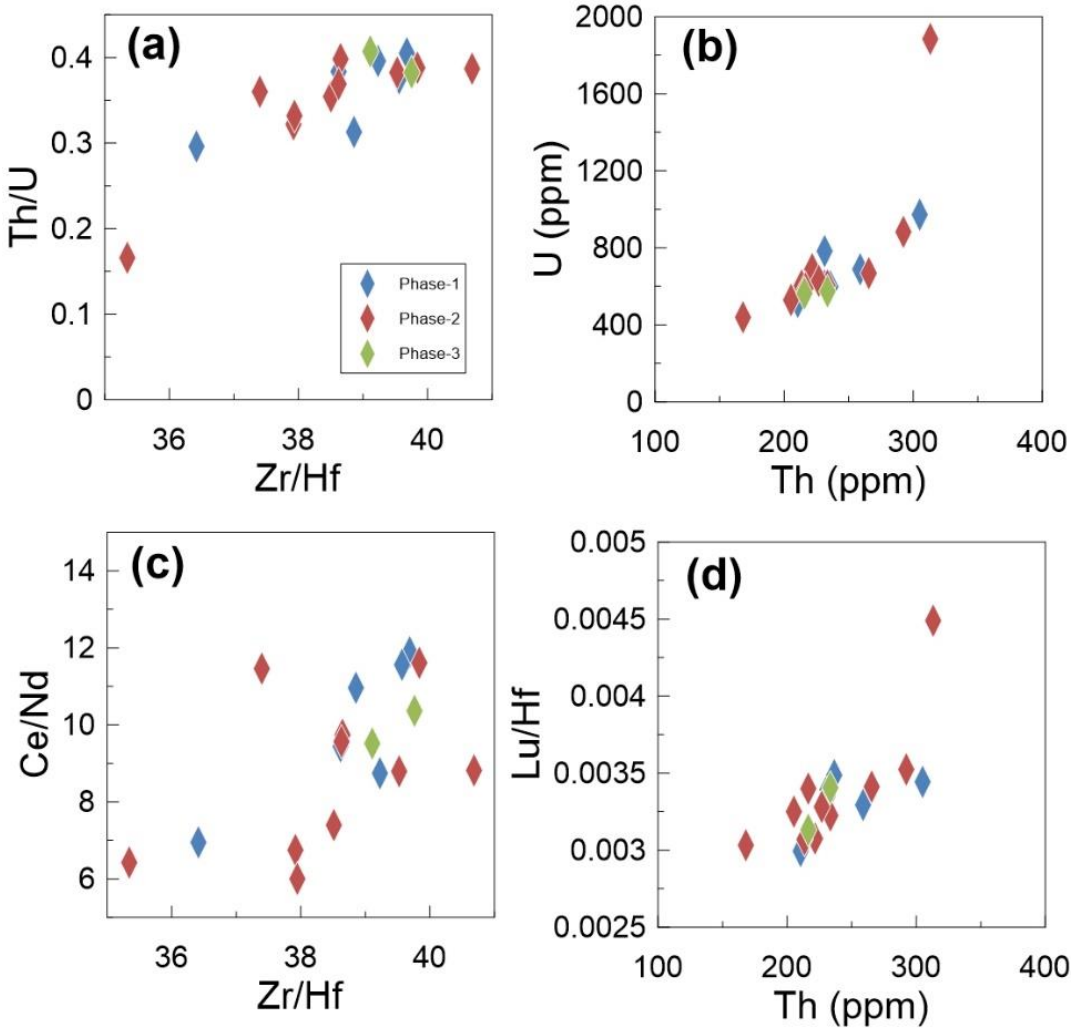

Fig. 4.16 Plot of Th/U *vs* Zr/ Hf (a); and Th *vs* U (ppm) (b); Ce/Nd *vs* Zr/ Hf and Lu/Hf *vs* Th (ppm) of zircons from the Qitianling granites.

the Zr/Hf ratio increases, the Th/U ratio seems also to increase (Fig. 4.16). As expected, HREE contents are higher than LREE. The highest LREE element is Ce, which is up to

~17 ppm while for HREE elements Yb can be up to ~365 ppm.

Like other typical magmatic zircons, in the chondrite normalized REE diagram (Fig. 4.17), all zircons from Qitianling pluton are rich in HREE relative to the LREE with a steeply-rising slope pattern and a La_N/ Yb_N ratio as 0.0014, on average. Besides, zircon displays both positive Ce-anomaly (δCe=18) and negative Eu-anomaly (δEu=0.08). The chondrite normalized REE patterns from the different Qitianling phases (as distinguished in the map) are similar.

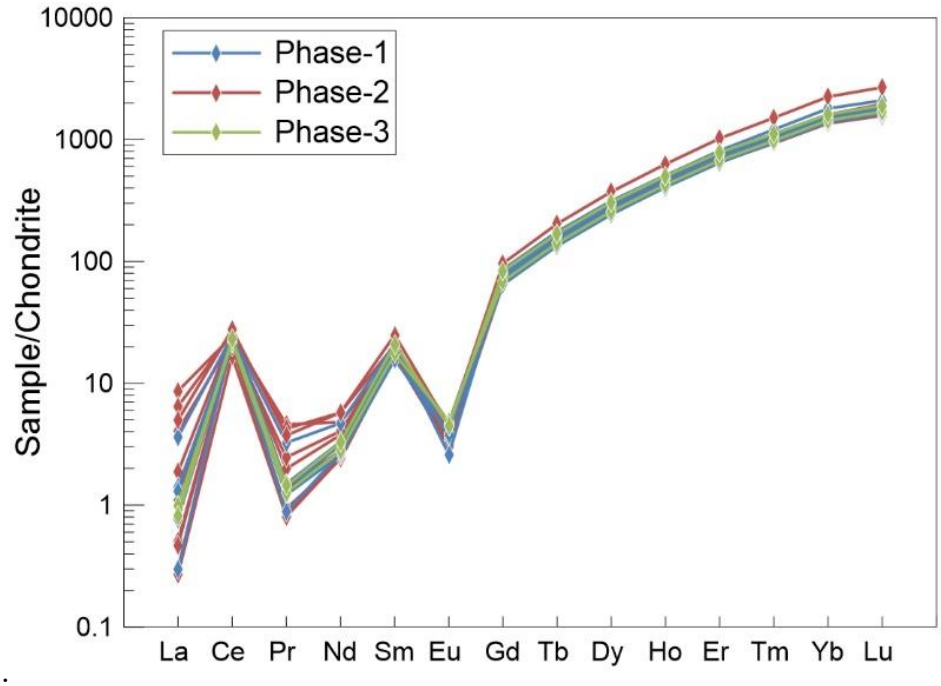

Fig. 4.17 Chondrite-normalized REE diagram of zircons from Qitianling granite.

4.4.2 Geochronology of Amphibole and Biotite

Twelve samples were selected from U-Pb dating samples for ^{40}Ar-^{39}Ar dating. They are QTL04, QTL10, QTL25, SC1442A, SC1445, SC1452, SC1458, SC1462, SC1474, SC1475, SC1477, SC1479. The locations and the lithology characters of them are given above (4.4.1.1). Both amphibole and biotite were picked out from 3 samples (SC1452, SC1458, SC1462), while for the rest of 9 samples, only biotite was picked out for ^{40}Ar-^{39}Ar dating.

The selected amphibole grains were fresh and euhedral. The have a prismatic shape with dark green and black colors. The size of the amphibole grains ranges from 500 μm to 1000 μm in length. The selected biotite grains are sheetlike and are mainly between 500 μm and 1000 μm in length. They are brown to black depending on the thickness of the crystal under the microscope. A highly perfect basal cleavage can be observed often for the biotite. (Fig. 4.18).

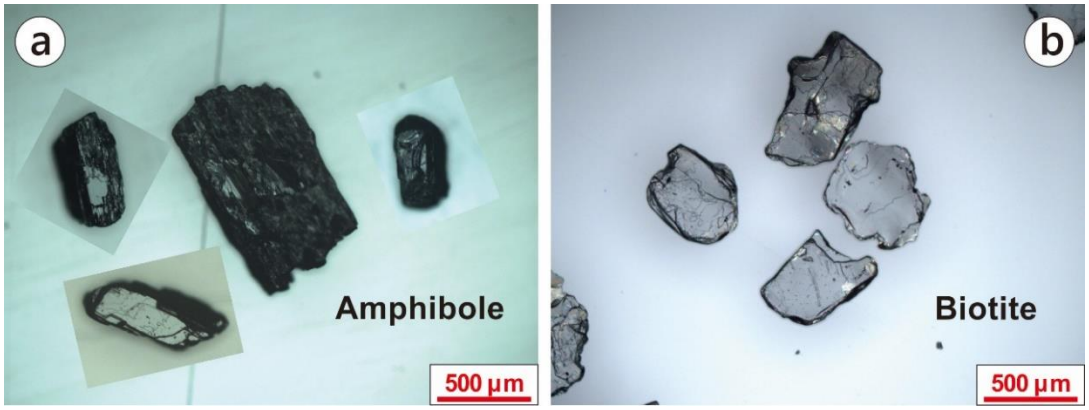

Fig. 4.18 Selected representative biotite and amphibole grains of Qitianling granite.

Analytical methods of ^{40}Ar-^{39}Ar dating are described in Chapter 3 and analytical results of Qitianling granite in detail are shown in Appendix Appendix table 7. All the ^{40}Ar-^{39}Ar isotopic analyses of amphibole from 3 samples gave ages between 151 to 153 Ma while biotite from 12 samples gave age between 151 to 155 Ma. More detailed information of each sample are given below (Fig. 4.19):

(1) SC1452 : ^{40}Ar-^{39}Ar dating of amphibole (N84) yielded a plateau age of 153.4±0.4 Ma. As for biotite, two grains (N88 and N89) were analyzed and gave a plateau age of 151.9 ± 0.5 Ma and 154.0 ± 1.2 Ma, respectively. The final pooled high-temperature age (PHTA) of N88 and N89 is 152.6±0.8 Ma which represents the biotite age of this sample (Fig. 4.19 a-d).

(2) SC1458 : Two grains of amphibole (N82 and N83) were measured and gave ^{40}Ar-^{39}Ar ages at 151.0 ± 0.5 Ma and 152.2 ± 0.7 Ma, respectively. The combined ages of both amphiboles gave the age at 151.5±0.5 Ma. While the three biotite grains yielded the ages of 153.0±0.6 Ma, 151.8 ± 1.1 Ma and 152.4±0.5 Ma, respectively. The final PHTA is 152.6±0.4 Ma for biotite (Fig. 4.19e-k).

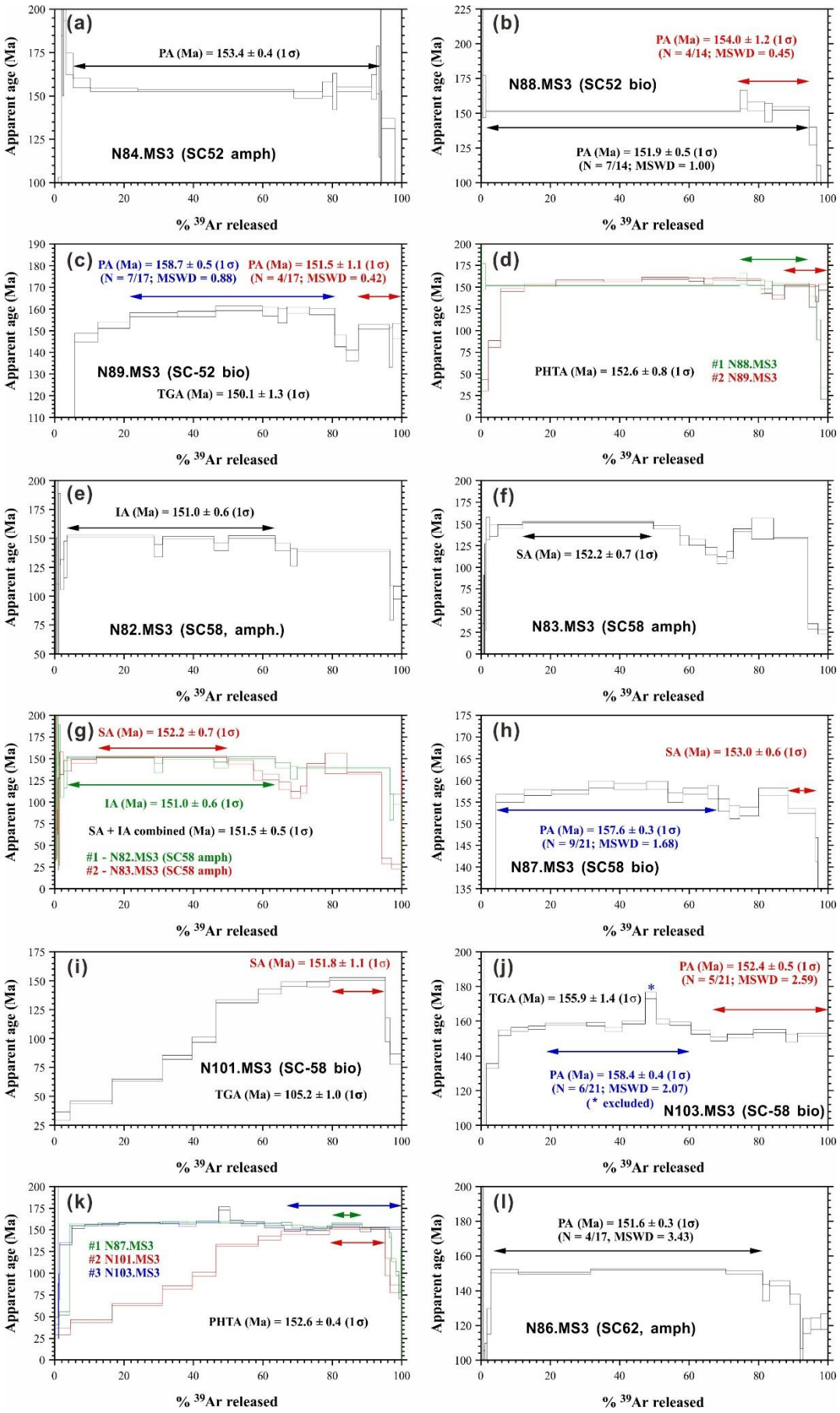
(a)
PA (Ma) = 153.4 ± 0.4 (1σ)
N84.MS3 (SC52 amph)
(b)
PA (Ma) = 154.0 ± 1.2 (1σ)
(N = 4/14; MSWD = 0.45)
N88.MS3 (SC52 bio)
PA (Ma) = 151.9 ± 0.5 (1σ)
(N = 7/14; MSWD = 1.00)
(c)
PA (Ma) = 158.7 ± 0.5 (1σ)
(N = 7/17; MSWD = 0.88)
PA (Ma) = 151.5 ± 1.1 (1σ)
(N = 4/17; MSWD = 0.42)
N89.MS3 (SC-52 bio)
TGA (Ma) = 150.1 ± 1.3 (1σ)
(d)
PHTA (Ma) = 152.6 ± 0.8 (1σ)
#1 N88.MS3
#2 N89.MS3
(e)
IA (Ma) = 151.0 ± 0.6 (1σ)
N82.MS3 (SC58, amph.)
(f)
SA (Ma) = 152.2 ± 0.7 (1σ)
N83.MS3 (SC58 amph)
(g)
SA (Ma) = 152.2 ± 0.7 (1σ)
IA (Ma) = 151.0 ± 0.6 (1σ)
SA + IA combined (Ma) = 151.5 ± 0.5 (1σ)
#1 - N82.MS3 (SC58 amph)
#2 - N83.MS3 (SC58 amph)
(h)
SA (Ma) = 153.0 ± 0.6 (1σ)
PA (Ma) = 157.6 ± 0.3 (1σ)
(N = 9/21; MSWD = 1.68)
N87.MS3 (SC58 bio)
(i)
SA (Ma) = 151.8 ± 1.1 (1σ)
N101.MS3 (SC-58 bio)
TGA (Ma) = 105.2 ± 1.0 (1σ)
(j)
PA (Ma) = 152.4 ± 0.5 (1σ)
(N = 5/21; MSWD = 2.59)
TGA (Ma) = 155.9 ± 1.4 (1σ)
*
PA (Ma) = 158.4 ± 0.4 (1σ)
(N = 6/21; MSWD = 2.07)
(* excluded)
N103.MS3 (SC-58 bio)
(k)
#1 N87.MS3
#2 N101.MS3
#3 N103.MS3
PHTA (Ma) = 152.6 ± 0.4 (1σ)
(l)
PA (Ma) = 151.6 ± 0.3 (1σ)
(N = 4/17, MSWD = 3.43)
N86.MS3 (SC62, amph)
Apparent age (Ma)
% 39Ar released

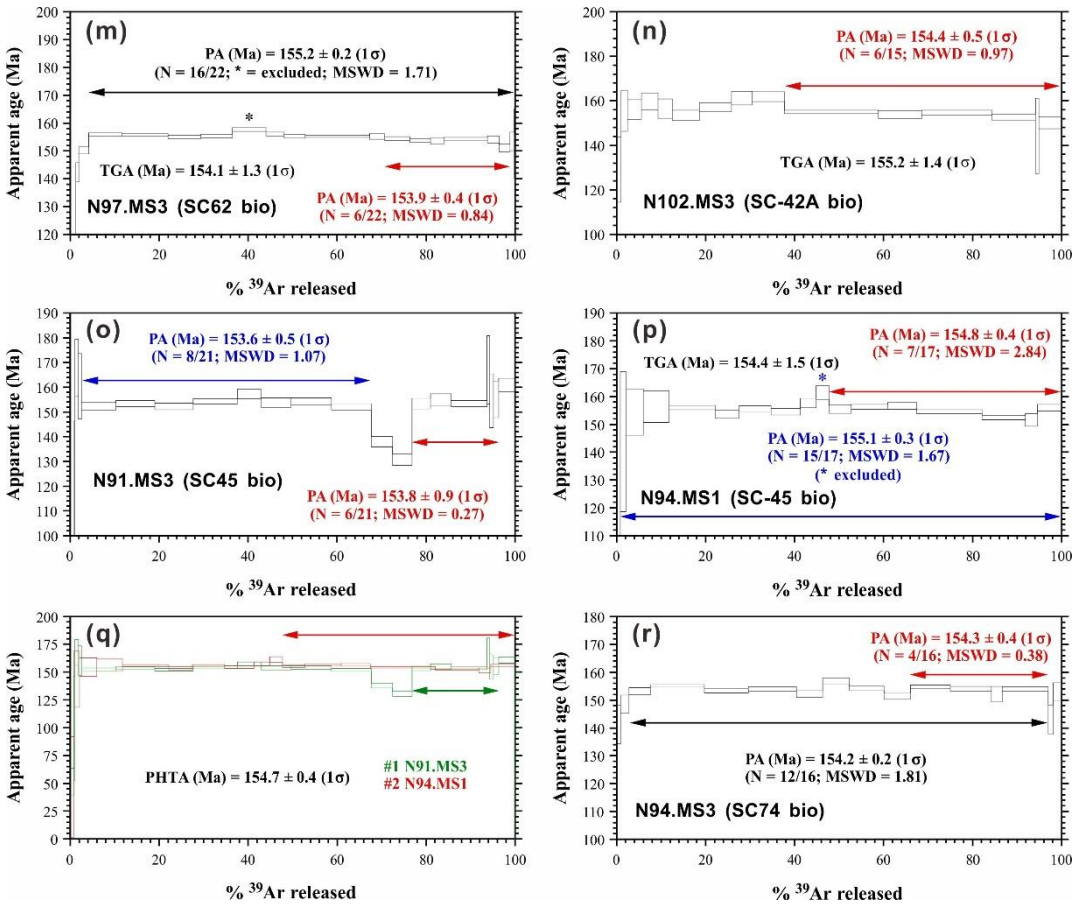

Fig. 4.19 The ^{40} Ar/ ^{39}Ar age spectrum diagrams for selected biotite and amphibole grains of Qitianling granite. (continue)

(3) SC1462 : One amphibole grain (N86) and one biotite grain (N97) were analyzed and gave a plateau age at 151.6 ± 0.3 Ma and 155.2 ± 0.2, respectively (Fig. 4.19i and j).

(4) SC1442A : One biotite grain was analyzed and gave a ^{40}Ar-^{39}Ar plateau age at 155.1± 0.5 Ma (Fig. 4.19n).

(5) SC1445 : Two biotite grains (N91 and N94.MS1) were analyzed and gave a ^{40}Ar-^{39}Ar plateau age of 153.8±0.9 Ma and 154.8±0.4, respectively. The final PHTA is 154.7±0.4 Ma for biotite (Fig. 4.19o-q).

(6) SC1474 : One biotite grain (N94.MS3) was analyzed and gave a ^{40}Ar-^{39}Ar plateau age of 154.3± 0.4 Ma (Fig. 4.19r).

(7) SC1475 : Two biotite grains (N93 and N104) were analyzed and the ^{40}Ar-^{39}Ar plateau ages are 152.2± 0.6 Ma and 151.7± 1.1 Ma which gave a final PHTA at 152.1±0.5 Ma for biotite (Fig. 4.19s-u).

(8) SC1477 : One biotite grain (N95) gave a ^{40}Ar-^{39}Ar plateau age at 154.1± 0.2 Ma(Fig. 4.19v).

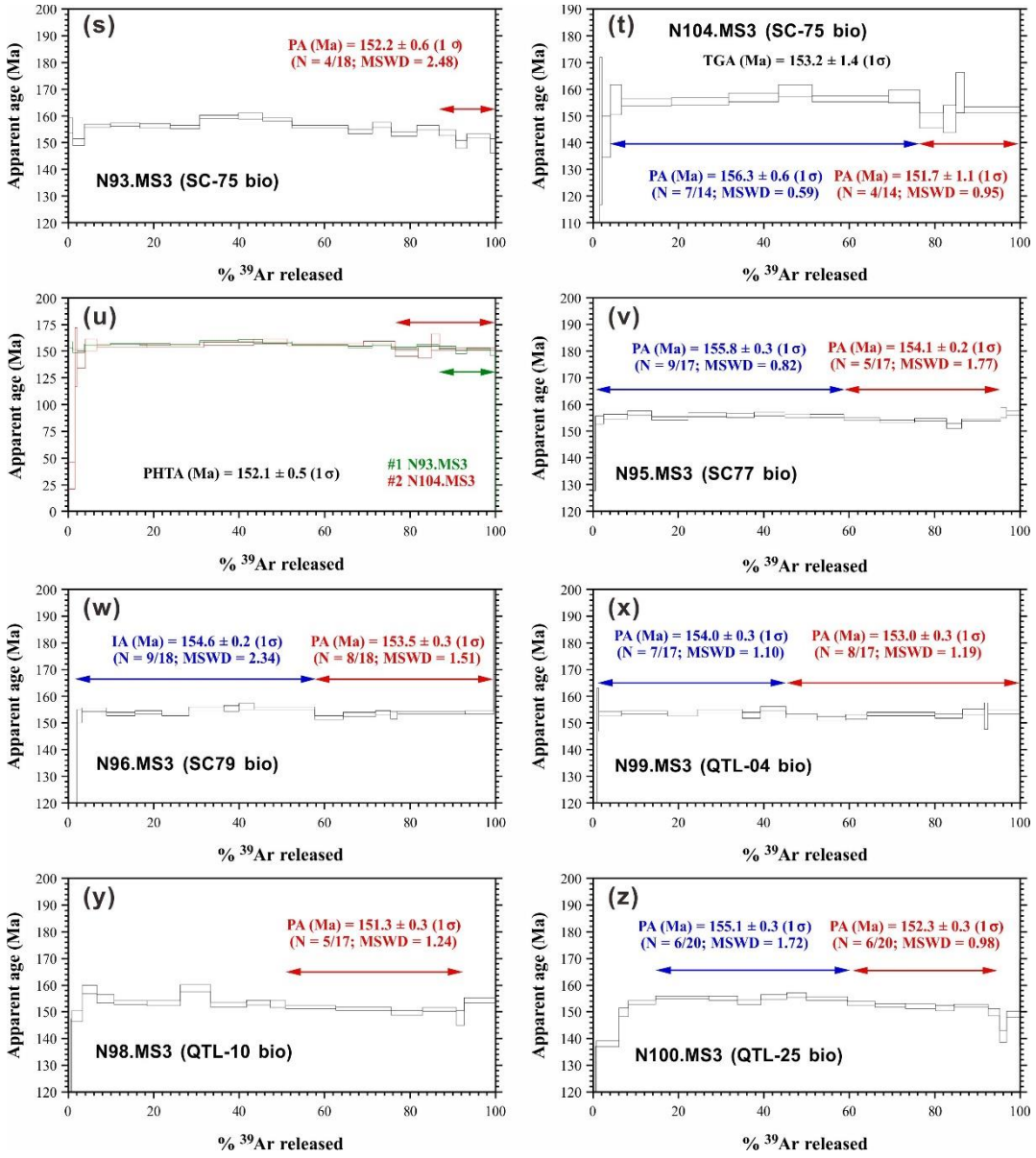

Fig. 4.19 The ^{40} Ar/ ^{39}Ar age spectrum diagrams for selected biotite and amphibole grains of Qitianling granite.

(9) SC1479 : One biotite grain (N96) gave a ^{40}Ar-^{39}Ar plateau age at 153.5± 0.3 Ma (Fig. 4.19w).

(10) QTL04 : One biotite grain (N99) gave a ^{40}Ar-^{39}Ar plateau age at 153.0± 0.3 Ma (Fig. 4.19x).

(11) QTL10 : One biotite grain (N98) gave a ^{40}Ar-^{39}Ar plateau age at 151.3± 0.3 Ma (Fig. 4.19y).

(12) QTL25 : One biotite grain (N100) gave a ^{40}Ar-^{39}Ar plateau age at 152.3± 0.3 Ma (Fig. 4.19z).

The different ages of Qitianling granite are summarized in table 4.1. The significance of these ages dates is discussed later in this chapter.

Sample	Phase	Lab#	Preferred age (Ma) (Ma ± 1 σ)		Final/Pooled age (Ma ± 1 σ)	U/Pb age (Ma ± 1 σ)
SC52	Amp	N84.MS3	PA	153.4±0.4	**153.4±0.4**	157.4±1.4
	Bt1	N88.MS3	HTPA	154.0±1.2	**152.6±0.8**	
	Bt2	N89.MS3	HTPA	151.5±1.1		
SC58	Amp1	N82.MS3	IA	151.0±0.6	**151.5±0.5**	157.2±1.4
	Amp2	N83.MS3	SA	152.2±0.7		
	Bt1	N87.MS3	SA	153.0±0.6	**152.6±0.4**	
	Bt2	N101.MS3	SA	151.8±1.1		
	Bt3	N103.MS3	PA	152.4±0.5		
SC62	Amp	N86.MS3	PA	151.6±0.3	**151.6±0.3**	158.3±1.4
	Bt	N97.MS3	HTPA	153.9±0.4	**153.9±0.4**	
SC42A	Bt	N102.MS3	HTPA	154.4±0.5	**154.4±0.5**	155.0±1.9
SC45	Bt1	N91.MS3	HTPA	153.8±0.9	**154.6±0.4**	154.7±1.9
	Bt2	N94.MS1	HTPA	154.8±0.4		
SC74	Bt	N94.MS3	HTPA	154.3±0.4	**154.3±0.4**	157.9±1.7
SC75	Bt1	N93.MS3	HTPA	152.2±0.6	**152.1±0.5**	154.0±2.0
	Bt2	N104.MS3	HTPA	151.7±1.1		
SC77	Bt	N95.MS3	HTPA	154.1±0.2	**154.1±0.2**	154.7±1.7
SC79	Bt	N96.MS3	HTPA	153.5±0.3	**153.5±0.3**	156.0±2.0
QTL04	Bt	N99.MS3	HTPA	153.0±0.3	**153.0±0.3**	155.9±1.6
QTL10	Bt	N98.MS3	HTPA	151.3±0.3	**151.3±0.3**	152.9±2.6
QTL25	Bt	N100.MS3	HTPA	152.3±0.3	**152.3±0.3**	154.0±2.0

Table 4.1 Summary of ^{40}Ar-^{39}Ar ages of amphibole and biotite from 12 Qitianling granite samples comparing with the zircon U-Pb ages. PA = plateau age; IA = integrated age; SA = single-step age; PHTA = pooled high-temperature age.

4.5 Discussion

4.5.1 Classification of Qitianling granites: A-type

In 1974, Chappell and White first proposed that granites fall into two main types, depending on their source protoliths: I-types have igneous protoliths while S-types have

sedimentary protoliths. Subsequently, one more granite type, M-type, was defined to quote granites derived directly from mantle magmas or subducted oceanic crust. The definition of A-type granites was then proposed first by Loiselle and Wones in 1979. The criteria of A-type granites include the tectonic setting and the geochemical characteristics, i.e. they are not directly related to the protolith: “anorogenic”, “alkaline” and “anhydrous” are the key terms typifying A-type granites. On the basis of trace elements (Rb, Ce, Y, Nb, Sc, Zr, Hf, Ta, Ga), Eby (1990, 1992) further subdivided A-type granites into the A1 subtype (with trace elements similar to oceanic-island basalts) and the A2 subtype (A1,Y/Nb<1.2 and A2,Y/Nb>1.2), with trace elements similar to continental crust or island-arc basalts. Generally, A1 subtypes are emplaced in continental rift environments or associated with mantle plumes or hot spots and mainly derive from a mantle source with limited crustal contribution: while A2 subtype granites are mainly emplaced in post-collisional or post-orogenic environments and derive from continental crust with minor mantle contamination. The consensus now is that A-type granites are not only peralkaline but also metaluminous and sometimes even peraluminous (King et al., 1997). Peralkaline A-type granites are characterized by alkali mafic minerals including riebeckite, arfvedsonite and sodic pyroxene. Aluminous A-type granites often contain annite and Fe-rich calcic- or sodic-calcic amphibole (Wu et al., 2002). The geochemistry of A-type granites is also characterized by high FeO_T/MgO ratios, high halogen (F, Cl) and HFSE (Zr, Nb, Y) contents (Bonin, 1978, 2007; Collins et al., 1982; Whalen et al., 1987; Rajesh, 2000; Martin, 2006). Available experimental works indicate that A-type granites can be also relatively rich in H_2O (> 2 wt. %) (e.g. Clemens et al., 1986; Dall’Agnol et al., 1999; Klimm et al., 2003; Bogaerts et al., 2006).

As mentioned before, Qitianling granites are mainly metaluminous (A/CNK =1 on average) with high contents of alkalis ($Na_2O + K_2O$=7.3 on average) being rather rich in LILE (Rb=478 ppm, Sr=107 ppm, Ba=301ppm on average) and HFSE (Zr=215 ppm, Nb=33 ppm, Ce=134 ppm, Y=44 ppm on average). The total REE is up to 665 ppm and

Ga is 22.43 ppm on average. In the diagram (Na_2O + K_2O) vs 10000Ga/Al and Zr+Nb+Ce+Y -10000Ga/Al (Fig. 4.20), almost all data, including the mafic enclaves, plot in the field of A-type granites (Whalen et al., 1987).

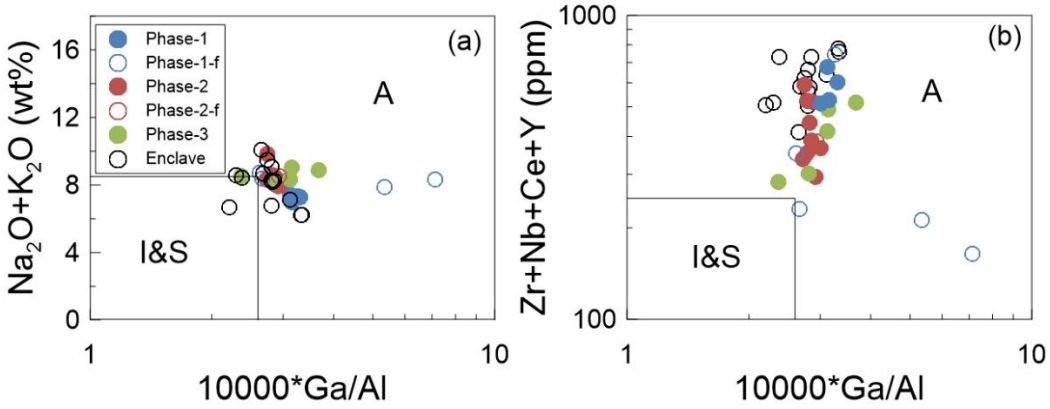

Fig. 4.20 Plot of (Na_2O + K_2O) *vs* 10000Ga/Al and Zr+Nb+Ce+Y *vs* 10000Ga/Al of the Qitianling granites and mafic enclave after Whalen et al., 1987. A: A-type granite, I: I- type granite; S: S-type granite.

According to the subdivision criteria of A-type granite by Eby 1992, most of the compositions of Qitianling granites and mafic enclaves belong to the A2 subtype granite though some mafic enclaves and two fine-grained granites from phase-1 plot within the field of A1 subtype (Fig. 4.21). One of these fine-grained granite, from the northern part of Qitianling pluton and near to Xintianling tungsten ore deposit, has a very low content of Nb and REE. The A2 subtype field indicates that Qitianling granite has a mostly a continental crust source with a small mantle contribution.

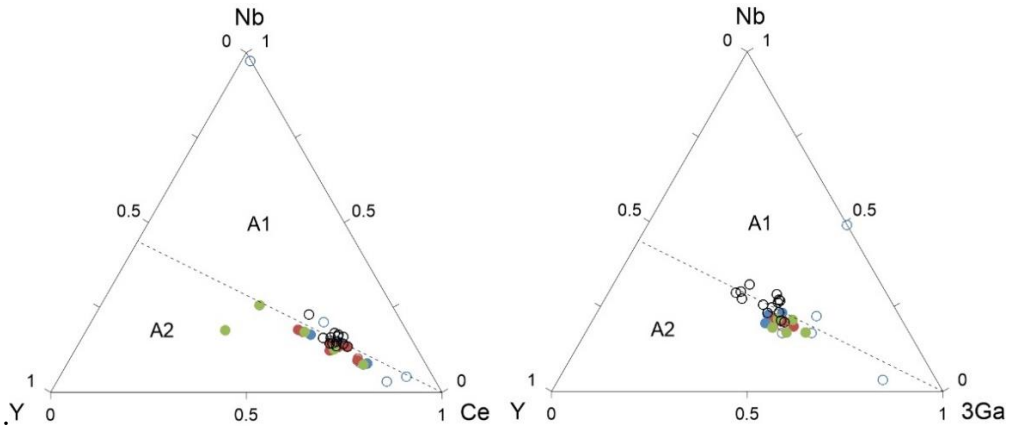

Fig. 4.21 Plot of Qitianling granite and mafic enclave in (a) Ce-Nb-Y and (b) 3*Ga-Nb-Y diagrams of Eby (1992) for subdivision of A1-type and A2-type granites.

As for the tectonic environment during their production, trace element discrimination diagrams proposed by Pearce et al., 1984, show that Qitianling granites and associated enclaves fall mostly in the field of the "within plate granites" (WPG) area and only a few samples plot within the syn-collision (syn-COLG) and volcanic arc (VAG) fields (Fig. 4.22).

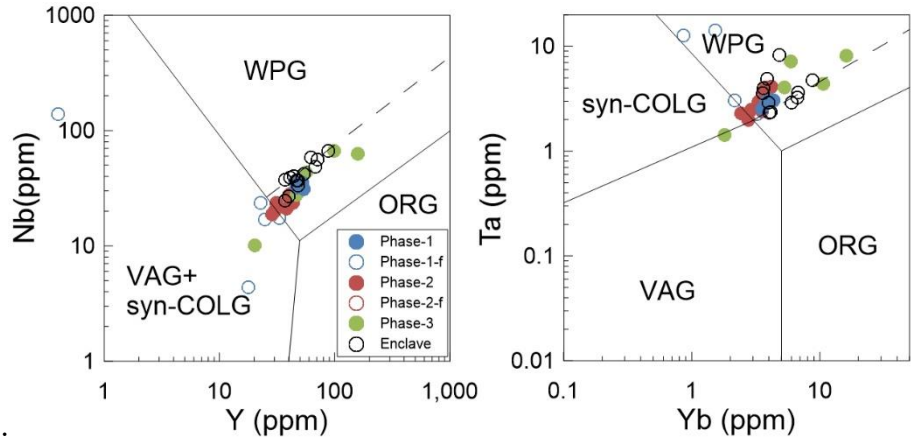

Fig. 4.22 Plot of Nb *vs* Y (a) and Ta *vs* Yb (b) discriminant diagrams for syn-collision granites (syn-COLG), volcanic arc granites (VAG), within plate granites (WPG) and ocean ridge granites (ORG) for Qitianling granites and mafic enclave. The dashed line represents the upper compositional boundary for ORG from anomalous ridge segments (after Pearce et al., 1984).

4.5.2 Temperature, pressure, oxygen fugacity condition constraints from natural mineral compositions

4.5.2.1 Temperature conditions

Temperature is an essential factor controlling magma emplacement. Watson and Harrison (1983) have experimentally calibrated the zirconium concentration in silicate melts saturated in zircon. They found that the temperature of zircon saturation varies with the melt composition and derived the following empirical equation:

$$\ln D_{Zr}^{zircon/melt} = \{- 3.80 - [0.85(M - 1)]\} + 12900/T,$$

with M= cation ratio (Na + K + 2Ca)/ (Al- Si) (see Hanchar and Watson, 2003). We

used this method to provide a first estimate of the temperature of Qitianling granites (Appendix table 1). The zircon-saturation temperature of Qitianling varyies from 636°C to 877°C with an average value of 796°C. In detail, phase-1, phase-2 and phase-3 granites yield 830°C, 809 °C and 785 °C on average, respectively. In addition, even though mafic enclaves contain much more mafic minerals compared to granites, and have higher zirconium content than granites, their calculated zircon-saturation temperatures vary from 741°C to 826 °C, with an average of 796 °C, which is essentially identical to that of the host granites. This reflects the strong compositional control on zircon saturation as expressed by the M parameter in the equation above (M=2.15 on average for mafic enclaves and 1.46 for granites).

What is more, amphibole is often observed in some intermediate-acid granites of Qitianling pluton. On the basis of mineral intergrowth association and textural observations, amphibole is usually inferred to be a rather early crystallized mineral. A first direct evidence was provided by the crystallization experiment conducted by Bowen (1956), later confirmed by, for instance, Dall'Agnol et al (1999). Therefore, the crystallization temperature of magmatic amphibole can be regarded as a proxy of the emplacement temperature for amphibole-bearing granites. Accordingly, two amphibole thermometers were used for the Qitianling pluton in this study. The first is the amphibole-plagioclase thermometer proposed by Holland and Blundy (1994): we used the reaction: edenite + albite = richterite + anorthite, to calculate temperatures of amphibole-bearing granites. Representative amphiboles from phase-1 yield a temperature range between 742 °C and 828°C whereas for phase-2, the temperature is between 655 °C and 739°C.

The second amphibole thermometer has been proposed by Putirka (2016), with the following equation:

$$T(°C) = 1781 - 132.74[Si^{Amp}] + 116.6[Ti^{Amp}] - 69.41[Fe_t^{Amp}] + 101.62[Na^{Amp}]$$

The temperature range of phase-1 varies from 725 °C to 782°C with an average value of 759 °C, while for phase-2 retrieved temperatures are a bit lower varying from 720 °C to 779°C with an average temperature of 743°C.

That zircon has a higher temperature (830 °C on average for phase-1) compared to amphibole (780 °C on average for phase-1), may simply reflect that zircon crystallize earlier (zircon often occurs as inclusions in rock-forming minerals). The above evidence led us to conclude that the Qitianling magma experienced a temperature of at least 800 °C during its crystallization.

4.5.2.2 Pressure of emplacement

Amphibole is also a mineral which is sensitive to pressure. Different amphibole barometers have been proposed relating the Al_{tot} of amphibole to pressure. The results for Qitianling pluton are shown on Fig. 4.23 and listed in table 4.2.

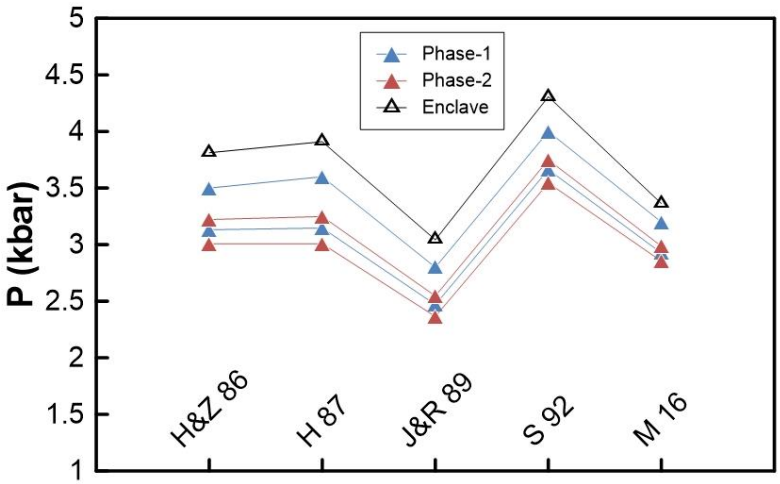

Fig. 4.23 Plot of calculated average pressure results of amphiboles from the Qitianling granites and enclave by different geobarometers. The amphibole compositional data of enclaves are from Zhao et al., 2012. The information on different barometers is given in Table 4.3.

Al_{tot} ranges from 1.2 to 1.7 for phase-1 and from 1.3 to 1.8 for phase-2 while for the mafic enclaves, the range is narrower (Al_{tot} 1.5-1.6). Of the different barometers (Fig. 4.23), that of Johnson and Rutherford, 1989 gives a lowest pressure (2.7 kbar on

average for phase-1; 2.5 kbar on average for phase-2; 3 kbar on average for mafic enclave) while that from Schmidt, 1992 gives the highest pressure: phase-1: 3.9 kbar, phase-2: 3.6 kbar and mafic enclave: 4.3 kbar.

Altogether, the calculations above suggest that the emplacement pressure of Qitianling pluton was around 3.2±1 kbar.

Barometer (in kbar)	Phase-1		Phase-2		E
	QTL-38C	SC14-42	QTL-14A	QTL-13	
Hammarstrom & Zen 86	3.5 (2.7-4.7)	3.1 (2.2-3.7)	3.2 (2.5-4.3)	3.0 (2.5-3.8)	3.8 (3.6-4.1)
Hollister et al. 87	3.6 (2.7-4.6)	3.1 (2.1-3.8)	3.2 (2.5-4.5)	3.0 (2.4-3.9)	3.9 (3.7-4.2)
Johnson & Rutherford 89	2.8 (2.1-3.8)	2.5 (1.7-3.0)	2.5 (2.0-3.5)	2.4 (1.9-3.1)	3.0 (2.9-3.2)
Schmidt 92	4.0 (3.2-5.1)	3.7 (2.8-4.2)	3.7 (3.1-4.8)	3.5 (3.1-4.3)	4.3 (4.1-4.5)
Mutch et al. 2016	3.2 (2.7-4.0)	2.9 (2.4-3.3)	3.0 (2.6-3.7)	2.9 (2.5-3.4)	3.4 (3.2-3.5)
Average	3.4	3.1	3.1	3.0	3.7

Table. 4.2 Pressure calculation results using the amphiboles from the Qitianling granites and enclaves and different geobarometers.

Hammarstrom and Zen, 1986 : $P= -3.92+5.03*Al_{tot}$;

Hollister et al., 1987: $P= -4.76+5.64* Al_{tot}$;

Johnson and Rutherford, 1989 : $P= -3.46+4.23* Al_{tot}$;

Schmidt, 1992: $P= -3.01+4.76* Al_{tot}$;

Mutch et al., 2016: $P= 0.5+0.3318* Al_{tot} +0.9954*(Al_{tot})^2$;

The amphibole compositional data of enclaves are from Zhao et al., 2012.

4.5.2.3 Redox state

The redox state is also a parameter of utmost importance (e.g., Dall'Agnol et al., 1999), in particular whenever ore processes associated to granite magmas are concerned.

Different redox states may have a huge influence on mineralization processes. As we know, a large-scale tin deposit (Furong) is located inside the Qitianling pluton. Constraining the oxygen fugacity condition prevailing during Qitianling magma crystallisation can help us to better understand the tin-deposits associated to this pluton.

Fe–Ti oxides (magnetite and ilmenite) can be divided into magnetite (Fe_3O_4) - ulvospinel (Fe_2TiO_4) series and hematite (Fe_2TiO_4)-ilmenite ($FeTiO_3$) series solid solutions also termed for short spinel and rhombohedral series, respectively. The phase-equilibrium studies in the system FeO-Fe_2O_3-TiO_2 investigated by Buddington and Lindsley, (1964) have shown that the composition of Fe–Ti oxides pair in equilibriumwith each other is a function of both temperature and oxygen fugacity.

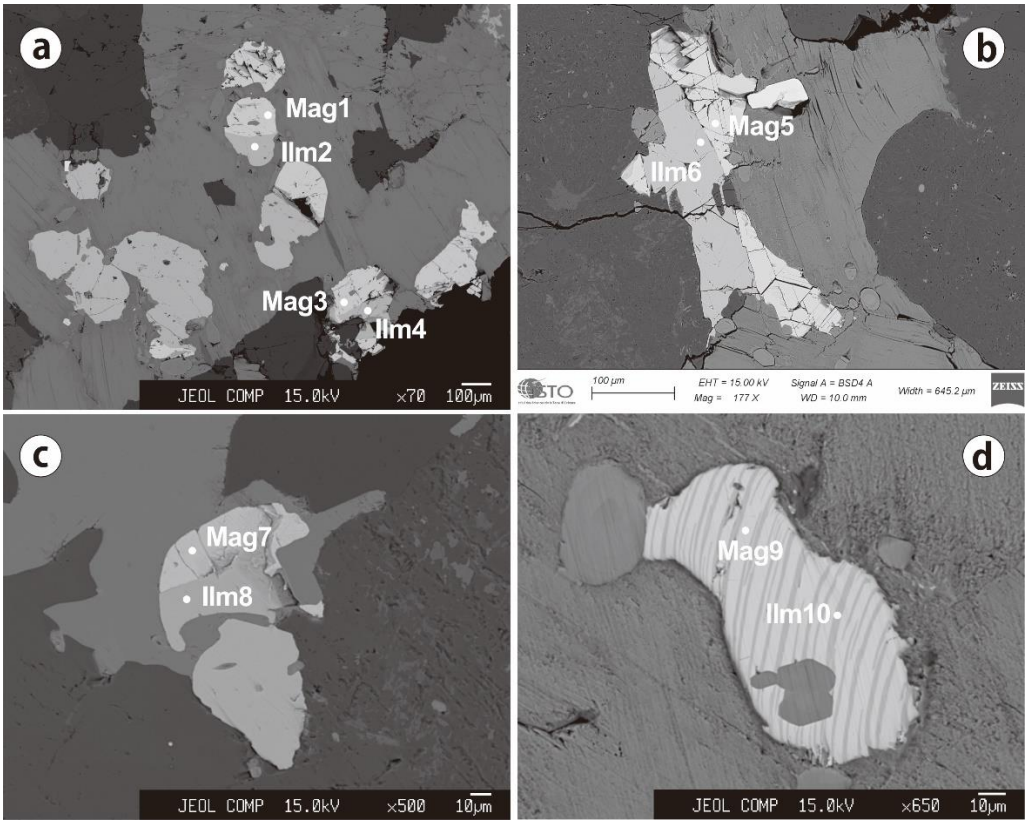

Fig. 4.24 BSE (back-scattered electron) images of magnetite and ilmenite from Phase-1(a, b) and Phase-2 (c, d). Abbreviations: Mag, magnetite; Ilm, ilmenite.

The Fe–Ti oxides of Qitianling pluton are mainly ilmenite and magnetite. Usually ilmenite and magnetite have an intergrowth relationship and occur as inclusions in

	Mag-1	Ilm-2	Mag-3	Ilm-4	Mag-5	Ilm-6	Mag-7	Ilm-8	Mag-9	Ilm-10
SiO2	0.12	0.04	0.12	0.11	0.51	0.06	0.00	0.00	0.00	0.00
TiO2	1.51	48.80	1.02	50.10	0.84	49.35	2.44	50.72	1.13	49.02
Al2O3	0.22	0.02	0.32	0.03	0.27	0.02	0.08	0.01	0.10	0.03
FeO(T)	91.61	45.85	92.95	46.76	92.54	46.91	89.45	48.36	90.32	44.58
MnO	0.18	2.57	0.04	2.96	0.00	2.84	0.27	2.87	0.09	4.98
MgO	0.02	0.02	0.00	0.06	0.10	0.04	0.13	0.01	0.01	0.00
CaO	0.04	0.03	0.03	0.02	0.16	0.02	0.00	0.00	0.00	0.00
Na2O	0.04	0.00	0.01	0.02	0.02	0.05	0.00	0.00	0.00	0.00
K2O	0.07	0.05	0.02	0.02	0.02	0.00	0.00	0.00	0.00	0.00
Sum:	93.81	97.40	94.50	100.07	94.44	99.29	92.37	101.98	91.65	98.61
Calc. Methods:	Mol % Usp	Mol % Ilm	Mol % Usp	Mol % Ilm	Mol % Usp	Mol % Ilm	Mol % Usp	Mol % Ilm	Mol % Usp	Mol % Ilm
C1967	0.048	0.950	0.034	0.950	0.043	0.942	0.071	0.941	0.033	0.941
A1968	0.041	0.947	0.029	0.946	0.024	0.938	0.064	0.938	0.032	0.934
L& S1982	0.044	0.947	0.029	0.946	0.024	0.938	0.072	0.938	0.033	0.934
S1983	0.044	0.949	0.030	0.949	0.024	0.940	0.071	0.940	0.033	0.938
Method1										
X'Usp & X'Ilm	T (°C)		T (°C)		T (°C)		T (°C)		T (°C)	
C1967	502		476		506		548		488	
A1968	494		470		468		543		493	
L& S1982	499		471		468		553		496	
S1983	496		468		465		549		492	
Average:	498		471		477		548		492	
Method2										
X'Usp & X'Ilm from:		log fO_2		log fO_2		log fO_2		log fO_2		log fO_2
C1967	586	-19.95	572	-20.21	595	-19.13	616	-18.74	586	-19.21
A1968	584	-19.77	572	-19.87	577	-19.20	617	-18.47	594	-18.63
L& S1982	586	-19.73	573	-19.87	576	-19.22	622	-18.39	596	-18.60
S1983	584	-19.91	569	-20.17	574	-19.43	619	-18.58	591	-18.92
Average:	585	-19.84	571	-20.03	580	-19.24	619	-18.55	592	-18.84
Method3										
X'Usp & X'Ilm from:		log fO_2		log fO_2		log fO_2		log fO_2		log fO_2
C1967	599		582		609		633		598	
A1968	596	-19.37	582	-19.51	586	-18.85	634	-18.05	606	-18.26
L& S1982	599	-19.32	583	-19.51	586	-18.87	640	-17.96	608	-18.23
S1983	596	-19.50	578	-19.81	583	-19.08	636	-18.14	603	-18.55
Average:	597	-19.40	581	-19.61	591	-18.93	636	-18.05	604	-18.35
Average all	560	-19.65	541	-19.85	549	-19.11	601	-18.33	562	-18.63

Table. 4.3 Temperature and oxygen fugacity calculation results of ilmenite and magnetite from the Qitianling granites by different geothermobarometer.

Different calculation methods of X'Usp & X'Ilm: Carmichael, 1967; Anderson, 1968; Lindsley & Spencer, 1982; Stormer, 1983.

Different geothermobarometer:

Method1 by Powell & Powell, 1977;

Method2 by Spencer & Lindsley, 1981;

Method3 by Andersen & Lindsley, 1985;

biotite. Occasionally, they can occur interstitially along with other rock forming minerals. Ilmenite trellis lamellae exsolution is often observed in magnetite for Qitianling pluton, which is typically regarded as a secondary texture (Dall'Agnol et al. 1997). To explore the redox state of Qitianling pluton, both homogeneous intergrowth ilmenite and magnetite pair and exsolution ilmenite and magnetite pair from phase-1 and phase-2 were chosen for the calculations (Fig. 4.24). We used the program ILMAT:

A Magnetite-Ilmenite Geothermobarometry Program (version 1.20)) of magnetite and ilmenite for estimating the temperature and oxygen fugacity condition (Lepage 2003). The composition of ilmenite and magnetite corresponding to the BSD images (Fig. 4.24) are listed in Table 4.3. The mole proportions of ulvospinel and ilmenite were calculated by different methods from Carmichael, 1967; Anderson, 1968; Lindsley & Spencer, 1982; Stormer, 1983. Using the geothermobarometer of Powell & Powell, 1977; Spencer & Lindsley, 1981; Andersen & Lindsley, 1985, the Fe-Ti oxides temperature of phase-1 is 560 °C on average, whereas for phase-2 it is 582 °C. The corresponding oxygen fugacities fall above the Ni-NiO oxygen buffer which indicates relatively oxidizing conditions. It is worth pointing out that the calculated temperatures are significantly below the solidus temperature of the granite magma system, and it is not known whether these oxygen fugacities still represent the magma redox state (Fig. 4.25).

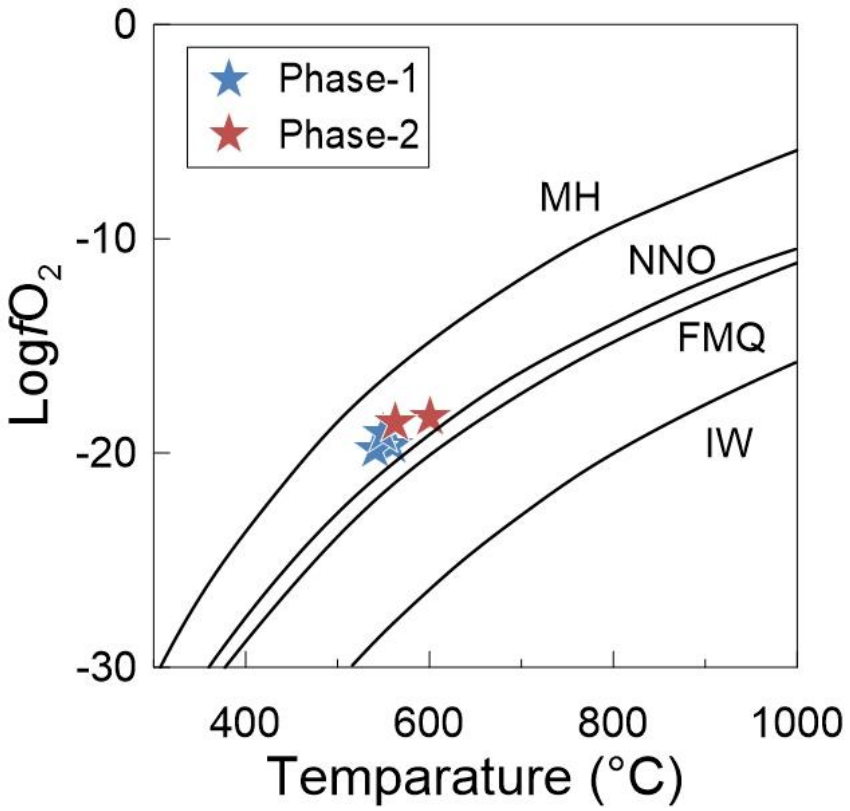

Fig. 4.25 Log oxygen fugacity *vs* Temperature diagram showing the redox state of Qitianling pluton reflected by Ti-Fe oxides. (Modified after Frost, 1991).

(ppm)	La	Ce	Pr	Nd	Sm	Eu	Gd	Dy	Lu	Hf	Zr	zircon
rock QTL-21b	200.00	326.00	29.90	80.80	9.21	0.58	8.69	3.64	0.33	9.98	377	Ce(IV)/Ce(III)
zircon qtl21b-01	0.09	14.59	0.09	1.05	2.47	0.18	12.15	54.04	37.74	12340		55
zircon qtl21b-02	0.02	15.15	0.03	0.96	1.97	0.25	12.24	58.09	39.78	13388		93
zircon qtl21b-03	1.39	13.96	0.44	3.19	3.55	0.21	15.50	78.87	47.57	13129		32
zircon qtl21b-04	0.15	17.73	0.10	1.25	2.87	0.19	17.15	83.65	62.70	14850		81
zircon qtl21b-05	0.07	14.27	0.06	0.80	1.94	0.15	11.73	55.53	39.80	12669		91
zircon qtl21b-06	0.27	12.20	0.09	0.63	1.81	0.09	8.92	44.09	30.76	12256		70
zircon qtl21b-07	0.07	14.18	0.08	0.79	1.45	0.15	10.47	49.45	36.10	13770		145
zircon qtl21b-08	0.35	16.43	0.18	1.57	2.30	0.12	13.26	61.23	47.91	14745		91
zircon qtl21b-09	0.08	12.30	0.08	0.88	2.09	0.15	11.32	52.23	35.16	13031		60
zircon qtl21b-10	0.46	11.54	0.23	1.49	2.50	0.35	14.58	68.29	41.64	12238		46
zircon qtl21b-11	1.59	20.76	0.81	4.02	3.51	0.22	14.84	64.78	45.22	12757		47
zircon qtl21b-12	0.02	9.62	0.06	0.75	2.71	0.33	16.16	70.60	44.66	12679		35
zircon qtl21b-13	0.06	16.44	0.06	1.02	2.80	0.18	13.86	65.18	41.82	12642		53
zircon qtl21b-14	0.91	22.30	0.29	3.31	4.56	0.46	24.58	104.49	66.30	13230		43
zircon qtl21b-15	0.56	17.02	0.24	2.15	2.72	0.25	12.27	58.16	40.62	13798		57
zircon qtl21b-16	0.66	16.77	0.30	2.14	3.15	0.19	17.10	77.10	45.99	12628		47
AV-zircon	0.42	15.33	0.20	1.63	2.65	0.22	14.13	65.36	43.99	13134		65
SD												29
rock QTL-25	69.70	122.00	12.00	36.20	5.57	0.47	4.85	4.21	0.41	5.55	175	
zircon qt25-01	0.11	13.78	0.09	0.87	1.80	0.12	11.20	51.62	36.69	12747		78
zircon qt25-02	0.86	15.79	0.20	1.47	1.84	0.13	8.87	45.56	34.66	13079		82
zircon qt25-03	1.86	16.05	0.42	3.05	2.83	0.13	19.95	100.95	72.55	14623		71
zircon qt25-04	1.30	16.03	0.44	2.53	2.79	0.14	13.12	59.86	39.31	12459		41
zircon qt25-05	0.51	15.76	0.24	2.65	5.43	0.32	27.69	110.37	57.08	12889		15
zircon qt25-06	0.04	13.41	0.06	1.14	2.62	0.22	14.66	68.08	46.10	13670		45
zircon qt25-07	0.04	13.69	0.05	0.70	1.25	0.22	9.10	45.35	33.55	12741		145
zircon qt25-08	0.74	20.23	0.17	2.33	2.81	0.18	15.17	68.20	47.48	14931		61
zircon qt25-09	0.05	7.81	0.10	1.97	4.28	0.20	22.59	88.05	46.38	11538		9
zircon qt25-10	0.05	12.87	0.03	0.76	1.71	0.18	9.47	46.08	35.43	13102		79
zircon qt25-11	0.02	5.40	0.04	1.23	2.93	0.21	15.82	71.48	43.24	12686		13
zircon qt25-12	4.41	23.66	1.24	5.90	3.52	0.19	12.83	57.02	37.39	13499		37
zircon qt25-13	0.29	9.78	0.06	0.65	1.43	0.12	6.94	37.12	29.72	13378		72
zircon qt25-14	0.29	17.40	0.35	3.93	6.22	0.57	27.07	112.10	61.14	13166		13
AV-zircon	0.75	14.40	0.25	2.08	2.96	0.21	15.32	68.70	44.34	13179		54
SD												38
rock QTL-04	80.80	145.00	13.80	43.30	7.26	0.26	7.03	6.23	0.69	6.51	195	
zircon qtl04-01	0.07	11.11	0.03	0.62	1.26	0.14	7.97	42.37	34.21	12494		102
zircon qtl04-02	0.15	15.09	0.09	0.90	1.99	0.17	10.94	54.32	36.83	11383		60
zircon qtl04-03	0.49	17.13	0.18	1.57	2.42	0.19	11.87	56.12	42.01	14031		54
zircon qtl04-04	0.58	15.45	0.16	1.58	2.56	0.17	13.40	63.33	37.56	11155		38
zircon qtl04-05	0.03	13.16	0.05	0.75	1.64	0.16	9.81	48.11	34.14	13530		71
zircon qtl04-06	0.25	14.93	0.09	1.48	2.82	0.20	14.21	65.83	41.79	13288		33
zircon qtl04-07	0.07	12.66	0.08	1.14	2.73	0.34	13.88	59.80	37.13	11780		27
zircon qtl04-08	1.35	20.44	0.39	2.55	2.52	0.14	13.79	62.98	45.02	14721		63
zircon qtl04-09	0.56	20.35	0.24	1.84	2.71	0.25	15.92	76.00	54.13	15989		64
zircon qtl04-10	0.09	18.00	0.14	1.34	2.80	0.22	14.75	67.26	42.93	14379		42
zircon qtl04-11	0.03	13.75	0.05	0.92	2.09	0.18	12.53	60.41	39.49	13137		53
zircon qtl04-12	0.06	9.58	0.10	1.78	3.77	0.29	19.77	83.66	45.96	12532		13
zircon qtl04-13	0.16	11.27	0.08	1.19	2.48	0.26	15.20	70.29	45.39	14779		35
zircon qtl04-14	0.48	15.46	0.23	1.18	2.12	0.23	11.76	59.33	42.31	14836		62
zircon qtl04-15	0.57	17.32	0.44	2.40	2.47	0.21	12.00	57.67	40.29	13563		50
zircon qtl04-16	0.13	9.23	0.08	1.15	3.55	0.39	17.52	81.20	48.64	13367		15
AV-zircon	0.32	14.68	0.15	1.40	2.50	0.22	13.46	63.04	41.74	13435		49
SD												23

Table. 4.4 Zircon and whole-rock trace-element data with calculated Ce^{4+}/Ce^{3+} ratios in zircon.

Besides Fe–Ti oxides, zircon has been shown to be a potential proxy for inferring magma oxidation state (Ballard et al., 2002; Trail et al., 2011, 2012; Smythe and Brenan,

2016). As an accessory mineral, zircon is relatively stable and durable, with high contents of REE (usually is HREE) in particular Ce. Usually, Ce is present in zircon as either Ce^{4+} or Ce^{3+}, Ce^{4+} being more compatible when compared to Ce^{3+} because its ionic radii (0.97 Å) is similar to that of Zr^{4+} (0.84 Å) (Shannon, 1976; Hoskin and Schaltegger, 2003). Therefore, the Ce^{4+}/Ce^{3+} ratio in zircon may mirror the redox state of the coexisting melt (Ballard et al., 2002; Trail et al., 2011, 2012).

We used the method of Ballard et al., 2002 on zircons from Qitianling to estimate the Ce^{4+}/Ce^{3+} ratio (for details on the calculation procedure see Ballard et al., 2002). The results are shown in the Table 4.4. Sample QTL-21b from phase-1 has a Ce^{4+}/Ce^{3+} ratio at 65 on average (SD=29), while for sample QTL-25 from phase-2 and sample QTL-04 from phase-3 are 54 (SD=38) and 49 (SD=23), respectively. Those ratios are relatively low when compared to those of zircons of intrusions associated to porphyry copper deposits in northern Chile: these display a Ce^{4+}/Ce^{3+} ratio >300 (Ballard et al., 2002). The low value of Ce^{4+}/Ce^{3+} ratio in zircon of Qitianling pluton hence suggests that the magma system of Qitianling may have a rather reduced oxygen fugacity.

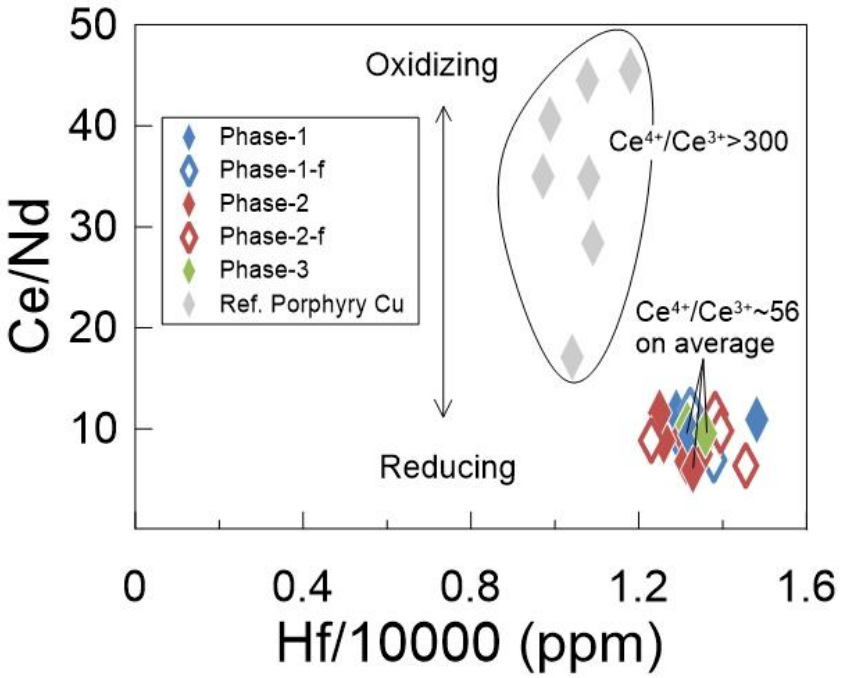

Fig. 4.26 Plot of Ce/Nd *vs* Zr/10000 of zircons from the Qitianling granites and Chile. Reference data are from porphyry copper deposits of northern Chile (Ballard et al., 2002).

Similar evidence come when using the works of Trail et al (2011) and Chelle-Michou et al (2014). Trail et al (2011) experimentally confirmed that the Ce anomaly ($(Ce/Ce^*)_N = Ce_N / (La_N * Pr_N)^{1/2}$) is indeed a function of oxygen fugacity. Because the La and Pr contents in zircon are very low, Chelle-Michou et al (2014) suggested that Ce/Nd ratio can be used as a proxy for the zircon Ce anomaly. On Fig 4.23, we compare the data from porphyry copper deposits of northern Chile (arc setting) and Qitianling: except for one sample which has a Ce/Nd ratio around 17, all Chilean samples have Ce/Nd ratio higher than 25 and the highest is up to ~45. In contrast the Ce/Nd ratios from Qitianling are all below 12 which suggest that the oxygen fugacity of Qitianling magma was rather reduced when compared to those from Chile (Fig. 4.26).

4.5.3 Geochronological constraints on Qitianling pluton

4.5.3.1 Emplacement age

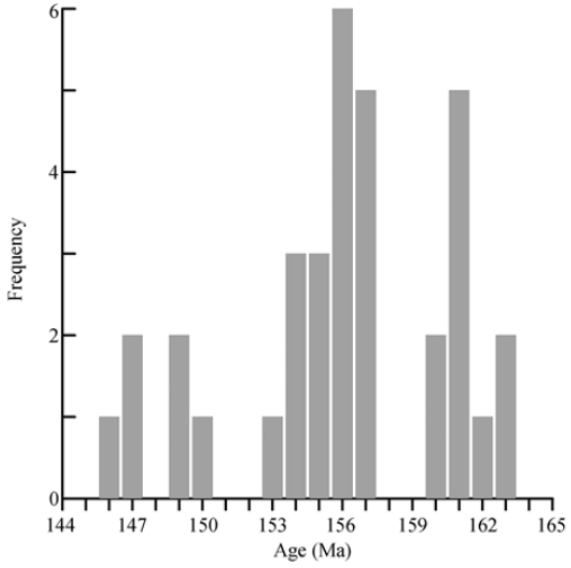

Fig. 4.27 Histogram of Zircon U-Pb ages for Qitianling pluton (Zhu et al., 2009).

Zhu et al (2009) carried out a systematic age study on Qitianling pluton. Using the analyses of 32 samples and available literature data (Li et al., 2006; Zhu et al., 2003; Zhu et al., 2005; Fu et al., 2004; Li et al., 2005; Zhao et al., 2006), they concluded that

Qitianling is a multi-stage composite pluton. Three main emplacement stages were defined: 163-160 Ma, 157-153 Ma and 150-146 Ma (Fig. 4.27), broadly corresponding to three rock types: hornblende-biotite monzonitic granites for the first stage; biotite±amphibole granites for the second stage and fine-grained (locally porphyritic) biotite granites for the third stage.

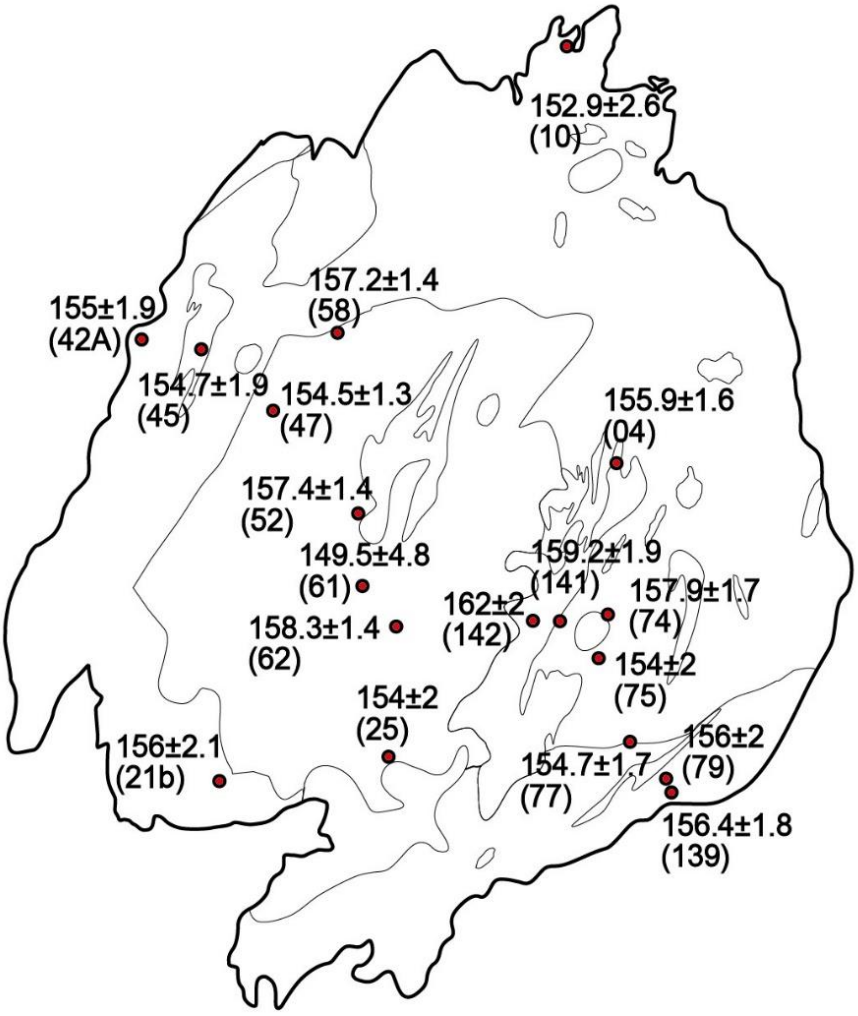

Fig. 4.28 Zircon U-Pb ages distribute in different Phases.

For this study, we have selected 18 samples to further explore the emplacement age of Qitianling pluton, in order to confirm whether the pluton was constructed during three major pulses. The distribution of all 18 samples is shown on Fig. 4.28. Among those samples, 6 samples from phase-1 (including 2 fined- grain samples) have ages varying between 159 Ma and 152 Ma with an average age of 156 Ma. The 10 samples

from phase 2, including 4 fined- grain samples, have ages between 158 Ma and 150 Ma with an average age 155 Ma. The 2 samples from phase-3 yield an age of 162 Ma and 156 Ma.

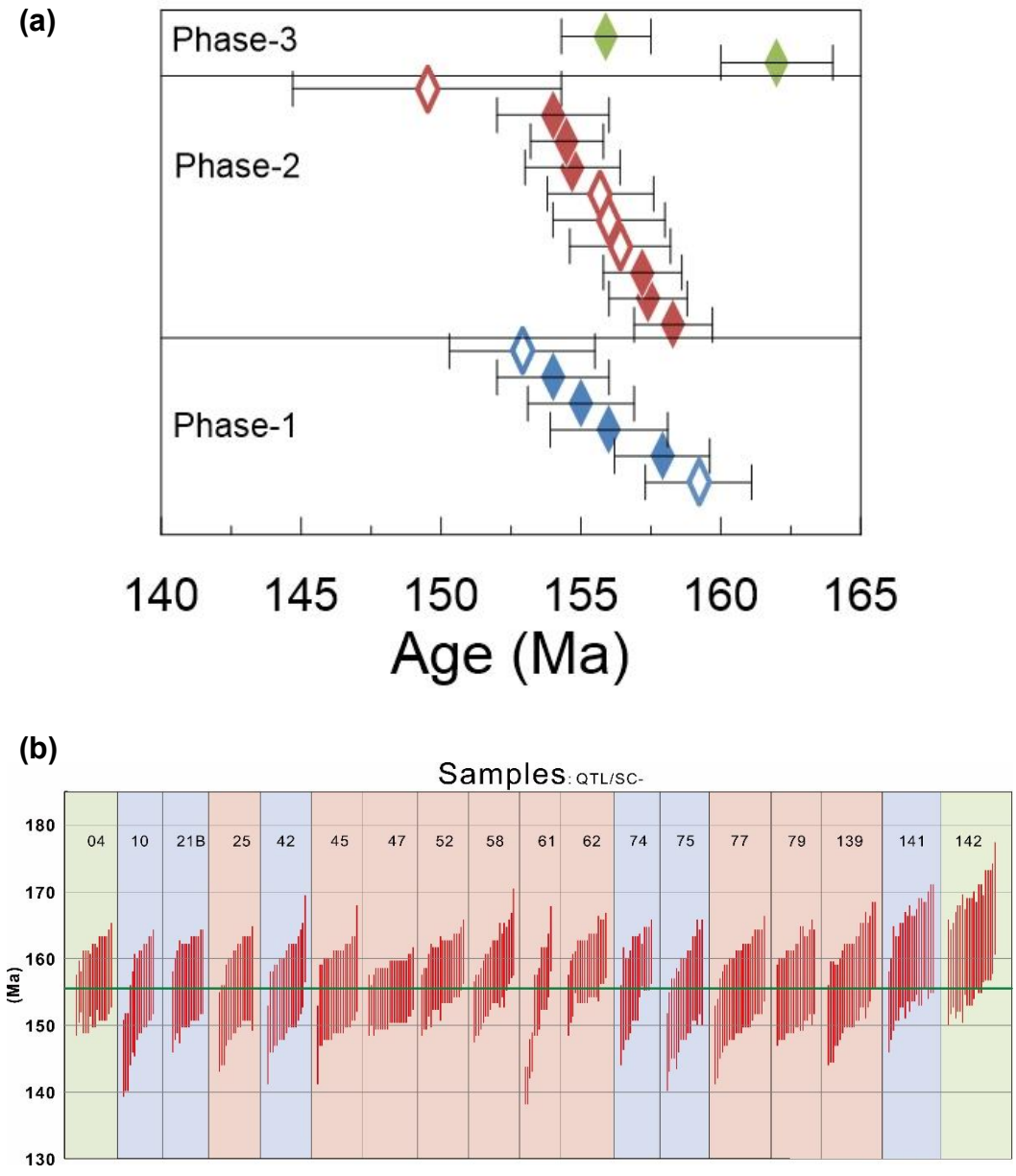

Fig. 4.29 Zircon Concordia U-Pb ages (a) and weighted mean ages (b) from different Phases. The Symbols in (a) are as in Fig. 4.26.

Fig. 4.29 a shows the age distribution obtained for each phase. Clearly our new data indicate that there is considerable time overlap between phases 1, 2 and 3, most of the ages falling in the time interval 150-160 Ma with an average age at 156 Ma (Fig. 4.29 b). Hence, our data do not confirm the proposal made by Zhu et al (2009). In

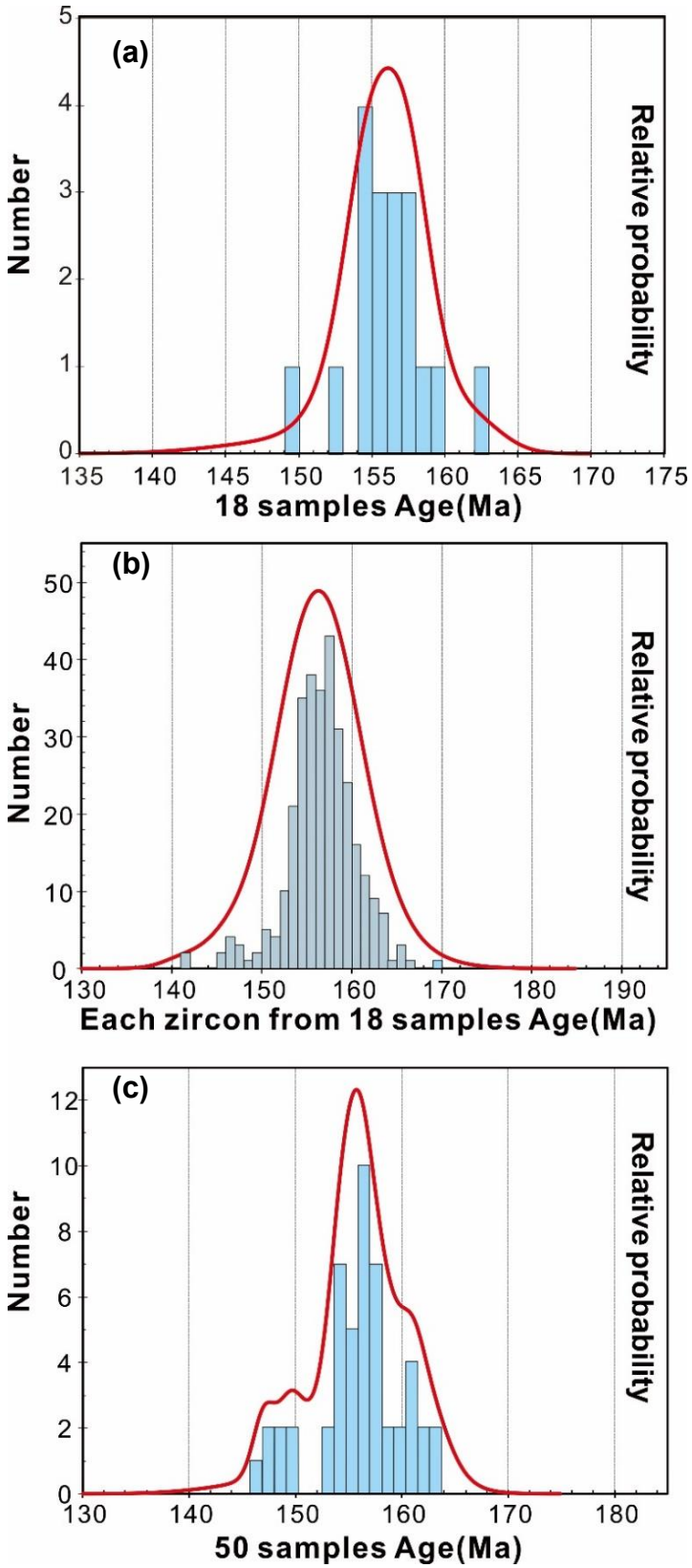

Fig. 4.30 Histogram of Zircon U-Pb ages of Qitianling pluton. (a) 18 samples from this study; (b)each zircon from the 18 samples of this study; (c) 18 samples from this study and 32 samples from Zhu et al., 2009.

particular, one of the oldest age obtained corresponds to phase 3. Our 18 samples show a symmetric unimodal distribution curve, in lieu of the trimodal one obtained previously, with a peak distribution centered at around 156 Ma (Fig. 4.30 a). The age of each zircon also displays a similar unimodal distribution curve (Fig. 4.30 b). When our data are lumped together with those of Zhu et al. (2009), a broad unimodal distribution curve emerges with two small peaks at ~148 Ma and ~161 Ma (Fig. 4.29 c). This therefore suggests that Qitianling pluton was constructed via a broadly continuous inflow of magma in the upper crust, which started at around 160 Ma, progressively increased till peaking at 156 Ma, and subsequently decreased at the same rate, till full cessation at around 147 Ma. Such a continuous magma inflow is also supported by the SHRIMP U-Pb chronological work conducted by Zhao et al. (2006). In their more spatially resolved analyses of single zircons, one zircon grain shows a rather wide crystallization age range (core: 159.1 ± 0.9 and rim: 151.9 ± 2.2; Fig. 4.31a). From the cathodoluminescence image of Zhao et al. (2006), it is apparent that the core and the rim parts of the crystal have the same type of oscillatory zoning. Moreover, the core part has clearly an angular shape which is different form the rounded shape of the inherited zircon core shown in Fig. 4.31b. We thus suggest that the zircon from Fig. 4.31a provides evidence for the continuous inflow of magma during the construction of Qitianling pluton which spanned several millions years (at least 7 Ma according to this single zircon).

The difference between the main peak around 156 Ma and two small peaks (~148 Ma and ~161 Ma) possibly reflects that the rate of continuous inflow of magma varied during intrusion in the upper crust. There are two possibilities to explain the peak of inflow at around 156 Ma: one is that a single huge magma injection occurred at that time, and the other is that thousands of small batches were delivered during a short period. The first scenario is inconsistent with field observations that indicate that there is no strong deformation at the margin of the pluton and its country rock. As for the second explanation, the anisotropy of magnetic susceptibility (AMS) measurements of

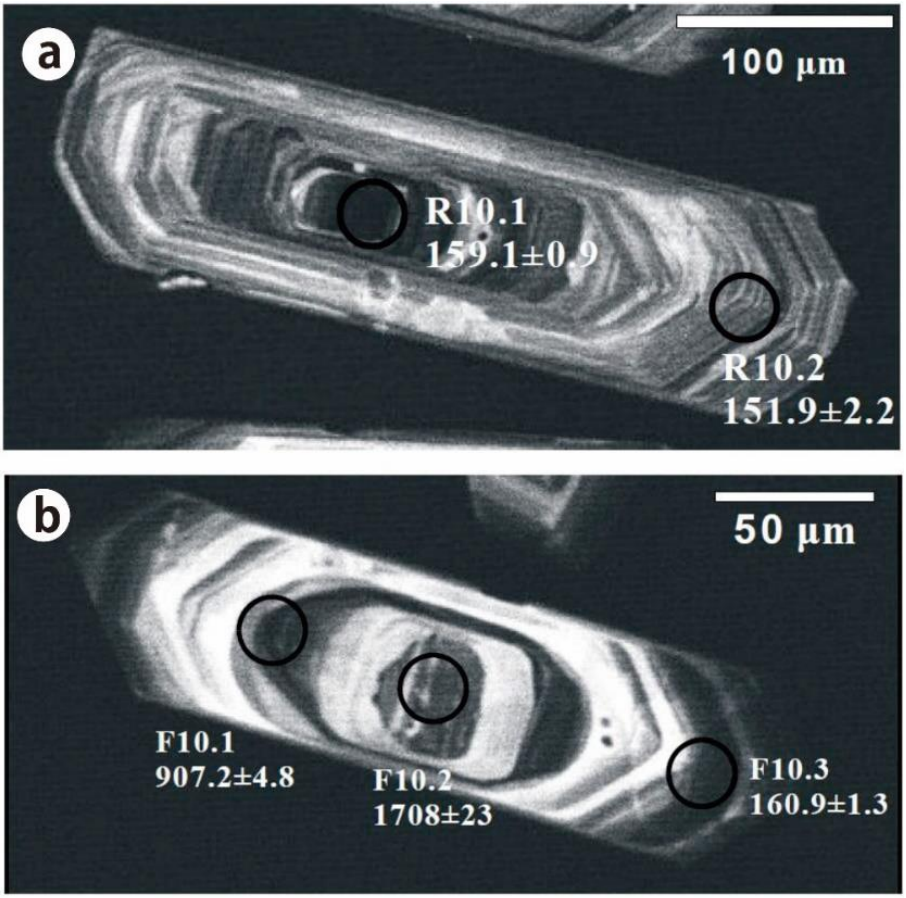

Fig. 4.31 The cathodoluminescence (CL) images of Zircon and the in situ SHRIMP U-Pb ages of zircon grain from Qitianling granite. Image and data are from Zhao et al., 2006

Liu et al., 2018 show that the magnetic foliations are horizontal while magnetic lineations are scattered which indicate that the inflow of magma was mostly horizontal (at the present level of observation) during the final stages of consolidation. The lack of deformation, as well as the limited extent of thermal aureole surrounding the pluton, both suggest that the inflow of magma at Qitianling occurred continuously via addition of small amounts of batches. The contact between phase-1 and phase-2 is not well exposed, so no information can be acquired from field observations on the intrusive relationships between these two phases. In contrast, the contact between fine grained granite and coarse to medium-grained granites has been observed in the field. One example is from the southwest part of the pluton, where Xie et al., 2013 reported a tin-mineralized topaz rhyolite dike with granitic enclaves. Geochronology results give crystallisation ages of 147.15±0.45 Ma (handpicked grains) and 150.0 ±2.0 Ma

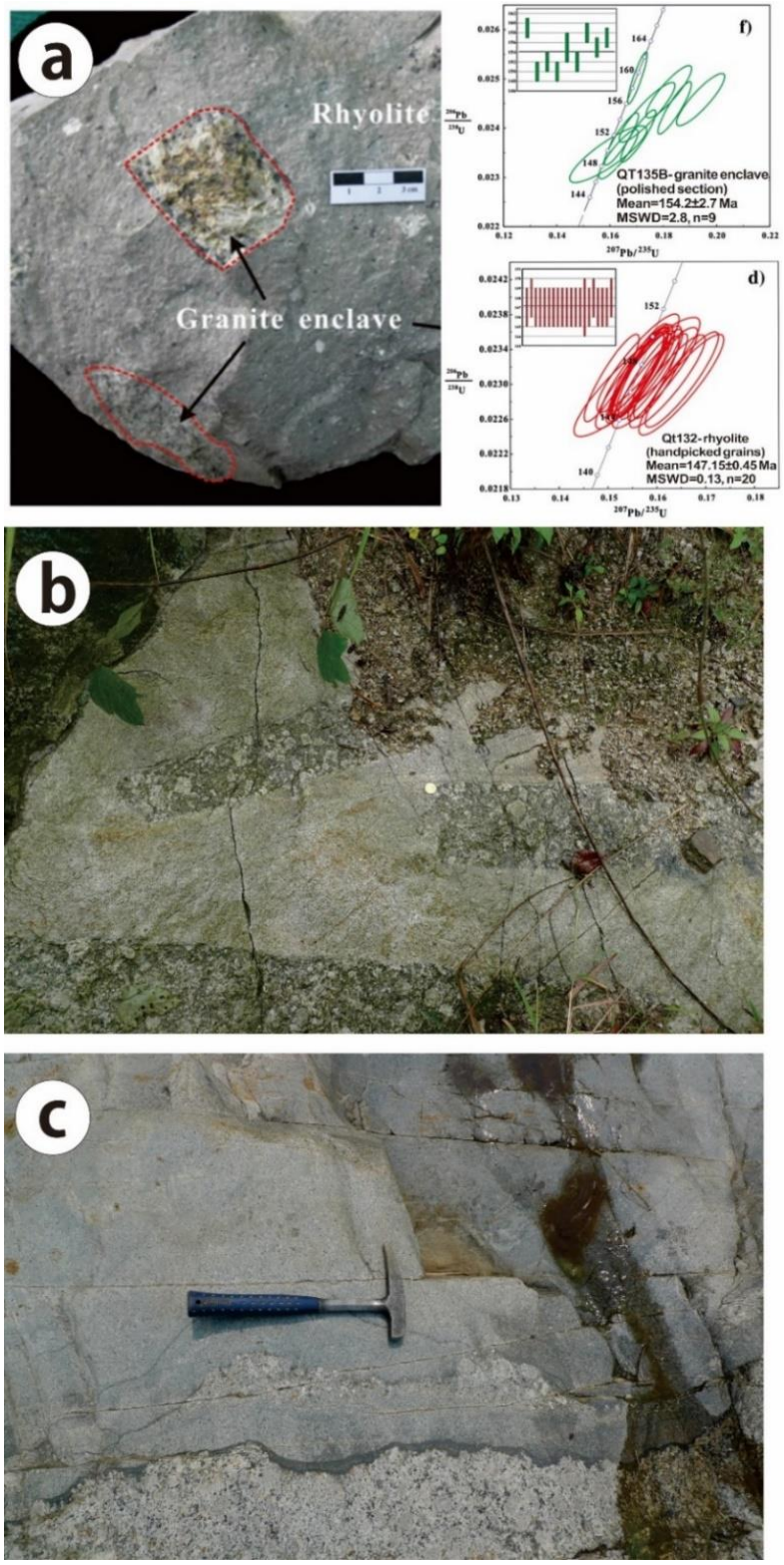

Fig. 4.32 Contact relationships between fine grained and coarse grained granites of Qitianling pluton. Image (a) is cited from Xie et al., 2013; granitic enclave age is in green colour with a mean U-Pb age in 154.2±2.7 Ma; rhyolite is in red colour with a mean U-Pb age in 147.15±0.45 Ma. Photo (b) is using the coin (golden) as the scale; Photo (c) shows the chilled margin between a coarse grained (sample QTL-21B dated at 156±2.1 Ma) and a fine grained granite.

(polished section) for the topaz rhyolite dike and of 154.2±2.7 Ma for the granitic enclave (Fig. 4.32a). Two other examples are from near the eastern and southwestern borders. For the former, angular shaped coarse grained granite fragments are included in a fine grained granite (Fig. 4.32b) whereas in the latter, a fine grained granite intrudes a coarse grained granite (sample QTL-21B with an age at 156.0 ±2.1 Ma) with a chilled margin (Fig. 4.32c). These observations demonstrate that when the fine grained granite magma was emplaced, the coarse grained variety was already solid and even cold. However, an important information that should be kept in mind is that fine grained granites are not necessarily equal to a late emplacement. Among our 18 samples, fine grained or medium/fine grained granites have ages varying from 149.5±4.8 Ma to 162 ±2 Ma which show that the fine grained magma variety was produced during the entire period of pluton emplacement. Our results coincide with those of Zhu et al. (2009), who showed that the fine grained granite has an age range varying from 147±1 Ma to 163 ±3 Ma. It is worth noting that, besides source processes (Fig. 4.32), another possibility to generate fine grained evolved granites is by in situ fractionation: such a mechanism would imply however that evolved magmas are predominantly produced during the latest stages of magma crystallization, which is at variance from geochronological constraints.

Therefore, based on our data as well as on previous findings, we suggest that the magma emplacement of Qitianling pluton was broadly continuous, starting at around 160 Ma with many small amounts of magma batches, whose intrusion rate progressively increased until around 156 Ma and then slowed down by about ~150 Ma: thereafter the main mass of magma body started to cool down while small increments of magma were added till ~ 147 Ma. Overall the data thus suggest that the thermal anomaly responsible for the melting of the lower crust at the origin of Qitianling pluton lasted at least 10 Ma, and was perhaps twice as long.

4.5.3.2 Cooling age

Many minerals incorporating various radio-isotopic systems were exploited as dating techniques. The isotopic geochemical analyses of these different minerals can provide thermal history information using the widely different closure temperature ranges, which greatly helped develop the geochronology and thermochronology (Reiners et al., 2005; Braun et al., 2006). The minerals chosen as chronometers mainly rely on the hypothesis that as the system cools down, the daughter products of decay of radiogenic isotopes and the parent existing element stop diffusing when below their closure temperature (Dodson, 1973). Most common chronometers include U-Pb dating of apatite, zircon, monazite and titanite, K-Ar and Ar-Ar dating of amphibole, biotite, muscovite and K-feldspars, (U–Th)/He dating of apatite, fluorite and zircon. Among them the popular with relatively high closure temperature is zircon U-Pb system whose closure temperature is in excess of 900 °C (Cherniak and Watson, 2001). Another thermochronometer widely used for dating metamorphic/magmatic processes is Ar-Ar system of amphibole and biotite, which have the closure temperature range around at 400-600°C and 350-400 °C, respectively (Harrison and McDougall, 1982; McDougall and Harrison, 1999; Scaillet, 2000; Meert et al., 2001). The ranges of closure temperature of different minerals are summarized in Fig. 4.33. More recently, the U-Pb dating of some ore-forming minerals (cassiterite and columbite-group-minerals) has been widely used by economic geologists (Che et al., 2015; Zhang et al., 2017).

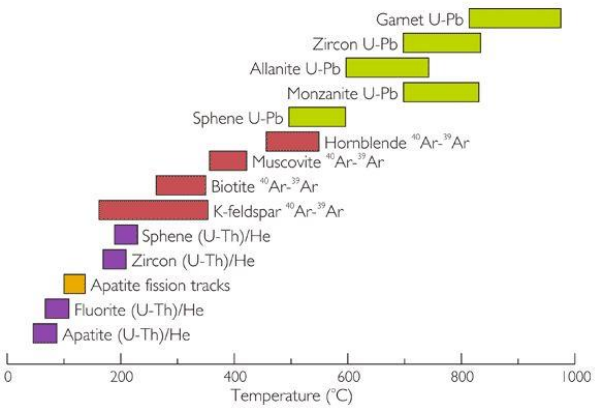

Fig. 4.33 The closure temperature of different minerals used in thermochronologic systems.

The results of Ar-Ar dating of amphibole and biotite in our study suggest that the age recorded by these minerals are mainly between 151 Ma and 155 Ma which is consistent with previous Ar-Ar dating studies: Mao et al. (2004) and Bai et al. (2005) demonstrated that the biotite from the coarse-medium grained amphibole-biotite granite of Qitianling pluton gave an Ar-Ar age of 157.5 ± 0.3 Ma and 155.1 ±1.8 Ma, respectively. Compared with the result of the zircon U-Pb age (see Fig. 4.34), the Ar-Ar ages of each sample are close (within 5 Ma) but younger than U-Pb ages, which indicate that these Ar-Ar ages represent the cooling age or crystallization age (approximate) of amphibole and biotite. This result is consistent with the facts that: 1) no conspicuous foliation or lineation has been observed from the Qitianling granite; 2) the contact between the granite and the country rocks is sharp, undeformed and with small thermal aureoles which prove that the deformation is relatively weak along the boundary. This indicates that after the main magma emplacement, the Qitianling pluton cooled down slowly and didn't experienced any other tectono-thermal events that could have reset the chronometers until to nowadays.

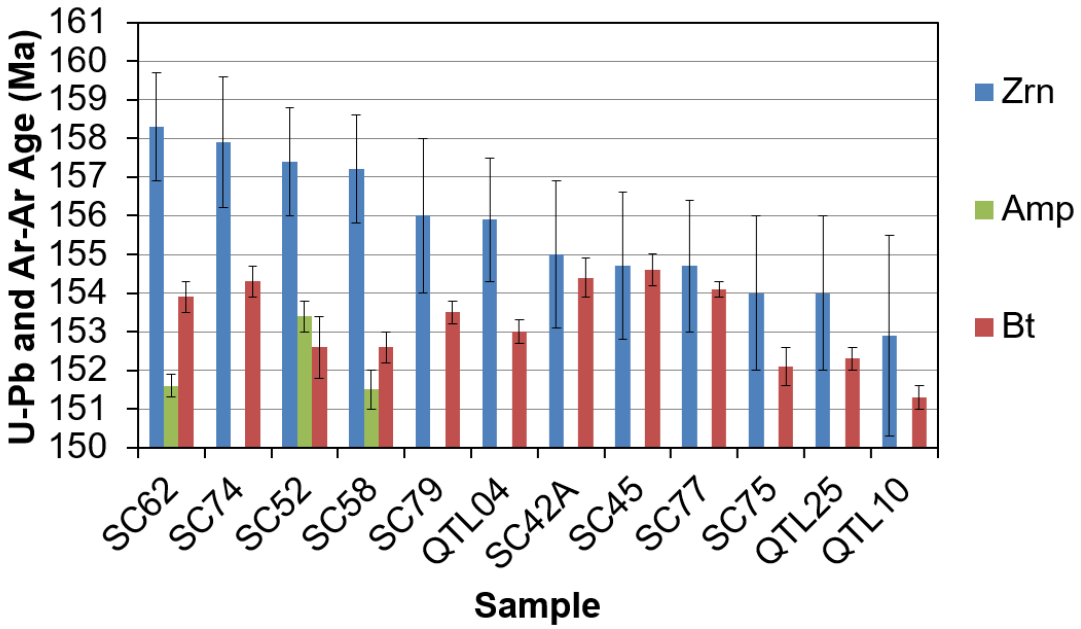

Fig. 4.34 The zircon U-Pb age and amphibole-biotite Ar-Ar age of Qitianling granite.

Three samples of Qitianling granite were chosen for all zircon U-Pb dating,

amphibole and biotite Ar-Ar dating (Fig. 4.34). Sample SC52 is located in the central part of the pluton, and the age acquired from zircon, amphibole and biotite of this sample are 157.5±1.4 Ma, 153.4±0.4 Ma and 152.6±0.8 Ma, respectively. Sample SC58 was collected from the northwest part of the pluton, the three types of dating of this sample gave age at 157.2±1.4 Ma, 151.5±0.4 Ma and 152.6±0.4 Ma, respectively. As for the sample SC62 which is in southwest, the zircon U-Pb, amphibole and biotite Ar-Ar age are 158.3±1.4 Ma, 151.6±0.3 Ma and 153.9±0.4 Ma, respectively. As we mentioned above, the range of closure temperature for zircon (U-Pb), amphibole (Ar-Ar) and biotite (Ar-Ar) are around 750-900°C, 400-600°C and 350-400 °C. When compared with other two samples, sample SC52 displays an ideal progressive cooling trend (ie biotite ages are younger than those of amphibole) thus was used as the cooling rate modeling (Fig. 4.35). From this sample, assuming that 5 Ma is the maximum gap between zircon age and biotite age and taking the lower limit value of the closure temperature of zircon (750°C), amphibole (400°C) and biotite (350°C), we can simply acquire the cooling curve. The slope of linear fitting equation of Sample SC52 is around 80, therefore suggesting that the cooling rate was 80°C/Ma (in this temperature interval).

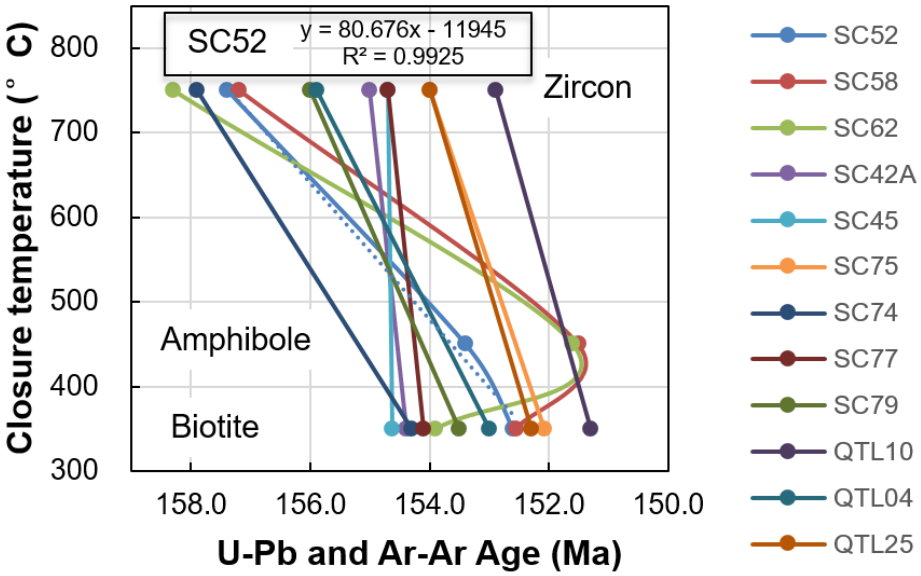

Fig. 4.35 Modeling of the cooling history deduced from geochronological data of the Qitianling granite.

For the other nine samples only the zircon U-Pb age and biotite Ar-Ar age were

acquired (Fig. 4.33, 4.34). If we exclude ages affected by large error bars, the difference between the two ages of each sample varies from 0.1 to 3.6 Ma (Fig. 4.35; 4.36). Interestingly, the samples with a small age difference such as SC42A (0.6 Ma), SC45 (0.1 Ma) and SC77 (0.6 Ma), appear to be located near the margin of the pluton while those with relative high age gap value e.g. SC74 (3.6 Ma) and QTL04 (2.9 Ma) tend to occur in the central part of the pluton, in particular for the three samples (SC52, SC58 and SC62) which give the highest age gap value (4.8 Ma) among all samples. In an ideal situation, this can be explained by the fact that from the central part to the marginal part of the pluton, heat loss increased rapidly such that the closure temperature of the Ar-Ar isotopic system of biotites from the periphery of the pluton was rapidly reached after emplacement (Fig. 4.36). That the central part of the pluton remained hotter for longer period suggests also that the magma main feeding zone was relatively focused in the core of the pluton.

The geochronological results gained on Qitianling pluton can be compared with thermal simulations of a cooling magma body in the crust. For instance, the simulations of Nabelek et al. (2012) show that a 2 km thick granite magma body intruded at 6 km depth, with an emplacement temperature of 900°C (initial host rock temperature at about 300°C) reaches a temperature of 400°C (ie the closure temperature of amphibole) in its core only after 100 kyr. This shows that emplacement of Qitianling through a single major pulse of magma is highly unlikely on thermal and geochronological grounds. Annen et al (2006) have modelled the thermal evolution of the Manaslu granite, a 5 km thick leucogranite body emplaced at 10-12 km depth (ie similar to Qitianling) in the Himalayan orogen. Their model shows that in order to maintain temperatures hotter that 350-400°C inside the main magma body for several Ma after the onset of emplacement, a slow intrusion rate (about 1 mm/year) during a protracted time interval (several Ma) is required (see their Figure 14). Altogether, field and laboratory data thus suggest that the Qitianling granite was slowly built via the addition of small magma batches. An indication about the size (thickness) of individual intrusions is given by the

limited extend of the thermal aureole surrounding the pluton (typically <30 m). Here also, thermal modelling shows that the thermal aureole is broadly proportional to the thickness of intrusion (see Annen et al., 2006), hence, intruded magma batches probably had thicknesses of about 30-100 m. For comparison, the simulations of Nabelek et al (2012) give an aureole size thicker than 2 km (for an instantaneously emplaced 2 km granite lense). Future, dedicated, thermal simulations will allow to further refine the thermal evolution of the Qitianling granite and its relationships with the regional geological evolution.

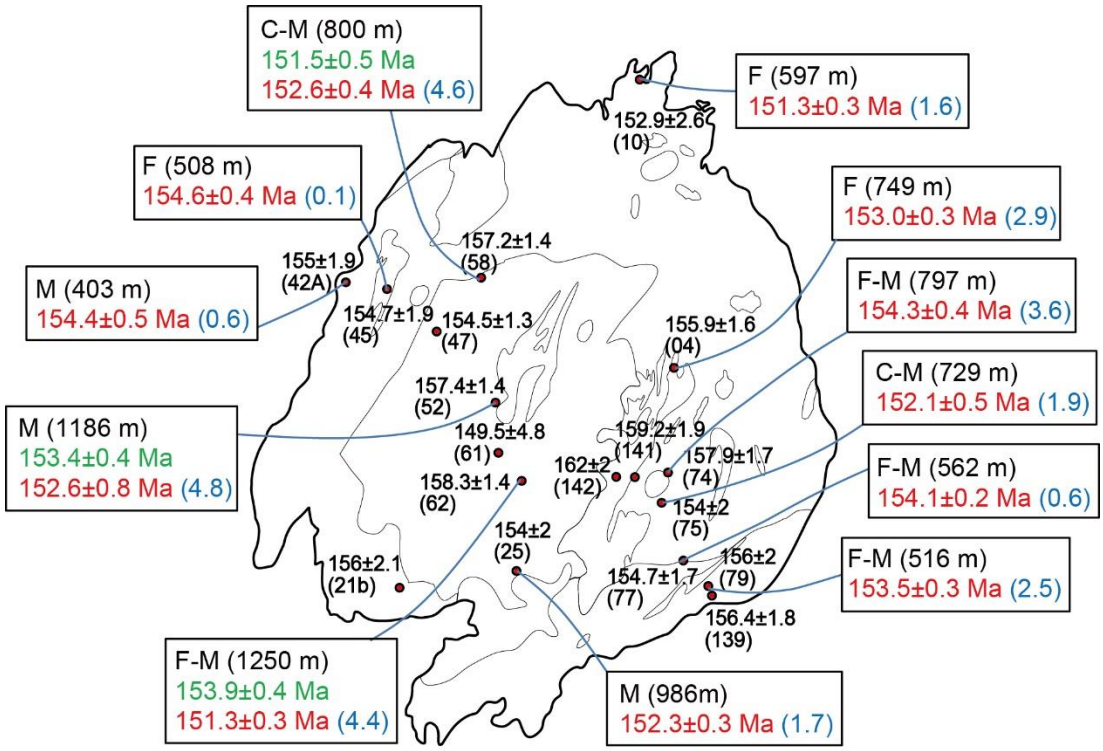

Fig. 4.36 The age distribution of Qitianling pluton. Red plots are the position where the sample were collected. The ages within the pluton in dark are the zircon U-Pb age (Ma). Under the zircon age, the number in the parentheses are the number of samples. Amphibole Ar-Ar ages (Ma) are in green while biotite Ar-Ar ages (Ma) are in red. The blue numbers in the parentheses are the difference between the zircon U-Pb age and biotite Ar-Ar age. F: fined-grain granite; M: medium-grain granite; C: coarse-grain granite. The number behind the lithology is the altitude of the samples.

4.6 Summary

Qitianling pluton consisted of three main phases: phase-1, porphyritic, medium- to coarse-grained amphibole-biotite-rich monzonitic granite; phase-2, medium-grained biotite±amphibole-bearing granite; phase-3, fine-grained, biotite-bearing granite. The geochemical data show that Qitianling pluton is metaluminous, and belongs to aluminous A-type granites (A_2 post- orogenic subtype) with high Ga/Al ratio and high contents of HFSE (Zr, Nb, Ce, Y) and REE. Harker and REE spider diagrams show that the Qitianling pluton display well organised fractionation trends.

The emplacement conditions of Qitianling pluton have been constrained using different mineral thermobarometers. Zircon-saturation temperature and amphibole-plagioclase thermometry suggest that the early emplacement temperature condition of Qitianling was at least of 800°C. Amphibole barometry suggests in turn that pressure was around 3.2±1 kbar. As for the redox state, restored Ti-Fe oxides compositions suggest an fO2 slightly above the NNO oxygen buffer, but the corresponding temperatures are largely below solidus. In contrast, based on the Ce content and Ce^{4+}/Ce^{3+} ratio in zircon, the redox state for Qitianling pluton is inferred to have been relatively reduced (when compared to that of arc-magmas). These two last observations suggest that the Qitianling pluton may have experienced an oxidation event during its evolution, perhaps at the subsolidus hydrothermal stage.

Radiometric data show that the emplacement of Qitianling pluton occurred during Jurassic times. We have found crystallization ages (Zircon U-Pb age) for Qitianling pluton ranging between 149.5±4.8 Ma to 162±2 Ma being coincident with previous constraints (146±5 Ma to 163±3 Ma). As shown in the frequency distribution histogram, most of our samples are distributed between 154 Ma and 158 Ma, which suggests that the main emplacement period was around 156 Ma. When combined with the results of previous studies, two small peaks (~148 Ma and ~161 Ma) appear, which

could correspond to slightly enhanced magma production rates during these periods. Combining these constraints with field observations, we suggest that the emplacement of Qitianling pluton occurred via incremental addition of small magma batches in a broadly continuous manner, but the rate of intrusion during pluton building varied, increasing till around 156 Ma, and then slowing down to around 148 Ma which is the youngest dated intrusion. The Ar-Ar dating of Qitianling granite shows that the amphibole and biotite record ages ranging from 151 Ma to 155 Ma which represent the cooling age of Qitianling. Located in the central part of the pluton, sample SC-52 acquired the ages from zircon (U-Pb system at 157.5±1.4 Ma), amphibole (Ar-Ar system at 153.4±0.4 Ma) and biotite (Ar-Ar system at 152.6±0.8 Ma) which give a cooling rate of 80°C / Ma for the cooling process of Qitianling pluton. The difference between zircon U-Pb age and biotite Ar-Ar age from each sample demonstrates that the ages gap value is positively associated with the distance from contact of the pluton.

Chapter 5 Phase equilibria of Qitianling Granite and emplacement condition constraint

5.1 Introduction

In Southern China, Mesozoic (~66-251 Ma) granitic rocks (sensu lato) make up a large proportion (~60 %) of the exposed crust, with an overall exposure of ~135,000 km^2 (e.g. Zhou et al., 2006). Jurassic plutons (~142-180 Ma) comprise ~50% of the exposed intrusions, many of which are associated with rare metal (W, Sn, Nb, Ta, Zr, U, REE) deposits of economic significance (Chen et al., 2013; Wang et al., 2017; Zhu et al., 2008; Jiang et al., 2008; Shu et al., 2013). Among them, many intrusions are metaluminous to slightly peraluminous A-type granites compositions which are characterized, interalia, by high Ga/Al and FeO_t/MgO ratios, high contents of Zr, Nb, Y, Ce, and Fe-rich minerals (Chappell and White, 1974, 2001; White and Chappell, 1977; Bonin, 2007; Collins et al., 1982; Whalen et al., 1987; Rajesh, 2000; Martin, 2006; Li et al., 2007; Fu et al., 2004). Knowledge of intensive system parameters prevailing during the crystallization of such huge amount of granites is important to unravel Mesozoic crust formation and evolution in southern China as well as for guiding mining exploration efforts in this area. In particular, constraints on system/melt H_2O content and oxygen fugacity are of fundamental importance for qualitatively and quantitatively assessing ore element concentration, solubility, and transport paths.

The conventional method for constraining the emplacement conditions of granites has been to use experimentally- or empirically calibrated geothermometers and geobarometers (e.g. Hammarstrom and Zen 1986; Anderson, 1996; Anderson et al., 2008; Mutch et al., 2016; Putirka and Keith, 2016). Such an approach does not, however, constrain accurately melt water content or oxygen fugacity, while estimates on crystallization pressure and temperature bear variable and often significant

uncertainties. Previous work has shown that such constraints may be gained from phase equilibrium experiments performed on representative compositions (e.g. Clemens et al., 1981, 1986; Scaillet et al., 1995; Dall'Agnol et al., 1999; Klimm et al., 2003).

Our choice of experimental conditions was based on P-T estimates gathered from previous studies and our own data. Calculated zircon saturation temperatures are between ~715 and 875 °C, (Appendix table 1 and Zhao et al. 2005), which is in the range typical for alkali-rich granitic magmas (e.g. cf. Collins et al. 2016). Hornblende-plagioclase and hornblende thermobarometry (Holland and Blundy, 1994; Hammarstrom and Zen, 1986; Hollister et al., 1987; Johnson and Rutherford, 1989; Schmidt, 1992; Anderson and Smith, 1995) yield calculated crystallization temperatures of ~750-820°C and pressures of ~360±90 MPa (Zhao et al. 2005). Zr-in-titanite thermometry of rare, euhedral, titanite crystal cores records crystallization temperatures of ~720-780°C (Xie et al. 2010). The common presence of magnetite and the composition of biotite (Fe-rich) have been used to infer magmatic crystallization over a wide range of oxygen fugacity, between the NNO and the MH (Fe_2O_3-Fe_3O_4) buffers (Zhao et al., 2005; Wang et al., 2017). The restored compositions of spatially associated magnetite and ilmenite (using a broad beam during electron probe analyses of exsolved oxides) suggest last equilibration below the solidus at ~580°C at an oxygen fugacity around NNO+1 (Table 4.3). The melt H_2O content of the Qitianling magmas remains unconstrained, but the presence of amphibole suggests that melt H_2O contents were ≥4 wt% (e.g. cf. Naney 1983; Dall'Agnol et al. 1999).

Accordingly, temperature was varied between 660 and 900 °C and pressure between ~100 and ~700 MPa. Most experiments were carried out at ~200-300 MPa, but some additional experiments were performed at ~100, ~400 and ~700 MPa. Oxygen fugacity was varied between ~NNO+2.4 and ~NNO-1.3, most experiments being performed between ~NNO+2.4 and ~NNO-1.3. Melt H_2O content was varied between ~3.0 and ~8.6 wt % by varying pressure and fluid composition (XH_2O) (see below).

Three representative samples of the two main Qitianling rock types (one phase-1 and two phase-2 samples), were chosen as raw starting materials. The phase-3 biotite granite was not selected because all exposed rocks are significantly altered. The selected starting material samples have SiO2 contents of ~65.7 wt % (phase-1 granite, sample QTL38C), ~68.1 wt % (phase-2 granite, sample QTL14A), and ~70.9 wt % (phase-2 granite, sample QTL13) (Appendix table 8). The details of starting materials preparation see in Chapter 3. Nineteen experiments were performed with a total of 166 individual charges. Experiments performed above 800 °C lasted ~140-350 hours (~6-15 days), while those performed below 800 °C lasted ~470-1350 hours (~20-56 days) (Appendix table 9).

5.2 Experimental results

5.2.1 Phase relations

(1) Phase-1 amphibole-biotite granite

At 200 MPa and ~NNO-1.5, Lpx, Cpx, Pl, Amp, Kfs, Qtz, Ilm, Mt, and Gl (0-90%) crystallized from phase-1 composition (Appendix table 9; Fig. 5.1a) (sample QTL-38C, ~65 wt% SiO_2). Ilm, Lpx, and Cpx are the near-liquidus phases (Fig. 5.1a). Lpx stability is limited to ≥750-800°C, while Cpx is present in all charges except for one Amp-rich charge crystallized at 800°C and H_2O-saturation. Amp appears at <900°C and for a melt H_2O content (H_2O_{melt}) >5.5 wt %, but its appearance is limited to >700-750°C, Amp being not a stable solidus or near-solidus phase at 200 MPa. The Amp stability field is limited to H_2O_{melt} > 5.5 wt % at 850°C and >6 wt % at 800°C, having thus a remarkably

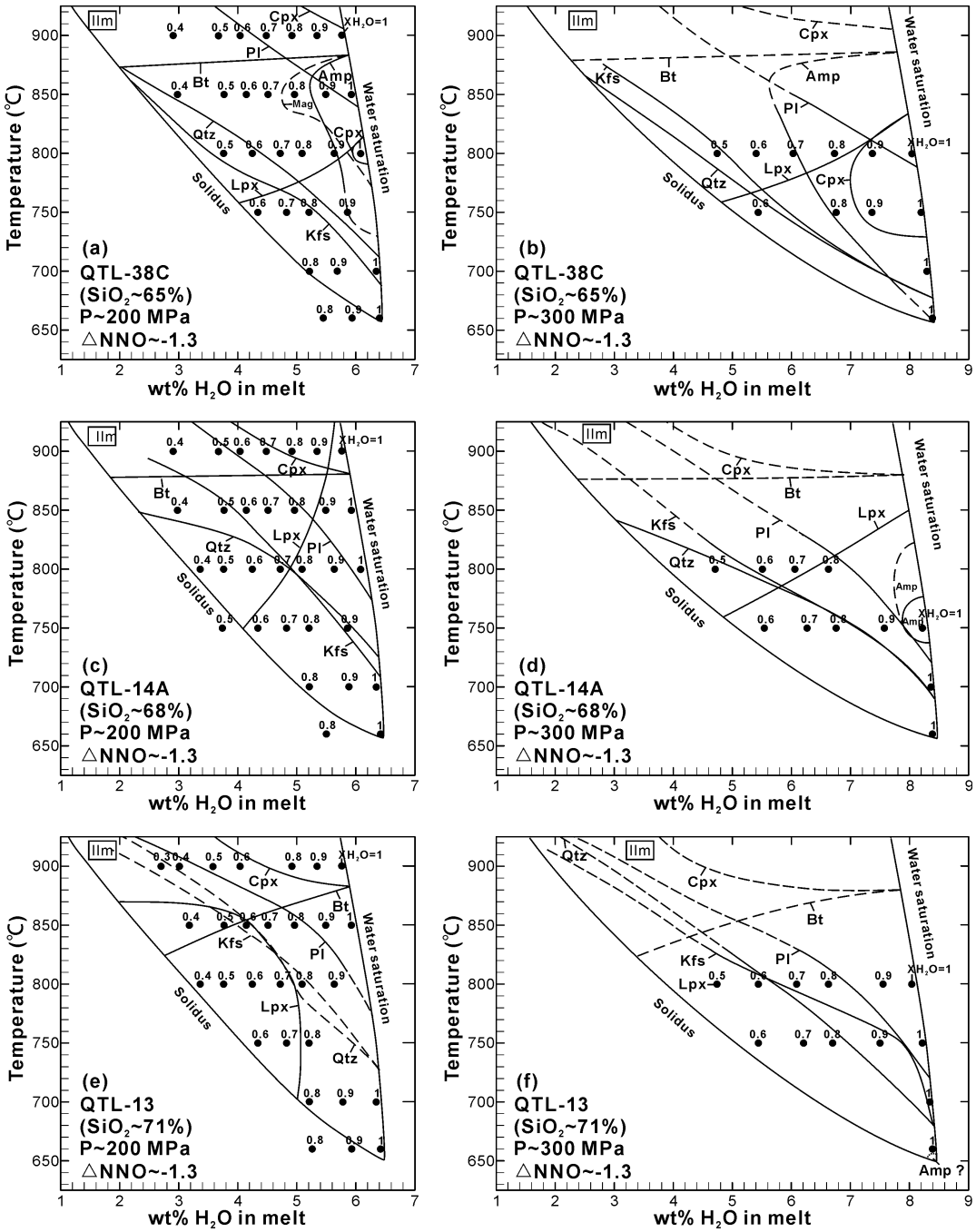

Fig. 5.1 Isobaric phase diagram at 200 MPa and 300 MPa of three compositions (QTL38C; QTL14A; QTL13) as a function of temperature and melt H_2O content. The number above each charge is the $XH_2O= [H_2O/ (H_2O+CO_2)]$ in mole. Solidus curves are based on the observation in our charges and Johannes and Holtz (1990). Minerals abbreviations: Ilm: ilmenite; Mag: magnetite; Cpx: clinopyroxene; Opx: orthopyroxene (low- Ca pyroxene); Amp: amphibole; Bt: biotite; Pl: plagioclase; Kfs: K-feldspar; Qtz: quartz.

narrow stability field (Fig. 5.1a). Bt appears below 900°C and is stable over the entire range of explored H_2O_{melt} (i.e. ~3-6.4 wt %). Pl crystallizes below 900°C at low H_2O_{melt} (<4 wt %) and below 825°C at H_2O saturation. The Qtz and Kfs saturation curves are subparallel to the Pl saturation and the inferred solidus curves. Ilm is present in all charges. Mag has been observed at 800°C and 850°C in H_2O-rich charges, where it coexists with Ilm.

Crystallization at 300 MPa produces phase relations similar to those determined at 200 MPa (Fig. 5.1b versus 5.1a). Cpx formed in all but four charges (at 800 and 750 °C and H_2O_{melt} >~7 wt %). Lpx stability is limited to >800 °C at H_2O saturation and to >~750 °C at H_2O_{melt} <5 wt %. Amp and Bt are likely stable at >800 °C according to the experiments at 200 MPa, but their maximum stability field was not determined. When compared with the stability at 200 MPa, Amp stability is still restricted to high melt H_2O, i.e. H_2O_{melt} >~6 wt %, but extends to a significantly lower temperature, ie at least ~675 °C (instead of ~750 °C). Amphibole is thus stable at near-solidus conditions, but it appears to be absent from our 660 °C, H_2O-saturated charge. As at 200 MPa, Pl crystallization at H_2O saturation occurs after Amp (at <800 °C). Qtz and Kfs are the last tectosilicate phases to appear as temperature decreases. Kfs crystallises before Qtz at low H_2O_{melt}, unlike at 200 MPa where Qtz always crystallises first relative to Kfs. Ttn was detected in some charges at ~700°C and at ~800°C crystallized at oxidizing conditions, while charges crystallized at reducing conditions showed no Ttn.

(2) Intermediate phase-2 biotite-amphibole granite

At 200 MPa, amphibole did not crystallize from the phase-2 composition (Fig. 5.1c) (sample QTL-14A, ~68 wt% SiO_2). Ilm and Lpx are the liquidus phases, while Mag was not observed. Cpx appears at 900°C and at H_2O_{melt} >5 wt %. Bt crystallises at <900°C displaying a stability field similar to that in phase-1 (Fig. 5.1c versus 5.1a). Compared to phase-1, the Pl stability field is depressed to slightly lower temperature, i.e. occurring at ~850 °C at ~4 wt % H_2O_{melt} and below 800 °C at H_2O saturation. The

stability fields of Kfs and Qtz are slightly larger than those determined for the phase-1 composition. Crystallization at 300 MPa yields results similar to those at 200 MPa, with one key exception: Amp crystallizes at ~750°C at H_2O-saturation (Fig. 5.1d). Ttn was observed in oxidizing experiments at 700°C and 800°C and in some reducing experiments at 660°C and 700°C (Appendix table 9).

(3) Evolved phase-2 biotite±amphibole granite

At 200 MPa, the evolved phase-2 biotite±amphibole granite (sample QTL13, ~71 wt % SiO_2), crystallizes essentially the same mineral assemblage as the intermediate phase-2 composition, ie Ilm, Lpx, Cpx, Pl, Kfs, Qtz, Ttn, only lacking Mag. The phase relationships closely compare to those determined for the intermediate phase 2 composition (Fig. 5.1e and 5.1c), except that the stability fields for Lpx and Bt differ. Lpx is no longer a near-liquidus phase, it crystallizes below 900°C and at H_2O_{melt} of <5 wt %. Bt stability becomes sensitive to melt water content. At H_2O_{melt} of ~2-3 wt %, it crystallizes at <800°C, while it appears below 850°C at H_2O saturation. Ttn is also present at 660 °C and 700 °C (300 and 400 MPa), which is similar to intermediate phase-2. The phase relations determined at 300 MPa do not significantly differ from those at 200 MPa (Fig. 5.1f).

Phase relations summary

Apart from Bt, which displays similar stability fields for all three compositions, the variation in saturation curves summarized above shows that even relatively minor compositional variations critically affect phase relationships (e.g. as previously observed for other compositions, for example, by Cadoux et al., 2014 or Scaillet et al. 2016). The most notable variation is observed for Amp and Lpx. For both phases, the stability fields progressively shrink with evolving bulk-rock composition. Another notable feature is the peritectic relationship between Cpx and Amp, i.e. Cpx is absent in low-temperature and H_2O-saturated charges whenever Amp is stable. Our results

show also that increasing pressure enlarges the stability field of Amp towards lower temperature, a reflection of the increase in H_2O melt solubility. Yet, the low-temperature limb of the Amp field does not straddle the solidus at 300 MPa, while it is close to it. We attribute this to a redox effect, i.e. we posit that our fO_2 was slightly too oxidizing compared to conditions at which Amp crystallizes at the solidus. Indeed, Dall'Agnol et al. (1999) have shown that low fO_2 displaces the stability field of Amp downward in a T-H_2O_{melt} projection, where Amp replaces Cpx at near solidus and H_2O-rich conditions. The scarce occurrence of Amp in evolved phase-2 rocks suggests that the stability field of this phase for this composition probably lies at near-solidus and H_2O-saturated conditions, as tentatively shown in Fig. 5.1f.

5.2.2 Phase compositions

5.2.2.1 Plagioclase

The maximum Pl An content decreases from the most mafic to the most felsic composition, i.e. from ~An54-23 to ~An51-20 to ~An45-12 %, respectively. For each composition, the An content of Pl increases systematically with temperature and H_2O_{melt} (and therefore with pressure as pressure increases H_2O melt solubility) as observed in previous studies (e.g. Dall'agnol et al., 1999; Scaillet and Evans, 1999; Klimm et al., 2003; Bogaerts et al., 2006; Klimm et al., 2008) (Fig 5.2). The Or content of Pl, in contrast, increases when both temperature and H_2O_{melt} decrease (Appendix table 10). The An content of Pl formed at oxidizing conditions is higher compared to Pl crystallized at reducing conditions (e.g. with a maximum difference of ~An15 in our experiments) (Appendix table 10). A similar finding was reported by Dall'Agnol et al. (1999).

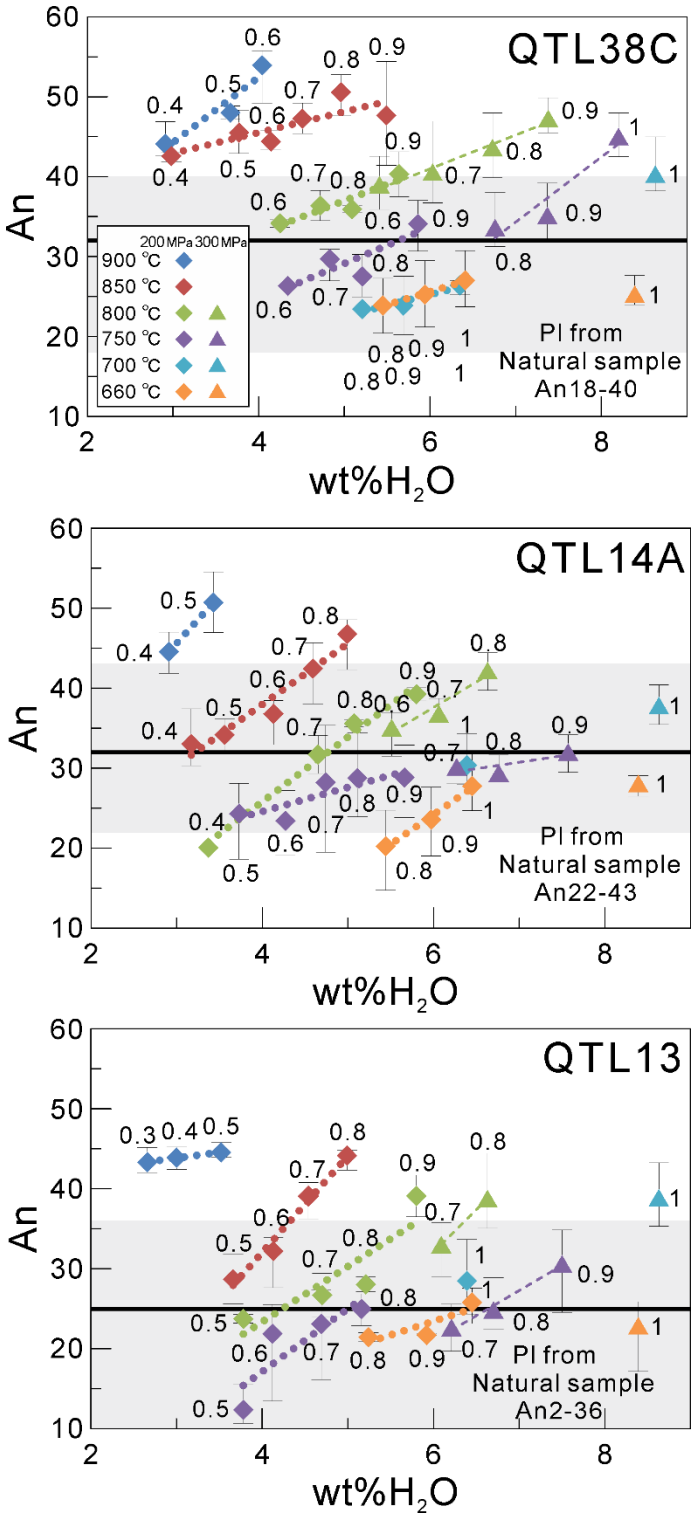

Fig. 5.2 An content of experimental plagioclase at 200MPa and 300MPa plotted as a function of melt H_2O content in different temperature (see in different colors) conditions with compositions of natural plagioclases (shaded area in grey color) from 3 samples. The bold black line is the average An value of Natural plagioclase. The number above each spot is the XH_2O from each charge.

5.2.2.2 Pyroxenes

Both Lpx and Cpx are observed in our crystallization experiments at most conditions, including the near-solidus experiments, yet they are absent from the natural samples. Cpx has <8.7 wt % Al_2O_3 and <2.7 wt % Na_2O. Diopside formed at 850 °C and 800°C, at H_2O saturation and either reducing conditions (~NNO-1.3) or oxidizing conditions (~NNO+2.4). Hedenbergite crystallized in experiments at <800 °C and at reducing conditions (~NNO-1.3). At 900°C-800°C and at H_2O-undersaturated conditions, Cpx has augite composition. Its Wo content increases with increasing XH_2O,

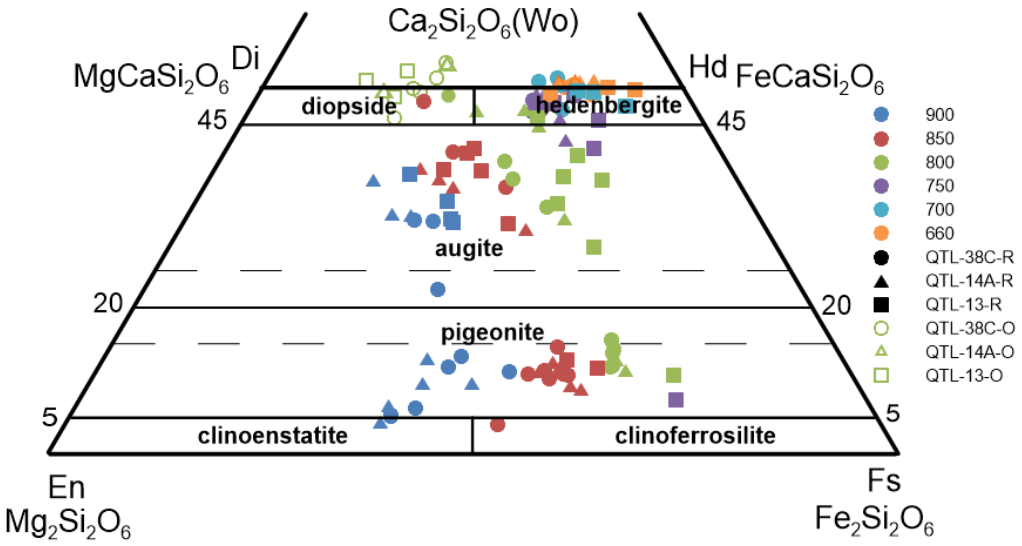

Fig. 5.3 Compositions of experimental pyroxene from the 3 samples at different temperatures in classification diagram. Solids symbol are the pyroxenes from reducing (~NNO-1.3) condition.● represent composition QTL38C; ▲ represent composition QTL14A; ■ represent composition QTL13. Those unfilled symbols represent the pyroxenes from oxidizing (~NNO+2.4) condition of 3 compositions.

while its Fs content increases with decreasing temperature.

Lpx is mostly pigeonite, except for crystals in two charges (900°C, XH_2O=0.9; 850°C, XH_2O=1), which are clinoenstatite and clinoferrosilite. Lpx has <7 wt % Al_2O_3 and <1 wt % Na_2O. Its Wo content increases with decreasing XH_2O (contrary to Cpx), while its Fs content increases with decreasing temperature (Fig 5.3; Appendix table 11).

5.2.2.3 Amphibole

Amp produced in our experiments is always calcic (>1.5 apfu (Ca, Na); Na< 0.5 apfu). According to Leake et al. (1997, 2003), it classifies as hornblende, pargasite, magnesiohastingsite, ferropargasite, ferroedenite, or edenite. Its TiO_2 content ranges from ~0.8 wt % to ~2.3 wt %. Al^{tot} shows a broad positive correlation with pressure,

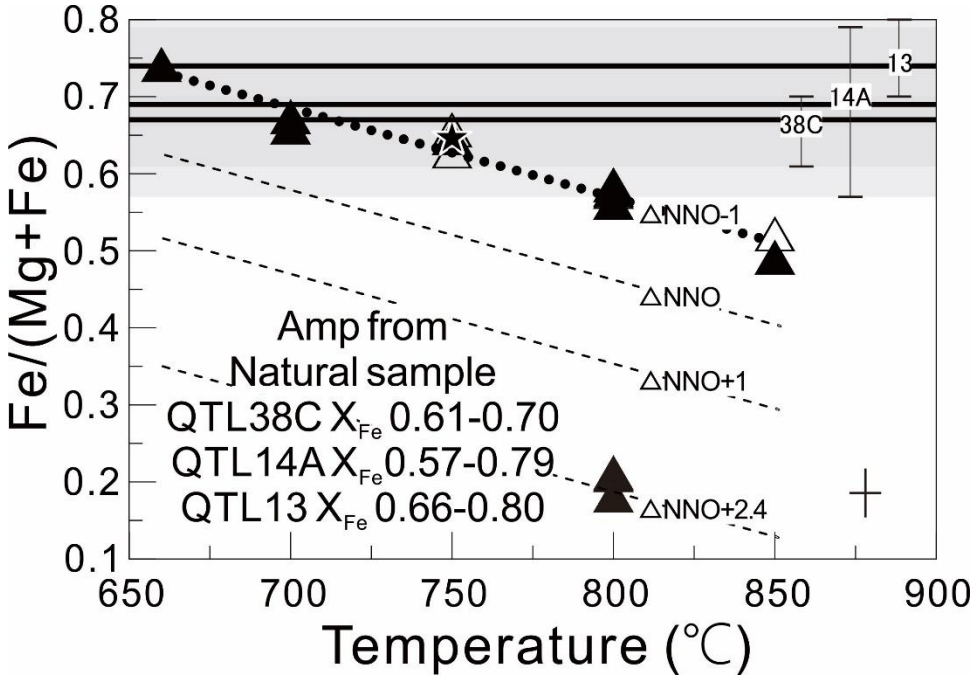

Fig. 5.4 Compositions of experimental amphiboles at water saturation (▲) and below water saturation (△) plotted as a function of temperature with compositions of natural amphibole (shaded area). Triangles represent the experimental amphibole crystallized from composition QTL-38 while the solid star represents those from composition 14A. The grey area are the range of Fe/(Mg+Fe) of natural amphiboles from 3 samples whereas the bold black lines are the average Fe/(Mg+Fe) value. The horizonal bar is the maximum uncertainty of temperature; the vertical bar is the maximum uncertainty of Fe/(Mg+Fe).

though there is not a simple linear relationship. For instance, at ~NNO+2.4 and 800°C, the Al^{tot} of Amp crystallized from the phase-1 composition at 200 MPa, 360 MPa and 700 MPa, is 1.48, 1.70 and 1.65 apfu, respectively. The X_{Fe} [Fe/(Fe+Mg)] content increases with temperature and decreases with oxygen fugacity. X_{Fe} also increases slightly with decreasing H_2O_{melt} (Fig 5.4). It does not vary obviously, however, with

pressure: at ~NNO+2.5 and 800°C, the X_{Fe} [Fe/(Fe+Mg)] at 200, 300 and 700 MPa, is 0.21, 0.21, and 0.18, respectively. Amp produced in phase-1 and phase-2 compositions have similar compositions, notably in terms of XFe: for instance, at 300 MPa, 750°C and ~NNO-1.3, XFe of Amp is 0.65 in both phase-1 and phase-2 experiments. Therefore, pressure and bulk compositional effects on Amp X_{Fe} are very small (Appendix table 12).

5.2.2.4 Biotite

Bt grain size is small in all charges (<10 μm) which, together with its high aspect ratio, made glass contamination unavoidable during EMP analysis. Bt analyses with high degrees of glass contamination (i.e. with K_2O<6 wt % and >10% contamination) were not considered. All other data are original, i.e. uncorrected compositions. Bt contains ~1-5 wt % TiO_2. The crystals have X_{Fe} values in the range of 0.42-0.75 (Appendix table 13), which increase with decreasing temperature and H_2O_{melt}, the trend being similar to that of Amp. Similarly to Amp, Bt crystallized in all three compositions (which have different Fe_{tot} content) at the same P-T-fO_2 conditions have comparable X_{Fe} (Fig 5.5).

5.2.2.5 Fe-Ti oxides

Due to their small grain size, good quality analyses of Fe-Ti oxide minerals were difficult to obtain. At reducing conditions, Ilm has relatively high FeO and low Fe_2O_3 contents (calculated at ~30-44 wt % and ~1-10 wt %, respectively), with ilmenite contents of 86-99 mol %. Ilmenite content increases with temperature and decreases with H_2O_{melt}. The MnO content of all experimental Ilm is <2.2 wt %, increasing when temperature decreases, while the MgO content increases with temperature, up to a maximum of ~3.8 wt %. Mag formed at ~NNO+2.4 has ulvöspinel (Usp) contents in the range of 21-37 mol%. At 800 °C, water saturation, and NNO-1.5, Mag in phase-1

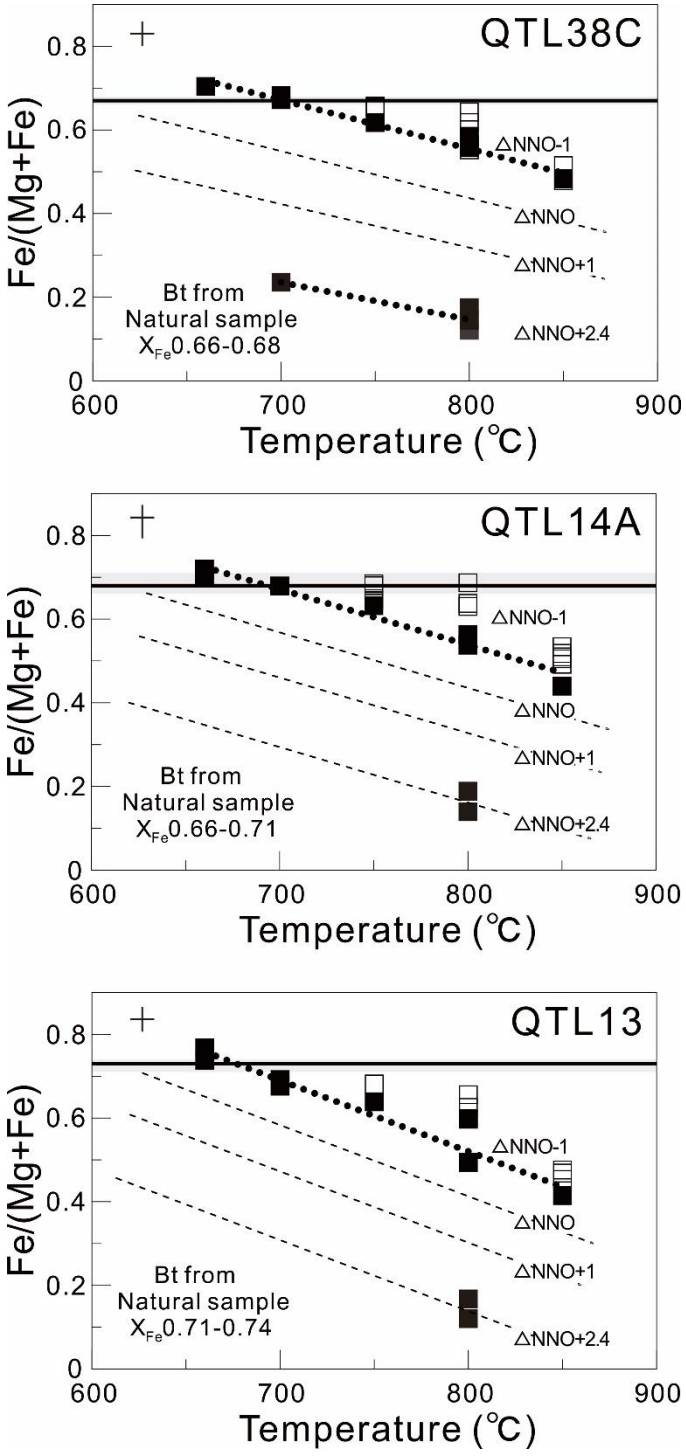

Fig. 5.5 Compositions of experimental biotite at water saturation (■) and below water saturation (□) plotted as a function of temperature and compositions of the natural biotites (shaded areas in grey color). The grey area are the range of Fe/(Mg+Fe) of natural biotites from 3 samples whereas the bold black lines are the average Fe/(Mg+Fe) values. The horizonal bar is the maximum uncertainty of temperature; the vertical bar is the maximum uncertainty of Fe/(Mg+Fe).

run products has a higher Usp content (41 mol%) compared to run products formed at oxidizing conditions (37 mol%). The bulk rock composition also affects Mag composition. For instance, at 200 MPa, 800 °C, water saturation and ~NNO+2.4, the Usp content decreases from the phase 1 to phase 3 compositions from 37 to 24 mol% (Appendix table 14).

5.2.2.6 Titanite

Ttn was observed in all three compositions but only at water-saturated conditions. At oxidizing conditions, Ttn crystallized at 800 °C (700 MPa) and 700°C (200 MPa) in phase-1 and intermediate phase-2 compositions. At reducing conditions, Ttn crystallized only at ≤700 °C, but ≥300MPa. Ttn has ~1.7-5 Al_2O_3, ~27-32 wt % TiO_2, and ~22-26 wt % CaO. With increasing crystallization pressure, Ttn Al_2O_3 content appears to decrease, while TiO_2 and CaO contents appear to increase.

5.2.2.7 Glass

Except for some crystal-rich charges at low H_2O_{melt}, the compositions of residual glasses were successfully analyzed by EMP. All glasses analyzed are homogeneous within the error of the method (see details in Appendix table 15). The residual glasses from our three series of experiments show closely comparable and coherent compositional trends, though they differ in absolute values. Glasses become more evolved as temperature and H_2O_{melt} decrease, being predominantly metaluminous. The composition of residual glasses produced at 200-300 MPa and reducing (~NNO-1.3) conditions are shown in Harker diagrams (Fig 5.6). Glass Al_2O_3 content significantly varies as a function of Pl abundance. In Pl-free charges at 200 MPa, Al_2O_3 shows minor variation (~14.8-15.5 wt % for phase-1 composition (QTL-38); ~14-15 wt % for intermediate phase-2 composition (QTL-14); ~13.8-14.3 wt % for evolved phase-2 composition (QTL-13), while it decreases significantly once Pl crystallizes. At temperatures higher than 700°C, the fact that the K_2O content increases with decreasing

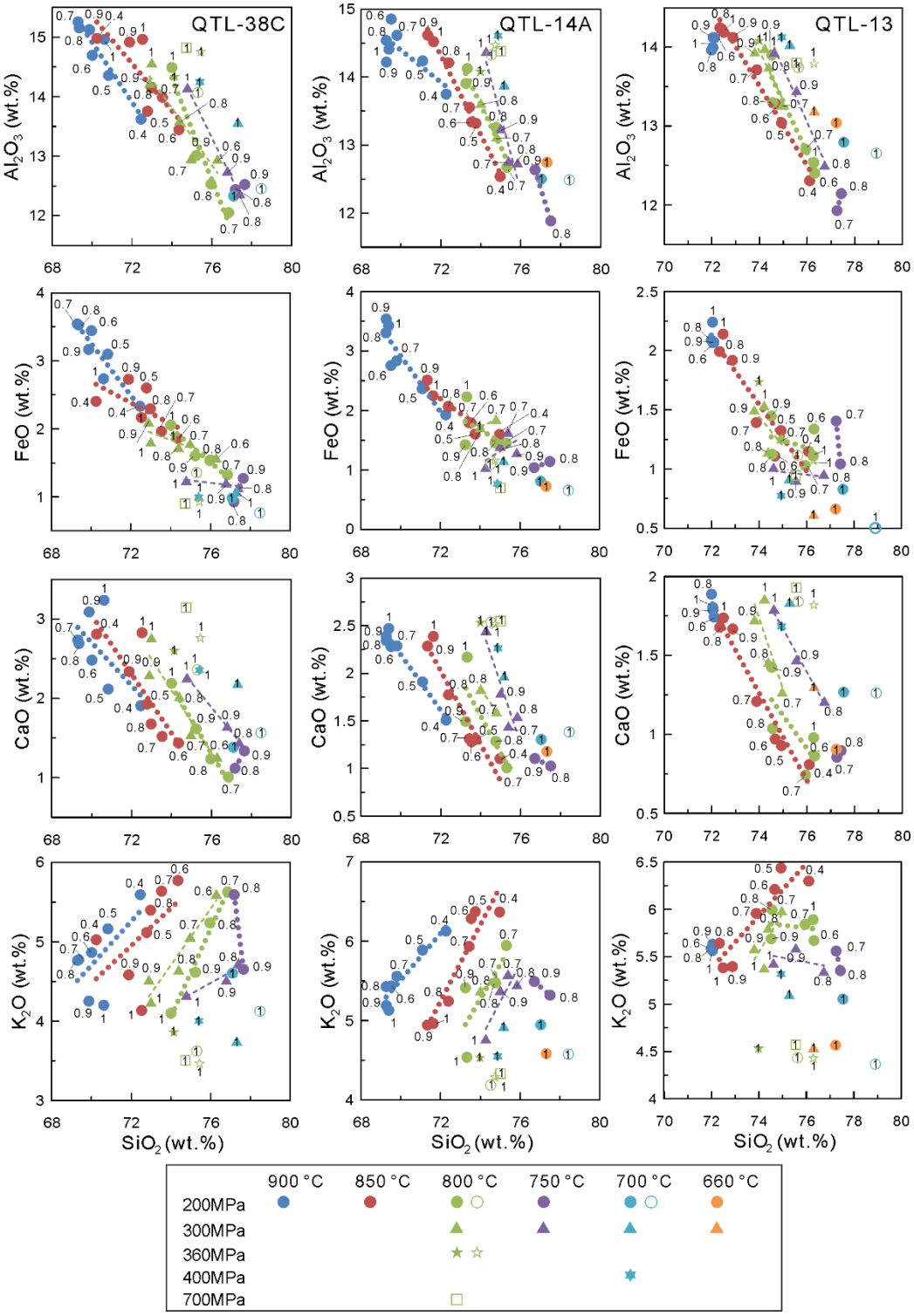

Fig. 5.6 Variation of residual glass compositions (on average) of samples QTL38C, QTL14A, QTL13 at different pressure, temperature, oxygen fugacity and melt H2O content conditions. Solid symbols and empty symbols represent those glass from reducing (~NNO-1.3) and oxidizing (~NNO+2.4) charges, respectively. The numbers attached to the symbols are the XH_2O values from each charge.

H_2O_{melt} reflects that at low H_2O_{melt} Bt crystallizes in relatively low proportion. Similarly, CaO and FeO (and TiO_2, not shown) contents continuously decrease with increasing degrees of crystallization, reflecting increasing precipitation of ferro-magnesian phases.

5.3 Discussion

5.3.1 Attainment of equilibrium

This study has used a standard procedure of crystallization which has been shown to allow attainment of equilibrium conditions in granitic systems (e.g. Clemens et al., 1981; 1986; Scaillet et al., 1995; Klimm et al., 2003; Pichavant, 1987; Pichavant et al., 2007). The textures and compositional attributes of our run products do not depart from those reported in previous studies on similar starting materials. The main features are that (1) the phases are homogeneously distributed, (2) the composition of minerals and glass in single charges is also homogeneous within the uncertainty of the method, (3) phase assemblages and compositions vary systematically with experimental parameters, and (4) mineral textures are also homogeneous, including those in highly crystallized charges. As outlined below, the experimental results reproduce the main petrological characteristics of the rocks selected for the experiments, showing that the investigated P-T-H_2O_{melt}-fO_2 space has captured the natural framework of magma evolution in the upper crust.

5.3.2 Comparison with previous phase-equilibrium studies

Several experimental studies have previously explored phase-equilibrium relations for metaluminous silicic rocks at conditions broadly comparable to those examined here (Appendix table 8). The study of Bogaerts et al. (2006) was carried out on a granodiorite composition (sample 98N06 from the Lyngdal massif in Norway) that

closely compares to our phase-1 granite composition except for its slightly higher Al_2O_3, CaO, Na_2O and K_2O contents. The Pinatubo dacite is also similar in composition to the Qitianling phase-1 granite except for its higher Al_2O_3, CaO, Na_2O and lower FeO and K_2O content. The phase-2 Qitianling granites compare to the Jamon (Dall'Agnol et al., 1999), Wangrah (Klimm et al., 2003), and Watergums (Clemens et al., 1986) granites. The Jamon and the AB412-Wangrah compositions are similar to the intermediate phase-2 composition (sample QTL14A), having higher contents of SiO_2 (by ~2 wt %) and Na_2O (by ~0.5 wt %) and lower contents of Al_2O_3 (by ~1 wt %) and K_2O (by ~1 wt %). The AB422-Wangrah and Watergums granites are similar to the evolved phase-2 composition (sample QTL-13), with higher contents of SiO_2 (by 1-2 wt %), slightly lower contents of Al_2O_3 (by ~1 wt %) and K_2O (by 0.5-1 wt %).

Both Qitianling phase-1 (QTL-38C) and the 98N06-Lyngdal granite (Bogaerts et al., 2006), show similar Bt and Amp upper thermal stability (around 875°C). The minimum H_2O_{melt} for Amp crystallization is also close to 5.5-6 wt % in both cases. The Pl in-curve at ~8 wt % H_2O_{melt} is equally near 750°C in both experimental series. The stability field of Mag, however, is smaller in our experiments compared to the Lyngdal granite experiments, which likely reflects the lower oxygen fugacity of our experiments (NNO-1.3 versus NNO-0.4 to NNO+0.8) and not bulk compositional effects. In contrast, the phase relationships of the Pinatubo dacite (at 220 MPa, NNO to NNO+2.7; Scaillet and Evans, 1999) differ from those determined for our phase-1 composition in that Cpx does not crystallize from the Pinatubo composition (at 220 MPa), that Amp thermal stability is higher (extending to over 900 °C), and that the thermal stability of biotite is ≤750°C. These differences can be ascribed to higher CaO and lower K_2O contents of the Pinatubo as compared to our phase-1 Qitianling starting material.

The comparison between the intermediate phase-2 Qitianling granite and the Jamon granite provides a further illustration of K_2O compositional control, in particular on the stability field of Amp. In the Jamon granite composition (K_2O~3.4 wt%), at ~300

MPa and NNO-1.5, Amp is stable up to 820°C and at H_2O_{melt} >4 wt%, while at similar P and fO_2 Amp was only found in one charge in our experiments on the intermediate phase-2 composition (K_2O~5.3 wt%), ie at 750°C, H_2O_{melt} ~8 wt % and NNO-1.3. The K_2O-rich character of Qitianling granites (compared to Jamon) (~5.3 versus 3.4 wt%), likely favours Bt over Amp, especially at high H_2O_{melt}. The experiments on the Jamon granite further show that increasing fO_2 (from ~NNO-1.5 to NNO+2.5) displaces the stability of Amp toward higher temperatures, so that Amp is no more present at the solidus under high fO_2 (see also Naney, 1983). Our experiments were, on average, slightly more oxidizing than those of Dall'Agnol et al (1999) (~NNO-1.3 versus ~NNO-1.5 for the reducing experimental series) and the small Amp stability fields determined for the Qitianling compositions is both related to an fO_2 effect and to the high K_2O content of the whole rock.

Our evolved phase-2 starting material (QTL-13) has the highest K_2O content (5.4 wt %) of all previously studied A-type granites, most closely approaching that of the AB422-Wangrah granite (4.9 wt % K_2O; Klimm et al., 2003). Both the evolved phase-2 and the AB422-Wangrah experimental series did not crystallize Amp and display similar Bt stability fields. The Watergums granite experiments (Clemens et al., 1986) also did not produce Amp but Bt, even though the Bt stability field is small (limited to >4 wt % H_2O_{melt} and ≤ 750°C) when compared to our results. This may be due to the low pressure (100 MPa for Watergums) and to the slightly lower K_2O content (~4.2 wt %) of the Watergums compared to the evolved phase-2 Qitianling granite.

Overall, the above comparison shows that high CaO and Al_2O_3 concentrations in metaluminous silicic to intermediate magmas increase the Pl stability field (at the expense of Cpx), while elevated K_2O enlarges that of Bt at the expense of Amp, shrinking the Amp field towards high H_2O_{melt}. Available experimental data indicate that amphibole crystallization is inhibited in SiO_2-rich (>70 wt%) and K_2O-rich (>4.5 wt%) magmas stored in shallow crust (≤ 300 MPa).

5.3.3 Crystallization conditions of the Qitianling granite (P-T -H_2O_{melt}-fO_2)

5.3.3.1 Pressure

At 200 MPa, only the phase-1 composition produced Amp, but not the phase-2 composition, which is in contrast with the occurrence of Amp in phase-2 rocks. Amp is moreover not a near solidus phase in the 200 MPa experiments (it only crystallized at >700 °C), yet it is inferred to have been a stable solidus phase in the natural system as Amp crystals are largely unzoned and as they do not show evidence for breakdown to either Bt or Ttn. At 300 MPa, in contrast, Amp is stable in the experiments using the phase-1 and the intermediate phase-2 composition (QTL14A), with a stability field extending to within <50 °C of the solidus. Amp is still absent from the crystallization products of the evolved phase-2 composition though, further suggesting that the crystallization conditions of the natural system were closely approached but not perfectly matched for all rocks. The average Al_{tot} content of the natural Amp in phase-1 and phase-2 granites is ~1.4-1.5, i.e. slightly higher than the Al content of the experimental Amp produced at 700°C and 300 MPa (Al_{tot} =1.43), yet significantly lower than the Al content of Amp produced at 700°C and 400 MPa (Al_{tot}=1.77). In our reducing experiments, Ttn was also observed only at ≥300 MPa, which is also in agreement with crystallization at moderately high pressure. In combination, we take the natural and the experimental phase relations and the amphibole compositions to conclude that the Qitianling magmas crystallized at ≥300 and <350 MPa.

This pressure range is in agreement with that retrieved using the natural amphibole compositions and various amphibole and amphibole-plagioclase barometers (360±90 MPa, Zhao et al., 2005; Appendix table 12). In combination they point to an emplacement depth of ~12-13 km, if we assume an average crustal density of 2600 kg/m^3. Gravimetry data indicate that the exposed rocks of the pluton represent the near-roof zone of a ~5 km thick intrusion (Liu et al. in revision), thus constraining pluton

emplacement at a mid-crustal depth of ~12-13 to ~17-18 km and at pressures of >300 to ~450 MPa. The inferred emplacement pressure and depth are higher than those typical for evolved magmatic reservoirs in arcs or anorogenic settings (typically ≤100-250 MPa, e.g. Scaillet et al., 1998; Mahood, 1984; Scaillet and Macdonald, 2001), but they compare to those of crustally-derived magmas emplaced within thick crust (typically at <400-500 MPa) (e.g. cf. Chaussard and Amelung 2014; Scaillet et al., 1995; Scaillet et al., 2016).

5.3.3.2 Temperature

Ilm or Ilm+Cpx are already present at 900 °C, the maximum temperature that we have explored in our experiments. This suggests that the Qitianling magmas formed at ~≥900 °C. The zircon saturation temperatures of the Qitianling granites are significantly lower (~715-875 °C, ~815°C on average), implying that zircon saturated late and that little to no zircon was inherited from the source, which is consistent with the magmatic zoning patterns and the scarcity of old, inherited zircon cores (e.g. Zhu et al., 2009). Pl of the natural samples has ~An43 to ~An02 composition. For crystallization under H_2O-rich conditions (as implied by amphibole occurrence), and at a pressure ≥300 MPa, the An range of Pl records crystallization at ≤700-750 °C (cf. Fig.5.2). Compositional plateau zones with ~An32, ~An32 and ~An25 of natural Pl in our phase-1, intermediate phase-2, and evolved phase-2 samples are matched by experimentally produced Pl crystallized at≤700 and 660 °C and at H_2O saturation.

That natural Amp in phase-1 and phase-2 granites has an X_{Fe} of ~0.6-0.8 which indicates that all crystals equilibrated at ≤800 °C. That the largest proportion of Amp has an X_{Fe} of ~0.7 highlights that they crystallized at near-solidus conditions at ≤660 °C if crystallization took place at H_2O saturation and at ~NNO-1±0.5 (as discussed further below). The Si content of the natural Amp crystals is, however, slightly lower than that of the crystals formed in our 300 MPa near-solidus experiments (~6.6 versus ~6.9 apfu), which we interpret to reflect the slightly higher crystallization pressure of the natural

crystals (at >300 and <350 MPa). Bt in the natural granites commonly includes Ti-Fe oxides and it is locally included in Amp (as euhedral-subhedral crystals), consistent with the interpretation that it commenced crystallization at high-temperature (but below 850 °C; cf. Fig. 5.1). At ~NNO-1±0.5, the Bt XFe of ~0.7 records crystallization (and/or re-equilibration) at ~650°C (Figs. 5.4, 5.5), ie similar to the compositional record of both Amp and Pl.

The comparison of Amp, Bt, and Pl compositions in the natural samples with our experimental run products highlights that the main mass of the Qitianling minerals record near solidus conditions at ≤660-700 °C. This is in contrast to the amphibole and amphibole-plagioclase crystallization temperatures estimated using the natural mineral compositions and the calibrations of Anderson and Smith (1995) and Putirka and Keith (2016), which both yield calculated crystallization temperatures of ~750-800 °C. The reason for the high calculated temperatures is that the Qitianling Amp has relatively low Si contents (~6.4-6.7 apfu), which reflects its crystallization at fairly reducing conditions(<NNO to ~NNO-1.3; Appendix table 12), where residual melts have relatively lower-SiO_2 contents compared to melts produced under more oxidizing conditions (Fig. 5.6). Anderson and Smith (1995) caution that their calibration should not be applied to Amp crystallized at <NNO. Putirka and Keith (2016) does not suggest any such restriction for the application of their Amp thermometers (equations 5 and 6). Our results show that for the compositions and crystallization conditions considered here, temperatures are significantly overestimated (1) for amphibole crystallized at oxidizing conditions and (2) for amphibole crystallized at low temperatures (at <750 °C). We therefore conclude that redox conditions should be defined prior to carrying out thermometric calculations based on amphibole chemistry.

5.3.3.3 Melt H_2O content

Amp is characteristic for the phase-1 and phase-2 Qitianling granites. The minimum H_2O_{melt} at which Amp stabilized in our crystallization experiments is ~5.5-

6.0 wt % at 850-800 °C and 200 MPa, highlighting that the natural magmas must have been H_2O-rich. At 300 MPa, Amp crystallization requires even higher H_2O_{melt}, i.e. ~6.5 wt % for phase-1 and ~8 wt % for intermediate phase-2, and thus H_2O_{melt} at or very near saturation. The rim compositions of the natural Pl crystals (~An20 for phase-1 and intermediate phase-2 and ~An2 for the evolved phase-2) are consistent with crystallization at or below 660 °C near H_2O-saturation. For an inferred crystallization pressure of ≥300 MPa, we thus construe that the Qitianling magmas crystallized at H_2O_{melt} ≥7.5-8.0 wt %. The low-Fe Amp and high-An Pl compositions (Fig. 5.4) in some of the natural crystal cores further indicate that H_2O_{melt} ≥7.5-8.0 wt % was already achieved at ~750-800 °C at relatively low crystallinities of ~15-30 wt% (Appendix table 9). This in turn suggests that liquidus H_2O_{melt} was >5-6 wt%, and thus significantly higher than that typical for A-type granites (i.e. ≤2.5-4.5 wt% H_2O; e.g. Clemens et al., 1986; Bonin, 2007). The high melt H_2O contents may relate to dehydration partial melting of hydrous source minerals such as amphibole and biotite, which may yield initial H_2O_{melt} of up to 8.8 wt% (cf. Beard and Lofgren, 1991). An alternative explanation is that fluids were derived from mantle-derived magmas underplated in the lower crust (inferred to have provided most of the heat for generating the crustal melts and Jurassic granites in SE China and to be volumetrically important in the lower crust; e.g. Zhao et al. 2012) and fluxed the granitic source(s), although it is not certain that such fluids would have been H_2O-rich (to comply with our inferred XH_2O of ~1, Fig. 5.1).

5.3.3.4 Oxygen fugacity

In our ~NNO+2.4 experiments, Mag is the only oxide, while Mag and Ilm coexist in the natural samples, ruling out such oxidizing conditions. In our reducing experiments at ~NNO-1.3, both Ilm and Mag coexist at ≤850 °C. The compositions of amphibole and biotite, in particular their Fe/(Fe+Mg) ratios, are also well reproduced in our reduced runs at near solidus temperatures (Fig. 5.4, 5.5), suggesting similarly

low fO_2. While Ttn has been found in evolved magmas crystallized at oxidizing conditions (~NNO+2.5; e.g. Dall'Agnol et al. 1999), it is, however, also present in our experiments performed at reducing conditions (~NNO-1.3) at 300 and 400 MPa, at $\leqslant$ 700°C, and at H_2O saturation (see also Xirouchakis and Lindsley, 1998). Taken together, our results thus suggest that the Qitianling magma(s) evolved at redox conditions around NNO-1±0.5. This range is lower than that inferred by Zhao et al. (2005) based on calculated biotite Fe^{2+}/Fe^{3+} composition: the estimated fO_2 with this method ranges between the NNO and the MH buffers. We note, however, that the granitic samples studied by Zhao et al. (2005) are spatially associated with the Furong tin deposit, and thus that these samples may have crystallized at, or evolved to, a different oxygen fugacity than the main intrusion, which we have characterized in our study. We also note that redox conditions may have increased during subsolidus cooling, i.e. during hydrothermal alteration that produced the tin deposit. In support of this are the Fe-Ti oxides whose restored compositions yield fO_2 around NNO+1 (for temperatures around 580°C). This subsolidus oxidation event may have increased the Fe^{3+}/Fe^{2+} ratio of biotites.

5.3.4 Geochemical evolution of the Qitianling pluton

The phase-1 to phase-3 granites of the Qitianling pluton could (1) be related by fractionation or (2) represent source partial melts with variably evolved composition. The uncertainties associated when using plutonic rocks as proxies of liquid composition

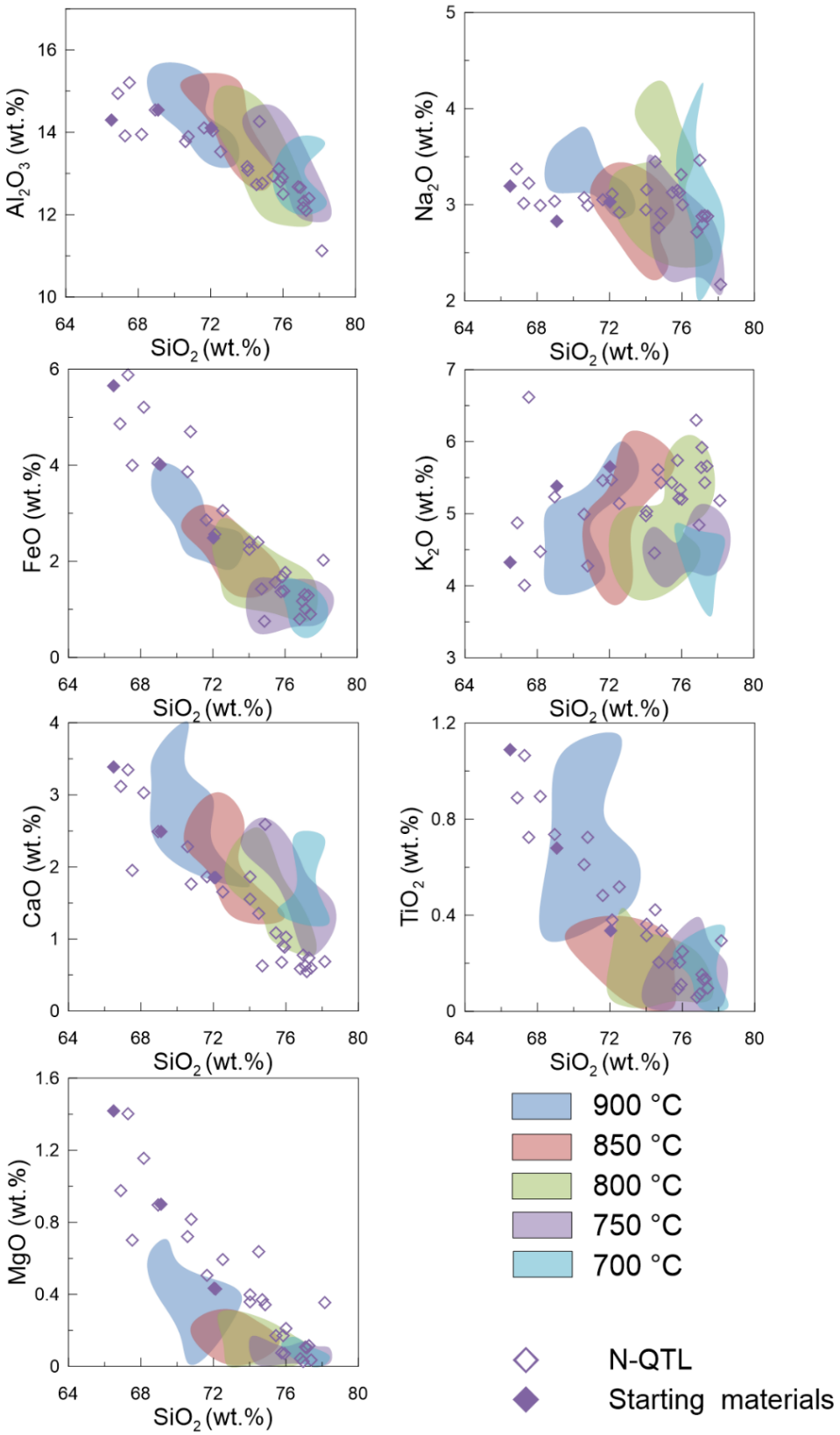

Fig. 5.7a The whole rock composition of natural samples (◇) (normalized to 100 wt %) compared to the residual glass compositions from phase 1 composition (QTL38C).

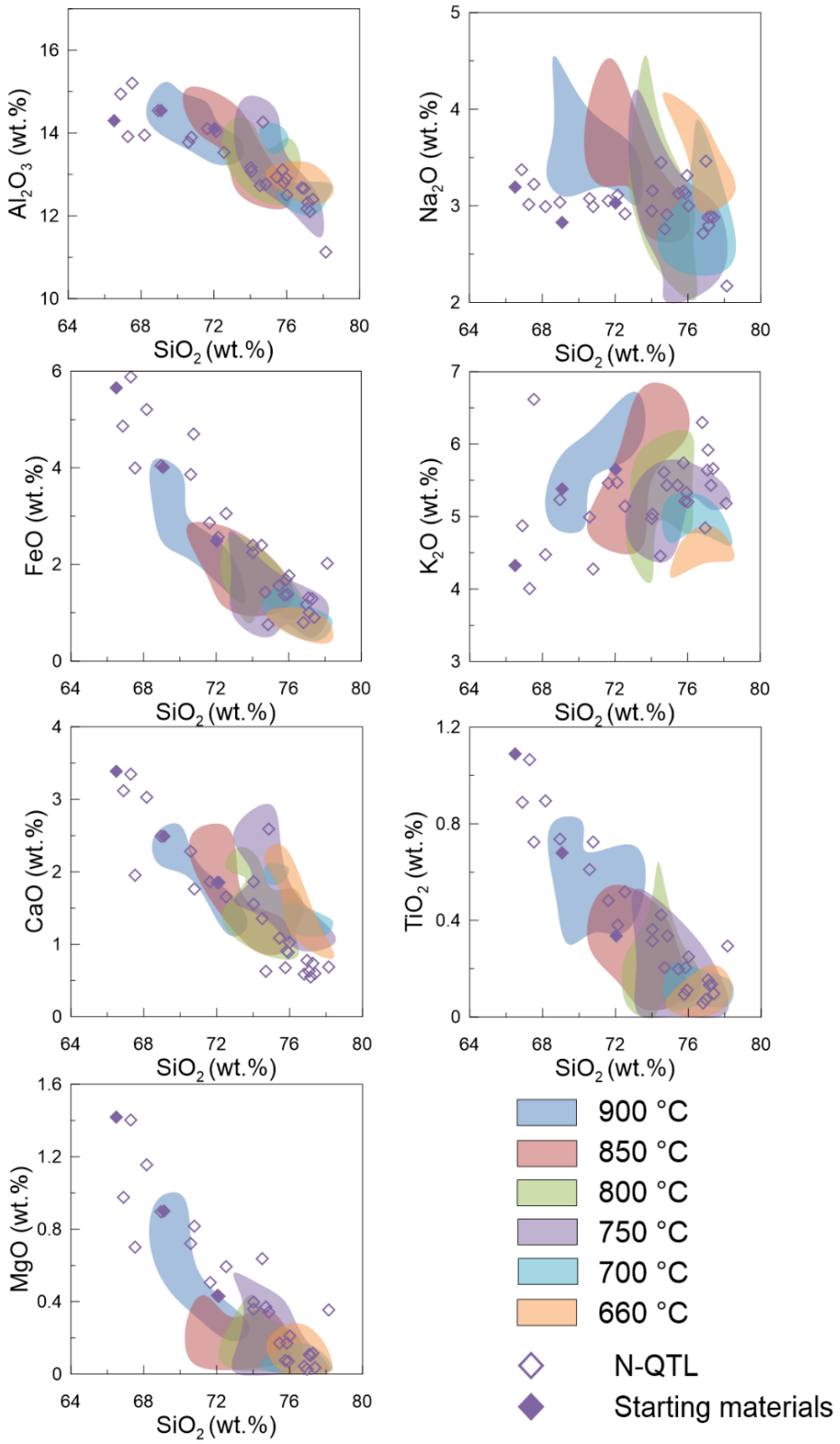

Fig. 5.7b The whole rock composition of natural samples (◇) (normalized to 100 wt %) compared to the residual glasses from intermediate phase 2 composition (QTL14A).

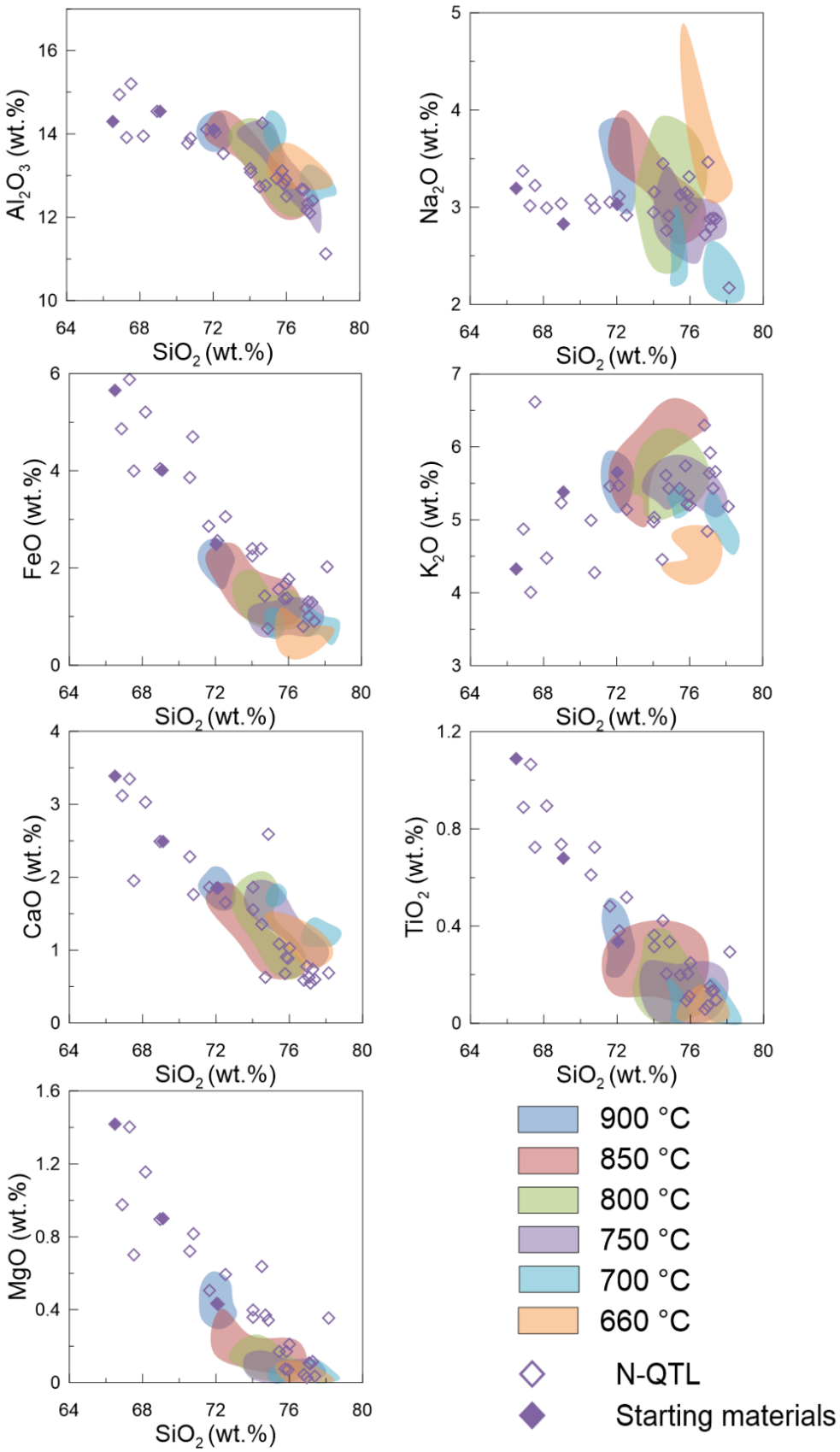

Fig. 5.7c The whole rock composition of natural samples (◇) (normalized to 100 wt %) compared to the residual glasses from evolved phase 2 composition (QTL13).

(e.g. see Pitcher (1997) for a detailed discussion), makes difficult to interpret in detail the compositional variations displayed by the whole suite (Fig. 5.7a-c). Yet, the following observations can be made. Firstly, liquids obtained from the crystallization of our most mafic starting material, (the phase-1 composition, QTL-38C), match the composition of the phase-2 granites at temperatures of ~900°C to 850°C and the composition of the most evolved, phase-3, granites at temperatures of ≤750°C (Fig. 5.7.a). Residual liquids from phase-2 magma at ≤700 °C equally match the most evolved whole-rock compositions of the pluton. This indicates that the more evolved rocks of the pluton (i.e. phase-2 and/or phase-3 granites) may represent low-temperature differentiates of magma equivalent to the phase-2 and/or phase-1 whole-rock compositions. Secondly, if compositions with <~72 wt% SiO_2 were not reproduced is due to the fact that we did not explore temperatures higher than 900°C, which would have produced crystal-poorer run products with lower-SiO_2 glass compositions. Experiments at 950°C would presumably extend the experimental trend toward more mafic compositions, approaching the bulk composition of our starting materials, hence reproducing the entire natural compositional field. Thirdly, the effect of variable pressure and H_2O_{melt} on experimental liquids is subtle, but nevertheless significant for the range explored. In particular, at 200 MPa, liquid CaO contents are notably lower and the liquid Na_2O and K_2O contents are notably higher than for liquids produced at ≥300 MPa (Fig. 5.6; Appendix table 15).

If such a shallow fractionation took place, then mafic cumulates should be present somewhere in the system. Granitoid rocks more mafic than those exposed in the Qitianling pluton exist in the Jurassic Huashan pluton, which crops out ~200 km southwest of the Qitianling pluton. The Huashan pluton is compositionally and mineralogically similar to Qitianling (Feng et al., 2012), save for the occurrence of more mafic varieties (the Niumiao unit with ~58-60 wt% SiO_2, ~14 wt% Al_2O_3, ~7 wt% FeO, ~5-6 wt% CaO, ~3 wt% Na_2O and ~4 wt% K_2O), which extend the Qitianling whole-rock compositional trends towards more mafic compositions. These mafic rocks

could represent the cumulated counterpart magmas, which at Qitianling would be present at a level below exposure.

Overall, that the experimentally-determined liquid lines of descent at 300 MPa and ~NNO-1±0.5 closely compare to those of the whole-rock compositional trends is thus taken to suggest that some fractionation of a relatively homogeneous bulk (source-derived) magma took place at or close to the emplacement level. Interestingly, taken at face value, the geochemical trends preserved within the pluton correspond to a temperature range of 900-660°C (Fig. 5.7).

5.4 Summary

Our experimental study on three different compositions of the Qitianling granite in Southern China shows that the magmas were both hot and water-rich, emplaced in the mid crust (10-12 km), and that their redox state was below NNO (at ~NNO-1±0.5) during crystallization. Our experimental results, and their comparison with previous experimental studies reveal clearly that amphibole stability in potassium-rich granites is limited to water-rich conditions. The usual minimum H_2O_{melt} content necessary for calcic amphibole crystallization in metaluminous silicate melts is widely quoted at around 4 wt %. Our results show this minimum is close to 6 wt % for K_2O-rich silicic magmas. The data also show that the geochemical trends displayed by the pluton can partly result from shallow level crystallization, yet they do not rule out source inheritance as a controlling factor.

Chapter 6 Experimental study on Fe/(Fe+Mg) in amphibole and biotite, an oxygen barometer for intermediate or acid-intermediate (granitoids) magma system

6.1 Introduction

Oxygen fugacity is a significant parameter in either volcanic or plutonic systems (Scaillet et al., 1998; Scaillet and Gaillard, 2011; Ishihara, 1977). The redox state of a magma has a huge effect on its crystallization order, or on the proportion and composition of minerals during the cooling period (Grove and Baker, 1984; Dall'Agnol et al., 1999; Berndt et al., 2005). What is more, this effect is also seen in partition coefficients of many elements in the magma, which may have a strong control on its metallogenic behavior during the magmatic or post-magmatic (hydrothermal) stage (Bindeman et al., 1998; Ballard et al., 2002; Belvin, 2004; Aigner-Torres et al., 2007). Since evaluating the oxygen fugacity of magma system allows us to better understand rock forming and ore forming processes, several oxybarometers and redox proxies have been developed over the years.

Based on the correlation between oxygen fugacity and multivalent elements in minerals and melts, the quantitative evaluation of the redox state in magma and fluid becomes possible. For instance, using the "ternary" biotite solid solutions and the stoichiometric calculations of Fe^{3+} and Fe^{2+} in biotite, Wones and Eugster (1965) proposed a biotite-oxybarometer. Ti-Fe oxides, e.g. magnetite and ilmenite, are also widely used as a redox state sensor (Powell and Powell, 1977; Spencer and Lindsley, 1981; Andersen and Lindsley, 1985). Similarly, on the basis of reaction $2Fe_2O_3$ (in ilmenite) + $4TiO_2$ (rutile) = $4FeTiO_3$ (in ilmenite) + O_2, Zhao et al. (l999) proposed a rutile–ilmenite oxybarometer. Ottonello et al. (2001) and Moretti (2005) used a thermodynamic model to calculated Fe in silicate melts and glass depending on the

redox state, so that the iron redox ratio of glasses can be used as an oxybarometer (e.g., Kress and Carmichael, 1991). France et al. (2010) used the partition coefficients of Fe^{3+} and Fe^{2+} in plagioclase and clinopyroxene, to provide a plagioclase-clinopyroxene oxybarometer. More recently, accessory minerals, e.g. zircon and apatite, have been also used as new redox proxies, based on the behaviour of Mn, Ce and Eu (Burnham and Berry, 2012; Trail et al., 2012; Miles et al., 2014; Smythe and Brenan, 2016).

Below, using our phase equilibrium experiments presented in Chapter 5, complemented by a few more experiments, we develop a model aimed at setting up an oxybarometer which can be used in intermediate or acid-intermediate magma compositions, ie for granitic rocks sensu lato, in which either amphibole or biotite, or both, are present.

6.2 Starting materials of oxygen fugacity experiments

In addition to the ~NNO+3 and ~NNO-1.3 crystallization experiments already presented, two experiments at an oxygen fugacity of ~NNO and ~NNO+1 (at 300MPa and 800 °C) were carried out to explore in greater detail the oxygen fugacity effect on the composition of amphibole and biotite. The running times of those two runs were 188 hours and 284 hours, respectively. To test the effect of whole rock composition, in addition to our 3 Qitianling samples (QTL-38C, QTL-14A and QTL-13), we used 3 other compositions: e.g. Santa Maria dacite (with 65.4 wt% of SiO_2 and $Fe\#_w = FeO_{tot}/(FeO_{tot}+MgO)$ 0.79, Rose, 1987), Pinatubo dacite (with 65.5 wt% of SiO_2 and Fe# = 0.68, Scaillet and Evans, 1999) and Jamon hornblende biotite monzogranite (with 70.62 wt% of SiO_2 and Fe#= 0.86, Dall'Agnol et al., 1999). For the Qitianling, Pinatubo and Santa Maria compositions, we carried out crystallization experiments using the dry glass as the starting material while for Jamon and one sample from Qitianling (QTL-38C) we carried out melting experiments using the bulk rock powder as the starting material. The compositions of different starting materials are shown in Appendix table

16. All charges were water-saturated, with about 10 to 15 wt% added water, depending on pressure.

All crystallization and melting experiments were conducted using internally heated pressure vessels. The different oxygen fugacity conditions were controlled by adding different amounts of H_2. The preparation of capsules for melting experiments is similar to crystallization experiments, except that the material loaded into the capsules for melting experiments is the bulk rock powder in lieu of the dry glass powder. The details of capsules preparation for crystallization experiments are described in Chapter 3.

6.3 Experimental results

6.3.1 Crystallization experiments

The results of crystallization experiments of Qitianling granite which were conducted under reducing conditions (~NNO-1.3) are discussed in Chapter 5. Here, we focus on the run products of other compositions (Santa Maria dacite; Pinatubo dacite and Jamon granite) and on those from Qitianling granite obtained at oxidizing (~NNO+2.3) or relatively oxidizing conditions (~NNO and ~NNO+1). All experimental results are listed in Appendix table 17.

For the 3 compositions of Qitianling granite, magnetite (Mag), ilmenite (Ilm), clinopyroxene (Cpx), amphibole (Amp), biotite (Bt), plagioclase (Pl), titanite (Ttn) and glass (Gl) were produced in the crystallization experiments at 800°C, 200 MPa-670MPa, ~NNO- ~NNO+2.4 and H_2O-saturation conditions. At NNO~+2.4, 200 MPa, in the charges of composition QTL-38, Cpx, Amp, Bt, Mag and Pl crystallized. As pressure increases from 360 MPa to 670 MPa, Pl disappears and at 670 MPa, Ttn is present. At 670 MPa, in the charges with 15 wt% added water, Amp was not observed. In all these oxidized charges, Mag is the only Ti-Fe oxide. For the compositions of QTL-14A and QTL-13, at NNO~+2.4, the same mineral phases crystallised, except Amp and Pl. At around NNO+1, with Bt and Mag, Ilm crystallize in all 3 Qitianling

compositions. Like the experiments at NNO~+2.4, Amp crystallised only in composition QTL-38 while Cpx was observed in compositions QTL-14A and QTL-13.

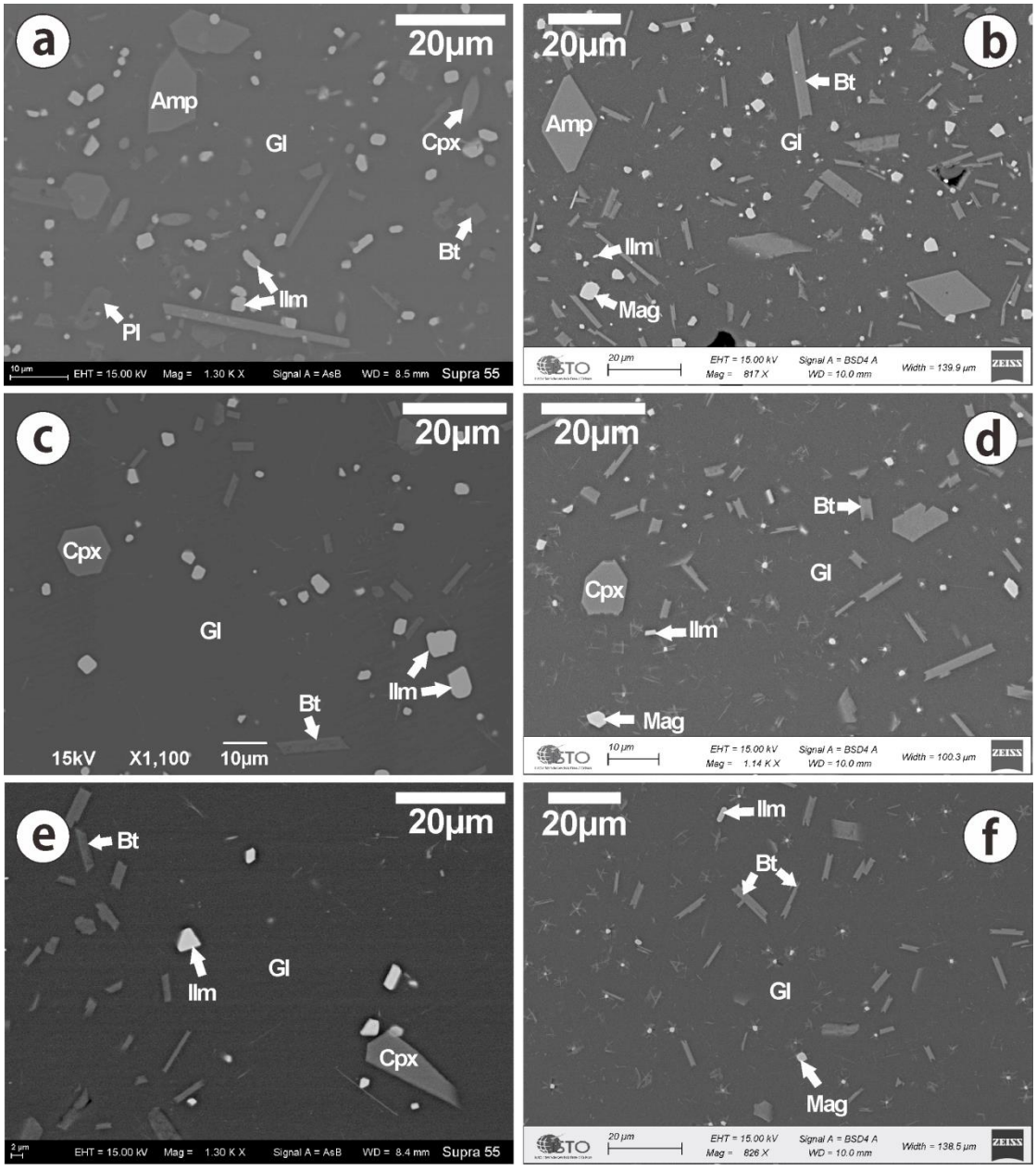

Fig. 6.1 Back-scattered electron (BSE) images of experimental run products (crystallization experiment) of Qitianling granite at ~NNO-1.3, 800°C, 200 MPa and water saturation (a,c,e), and at ~NNO, 800°C, 300MPa and water saturation(b,d,f). a,b are run products of QTL-38; c,d are run products of QTL-14; e,f are run products of QTL-13. Abbreviations: Ilm: ilmenite; Mag: magnetite; Cpx: clinopyroxene; Amp: amphibole; Bt: biotite; Pl: plagioclase; Gl: glass.

Pl was only observed in composition QTL-13.

At NNO, the phase assemblages are the same than those at NNO+1 for the three compositions, except that Pl is not stable. Representative back-scattered electron (BSE) images of run products of Qitianling granite are shown in Fig 6.1

Representative back-scattered electron (BSE) images of run products of Santa Maria and Pinatubo dacites are shown in Fig 6.2. At ~NNO-1.3, from 700°C to 800°C and between 200 MPa and 400 MPa, Amp, Ilm, Pl are present in all the experiments of Santa Maria composition (Fig 6.2 a,c). Because the crystallized phases at 660°C are too small to be identified, these results were not included in our discussion. When oxygen

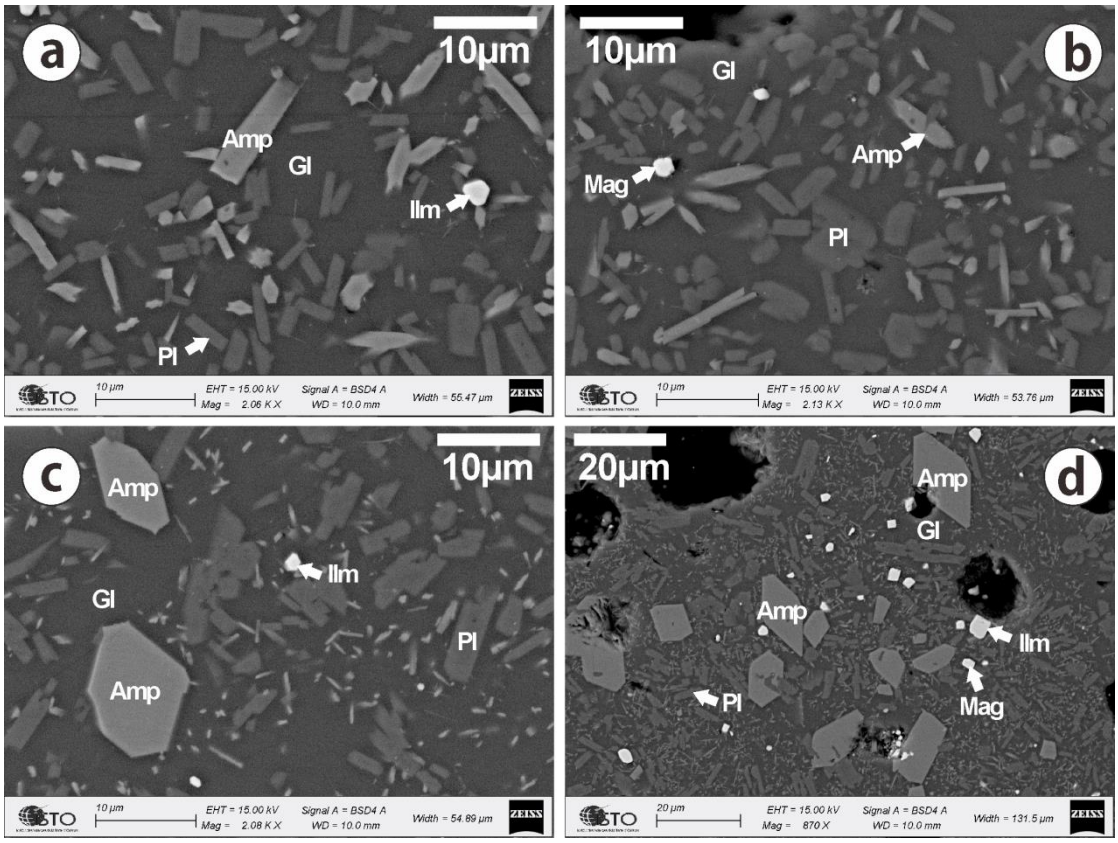

Fig. 6.2 Back-scattered electron (BSE) images of experimental run products (crystallization experiment) of Santa Maria (a,b) and Pinatubo (c,d) dacites at ~NNO-1.3, 800°C, 300MPa and water saturation(a,c); and at ~NNO+1, 800°C, 300MPa and water saturation(b,d). Abbreviations are the same as Fig.6.1.

fugacity increases to ~NNO, at 300 MPa and 800°C, Amp and Pl still crystallize while magnetite becomes the dominant oxide (Fig 6.2 b, d). Similar phase assemblages can be observed at ~NNO+1, 300 MPa and 800°C.

For the Pinatubo composition, at ~NNO-1.3, from 700°C to 800°C and 200 MPa and 400 MPa, Amp, Ilm and Pl crystallized, Qtz being present as well at 700°C and 200 MPa. At ~NNO and ~NNO+1, 800°C and 300 MPa, in addition to Amp, Ilm, Pl, Mag also crystallized.

6.3.2 Melting experiments

Representative back-scattered electron (BSE) images of run products are shown in Fig 6.3. At 660 °C, 200 MPa and ~NNO-1.3, the bulk rock powder of Jamon hornblende biotite monzogranite and Qitianling amphibole-biotite granite (QTL-38C) do not display glass, being therefore below solidus at this pressure. Amp, Ilm, Mag, Bt,

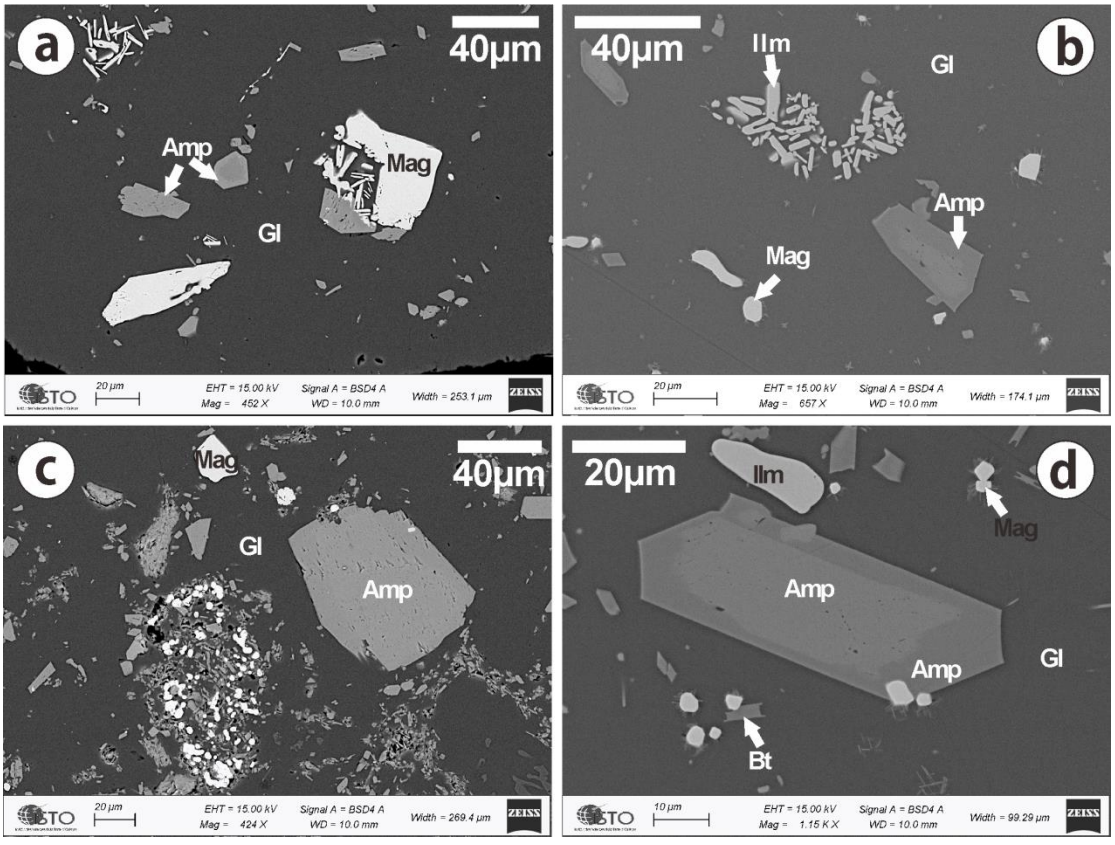

Fig. 6.3 Back-scattered electron (BSE) images of experimental run products (melting experiments) of Jamon (a,b) and Qitianling QTL-38 (c,d) granites at ~NNO-1.3, 700°C, 400 MPa and water saturation(a,c); and at ~NNO, 800°C, 300 MPa and water saturation(b,d). Abbreviations are the same as Fig.6.1.

Pl, Kfs and Qtz were well preserved in the charges. As temperature increased to 700°C, glass was observed in the charge of Qitianling composition. Qtz, Kfs and Pl were partially melted with a round shape and reaction rims can be observed in Amp and Bt. However, for the Jamon composition, glass pockets were difficult to found. At 700°C and 400 MPa, Qtz, Kfs and Pl are absent in the Jamon granite while for Qitianling granite only Kfs and Qtz disappeared. Mag and Ilm start to melt. Amp and Bt have re-equilibrated rims, some small isolated euhedral Amp crystals being also present (Fig. 6.3 a versus c). At 750°C, 300 MPa, the Qitianling composition has the same phase assemblages with a slightly higher melting degree when compared to the charge at 700°C, 400MPa.

At 800 °C, 300 MPa and ~NNO, the melting degree increased further as anticipated. In both compositions, Pl melted out totally. Mag and Ilm partially melted having a typical round shape, some small recrystallized angular oxides being present as well. Amp also partially melted having re-equilibrated angular rims. Bt was no longer observed in the melting experiment of Jamon composition, while some large Bt still persists in Qitianling with a re-equilibrated texture (Fig. 6.3 b versus d). At 800 °C, 300MPa and ~NNO+1, the phase assemblages are similar to those at ~NNO for both compositions.

6.3.3 Phase chemistry

6.3.3.1 Amphibole

Amp data were collated from 22 charges of different starting materials including 13 crystallization and 9 melting experiments (Appendix table 17). Besides, Amp data from 12 charges of Qitianling compositions at reducing condition (11 charges of QTL-38 and 1 charge of QTL-14) are also included (Appendix table 12 in chapter 5). All representative compositions of Amp are given in Appendix table 18. Microprobe analyses show that all the experimental Amp from different starting materials belong to

the calcic group Amp (Leake et al., 1997, 2003). For Qitianling compositions, at 800 °C, from 200 MPa to 670 MPa, at ~NNO+2.4, ~NNO+1 and ~NNO and water-saturated conditions, only QTL-38 composition successfully crystallized Amp. Al_{tot} of those Amp ranges between 1.48 and 1.70 a.p.f.u. Fe#= molar $Fe_{tot}/(Fe_{tot}+Mg)$ ranges from 0.18 to 0.48. At reducing condition (~NNO-1.3) and 800°C, Fe# rises up to 0.58. At a fixed temperature, as pressure increase (from 200 MPa to 670 MPa), Fe# slightly changes: e.g. at 800°C and ~NNO+2.4, Fe# = 0.21, 0.21, 0.18 at 200MPa, 360MPa and 670MPa, respectively. Similar results are obtained at reducing conditions. At 800°C

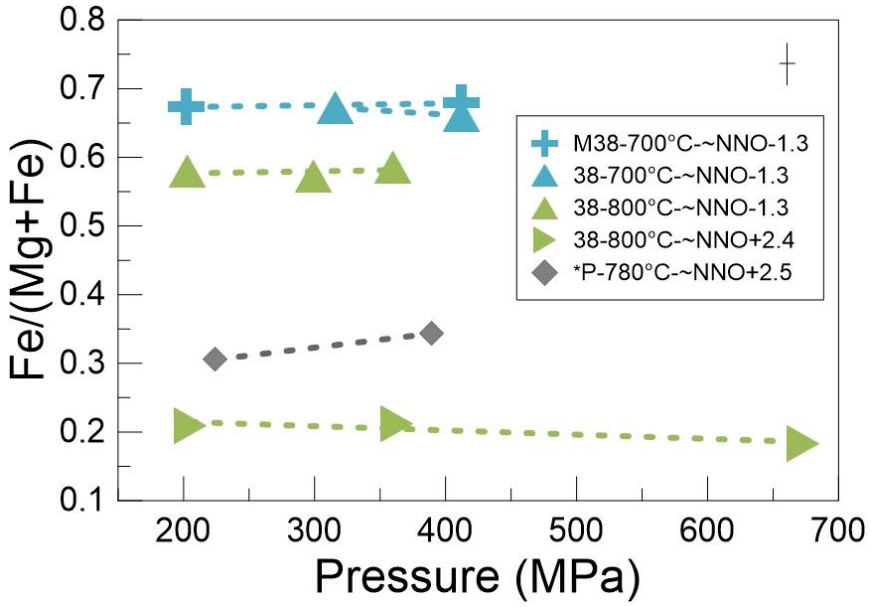

Fig. 6.4 Fe#= $Fe_{tot}/(Fe_{tot}+Mg)$ of experimental amphiboles plotted as a function of pressure. 38 stands for Qitianling granite (QTL-38C); M38 stands for melting experiment of QTL-38C; *P are the data of experimental Amp compositions of Pinatubo dacite from Scaillet and Evans, 1999. Vertical error bar gives the standard deviation of Fe#, and the horizontal bar gives the uncertainty on pressure.

and ~NNO-1.3, Fe# = 0.58, 0.57 and 0.59 at 200 MPa, 300 MPa and 360 MPa, respectively. Melting experiments at different pressures also show a similar Fe# behaviour. These results indicate that the effect of pressure on the Fe# of Amp in the investigated range (from 200 MPa to 700 MPa) is marginal. At a constant temperature and similar oxygen fugacity condition, Amp from the Pinatubo experiments (Scaillet and Evans (1999)) shows a slight increase of its Fe# from 220 MPa to 390 MPa, which

remains moderate however. (Fig. 6.4).

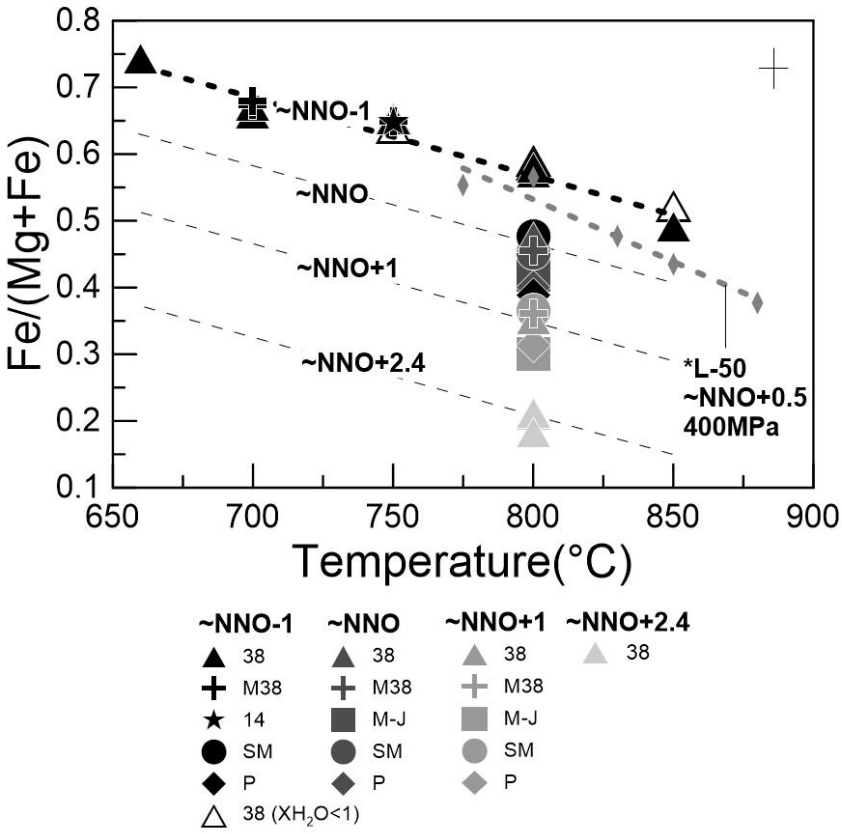

Fig. 6.5 Fe#= $Fe_{tot}/(Fe_{tot}+Mg)$ of experimental amphiboles plotted as a function of pressure. Different symbols represent different starting materials: 38 stands for Qitianling granite (QTL-38C); M38 stands for melting experiment of QTL-38C; 14 stands for Qitianling granite (QTL-14A); M-J stands for melting experiment of Jamon granite; SM stands for Santa Maria dacite and P stands for Pinatubo dacite; *L are experimental Amp of Lyngdal granodiorite from Bogaerts et al., 2006. All solid symbols are at water saturation condition ($XH_2O=1$) while empty symbols are from water under saturation conditions ($XH_2O<1$). The vertical error bar is the standard deviation of Fe#, and the horizontal bar is the uncertainty of temperature.

As for the Santa Maria dacite composition, Amp crystallized at 200 MPa to 400 MPa has a Al_{tot} which ranges between 1.4 and 1.7. At 700°C, ~NNO-1.4 and 400 MPa, Amp has the highest Fe# value (= 0.53). At the same oxygen fugacity condition and 800°C, Fe# decreases to 0.47. When fO2 increases from NNO to NNO+1, Fe# decreases from 0.45 to 0.37. Similar results are obtained with the Pinatubo composition: Al_{tot} varies from 1.0 to 1.7 from 200 MPa to 400 MPa. At ~NNO-1.4, Amp at 700°C

and 400 MPa has an Fe# = 0.45 while at 800°C Fe# = 0.39. As oxygen fugacity increases, Fe# = 0.40 and 0.31, at ~NNO and ~NNO+1, respectively (Fig. 6.4).

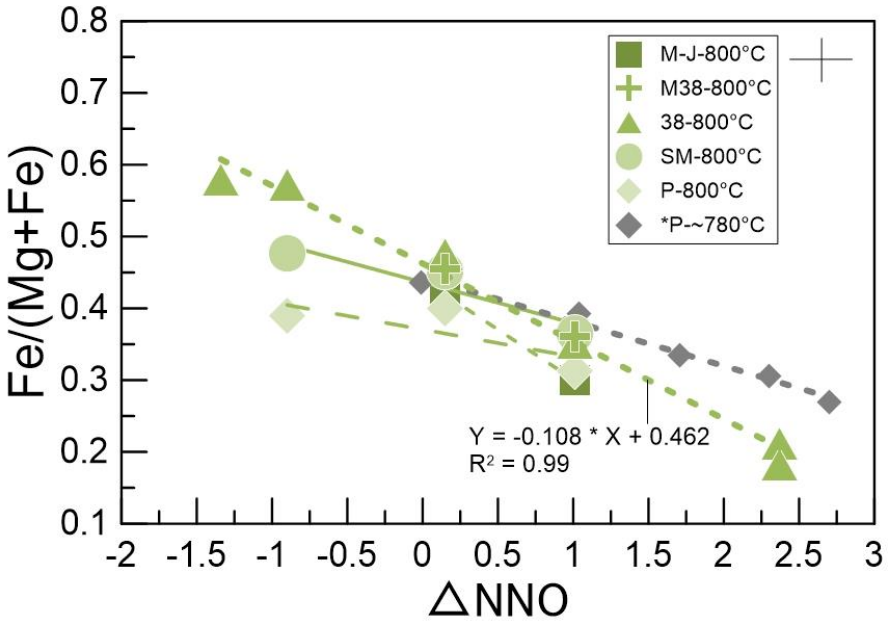

Fig. 6.6 Fe#= $Fe_{tot}/(Fe_{tot}+Mg)$ of experimental amphiboles ($XH_2O=1$) plotted as a function of oxygen fugacity (△ NNO=logfO_2exp-logfO_2NNO). *P are the data of experimental Amp composition cited form Scaillet and Evans, 1999. Vertical error is the maximum standard deviation of Fe#, and the horizontal bar is the maximum uncertainty of oxygen fugacity (△NNO).

In the melting experiments of Jamon and Qitianling (QTL-38) granites, most large relict Amp crystals display core and rim texture (Fig. 6.3). Amp rim compositions are similar to small euhedral Amp. The Amp rim in Jamon granite composition has an Al_{tot} ranging from 1.0 to 1.5 while the Altot core varies from 1.0 to 1.3 which is close to the natural Amp composition (Al_{tot} is 1.2-1.4, Dall'Agnol et al., 1999). The highest Fe# of the Amp rim is 0.72 at 700°C, ~NNO-1.4. At 800°C and more oxidizing conditions (~NNO and ~NNO+1), Fe# = 0.42 and 0.3, respectively. For the composition of Qitianling granite QTL-38, Amp rims have an Al_{tot} varying from 1.36 to 1.81 when the melting conditions are 700°C-800°C, 200 MPa - 400 MPa, ~NNO-1.3- ~NNO+1. At reducing conditions (~NNO-1.3) and 700 °C, Fe# = 0.67 and 0.68 at 200 MPa and 400 MPa, respectively. At 750 °C, Fe# = 0.65. At 800°C, Fe# = 0.46 and 0.36 at ~NNO and

~NNO+1, respectively. For the composition QTL-38, at the same experimental conditions (T, P, fO_2 and H_2O content), the composition of the rim of the Amp in the melting experiments is close to the composition of the Amp from the crystallization experiment (e.g. at 700 °C, 400MPa, ~NNO-1 and water saturation, the Fe# of the Amp rim from the melting experiment is 0.66 and that from the crystallization experiment is 0.68).

In a summary, the oxygen fugacity effect on Amp depends on the composition of the starting material (Fig. 6.6). At 800°C, 1) at ~NNO+2.4, Fe# of Amp from Qitianling is around 0.20, while for those from Pinatubo (Scaillet and Evans, (1999)) Fe# is around 0.31 (at 781°C). Note that in addition to the composition, this difference may be also caused by the temperature, since the temperature gap is up to 20°C. 2) At ~NNO+1 and ~NNO, Amp crystallized from different starting materials have similar Fe#: e.g. at ~NNO+1, Fe# of Amp is 0.30 for M-J (Jamon melting experiment), 0.36 for M-38(QTL38 melting experiment), 0.35 for Qitianling QTL38, 0.37 for Santa Maria dacite and 0.31 for Pinatubo dacite; at ~NNO, Fe# of Amp is 0.42 for M-J (Jamon melting experiment), 0.46 for M-38 (QTL38 melting experiment), 0.48 for Qitianling QTL38, 0.45 for Santa Maria dacite and 0.40 for Pinatubo dacite. 3) In contrast, at ~NNO-1, the Fe# of Amp displays obvious differences depending on different starting materials. For Qitianling granite, Santa Maria and Pinatubo dacites, the Fe# of Amp is ~0.58, 0.47 and 0.39, respectively. The difference of Fe# of Amp among different starting materials reflects the FeO_t/ (FeO_t+MgO) of bulk rock compositions: from Qitianling (QTL-38C), to Santa Maria and Pinatubo dacites, the bulk rock FeO_t/ (FeO_t+MgO) decreases from 0.81, to 0.79 to 0.68, respectively.

6.3.3.2 Biotite

Experimental Bt was only observed in Qitianling run products (QTL-38, QTL-14 and QTL-13) while in Santa Maria and Pinatubo compositions, Bt is not stable at the

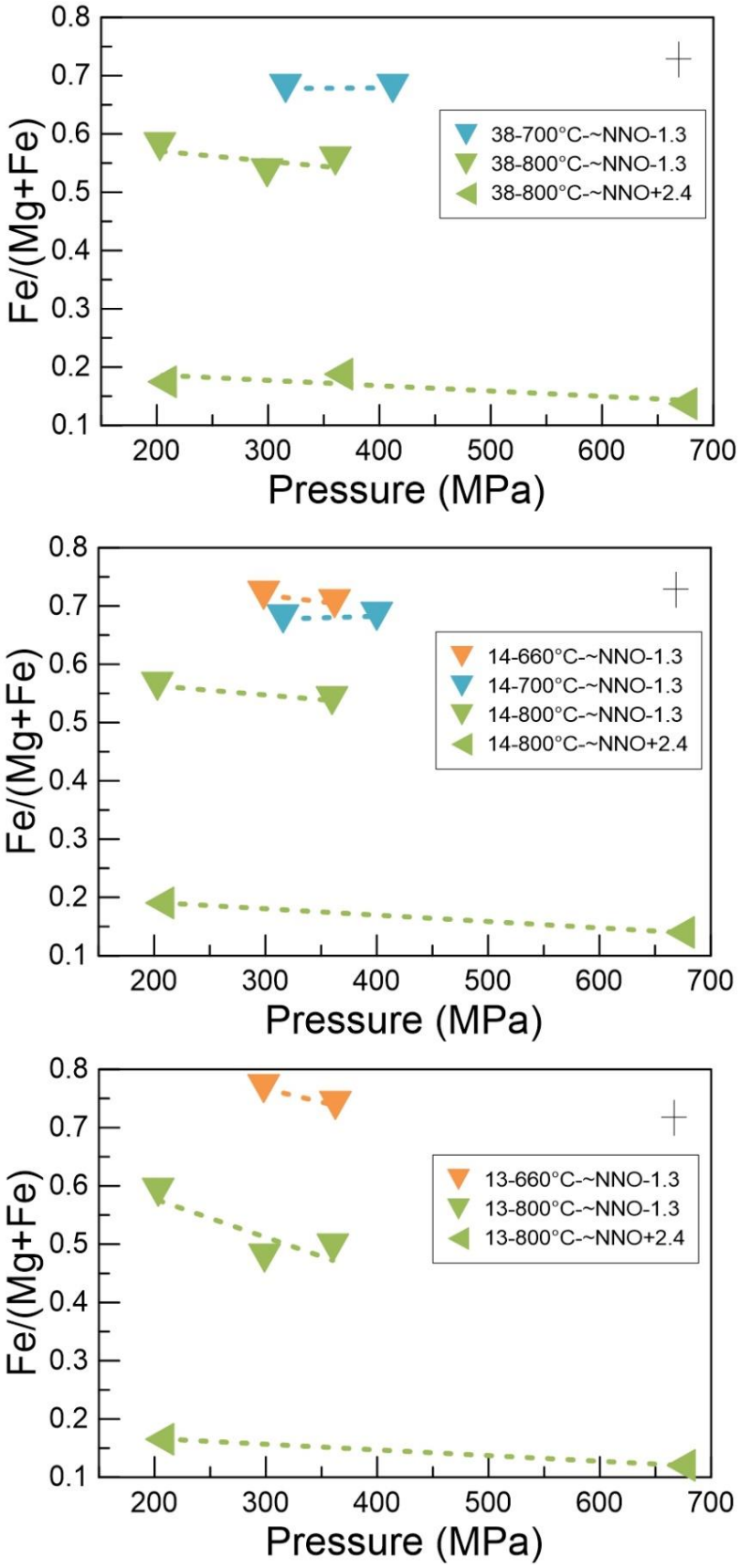

Fig. 6.7 Fe#= $Fe_{tot}/(Fe_{tot}+Mg)$ of experimental biotite plotted as a function of pressure.

experimental conditions of this study (Appendix table 17). The Bt composition (the recrystallized rim) from the melting experiment of Jamon granite is difficult to determine because of the contamination and the difficulty of distinguish with the Bt core and recrystallized Bt rim (Fig. 6.3). Therefore, Bt with K_2O lower than 6% and higher than 10% were excluded in this study. Representative compositions of Bt are given in Appendix table 19.

Experimental Bt from reducing conditions is close to annite while that from oxidizing condition is close to phlogopite. Bt has an Si (a.p.f.u) mostly between 5.0 and 6.5 and Al_{tot} (a.p.f.u) ranges from 1.9-2.6. The Fe# varies from 0.15 to 0.70. As for Amp, pressure effect on Fe# is negligible when compared to other experimental parameters (e.g. T and fO_2,). At 800 °C and water saturation, as pressure changes from 200 MPa to 670 MPa, the Fe# of Bt from the 3 Qitianling compositions is 0.12-0.19 at ~NNO+2.4 and 0.41-0.48 ~NNO-1. From mafic (QTL-38) to felsic (QTL-13) compositions, the pressure influence on Fe# becomes slightly larger (Fig. 6.7 a, b and c). As for the temperature effect, when temperature decrease, the Fe# of Bt increases systematically for all 3 compositions (Fig. 6.8): at around NNO-1 and water saturation conditions, the Fe# of Bt from QTL-38 are 0.48 (at 850°C), 0.53-0.58 (at 800°C), 0.62 (at 750°C), 0.68 (at 700°C) and 0.70 (at 660°C). Similar trends can be seen for the Bt of the 2 other more felsic compositions. Everything else being equal, the highest Fe# of experimental Bt (up to 0.74) is from the most felsic composition. (Fig. 6.8). Oxygen fugacity effect on Fe# of Bt is also similar to that of Amp, ie, as oxygen fugacity increases, Fe# decreases. For instance, at 800°C and water saturation, the Fe# of experimental Bt crystallized from the most mafic composition (QTL-38) at ~NNO-1, ~NNO, ~NNO+1 and ~NNO+2.5 are 0.53-0.58, 0.48, 0.34 and 0.14-0.19, respectively (Fig. 6.8a). This trend is also observed for Bt crystallized from the two other compositions. Similarly to the temperature effect, at a fixed oxygen fugacity, Bt from the most felsic composition tends to have the highest Fe# (e.g. at 800°C and ~NNO+1, Fe# of QTL38C, QTL14A and QTL13 are 0.34, 0.36 and 0.40, respectively).

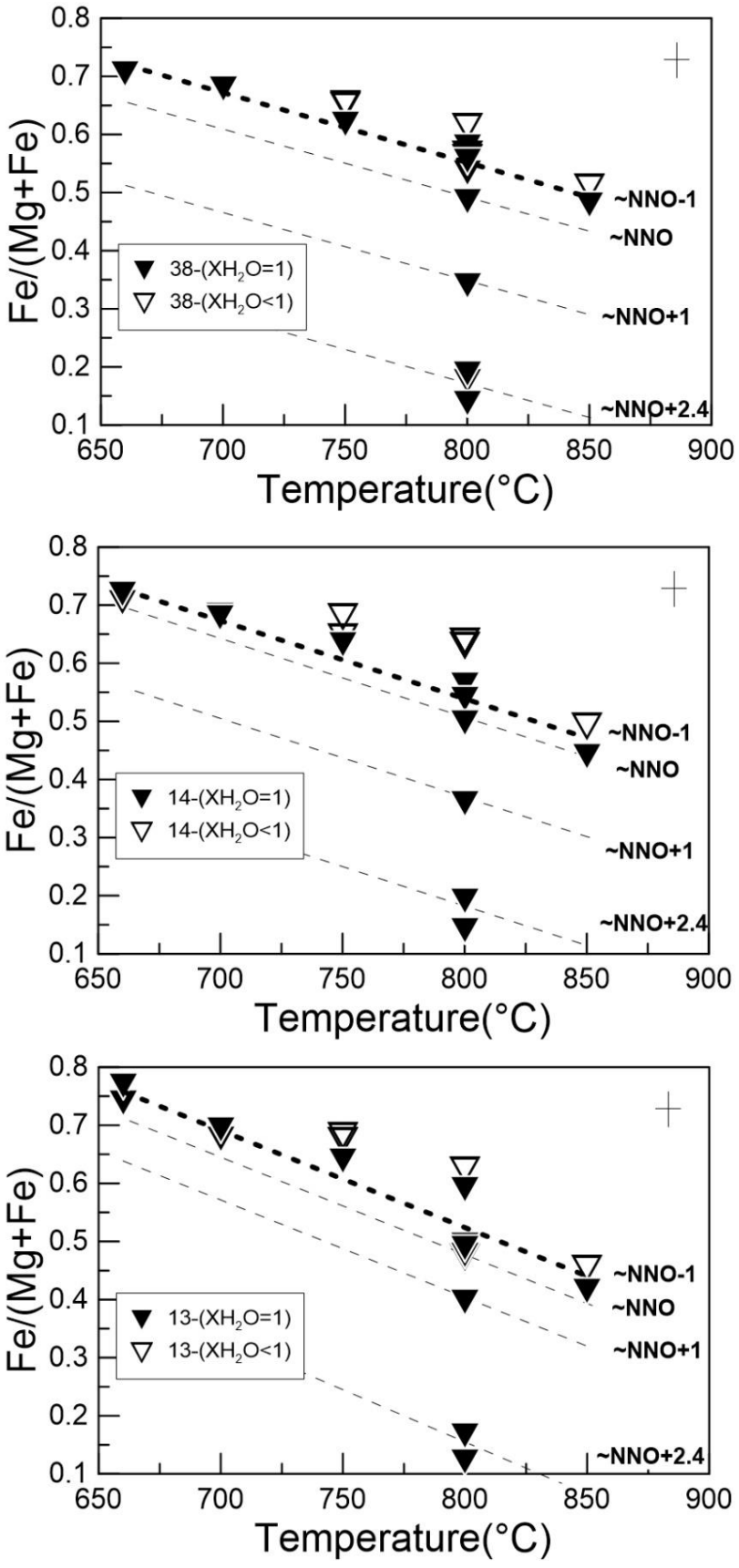

Fig. 6.8 Fe#= $Fe_{tot}/(Fe_{tot}+Mg)$ of experimental biotite plotted as a function of temperature.

At the same experiment condition including temperature(T), pressure(P), oxygen fugacity(fO_2) and water content (XH_2O), the Fe# of Amp is close to the Fe# of Bt, the Fe# of Amp being slightly higher than the Fe# of Bt (<0.04). In addition to the most mafic composition (QTL-38C, with bulk rock FeO_t/(FeO_t+MgO)=0.81), one charge of the intermediate felsic composition (QTL-14A, with bulk rock FeO_t/(FeO_t+MgO) = 0.82) also crystallized Amp and Bt which have the similar Fe# when compared with the most mafic composition at the same experimental conditions.(Fig. 6.9).

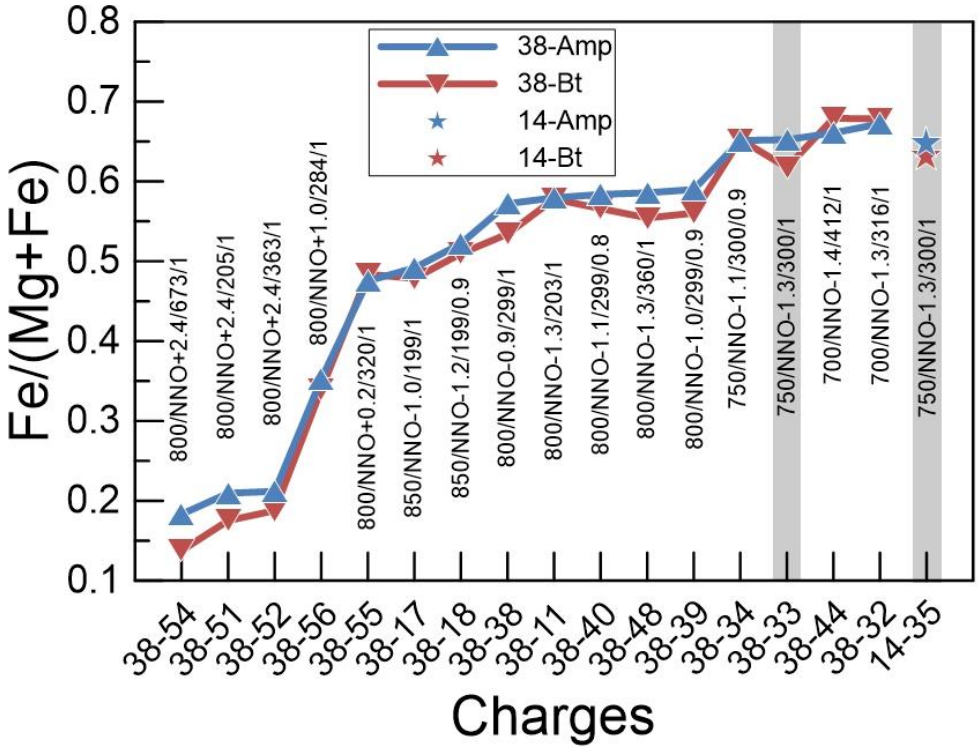

Fig. 6.9 Comparison of Fe#= Fe_{tot}/(Fe_{tot}+Mg) between experimental Amp (Blue) and Bt (Red) at the same experimental conditions. The label of each charge represents T(°C)/fO_2(NNO)/P(MPa)/XH_2O. The two charges marked in grey are from the same run which were at the same experimental conditions.

6.4 Oxygen fugacity barometer

6.4.1 Oxygen fugacity dataset

In order to extend the range of bulk composition for our oxygen fugacity barometer, in addition to our experimental results, part of the data from Dall'Agnol et al. (1999); Bogaerts et al. (2003); Klimm et al. (2003); Scaillet and Evans, (1999) and Prouteau and Scaillet, (2003); Scaillet, (1995); Scaillet and Macdonald, (2003) were considered in our modeling (Fig. 6.10； Appendix table 20&21). We first derive the oxygen barometer based on Amp composition, and then use the same approach for Bt.

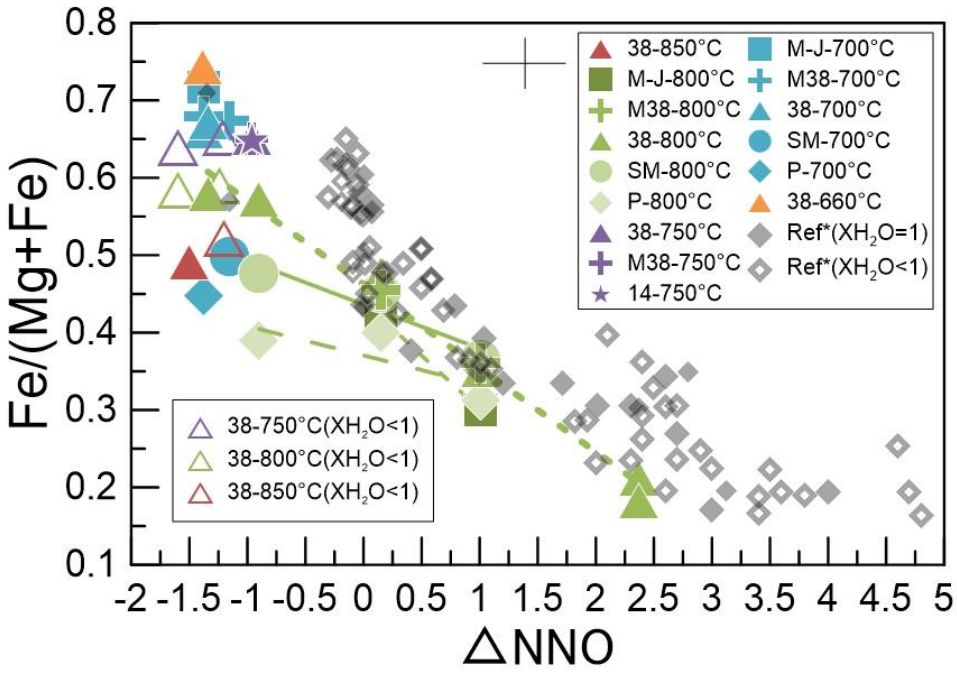

Fig. 6.10 Fe#= $Fe_{tot}/(Fe_{tot}+Mg)$ of experimental Amp plotted as a function of oxygen fugacity. Ref* are the data (in grey colour) of experimental Amp composition of Jamon granite from Dall'Agnol et al., 1999; Wangrah granite from Klimm et al., 2003; Lyngdal granodiorite from Bogaerts et al., 2006 and Bogaerts, 2003 and Pinatubo dacite from Scaillet and Evans, 1999; Prouteau and Scaillet, 2003. The vertical error is the standard deviation of Fe#, and the horizontal bar is the uncertainty of oxygen fugacity (△NNO).

6.4.2 Oxygen fugacity calibration modeling

6.4.2.1 Amphibole calibration

From Fig. 6.5 and Fig. 6.10, we can see that the composition of starting materials, oxygen fugacity, temperature and to some extent water in melt (via its role on fO_2) affect the Fe# of Amp. Therefore, combining Amp from other experimental starting materials (Jamon granite; Wangrah granite; Lyngdal granodiorite and Pinatubo dacite) with our experimental Amp, the following simple empirical oxygen barometer was derived:

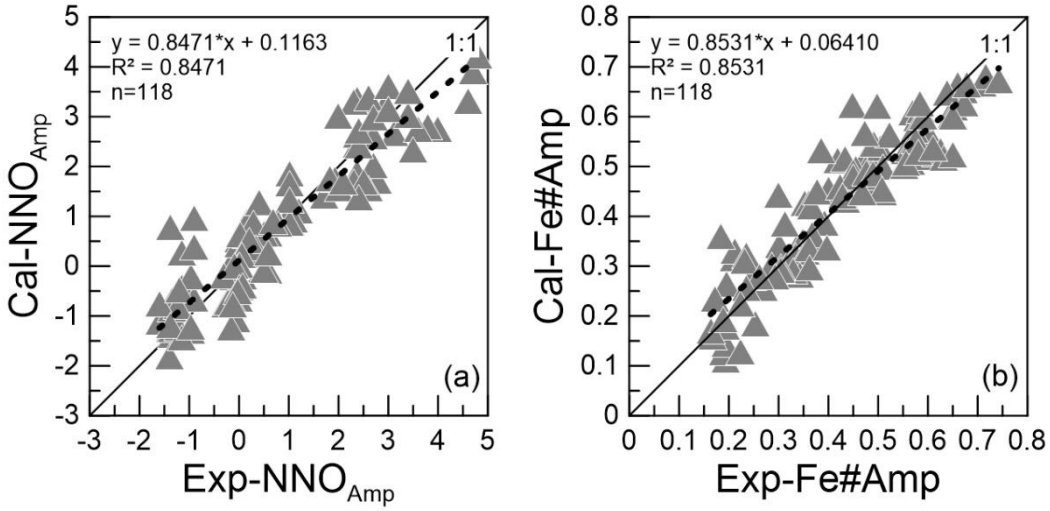

Fig. 6.11 Oxygen fugacity (NNO value) calculated using our modeling based on equation (1) vs. NNO value of experiments (a). Fe#= $Fe_{tot}/(Fe_{tot}+Mg)$ of Amp calculated vs. Fe#= $Fe_{tot}/(Fe_{tot}+Mg)$ of Amp measured in the experiments (b). Some Amp data are from Dall'Agnol et al., 1999; Bogaerts et al., 2006 and the studies of Bogaerts, 2003; Scaillet and Evans, 1999 and Prouteau and Scaillet, 2003.

$$\triangle NNO = -0.00254 \times T(°C) - 13.9602 \times Fe\#Amp + 0.00143 \times P(MPa) + 6.2809 \times Fe\#Amp \times Fe\#w + 0.2803 \times wTiO_2 - 2.1 \times w(Al_2O_3/SiO_2) + 0.2768 \times w(Na_2O/K_2O) + 5.9663 \quad (1)$$

where T is temperature in °C, Fe#Amp is $Fe_{tot}/(Fe_{tot}+Mg)$ of Amp in apfu, Fe#W is $FeO_{tot}/(FeO_{tot}+MgO)$ of whole rock composition, P is pressure in MPa, $wTiO_2$ is the

composition of whole rock, w(Al_2O_3/SiO_2) and w(Na_2O/K_2O) are the ratios of whole rock composition.

The comparison between calculated and measured fO2 is shown in Fig. 6.11a. showing that equation (1) reproduces reasonably well the experimental data (R^2=0.8157) over 6 log units of fO2 variation. Similar results also come when using the Fe# of Amp (Fig. 6.11b), equation (2):

$$Fe\#Amp = -0.0004418 \times T(°C) - 0.07625 \times \triangle NNO + 0.3272 \times Fe\#w + 0.0000967 \times P\ (MPa) + 0.5646 \quad (2)$$

6.4.2.2 Bt calibration

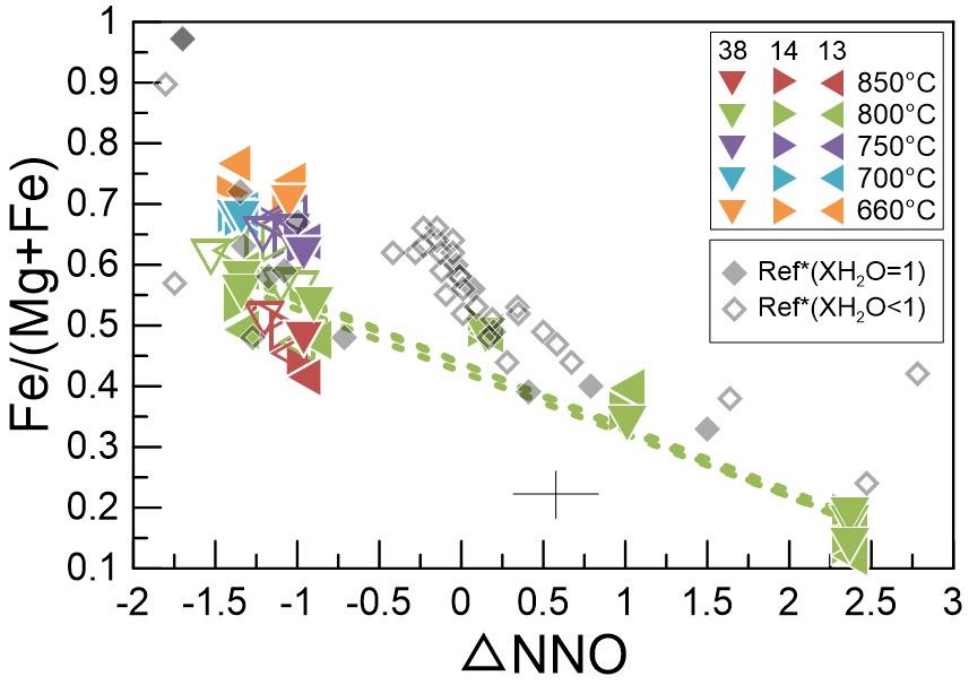

Fig. 6.12 Fe#= $Fe_{tot}/(Fe_{tot}+Mg)$ of experimental Bt plotted as a function of oxygen fugacity. Solid symbols represent water-saturated data while empty triangles stand for the data below H_2O saturation. Ref* are the data (in grey colour) of experimental Bt of Jamon granite from Dall'Agnol et al., (1999) Lyngdal granodiorite from Bogaerts et al. (2006) and Bogaerts (2003) and Pinatubo dacite from Scaillet and Evans (1999). The vertical error is the standard deviation of Fe#, while the horizontal bar is the uncertainty of oxygen fugacity (△NNO).

Just like for Amp, the Fe# value of Bt varies also with the oxygen fugacity,

temperature or water content in melt (Fig. 6.12). Therefore, we developed a Bt oxygen barometer with similar input parameters:

$$\triangle NNO = -0.0004 \times T(°C) - 0.0004 \times Fe\#Bt + 8.3772 \times Fe\#Bt \times Fe\#w + 0.0027 \times P(MPa) + 2.4082 \quad (3)$$

where T is temperature in °C, Fe#Bt is $Fe_{tot}/(Fe_{tot}+Mg)$ of Bt in apfu, Fe#W is $FeO_{tot}/(FeO_{tot}+MgO)$ of whole rock composition, and P is pressure in MPa.

Similarly, a model to calculate Fe#Bt of Bt is given by the following equation:

$$Fe\#Bt = -0.00034 \times T(°C) - 0.11339 \times \triangle NNO + 0.8056 \times Fe\#w + 0.000324 \times P(MPa) \quad (4)$$

Based on the equation (3) and (4), the calculated oxygen fugacity (in NNO) and Fe#Bt values from Bt are generally close to the experimental values (Fig. 6.13), though a significant dispersion is observed at high fO_2.

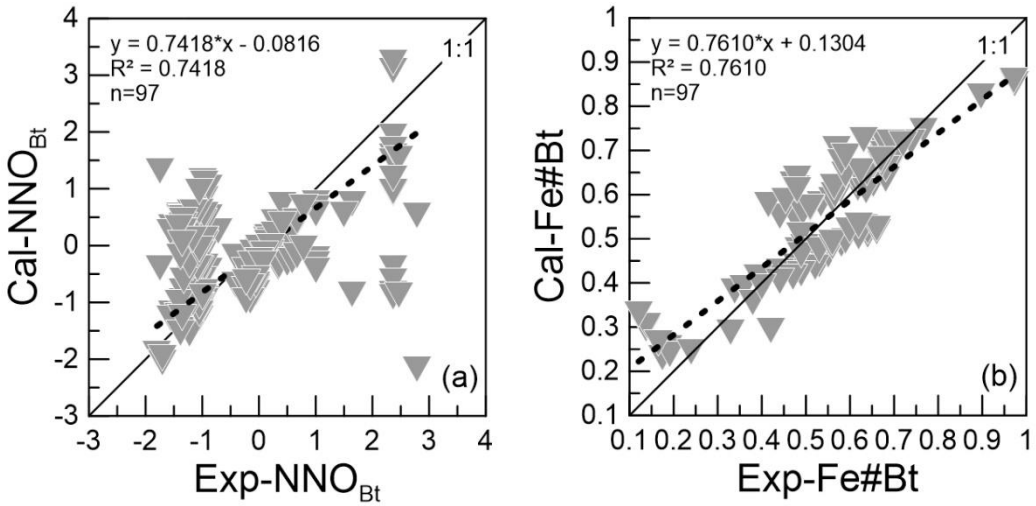

Fig. 6.13 Fe#= molar $Fe_{tot}/(Fe_{tot}+Mg)$ of Bt calculated use the equation (2) vs. Fe#= molar $Fe_{tot}/(Fe_{tot}+Mg)$ of Bt measured in experiments(a). Oxygen fugacity (NNO value) calculated using our modeling (based on Fe# of Bt), equation (2) vs. NNO value of experiments(b). Some Bt data are from Dall'Agnol et al., 1999; Bogaerts et al., 2006 and Bogaerts, 2003.

6.4.3 Oxygen fugacity modeling test and application

6.4.3.1 Modeling testing

In order to evaluate and test our oxygen fugacity models, the data of Fe# of bulk rock, Amp and Bt, temperature and pressure were collected from studies which used

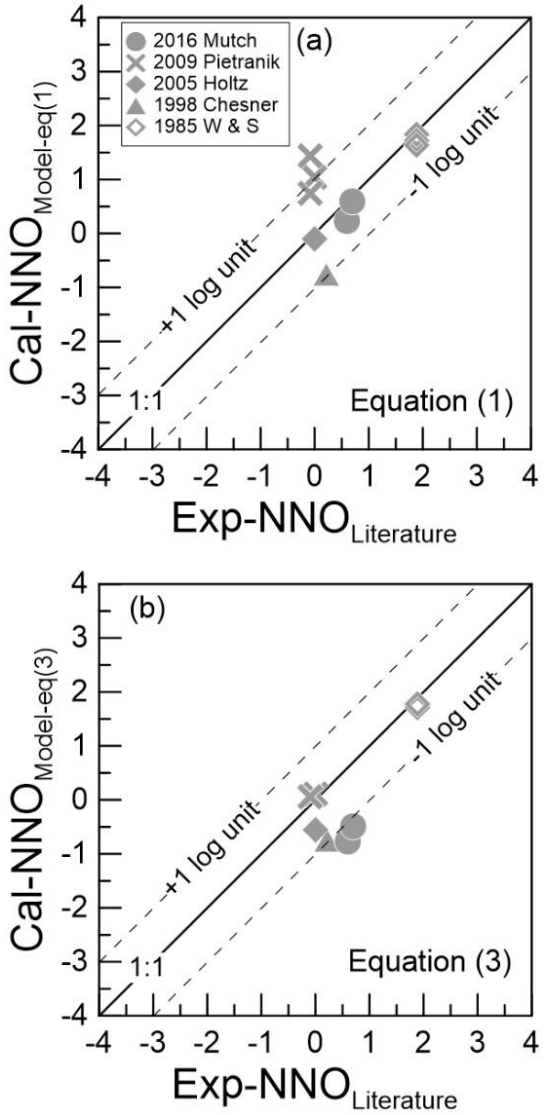

Fig. 6.14 Oxygen fugacity (NNO value) calculated using our model (based on (a): equation (1), (b): equation (3) vs. NNO value of literatures which are from Whitney and Stormer, 1985; Chesner, 1998; Holtz et al., 2005; Pietranik et al., 2009 and Mutch et al., 2016.

experimental petrology to infer magma emplacement conditions (Mutch et al., 2016; Pietranik et al., 2009; Holtz et al., 2005; Chesner, 1998; Whitney and Stormer,1985).

We only used experimental results providing the Fe# of bulk rock, Amp, Bt, the temperature, pressure and oxygen fugacity obtained on a single sample. Using our equations (1) and (3) based on the Fe# of both Amp, Bt and the whole rock composition, the pressure and the temperature data collected from the literatures above, we calculated the oxygen fugacity of those from Lluta Batholith tonalite, Gęsiniec quartz diorite, Unzen dacite, Toba Tuff and Fish Canyon Tuff and then compare these values against the oxygen fugacity constrained from other oxygen barometers in the literature. The results are summarized in Fig. 6.14. From Fig. 6.14 we can see that most of the calculated results using equations (1) and (3) are within ± 1 log unit range, and along with the 1:1 line (calculated oxygen fugacity vs. experimental oxygen fugacity) which demonstrate that our oxygen barometer modeling can retrieve reliable estimates on the oxygen fugacity of the magma system.

6.4.3.1 Application

Three Jurassic plutons in South China were chosen for estimating the oxygen fugacity condition using our oxygen fugacity modeling equations (1) and (3). These plutons are Jiuyishan, Huashan and Guposhan granites which are located on the southwest of Qitianling pluton, having a similar mineralogy, such as coarse-grained amphibole bearing biotite granite and coarse-medium grained biotite granite. The detailed description of these three plutons is given in Chapter 2. Five coarse-grained amphibole bearing biotite granite samples from three plutons were selected for the oxygen fugacity calculations. These are JYS-SC162A from Jiuyishan pluton, HS-SC172B and HS-SC176A from Huashan pluton, GPS-SC182 and GPS-SC183 from Guposhan pluton.

All the whole rocks, Amp and Bt compositional data of five samples are from this study expect the bulk rock compositions of Guposhan pluton which are from Wang et al., 2014. Since Wang et al. (2014) provided three compositions of coarse-grained amphibole bearing biotite granite, we use the average value to calculate the Fe# of

whole rock composition (Fe#w=0.82) in this study for GPS-SC182 and GPS-SC183 two samples. The Fe#w of the other three samples are: 1.00 for JYS-SC162A, 0.68 for HS-SC172B and 0.84 for HS-SC176A. The average Fe#Amp of five samples varies from 0.45-0.78 with a maximum standard deviation as ±0.02 (Fig. 6.15 a; c; e) and most of them are higher than 0.65 except sample HS-SC172B (Fe#Amp=0.45), which also has the lowest Fe#w value (Fe#w=0.68). This sample is located near the Niumiao diorite (Fe#w=0.65, Zhu et al., 2006) in the southeastern part of the Hushan pluton. The average Fe#Bt of five samples are between 0.51-0.73 with a maximum standard deviation of ±0.01 (Fig. 6.15 b; d; f). Not surprisingly, except sample HS-SC172B, the Fe#Bt of other four samples are higher than 0.66. For each single sample, the Fe#Amp is close to the Fe#Bt with a maximum difference of 0.06 (e.g. Fig. 6.15a and b). For each samples, temperature parameters were acquired using the Amp thermometer from Putirka, (2016): $T(°C) = 1781 - 132.74[\text{Si Amp}] + 116.6[\text{Ti Amp}] - 69.41[\text{Fe}_t\ \text{Amp}] + 101.62[\text{Na Amp}]$. Pressures were obtained from the revised Al-in-hornblende geobarometer proposed by Mutch et al., (2016): $P\ (\text{kbar}) = 0.5 + 0.331(8) \times \text{Al}_{\text{tot}} + 0.995(4) \times (\text{Al}_{\text{tot}})^2$.

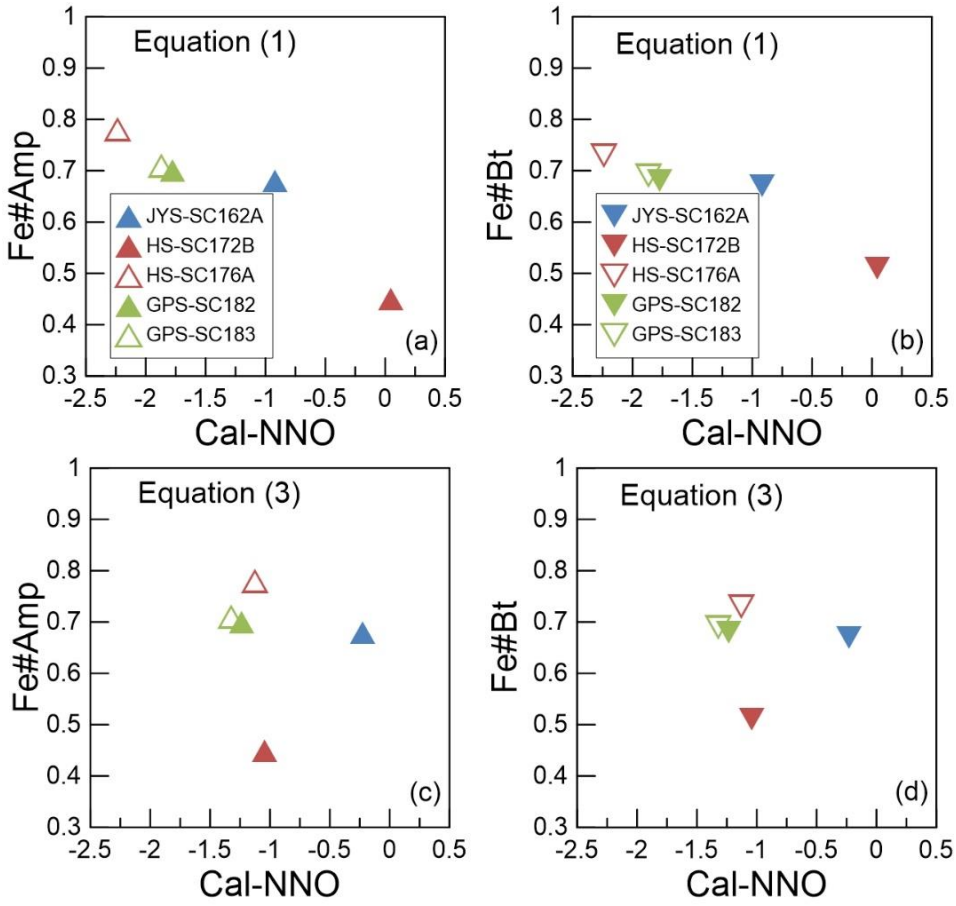

Fig. 6.15 Calculated oxygen fugacity results using equations (1) and (3) vs. the Fe#Amp and the Fe#Bt of Jiuyishan, Huashang and Guposhan granites. The error of oxygen fugacity estimation is ±1.

The calculated oxygen fugacity results using our equation (1) and (3) are shown in Fig. 6.15； Appendix table 22. Equation (1) gave an oxygen fugacity range from ~NNO -2.3 to ~NNO for five samples while with equations (3), the values range from ~NNO-1.5 to ~NNO. If we ignore the error (NNO±1) of the estimates, the oxygen fugacity conditions of Jiuyishan, Hushan, Guposhan three plutons are all below NNO which suggests a relative reduced environment during magma crystallization.

6.5 Summary

Our oxygen fugacity modeling is based on the phase equilibria of intermediate-

acid igneous rocks including Qitianling granite, Santa Maria dacite, Pinatubo dacite, Jamon granite, Lyngdal granodiorite which cover a SiO_2 content of bulk rock ranging from 60 wt% to 71 wt%. Combining the composition of rock forming minerals such as Amp and Bt we propose an empirical oxygen barometer. All the required parameters are temperature, pressure, whole rock composition, e.g. Fe#w (FeO_{tot}/ (FeO_{tot}+MgO) of whole rock composition), Fe#Amp (Fe_{tot}/(Fe_{tot}+Mg) of Amp) or Fe#Bt (Fe_{tot}/(Fe_{tot}+Mg) of Bt). These equations allow to calculate magmatic fO_2 to within 1 log unit error: the retrieved values most likely correspond to conditions during the late crystallization stage of the magma, owing to the easiness of re-equilibration of the used minerals. Application of our oxygen barometer to three Jurassic plutons (Jiuyishan, Huashan and Guposhan pluton) in South China demonstrates that the oxygen fugacity of those three plutons suggest a relative reduced redox environment, similar to that inferred for Qitianling granite.

Chapter 7 Differentiated Sn-Nb-Ta mineralization of rare-elemental granite：A case study in dyke 431 in South China

7.1 Introduction

Ongonite and topazite, described frequently in 1970s (Kovalenko et al., 1971; 1975; Eadington and Nashar, 1978), are two unusual types of felsic rock that are rich in rare elements. They are characterized by volcanic to shallow-intrusive textures, and abundant volatile-rich minerals (mainly topaz). Ongonite is defined as the phenocrystic subvolcanic analogue of granite that is rich in the rare elements Li and F (Kovalenko and Kovalenko, l976). Topazite has been used in reference to felsic dikes that consist mainly of quartz and topaz, for which mineralogical, textural, and field relationships suggest a magmatic origin (Eadington and Nashar, 1978). Mineralization associated with these two particular rock types has been described from many localities worldwide. Examples include W deposits associated with F-rich rhyolites (ongonites) from Ongon Khairkhan, Mongolia (Štemprok, 1991), the type locality of topaz rhyolite with W, Nb, Ta, and Sn mineralization (Burt, 1992), similar to topaz-albite granite, e.g., Limu in South China (Zhu et al., 2001), the French Massif Central (Cuney et al., 1992), Southern New Brunswick (Taylor, 1992), and the Eastern Desert, Egypt (Helba et al., 1997). The mineralization associated with topazite in South China is complex but dominated by Sn, such as deposits at Shicheng, Xunwu, Huichang, Yanbei and Taishun (Liu et al., 1996).

Although both ongonite and topazite are F-rich peraluminous rocks, their coexistence is not common. Kortemeier and Burt (1988) reported the first example of ongonite and topazite dikes occurring together in the Flying W Ranch area, Arizona, and they considered the rocks to be dominantly magmatic with fluorine-controlled transitions for both the ongonite and topazite, according to field, textural, mineralogical, and geochemical criteria. However, the ongonite and topazite in that area are not

strongly mineralized.

The No. 431 dike in the Xianghualing tin district of southern China contains both ongonite and topazite in spatial association (Chen, 1984; Du and Huang, 1984; Zhu and Liu, 1990; Zhu et al., 1993), and the typical mineralization involves Nb, Ta, and Sn. The coexistence of both ongonite and topazite in such a small-scale dike provides a unique opportunity to compare the rare-element mineralization in the two rock types. Our objective was to determine if the two rock types represent co-magmatic melts, and if so by which mechanisms they formed? Most interestingly, how can we explain the mineralization of these two different types of rock? We report comprehensive major and trace element whole-rock data, as well as detailed petrograpic observations and mineral compositional data determined using electron microprobe analysis (EMPA). We evaluate the genetic relationship between ongonite and topazite exposed in a narrow dike, and discuss differentiation trends, and particularly the coupled fractionation of F with Nb-Ta-Sn and the role of liquid immiscibility in their distribution between ongonite and topazite. We explore the potential role of oxides as an efficient container of rare metals and as a monitor of changes in fluid composition in mineralized highly-evolved silica systems. We believe that a detailed study of this kind provides an excellent framework for future investigations using advanced and new, evolving analytical techniques, particularly those targeting melt inclusions of the various mineral populations.

7.2 Geological setting and sampling of the Xianghualing No. 431 dike

The Xianghualing metallogenic district is located in the northern part of Linwu county, South Hunan province, which is in the center of the Nanling Range in South China. In terms of its tectonic setting, the Xianghualing district is situated where the middle part of the E-W-trending Nanling tectonic belt converges with the N-S-trending Leiyang-Linwu tectonic belt (Yuan et al., 2007). The Xianghualing district itself

consists of a tectono-magmatic anticlinal dome that is composed mainly of Paleozoic strata with minor Mesozoic and Cenozoic strata. The main part of the lower Paleozoic consists of Cambrian arenaceous, argillaceous, and siliceous rocks together with minor carbonates. The upper Paleozoic strata lie unconformably on the lower Paleozoic, and are dominated by Middle Devonian conglomerates, sandstones, and shales of the Tiaomajian Formation (D_2t); Middle Devonian limestones and dolomites of the Qiziqiao Formation (D_2q); Upper Devonian dolomitic limestones and sandstones of the Shetianqiao Formation (D_3s); and Carboniferous carbonates and clastic rocks (Yuan et al., 2008).

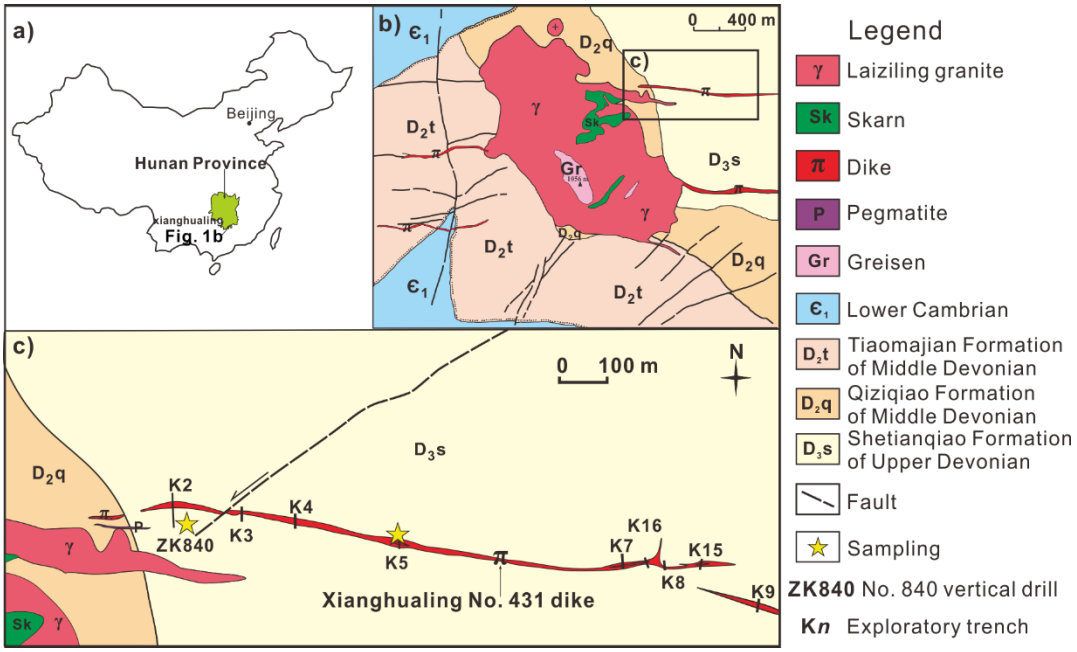

Fig. 7.1 Simplified geological map of the No. 431 dike, Hunan Province, South China (modified after Zhu et al., 2011). (a) Location of Hunan Province in China; (b) the No. 431 dike in close spatial association to the ~154-155 Ma Laiziling granite; and (c) the No. 431 dike is sharply intrudes into carbonate-dominated strata.

Jurassic red beds and Cretaceous continental clastic rocks are found scattered in small basins in the north and east of the district. Three early Yanshanian granite stocks have been identified in the area, and from south to north they are the Jianfengling granite (K-Ar age of 167 Ma; Mo et al., 1980), the Tongtianmiao granite, and the

Laiziling granite (154–155 Ma, zircon U-Pb dating; Zhu et al., 2011). The mineralization associated with these granites includes W, Sn, Nb, Ta, Be, F, Pb, and Zn. This is also the type locality of hsianghualite, the first new mineral named by a Chinese mineralogist in China (Huang et al., 1958).

The No. 431 dike is located ~ 70 m northeast of the Laiziling granite (E112° 34′ 06″; N25° 27′ 26″) (Fig. 7.1). It is ~ 1770 m long and 1.8 to 18.0 m wide. The dike dips to the south at 42°–78°. The dike intrudes Devonian carbonates along a sharp contact, and the dike margins are characterized by flow structures, chilled margins, and xenoliths of Devonian limestone (Zhu and Liu, 1990). There is no direct evidence that the dike connects with the Laiziling granite body. However, vertical drilling has proved that the intrusive contact of the granite is inclined beneath the dike at an angle of 40°, and it thus seems possible that granite and the No. 431 dike are connected at depth.

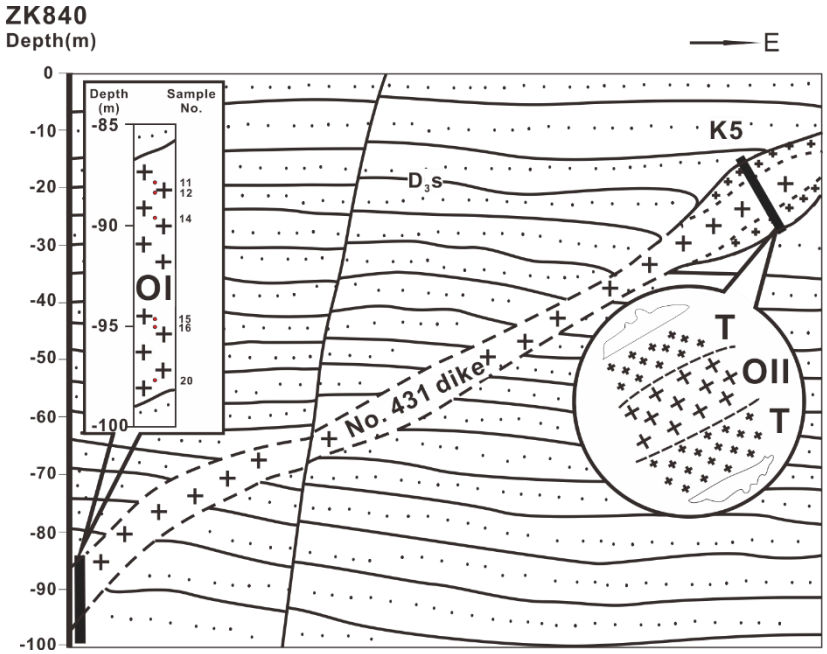

Fig. 7.2 Cross-section of the No. 840 vertical drill hole and the No. 5 trench across the No. 431 dike. Abbreviations: OI: ongonite I; OII: ongonite II; T: topazite.

Ground (or near-surface) trenches and subsurface drillings were carried out in the early 1970s in order to investigate the dike. Earlier work had described the dike as

heterogeneous, and it was classified as a topaz-bearing felsophyre and aplite (Du and Huang, 1984), but the later work of Zhu and Liu (1990) showed that the dike contains at least two major rock types, ongonite and topazite.

The samples we describe in this paper were collected from the No. 431 dike at two different locations. They capture the apparent petrographic variations both vertically and horizontally (Fig. 7.2). On the unexposed western side of the dike, the No. 840 drill revealed ongonite (the samples collected here are called ongonite I) between depths of –87.4 m and –96.3 m. The samples acquired from the eastern side of the dike are exposed in the No. 5 exploratory trench. They contain spatially associated ongonite (labeled ongonite II) and topazite. Ongonite II is from the central zone of the dike, whereas the topazite comes from the marginal zones (Huang et al., 1988).

7.3 Petrology and geochemistry of the No. 431 dike

The No. 431 dike is composed of ongonite and mica-bearing topazite. All the ongonite specimen are white and they have a porphyritic texture (0.1–1.0 mm) with a fine-grained groundmass. Ongonite I shows gradational zoning from a phenocryst-rich core zone to a phenocryst-poor topaz-bearing rim zone. Ongonite II appears unzoned, while topazite shows fine-scale layers subparallel to the dike margin. The phenocrysts in the ongonites are mainly K-feldspar, quartz, albite, zinnwaldite, and rarely topaz. Their sizes may reach 1.5 mm; the groundmass consists mainly of albite, quartz, topaz, and minor zinnwaldite (Fig. 7.3a, b). Nevertheless, some differences exist between the ongonites. First, small amounts of anhedral fluorite have been found in the matrix of ongonite I, while fluorite is very rare in ongonite II. Second, although topaz appears in all the ongonites, it is short and prismatic in ongonite I, and long and prismatic or needle-like in ongonite II (Fig. 7.3c, d). The topazite, locally present at ground level, is composed mostly of topaz, quartz, and zinnwaldite that delineate a flow structure (Fig. 7.3e). The acicular topaz generally occurs in the interstices of anhedral quartz, and it is

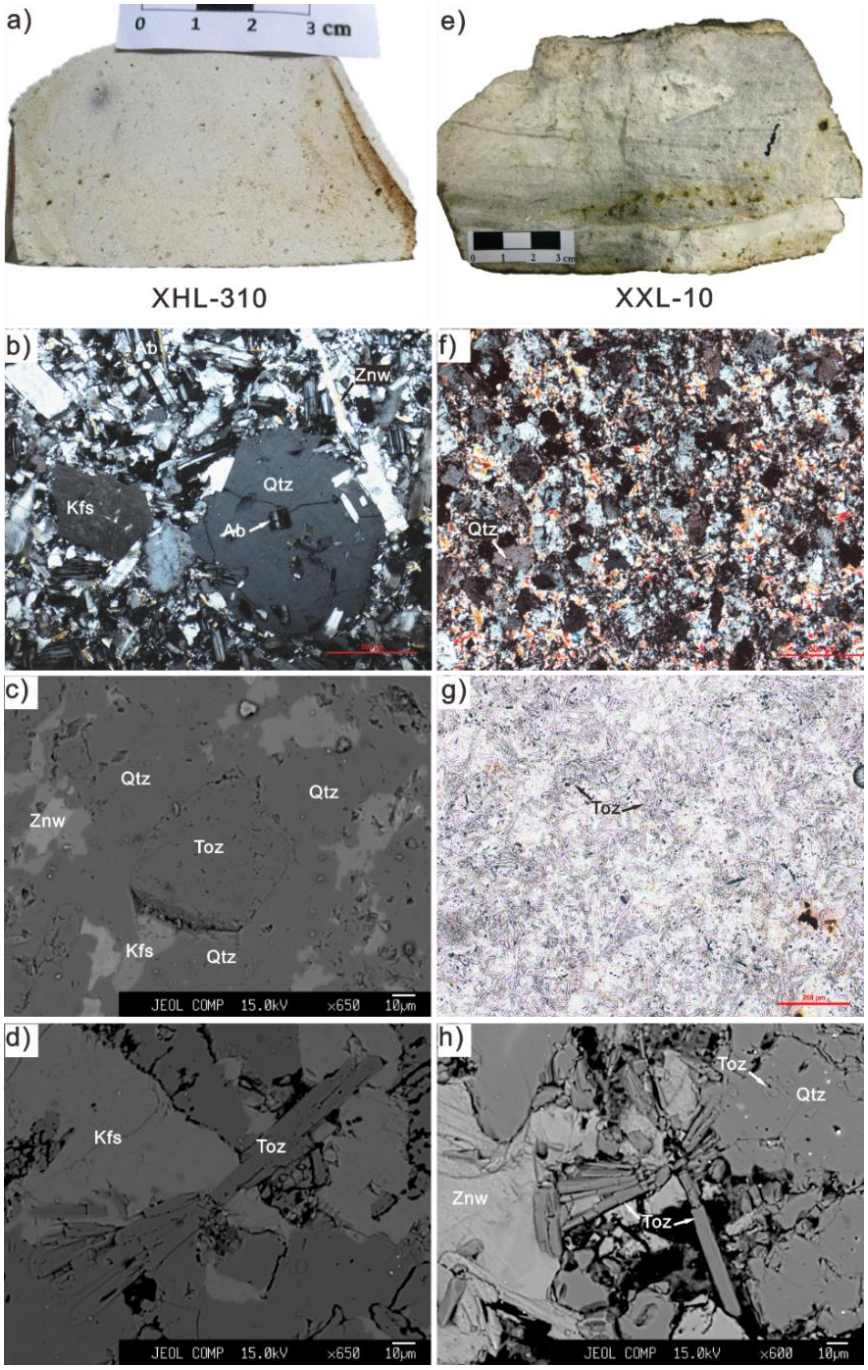

Fig. 7.3 Photographs, photomicrographs, and BSE (back-scattered electron) images of ongonite and topazite. (a) Fine-grained ongonite II with quartz phenocryst (gray); (b) quartz phenocryst in ongonite containing tabular albite crystals, under crossed polarized light; (c) short prismatic or columnar topaz in a groundmass of ongonite I (BSE); (d) needle-like topaz in a groundmass of ongonite II (BSE); (e) flow structure in fine-grained topazite; (f) anhedral quartz and zinnwaldite in topazite, under crossed polarized light; (g) abundant acicular and high-relief topaz in topazite, under plane polarized light; and (h) needle-like topaz in topazite (BSE). Minerals abbreviations: Qtz: quartz; Ab: albite; Kfs: K-feldspar; Znw: zinnwaldite; Tpz: topaz.

occasionally included in the quartz grains (Fig. 7.3f, g).

Details of the whole-rock major and trace-element compositions of the No. 431 dike are given in Appendix table 23. The data show that ongonite I and II have similar compositions characterized by relatively high contents of SiO_2 (on average, 68.59 wt.%)

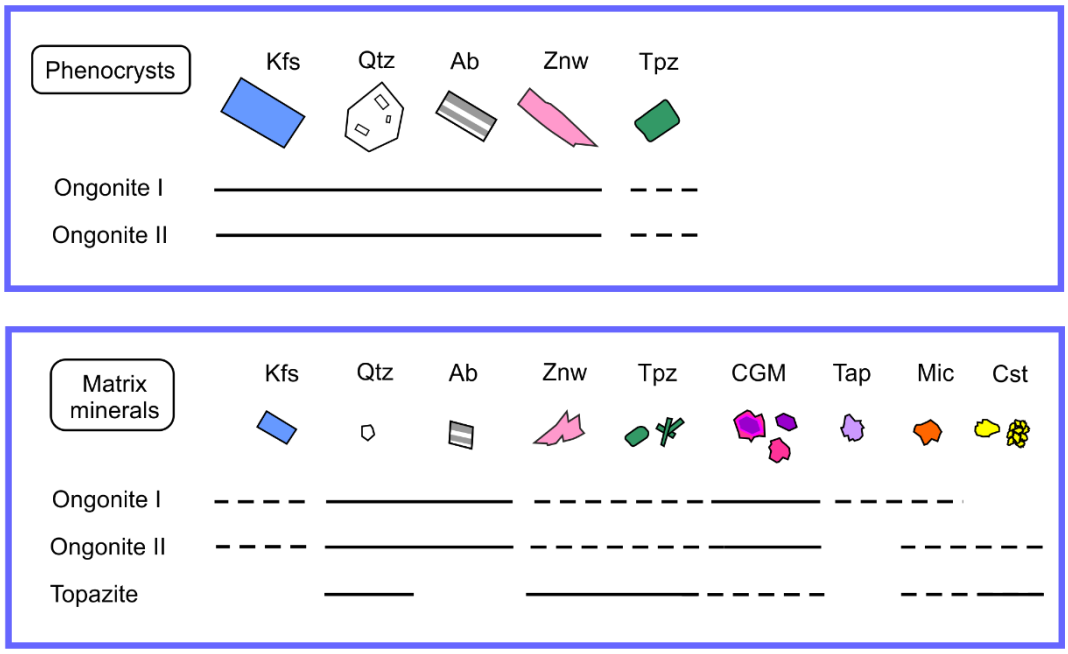

Fig. 7.4 The distribution of phenorysts and matrix minerals in ongonite I, ongonite II and topazite from the No. 431 dike. Minerals abbreviations: CGM: columbite-group minerals. Solid line signifies abundant presence of minerals. Dashed line signifies rare occurrence of minerals.

and Al_2O_3 (on average, 18.47 wt.%), where SiO_2 contents decrease and Al_2O_3 contents increase from ongonite I to ongonite II. The rocks have a strongly peraluminous character with an average ACNK value of 1.5 [Al_2O_3/ (Na_2O + K_2O + CaO) in molars], and high F contents (on average, 1.7 wt.%). These characteristics are typical of ongonites elsewhere (Kovalenko and Kovalenko, 1976; Štemprok, 1991). We further note that the marginal zone of ongonite I (against the country rocks) is enriched in F and Li relative to the ongonite I core zone (i.e., samples 10-11-20 versus samples 12-14; Appendix table 23. Moreover, two slight differences in the major element contents of the two sub-types of ongonites should not be ignored. Compared with ongonite II, ongonite I has higher contents of FeO_t and CaO (up to 3.03 and 1.00 wt.%, respectively), possibly corresponding to the higher mica and fluorite abundances. Relative to the

ongonites, the topazite has a lower SiO_2 content, ranging from 56.57 to 63.08 wt.%, and higher Al_2O_3 content (up to 27.77 wt.%, average of 25.14 wt.%) and significantly higher F contents (up to 6.22 wt.%, average of 5.44 wt.%). The whole-rock SiO_2 content and FeO_t/MnO decrease from ongonite I to ongonite II and topazite in the No. 431 dike, while Al_2O_3 increases (Appendix table 23). Compared to the ongonite rocks, the Na_2O content of the topazite is extremely low (<0.08 wt.% versus 3.80–6.88 wt.% for ongonites) while K_2O contents are relatively high, but variable (3.56–5.57 wt.% versus 1.05–4.59 wt.% for ongonites).

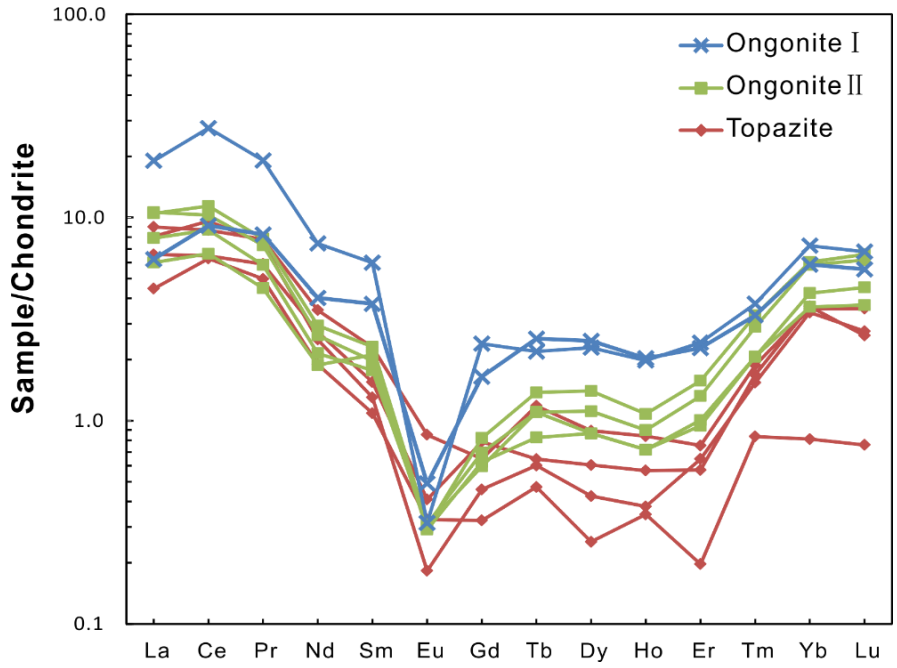

Fig. 7.5 Chondrite-normalized REE patterns for the No. 431 dike (chondrite REE values from Anders and Grevesse, 1989).

The samples from the No. 431 dike are enriched in Li, Rb, Cs, Nb, Ta, Be, Sn, W, and Hf, and depleted in Sr, Ba, P, and Ti, with significantly low Zr/Hf (on average 6.04 for ongonites and 4.23 for topazite) and Nb/Ta ratios (on average 1.55 for ongonites and 1.06 for topazite) (Appendix table 24; Fig. 3). The contents of the ore-forming elements Nb, Ta, Sn, and W are high, up to 248, 175, 62.6, and 68.5 ppm for the ongonites, and 223, 207, 802, and 771 ppm for the topazite, respectively. The contents of rare-earth elements (REE) in the ongonite and topazite samples are markedly low, and the normalized REE pattern is similar to the M tetrad effect of Takahashi (2002)

(Fig. 7.5). There are slight negative Eu anomalies; the δEu value for the ongonites and topazite average 0.22 and 0.47, and the $(La/Yb)_N$ ratio varies from 1.00 to 2.89 and 1.80 to 5.50, respectively.

7.4 Mineral chemistry

7.4.1 Feldspars

Feldspars, including K-feldspar and albite, are common in the ongonites but absent in the topazite. In the ongonites, K-feldspar exists mainly as subhedral phenocrysts up to 1 mm long, and locally it encloses albite. All K-feldspar has low Ab contents of 1.8–3.2 mol.%. Albite occurs mostly as euhedral to subhedral tabular phenocrysts, but may also be included within K-feldspar or quartz to form a snowball texture which is usually observed in granites rich in rare-elements (Pollard, 1989; Huang et al., 2002). Compositionally, the feldspars in the ongonites are nearly pure end members (K-feldspar has 1.79–3.18 mol.% Ab, and albite has 97.00–99.1 mol.% Ab) (Appendix table 24).

7.4.2 Mica

In the ongonites, mica occurs as phenocrysts about 0.1 to 1.5 mm in size, and is also present in the groundmass, but it is not as abundant as in the topazite, and it is only locally found as one of main rock-forming minerals. According to electron-microprobe analyses, the micas in the ongonites and topazite mostly classify as zinnwaldite, together with minor lepidolite and rare lithian muscovite (following the classification of Foster, 1960a, b). The FeO content in zinnwaldite from ongonite I may be up to 16.88 wt.%, while that in ongonite II is 6.62 wt.%, close to the composition of lepidolite. In contrast, the MnO content is highest in ongonite II (up to 2.78 wt.% MnO), but very low in ongonite I (only up to 0.95 wt.% MnO). Zinnwaldite from the topazite has FeO

and MnO contents of about 10 wt.% and 1.9 wt.%, respectively, and the composition is similar to the micas in the coexisting ongonite II. The F content of the zinnwaldite is on average 5.71 wt.% in ongonite I, while in ongonite II and the topazite the values are higher, with averages of 8.89 wt.% and 8.17 wt.%, respectively (Appendix table 25).

7.4.3 Topaz

Topaz is only observed as an accessory mineral in the ongonites, but it is one of the main rock-forming minerals in topazite, where it can reach approximately 30 vol.%. Two kinds of topaz crystal are found in the ongonites: short prisms in ongonite I and fine acicular crystals in ongonite II. They usually coexist with other rock-forming minerals in the groundmass. In the topazite, topaz occurs dominantly as small grains in the groundmass, rarely as phenocrysts, but it also forms aggregates with cassiterite (see below). Radial arrays of needle-like topaz characterize the groundmass, of which some are included in quartz phenocrysts. In addition, EMPA results indicate that the topaz is fluorine-dominated with F contents of 18.88 to 21.67 wt.% (Appendix table 24).

7.4.4 Niobium-tantalum oxides

Nb-Ta oxide minerals in the No. 431 dike include the columbite-group minerals which are always present, and the rarely observed tapiolite and microlite. The columbite-group minerals are present in all the ongonites and topazite to different degrees. Only a small amount of tapiolite is observed in ongonite I, while microlite occurs in the ongonites as well as the topazite. Most of the Nb-Ta oxides are present in association with rock-forming minerals such as quartz, albite, and mica. Approximately 400 electron-microprobe analyses were obtained from about 80 Nb-Ta oxide grains in the studied ongonites and topazite, and representative results are presented in Appendix table 26.

7.4.4.1 Niobium-tantalum oxides in ongonite I

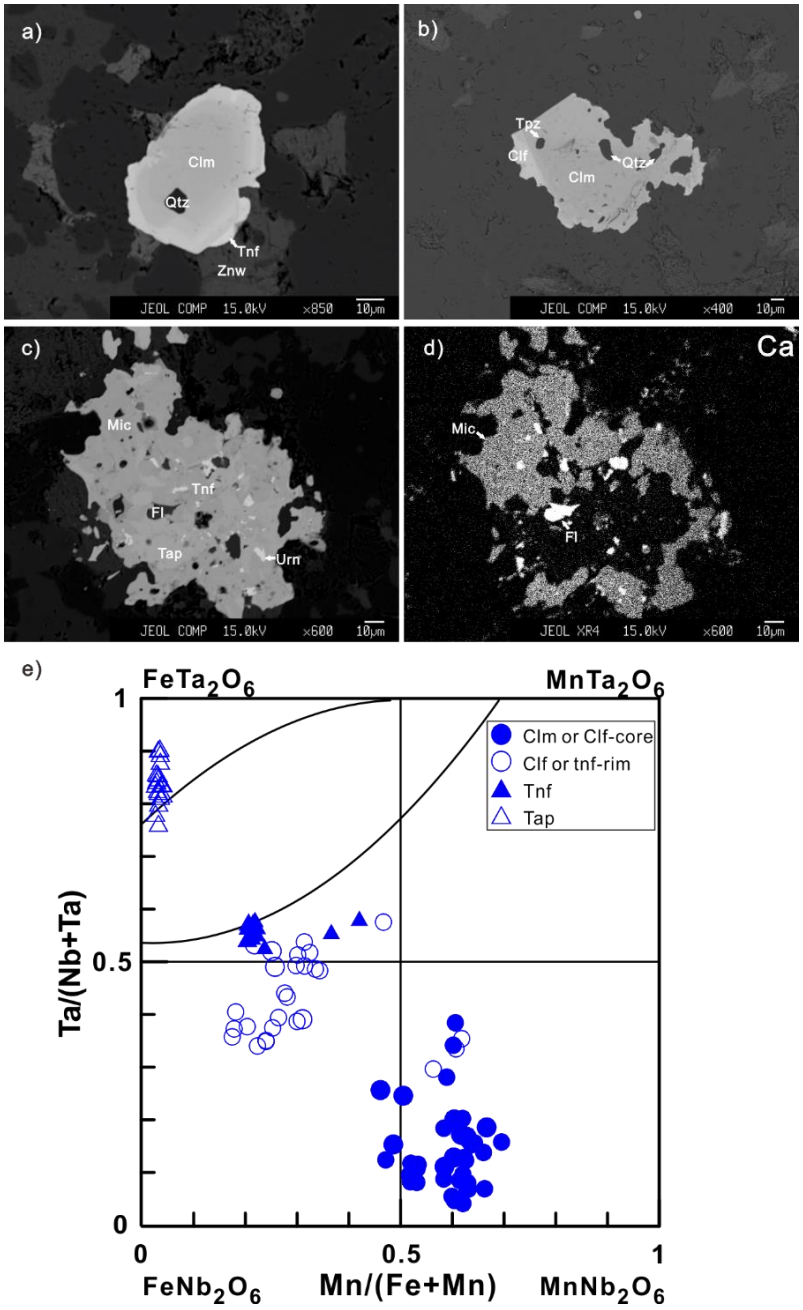

Fig. 7.6 BSE images and compositional classification of the columbite-group minerals and tapiolite from ongonite I. (a) Progressive zoning of columbite-(Mn) core with a rim of tantalite-(Fe); (b) columbite-(Mn) core and columbite-(Fe) rim with topaz and quartz inclusions; (c) microgranular aggregate of columbite-group minerals, tapiolite, and microlite; (d) X-ray scanning map showing the Ca distribution of (c); and (e) compositions of the columbite-group minerals and tapiolite in ongonite I, plotted on the Mn/(Fe + Mn) versus Ta/(Nb + Ta) quadrilateral diagram. Minerals abbreviations: Clf: columbite-(Fe); Clm: columbite-(Mn); Tnf: tantalite-(Fe); Tap: tapiolite-(Fe); Mic: microlite; Urn: uraninite; Fl: fluorite.

Columbite-group minerals appear in ongonite I mostly as fine grains less than 300 μm in size, which are commonly interstitial to the rock-forming minerals. Sometimes the columbite contains inclusions of quartz and topaz, indicating its simultaneous crystallization with those rock-forming minerals. Progressive zoning is occasionally observed in some crystals, characterized by increasing brightness in BSE images (Fig. 7.6a). In particular, the grains commonly display <20 μm wide, very bright rims (Fig. 7.6a, b). Electron-microprobe results indicate that the columbite-group minerals can be divided into two groups on the basis of their compositions. The dominant part in some zoned crystals displays variations in Mn/(Fe + Mn) (shortened hereafter as $Mn^{\#}$) from 0.46 to 0.70, and in Ta/(Nb + Ta) (shortened to $Ta^{\#}$) from 0.04 to 0.38. Overall, most of them fall into the field of columbite-(Mn) (Appendix table 26; Fig. 7.6e). The brightest outermost parts of the grains are tantalite-(Fe) or Ta-rich columbite-(Fe). They have moderate $Ta^{\#}$ of 0.30–0.58 and a variable $Mn^{\#}$ of 0.17–0.62.

Microgranular aggregates in the upper part of ongonite I make up the second-most important occurrence of Nb-Ta oxide minerals. Back-scattered electron images demonstrate that tantalite-(Fe) and tapiolite are the main minerals in the centers of the aggregates, and these are surrounded by many irregular microlite grains (Fig. 7.6c, d). Uraninite and fluorite may also be found in this complex association. The results of the analyses of tantalite-(Fe) show a restricted $Ta^{\#}$ ranging from 0.52 to 0.58 and a $Mn^{\#}$ ranging from 0.20 to 0.42. They plot precisely near the bottom boundary of the miscibility gap between tantalite and tapiolite (Černý et al., 1992). Tapiolite, a kind of highly Fe-dominated Ta-enriched oxide, has extremely high values of $Ta^{\#}$ and low values of $Mn^{\#}$, ranging from 0.76 to 0.91 and 0.03 to 0.04, respectively. Its composition plots close to the top boundary of the miscibility gap (Fig. 7.6e). The third main mineral in the aggregates is microlite, containing 8.69 wt.% Na_2O, 5.54 wt.% CaO, and 6.23 wt.% UO_2 on average (Appendix table 27). In addition, the fluorine content of the microlite in ongonite I is up to 4.23 wt.%, the highest of all the microlites from the different rocks of this dike.

In summary, the Nb-Ta oxides in ongonite I display an overall Ta dominance towards the marginal zones of ongonite I, especially for the structurally highest level, characterized first by the appearance of Ta-dominated minerals such as tapiolite and microlite, and second by the overall increasing $Ta^{\#}$ value in the columbite, as revealed in Fig. 7.7.

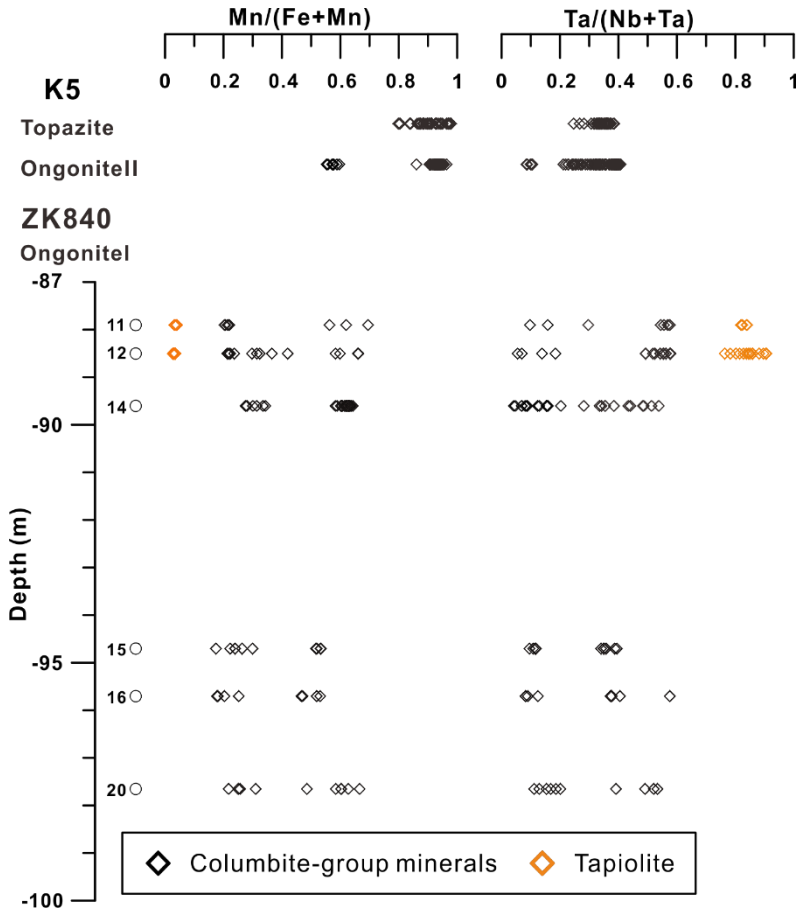

Fig. 7.7 Chemical variations of the columbite-group minerals and tapiolite from ongonite I (at depth from the drill hole), ongonite II and topazite.

7.4.4.2 Niobium-tantalum oxides in ongonite II

In comparison with ongonite I, the columbite-group minerals in ongonite II are compositionally simpler. Intergranular subhedral tabular crystals up to 100 μm long (Fig. 7.8a) that contain low $Ta^{\#}$ values of 0.09 to 0.11 and $Mn^{\#}$ values of 0.55 to 0.60 classify as columbite-(Mn) (Appendix table 26). Moreover, abundant subhedral to anhedral fine-grained crystals occur interstitially in ongonite II, and they have moderate

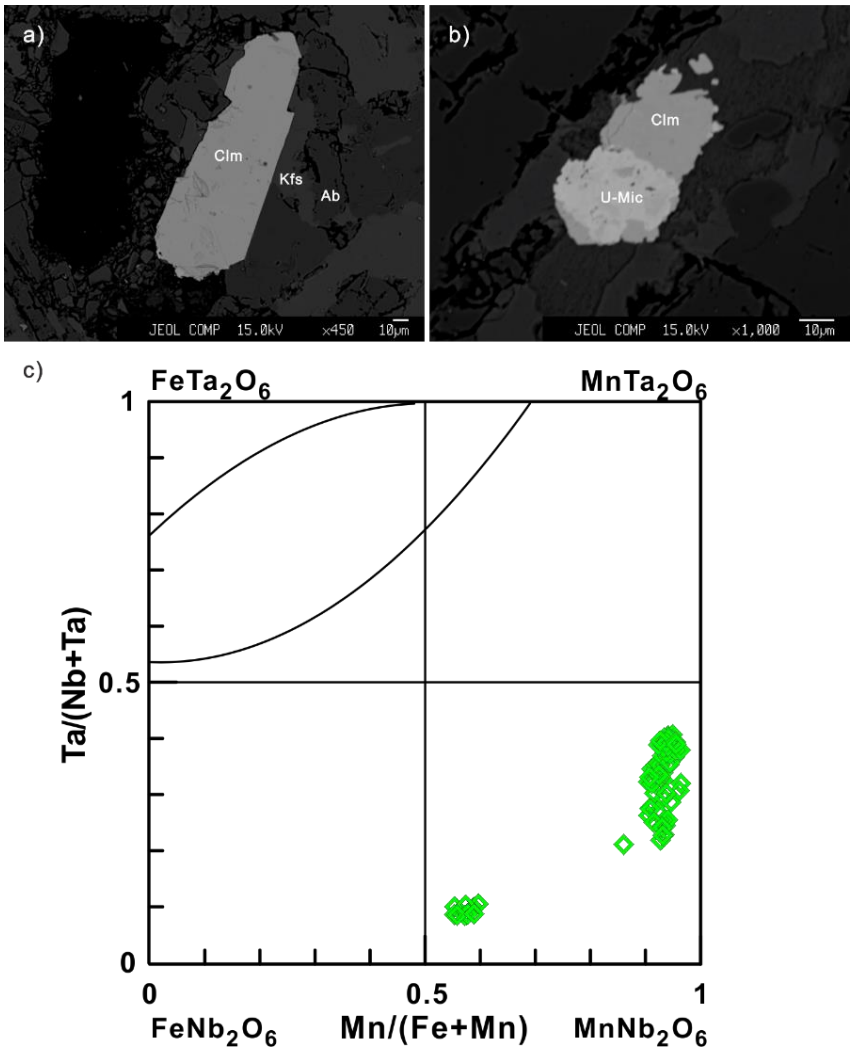

Fig. 7.8 BSE images and compositional classification of the columbite-group minerals. (a) Euhedral tabular columbite-(Mn) is interstitial to the rock-forming minerals, (b) columbite-(Mn) intergrowth with U-rich microlite, and (c) compositions of the columbite-group minerals from ongonite II, plotted on the Mn/(Fe + Mn) versus Ta/(Nb + Ta) quadrilateral diagram. Minerals abbreviations: U-Mic: uranomicrolite.

$Ta^{\#}$ values of 0.21 to 0.41 and high $Mn^{\#}$ values of 0.86 to 0.96. This type of columbite also classifies as columbite-(Mn). The columbite-(Mn) is characteristically enriched in tungsten with a maximum of 18.86 wt.% WO_3 and an average of 4.54 wt.%. The third type of columbite grains is part of a mineral association that includes microlite (Fig. 7.8b) and/or rutile + zircon, and these grains are commonly 10–50 μm in size. They have distinctively high values of $Ta^{\#}$ and $Mn^{\#}$, ranging from 0.32 to 0.37 and 0.91 to 0.94, respectively. All the columbite group minerals found in ongonite II are columbite-(Mn), and the latter two kinds of Nb-Ta oxide minerals share close positions in the

columbite-tantalite quadrilateral diagram (Fig. 7.8c). The associated microlite is characterized by high UO_2 contents up to 15.36 wt.% but low Na_2O and CaO levels. It could therefore be classified as uranomicrolite according to the classification suggested by Hogarth (1977) and Černý (1989).

Tantalian rutiles are only found in ongonite II as euhedral-subhedral crystals in aggregates of Nb-Ta oxide minerals, and they contain up to 21.92 wt.% Ta_2O_5 and trace amounts of Fe, Mn, Sn, and W.

7.4.4.3 Niobium-tantalum oxides in topazite

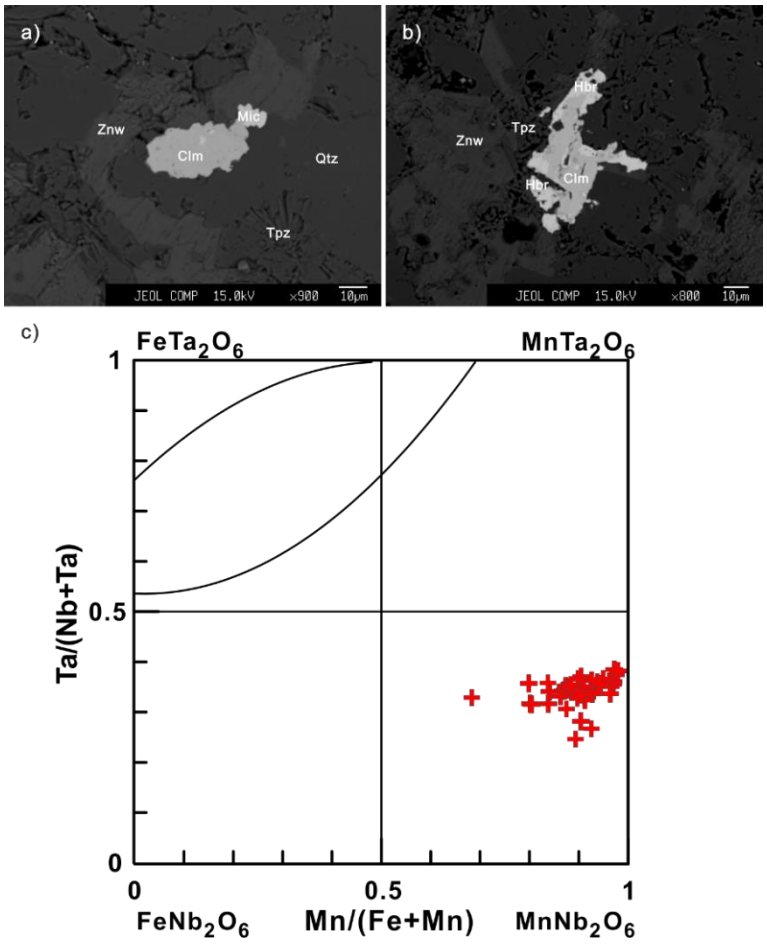

Fig. 7.9 BSE images and compositional classification of the columbite-group minerals from topazite. (a) Fine-grained columbite-(Mn) intergrown with U-rich microlite, interstitial to the rock-forming minerals; (b) subhedral columbite-(Mn) intergrown with hubnerite; and (c) compositions of the columbite-group minerals from topazite, plotted on the Mn/(Fe + Mn) versus Ta/(Nb + Ta) quadrilateral diagram.

In the topazite, columbite-group minerals are fewer and smaller in size (10–15 × 10–30 μm), and they commonly occur as subhedral crystals associated with microlite or hubnerite (Fig. 7.9a, b). Chemical analyses show that the columbite-group minerals also correspond to columbite-(Mn) in the classification diagram (Fig. 7.9c). Overall the $Ta^{\#}$ and $Mn^{\#}$ values of columbite-(Mn) in topazite overlap those in ongonite II. Subhedral to anhedral microlite is present along with the columbite-(Mn), and it is rich in uranium with up to 17.46 wt.% UO_2, which means it can be classified as an uranomicrolite. The association of columbite and microlite is consistent with the assemblage observed in the spatially associated ongonite II.

7.4.5 Cassiterite

Cassiterite is almost absent in ongonite I and scarce in ongonite II. It occurs as anhedral crystals or fine veinlets along zinnwaldite cleavages. In contrast, in the topazite, cassiterite is abundant as an accessory mineral. According to the textural evidence and mineral compositions, two main types of cassiterite may be distinguished in the topazite: disseminated cassiterite (cassiterite I) and aggregated cassiterite (cassiterite II), and they are considered below (Fig. 7.10; Appendix table 28).

(1) Cassiterite I occurs as independent euhedral to subhedral granular crystals (10–20 μm across), either in the interstices between topaz and quartz, or in a mineral association with zircon, columbite-(Mn), hubnerite, and/or microlite (Fig. 9a). The composition of cassiterite I is similar to that of magmatic cassiterite in pegmatites rich in rare metals (Černý, 1989; Neiva, 1996), and it is characterized by significant amounts of Ta (up to 7.77 wt.% Ta_2O_5), Nb (up to 4.01 wt.% Nb_2O_5), and W (up to 5.13 wt.% WO_3), together with minor Mn (up to 1.34 wt.% MnO) and Fe (up to 3.89 wt.% FeO). In the Nb + Ta vs. Fe + Mn diagram, cassiterite I is mostly dispersed along the 2:1 line, corresponding to the general substitution of columbite solid-solution in cassiterite: $3Sn^{4+} \Leftrightarrow 2\ (Nb, Ta)^{5+} + (Fe, Mn)^{2+}$, similar to that described by Černý and Ercit (1989) and Tindle and Breaks (1998).

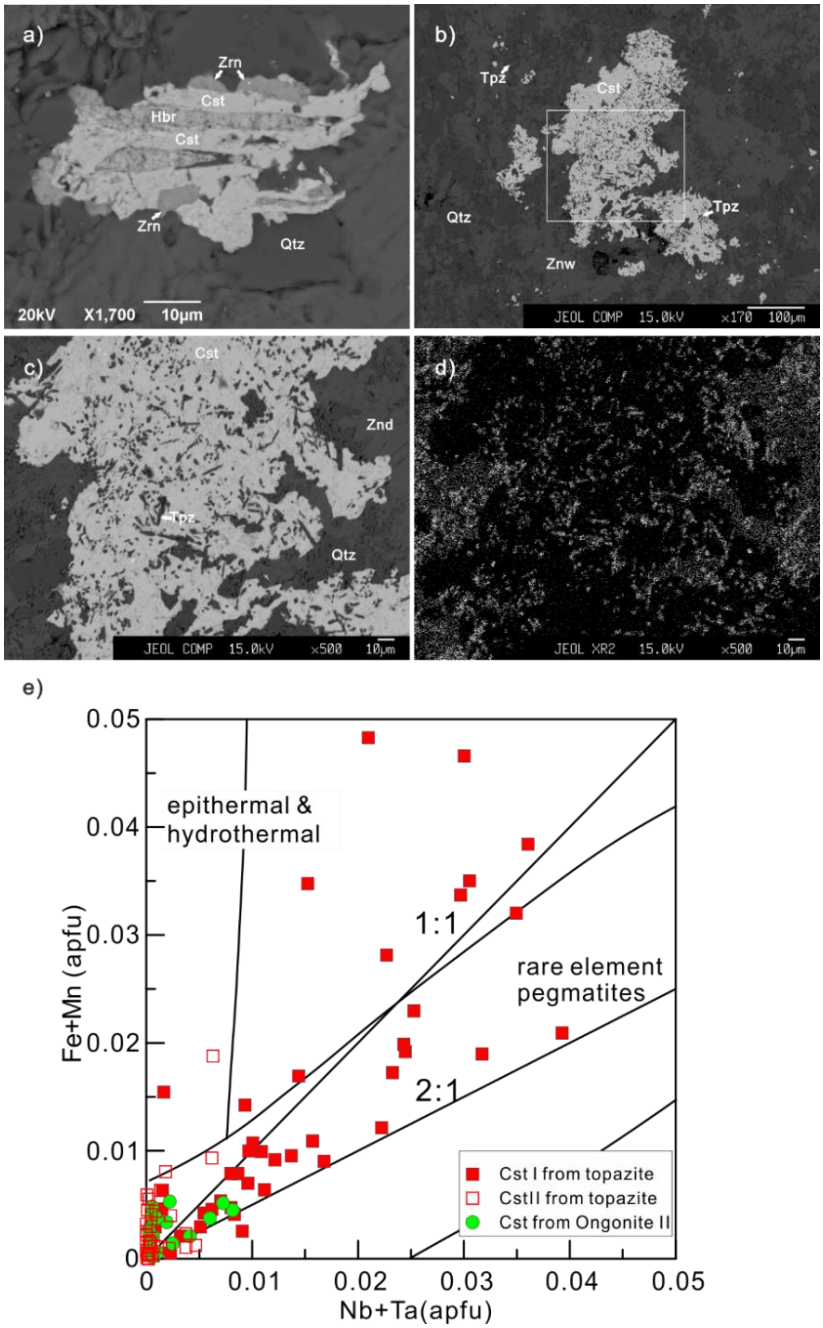

Fig. 7.10 BSE images and covariation diagram of (Nb + Ta) vs. (Fe + Mn) in cassiterite from ongonite II and topazite (after Tindle and Breaks, 1998). (a) Disseminated cassiterite (Cst I) intergrown with hubnerite and zircon; (b) aggregates of cassiterite (Cst II) intergrown with abundant topaz; (c) enlargement of part of (b) showing aggregates of cassiterite (Cst II) intergrown with abundant topaz; (d) X-ray scanning map showing the distribution of F of (b); and (e) covariation diagram of (Nb + Ta) vs. (Fe + Mn) for cassiterite from ongonite II and topazite (after Tindle and Breaks, 1998). Minerals abbreviations: Cst: cassiterite; Hbr: hubnerite; Zrn: zircon.

(2) Cassiterite II is typically present as micron-sized crystals in aggregates with needle-like topaz (Fig. 7.10b-d). Cassiterite II has low levels of trace elements (less

than 1 wt.%) (Fig. 7.10e). Moreover, minor amount of galena are locally found included in cassiterite II aggregates, suggesting their crystallization was part of a later hydrothermal process.

7.4.6 Varlamoffite

Varlamoffite is a hydrous Sn mineral only found in the topazite. It usually occurs in cavities, and occasionally it is associated with cassiterite. It contains 44.55 wt.% SnO_2 and 23.18 wt.% FeO, on average, and probably about 30 wt.% H_2O.

7.5 Discussion

7.5.1 Co-magmatic relationships between ongonite and topazite in the Xianghualing No. 431 dike

Although both ongonite and topazite have equivalents among granitic rocks that are rich in rare elements, their coexistence was only described in 1988 from the Flying W Ranch of Arizona (Kortemeier and Burt, 1988). In addition, Johnston and Chappell (1992) also described co-magmatic, topaz-bearing aplite (very similar to ongonite) and topazite. They suggested their co-magmatic origin on the basis of petrographic investigations, in spite of their presence in different dikes. The Xianghualing No. 431 dike exposes coexisting ongonite and topazite in a very small scale dike (less than 18 m wide). The two ongonite sub-types and the topazite of the No. 431 dike have highly evolved compositions with ~ 1.1–6.2 wt.% F, ~ 750 –6,250 ppm Li, and an ACNK index of > 1.1 to ~ 6.9, where the degree of differentiation increases from ongonite I over ongonite II to topazite. Additionally, both Nb/Ta and Zr/Hf ratios decrease from ongonite I to topazite. Compositionally, the ongonite and topazite rocks are very similar to F-rich, peraluminous, highly evolved, and volatile-rich eruptive rocks such as the Macusani glass in SE Peru (Pichavant et al., 1987) and topaz rhyolites (Raimbault and

Burnol, 1998; Breiter, 2012; Xie et al., 2013; Gioncada et al., 2014). Other topazites (Songling, Hailuoling, Tongkengzhang, Fenghuangdong and Yangbin) besides the Xianghualing No. 431 dike in southern China also share similar petrological and geochemical characteristics (Liu et al., 1996). Most of them contain quartz and topaz as the rock-forming minerals and occasionally have fine-grained zinnwaldite. They are generally relatively rich in SiO_2, strongly peraluminous and have a high content of F (up to 6.55 wt.%) (Liu et al., 1996). Trace elements of topazites are rich in HFSE (Nb, Ta, Sn, W, Zr and Hf) with high values of Rb/Sr and low values of Zr/Hf and Nb/Ta.

How the evolved magma emplaced in the No. 431 dike crystallized and how the ongonite types and topazite are related to each other is discussed in the following sections, using the compositional variation and the distribution of mineral assemblages, their textures, and composition. The main features we seek to explain are: (i) the strong increase in F, LiO_2, Sn, and W and the decrease in Na_2O from ongonite II to topazite; (ii) the highly porphyritic texture of ongonite I and II; (iii) the euhedral-subhedral phenocrysts in the ongonite I core zone and ongonite II, and the subrounded phenocrysts in the ongonite I rim zone and the topazite; and (iv) the highly contrasting abundance and mineral textures of topaz, Nb-Ta oxide minerals, and cassiterite in the two main rock types (Fig. 7.4).

Studies of natural examples and experimental results have demonstrated that liquid immiscibility may play an important role in the evolution volatile-rich magmatic system and particularly in the evolution of Li-F-rich granitic magmas (e.g., Roedder and Coombs, 1967; Roedder, 1992; Veksler, 2004; Peretyazhko et al., 2007; Kamenetsky and Kamenetsky, 2010; Veksler et al., 2012; Shchekina et al., 2013). High concentrations of alkali and earth alkali metals favor liquid immiscibility and high concentrations of non-silicate anions (e.g., F^-, CO_3^{2-}) permit their efficient separation. Low-pressure (72-100 MPa), high-temperature (650-1100 °C) experiments performed by Veksler et al. (2012) have revealed that in immiscible silicate-fluoride systems, the fluoride melt strongly partitions F, Li_2O, MgO, and CaO and moderately partitions

Al_2O_3, Na_2O, and K_2O. Trace elements that most strongly partition into the fluoride melt are W, Th, and the REEs. Additionally, in carbonate-silicate systems, the carbonate liquid strongly partitions Na_2O and CaO and moderately partitions K_2O, Mo, and W.

The strong and abrupt increase in the concentrations of F and LiO_2 from ongonite I and II to topazite and the increase in MgO from ongonite II to topazite in the No. 431 dike is thus consistent with unmixing of silicate and fluorite melts. The very low Na_2O content and the variable K_2O content of the topazite samples in the margin of the dike is not only suggested by the experimental silicate-fluoride partition coefficients, but could reflect the unmixing of carbonate species, as the dike wall rocks are dominated by carbonate strata. Trace-element partitioning could have also been governed by carbonate and fluorine species, as they seem to most strongly partition the ore minerals Nb, Ta, Sn, and W that are strongly enriched in the topazite of the No. 431 dike.

The presence of the phenocryst of K-feldspar, quartz, albite, zinnwaldite, minor topaz and columbite-(Mn) – in the structurally lower part (ongonite I; Fig.7.11a, b) and the near-surface part of the dike – suggest that early crystallization enriched the melt phase in elements including the network-modifiers Li and F and ore elements Sn and W (Time 1, ongonite II, Fig. 7.11c, d). The large size of the phenocrysts in ongonite indicates that crystal nucleation was slow relative to crystal growth (e.g., Hersum and Marsh, 2007; Pietro, 2008). Such crystallization is consistent with the presence of large amounts of volatiles and other network-modifiers and/or extended crystallization time (Swanson, 1977; Fenn, 1977).

In contrast, the strongly porphyritic texture of ongonite I and ongonite II with abundant fine-grained quartz and albite along with K-feldspar, zinnwaldite, topaz, and ore minerals is consistent with subsequent rapid crystallization (e.g., Fig. 7.3b). Such rapid crystallization is typically invoked to be triggered by supercooling as a function of decreasing temperature and/or the exsolution of volatile components from an

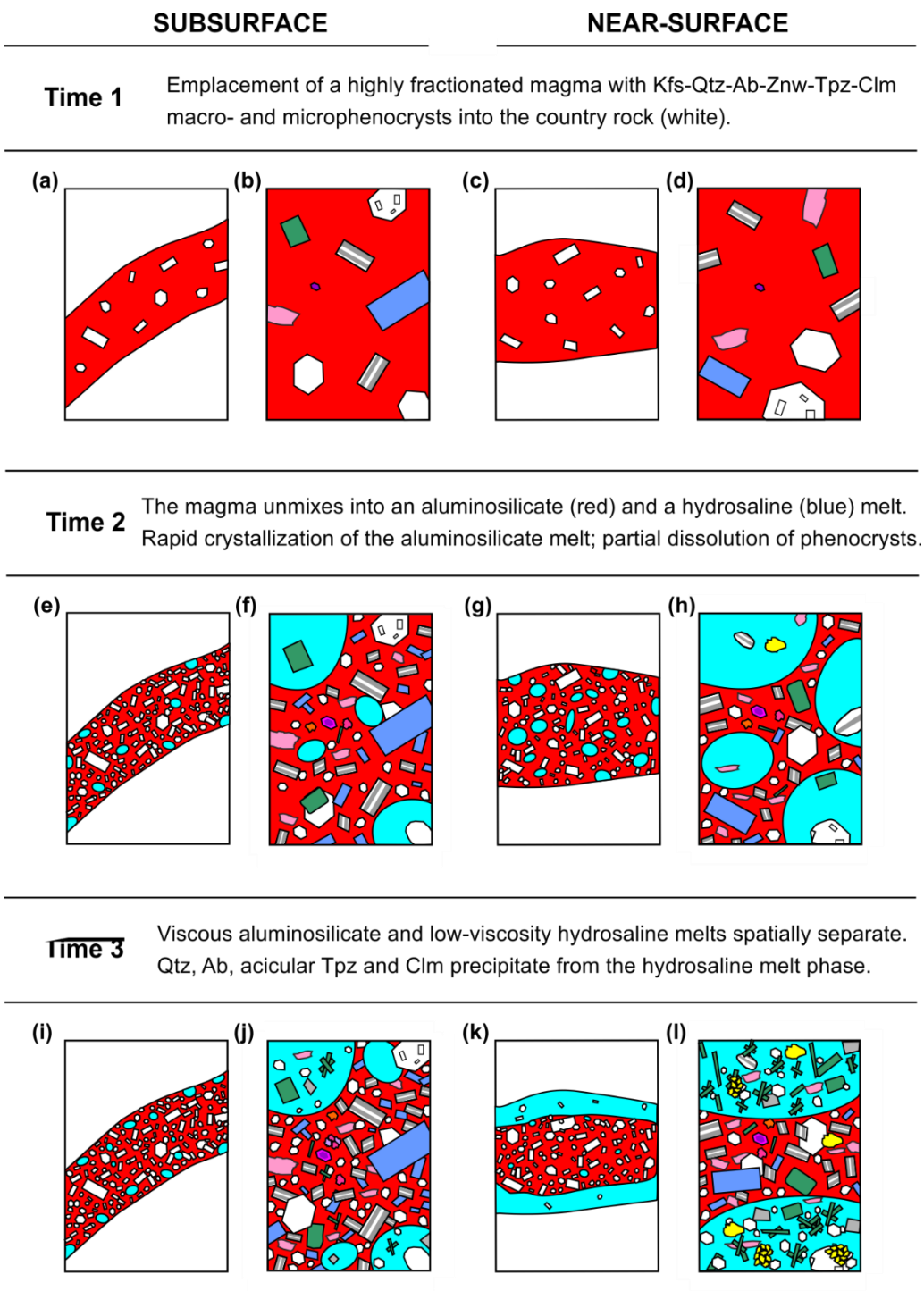

Fig. 7.11 The proposed magmatic evolution of the No. 431 dike now exposed at subsurface and near-surface locations. Crystallization of an initially homogeneous, highly differentiated magma was followed by unmixing of silicate- and fluoride-dominated melt phases that crystallized to ongonite and topazite, respectively

originally homogeneous melt phase (e.g., Cobbing et al., 1986; Breiter et al., 2005; Štemprok et al., 2008; London and Morgan, 2012). Crystallization as a result of abrupt

cooling alone is inconsistent with the occurrence of the most fractionated rocks, the topazite, along the margins of the No. 431 dike. Consistent with the compositional variation between ongonite and topazite rocks, we suggest that the fine-grained assemblage started to form when the granitic magma separated into aluminosilicate and hydrosaline melt phases that later crystallized ongonite and topazite lithologies, respectively (Time 2, Fig. 7.11 e-h).

Once the two melt phases had unmixed (Time 3), the low-viscosity hydrosaline melts appear to have segregated from the more viscous aluminosilicate melt towards the margin of the dike (Fig. 7.11 i-l). Possible driving forces for this segregation are discussed in the following section. Rare, subrounded silicate phenocrysts in the rim zone of ongonite II and topazite were likely entrained from the assemblage that crystallized from the originally homogeneous silicate melt phase. They were then partially resorbed while hosted by the hydrosaline melt phase (e.g., Fig. 7.11 f, h). At this stage, abundant quartz, topaz, zinnwaldite and ore minerals crystallized. Notably, most of the Sn that was originally present in the magma was carried in the hydrosaline melt to the margin of the dike, where cassiterite precipitated.

7.5.2 Comparison of ore mineral assemblages in the ongonites and topazite

The common accessory minerals in the No. 431 dike are columbite-tantalite, tapiolite, microlite, uraninite, rutile, hubnerite-ferberite, and zircon. Details of the distribution of the main ore minerals in the different rock types are provided in Appendix table 29.

As shown by the mineralogical descriptions, the ongonites and topazite in the No. 431 dike display distinct Nb-Ta-Sn oxide mineral associations. In the subsurface ongonite I, rare-metal elements are dominated by columbite-tantalite, together with tapiolite and microlite, but are free of cassiterite. Commonly, the subhedral Ta-poor columbite-(Mn) crystals are intergrown with rock-forming minerals, and they may

indicate early magmatic crystallization. The progressive zoning in columbite-(Mn), comprising an increase in the Ta content from core to rim, can be attributed to the gradual differentiation of the magma. The experimental work of Linnen and Keppler (1997) and Linnen (1998, 2004) suggests that the solubility of the Ta-rich end-member is higher than that of the Nb-rich member of columbite in peraluminous granites or pegmatite melts, similar to the relationship between the Fe-rich members relative to the Mn-rich members. Therefore, the coexisting tapiolite and tantalite-(Fe) represent the products of late-stage magmatic or possibly deuteric hydrothermal crystallization. Tapiolite is commonly found in pegmatites and granites that have undergone a highly evolved magmatic process (Černý et al., 1989a, b; Wang et al., 1997; Novák et al., 2003; Zhang et al., 2004; Beurlen et al., 2008; Chudik et al., 2008; Rao et al., 2009), and the fact that the tapiolite-tantalite pair plot at the appropriate boundary of the miscibility gap can probably be attributed to exsolution from an unstable homogeneous precursor (Černý et al., 1989a, b). Fluorite is usually present in the mineral assemblage of tapiolite, tantalite, and microlite, suggesting crystallization from an F-rich liquid. Overall, the variations in the composition of columbite-tantalite and tapiolite reflect a highly differentiated and relatively Fe-richer magma system.

In the near-surface ongonite (ongonite II), columbite-(Mn) also occurs, and it is associated with a small amount of cassiterite. In the topazite that coexists with ongonite II, Nb-Ta oxide minerals become less abundant, but their composition are similar to those in the ongonite II. Interestingly, there is an abundance of Nb-Ta oxide minerals in the ongonite, but a large amount of cassiterite only appears in the topazite. In particular, the cassiterite occurs as two distinct types. First, subhedral grains of cassiterite are associated with zircon and hubnerite (Fig. 7.9a), which may have crystallized from a melt phase; second, abundant, highly anhedral cassiterites with very fine-grained inclusion of topaz and varlamoffite in cavities may have crystallized at a later stage from an epigenetic hydrothermal fluid.

7.5.3 Differentiated Nb-Ta-Sn mineralization in the ongonites and topazite of the No. 431 dike

Granitic rocks rich in the rare elements are generally strongly enriched in F, and they are characterized by the crystallization of Nb-Ta-Sn ores, which may be directly linked to magmatic processes. Typical examples are found in the Beauvoir granite of the French Massif Central (Cuney et al., 1992; Wang et al., 1992), in the Yichun granite of Southern China (Belkasmi et al., 2000; Huang et al., 2002), and in the Czeck Podlesí granite (Breiter et al., 2007). It is particularly noted that Nb-Ta-Sn ores may be deposited at various stages of differentiation as coexisting columbite-tantalite and cassiterite are commonly disseminated in various facies of these granites. However, cassiterite may also be deposited in hydrothermal quartz veins, whereas columbite-tantalite is never found in such veins. In this study of the Xianghualing No. 431 dike, it was noted that the dike has two distinct types of rare-mental mineralization: Nb-Ta mineralization in the ongonites and Sn mineralization in the topazite. This apparently contrasting feature of Nb-Ta versus Sn mineralization differs from what is found in granites that are similarly enriched in rare-elements, and the difference may possibly be linked specifically to the highly F-enriched, high-level or near-surface emplacement of the Xianghualing Nb-Ta-Sn-enriched melt that permitted the efficient segregation of aluminosilicate and hydrosaline melts. As mentioned above, the ongonites of No. 431 dike are thought to be the product of extreme fractional crystallization of an F-rich granitic magma and unmixing of a silicate and fluoride-rich melt phases. The ore elements were likely present in the melt as complexes of TaF_8^{3-}, NbF_7^{2-}, and SnF_6^{2-}. The solubility of Nb, Ta, and Sn in the high-F fluids was maintained for a long time. At 600 ℃, 120–490 ppm Nb is required for columbite saturation in a melt with 2 wt.% F (Linnen and Keppler, 1997; Linnen, 1998). Simultaneously, the Nb- and Ta-complexes are sensitive to the Li-content in the melt. Breiter et al. (2007) confirmed that columbite often crystallized immediately after Li-mica (zinnwaldite), while the the Li-contents

decreased rapidly. As a result of both factors, the complexes of Nb and Ta were depolymerized easily, and the Nb-Ta minerals began to precipitate early from the ongonite melt. However, Bhalla et al. (2005) observed an increase in cassiterite solubility with increasing F in peraluminous melts. Obviously, the crystallization of abundant topaz in the ongonites and topazite would have rapidly caused a decrease in the activity of F in the melt. As a result, the cassiterite could crystallize during the post-magmatic and hydrothermal stages, and even varlamoffite could form in the cavities. Therefore, the increase in the F content of the melt that produced the No. 431 dike would inevitably have led to tin mineralization in the strongly F-enriched topazitic melts.

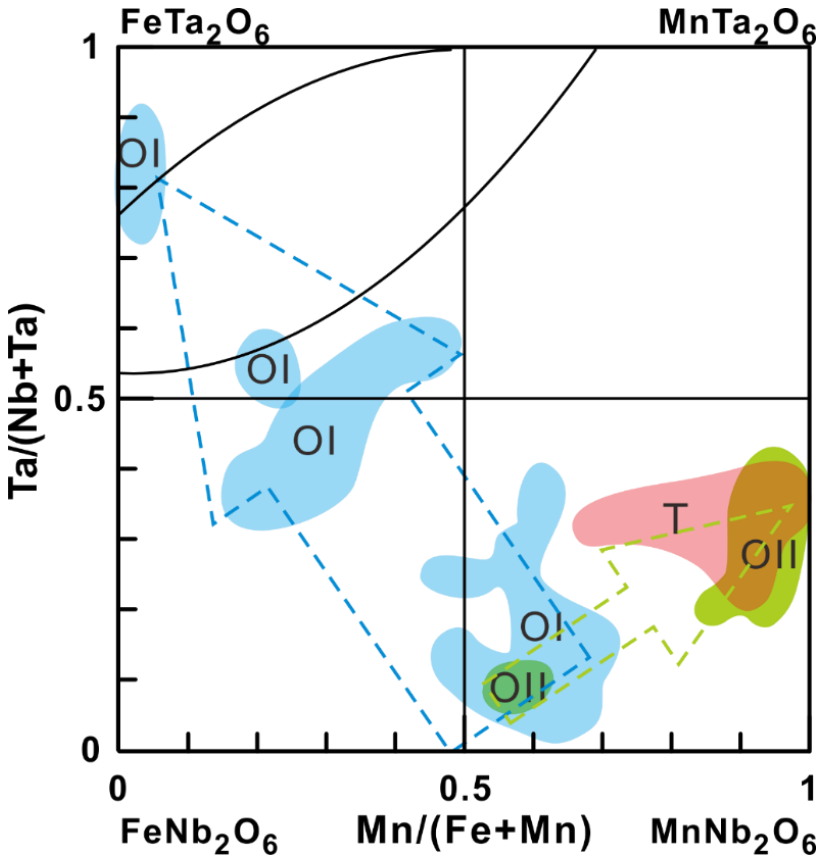

Fig. 7.12 Fractionation trends of the columbite-group minerals and tapiolite from the No. 431 dike. Arrows indicate direction of compositional fractionation. Abbreviations: OI: ongonite I; OII: ongonite II; T: topazite.

The observed trends of increasing Fe in columbite group minerals in ongonite I as compared to increasing Mn in columbite group minerals in ongonite II and topazite (Fig.

7.12; Appendix table 26) reflect a decrease of whole-rock FeO_t/MnO value from subsurface to near-surface (Appendix table 23). The compositional trends of the columbite minerals also concur with Mn-poor zinnwaldite in ongonite I and Mn-bearing zinnwaldite in ongonite II and topazite (Appendix table 25). We therefore interpret the two different compositional trends shown in Figure 7.12 to reflect the overall increase of differentiation from ongonite I to ongonite II and topazite.

7.5.4 A possible mechanism for the segregation of aluminosilicate and hydrosaline melts in the No. 431 dike

Aluminosilicate-dominated and hydrosaline melt phases as those inferred to have crystallized ongonite and topazite of the No. 431 dike differ in density and viscosity. Hydrosaline melts have low densities and low viscosities compared to aluminosilicate-dominated melts (Veksler and Thomas, 2002; Badanina et al., 2004; Veksler, 2004; Peretyazhko, 2010), and the density contrast of the two melt phases could thus have caused segregation of the hydrosaline melt into structurally higher positions. However, the zoning of both ongonite I from core to margin (as revealed in drill core) as well as ongonite II to topazite (as exposed in the exploratory trench) suggests that the hydrosaline melt separated towards both – the upper and the lower – dike margins, which cannot be explained by simple density-driven segregation. Temperature gradients between dike interior and country rocks could have also affected the segregation of the two melt phases. However, if temperature was the main driving force for segregation we would expect that the least evolved ongonite rocks would have crystallized along the colder dike margins and the more evolved ongonite rocks and topazite would have crystallized in the dike interior.

Another possible explanation – and our preferred interpretation – is that continued dike propagation/widening caused the partial (in ongonite I) to significant (from ongonite II to topazite) segregation of hydrosaline from aluminosilicate melt. Elastic propagation rates for fractures exceed viscous flow rates of silicate magmas (e.g., Rubin,

1993; Clarke et al., 1998), and dike propagation/widening will therefore create a pressure gradient and may shortly create a vacuum. The least viscous material of the dike – the hydrosaline melt – will have been instantly drawn into the low-pressure zone, and thereby largely separated from the aluminosilicate melt. The greater width of the dike as exposed in the exploratory trench relative to the drill core could reflect that the dike opened further at this structurally higher position, which caused a more advanced segregation of the two melt phases into ongonite II and topazite than at the structurally lower position with zoned ongonite I.

We believe that there might be records in the rocks such as melt inclusions of two immiscible melts, which may be present in minerals from both types of rocks and can be good for further studies. A detailed investigation of melt inclusions from the different mineral types and crystal populations will be ideally suited to test – and to refine – our proposed model. However, the detailed compositional and textural study presented here is an important guide for the sensible collection and interpretation of such data.

7.6 Summary

The Xianghualing No. 431 dike is composed of ongonite and topazite which are predominantly mineralized by Nb- and Ta-bearing and Sn-bearing ore minerals, respectively. Using the results of a combined petrological, mineralogical, and geochemical study of the small-scale dike, we have come to the following conclusions. Ongonite crystallized from an aluminosilicate magma that reached saturation in F and other volatile components. Upon exsolution of a hydrosaline melt phase (or phases), the aluminosilicate melt rapidly crystallized to a quartz-, K-feldspar-, and albite-dominated assemblage with Nb-Ta ore minerals of the columbite-tantalite, tapiolite and microlite as characteristic accessories. Topazite formed from the hydrosaline melt that segregated towards the margin of the small-scale dike, crystallizing a topaz-,

zinnwaldite-, and quartz-dominated assemblage. Exsolution of the two melt phases and their efficient segregation into core and rim zones of the dike may have been driven by dike propagation/widening subsequent to the initial dike emplacement. Melt inclusions should provide a detailed record of the proposed evolution and further provide compositional details on the fractionating liquids.

Chapter 8 Insights from experimental petrology for the understanding the mineralization and origin of Jurassic granites in South China

8.1 The relationship between emplacement conditions and tin mineralization

Phase equilibrium studies have shown that the Qitianling granite has a relatively high liquidus temperature (>900°C), it emplaced in the mid crust (~10-12 km), with a melt water content rich (≥5.5 wt.%) and at relatively reduced (oxygen fugacity around at NNO-1 ± 0.5) environment. Since the cassiterite U-Pb ages (159.9±1.9 Ma and 158.2±0.4 Ma) of Furong tin district (Yuan et al., 2011) are very close to the zircon U-Pb ages (range from 149.5±4.8 Ma to 162±2 Ma) of Qitianling granite, the emplacement condition should have influenced the tin mineralization. In the following, we discuss three main influence factors based on our experimental work.

The first controlling factor is oxygen fugacity. The solubility of SnO_2 study in a synthetic granite system under variable oxygen fugacity condition was firstly carried out by Ryabchikov et al. (1978). The experiments in the haplogranite-SnO_2-FeO-H_2O system indicate that at 750°C, 150 MPa, and oxygen fugacity between HM to NNO conditions, the solubility of Sn ranges from 1000 ppm to 2000 ppm, while at more reduced condition (MW), the solubility of Sn increased twice, demonstrating that low oxygen fugacity may enhance the solubility of Sn in the granite melt. This conclusion is also in agreement with the experiments conducted by Taylor and Wall, 1992. In their experiment, the haplogranite composition Or(11)-Ab(19)-Qtz(70) and SnO_2 crystals were chosen as the starting materials. Experiments were conducted at 750 °C, 200 MPa and different oxygen fugacities (e.g. run 1052 at ~logfO_2-14.18 and run 1050 at ~logfO_2-16.56). The results show that the solubility of Sn in run 1052 is 845 ppm ± 178, while in more reducing condition, the solubility of Sn in run 1050 is up to 2233

ppm±963. Using the diffusion profile method to avoid the loss of Sn to the noble-element capsule walls, Linnen et al. (1995) also investigated the cassiterite solubility at relatively high temperature (850°C) and 2 kbar in a haplogranitic melt system with 5.6 wt% of H_2O. Their result illustrated that at FMQ-0.84, the cassiterite solubility can be up to 28000 ppm while at FMQ+3.12, it just around ~800 ppm. All those experiments suggest therefore that low oxygen fugacity can be a significant constrain on the Sn incorporation in a granitic melt. Qitianling magma was emplaced at relative low oxygen fugacities (NNO-1±0.5), hence providing a beneficial environment for incorporating the Sn in the melt, at least during the early stages of its production/crystallisation. W-Sn related with reduced magma is also supported by other studies (e.g. Ishihara 1981; Lehmann 1990; Blevin and Chappell, 1992, 1995). Conversely, cassiterite precipitation will be favored by an increase in redox conditions. The increase in fO_2 we document between the magmatic stage (as inferred from our phase equilibrium experiments) and subsolidus conditions or magmatic-hydrothermal transition (as inferred from FeTi oxides of the pluton) may be one reason of ore production. The reason for such an increase in *f*O2 still demands to be defined however, but has been documented to occur on other plutonic systems (e.g., Pichavant et al., 2017).

The second controlling factor is temperature. During the partial melting of the lower crust and magma ascent or even with assimilation and magma mixing processes, high temperature plays an important role on extracting ore elements, especially in thoes anatectic melts. Stemprok (1990) summarized and compared the dry and hydrothermal experimental work about the solubility of tin in felsic magma. Based on the data from Stemprok and Voldfin (1978), Stemprok (1982), Barsukov et al. (1983), Nekrasov (1984) and Ryabchikov et al. (1978a, b), Stemprok (1990) proposed an equation ($1ogC_{SnO2}$= 2.4-2.94*1000/T, where T is in K and C is in mass.%), which demonstrates the relationship between the solubility of SnO_2(C) and temperature. In this equation, as temperature increases, the solubility of SnO_2 increases. High liquidus temperature of Qitianling magma also allows high concentration of tin being reached in the silicate

melt during the different geological process.

The third controlling factor is melt water content. Firstly, a widely demonstrated effect is that water plays a significant role in decreasing the solidus temperature and increasing the melt proportion. This also conduces to concentrate the ore element in the melt during the melting process. Secondly, the participation of water in the magma will decreased the viscosity of the melt which improved element diffusivities, the mobility of the magma and meanwhile the transportation of ore elements become faster and more flexible. Thirdly, water rich magmas also dissolve other volatiles such as chlorine, fluorine, boron and phosphorus which will be also helpful in capturing and transiting the ore elements such as Sn (Wolf and London, 1994; Webster et al., 1996; Webster, 1997; Xiong et al. 1998; Bhalla et al., 2005; Zimmer et al. 2010; Duc-Tin et al., 2007). The volatiles, such as F, have significant effect on concentrating Sn. The discussion on detail can also see in chapter 7, highly evolved 431 dyke study. The lowest melt water content of Qitianling magma was constrained as >5.5 wt% and the average of melt water content is around 6.5 wt %, which is relative rich when compared with other magma systems. After the emplacement of magma, as the batholith slowly cooled down, along with crystallization, exsolution of aqueous fluids generally occurred till the magmatic-hydrothermal transition. Zhao et al. (2011) investigated the fluid–rock interaction of Qitianling granite using boron and oxygen isotopes of bulk rock and found that exsolution of voluminous aqueous fluids from the Qitianling magma occurred at temperature >450°C, pointing out the contribution of magmatic fluids in ore generation. This result is consistent with the study of fluid inclusion of Qitianling Furong deposit by Shuang et al. (2009). Their homogenization temperature measurements show that the highest temperature is from the skarn-type ore with 400°C-450°C, while these from greisen and altered granite are 250°C-350°C. Besides, the H-O isotopes of quartz of greisen indicate that the H_2O equilibrium with quartz has a $\delta^{18}O$ ranging from -5.7‰ to 7.6‰ close to the magmatic fluid. This result is once again interpreted as reflecting the magmatic origin of ore-forming fluids.

8.2 A possible source of the Jurassic Qitianling granite in South China

Geochemical studies have shown that the Qitianling granites were originated from the partial melting of lower crustal rocks with a limited contribution (~10-20%) of mantle-derived melt (Zhao et al., 2012). The role of mantle-derived magmas has therefore been restricted to that of heating the lower crust (e.g. Zhu et al., 2009). Our results do not shed light on the source of the water, e.g. whether there was an excess fluid phase rich in water or if water came only from dehydration melting of hydrous minerals such as amphibole and biotite. In the following we take the second scenario as a working hypothesis since it is the most commonly invoked for lower crustal melting (e.g. Clemens and Watkins, 2001). We evaluate (1) possible source rock compositions, and (2) the conditions that may have produced the H_2O-rich Qitianling magmas with ≥5-6 wt % H_2O_{melt} initial and with a liquidus temperature of > 900°C. We first consider the REE compositions of the Qitianling whole rocks to infer the nature of residual phases in the source. The Qitianling rocks have high REE concentrations. The LREE concentrations and patterns of most Qitianling granites compare to those of amphibolite but more closely resemble those of garnet-biotite gneiss xenoliths in south China, which are interpreted as fragments of the lower crust (Li et al., 2001; Guo et al., 1997; Li, 1997). The HREE concentrations of the Qitianling granites also closely compare to those of the amphibolite and garnet-biotite gneiss xenoliths, except for some of the phase-3 rocks. The moderately steep to steep LREE patterns are interpreted to result from the segregation of pyroxene in the source (Rollinson, 1993). The pronounced Eu anomaly of the Qitianling granites similarly suggests that either (1) plagioclase was residual in the source rocks, or (2) that it was removed from the magmas at some stage in their evolution. The latter mechanism is suggested by the increase of the Eu anomaly from Phase-1 to Phase-3 (Fig 8.1). However and importantly, the overall relatively flat HREE patterns indicate that garnet was not a significant source constituent (e.g. Drummond and Defant, 1990), and thus that source partial melting

took place at ≤800-900 MPa (e.g. cf. Rapp and Watson, 1995), i.e. at depths of ≤24-27 km for a common crust density. This suggests that the garnet bearing xenolith gneisses of Southern China, if representative of one of the lower crustal lithologies that melted for the production of the Qitianling magmas, reflects the deeper crustal levels of the main melting zone.

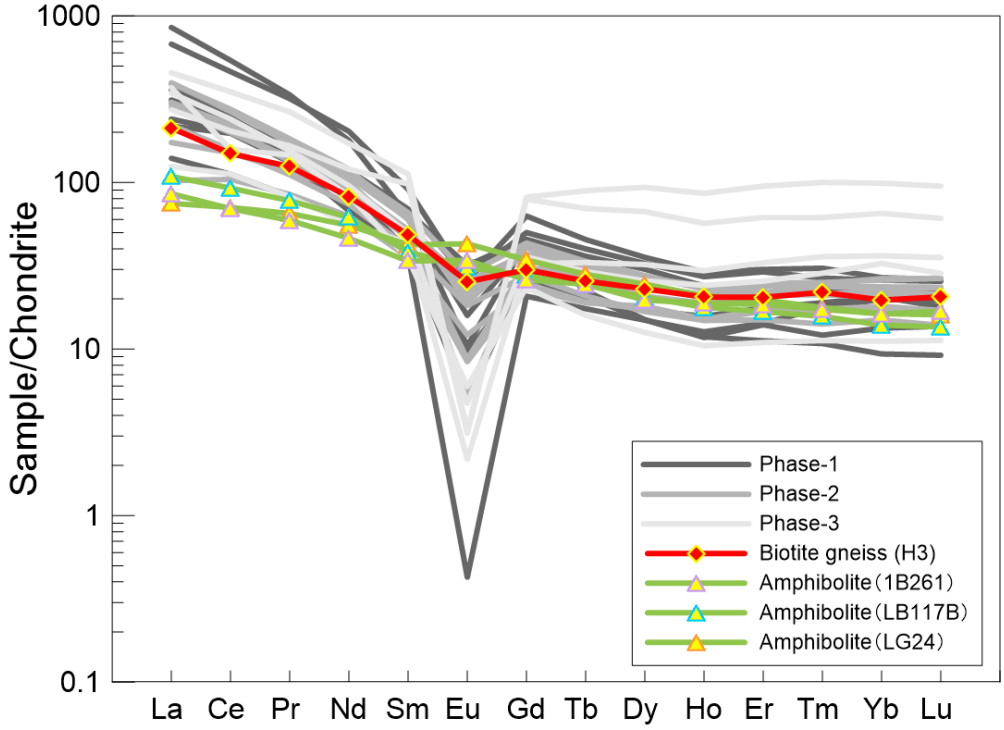

Fig. 8.1 Geological map of the Furong tin deposit and distribution of orebodies (cited from Yuan et al., 2011).

The garnet-bearing biotite gneiss xenoliths that could represent source rocks, have ~64-74 wt % SiO_2, ~11-15 wt % Al_2O_3, ~2-6 wt% FeO, ~1-2 wt% CaO, ~1-2 wt% Na_2O, and ~2-5 wt % K_2O) (Li et al., 2001; Guo et al., 1997). The amphibolites have ~49 wt % SiO_2, ~16-17 wt % Al_2O_3, ~11-12 wt % FeO, ~5 wt % CaO, ~3-4 wt % Na_2O, and ~1 wt % K_2O (Li, 1997).

Dehydration-melting experiments using a Bt gneiss (with 37 wt % Bt and ~63 wt % SiO_2) and a Qtz amphibolite (with 54 wt % Amp and ~60 wt % SiO_2) at 500-1000 MPa and 875-1000 °C produce melts with ~1.7-7.2 wt % H_2O for melt fractions of <30 wt % (Patino Douce and Beard ,1995). However, the SiO_2 content of the liquids produced by both Bt gneiss (SiO_2 ~70-76 wt %) and Qtz amphibolite (SiO_2 ~70-76 wt %) partial

melting is significantly higher than the SiO_2 content of the phase-1 Qitianling granite (~67 wt % SiO_2), while it closely compares to that of the intermediate phase-2 rocks. This however partly reflects the higher SiO_2 content of Qtz amphibolite used in the melting experiments of Patino Douce and Beard (1995) compared to that of the amphibolite in South China (60 wt % versus 49 wt %).

Amphibolite and greenschist rocks used in partial melting experiments by Beard and Lofgren (1991) have ~49-57 wt % SiO_2, (with ~34-50 wt% Amp) i.e. they are closer in composition to the amphibolites known in Southern China. Their results (in particular with their composition 478) show that at 690 MPa and 850-1000 °C, amphibolite dehydration melting produces liquids with ~3.8-6.3 wt % of H_2O_{melt} and low SiO_2 content (~66 wt %), i.e. close to the composition of the phase-1 Qitianling granites. The dehydration melting experiments conducted by Wolf and Wyllie (1994) at 1 GPa, 850-1000°C, and with starting materials similar to those of Beard and Lofgren (1991) (i.e with ~48 wt % SiO_2), yield liquids with ~52-66 wt % SiO_2.

However, all liquids produced by amphibolite partial melting have K_2O contents usually < 2 wt %, i.e. lower than phase 1 of Qitianling. We suggest that the elevated K_2O content reflects the contribution of biotite-bearing gneisses. A composite source made of amphibolite and biotite gneisses may be one of the interpretations for Qitianling granite source.

Altogether, the above comparison shows that it is possible to produce liquids with compositions akin to those of the most mafic variety cropping out in the Qitianling intrusion by partially melting lithologies similar to lower crustal xenoliths found in SE China. We therefore infer that a source made of amphibolite and biotite bearing rocks partially melted at pressure depths of around 800-900 MPa, and temperatures as high as 950°C, producing liquids with about 5-6 wt % H_2O_{melt}, can produce the most mafic liquids recorded at Qitianling. Under such conditions, experiments show that the melt fraction in the source remains relatively modest, ie lower than 30 wt % (Patino Douce and Beard, 1995). As our results show, such liquids may have subsequently fractionated

to produce the more evolved facies, such as phase-2 and phase-3 compositions. Such a fractionation may have occurred in a shallow reservoir, but fractionation at deeper levels, including at the source, cannot be excluded.

Appendix table 1 Major and trace elements of bulk rock samples from Qitianling, Jiuyishan, Guposhan and Huashan plutons

Pluton	Qitianling							
N	25°34'44"	25°32'58"	25°31'45"	25°32'58"	25°31'45"	25°27'09"	25°27'53"	25°34'12"
E	112°46'40"	112°59'12"	112°50'39"	112°59'12"	112°50'39"	112°47'59"	112°48'41"	112°48'17"
Sample	13-QTL-17	QT-38C	13-QTL-14B	QT-38	13-QTL-14A	13-QTL-21B	13-QTL-20	13-QTL-16
Lithology	CHBG	CHBG	M-FHBG	CHBG	MHBG	C-MBG	MHBG	MBG
(wt %)								
SiO_2	65.40	65.72	65.73	66.69	68.07	68.35	70.01	70.76
TiO_2	0.87	1.04	0.71	0.87	0.73	0.70	0.47	0.50
Al_2O_3	14.61	13.58	14.79	13.64	14.35	13.42	13.79	13.21
Fe_2O_3	1.20	1.68	1.54	2.86	1.12	0.75	0.99	0.87
FeO	3.68	4.22	2.51	2.52	2.98	3.86	1.90	2.20
MnO	0.09	0.10	0.05	0.12	0.07	0.05	0.05	0.06
MgO	0.95	1.37	0.68	1.13	0.89	0.79	0.49	0.58
CaO	3.05	3.27	1.90	2.97	2.46	1.70	1.82	1.61
Na_2O	3.30	2.95	3.14	2.93	3.00	2.89	2.98	2.84
K_2O	4.76	3.91	6.44	4.38	5.17	4.13	5.33	5.01
P_2O_5	0.28	0.33	0.22	0.28	0.24	0.22	0.14	0.16
LOI	1.01	0.91	1.75	1.12	1.29	2.47	1.13	1.34
Total	99.20	99.08	99.46	99.51	100.35	99.33	99.11	99.13
FeO_t	4.76	5.74	3.90	5.10	3.99	4.54	2.79	2.98
F	0.15	0.20	0.45	0.15	0.19	0.34	0.15	0.17
Na_2O+K_2O	8.07	6.86	9.58	7.30	8.17	7.02	8.31	7.86
K_2O/Na_2O	1.44	1.33	2.05	1.50	1.72	1.43	1.79	1.76
A/CNK	0.91	0.90	0.95	0.91	0.96	1.09	0.99	1.01
A/NK	1.38	1.50	1.22	1.43	1.36	1.45	1.29	1.31
FeO_t/MgO	4.99	4.18	5.71	4.51	4.50	5.74	5.65	5.16
FeO_t#	0.83	0.81	0.85	0.82	0.82	0.85	0.85	0.84
(ppm)								
Li	65.6	107	64.3	87	69.5	166	58.5	32
Be	8.18	6.07	9.58	4.17	9.25	8.31	9.77	11.5
Sc	12.8	15.1	10.6	12.9	10.9	9.7	8.1	11.3
V	58.8	85.3	29.4	70	51.7	40.6	28.5	29.9
Cr	12.4	19.8	7.13	17.2	13.8	13.6	11.2	9.97
Co	10.2	13.9	5.45	11.1	7.7	8.29	4.89	5.34
Ni	6.1	10.2	4.0	9.5	7.0	5.7	5.0	4.4
Cu	7.7	12.9	79.4	15.7	18.3	8.5	54.3	5.6

Zn	146	174	105	147	146	145	106	122
Ga	23.7	23.1	22	22.9	21.4	24.3	21.3	20.5
Rb	266	249	363	250	296	362	369	319
Sr	334	223	177	214	211	101	175	149
Y	46.6	52.5	46.2	54.3	41.2	45.4	39.9	41
Zr	295	318	424	313	321	360	201	315
Nb	31.8	35.2	30.8	30.9	27.3	35.6	27	27.8
Sb	0.593	0.594	0.873	0.543	0.903	0.51	0.888	0.489
Cs	12.2	16.4	43.2	14.8	24.3	21.2	22.6	14.2
Ba	821.2	502.3	862.9	554.2	887.2	359.1	631.9	425.2
La	73.4	56.5	40.8	159	65.8	92	65.5	71.1
Ce	140	121	90.8	279	132	162	120	134
Pr	15	13.9	10.4	28.4	14.2	15.9	12.5	14
Nd	53.2	53.5	39.7	91.6	52.3	52.1	43	48.9
Sm	9.78	10.2	7.68	13.4	9.71	8.88	7.63	8.91
Eu	1.78	1.50	1.43	1.44	1.57	0.89	1.23	1.06
Gd	8.98	9.84	7.32	12.37	8.52	8.31	7.23	8.08
Tb	1.31	1.45	1.08	1.65	1.22	1.17	0.974	1.15
Dy	7.32	7.93	6.48	8.63	6.71	6.64	5.9	6.51
Ho	1.33	1.51	1.3	1.61	1.27	1.29	1.13	1.33
Er	3.9	4.62	3.95	4.78	3.85	3.84	3.32	3.9
Tm	0.561	0.645	0.608	0.74	0.517	0.573	0.514	0.576
Yb	3.55	4.21	4.21	4.36	3.63	3.82	3.3	3.84
Lu	0.5	0.62	0.645	0.637	0.514	0.538	0.503	0.571
Hf	6.82	7.67	9.78	8.25	8.43	8.75	5.52	9.31
Ta	2.52	3.07	4.13	3.02	3.71	2.95	2.95	3.86
W	3.66	2.69	3.91	4.76	2.89	14.1	7.06	7.11
Tl	1.17	1.13	2.67	1.15	1.86	1.82	2	2.32
Pb	40.5	30.6	48	34.6	44.1	37.5	46.8	55.6
Bi	0.525	0.327	21.6	0.41	2.33	0.872	2.42	3.03
Th	24.9	22.6	28.7	47.9	41.1	59.7	51	53.5
U	13.7	5.62	17	6.85	11	11.1	13.6	15.2
Sn	21.4	12	25.3	6.73	22.8	6.67	12.8	13.7
∑REE	321	287	216	608	302	358	273	304
Rb/Sr	0.79	1.12	2.05	1.17	1.40	3.59	2.11	2.14
Zr/Hf	43.26	41.46	43.35	37.94	38.08	41.14	36.41	33.83
Nb/Ta	12.62	11.47	7.46	10.23	7.36	12.07	9.15	7.20
Th/U	1.82	4.02	1.69	6.99	3.74	5.38	3.75	3.52
Zr+Nb+Ce+Y	513.40	526.70	591.80	677.20	521.50	603.00	387.90	517.80
10000*Ga/Al	3.07	3.21	2.81	3.17	2.82	3.42	2.92	2.93

T_{zr}(℃)	812	821	854	822	832	863	797	844
Pluton	Qitianling							
N	25°29'52"	25°32'41"	25°34'45"	25°27'36"	25°26'37"	25°26'31"	25°27'27"	25°27'27"
E	112°51'24"	112°58'01"	112°46'17"	112°48'40"	112°51'13"	112°47'30"	112°51'20"	112°51'20"
Sample	13-QTL-13	13-QTL-01	13-QTL-19	13-QTL-24	13-QTL-26B	13-QTL-22	13-QTL-25A	13-QTL-25B
Lithology	FHBG	FG	M-FBG	MBG	FBG	FBG	M-FBG	M-FBG
(wt %)								
SiO_2	70.92	72.82	73.26	73.31	74.05	74.12	74.33	74.36
TiO_2	0.38	0.20	0.42	0.36	0.09	0.33	0.20	0.24
Al_2O_3	13.79	13.90	12.51	13.03	12.82	12.65	12.75	12.23
Fe_2O_3	0.60	0.53	0.67	0.55	0.39	0.22	0.36	0.50
FeO	1.97	0.91	1.76	1.73	0.99	0.54	1.21	1.28
MnO	0.04	0.03	0.03	0.03	0.02	0.01	0.03	0.03
MgO	0.42	0.36	0.63	0.40	0.07	0.34	0.17	0.21
CaO	1.82	0.61	1.33	1.85	0.66	2.56	1.07	1.01
Na_2O	3.06	2.69	3.39	2.92	3.08	2.88	3.08	2.94
K_2O	5.38	5.47	4.38	4.92	5.61	5.38	5.35	5.08
P_2O_5	0.12	0.23	0.12	0.11	0.02	0.09	0.05	0.06
LOI	1.17	1.73	1.42	1.34	1.41	1.28	1.09	1.28
Total	99.68	99.49	99.92	100.54	99.20	100.41	99.67	99.21
FeO_t	2.51	1.39	2.36	2.23	1.34	0.74	1.53	1.73
F	0.15	0.08	0.08	0.22	0.56	0.18	0.17	0.22
Na_2O+K_2O	8.44	8.16	7.77	7.84	8.69	8.26	8.43	8.02
K_2O/Na_2O	1.76	2.03	1.29	1.69	1.82	1.87	1.74	1.73
A/CNK	0.97	1.21	0.98	0.97	1.04	0.83	1.00	1.01
A/NK	1.27	1.34	1.21	1.29	1.15	1.20	1.17	1.18
FeO_t/MgO	5.92	3.87	3.77	5.64	18.33	2.19	9.18	8.41
FeO_t#	0.86	0.79	0.79	0.85	0.95	0.69	0.90	0.89
(ppm)								
Li	109	125	63.6	51.6	294	18	128	71.9
Be	12.3	13.3	7.49	6.13	39.7	11.8	8.37	20.8
Sc	8.1	8.9	5.0	7.1	6.2	7.3	5.7	5.4
V	25.2	20.1	1.26	22	3.63	21.2	8.93	10.5
Cr	14.9	14.2	9.81	28.3	9.73	8.12	7.16	7.11
Co	3.91	2.71	2.18	5.23	0.64	1.34	1.82	2.02
Ni	8.3	5.5	23.9	17.6	6.0	3.6	4.0	2.8
Cu	26.3	4.8	6075	14.4	2.5	3.4	2.0	3.4
Zn	137	88.9	1270	60.5	70.1	67.8	55.2	60.7
Ga	20.9	20.1	36	20.3	25.5	18.4	19.1	19.9

Rb	387	383	1148	343	750	368	452	446
Sr	142	82.2	70.7	136	18.5	128	51.3	76.6
Y	38.1	22.6	17.8	28.5	98.6	30.3	31.3	43.3
Zr	218	116	71.3	152	140	222	175	174
Nb	21	23.5	4.35	18.8	66.6	20.1	23.6	23.7
Sb	3.75	0.683	44.5	2.8	0.92	0.8	0.636	0.598
Cs	24.9	21.2	16.1	31.2	50	10.9	35.5	20.3
Ba	519.7	295.4	117.7	332.2	72.5	207.6	104.5	124.7
La	92.3	32.8	51.2	51.8	107	24.1	69.7	69.6
Ce	166	67.6	119	94.8	211	63	122	125
Pr	16.3	7.34	11.8	9.91	23.6	7.56	12	12.4
Nd	54.3	26.5	30.6	33.5	77.6	28.4	36.2	39.6
Sm	8.79	5.77	5.38	6.03	16.5	5.23	5.57	6.8
Eu	1.15	0.55	0.02	1.02	0.18	0.68	0.47	0.49
Gd	8.02	5.19	4.08	5.44	15.59	4.54	4.85	6.27
Tb	1.05	0.748	0.634	0.757	2.53	0.687	0.696	0.982
Dy	5.8	3.64	3.62	4.07	16.2	4.38	4.21	5.66
Ho	1.17	0.658	0.705	0.825	3.16	0.843	0.839	1.16
Er	3.53	1.78	2.27	2.38	9.8	2.66	2.75	3.82
Tm	0.51	0.261	0.428	0.342	1.49	0.415	0.42	0.599
Yb	3.56	1.52	3.23	2.43	10.6	2.78	2.93	4.3
Lu	0.52	0.223	0.475	0.337	1.48	0.404	0.414	0.646
Hf	6.65	3.19	6.94	4.22	6.51	6.15	5.55	5.87
Ta	2.39	1.58	2.39	2.28	4.37	1.97	2.48	3.03
W	0.901	14.2	2.25	4.77	10.1	1.11	3.42	5.37
Tl	2	1.92	6.38	2.18	4.18	1.43	2.14	2.37
Pb	83.3	56.6	478	41.5	73.1	42.4	46.4	51.3
Bi	0.99	0.0792	28.3	0.963	0.439	0.362	0.37	0.611
Th	56.2	21.6	33.4	44.1	66.9	77.9	66.8	74.1
U	18.9	7.81	34.3	12	23	15.7	23.4	25.5
Sn	18.2	27	113	11.4	23	25	14.6	18
∑REE	363	155	233	214	497	146	263	277
Rb/Sr	2.73	4.66	16.23	2.52	40.54	2.87	8.82	5.82
Zr/Hf	32.78	36.36	10.27	36.02	21.51	36.10	31.53	29.64
Nb/Ta	8.79	14.87	1.82	8.25	15.24	10.20	9.52	7.82
Th/U	2.97	2.77	0.97	3.68	2.91	4.96	2.85	2.91
Zr+Nb+Ce+Y	443.10	229.70	212.45	294.10	516.20	335.40	351.90	366.00
10000*Ga/Al	2.86	2.73	5.43	2.94	3.76	2.75	2.83	3.07
T_{zr}(℃)	803	774	716	774	777	790	791	793
Pluton	Qitianling							

N	25 °39'49"	25 °32'36"	25 °28'13"	25 °34'27"	25 °32'24"	25 °26'37"	25 °32'04"	25 °27'09"
E	112 °54'46"	112 °55'22"	112 °53'08"	112 °47'33"	112 °53'35"	112 °51'13"	112 °50'47"	112 °47'59"
Sample	13-QTL-10	13-QTL-04	QT-105	QT-122	13-QTL-03	13-QTL-26A	QT-123	13-QTL-21A
Lithology	FBG	FBG	FG	FG	FG	FBG	FG	FBG
(wt %)								
SiO_2	74.85	75.83	75.93	76.08	76.21	76.40	77.03	77.03
TiO_2	0.20	0.13	0.07	0.15	0.13	0.06	0.10	0.29
Al_2O_3	12.64	11.88	12.49	12.02	12.18	12.60	12.34	10.96
Fe_2O_3	0.63	0.22	0.26	0.50	0.21	0.31	0.67	0.53
FeO	1.09	1.06	0.92	0.83	0.80	0.51	0.29	1.52
MnO	0.03	0.02	0.03	0.02	0.02	0.01	0.01	0.03
MgO	0.17	0.11	0.03	0.11	0.10	0.04	0.04	0.35
CaO	0.90	0.72	0.77	0.62	0.54	0.59	0.60	0.67
Na_2O	3.08	2.83	3.42	2.84	2.76	2.70	2.87	2.14
K_2O	5.15	5.33	4.78	5.56	5.85	6.26	5.63	5.11
P_2O_5	0.05	0.02	0.01	0.03	0.03	0.02	0.01	0.08
LOI	0.94	0.86	1.13	0.93	0.96	1.22	0.70	1.18
Total	99.73	99.02	99.82	99.69	99.79	100.72	100.28	99.89
FeO_t	1.66	1.26	1.15	1.29	0.99	0.79	0.90	2.00
F	0.15	0.30	0.44	0.06	0.18	0.56	0.06	0.11
Na_2O+K_2O	8.23	8.16	8.19	8.41	8.61	8.96	8.50	7.25
K_2O/Na_2O	1.67	1.88	1.40	1.96	2.12	2.32	1.96	2.39
A/CNK	1.03	1.01	1.03	1.02	1.03	1.03	1.04	1.07
A/NK	1.19	1.14	1.16	1.12	1.12	1.12	1.14	1.21
FeO_t/MgO	9.82	11.07	42.63	12.25	9.84	18.44	25.63	5.73
FeO_t#	0.91	0.92	0.98	0.92	0.91	0.95	0.96	0.85
(ppm)								
Li	461	90.9	248	33.3	30	170	23.5	63.1
Be	6.5	18.7	6.98	21.7	15.8	7.2	6.6	2.01
Sc	6.7	6.1	4.5	4.9	5.4	6.1	4.7	5.3
V	1.31	4.52	1.96	4.34	4.26	2.09	1.34	14.8
Cr	5.95	5.22	7.18	5.5	5.41	3.27	13.3	6.99
Co	1.18	1.15	1.03	1.22	1.13	0.362	0.766	3.74
Ni	36.3	1.8	1.6	2.5	2.2	1.7	5.7	4.0
Cu	9540	2.0	3.4	10.4	4.9	2.1	2.0	4.3
Zn	1640	104	34.2	79.3	54.9	37.3	53.8	85.7
Ga	48.3	20	18.8	18.9	17.1	21.1	15.5	19.2
Rb	1110	500	674	478	485	740	398	335
Sr	53.1	29.2	14	34.7	34.3	16.2	25.5	68.7

Y	0.398	46.9	56.7	36.3	33	160	20.2	24.9
Zr	21.1	195	135	165	154	144	157	377
Nb	139	27.6	42.9	22.1	17.4	62.9	10.1	17
Sb	45.3	0.28	0.215	0.407	0.633	0.605	0.467	0.466
Cs	29.1	21.3	44.7	26.8	17.5	31.6	11.8	10.1
Ba	80.4	29.0	14.9	53.5	41.3	46.3	14.8	134.0
La	0.694	80.8	29.3	93.1	84.8	64.1	87.1	200
Ce	3.189	145	67.8	162	148	123	95.3	326
Pr	0.427	13.8	7.32	15.3	13.9	14.8	13	29.9
Nd	0.819	43.3	25.6	45.6	40.4	54.4	37.7	80.8
Sm	0.270	7.26	6.36	6.91	5.73	14.4	5.14	9.21
Eu	0.004	0.26	0.12	0.30	0.28	0.17	0.33	0.58
Gd	0.109	7.03	6.39	6.49	5.67	16.02	4.60	8.69
Tb	0.045	1.06	1.2	0.918	0.733	3.24	0.579	0.813
Dy	0.302	6.23	7.8	5.03	4.15	22.7	3.05	3.64
Ho	0.051	1.34	1.64	1.05	0.874	4.78	0.582	0.652
Er	0.212	4.06	5.24	3.27	2.8	15.1	1.74	2.22
Tm	0.063	0.691	0.867	0.575	0.459	2.42	0.272	0.293
Yb	0.865	5.31	5.9	3.78	3.34	16.1	1.81	2.17
Lu	0.121	0.691	0.859	0.568	0.435	2.31	0.274	0.333
Hf	4.6	6.51	6.97	5.81	5.22	8.77	5.1	9.98
Ta	115	4.07	7.17	4.02	0.834	8.12	1.42	1.11
W	12.7	13.1	14.9	12.1	2.63	14.1	2.1	3.02
Tl	4.58	2.53	3.79	1.97	2.86	4.11	1.9	1.64
Pb	606	64.2	52.8	51.2	46.9	66.2	46.4	44.5
Bi	10.8	1.66	1.35	1.32	30.4	1.29	0.276	1.11
Th	5.13	78.6	53.5	87.5	80.5	53.5	87.4	149
U	11.8	25.9	39.5	24.4	20	29.8	14	23
Sn	162	25.9	39.5	9.56	29.9	29.8	14	12.7
∑REE	7	317	166	345	312	354	251	665
Rb/Sr	20.90	17.13	48.11	13.77	14.13	45.69	15.62	4.87
Zr/Hf	4.59	29.95	19.37	28.40	29.50	16.42	30.78	37.78
Nb/Ta	1.21	6.78	5.98	5.50	20.86	7.75	7.11	15.32
Th/U	0.43	3.03	1.35	3.59	4.03	1.80	6.24	6.48
Zr+Nb+Ce+Y	163.69	414.50	302.40	385.40	352.40	489.90	282.60	744.90
10000*Ga/Al	7.22	3.18	2.84	2.97	2.65	3.16	2.37	3.31
T_{zr}(℃)	636	806	774	791	786	779	789	877

Pluton	Jiuyishan				Guposhan		Huashan			
Sample	SC14-160A	SC14-160B	SC14-162-A	SC14-162-BE	SC14-169	SC14-181	SC14-171AD	SC14-172B	SC14-176A	SC14-177B
Lithology	C-MBG	FBG	CBG		FBG	CBG		CHBG	CHBG	CBG
(wt %)										
SiO_2	75.07	74.47	75.88	67.44	73.28	73.41	57.69	62.22	66.20	73.15
TiO_2	0.17	0.26	0.06	0.60	0.22	0.18	1.57	1.24	0.65	0.68
Al_2O_3	13.24	12.58	13.36	14.68	13.63	14.22	14.55	14.25	14.91	12.61
Fe_2O_3	0.84	0.76	0.74	1.34	0.86	0.82	2.46	2.25	1.74	0.91
FeO	0.79	1.60	0.47	3.06	1.01	0.91	4.68	3.91	3.21	2.98
MnO	0.04	0.03	0.02	0.06	0.02	0.03	0.12	0.11	0.08	0.08
MgO	0.16	0.15	0.00	0.55	0.15	0.15	3.77	2.75	0.88	0.78
CaO	0.72	1.19	0.55	1.60	0.82	0.70	5.81	4.57	2.09	0.92
Na_2O	3.25	2.86	3.83	3.19	2.70	3.44	3.03	2.96	3.36	2.12
K_2O	5.08	5.01	4.71	5.79	6.20	5.57	3.62	3.88	5.27	4.79
P_2O_5	0.03	0.04	0.00	0.17	0.04	0.03	0.35	0.29	0.18	0.05
LOI	0.88	0.64	0.84	0.86	0.57	0.82	1.43	0.71	0.69	0.98
Total	100.27	99.58	100.46	99.35	99.50	100.29	99.08	99.14	99.25	100.05
FeO_t	1.54	2.28	1.14	4.27	1.78	1.65	6.89	5.93	4.78	3.79
F	0.19	0.21	0.25	0.23	0.10	0.20	0.12	0.11	0.25	0.11
Na_2O+K_2O	8.33	7.87	8.54	8.98	8.90	9.01	6.65	6.84	8.63	6.92
K_2O/Na_2O	1.56	1.75	1.23	1.82	2.30	1.62	1.20	1.31	1.57	2.26
A/CNK	1.09	1.02	1.08	1.02	1.08	1.10	0.75	0.82	0.99	1.22
A/NK	1.22	1.24	1.17	1.27	1.22	1.22	1.63	1.57	1.33	1.45
FeO_t/MgO	9.82	15.57	1093.44	7.78	12.00	11.08	1.83	2.16	5.45	4.88
FeO_t#	0.91	0.94	1.00	0.89	0.92	0.92	0.65	0.68	0.85	0.83
(ppm)										
Li	51.9	46.8	75.3	64.8	62	64.3	31.8	39.6	71.8	49.4
Be	7.2	4.8	6.99	7.42	2.75	6.88	3.07	3.69	5.92	3.09
Sc	9.9	11.2	8.29	13.5	10.9	10.1	16.5	15.4	14.4	11.5
V	9.58	7.61	1.54	23.3	7.44	6.9	156	133	35.1	52.8
Cr	3.53	1.83	1.62	2.06	2.04	2.34	96.3	44.3	3.87	32.3
Co	1.06	1.61	0.19	5.02	1.49	1.29	26.4	18.7	5.79	9.41
Ni	0.75	0.14	-0.09	0.67	1.47	1.46	42.3	19.5	2.71	15
Cu	1.92	1.74	0.15	5.24	2.24	1.75	29.1	19	5.46	9.83
Zn	152	116	37.1	206	96.8	139	125	106	111	161
Ga	19.1	19.5	22.8	21.6	19	21.1	20.3	20.3	24	17.6
Rb	370	279	490	348	309	415	187	212	353	239
Sr	41.1	42.5	4.18	90.7	64.8	61.6	527	438	183	147
Y	48.9	55.7	72.7	38.6	40.8	38.2	27.4	30.7	52	31.5

Zr	138	269	130	524	197	179	186	234	433	343
Nb	33.6	25.6	34.7	26.5	18.2	22.6	37.6	39.5	47.1	25.3
Sb	0.65	0.26	0.64	0.18	0.37	0.49	1.15	1.23	0.66	0.77
Cs	18.5	9.88	20.2	14.7	8.68	13.4	19.6	13.9	19.7	12
Ba	120	323	5.7	1040	775	323	678	718	574	548
La	35.2	67.6	12.2	47.6	60.5	45.4	50.5	55.5	82.8	69
Ce	71.5	141	31.7	91.2	127	86.9	101	118	175	150
Pr	8.72	16.8	4.14	10.8	14.5	10.4	11.5	13.3	19.6	16.2
Nd	32.7	61.5	17.1	40.8	53.3	36.8	41.6	47.6	69.6	57.3
Sm	7.34	11.8	5.97	7.96	10.1	7.23	7.52	8.64	13	9.88
Eu	0.39	0.75	0.05	1.38	1.02	0.55	1.93	1.91	1.45	1.46
Gd	7.22	10.76	7.28	7.49	8.82	6.26	6.91	7.45	12.01	8.14
Tb	1.31	1.77	1.55	1.16	1.31	0.99	0.95	1.09	1.8	1.13
Dy	7.91	9.51	10.7	6.33	7.04	5.76	5.19	5.54	9.58	5.87
Ho	1.6	1.89	2.32	1.29	1.35	1.16	0.93	1	1.82	1.19
Er	4.82	5.54	6.85	3.78	4.01	3.72	2.55	2.78	5.2	2.92
Tm	0.76	0.79	1.02	0.53	0.54	0.56	0.33	0.38	0.68	0.38
Yb	5.02	4.97	6.78	3.57	3.47	3.81	2.25	2.66	4.25	2.4
Lu	0.7	0.7	0.99	0.54	0.5	0.58	0.33	0.38	0.6	0.35
Hf	5.21	7.8	6.29	11.8	5.78	6.06	4.87	6.17	10.9	8.98
Ta	4.82	2.17	4.41	1.81	1.39	2.15	3.06	3.42	3.48	1.51
W	8.62	1.29	2.78	23.8	2.9	2.96	3.05	4.43	1.83	1.78
Tl	1.58	1.33	2.57	1.77	1.36	1.63	0.71	0.9	1.53	1.01
Pb	32.6	34.7	54.4	43.8	35.9	31.8	23	25.5	31.4	32.8
Bi	0.079	0.16	0.173	0.067	0.193	0.046	0.364	0.484	0.275	0.087
Th	45.8	40.7	41.9	22.8	29.2	42	21.1	25.2	65.2	38.7
U	12.30	8.40	14.84	5.64	5.95	10.15	8.02	9.00	19.93	5.26
Sn	3.04	3.51	16.5	3.44	3.01	8.88	3.81	4.85	9.51	4.62
∑REE	185	335	109	224	293	210	233	266	397	326
Rb/Sr	9.00	6.56	117.22	3.84	4.77	6.74	0.35	0.48	1.93	1.63
Zr/Hf	26.49	34.49	20.67	44.41	34.08	29.54	38.19	37.93	39.72	38.20
Nb/Ta	6.97	11.80	7.87	14.64	13.09	10.51	12.29	11.55	13.53	16.75
Th/U	3.72	4.85	2.82	4.04	4.91	4.14	2.63	2.80	3.27	7.36
Zr+Nb+Ce+Y	292.00	491.30	269.10	680.30	383.00	326.70	352.00	422.20	707.10	549.80
10000*Ga/Al	2.72	2.93	3.22	2.78	2.63	2.80	2.64	2.69	3.04	2.64
T_{zr}(℃)	780	834	774	888	808	801	728	771	862	876

Note: Abbreviations of lithology: C: coarse grained; M: medium grained; F: fine grained; H: hornblende; B: biotite; G: granite; E: enclave; D: diorite; A/CNK= $[Al_2O_3/(CaO+K_2O+Na_2O)]_{in\ mole}$; FeO_t= (FeO + Fe_2O_3 ×0.8998); FeO_t#= FeO_t /(FeO_t+MgO);

Tzr is calculated after Waston and Harrison, 1983.

Appendix table 2 Representative composition of amphibole from Qitianling, Jiuyishan, Guposhan and Huashan plutons

	Qitianling									
Sample	38C	38C	38C	38C	38C	14A	14A	14A	14A	14A
SiO_2	43.58	43.15	43.51	43.21	43.31	40.73	43.46	43.49	43.94	42.52
TiO_2	1.85	2.03	1.81	2.00	1.97	0.67	1.78	1.96	1.87	1.60
Al_2O_3	7.44	7.18	7.35	7.43	7.40	8.59	7.53	7.34	7.11	7.84
FeO	24.52	23.99	24.55	25.14	24.94	28.47	23.67	23.09	22.42	25.85
MnO	0.25	0.21	0.24	0.18	0.26	0.23	0.24	0.17	0.18	0.30
MgO	6.53	6.82	6.57	6.51	6.41	4.27	7.42	7.74	8.30	5.89
CaO	10.88	10.64	10.84	11.09	10.77	11.10	10.72	10.47	10.55	10.64
Na_2O	1.99	1.81	1.92	1.77	1.86	1.75	2.04	2.05	1.84	1.99
K_2O	1.23	1.26	1.22	1.17	1.21	1.60	1.15	1.15	1.18	1.28
F	0.34	0.35	0.35	0.31	0.35	0.40	0.57	0.63	0.57	0.47
Cl	0.19	0.17	0.18	0.17	0.17	1.44	0.27	0.20	0.16	0.40
Total	98.80	97.59	98.53	98.97	98.65	99.25	98.86	98.30	98.13	98.78
O=F,Cl	0.19	0.19	0.19	0.17	0.19	0.49	0.30	0.31	0.28	0.29
Total	98.61	97.40	98.35	98.80	98.47	98.75	98.56	97.98	97.85	98.50
Based on 23 Oxygen										
Si	6.729	6.714	6.728	6.660	6.691	6.479	6.668	6.682	6.720	6.610
Al iv	1.271	1.286	1.272	1.340	1.309	1.521	1.332	1.318	1.280	1.390
Al vi	0.084	0.030	0.067	0.009	0.038	0.089	0.029	0.012	0.001	0.047
Ti	0.214	0.237	0.211	0.232	0.228	0.080	0.206	0.226	0.216	0.188
Fe^{3+}	0.321	0.439	0.378	0.449	0.455	0.624	0.533	0.570	0.617	0.569
Fe^{2+}	2.845	2.683	2.797	2.792	2.767	3.164	2.504	2.398	2.250	2.792
Mn	0.033	0.027	0.032	0.024	0.034	0.031	0.032	0.022	0.024	0.039
Mg	1.503	1.582	1.515	1.496	1.477	1.012	1.696	1.773	1.892	1.366
Ca	1.800	1.773	1.795	1.831	1.782	1.892	1.763	1.723	1.728	1.773
Na	0.595	0.545	0.575	0.528	0.557	0.538	0.607	0.611	0.545	0.599
K	0.242	0.250	0.241	0.229	0.239	0.324	0.226	0.226	0.231	0.255
Total	15.64	15.57	15.61	15.59	15.58	15.75	15.60	15.56	15.50	15.63
Mg#	0.35	0.37	0.35	0.35	0.35	0.24	0.40	0.43	0.46	0.33
Fe#	0.68	0.66	0.67	0.68	0.68	0.79	0.64	0.62	0.60	0.71
Al	1.35	1.32	1.34	1.35	1.35	1.61	1.36	1.33	1.28	1.44
	Qitianling									
						SC14	SC14	SC14	SC14	SC14
Sample	13	13	13	13	13	52	52	52	52	52
SiO_2	42.55	41.69	42.15	42.54	42.61	41.46	42.12	43.29	42.83	42.49
TiO_2	1.36	1.86	1.28	1.67	1.51	0.84	2.02	2.00	1.81	1.87
Al_2O_3	6.79	7.53	7.09	6.90	7.01	8.34	7.68	7.72	7.89	7.90
FeO	27.19	25.47	26.34	26.76	24.32	25.94	23.39	20.77	21.02	21.75

MnO	0.31	0.38	0.40	0.32	0.34	0.50	0.77	0.38	0.41	0.48
MgO	4.44	5.13	5.00	4.78	6.46	5.41	6.18	8.19	7.76	7.55
CaO	10.62	10.67	10.62	10.37	10.48	10.79	10.59	10.79	10.67	10.66
Na_2O	2.02	2.39	2.16	2.10	2.26	1.99	2.00	2.11	1.99	2.09
K_2O	1.18	1.14	1.21	1.18	1.23	1.42	1.26	1.37	1.30	1.31
F	0.78	0.86	0.88	0.81	1.06	1.71	1.79	1.65	2.41	2.27
Cl	0.36	0.22	0.30	0.20	0.14					
Total	97.60	97.34	97.43	97.64	97.40	98.40	97.79	98.27	98.08	98.36
O=F,Cl	0.41	0.41	0.44	0.39	0.48	0.72	0.76	0.69	1.01	0.96
Total	97.19	96.93	96.99	97.25	96.93	97.68	97.04	97.58	97.06	97.40
Based on 23 Oxygen										
Si	6.813	6.672	6.741	6.768	6.734	6.564	6.668	6.715	6.709	6.651
Al iv	1.187	1.328	1.259	1.232	1.266	1.436	1.332	1.285	1.291	1.349
Al vi	0.093	0.092	0.077	0.063	0.039	0.121	0.102	0.127	0.167	0.109
Ti	0.164	0.224	0.154	0.200	0.179	0.100	0.240	0.234	0.213	0.220
Fe^{3+}	0.255	0.154	0.319	0.347	0.377	0.557	0.288	0.196	0.252	0.330
Fe^{2+}	3.386	3.253	3.204	3.213	2.838	2.878	2.809	2.498	2.503	2.517
Mn	0.042	0.051	0.055	0.043	0.045	0.067	0.103	0.050	0.054	0.064
Mg	1.060	1.224	1.192	1.134	1.522	1.278	1.458	1.895	1.811	1.761
Ca	1.822	1.829	1.820	1.768	1.775	1.830	1.797	1.794	1.791	1.788
Na	0.626	0.742	0.668	0.648	0.693	0.610	0.614	0.634	0.604	0.634
K	0.242	0.233	0.247	0.238	0.247	0.287	0.254	0.272	0.260	0.261
Total	15.69	15.80	15.74	15.65	15.72	15.73	15.66	15.70	15.66	15.68
Mg#	0.24	0.27	0.27	0.26	0.35	0.31	0.34	0.43	0.42	0.41
Fe#	0.77	0.73	0.75	0.76	0.68	0.73	0.68	0.59	0.60	0.62
Al	1.28	1.42	1.34	1.29	1.30	1.56	1.43	1.41	1.46	1.46

	Qitianling									
	SC14	SC14	SC14	SC14	SC14	SC14	SC14	SC14	SC14	SC14
Sample	42	42	42	42	42	62	62	62	62	62
SiO_2	42.25	42.62	42.02	42.82	42.56	43.01	43.26	43.22	42.48	43.44
TiO_2	1.78	1.82	2.08	1.85	1.85	1.04	0.72	1.17	1.88	1.11
Al_2O_3	8.18	7.46	7.50	7.77	7.65	7.28	6.84	7.67	7.81	7.51
FeO	23.44	23.94	23.46	22.30	22.79	23.81	24.94	22.75	22.31	22.79
MnO	0.44	0.50	0.56	0.47	0.42	0.78	0.67	0.77	0.63	0.45
MgO	6.23	6.81	6.60	7.28	7.31	6.28	6.36	7.26	7.04	6.55
CaO	10.47	10.67	10.44	10.64	10.74	10.84	10.89	10.80	10.77	10.87
Na_2O	2.02	1.85	1.88	1.80	1.88	1.88	1.79	1.88	1.96	1.87
K_2O	1.29	1.10	1.31	1.28	1.14	1.19	1.19	1.33	1.37	1.23
F	1.54	0.99	1.42	1.43	1.25	2.26	1.36	2.08	2.05	1.88
Cl										
Total	97.63	97.74	97.28	97.63	97.60	98.37	98.03	98.93	98.32	97.71
O=F,Cl	0.65	0.42	0.60	0.60	0.53	0.95	0.57	0.88	0.86	0.79

Total	96.98	97.32	96.68	97.03	97.07	97.41	97.45	98.05	97.45	96.91
Based on 23 Oxygen										
Si	6.658	6.645	6.633	6.685	6.643	6.793	6.794	6.718	6.671	6.858
Al iv	1.342	1.355	1.367	1.315	1.357	1.207	1.206	1.282	1.329	1.142
Al vi	0.178	0.017	0.028	0.115	0.051	0.148	0.061	0.124	0.115	0.256
Ti	0.211	0.214	0.247	0.218	0.217	0.124	0.085	0.136	0.222	0.132
Fe^{3+}	0.331	0.569	0.473	0.405	0.483	0.329	0.523	0.458	0.273	0.125
Fe^{2+}	2.758	2.553	2.623	2.507	2.491	2.816	2.752	2.499	2.657	2.884
Mn	0.059	0.066	0.075	0.061	0.056	0.104	0.089	0.101	0.084	0.060
Mg	1.463	1.582	1.554	1.693	1.702	1.479	1.490	1.682	1.649	1.542
Ca	1.768	1.782	1.766	1.779	1.797	1.834	1.833	1.798	1.812	1.838
Na	0.617	0.558	0.577	0.545	0.569	0.575	0.546	0.567	0.598	0.573
K	0.259	0.219	0.264	0.255	0.227	0.241	0.239	0.265	0.275	0.248
Total	15.64	15.56	15.61	15.58	15.59	15.65	15.62	15.63	15.68	15.66
Mg#	0.35	0.38	0.37	0.40	0.41	0.34	0.35	0.40	0.38	0.35
Fe#	0.68	0.66	0.66	0.63	0.63	0.68	0.68	0.63	0.64	0.66
Al	1.52	1.37	1.40	1.43	1.41	1.36	1.27	1.41	1.44	1.40

	Jiuyishan					Huashan				
Sample	162	162	162	162	162	176A	176A	176A	176A	176A
SiO_2	40.94	40.72	40.74	41.71	41.96	40.15	40.00	40.48	40.17	40.02
TiO_2	1.53	1.22	1.53	1.61	1.49	1.08	1.14	1.43	1.11	0.87
Al_2O_3	8.22	8.19	8.25	7.72	7.61	9.65	9.58	8.71	9.52	9.41
FeO	24.49	25.21	24.94	24.56	24.16	26.78	27.37	27.27	27.15	27.09
MnO	0.79	0.66	0.63	0.59	0.75	0.71	0.70	0.71	0.65	0.67
MgO	6.28	6.42	6.42	6.30	6.74	4.44	4.08	4.41	4.50	4.38
CaO	11.18	10.81	10.87	10.83	10.84	11.47	11.59	11.37	11.39	11.70
Na_2O	1.89	1.80	1.89	1.88	1.89	2.14	1.75	2.06	2.10	1.94
K_2O	0.98	0.97	1.10	0.99	0.84	1.37	1.22	1.16	1.36	1.33
F	1.15	1.12	0.96	0.78	1.06	0.79	0.32	0.61	0.75	0.37
Cl	0.19	0.20	0.13	0.18	0.14	0.15	0.18	0.36	0.16	0.16
Total	97.63	97.32	97.44	97.16	97.47	98.73	97.91	98.56	98.85	97.93
O=F,Cl	0.53	0.52	0.43	0.37	0.48	0.37	0.17	0.34	0.35	0.19
Total	97.10	96.80	97.01	96.79	97.00	98.37	97.74	98.22	98.50	97.74
Based on 23 Oxygen										
Si	6.467	6.416	6.414	6.576	6.576	6.370	6.365	6.432	6.353	6.382
Al iv	1.531	1.521	1.530	1.424	1.406	1.630	1.635	1.568	1.647	1.618
Al vi	0.000	0.000	0.000	0.010	0.000	0.175	0.162	0.064	0.128	0.151
Ti	0.181	0.145	0.182	0.191	0.176	0.129	0.136	0.171	0.132	0.104
Fe^{3+}	0.614	0.964	0.816	0.597	0.706	0.361	0.465	0.422	0.476	0.389
Fe^{2+}	2.621	2.359	2.469	2.642	2.460	3.192	3.176	3.202	3.115	3.225
Mn	0.106	0.088	0.084	0.079	0.100	0.095	0.094	0.096	0.087	0.090
Mg	1.479	1.508	1.506	1.481	1.575	1.049	0.967	1.045	1.062	1.041

Ca	1.892	1.824	1.833	1.830	1.821	1.950	1.975	1.936	1.930	1.999
Na	0.577	0.550	0.576	0.575	0.574	0.659	0.539	0.634	0.644	0.601
K	0.197	0.196	0.221	0.200	0.168	0.278	0.247	0.235	0.273	0.271
Total	15.67	15.57	15.63	15.60	15.56	15.89	15.76	15.80	15.85	15.87
Mg#	0.36	0.39	0.38	0.36	0.39	0.25	0.23	0.25	0.25	0.24
Fe#	0.69	0.69	0.69	0.69	0.67	0.77	0.79	0.78	0.77	0.78
Al	1.53	1.52	1.53	1.43	1.41	1.80	1.80	1.63	1.77	1.77
					Guposhan					
Sample	182	182	182	182	182	183	183	183	183	183
SiO_2	42.21	42.96	42.32	41.73	41.52	41.06	42.38	41.78	42.52	42.84
TiO_2	1.67	1.52	1.48	1.67	1.69	1.61	1.55	1.63	1.50	1.62
Al_2O_3	8.50	7.73	7.84	8.85	8.18	8.18	7.77	8.01	7.17	7.48
FeO	24.75	24.43	24.13	24.45	24.58	24.93	25.46	24.92	24.76	24.67
MnO	0.85	0.80	0.79	0.81	0.80	0.84	0.89	0.87	0.88	0.92
MgO	6.19	6.46	6.43	5.92	6.28	5.66	5.88	5.81	6.30	6.27
CaO	11.10	11.38	11.52	10.82	11.04	10.77	10.44	10.21	10.27	10.29
Na_2O	2.05	1.95	2.00	1.95	2.03	2.13	1.93	1.99	2.00	2.04
K_2O	0.98	0.96	0.96	1.08	1.02	1.06	1.02	0.97	0.85	0.91
F	0.52	0.44	0.37	0.29	0.39	0.32	0.42	0.40	0.50	0.54
Cl	0.35	0.25	0.25	0.28	0.33	0.27	0.28	0.29	0.24	0.23
Total	99.17	98.89	98.08	97.84	97.84	96.82	98.03	96.89	96.97	97.79
O=F,Cl	0.30	0.24	0.21	0.18	0.24	0.19	0.24	0.23	0.27	0.28
Total	98.87	98.65	97.87	97.65	97.61	96.62	97.79	96.66	96.71	97.51
Based on 23 Oxygen										
Si	6.523	6.652	6.621	6.507	6.502	6.518	6.597	6.568	6.665	6.660
Al iv	1.477	1.348	1.379	1.493	1.498	1.482	1.403	1.432	1.324	1.340
Al vi	0.071	0.063	0.066	0.134	0.011	0.048	0.023	0.052	0.000	0.030
Ti	0.194	0.177	0.174	0.196	0.199	0.192	0.181	0.193	0.177	0.189
Fe^{3+}	0.534	0.377	0.307	0.551	0.566	0.517	0.749	0.752	0.767	0.710
Fe^{2+}	2.664	2.785	2.850	2.637	2.653	2.793	2.565	2.525	2.479	2.498
Mn	0.111	0.105	0.105	0.107	0.106	0.112	0.117	0.116	0.117	0.120
Mg	1.426	1.492	1.499	1.376	1.467	1.338	1.365	1.363	1.472	1.452
Ca	1.838	1.888	1.930	1.808	1.852	1.831	1.741	1.720	1.725	1.714
Na	0.614	0.586	0.607	0.588	0.617	0.656	0.583	0.607	0.607	0.614
K	0.194	0.190	0.192	0.214	0.204	0.214	0.203	0.195	0.169	0.179
Total	15.65	15.66	15.73	15.61	15.67	15.70	15.53	15.52	15.50	15.51
Mg#	0.35	0.35	0.34	0.34	0.36	0.32	0.35	0.35	0.37	0.37
Fe#	0.69	0.68	0.68	0.70	0.69	0.71	0.71	0.71	0.69	0.69
Al	1.55	1.41	1.44	1.63	1.51	1.53	1.43	1.48	1.32	1.37

Mg#=Mg/(Mg+Fe^{2+}); Fe#=Fetot/(Fetot+Mg); Altot= Al iv+ Al vi

Appendix table 3 Representative composition of feldspars from Qitianling pluton

	38C Pl	38C Pl	38C Pl	38C Pl	38C Pl	38C Pl	38C Pl	38C Pl	38C Pl	38C Pl
SiO_2	61.15	62.58	61.31	61.50	60.41	60.43	60.27	64.10	59.14	58.37
Al_2O_3	24.91	23.98	25.13	24.86	25.61	25.41	25.65	23.91	26.31	26.87
FeO	0.16	0.10	0.15	0.16	0.19	0.24	0.17	0.17	0.25	0.16
MnO	0.01	0.00	0.00	0.02	0.00	0.01	0.00	0.03	0.01	0.03
MgO	0.00	0.00	0.00	0.00	0.01	0.00	0.00	0.03	0.00	0.01
CaO	6.08	5.25	6.10	5.57	6.89	6.73	6.86	4.42	7.87	8.42
Na_2O	8.10	8.61	8.02	8.11	7.52	7.70	7.73	8.68	6.89	6.82
K_2O	0.38	0.51	0.33	0.27	0.44	0.43	0.39	0.37	0.45	0.27
Total	100.78	101.02	101.04	100.48	101.08	100.95	101.08	101.71	100.92	100.96
Cations per 16 oxygens										
Si	5.403	5.503	5.399	5.434	5.334	5.343	5.324	5.574	5.245	5.183
Al	2.595	2.486	2.608	2.589	2.665	2.649	2.671	2.451	2.750	2.812
Fe	0.012	0.007	0.011	0.012	0.014	0.018	0.013	0.012	0.018	0.012
Ca	0.575	0.494	0.576	0.527	0.652	0.637	0.649	0.412	0.747	0.801
Na	1.387	1.468	1.370	1.390	1.288	1.321	1.325	1.464	1.185	1.175
K	0.042	0.057	0.037	0.031	0.050	0.049	0.043	0.041	0.051	0.030
Total	10.014	10.016	10.000	9.982	10.003	10.017	10.025	9.954	9.997	10.013
Ca+Na+K	2.005	2.019	1.983	1.948	1.990	2.007	2.017	1.917	1.983	2.006
Ab	69	73	69	71	65	66	66	76	60	59
An	29	24	29	27	33	32	32	21	38	40

Or	2	3	2	2	3	2	2	2	3	2
	14	14	14	14	14	14	14	14	14	14
	Pl	Pl	Pl	Pl	Pl	Kfs	Kfs	Kfs	Kfs	Kfs
SiO_2	60.36	59.27	59.25	59.25	62.40	66.59	65.44	63.70	64.41	66.77
Al_2O_3	24.40	24.49	24.86	24.86	22.79	18.16	19.14	18.36	18.69	18.68
FeO	0.34	0.18	0.05	0.05	0.04	0.34	0.52	2.96	0.78	0.26
MnO	0.00	0.00	0.00	0.00	0.00	0.00	0.00	0.00	0.02	0.01
MgO	0.01	0.03	0.02	0.02	0.01	0.17	0.13	0.06	0.02	0.00
CaO	7.11	6.76	7.03	7.03	4.98	0.69	0.90	0.57	0.55	0.14
Na_2O	7.37	7.77	7.58	7.58	8.64	1.76	1.71	1.52	1.53	1.68
K_2O	0.31	0.26	0.31	0.31	0.43	12.65	13.41	13.15	12.99	14.75
Total										
Cations per 16 oxygens										
Si	5.392	5.360	5.338	5.338	5.574	6.051	5.938	5.898	5.961	6.003
Al	2.570	2.610	2.641	2.641	2.400	1.945	2.047	2.004	2.039	1.980
Fe	0.026	0.013	0.004	0.004	0.003	0.026	0.039	0.229	0.060	0.019
Ca	0.681	0.655	0.679	0.679	0.477	0.067	0.087	0.056	0.054	0.013
Na	1.276	1.362	1.323	1.323	1.496	0.309	0.302	0.273	0.274	0.292
K	0.035	0.030	0.035	0.035	0.049	1.466	1.552	1.553	1.534	1.692
Total	9.979	10.031	10.021	10.021	9.999	9.864	9.965	10.013	9.923	9.999
Ca+Na+K	1.992	2.047	2.038	2.038	2.022	1.843	1.941	1.882	1.862	1.998
Ab	64	67	65	65	55	17	16	15	15	15
An	34	32	33	33	43	4	4	3	3	1
Or	2	1	2	2	2	80	80	82	82	85
	13	13	13	13	13	13	13	13	13	13

	Pl	Pl	Pl	Pl	Pl	Pl	Pl	Pl	Kfs	Kfs
SiO_2	61.16	59.96	60.15	62.81	62.49	60.31	63.78	60.85	67.08	65.70
Al_2O_3	24.35	24.15	24.36	22.84	22.56	24.46	21.72	24.07	18.61	19.44
FeO	0.14	0.19	0.03	0.24	0.18	0.36	0.04	0.00	0.43	0.40
MnO	0.06	0.21	0.00	0.00	0.00	0.01	0.02	0.06	0.00	0.00
MgO	0.01	0.00	0.00	0.04	0.00	0.00	0.00	0.01	0.00	0.01
CaO	6.53	7.06	6.86	5.42	5.32	6.67	4.50	6.77	0.30	1.27
Na_2O	7.58	7.10	7.32	7.80	8.09	7.48	9.00	7.22	1.93	2.23
K_2O	0.37	0.41	0.31	0.42	0.54	0.24	0.58	0.41	13.44	11.67
Total										
Cations per 16 oxygens										
Si	5.434	5.406	5.406	5.588	5.589	5.399	5.672	5.446	6.024	5.936
Al	2.550	2.566	2.580	2.395	2.378	2.581	2.277	2.539	1.970	2.070
Fe	0.010	0.014	0.002	0.018	0.014	0.027	0.003	0.000	0.032	0.031
Ca	0.622	0.682	0.661	0.517	0.510	0.639	0.429	0.649	0.029	0.123
Na	1.306	1.241	1.276	1.345	1.403	1.299	1.553	1.254	0.336	0.390
K	0.042	0.047	0.035	0.047	0.061	0.027	0.066	0.047	1.540	1.345
Total	9.965	9.955	9.960	9.910	9.954	9.973	9.999	9.935	9.929	9.896
Ca+Na+K	1.970	1.969	1.972	1.909	1.974	1.966	2.047	1.950	1.904	1.859
Ab	66	63	65	70	71	66	76	64	18	21
An	32	35	34	27	26	33	21	33	2	7
Or	2	2	2	2	3	1	3	2	81	72

Appendix table 4 Representative composition of biotite from Qitianling, Jiuyishan, Guposhan and Huashan plutons

	Qitianling									
Sample	38C	38C	38C	38C	38C	14A	14A	14A	14A	14A
SiO_2	36.67	36.05	36.48	36.48	36.37	36.49	36.20	37.59	36.79	36.42
TiO_2	4.57	4.16	4.21	4.52	3.60	4.51	4.50	4.45	4.41	4.94
Al_2O_3	11.36	11.46	11.61	11.47	11.72	11.24	10.79	11.28	11.25	11.35
FeO	26.79	26.37	27.23	26.92	27.43	27.05	26.62	26.65	26.99	27.81
MnO	0.11	0.14	0.11	0.13	0.13	0.12	0.17	0.13	0.13	0.11
MgO	7.54	7.75	7.40	7.63	7.94	7.21	7.34	7.55	7.19	6.39
CaO	0.00	0.00	0.00	0.00	0.00	0.00	0.04	0.00	0.00	0.02
Na_2O	0.17	0.15	0.14	0.16	0.10	0.15	0.12	0.11	0.07	0.13
K_2O	9.21	9.28	9.09	9.38	9.43	9.06	8.88	8.85	8.75	8.69
F	0.21	0.20	0.19	0.19	0.19	0.45	0.45	0.41	0.39	0.52
Cl	0.61	0.59	0.44	0.57	0.28	0.62	0.57	0.54	0.47	0.27
O=F,Cl	0.22	0.22	0.18	0.21	0.14	0.33	0.32	0.29	0.27	0.28
Total	97.00	95.91	96.72	97.23	97.04	96.57	95.37	97.27	96.17	96.35
Based on 22 Oxygen										
Si	5.712	5.615	5.682	5.682	5.666	5.684	5.639	5.856	5.731	5.673
Al iv	2.086	2.129	2.140	2.105	2.159	2.067	2.008	2.046	2.071	2.090
Al vi	0.000	0.000	0.000	0.000	0.000	0.000	0.000	0.000	0.000	0.000
Ti	0.535	0.493	0.495	0.529	0.423	0.529	0.535	0.515	0.518	0.581
Fe^{2+}	3.490	3.477	3.563	3.507	3.586	3.530	3.514	3.429	3.526	3.635
Mn	0.015	0.018	0.015	0.018	0.017	0.016	0.023	0.017	0.017	0.014
Mg	1.751	1.822	1.725	1.771	1.850	1.678	1.727	1.732	1.675	1.488
Ca	0.000	0.000	0.000	0.000	0.001	0.000	0.007	0.000	0.000	0.003
Na	0.050	0.045	0.044	0.047	0.030	0.045	0.038	0.033	0.022	0.038
K	1.830	1.866	1.815	1.865	1.880	1.803	1.789	1.737	1.745	1.733
Cl	0.160	0.158	0.116	0.150	0.073	0.165	0.152	0.140	0.125	0.071
F	0.102	0.100	0.093	0.094	0.094	0.223	0.227	0.200	0.194	0.256
Total	15.47	15.47	15.48	15.52	15.61	15.35	15.28	15.37	15.31	15.26
Fe#	0.67	0.66	0.67	0.66	0.66	0.68	0.67	0.66	0.68	0.71

	Qitianling									
Sample	13	13	13	13	13	4	4	4	4	4
SiO_2	36.72	36.71	36.21	36.01	36.17	35.34	35.87	35.13	36.15	35.57
TiO_2	4.26	4.06	3.94	3.77	3.77	2.70	2.91	3.13	2.94	2.98
Al_2O_3	13.23	13.08	13.24	13.08	13.34	15.13	14.84	15.12	15.17	14.84
FeO	28.22	27.64	27.09	27.25	27.20	28.98	28.50	27.38	28.14	29.17
MnO	0.12	0.13	0.17	0.13	0.15	0.48	0.47	0.46	0.52	0.57

MgO	5.75	5.78	6.25	5.88	6.05	2.61	2.82	2.77	2.71	2.73
CaO	0.00	0.00	0.00	0.00	0.00	0.00	0.02	0.00	0.00	0.04
Na_2O	0.10	0.10	0.12	0.13	0.14	0.16	0.11	0.13	0.10	0.15
K_2O	8.81	8.89	8.89	8.84	8.68	8.89	9.32	9.44	9.06	8.70
F	0.46	0.52	0.43	0.46	0.37	0.84	0.99	1.20	0.66	0.68
Cl	0.80	0.74	1.31	1.10	1.17	0.31	0.36	0.35	0.30	0.30
O=F,Cl	0.37	0.39	0.47	0.44	0.42	0.42	0.50	0.58	0.34	0.35
Total	98.09	97.27	97.17	96.21	96.62	95.00	95.72	94.52	95.39	95.36
Based on 22 Oxygen										
Si	5.719	5.719	5.641	5.610	5.634	5.504	5.588	5.473	5.632	5.540
Al iv	2.281	2.281	2.359	2.390	2.366	2.496	2.412	2.527	2.368	2.460
Al vi	0.112	0.098	0.057	0.021	0.081	0.331	0.329	0.286	0.446	0.309
Ti	0.492	0.471	0.459	0.444	0.442	0.322	0.343	0.372	0.348	0.355
Fe^{2+}	3.622	3.568	3.506	3.565	3.541	3.843	3.737	3.614	3.705	3.863
Mn	0.016	0.017	0.022	0.017	0.019	0.064	0.062	0.061	0.069	0.077
Mg	1.316	1.329	1.442	1.372	1.404	0.617	0.660	0.652	0.635	0.644
Ca	0.000	0.000	0.000	0.001	0.000	0.000	0.004	0.000	0.000	0.006
Na	0.031	0.031	0.035	0.040	0.043	0.049	0.034	0.039	0.031	0.046
K	1.725	1.751	1.756	1.764	1.723	1.798	1.865	1.901	1.818	1.758
Cl	0.208	0.192	0.343	0.291	0.309	0.095	0.113	0.115	0.100	0.105
F	0.221	0.255	0.208	0.225	0.183	0.479	0.582	0.735	0.418	0.450
Total	15.31	15.27	15.28	15.22	15.25	15.02	15.03	14.92	15.05	15.06
Fe#	0.73	0.73	0.71	0.72	0.72	0.86	0.85	0.85	0.85	0.86

	Jiuyishan					Huashan				
Sample	162	162	162	162	162	176A	176A	176A	176A	176A
SiO_2	35.85	35.33	35.54	34.96	35.27	35.70	35.64	35.64	35.61	35.07
TiO_2	3.78	4.23	4.40	4.23	4.36	2.89	3.39	3.53	3.74	3.80
Al_2O_3	12.02	12.07	11.82	11.91	11.82	13.58	13.16	13.89	13.47	13.49
FeO	26.76	27.27	26.48	26.47	27.20	28.80	28.57	27.95	29.00	29.12
MnO	0.43	0.70	0.58	0.79	0.59	0.38	0.40	0.35	0.39	0.44
MgO	7.71	7.35	7.31	7.36	7.45	6.37	6.24	6.08	5.93	5.71
CaO	0.02	0.00	0.00	0.00	0.01	0.07	0.06	0.07	0.03	0.00
Na_2O	0.18	0.15	0.17	0.20	0.20	0.17	0.22	0.25	0.29	0.10
K_2O	7.68	7.58	7.69	7.73	7.39	8.79	8.73	8.79	8.64	8.99
F	1.30	1.04	1.34	0.81	1.06	0.55	0.73	0.51	0.87	0.86
Cl	0.12	0.09	0.07	0.10	0.13	0.17	0.16	0.18	0.22	0.19
O=F,Cl	0.58	0.46	0.58	0.37	0.48	0.27	0.34	0.26	0.42	0.41
Total	95.29	95.35	94.81	94.20	95.00	96.93	96.61	96.73	97.36	96.97
Based on 22 Oxygen										
Si	5.097	5.023	5.052	4.970	5.015	5.075	5.067	5.068	5.063	4.986
Al iv	2.192	2.219	2.165	2.223	2.177	2.490	2.412	2.544	2.445	2.469
Al vi	0.000	0.000	0.000	0.000	0.000	0.000	0.000	0.000	0.000	0.000

Ti	0.440	0.496	0.514	0.504	0.513	0.338	0.396	0.412	0.433	0.444
Fe^{2+}	3.462	3.556	3.443	3.506	3.556	3.748	3.715	3.632	3.734	3.781
Mn	0.056	0.092	0.076	0.106	0.078	0.050	0.052	0.046	0.050	0.058
Mg	1.777	1.708	1.694	1.739	1.735	1.478	1.446	1.408	1.362	1.322
Ca	0.003	0.000	0.000	0.000	0.001	0.012	0.011	0.011	0.005	0.000
Na	0.055	0.044	0.052	0.063	0.059	0.051	0.066	0.075	0.086	0.031
K	1.515	1.508	1.525	1.562	1.474	1.745	1.732	1.743	1.698	1.782
Cl	0.031	0.024	0.019	0.028	0.035	0.044	0.042	0.048	0.057	0.049
F	0.638	0.514	0.661	0.408	0.525	0.270	0.361	0.252	0.425	0.424
Total	14.60	14.65	14.52	14.67	14.61	14.99	14.90	14.94	14.88	14.87
Fe#	0.66	0.68	0.67	0.67	0.67	0.72	0.72	0.72	0.73	0.74
	Guposhan									
Sample	182	182	182	182	182	183	183	183	183	183
SiO_2	35.59	36.43	35.68	35.80	35.52	35.51	36.06	35.55	35.86	35.76
TiO_2	3.85	3.46	4.32	4.50	4.05	3.73	3.69	3.64	3.69	4.06
Al_2O_3	13.39	13.36	13.43	13.90	13.59	12.67	12.75	12.70	12.82	12.71
FeO	26.57	26.28	26.65	26.07	25.91	27.45	26.99	26.44	26.82	26.99
MnO	0.34	0.36	0.46	0.45	0.41	0.46	0.48	0.48	0.48	0.49
MgO	7.54	7.35	6.94	6.95	6.91	6.83	7.29	6.87	7.05	6.85
CaO	0.00	0.00	0.03	0.04	0.05	0.01	0.00	0.00	0.00	0.00
Na_2O	0.06	0.05	0.17	0.13	0.13	0.10	0.14	0.09	0.07	0.07
K_2O	9.07	8.70	8.45	8.35	8.49	9.02	9.23	9.05	9.12	9.05
F	0.64	0.59	0.66	0.51	0.51	0.48	0.56	0.42	0.43	0.54
Cl	0.17	0.15	0.17	0.14	0.13	0.12	0.13	0.13	0.11	0.14
O=F,Cl	0.31	0.28	0.31	0.25	0.24	0.23	0.26	0.20	0.21	0.26
Total	96.59	96.17	96.33	96.33	95.20	95.90	96.77	94.96	96.03	96.13
Based on 22 Oxygen										
Si	5.060	5.180	5.073	5.090	5.050	5.048	5.127	5.054	5.098	5.084
Al iv	2.438	2.430	2.444	2.525	2.502	2.345	2.329	2.367	2.363	2.337
Al vi	0.000	0.000	0.000	0.000	0.000	0.000	0.000	0.000	0.000	0.000
Ti	0.447	0.401	0.501	0.521	0.476	0.440	0.430	0.433	0.434	0.477
Fe^{2+}	3.433	3.392	3.442	3.362	3.386	3.607	3.498	3.498	3.510	3.523
Mn	0.044	0.048	0.061	0.059	0.054	0.061	0.062	0.064	0.064	0.064
Mg	1.736	1.692	1.599	1.597	1.609	1.600	1.683	1.620	1.643	1.594
Ca	0.000	0.000	0.005	0.006	0.008	0.001	0.000	0.001	0.000	0.000
Na	0.019	0.016	0.051	0.038	0.040	0.030	0.041	0.029	0.022	0.020
K	1.787	1.714	1.665	1.643	1.692	1.807	1.825	1.825	1.821	1.802
Cl	0.045	0.040	0.044	0.038	0.033	0.032	0.033	0.034	0.029	0.036
F	0.310	0.288	0.320	0.246	0.252	0.239	0.273	0.208	0.212	0.268
Total	14.96	14.87	14.84	14.84	14.82	14.94	15.00	14.89	14.95	14.90
Fe#	0.66	0.67	0.68	0.68	0.68	0.69	0.68	0.68	0.68	0.69

Fe#=Fetot/(Fetot+Mg)

Appendix table 5 Representative composition of titanite from Qitianling pluton

	Phase-1				Phase-2				Phase-3			
		n=29				n=25				n=14		
(wt.%)		Average	SD	Range		Average	SD	Range		Average	SD	Range
SiO_2	29.77	29.88	0.68	28.84-31.70	30.38	30.25	0.60	29.06-32.49	29.96	30.07	0.29	29.54-30.64
TiO_2	33.28	32.49	2.47	28.92-38.07	30.33	30.61	0.78	28.82-31.9	31.35	30.89	0.84	29.29-32.32
Al_2O_3	2.39	3.33	1.16	2.16-7.75	3.89	3.44	0.35	2.87-4.40	2.86	3.41	0.39	2.86-4.34
Fe_2O_3	2.06	2.12	0.67	0.68-3.18	1.52	2.39	0.35	1.52-2.98	2.21	2.41	0.52	1.81-3.38
MnO	0.02	0.12	0.09	0.00-0.31	0.00	0.08	0.09	0.00-0.28	0.00	0.06	0.06	0.00-0.16
MgO	0.02	0.03	0.03	0.00-0.11	0.18	0.13	0.05	0.07-0.25	0.09	0.10	0.03	0.04-0.15
CaO	26.64	27.44	1.38	25.52-30.33	27.05	27.26	0.32	26.49-27.8	26.92	27.29	0.31	26.7-27.86
Na_2O	0.02	0.03	0.03	0.00-0.10	0.04	0.05	0.03	0.00-0.12	0.07	0.04	0.03	0.00-0.09
K_2O	0.00	0.01	0.02	0.00-0.09	0.00	0.03	0.03	0.00-0.12	0.00	0.02	0.03	0.00-0.11
F	0.01	0.01	0.01	0.00-0.04	0.00	0.01	0.01	0.00-0.03	0.00	0.01	0.01	0.00-0.02
Cl	1.47	0.83	0.80	0.41-2.92	2.34	2.23	0.50	1.08-3.06	1.75	1.82	0.46	1.30-2.89
O=F,Cl	0.33	0.19			0.53	0.51			0.40	0.41		
Total	95.34	96.11			95.21	95.97			94.82	95.69		
Structural formula calculated based on Σ cations=3												
Si(apfu)	0.983	0.965			0.994	0.983			0.989	0.978		
Ti	0.827	0.789			0.746	0.748			0.779	0.756		
Al	0.093	0.126			0.150	0.132			0.111	0.131		
Fe^{3+}	0.051	0.052			0.037	0.059			0.055	0.059		
Mn	0.000	0.003			0.000	0.002			0.000	0.002		
Mg	0.001	0.001			0.006	0.005			0.003	0.003		
Ca	0.943	0.949			0.948	0.950			0.953	0.951		
Na	0.001	0.002			0.002	0.003			0.004	0.002		
K	0.000	0.001			0.000	0.001			0.000	0.001		
F	0.000	0.000			0.000	0.000			0.000	0.000		
Cl	0.041	0.023			0.066	0.063			0.049	0.051		

Appendix table 6 LA-ICP-MS U-Pb data for zircon from Qitianling pluton

No.	Compositions			Atomic rations							
	Th(ppm)	U(ppm)	Th/U	$^{207}Pb/^{235}U$	1σ	$^{206}Pb/^{238}U$	1σ	$t_{207/235}$ (Ma)	1σ	$t_{206/238}$ (Ma)	1σ
QTL04: Fine grained biotite granite (25 °32'36''N; 112 °55'22''E)											
qtl04-01	278	598	0.46	0.16594	0.00753	0.0244	0.00046	156	7	155	3
qtl04-02	341	573	0.60	0.16545	0.00582	0.02462	0.00041	155	5	157	3
qtl04-03	270	524	0.51	0.16819	0.01217	0.02463	0.00064	158	11	157	4
qtl04-04	266	442	0.60	0.17072	0.01211	0.02471	0.00064	160	11	157	4
qtl04-05	275	444	0.62	0.16655	0.00787	0.02408	0.00046	156	7	153	3
qtl04-06	311	549	0.57	0.16748	0.00808	0.02442	0.00049	157	7	156	3
qtl04-07	219	363	0.60	0.16673	0.01335	0.02459	0.0007	157	12	157	4
qtl04-08	355	637	0.56	0.16656	0.00542	0.02426	0.00039	156	5	155	2
qtl04-09	282	491	0.57	0.17104	0.00911	0.02483	0.00071	160	8	158	4
qtl04-10	263	442	0.60	0.16608	0.00694	0.02469	0.00066	156	6	157	4
qtl04-11	554	667	0.83	0.16506	0.00747	0.02495	0.00068	155	7	159	4
qtl04-12	386	659	0.59	0.16124	0.00644	0.02436	0.00065	152	6	155	4
qtl04-13	382	631	0.60	0.16323	0.00705	0.0244	0.00066	154	6	155	4
qtl04-14	194	288	0.67	0.16627	0.00825	0.02447	0.00069	156	7	156	4
qtl04-15	319	550	0.58	0.15979	0.0068	0.02447	0.00066	151	6	156	4
qtl04-16	359	705	0.51	0.16018	0.00687	0.02441	0.00066	151	6	155	4
QTL10: Fine grained biotite granite (25°39'49''N; 112 °54'46''E)											
qtl10-01	379	679	0.56	0.16635	0.00691	0.02465	0.00067	156	6	157	4
qtl10-02	303	607	0.50	0.15439	0.00918	0.02357	0.0007	146	8	150	4
qtl10-03	466	1921	0.24	0.17024	0.00846	0.02461	0.0007	160	7	157	4

qtl10-04	314	692	0.45	0.16697	0.00779	0.02297	0.00064	157	7	146	4
qtl10-05	300	533	0.56	0.16838	0.00714	0.02443	0.00066	158	6	156	4
qtl10-06	309	867	0.36	0.16454	0.00778	0.02419	0.00067	155	7	154	4
qtl10-07	264	419	0.63	0.16082	0.00913	0.02382	0.00069	151	8	152	4
qtl10-08	179	342	0.52	0.16736	0.01066	0.02407	0.00073	157	9	153	5
qtl10-09	332	616	0.54	0.1628	0.00638	0.02444	0.00064	153	6	156	4
qtl10-10	264	501	0.53	0.16781	0.00685	0.0248	0.00065	158	6	158	4
qtl10-11	294	400	0.74	0.16943	0.00936	0.02436	0.00071	159	8	155	4
qtl10-12	281	845	0.33	0.15388	0.00616	0.0229	0.00061	145	5	146	4
qtl10-13	227	390	0.58	0.16556	0.00778	0.02434	0.00067	156	7	155	4
qtl10-14	323	791	0.41	0.16015	0.00654	0.02279	0.00061	151	6	145	4
QTL21B: Coarse-medium grained biotite granite (25°27'09'N; 112 °47'59''E)											
qtl-21b-01	364	573	0.64	0.16616	0.00604	0.02474	0.00065	156	5	158	4
qtl-21b-02	358	607	0.59	0.17168	0.00641	0.02459	0.00065	161	6	157	4
qtl-21b-03	349	598	0.58	0.167	0.0063	0.02458	0.00065	157	5	157	4
qtl-21b-04	342	526	0.65	0.1649	0.00693	0.02471	0.00067	155	6	157	4
qtl-21b-05	281	722	0.39	0.16913	0.00591	0.02444	0.00064	159	5	156	4
qtl-21b-06	368	593	0.62	0.16731	0.00654	0.02441	0.00066	157	6	155	4
qtl-21b-07	330	541	0.61	0.17028	0.00661	0.02443	0.00066	160	6	156	4
qtl-21b-08	256	381	0.67	0.16463	0.007	0.02476	0.00067	155	6	158	4
qtl-21b-09	207	300	0.69	0.16705	0.00818	0.02464	0.00069	157	7	157	4
qtl-21b-10	359	537	0.67	0.16092	0.00925	0.02418	0.00071	152	8	154	4
qtl-21b-11	167	254	0.66	0.15935	0.01033	0.02432	0.00074	150	9	155	5
qtl-21b-12	217	509	0.43	0.15908	0.00657	0.02448	0.00065	150	6	156	4
qtl-21b-13	311	498	0.62	0.16717	0.00724	0.02393	0.00064	157	6	152	4
qtl-21b-14	259	413	0.63	0.15984	0.00757	0.02444	0.00067	151	7	156	4
QTL25: Medium grained biotite granite (25°27'27''N; 112 °51'20''E)											
qtl-25-01	237	420	0.57	0.02419	0.00063	0.00799	0.00083	153	6	154	4
qtl-25-02	299	495	0.61	0.0242	0.00064	0.00748	0.0008	153	6	154	4

qtl-25-03	314	525	0.60	0.02347	0.00062	0.00773	0.00084	152	6	150	4
qtl-25-04	147	218	0.67	0.02435	0.00067	0.00761	0.00086	159	8	155	4
qtl-25-05	415	670	0.62	0.02458	0.00064	0.00754	0.00097	156	6	157	4
qtl-25-06	275	457	0.60	0.02403	0.00066	0.00785	0.00106	159	7	153	4
qtl-25-07	350	567	0.62	0.02356	0.00063	0.00738	0.00102	156	7	150	4
qtl-25-08	317	572	0.55	0.02462	0.00064	0.00748	0.00077	161	6	157	4
qtl-25-09	246	429	0.57	0.02458	0.00069	0.00757	0.00084	160	8	157	4
qtl-25-10	189	359	0.52	0.02462	0.00068	0.0079	0.00088	158	7	157	4
qtl-25-11	317	505	0.63	0.02339	0.00062	0.00679	0.00076	150	6	149	4
qtl-25-12	203	323	0.63	0.02467	0.00072	0.00697	0.00086	158	8	157	5
qtl-25-13	212	551	0.39	0.02449	0.00065	0.00788	0.00099	159	6	156	4
qtl-25-14	330	534	0.62	0.02449	0.00065	0.00717	0.00095	160	6	156	4
qtl-25-15	222	327	0.68	0.02439	0.0007	0.00678	0.00095	157	8	155	4
SC1442: Coarse-medium grained amphibole biotite granite (25°34'46"N; 112 °46'33"E)											
sc42-01	237	401	0.59	0.17104	0.00708	0.02467	0.00065	160	6	157	4
sc42-02	258	432	0.60	0.16147	0.00698	0.02436	0.00065	152	6	155	4
sc42-03	205	315	0.65	0.15867	0.00722	0.02311	0.00062	150	6	147	4
sc42-04	483	643	0.75	0.15615	0.00628	0.02416	0.00064	147	6	154	4
sc42-05	352	492	0.72	0.15426	0.00745	0.02447	0.00067	146	7	156	4
sc42-06	261	461	0.57	0.16598	0.00696	0.02422	0.00065	156	6	154	4
sc42-07	349	575	0.61	0.16984	0.00686	0.02423	0.00064	159	6	154	4
sc42-08	364	586	0.62	0.16194	0.00666	0.02392	0.00064	152	6	152	4
sc42-09	321	536	0.60	0.17061	0.00683	0.02398	0.00064	160	6	153	4
sc42-10	312	516	0.60	0.16847	0.0069	0.02394	0.00064	158	6	153	4
sc42-11	239	487	0.49	0.1742	0.00661	0.02562	0.00068	163	6	163	4
sc42-12	347	566	0.61	0.163	0.00646	0.02388	0.00064	153	6	152	4
sc42-13	246	486	0.51	0.16212	0.00655	0.02454	0.00066	153	6	156	4
sc42-14	399	672	0.59	0.1691	0.0069	0.02452	0.00067	159	6	156	4
sc42-15	147	179	0.82	0.15981	0.00899	0.02448	0.00071	151	8	156	4

sc42-16	306	496	0.62	0.16773	0.00676	0.02495	0.00068	157	6	159	4
sc42-17	317	523	0.61	0.16506	0.00685	0.0248	0.00068	155	6	158	4
SC1445: Medium-fine grained biotite granite (25°34'36"N; 112°47'38"E)											
sc45-01	372	649	0.57	0.16016	0.00591	0.02426	0.00065	151	5	155	4
sc45-02	220	345	0.64	0.15844	0.00749	0.02434	0.00068	149	7	155	4
sc45-03	83	1178	0.07	0.16808	0.00654	0.02396	0.00065	158	6	153	4
sc45-04	304	478	0.64	0.16991	0.0087	0.02452	0.00071	159	8	156	4
sc45-05	381	618	0.62	0.16792	0.00643	0.02416	0.00065	158	6	154	4
sc45-06	269	437	0.62	0.16562	0.0069	0.02419	0.00066	156	6	154	4
sc45-07	249	418	0.60	0.17312	0.00707	0.02464	0.00067	162	6	157	4
sc45-08	194	361	0.54	0.1597	0.01121	0.02507	0.0008	150	10	160	5
sc45-09	568	572	0.99	0.15508	0.00742	0.02306	0.00065	146	7	147	4
sc45-10	209	489	0.43	0.16312	0.00649	0.02439	0.00065	153	6	155	4
sc45-11	334	476	0.70	0.16421	0.00664	0.02454	0.00066	154	6	156	4
sc45-12	248	420	0.59	0.1683	0.00702	0.02419	0.00066	158	6	154	4
sc45-13	411	714	0.58	0.15851	0.00678	0.02446	0.00066	149	6	156	4
sc45-14	290	540	0.54	0.16045	0.00638	0.02431	0.00065	151	6	155	4
sc45-15	294	508	0.58	0.16468	0.00779	0.02423	0.00068	155	7	154	4
sc45-16	171	344	0.50	0.15615	0.01377	0.02459	0.00068	147	12	157	4
sc45-17	358	549	0.65	0.15738	0.00793	0.02405	0.00068	148	7	153	4
sc45-18	305	479	0.64	0.17048	0.00698	0.02426	0.00066	160	6	155	4
SC1447: Medium grained biotite granite (25°33'31"N; 112°49'02"E)											
sc47-01	310	523	0.59	0.16609	0.00662	0.02461	0.00043	156	6	157	3
sc47-02	267	457	0.58	0.16631	0.00826	0.02398	0.00047	156	7	153	3
sc47-03	149	367	0.41	0.1687	0.00606	0.02451	0.0004	158	5	156	3
sc47-04	305	588	0.52	0.1676	0.00547	0.02401	0.00039	157	5	153	2
sc47-05	313	552	0.57	0.1667	0.0058	0.02432	0.0004	157	5	155	3
sc47-06	308	493	0.62	0.17049	0.00576	0.0242	0.0004	160	5	154	3
sc47-07	315	550	0.57	0.16675	0.00577	0.02434	0.0004	157	5	155	3

sc47-08	303	604	0.50	0.16749	0.00588	0.02433	0.00041	157	5	155	3
sc47-09	377	671	0.56	0.16736	0.00789	0.02433	0.00048	157	7	155	3
sc47-10	309	513	0.60	0.16703	0.00597	0.02425	0.00041	157	5	154	3
sc47-11	278	486	0.57	0.16741	0.00826	0.02412	0.00049	157	7	154	3
sc47-12	265	503	0.53	0.16758	0.00707	0.02435	0.00045	157	6	155	3
sc47-13	223	439	0.51	0.16049	0.00603	0.02435	0.00042	151	5	155	3
sc47-14	403	608	0.66	0.16302	0.00687	0.02412	0.00045	153	6	154	3
sc47-15	401	1296	0.31	0.16131	0.00536	0.02432	0.00041	152	5	155	3
sc47-16	296	476	0.62	0.16141	0.00761	0.02435	0.00048	152	7	155	3
sc47-17	504	697	0.72	0.16406	0.00884	0.0241	0.00052	154	8	154	3
sc47-18	295	530	0.56	0.16375	0.00664	0.02419	0.00044	154	6	154	3
sc47-19	184	402	0.46	0.1628	0.00687	0.02442	0.00045	153	6	156	3
sc47-20	284	484	0.59	0.1636	0.00718	0.02409	0.00046	154	6	153	3
SC1452: Coarse-medium grained amphibole biotite granite (25°31'46"N; 112°50'39"E)											
sc52-01	234	388	0.60	0.16438	0.00581	0.02471	0.00042	155	5	157	3
sc52-02	231	403	0.57	0.16576	0.00927	0.02514	0.00054	156	8	160	3
sc52-03	295	498	0.59	0.1676	0.00574	0.02451	0.00041	157	5	156	3
sc52-04	405	596	0.68	0.17284	0.00634	0.02472	0.00043	162	5	157	3
sc52-05	152	296	0.51	0.1686	0.00849	0.02502	0.0005	158	7	159	3
sc52-06	253	472	0.54	0.16888	0.0067	0.02501	0.00044	158	6	159	3
sc52-07	330	502	0.66	0.16821	0.00575	0.02492	0.00042	158	5	159	3
sc52-08	221	387	0.57	0.16991	0.00668	0.02481	0.00044	159	6	158	3
sc52-09	223	409	0.55	0.16762	0.00752	0.02522	0.00047	157	7	161	3
sc52-10	120	224	0.54	0.16922	0.0087	0.02458	0.0005	159	8	157	3
sc52-11	314	545	0.58	0.16844	0.00581	0.02475	0.00042	158	5	158	3
sc52-12	279	454	0.62	0.16735	0.00568	0.02422	0.0004	157	5	154	3
sc52-13	288	467	0.62	0.1678	0.00693	0.0248	0.00045	158	6	158	3
sc52-14	369	481	0.77	0.16685	0.01078	0.02457	0.0006	157	9	156	4
sc52-15	253	458	0.55	0.16616	0.00578	0.024	0.0004	156	5	153	3

sc52-16	270	510	0.53	0.16611	0.00636	0.02419	0.00042	156	6	154	3
sc52-17	228	467	0.49	0.16698	0.00664	0.02482	0.00044	157	6	158	3
sc52-18	344	706	0.49	0.16625	0.00585	0.02487	0.00042	156	5	158	3
sc52-19	226	375	0.60	0.16591	0.00966	0.02465	0.00056	156	8	157	4
SC1458: Coarse-medium grained amphibole biotite granite (25°34'59"N; 112 °50'14"E)											
sc58-01	290	552	0.53	0.16823	0.00618	0.02522	0.00046	158	5	161	3
sc58-02	257	441	0.58	0.16961	0.012	0.02572	0.00069	159	10	164	4
sc58-03	302	544	0.55	0.16654	0.00991	0.02492	0.00059	156	9	159	4
sc58-04	127	184	0.69	0.16627	0.00908	0.02484	0.00051	156	8	158	3
sc58-05	257	448	0.57	0.16561	0.00851	0.02481	0.00052	156	7	158	3
sc58-06	230	432	0.53	0.16527	0.00733	0.02408	0.00047	155	6	153	3
sc58-07	299	527	0.57	0.16788	0.0059	0.02547	0.00044	158	5	162	3
sc58-08	324	543	0.60	0.17002	0.00553	0.02519	0.00043	159	5	160	3
sc58-09	265	474	0.56	0.1674	0.0054	0.02455	0.00042	157	5	156	3
sc58-10	290	575	0.50	0.1677	0.00691	0.02466	0.00046	157	6	157	3
sc58-11	294	559	0.53	0.1738	0.00593	0.02495	0.00042	163	5	159	3
sc58-12	321	518	0.62	0.17242	0.01053	0.02503	0.00058	162	9	159	4
sc58-13	219	384	0.57	0.17038	0.00702	0.02454	0.00045	160	6	156	3
sc58-14	189	363	0.52	0.17225	0.00612	0.02395	0.00041	161	5	153	3
sc58-15	283	548	0.52	0.17103	0.00635	0.02421	0.00042	160	6	154	3
sc58-16	222	384	0.58	0.17047	0.00636	0.02441	0.00043	160	6	155	3
sc58-17	271	483	0.56	0.16216	0.0058	0.02393	0.00041	153	5	152	3
sc58-18	272	472	0.57	0.17246	0.00483	0.02474	0.0004	162	4	158	3
SC1461: Medium-fine grained biotite granite (25°30'30"N; 112 °50'42"E)											
sc61-01	190	270	0.70	0.17063	0.00817	0.02468	0.00049	160	7	157	3
sc61-02	301	543	0.55	0.17081	0.00529	0.02499	0.00041	160	5	159	3
sc61-03	491	804	0.61	0.15408	0.00396	0.02214	0.00034	146	3	141	2
sc61-04	386	871	0.44	0.15418	0.00399	0.02209	0.00034	146	4	141	2
sc61-05	294	475	0.62	0.17238	0.00707	0.02469	0.00045	161	6	157	3

sc61-06	272	630	0.43	0.17237	0.00672	0.02563	0.00048	161	6	163	3
sc61-07	189	395	0.48	0.16801	0.00806	0.02419	0.0005	158	7	154	3
sc61-08	220	326	0.67	0.17823	0.00699	0.02469	0.00044	167	6	157	3
sc61-09	295	492	0.60	0.1651	0.00948	0.02402	0.00053	155	8	153	3
sc61-10	115	167	0.69	0.1617	0.0098	0.02405	0.00051	152	9	153	3
sc61-11	675	1663	0.41	0.1667	0.00322	0.02279	0.00033	157	3	145	2
sc61-12	300	598	0.50	0.15841	0.00485	0.02295	0.00037	149	4	146	2
SC1462: Coarse-medium grained amphibole biotite granite (25°29'55"N; 112°51'21"E)											
sc62-01	438	813	0.54	0.16688	0.0046	0.02475	0.00039	157	4	158	2
sc62-02	267	571	0.47	0.1666	0.00567	0.02407	0.00041	156	5	153	3
sc62-03	226	412	0.55	0.17008	0.00544	0.02477	0.00042	159	5	158	3
sc62-04	321	571	0.56	0.16971	0.00743	0.02493	0.0005	159	6	159	3
sc62-05	309	559	0.55	0.17202	0.00809	0.02503	0.00052	161	7	159	3
sc62-06	217	485	0.45	0.1714	0.00592	0.02487	0.00043	161	5	158	3
sc62-07	374	692	0.54	0.17026	0.00838	0.02438	0.00052	160	7	155	3
sc62-08	325	542	0.60	0.17059	0.00741	0.02486	0.00049	160	6	158	3
sc62-09	283	539	0.53	0.16882	0.00842	0.02492	0.00052	158	7	159	3
sc62-10	360	600	0.60	0.16766	0.00503	0.02482	0.0004	157	4	158	3
sc62-11	277	448	0.62	0.1741	0.0064	0.025	0.00044	163	6	159	3
sc62-12	269	470	0.57	0.16763	0.00496	0.02457	0.0004	157	4	156	3
sc62-13	153	508	0.30	0.17208	0.01089	0.02511	0.00062	161	9	160	4
sc62-14	233	382	0.61	0.17432	0.00695	0.02524	0.00046	163	6	161	3
sc62-15	238	412	0.58	0.17821	0.00818	0.02533	0.0005	167	7	161	3
sc62-16	294	476	0.62	0.17642	0.00524	0.02542	0.00041	165	5	162	3
sc62-17	165	315	0.52	0.17162	0.0071	0.02488	0.00046	161	6	158	3
SC1474: Medium-fine grained biotite granite (25°29'54"N; 112°55'15"E)											
sc74-01	199	308	0.65	0.16695	0.00626	0.02491	0.00044	157	5	159	3
sc74-02	483	843	0.57	0.16847	0.00406	0.02492	0.00038	158	4	159	2
sc74-03	392	661	0.59	0.16943	0.00586	0.02534	0.00043	159	5	161	3

sc74-04	295	496	0.59	0.16724	0.00575	0.0251	0.00042	157	5	160	3
sc74-05	231	377	0.61	0.1682	0.00739	0.02513	0.00048	158	6	160	3
sc74-06	256	423	0.60	0.16748	0.0066	0.02519	0.00046	157	6	160	3
sc74-07	234	477	0.49	0.16561	0.00667	0.02459	0.00069	156	6	157	4
sc74-08	170	256	0.66	0.17352	0.0069	0.0247	0.00069	162	6	157	4
sc74-09	309	491	0.63	0.16332	0.0069	0.02352	0.0007	154	6	150	4
sc74-10	389	715	0.54	0.16537	0.00468	0.02469	0.00065	155	4	157	4
sc74-11	296	496	0.60	0.16717	0.00526	0.02426	0.00064	157	5	155	4
sc74-12	410	549	0.75	0.16436	0.01026	0.02417	0.00083	155	9	154	5
sc74-13	361	503	0.72	0.1662	0.00738	0.02419	0.0007	156	6	154	4
sc74-14	320	548	0.58	0.16637	0.00564	0.02418	0.00065	156	5	154	4
SC1475: Coarse grained biotite granite (25°29'17"N; 112 °55'12"E)											
sc75-01	399	715	0.56	0.16772	0.00598	0.02429	0.00067	157	5	155	4
sc75-02	324	562	0.58	0.16824	0.00788	0.02421	0.00068	158	7	154	4
sc75-03	478	725	0.66	0.15602	0.00572	0.02296	0.00061	147	5	146	4
sc75-04	250	448	0.56	0.16713	0.0083	0.02489	0.00075	157	7	158	5
sc75-05	268	433	0.62	0.16773	0.00868	0.02429	0.00071	157	8	155	4
sc75-06	314	478	0.66	0.16697	0.00614	0.02462	0.00067	157	5	157	4
sc75-07	249	437	0.57	0.16847	0.00643	0.02475	0.00068	158	6	158	4
sc75-08	309	514	0.60	0.16818	0.01001	0.02474	0.00074	158	9	158	5
sc75-09	402	570	0.71	0.1615	0.00616	0.0237	0.00063	152	5	151	4
sc75-10	332	833	0.40	0.16816	0.00722	0.0241	0.00068	158	6	154	4
sc75-11	704	724	0.97	0.16305	0.00712	0.02331	0.00064	153	6	149	4
sc75-12	218	381	0.57	0.16545	0.00735	0.0242	0.00066	155	6	154	4
sc75-13	258	430	0.60	0.1666	0.00643	0.02463	0.00066	156	6	157	4
sc75-14	242	404	0.60	0.16282	0.00723	0.02387	0.00066	153	6	152	4
sc75-15	262	428	0.61	0.16435	0.00776	0.02366	0.00066	155	7	151	4
sc75-16	157	266	0.59	0.16422	0.01221	0.02369	0.00078	154	11	151	5
SC1477: Coarse-medium grained biotite granite (25°28'11"N; 112 °55'48"E)											

sc77-01	239	398	0.60	0.1751	0.00814	0.02478	0.00068	164	7	158	4
sc77-02	303	528	0.57	0.17338	0.00687	0.02508	0.00066	162	6	160	4
sc77-03	356	544	0.66	0.17879	0.00801	0.02436	0.00067	167	7	155	4
sc77-04	290	499	0.58	0.17577	0.00904	0.02406	0.00069	164	8	153	4
sc77-05	266	440	0.60	0.1688	0.00777	0.02485	0.00068	158	7	158	4
sc77-06	198	364	0.55	0.16615	0.00697	0.02424	0.00065	156	6	154	4
sc77-07	291	488	0.60	0.16673	0.00706	0.02448	0.00066	157	6	156	4
sc77-08	388	563	0.69	0.17178	0.00675	0.02484	0.00066	161	6	158	4
sc77-09	307	398	0.77	0.16359	0.00868	0.02381	0.00068	154	8	152	4
sc77-10	230	419	0.55	0.17382	0.00718	0.02486	0.00067	163	6	158	4
sc77-11	292	622	0.47	0.16588	0.00653	0.02449	0.00065	156	6	156	4
sc77-12	195	371	0.52	0.1659	0.00846	0.02427	0.00071	156	7	155	4
sc77-13	295	474	0.62	0.16642	0.00736	0.02465	0.00067	156	6	157	4
sc77-14	163	326	0.50	0.16811	0.00772	0.02452	0.00069	158	7	156	4
sc77-15	378	765	0.49	0.15903	0.00615	0.02316	0.00063	150	5	148	4
sc77-16	408	736	0.55	0.16783	0.00731	0.02424	0.0007	158	6	154	4
sc77-17	352	597	0.59	0.16738	0.00817	0.02398	0.00067	157	7	153	4
sc77-18	282	492	0.57	0.16653	0.0082	0.02451	0.00068	156	7	156	4
sc77-19	309	512	0.60	0.16839	0.00924	0.02364	0.00069	158	8	151	4
sc77-20	234	393	0.60	0.16803	0.00832	0.02417	0.00068	158	7	154	4
sc77-21	262	398	0.66	0.16838	0.00738	0.02427	0.00067	158	6	155	4
sc77-22	305	501	0.61	0.16637	0.00679	0.02313	0.00062	156	6	147	4
SC1479: Fine grained biotite granite (25°27'12"N; 112 °56'31"E)											
sc79-01	296	547	0.54	0.16987	0.00886	0.02462	0.00075	159	8	157	5
sc79-02	323	341	0.95	0.17163	0.00969	0.02473	0.00073	161	8	157	5
sc79-03	337	517	0.65	0.16878	0.00779	0.02434	0.00067	158	7	155	4
sc79-04	347	671	0.52	0.17133	0.00682	0.0246	0.00066	161	6	157	4
sc79-05	386	662	0.58	0.17292	0.00685	0.02481	0.00065	162	6	158	4
sc79-06	232	411	0.57	0.17582	0.00744	0.02439	0.00066	164	6	155	4

sc79-07	388	670	0.58	0.16679	0.00596	0.02448	0.00065	157	5	156	4
sc79-08	434	764	0.57	0.17716	0.00689	0.02447	0.00064	166	6	156	4
sc79-09	374	566	0.66	0.16913	0.00884	0.02489	0.00074	159	8	158	5
sc79-10	357	599	0.60	0.16351	0.00629	0.02394	0.00063	154	5	153	4
sc79-11	295	515	0.57	0.16774	0.0084	0.02459	0.00071	157	7	157	4
sc79-12	320	555	0.58	0.16397	0.00682	0.02427	0.00065	154	6	155	4
sc79-13	441	824	0.54	0.16302	0.00571	0.02421	0.00063	153	5	154	4
sc79-14	252	449	0.56	0.16457	0.00854	0.02425	0.00069	155	7	154	4
sc79-15	334	548	0.61	0.16518	0.00795	0.02422	0.00067	155	7	154	4
sc79-16	378	613	0.62	0.16695	0.00691	0.02429	0.00065	157	6	155	4
sc79-17	321	547	0.59	0.16736	0.00637	0.0248	0.00066	157	6	158	4
SC14139: Medium-fine grained biotite granite (25°26'57"N; 112°56'35"E)											
sc139-01	348	455	0.77	0.17037	0.0081	0.02504	0.0007	160	7	159	4
sc139-02	323	534	0.60	0.16919	0.00723	0.02443	0.00068	159	6	156	4
sc139-03	280	461	0.61	0.1709	0.00711	0.02445	0.00067	160	6	156	4
sc139-04	297	498	0.60	0.16949	0.00693	0.02437	0.00066	159	6	155	4
sc139-05	265	449	0.59	0.16411	0.00821	0.02397	0.00068	154	7	153	4
sc139-06	502	1100	0.46	0.16761	0.00614	0.02412	0.00064	157	5	154	4
sc139-07	599	721	0.83	0.15945	0.00924	0.02353	0.0007	150	8	150	4
sc139-08	456	697	0.65	0.16779	0.00636	0.02406	0.00065	157	6	153	4
sc139-09	350	422	0.83	0.16764	0.00787	0.02451	0.0007	157	7	156	4
sc139-10	385	613	0.63	0.16242	0.00723	0.02453	0.00067	153	6	156	4
sc139-11	415	523	0.79	0.16855	0.00676	0.02443	0.00068	158	6	156	4
sc139-12	438	664	0.66	0.17059	0.0062	0.02521	0.00068	160	5	160	4
sc139-13	245	430	0.57	0.17042	0.00817	0.02497	0.0007	160	7	159	4
sc139-14	238	383	0.62	0.17026	0.00724	0.0247	0.00068	160	6	157	4
sc139-15	268	469	0.57	0.17368	0.00689	0.02539	0.00069	163	6	162	4
sc139-16	375	516	0.73	0.17092	0.00706	0.02465	0.00067	160	6	157	4
sc139-17	180	270	0.67	0.16839	0.01047	0.02491	0.00078	158	9	159	5

sc139-18	309	456	0.68	0.17412	0.00688	0.02495	0.00068	163	6	159	4
sc139-19	294	517	0.57	0.16564	0.00971	0.02379	0.00077	156	8	152	5
sc139-20	253	429	0.59	0.17338	0.00827	0.02543	0.00071	162	7	162	4
sc139-21	496	880	0.56	0.16479	0.01167	0.02381	0.0008	155	10	152	5
SC14141: Medium-fine grained biotite granite (25°29'54"N; 112 °54'26"E)											
sc141-01	335	568	0.59	0.17277	0.0068	0.02542	0.00069	162	6	162	4
sc141-02	393	683	0.58	0.16302	0.00731	0.0239	0.00068	153	6	152	4
sc141-03	294	410	0.72	0.17486	0.00868	0.02522	0.00071	164	8	161	4
sc141-04	228	411	0.55	0.17578	0.00772	0.02541	0.00071	164	7	162	4
sc141-05	271	451	0.60	0.1761	0.00764	0.02503	0.00069	165	7	159	4
sc141-06	331	533	0.62	0.17196	0.00814	0.02515	0.00071	161	7	160	4
sc141-07	207	347	0.60	0.16184	0.00824	0.02412	0.00069	152	7	154	4
sc141-08	341	548	0.62	0.173	0.00718	0.02524	0.00072	162	6	161	5
sc141-09	266	456	0.58	0.17206	0.00796	0.02549	0.00074	161	7	162	5
sc141-10	198	300	0.66	0.17288	0.00848	0.02565	0.00074	162	7	163	5
sc141-11	381	575	0.66	0.16895	0.00783	0.0247	0.00073	159	7	157	5
sc141-12	291	512	0.57	0.16958	0.00891	0.02515	0.00077	159	8	160	5
sc141-13	337	537	0.63	0.17256	0.00754	0.02525	0.00073	162	7	161	5
sc141-14	237	394	0.60	0.17468	0.01006	0.02555	0.00076	163	9	163	5
sc141-15	342	561	0.61	0.16939	0.00666	0.02491	0.00069	159	6	159	4
sc141-16	349	600	0.58	0.16817	0.00708	0.02465	0.00068	158	6	157	4
sc141-17	148	223	0.67	0.17061	0.01192	0.02496	0.00079	160	10	159	5
sc141-18	217	380	0.57	0.16765	0.00804	0.02468	0.0007	157	7	157	4
sc141-19	317	497	0.64	0.17441	0.00738	0.02519	0.00068	163	6	160	4
sc141-20	175	315	0.55	0.16757	0.00819	0.02511	0.00071	157	7	160	4
SC14142: Medium-fine grained biotite granite (25°29'54"N; 112 °53'58"E)											
sc142-01	184	250	0.73	0.17143	0.00836	0.02489	0.00075	161	7	158	5
sc142-02	265	451	0.59	0.17168	0.00754	0.02514	0.00074	161	7	160	5
sc142-03	325	537	0.61	0.17152	0.00679	0.02529	0.0007	161	6	161	4

sc142-04	193	322	0.60	0.17056	0.00885	0.02515	0.00078	160	8	160	5
sc142-05	338	613	0.55	0.17147	0.01222	0.02509	0.00089	161	11	160	6
sc142-06	333	583	0.57	0.17081	0.00523	0.02478	0.00068	160	5	158	4
sc142-07	257	429	0.60	0.17198	0.00725	0.0253	0.00075	161	6	161	5
sc142-08	256	441	0.58	0.17088	0.00562	0.02492	0.00069	160	5	159	4
sc142-09	153	141	1.08	0.16993	0.01178	0.02524	0.00082	159	10	161	5
sc142-10	290	496	0.59	0.16917	0.0099	0.02493	0.00082	159	9	159	5
sc142-11	275	471	0.58	0.17933	0.00641	0.02599	0.00072	167	6	165	5
sc142-12	196	350	0.56	0.17811	0.00698	0.02564	0.00074	166	6	163	5
sc142-13	312	563	0.55	0.17129	0.00564	0.0261	0.00074	161	5	166	5
sc142-14	227	372	0.61	0.17644	0.00627	0.02659	0.00075	165	5	169	5
sc142-15	200	294	0.68	0.17971	0.00843	0.02592	0.00078	168	7	165	5
sc142-16	272	429	0.63	0.17654	0.00628	0.02548	0.00072	165	5	162	5
sc142-17	110	181	0.61	0.17	0.00908	0.02534	0.00076	159	8	161	5
sc142-18	147	220	0.67	0.17603	0.00809	0.02597	0.00077	165	7	165	5
sc142-19	258	416	0.62	0.16996	0.00736	0.02565	0.00073	159	6	163	5
sc142-20	235	413	0.57	0.1693	0.00618	0.02537	0.0007	159	5	162	4
sc142-21	510	925	0.55	0.17161	0.00499	0.02568	0.00069	161	4	163	4

Appendix table 7 The Ar-Ar dating data of amphibole and biotite from Qitianling pluton

Step #	$^{39}Ar_K$ (V)	$^{36}Ar_{atm}/^{39}Ar_K$ (±1σ)			$^{37}Ar_{Ca}/^{39}Ar_K$			$^{38}Ar_{Cl}/^{39}Ar_K$			%$^{40}Ar^*$	$^{40}Ar^*/^{39}Ar_K$ (±1σ)					
N82.MS3		J = .2740E-02 ± .2407E-04															
# 1	6.70E-07	1.51E+01	±	1.48E+00	8.71E+00	±	2.27E+01	-1.27E-01	±	6.72E-02	-1.3	-55.27	±	35.91	-296.3	±	209.2
# 2	9.39E-08	6.02E-01	±	5.59E-01	5.36E-01	±	1.64E+02	-6.07E-01	±	5.12E-01	29.7	75.30	±	131.70	338.4	±	539.6
# 3	1.09E-06	1.25E-01	±	3.59E-02	-1.39E-01	±	1.33E+01	-2.84E-02	±	3.11E-02	32.1	17.43	±	10.90	84.2	±	51.4
# 4	9.81E-07	3.51E-02	±	3.81E-02	-4.62E+00	±	1.57E+01	-2.41E-02	±	3.04E-02	65.5	19.70	±	11.90	94.9	±	55.8
# 5	1.02E-06	-6.23E-02	±	3.88E-02	-5.38E+00	±	1.50E+01	-4.21E-02	±	3.07E-02	210.3	35.10	±	12.22	165.7	±	55.1
# 6	9.33E-07	1.37E-02	±	4.10E-02	1.06E+01	±	1.62E+01	-2.01E-02	±	3.24E-02	80.8	17.06	±	12.81	82.4	±	60.5
# 7	1.79E-06	8.50E-02	±	2.18E-02	-4.27E+00	±	8.93E+00	3.64E-03	±	1.92E-02	57.1	33.45	±	6.83	158.2	±	30.9
# 8	4.41E-06	1.92E-02	±	8.76E-03	5.81E+00	±	4.04E+00	8.36E-03	±	7.74E-03	81.4	24.83	±	2.83	118.8	±	13.1
# 9	3.61E-06	9.99E-03	±	1.07E-02	8.63E+00	±	4.81E+00	2.40E-02	±	8.80E-03	90.4	27.69	±	3.45	131.9	±	15.9
# 10	1.06E-04	3.55E-03	±	3.69E-04	4.31E+00	±	1.69E-01	1.79E-02	±	6.06E-04	96.8	32.05	±	0.19	151.9	±	0.9
# 11	1.06E-05	1.01E-02	±	3.70E-03	3.40E+00	±	1.59E+00	1.94E-02	±	3.65E-03	90.8	29.32	±	1.21	139.4	±	5.5
# 12	6.21E-05	5.86E-03	±	6.46E-04	3.68E+00	±	2.86E-01	1.55E-02	±	9.91E-04	94.8	31.79	±	0.22	150.7	±	1.0
# 13	1.74E-05	6.79E-03	±	2.20E-03	3.82E+00	±	9.43E-01	1.70E-02	±	2.20E-03	93.8	30.08	±	0.75	142.9	±	3.4
# 14	5.64E-05	2.13E-03	±	6.51E-04	3.24E+00	±	3.22E-01	1.34E-02	±	7.87E-04	98.1	31.94	±	0.25	151.4	±	1.1
# 15	1.86E-05	9.09E-03	±	2.10E-03	3.20E+00	±	8.26E-01	1.18E-02	±	2.15E-03	91.8	29.99	±	0.70	142.5	±	3.2
# 16	8.36E-06	2.29E-02	±	5.08E-03	5.65E+00	±	1.92E+00	1.72E-02	±	4.46E-03	80.6	28.05	±	1.63	133.6	±	7.5
# 17	1.12E-04	1.01E-02	±	3.71E-04	3.24E+00	±	1.74E-01	1.25E-02	±	4.42E-04	90.8	29.33	±	0.17	139.5	±	0.8
# 18	3.97E-06	1.50E-01	±	1.06E-02	5.77E+00	±	3.77E+00	7.51E-03	±	8.25E-03	30.6	19.56	±	3.19	94.2	±	15.0
# 19	1.04E-05	1.02E-02	±	3.73E-03	3.24E+00	±	1.53E+00	9.67E-03	±	3.55E-03	87.7	21.50	±	1.19	103.3	±	5.6
Total	4.20E-04	3.30E-02	±	4.40E-04	3.69E+00	±	1.70E-01	1.40E-02	±	4.18E-04	75.6	30.24	±	0.15	143.6	±	1.4
N83.MS3		J = .2740E-02 ± .2407E-04															
# 1	2.13E-06	1.66E+01	±	8.88E-01	1.07E+01	±	6.90E+00	1.28E-03	±	5.57E-02	-1.8	-87.45	±	21.58	-494.3	±	140.3

# 2	1.12E-07	3.40E+01	±	2.61E+01	9.69E+01	±	1.58E+02	-6.40E-01	±	7.03E-01	0.4	40.41	±	197.50	189.5	±	879.0
# 3	2.82E-07	2.06E+00	±	6.58E-01	-2.33E+01	±	5.64E+01	-2.24E-01	±	1.65E-01	7.1	46.37	±	73.60	215.8	±	322.8
# 4	2.06E-06	1.42E+00	±	8.11E-02	1.44E+01	±	8.35E+00	-5.43E-02	±	2.30E-02	-0.8	-3.41	±	10.46	-17.0	±	52.2
# 5	1.22E-06	4.10E-01	±	5.87E-02	1.30E+01	±	1.34E+01	-2.53E-02	±	3.75E-02	1.5	1.79	±	16.78	8.8	±	82.6
# 6	1.07E-06	3.78E-01	±	6.54E-02	-9.48E+00	±	1.44E+01	-5.31E-02	±	4.05E-02	-6.3	-6.58	±	18.95	-32.9	±	95.4
# 7	1.93E-06	3.47E-01	±	3.64E-02	7.57E+00	±	8.04E+00	1.54E-02	±	2.30E-02	13.5	15.96	±	10.62	77.2	±	50.3
# 8	7.40E-06	1.02E-01	±	8.73E-03	6.56E+00	±	2.15E+00	2.22E-02	±	6.98E-03	50.4	30.48	±	2.86	144.7	±	13.0
# 9	1.45E-05	4.24E-02	±	4.28E-03	6.88E+00	±	1.06E+00	2.93E-02	±	3.12E-03	70.6	29.98	±	1.45	142.4	±	6.6
# 10	4.66E-05	3.10E-02	±	1.37E-03	4.68E+00	±	4.02E-01	3.10E-02	±	1.80E-03	77.2	30.98	±	0.49	147.0	±	2.2
# 11	2.44E-04	6.17E-03	±	2.66E-04	4.03E+00	±	9.05E-02	2.39E-02	±	5.61E-04	94.6	32.12	±	0.15	152.2	±	0.7
# 12	4.98E-05	1.53E-02	±	1.28E-03	4.43E+00	±	3.14E-01	1.73E-02	±	1.08E-03	87.2	30.77	±	0.44	146.1	±	2.0
# 13	1.70E-05	1.81E-02	±	3.58E-03	4.67E+00	±	9.47E-01	1.75E-02	±	3.79E-03	83.7	27.43	±	1.21	130.8	±	5.5
# 14	3.05E-05	3.04E-02	±	2.12E-03	6.80E+00	±	5.20E-01	2.36E-02	±	1.73E-03	75.1	27.02	±	0.71	128.9	±	3.3
# 15	2.17E-05	2.22E-02	±	2.84E-03	5.85E+00	±	7.89E-01	2.18E-02	±	2.87E-03	79.1	24.81	±	0.95	118.7	±	4.4
# 16	1.81E-05	3.80E-01	±	4.02E-03	5.02E+00	±	9.64E-01	1.45E-02	±	2.28E-03	16.8	22.59	±	0.85	108.4	±	4.0
# 17	1.25E-05	1.08E-01	±	2.68E-03	4.86E+00	±	1.38E+00	1.71E-02	±	3.15E-03	42.8	23.88	±	0.85	114.3	±	4.0
# 18	3.36E-05	1.80E-02	±	9.45E-04	5.59E+00	±	5.79E-01	2.33E-02	±	2.19E-03	85.0	30.08	±	0.36	142.9	±	1.7
# 19	4.15E-05	1.34E-02	±	7.69E-04	6.34E+00	±	4.98E-01	1.69E-02	±	1.19E-03	88.5	30.47	±	2.60	144.7	±	11.9
# 20	6.43E-05	1.61E-02	±	4.54E-04	7.89E+00	±	2.80E-01	2.02E-02	±	6.45E-04	85.5	28.04	±	0.21	133.5	±	1.0
# 21	1.86E-05	4.53E-02	±	2.13E-03	4.64E+00	±	8.40E-01	1.29E-02	±	1.90E-03	32.8	6.53	±	0.68	32.0	±	3.3
# 22	1.85E-05	6.91E-02	±	1.78E-03	2.30E+00	±	8.41E-01	4.22E-03	±	2.09E-03	20.4	5.22	±	0.57	25.6	±	2.8
# 23	4.68E-07	1.59E-01	±	6.63E-02	3.49E-01	±	3.30E+01	-5.21E-02	±	6.62E-02	14.8	8.17	±	20.81	40.0	±	100.6
Total	6.48E-04	9.80E-02	±	4.77E-04	5.09E+00	±	1.25E-01	2.08E-02	±	4.57E-04	49.2	28.03	±	0.23	133.5	±	1.5

N84.MS3		J = .2741E-02 ± .2408E-04														
# 1	3.24E-06	2.03E+00	±	1.82E-01	-1.03E+00	±	2.81E+00	-1.17E-02	±	1.48E-02	-1.4	-8.48	±	7.59	-42.4	±	38.4
# 2	4.30E-06	3.31E-01	±	2.60E-02	3.80E-01	±	2.51E+00	1.51E-02	±	1.30E-02	-7.1	-6.53	±	5.02	-32.6	±	25.3
# 3	7.29E-06	9.11E-02	±	9.31E-03	2.91E-01	±	1.27E+00	9.33E-03	±	5.21E-03	40.6	18.37	±	3.07	88.6	±	14.4
# 4	2.87E-06	5.84E-03	±	2.20E-02	1.71E+00	±	3.64E+00	2.19E-02	±	1.46E-02	96.6	48.40	±	9.13	224.7	±	39.9

# 5	2.60E-06	2.71E-02	±	2.37E-02	2.61E+00	±	3.26E+00	2.24E-02	±	1.60E-02	83.6	40.88	±	9.34	191.6	±	41.5
# 6	5.16E-06	7.99E-03	±	1.22E-02	3.60E+00	±	1.83E+00	2.34E-02	±	7.24E-03	95.1	46.18	±	4.96	215.0	±	21.8
# 7	1.60E-05	1.62E-02	±	4.10E-03	4.10E+00	±	9.01E-01	2.85E-02	±	3.03E-03	88.2	35.71	±	1.39	168.5	±	6.3
# 8	3.90E-05	7.95E-03	±	1.74E-03	5.22E+00	±	4.15E-01	3.11E-02	±	1.84E-03	93.4	33.31	±	0.59	157.6	±	2.7
# 9	1.07E-04	6.10E-03	±	6.25E-04	4.61E+00	±	2.30E-01	3.00E-02	±	8.02E-04	94.7	32.45	±	0.23	153.7	±	1.0
# 10	3.53E-04	3.50E-03	±	2.05E-04	4.50E+00	±	7.02E-02	3.01E-02	±	3.15E-04	96.9	32.34	±	0.13	153.2	±	0.6
# 11	6.47E-05	2.98E-03	±	1.02E-03	4.55E+00	±	2.70E-01	2.90E-02	±	1.05E-03	97.3	31.76	±	0.39	150.6	±	1.8
# 12	2.40E-05	9.80E-05	±	2.73E-03	4.44E+00	±	6.65E-01	2.87E-02	±	3.24E-03	99.9	32.52	±	0.93	154.1	±	4.2
# 13	9.29E-06	3.74E-04	±	7.00E-03	1.42E+00	±	1.72E+00	3.77E-02	±	5.69E-03	99.7	32.22	±	2.31	152.7	±	10.5
# 14	7.75E-05	6.82E-04	±	6.30E-04	5.20E+00	±	2.85E-01	2.90E-02	±	6.47E-04	99.4	32.48	±	0.28	153.8	±	1.3
# 15	1.22E-05	-8.32E-04	±	4.01E-03	5.61E+00	±	1.43E+00	2.64E-02	±	3.48E-03	100.8	32.80	±	1.58	155.3	±	7.2
# 16	6.17E-06	-1.24E-04	±	7.97E-03	9.62E+00	±	3.05E+00	2.53E-02	±	5.84E-03	100.1	34.95	±	3.07	165.0	±	13.9
# 17	3.25E-06	9.14E-03	±	1.52E-02	1.52E+00	±	5.62E+00	1.59E-02	±	1.13E-02	91.7	29.73	±	5.78	141.3	±	26.4
# 18	1.16E-06	-2.09E-02	±	4.33E-02	-8.62E-01	±	1.55E+01	5.00E-03	±	2.99E-02	130.2	26.60	±	16.26	127.0	±	75.0
# 19	4.97E-07	4.08E-02	±	1.03E-01	-4.27E+00	±	3.64E+01	-2.42E-02	±	6.54E-02	-199.1	-8.03	±	38.17	-40.1	±	193.0
# 20	3.11E-05	1.11E-02	±	1.57E-03	5.41E+00	±	5.66E-01	2.93E-02	±	1.31E-03	89.6	28.17	±	0.64	134.2	±	2.9
# 21	1.41E-05	1.88E-02	±	3.74E-03	1.08E+00	±	1.30E+00	1.40E-03	±	2.78E-03	54.3	6.59	±	1.37	32.3	±	6.7
# 22	9.00E-07	3.15E-02	±	5.40E-02	1.74E+01	±	1.94E+01	3.22E-02	±	3.66E-02	81.1	39.87	±	20.82	187.1	±	92.8
Total	7.85E-04	1.55E-02	±	3.58E-04	4.49E+00	±	9.98E-02	2.86E-02	±	3.27E-04	87.3	31.48	±	0.14	149.3	±	1.4
N85.MS3		J = .2740E-02 ± .2406E-04															
# 1	2.22E-06	8.61E-01	±	7.20E-02	2.42E+01	±	6.93E+00	4.27E-03	±	4.01E-02	-7.1	-16.77	±	28.23	-84.9	±	146.3
# 2	7.28E-07	7.42E+00	±	6.54E-01	1.47E+01	±	1.99E+01	-2.53E-05	±	1.39E-01	-4.6	-96.51	±	85.74	-554.1	±	576.2
# 3	1.08E-06	7.49E+00	±	5.13E-01	1.97E+01	±	1.26E+01	-8.41E-02	±	9.17E-02	-4.1	-86.92	±	58.64	-490.7	±	380.5
# 4	1.20E-06	3.60E+00	±	2.15E-01	2.50E+01	±	1.21E+01	-1.05E-01	±	7.83E-02	-3.3	-34.17	±	52.35	-177.3	±	285.5
# 5	6.99E-07	3.02E+00	±	3.19E-01	1.39E+01	±	2.03E+01	1.06E-01	±	1.33E-01	-0.6	-4.96	±	89.01	-24.7	±	446.0
# 6	9.97E-07	1.04E+01	±	7.30E-01	5.72E+01	±	1.58E+01	-3.56E-02	±	1.04E-01	-5.9	#####	±	65.99	#####	±	614.3
# 7	3.32E-06	1.90E+00	±	7.04E-02	2.35E+02	±	8.62E+00	5.12E-04	±	2.85E-02	-29.0	#####	±	19.72	-765.3	±	149.0
# 8	2.76E-06	1.21E+00	±	4.99E-02	1.42E+02	±	7.30E+00	-4.90E-02	±	2.22E-02	-1.6	-5.60	±	7.50	-27.9	±	37.6

# 9	2.47E-06	5.22E-01	±	3.24E-02	4.50E+01	±	5.28E+00	-3.23E-02	±	2.11E-02	2.8	4.50	±	8.37	22.1	± 40.9
# 10	2.41E-06	3.81E-01	±	3.18E-02	3.89E+01	±	6.41E+00	4.52E-03	±	2.39E-02	7.8	9.45	±	8.35	46.1	± 40.2
# 11	7.36E-07	2.84E-01	±	9.64E-02	3.45E+01	±	1.65E+01	-1.41E-02	±	8.33E-02	-22.0	-15.13	±	27.30	-76.4	± 140.8
# 12	1.23E-06	2.21E-01	±	5.91E-02	-2.05E+00	±	9.76E+00	-1.46E-02	±	4.37E-02	-6.4	-3.94	±	17.04	-19.6	± 85.2
# 13	1.76E-06	2.09E-01	±	3.99E-02	1.30E+01	±	7.52E+00	-1.01E-02	±	3.37E-02	15.4	11.20	±	11.68	54.5	± 56.0
# 14	1.94E-06	1.09E-01	±	3.43E-02	4.34E-01	±	6.60E+00	-3.97E-04	±	2.78E-02	32.3	15.40	±	10.31	74.5	± 48.9
# 15	2.94E-06	1.44E-01	±	2.35E-02	4.70E-01	±	4.12E+00	-8.11E-04	±	1.85E-02	32.2	20.24	±	6.95	97.4	± 32.5
# 16	8.39E-06	3.46E-01	±	9.86E-03	3.85E+00	±	1.53E+00	6.87E-03	±	7.94E-03	14.1	16.77	±	2.46	81.0	± 11.6
# 17	1.36E-05	2.25E-01	±	5.74E-03	1.72E+00	±	9.58E-01	9.58E-03	±	4.76E-03	14.3	11.05	±	1.58	53.8	± 7.6
# 18	1.84E-05	1.42E+00	±	1.57E-02	3.45E+00	±	6.63E-01	-3.18E-03	±	4.99E-03	1.4	5.94	±	2.17	29.1	± 10.6
# 19	2.62E-05	4.36E-01	±	4.12E-03	8.75E-01	±	4.54E-01	4.51E-03	±	2.76E-03	5.2	7.07	±	0.94	34.6	± 4.6
# 20	8.71E-07	1.31E-02	±	7.68E-02	1.97E+01	±	1.40E+01	5.57E-02	±	6.46E-02	87.7	27.61	±	23.32	131.6	± 107.2
Total	9.39E-05	9.47E-01	±	6.91E-03	1.88E+01	±	6.59E-01	-1.33E-03	±	3.63E-03	-0.4	-1.22	±	1.99	-6.0	± 9.8
N86.MS3		J = .2740E-02 ± .2406E-04														
# 1	4.30E-06	4.87E+00	±	1.28E-01	-3.22E-01	±	3.10E+00	1.20E-02	±	1.83E-02	-0.3	-3.60	±	7.15	-17.9	± 35.7
# 2	1.60E-06	2.95E-01	±	3.54E-02	-7.99E+00	±	9.33E+00	-1.12E-02	±	3.18E-02	28.8	35.12	±	10.66	165.7	± 48.1
# 3	4.58E-06	2.06E-01	±	1.07E-02	2.41E+00	±	2.99E+00	2.18E-02	±	1.03E-02	23.2	18.42	±	3.54	88.8	± 16.7
# 4	5.28E-06	7.42E-01	±	1.79E-02	5.74E+00	±	3.43E+00	8.05E-04	±	1.12E-02	8.3	19.84	±	3.09	95.5	± 14.5
# 5	1.09E-05	2.39E-01	±	5.18E-03	2.73E+00	±	1.33E+00	1.37E-02	±	5.34E-03	26.6	25.62	±	1.60	122.4	± 7.4
# 6	7.39E-05	2.31E-02	±	5.50E-04	4.34E+00	±	2.35E-01	2.42E-02	±	1.22E-03	82.4	31.93	±	0.25	151.3	± 1.1
# 7	1.95E-04	9.17E-03	±	1.73E-04	3.78E+00	±	9.85E-02	2.05E-02	±	4.04E-04	92.1	31.66	±	0.14	150.1	± 0.6
# 8	3.67E-04	3.60E-03	±	1.05E-04	3.56E+00	±	6.52E-02	2.04E-02	±	3.60E-04	96.8	32.16	±	0.08	152.3	± 0.4
# 9	9.92E-05	6.81E-03	±	4.51E-04	3.86E+00	±	1.74E-01	1.99E-02	±	6.85E-04	94.1	31.78	±	0.21	150.6	± 0.9
# 10	1.83E-05	3.72E-02	±	2.78E-03	2.54E+00	±	7.14E-01	1.38E-02	±	3.12E-03	72.7	29.21	±	1.05	138.9	± 4.8
# 11	5.54E-05	1.97E-02	±	7.96E-04	3.28E+00	±	2.67E-01	1.29E-02	±	1.10E-03	83.9	30.39	±	0.34	144.3	± 1.5
# 12	2.76E-05	4.66E-02	±	1.65E-03	4.49E+00	±	5.92E-01	1.62E-02	±	2.17E-03	67.4	28.38	±	0.64	135.1	± 2.9
# 13	8.47E-06	3.60E-01	±	8.37E-03	1.01E-01	±	1.63E+00	1.15E-02	±	6.25E-03	15.8	20.00	±	2.24	96.3	± 10.5
# 14	2.01E-05	6.09E-02	±	2.56E-03	6.49E+00	±	7.86E-01	1.68E-02	±	2.71E-03	58.2	25.05	±	0.95	119.7	± 4.4

# 15	2.64E-05	6.00E-02	±	1.90E-03	3.85E+00	±	5.75E-01	1.05E-02	±	2.65E-03	58.8	25.33	±	0.72	121.1	± 3.3
# 16	2.04E-05	6.61E-02	±	2.67E-03	1.61E+00	±	8.11E-01	5.72E-03	±	2.53E-03	56.7	25.61	±	0.98	122.3	± 4.5
# 17	3.43E-07	-3.99E-01	±	1.77E-01	-9.52E+01	±	5.23E+01	-1.27E-01	±	1.46E-01	431.9	153.50	±	69.15	633.5	± 240.6
Total	9.39E-04	4.74E-02	±	2.19E-04	3.61E+00	±	7.12E-02	1.89E-02	±	3.02E-04	68.7	30.80	±	0.09	146.2	± 1.3
N87.MS3		J = .2740E-02 ± .2407E-04														
# 1	3.94E-05	3.12E-01	±	3.85E-03	5.38E-02	±	6.33E-01	5.25E-03	±	2.58E-03	9.1	9.24	±	0.90	45.1	± 4.3
# 2	9.46E-05	5.40E-02	±	1.39E-03	4.59E-01	±	2.61E-01	7.94E-03	±	9.88E-04	41.0	11.10	±	0.41	54.1	± 2.0
# 3	2.54E-04	1.61E-03	±	3.88E-04	1.72E-01	±	9.88E-02	6.68E-03	±	4.68E-04	98.6	32.93	±	0.20	155.9	± 0.9
# 4	2.47E-04	6.64E-05	±	3.99E-04	-8.00E-02	±	9.80E-02	5.47E-03	±	4.77E-04	99.9	33.22	±	0.16	157.2	± 0.7
# 5	3.37E-04	-2.13E-04	±	2.87E-04	9.58E-02	±	7.90E-02	4.78E-03	±	4.30E-04	100.2	33.24	±	0.11	157.3	± 0.5
# 6	2.27E-04	-1.88E-04	±	4.28E-04	-4.13E-02	±	1.07E-01	5.05E-03	±	5.81E-04	100.2	33.64	±	0.18	159.1	± 0.8
# 7	2.94E-04	8.27E-04	±	3.29E-04	-1.13E-02	±	8.16E-02	4.63E-03	±	3.62E-04	99.3	33.52	±	0.16	158.6	± 0.7
# 8	1.93E-04	3.67E-04	±	5.06E-04	1.63E-01	±	1.32E-01	4.35E-03	±	6.08E-04	99.7	33.59	±	0.20	158.9	± 0.9
# 9	1.37E-04	1.03E-03	±	7.03E-04	6.48E-02	±	1.76E-01	4.40E-03	±	6.81E-04	99.1	32.98	±	0.25	156.1	± 1.1
# 10	2.25E-04	2.86E-04	±	4.35E-04	3.00E-01	±	1.09E-01	4.96E-03	±	5.29E-04	99.8	33.28	±	0.15	157.5	± 0.7
# 11	9.39E-05	3.34E-04	±	1.03E-03	3.49E-01	±	2.58E-01	4.45E-03	±	1.13E-03	99.7	33.25	±	0.34	157.3	± 1.5
# 12	1.01E-04	7.81E-04	±	9.53E-04	1.17E-01	±	2.40E-01	4.66E-03	±	1.01E-03	99.3	32.59	±	0.30	154.3	± 1.4
# 13	9.32E-05	1.05E-03	±	1.03E-03	-6.20E-02	±	2.61E-01	4.11E-03	±	9.75E-04	99.1	32.23	±	0.32	152.7	± 1.5
# 14	1.71E-04	1.23E-03	±	5.58E-04	1.53E-01	±	1.44E-01	5.70E-03	±	5.59E-04	98.9	32.25	±	0.22	152.8	± 1.0
# 15	2.67E-04	1.28E-04	±	3.56E-04	1.94E-01	±	9.27E-02	5.35E-03	±	4.57E-04	99.9	33.26	±	0.17	157.4	± 0.8
# 16	2.48E-04	6.51E-04	±	1.64E-04	2.60E-01	±	6.44E-02	4.63E-03	±	4.15E-04	99.4	32.31	±	0.14	153.0	± 0.6
# 17	2.05E-05	1.47E-03	±	1.94E-03	-8.43E-02	±	7.86E-01	1.46E-04	±	2.95E-03	98.6	30.31	±	0.62	144.0	± 2.8
# 18	3.89E-05	1.04E-02	±	1.08E-03	4.81E-01	±	4.42E-01	3.33E-03	±	1.78E-03	88.7	24.10	±	0.36	115.4	± 1.7
# 19	2.66E-05	1.14E-02	±	1.48E-03	1.89E-01	±	6.24E-01	1.00E-03	±	2.00E-03	86.1	20.81	±	0.49	100.0	± 2.3
# 20	1.51E-05	3.44E-02	±	2.63E-03	1.10E+00	±	1.13E+00	5.25E-03	±	3.65E-03	60.2	15.38	±	0.82	74.5	± 3.9
# 21	1.19E-05	7.21E-03	±	3.74E-03	-8.39E-01	±	1.45E+00	5.90E-03	±	4.47E-03	92.4	25.75	±	1.20	123.0	± 5.5
Total	3.14E-03	6.44E-03	±	1.29E-04	1.30E-01	±	3.32E-02	5.04E-03	±	1.48E-04	94.4	31.78	±	0.05	150.7	± 1.3

N88.MS3		J = .2741E-02 ± .2408E-04															
# 1	1.45E-07	4.56E+00	±	2.39E+00	-3.40E+01	±	1.12E+02	5.98E-01	±	4.27E-01	-9.5	#####	±	112.50	-694.1	±	817.2
# 2	2.92E-08	2.89E+00	±	7.80E+00	4.18E+02	±	1.24E+03	-6.55E-01	±	2.18E+00	-42.5	#####	±	810.50	#####	±	#####
# 3	5.19E-07	1.58E-01	±	8.43E-02	-3.63E+01	±	3.12E+01	-1.48E-03	±	7.32E-02	30.0	19.97	±	25.26	96.1	±	118.4
# 4	1.06E-06	3.62E-03	±	3.89E-02	2.07E+01	±	1.80E+01	-3.57E-03	±	3.67E-02	97.6	44.15	±	12.69	206.1	±	56.0
# 5	4.16E-06	1.56E-02	±	1.06E-02	-2.15E+00	±	3.68E+00	2.55E-02	±	8.84E-03	88.2	34.30	±	3.34	162.1	±	15.1
# 6	3.19E-04	6.52E-03	±	1.75E-04	3.74E+00	±	6.67E-02	1.48E-02	±	4.64E-04	94.3	31.99	±	0.11	151.6	±	0.5
# 7	9.28E-06	-4.46E-03	±	4.51E-03	2.10E+00	±	1.90E+00	1.83E-02	±	4.61E-03	104.1	33.85	±	1.46	160.1	±	6.6
# 8	2.15E-05	-6.36E-04	±	2.05E-03	2.89E+00	±	8.49E-01	1.59E-02	±	2.11E-03	100.6	32.79	±	0.69	155.2	±	3.1
# 9	9.71E-06	3.18E-03	±	4.46E-03	4.19E+00	±	1.75E+00	1.90E-02	±	4.60E-03	97.1	31.75	±	1.50	150.5	±	6.8
# 10	4.64E-05	1.14E-03	±	9.03E-04	4.29E+00	±	4.73E-01	1.78E-02	±	1.04E-03	99.0	32.43	±	0.30	153.6	±	1.4
# 11	9.31E-06	1.93E-02	±	4.46E-03	1.49E+00	±	1.76E+00	1.57E-02	±	4.98E-03	83.1	28.02	±	1.43	133.5	±	6.5
# 12	5.20E-06	3.58E-02	±	7.89E-03	4.90E+00	±	3.15E+00	8.72E-05	±	7.67E-03	66.5	20.99	±	2.47	100.9	±	11.6
# 13	8.97E-06	3.27E-02	±	4.62E-03	2.49E-01	±	1.76E+00	5.80E-03	±	4.26E-03	36.8	5.63	±	1.43	27.6	±	7.0
# 14	1.50E-07	3.08E-02	±	2.73E-01	-1.41E+02	±	1.25E+02	3.66E-01	±	3.13E-01	64.2	16.31	±	85.30	78.9	±	403.7
Total	4.36E-04	8.42E-03	±	3.73E-04	3.53E+00	±	1.50E-01	1.53E-02	±	4.84E-04	92.6	31.32	±	0.14	148.6	±	1.4

N89.MS3		J = .2741E-02 ± .2408E-04															
# 1	3.57E-05	8.89E-02	±	4.48E-03	1.02E+00	±	5.36E-01	6.34E-03	±	2.60E-03	22.4	7.58	±	1.35	37.1	±	6.5
# 2	5.82E-05	2.33E-02	±	2.71E-03	2.11E-01	±	3.27E-01	4.56E-03	±	1.58E-03	71.7	17.49	±	0.83	84.5	±	3.9
# 3	1.12E-04	-1.43E-04	±	1.39E-03	-6.71E-02	±	1.77E-01	4.76E-03	±	7.81E-04	100.1	30.95	±	0.44	146.9	±	2.0
# 4	1.51E-04	1.46E-03	±	1.04E-03	6.54E-02	±	1.27E-01	5.23E-03	±	6.43E-04	98.7	32.22	±	0.34	152.7	±	1.5
# 5	2.27E-04	3.97E-04	±	6.89E-04	3.86E-02	±	9.22E-02	5.66E-03	±	5.54E-04	99.7	33.27	±	0.23	157.4	±	1.0
# 6	1.81E-04	5.70E-04	±	8.72E-04	-4.05E-02	±	1.07E-01	4.85E-03	±	5.96E-04	99.5	33.32	±	0.28	157.7	±	1.3
# 7	2.25E-04	1.30E-03	±	7.00E-04	4.29E-03	±	7.94E-02	6.74E-03	±	5.40E-04	98.9	33.93	±	0.24	160.4	±	1.1
# 8	7.26E-05	-5.02E-04	±	1.32E-03	2.45E-01	±	2.63E-01	2.92E-03	±	1.19E-03	100.4	33.59	±	0.46	158.9	±	2.1
# 9	4.25E-05	1.89E-03	±	2.29E-03	1.07E-01	±	4.42E-01	3.20E-03	±	1.81E-03	98.4	33.18	±	0.75	157.0	±	3.4
# 10	1.09E-04	8.25E-04	±	8.96E-04	9.81E-02	±	1.74E-01	4.55E-03	±	7.22E-04	99.3	33.75	±	0.30	159.6	±	1.4
# 11	1.20E-04	3.53E-03	±	8.20E-04	1.16E-01	±	1.61E-01	6.30E-03	±	7.43E-04	97.0	33.60	±	0.33	158.9	±	1.5

# 12	5.34E-05	1.38E-02	±	1.86E-03	4.15E-01	±	3.65E-01	6.12E-03	±	1.62E-03	88.2	30.62	±	0.61	145.4	± 2.8
# 13	5.84E-05	3.36E-02	±	1.69E-03	3.09E-01	±	3.48E-01	5.16E-03	±	1.34E-03	74.6	29.13	±	0.55	138.6	± 2.5
# 16	1.48E-04	4.48E-03	±	6.66E-04	-6.05E-02	±	1.35E-01	5.00E-03	±	7.28E-04	96.0	32.04	±	0.24	151.8	± 1.1
# 17	1.54E-05	1.69E-02	±	6.30E-03	1.52E-01	±	1.21E+00	6.87E-03	±	5.34E-03	85.7	29.95	±	2.02	142.3	± 9.2
# 18	4.27E-05	1.45E-02	±	2.36E-03	2.02E-01	±	4.55E-01	3.77E-03	±	1.98E-03	88.1	31.63	±	0.75	150.0	± 3.4
# 19	1.40E-06	-4.30E-02	±	7.09E-02	1.98E+00	±	1.38E+01	3.14E-02	±	5.47E-02	176.1	29.38	±	22.41	139.7	± 102.5
Total	1.65E-03	6.03E-03	±	3.14E-04	8.79E-02	±	4.82E-02	5.30E-03	±	2.33E-04	94.7	31.65	±	0.10	150.1	± 1.3

N90.MS3		J = .2739E-02 ± .2405E-04														
# 1	7.15E-06	1.44E-01	±	2.16E-02	-4.85E-02	±	2.36E+00	-4.82E-03	±	1.40E-02	31.6	19.66	±	6.28	94.6	± 29.5
# 2	3.80E-05	1.02E-01	±	3.96E-03	1.67E-01	±	4.80E-01	6.50E-03	±	2.78E-03	39.5	19.66	±	1.17	94.6	± 5.5
# 3	8.68E-05	9.21E-03	±	2.07E-03	1.05E-01	±	2.03E-01	8.00E-03	±	1.24E-03	91.6	29.62	±	0.64	140.7	± 2.9
# 4	1.32E-04	2.52E-03	±	9.31E-04	-5.50E-02	±	1.33E-01	7.11E-03	±	8.22E-04	97.7	32.03	±	0.32	151.7	± 1.5
# 5	2.01E-04	-1.34E-04	±	2.57E-04	-2.30E-02	±	9.27E-02	4.44E-03	±	5.89E-04	100.1	32.87	±	0.14	155.5	± 0.6
# 6	1.25E-04	6.58E-05	±	3.99E-04	1.14E-01	±	1.47E-01	3.70E-03	±	8.13E-04	99.9	32.98	±	0.20	156.1	± 0.9
# 7	3.45E-04	3.13E-04	±	1.40E-04	4.71E-02	±	5.38E-02	4.32E-03	±	3.65E-04	99.7	34.59	±	0.10	163.3	± 0.4
# 8	1.62E-04	1.33E-03	±	3.18E-04	2.48E-01	±	1.11E-01	3.63E-03	±	6.50E-04	98.8	32.77	±	0.21	155.1	± 1.0
# 9	1.20E-04	1.68E-03	±	4.06E-04	1.51E-01	±	1.66E-01	4.53E-03	±	9.50E-04	98.5	32.59	±	0.19	154.3	± 0.8
# 10	7.52E-05	2.07E-04	±	6.35E-04	1.75E-01	±	2.38E-01	5.27E-03	±	1.40E-03	99.8	33.49	±	0.29	158.4	± 1.3
# 11	1.27E-04	1.36E-03	±	3.88E-04	-1.46E-02	±	1.40E-01	4.26E-03	±	9.18E-04	98.8	33.64	±	0.19	159.0	± 0.9
# 12	1.41E-04	2.38E-03	±	3.51E-04	2.17E-02	±	1.25E-01	4.95E-03	±	8.08E-04	98.0	33.72	±	0.16	159.4	± 0.7
# 13	1.34E-04	1.66E-03	±	3.67E-04	7.16E-02	±	1.37E-01	4.88E-03	±	8.52E-04	98.6	33.84	±	0.17	159.9	± 0.8
# 14	1.55E-04	7.79E-04	±	3.08E-04	-9.93E-02	±	1.15E-01	5.01E-03	±	7.19E-04	99.3	33.35	±	0.15	157.7	± 0.7
# 15	1.81E-04	1.43E-03	±	2.83E-04	-5.66E-03	±	9.68E-02	4.88E-03	±	5.89E-04	98.7	33.19	±	0.16	157.0	± 0.7
# 16	1.45E-04	7.99E-04	±	3.31E-04	-2.84E-02	±	1.25E-01	4.66E-03	±	8.07E-04	99.3	32.86	±	0.14	155.5	± 0.6
# 17	1.25E-04	4.93E-04	±	3.96E-04	-3.07E-01	±	1.43E-01	4.44E-03	±	8.05E-04	99.6	32.96	±	0.21	156.0	± 0.9
# 18	7.00E-05	-1.06E-03	±	6.90E-04	-2.82E-01	±	2.58E-01	4.69E-03	±	1.43E-03	101.0	33.20	±	0.34	157.0	± 1.5
# 19	2.50E-04	3.06E-06	±	1.99E-04	3.33E-02	±	7.39E-02	4.87E-03	±	4.35E-04	100.0	33.87	±	0.13	160.0	± 0.6
# 20	4.20E-04	3.89E-04	±	1.12E-04	6.67E-02	±	4.59E-02	4.19E-03	±	3.21E-04	99.7	34.53	±	0.12	163.1	± 0.5

# 21	1.33E-04	-5.92E-04	±	3.70E-04	3.19E-01	±	1.52E-01	3.95E-03	±	7.90E-04	100.5	32.95	±	0.18	155.9	± 0.8
# 22	4.55E-06	1.08E-03	±	1.14E-02	5.82E+00	±	3.95E+00	4.18E-03	±	2.15E-02	98.9	28.09	±	4.22	133.8	± 19.4
# 23	4.97E-06	-8.31E-03	±	2.81E-02	3.04E+00	±	3.59E+00	4.72E-03	±	1.98E-02	108.5	31.19	±	8.65	147.9	± 39.4
Total	3.18E-03	2.45E-03	±	1.23E-04	4.95E-02	±	2.74E-02	4.67E-03	±	1.66E-04	97.9	33.20	±	0.05	157.0	± 1.3
N91.MS3		J = .2741E-02 ± .2408E-04														
# 1	4.54E-06	1.23E-01	±	8.56E-03	-1.15E+00	±	4.50E+00	-1.75E-02	±	1.22E-02	22.6	10.59	±	2.49	51.6	± 12.0
# 2	1.04E-06	2.31E-02	±	3.24E-02	7.44E+00	±	2.15E+01	-6.13E-02	±	5.10E-02	75.2	20.69	±	10.04	99.5	± 47.0
# 3	4.17E-06	1.14E-02	±	8.02E-03	3.21E+00	±	5.19E+00	-1.90E-03	±	1.32E-02	91.3	35.58	±	2.58	167.9	± 11.6
# 4	4.22E-06	2.73E-03	±	9.21E-03	3.98E+00	±	5.63E+00	9.71E-03	±	1.33E-02	97.7	33.95	±	2.94	160.5	± 13.3
# 5	4.19E-05	1.19E-02	±	9.23E-04	-1.05E-01	±	5.25E-01	5.89E-03	±	1.58E-03	90.1	32.15	±	0.34	152.4	± 1.5
# 6	4.74E-05	5.99E-03	±	7.33E-04	2.09E-01	±	4.56E-01	8.73E-03	±	1.42E-03	94.8	32.40	±	0.26	153.5	± 1.2
# 7	4.67E-05	3.50E-03	±	7.20E-04	-3.56E-02	±	4.47E-01	6.18E-03	±	1.36E-03	96.9	32.13	±	0.29	152.3	± 1.3
# 8	5.42E-05	3.96E-03	±	6.77E-04	1.05E-01	±	3.98E-01	6.91E-03	±	1.53E-03	96.5	32.59	±	0.25	154.4	± 1.1
# 9	2.88E-05	2.59E-03	±	1.20E-03	-1.62E-01	±	7.39E-01	6.82E-03	±	2.28E-03	97.8	33.23	±	0.42	157.3	± 1.9
# 10	3.71E-05	2.13E-03	±	1.02E-03	2.38E-01	±	5.86E-01	6.81E-03	±	1.59E-03	98.1	32.49	±	0.41	153.9	± 1.9
# 11	4.90E-05	3.59E-03	±	8.18E-04	4.57E-01	±	4.42E-01	8.44E-03	±	1.24E-03	96.9	32.58	±	0.32	154.3	± 1.5
# 12	4.89E-05	-1.20E-04	±	6.84E-04	2.17E-01	±	4.40E-01	6.58E-03	±	1.27E-03	100.1	32.09	±	0.29	152.1	± 1.3
# 13	2.59E-05	5.27E-03	±	1.38E-03	5.93E-01	±	8.58E-01	5.84E-03	±	2.29E-03	94.9	29.02	±	0.47	138.1	± 2.1
# 14	2.40E-05	8.66E-03	±	1.43E-03	-1.68E+00	±	9.24E-01	5.52E-03	±	2.36E-03	91.5	27.44	±	0.49	130.8	± 2.3
# 15	2.24E-05	-6.27E-04	±	1.21E-03	-9.15E-01	±	7.91E-01	7.53E-03	±	1.83E-03	100.6	32.39	±	0.46	153.5	± 2.1
# 16	2.52E-05	1.45E-01	±	1.78E-03	-9.06E-01	±	7.00E-01	6.57E-03	±	2.16E-03	43.3	32.74	±	0.52	155.1	± 2.4
# 17	4.40E-05	4.67E-05	±	6.67E-04	-8.57E-01	±	4.09E-01	5.89E-03	±	9.92E-04	100.0	32.39	±	0.26	153.5	± 1.2
# 18	3.15E-06	5.72E-04	±	7.70E-03	4.25E+00	±	5.31E+00	-5.85E-03	±	1.14E-02	99.5	35.40	±	3.05	167.1	± 13.8
# 19	4.46E-06	5.69E-03	±	6.27E-03	-1.78E+00	±	3.78E+00	1.17E-02	±	1.00E-02	95.1	32.64	±	2.40	154.6	± 10.9
# 20	6.51E-06	-5.18E-04	±	4.51E-03	1.35E+00	±	3.01E+00	8.47E-03	±	6.08E-03	100.5	32.78	±	1.64	155.2	± 7.4
# 21	2.04E-05	1.52E-03	±	1.26E-03	-7.51E-02	±	9.08E-01	4.65E-03	±	1.83E-03	98.7	34.04	±	0.60	160.9	± 2.7
Total	5.44E-04	1.13E-02	±	2.84E-04	-2.54E-02	±	1.73E-01	6.36E-03	±	4.75E-04	90.5	31.97	±	0.10	151.5	± 1.4

N92.MS3		J = .2741E-02 ± .2408E-04															
# 1	2.56E-05	1.31E-01	±	1.30E-01	-2.89E-01	±	1.63E+00	7.03E-03	±	4.66E-02	1.7	0.68	±	38.07	3.4	±	187.9
# 2	1.69E-04	1.01E-02	±	1.95E-02	1.69E-01	±	2.48E-01	5.26E-03	±	7.07E-03	84.5	16.25	±	5.77	78.6	±	27.3
# 3	2.59E-04	-2.50E-04	±	1.28E-02	1.20E-01	±	1.63E-01	5.53E-03	±	4.62E-03	100.2	30.81	±	3.79	146.3	±	17.3
# 4	1.19E-04	-1.01E-02	±	2.77E-02	-2.52E-01	±	3.50E-01	4.38E-03	±	1.00E-02	108.9	36.59	±	8.24	172.5	±	37.0
# 5	2.29E-04	-1.22E-02	±	1.44E-02	-1.28E-01	±	1.86E-01	3.63E-03	±	5.24E-03	110.6	37.85	±	4.30	178.1	±	19.3
# 6	2.07E-04	-1.52E-02	±	1.60E-02	-8.56E-02	±	2.04E-01	4.06E-03	±	5.77E-03	113.1	38.69	±	4.76	181.8	±	21.3
# 7	1.85E-04	6.12E-02	±	1.83E-02	4.74E-01	±	2.34E-01	1.11E-02	±	6.68E-03	42.4	13.32	±	5.39	64.7	±	25.7
# 8	1.40E-04	-1.51E-02	±	2.36E-02	-1.86E-03	±	3.00E-01	5.67E-03	±	8.56E-03	113.1	38.59	±	7.05	181.4	±	31.5
# 9	2.64E-04	-5.76E-04	±	1.25E-02	-1.81E-01	±	1.62E-01	5.86E-03	±	4.54E-03	100.5	35.34	±	3.73	166.8	±	16.8
# 10	2.74E-04	7.91E-04	±	1.50E-04	-2.35E-02	±	7.47E-02	5.59E-03	±	3.79E-04	99.3	33.88	±	0.12	160.2	±	0.5
# 11	1.22E-04	7.73E-04	±	3.23E-04	5.37E-02	±	1.59E-01	5.11E-03	±	6.06E-04	99.3	33.41	±	0.17	158.1	±	0.8
# 12	1.72E-04	5.07E-04	±	2.48E-04	-9.85E-02	±	1.14E-01	4.74E-03	±	4.10E-04	99.6	33.87	±	0.15	160.2	±	0.7
# 13	9.02E-05	-5.14E-05	±	4.61E-04	-5.71E-02	±	2.16E-01	5.18E-03	±	6.53E-04	100.0	37.48	±	4.00	176.4	±	18.0
# 14	1.91E-04	2.73E-04	±	2.10E-04	6.29E-02	±	1.04E-01	5.15E-03	±	4.90E-04	99.8	34.07	±	0.15	161.1	±	0.7
# 15	2.33E-04	6.54E-04	±	1.76E-04	8.17E-02	±	8.57E-02	5.87E-03	±	4.66E-04	99.4	34.10	±	0.11	161.2	±	0.5
# 16	1.07E-04	8.98E-04	±	3.59E-04	1.60E-01	±	1.90E-01	4.86E-03	±	5.99E-04	99.2	34.44	±	0.16	162.8	±	0.7
# 17	2.76E-05	6.93E-04	±	1.44E-03	-2.74E-01	±	6.90E-01	3.03E-03	±	2.39E-03	99.4	33.92	±	0.59	160.4	±	2.6
# 18	1.84E-04	2.01E-04	±	2.18E-04	-1.84E-02	±	1.12E-01	5.73E-03	±	6.72E-04	99.8	34.26	±	0.13	162.0	±	0.6
# 19	1.62E-04	1.81E-04	±	2.55E-04	2.28E-01	±	1.35E-01	5.45E-03	±	5.98E-04	99.8	34.40	±	0.13	162.6	±	0.6
# 20	2.34E-04	2.76E-04	±	1.83E-04	5.85E-02	±	8.76E-02	6.17E-03	±	4.88E-04	99.8	33.80	±	0.13	159.8	±	0.6
# 21	1.72E-04	2.60E-05	±	2.41E-04	2.29E-01	±	1.22E-01	4.49E-03	±	5.15E-04	100.0	33.53	±	0.13	158.6	±	0.6
# 22	1.46E-04	9.74E-04	±	2.75E-04	1.12E-01	±	1.33E-01	5.38E-03	±	6.12E-04	99.1	33.09	±	0.13	156.6	±	0.6
# 23	5.32E-05	2.24E-03	±	7.72E-04	3.89E-01	±	4.30E-01	5.18E-03	±	1.10E-03	98.0	32.57	±	0.35	154.3	±	1.6
# 24	4.63E-05	-4.75E-04	±	9.26E-04	-1.70E-01	±	4.12E-01	2.36E-03	±	1.36E-03	100.4	32.97	±	0.40	156.1	±	1.8
# 25	1.27E-04	-3.62E-04	±	3.31E-04	-1.27E-01	±	1.71E-01	6.11E-03	±	8.10E-04	100.3	33.47	±	0.15	158.4	±	0.7
# 27	3.38E-05	9.34E-04	±	6.60E-04	7.24E-01	±	8.77E-01	4.18E-03	±	1.78E-03	99.2	32.57	±	0.37	154.3	±	1.7
# 28	1.14E-05	-1.31E-03	±	1.77E-03	-1.68E+00	±	2.53E+00	7.28E-03	±	4.37E-03	101.2	33.51	±	0.79	158.6	±	3.6
# 29	5.95E-06	-1.53E-03	±	3.29E-03	-2.45E+00	±	4.92E+00	5.19E-03	±	8.51E-03	101.4	33.03	±	1.47	156.4	±	6.7

# 30	6.93E-05	2.19E-04	±	3.67E-04	-3.66E-03	±	4.18E-01	4.49E-03	±	8.02E-04	99.8	33.23	±	0.17	157.3	± 0.8
# 31	4.29E-05	6.96E-04	±	5.39E-04	-5.76E-02	±	6.79E-01	1.87E-03	±	1.32E-03	99.4	33.03	±	0.26	156.4	± 1.2
# 32	1.15E-05	8.69E-04	±	2.06E-03	1.97E+00	±	2.49E+00	-1.59E-03	±	4.61E-03	99.2	33.60	±	0.83	158.9	± 3.8
# 33	1.30E-05	-7.19E-03	±	2.24E-03	-3.80E+00	±	2.22E+00	2.59E-02	±	3.68E-03	106.3	35.57	±	0.98	167.8	± 4.4
Total	4.13E-03	1.92E-03	±	2.41E-03	2.29E-02	±	4.10E-02	5.46E-03	±	8.78E-04	98.3	32.65	±	0.72	154.6	± 3.5
N93.MS3		J = .2739E-02 ± .2404E-04														
# 1	1.84E-05	1.15E-02	±	1.81E-03	7.37E-01	±	1.04E+00	8.20E-03	±	3.90E-03	90.7	33.07	±	0.62	156.4	± 2.8
# 2	4.92E-05	4.54E-03	±	5.48E-04	1.11E-01	±	3.62E-01	3.65E-03	±	1.56E-03	95.9	31.69	±	0.28	150.2	± 1.3
# 3	1.12E-04	1.57E-04	±	2.56E-04	-2.15E-01	±	1.76E-01	3.45E-03	±	7.78E-04	99.9	33.05	±	0.14	156.4	± 0.6
# 4	1.25E-04	6.59E-04	±	2.39E-04	-5.28E-03	±	1.53E-01	3.36E-03	±	7.00E-04	99.4	33.15	±	0.11	156.8	± 0.5
# 5	1.28E-04	4.89E-04	±	2.42E-04	1.34E-02	±	1.39E-01	4.42E-03	±	7.66E-04	99.6	33.03	±	0.20	156.3	± 0.9
# 6	1.27E-04	3.60E-04	±	2.24E-04	4.66E-02	±	1.56E-01	5.34E-03	±	7.55E-04	99.7	32.96	±	0.14	155.9	± 0.6
# 7	1.65E-04	3.18E-04	±	1.80E-04	1.73E-01	±	1.04E-01	4.77E-03	±	5.04E-04	99.7	33.79	±	0.16	159.7	± 0.7
# 8	1.03E-04	-4.02E-05	±	2.66E-04	3.29E-01	±	1.98E-01	4.00E-03	±	8.81E-04	100.0	33.86	±	0.26	160.0	± 1.2
# 9	1.25E-04	7.04E-04	±	2.42E-04	1.63E-01	±	1.41E-01	5.29E-03	±	6.87E-04	99.4	33.58	±	0.12	158.7	± 0.6
# 10	2.39E-04	6.57E-04	±	1.34E-04	4.80E-02	±	7.18E-02	3.95E-03	±	3.72E-04	99.4	32.97	±	0.10	156.0	± 0.5
# 11	1.03E-04	-4.73E-05	±	3.56E-04	1.03E-01	±	1.82E-01	3.85E-03	±	8.80E-04	100.0	32.58	±	0.17	154.2	± 0.8
# 12	8.08E-05	-2.74E-04	±	4.60E-04	1.88E-01	±	2.23E-01	4.55E-03	±	1.05E-03	100.2	33.13	±	0.21	156.7	± 0.9
# 13	1.09E-04	5.59E-04	±	3.46E-04	-2.93E-01	±	1.65E-01	3.33E-03	±	7.48E-04	99.5	32.39	±	0.17	153.3	± 0.8
# 14	9.43E-05	3.03E-04	±	3.98E-04	1.80E-01	±	1.92E-01	3.29E-03	±	9.02E-04	99.7	32.91	±	0.19	155.7	± 0.9
# 15	7.20E-05	-2.82E-04	±	5.72E-04	-9.34E-02	±	2.67E-01	3.16E-03	±	1.08E-03	100.3	32.48	±	0.24	153.7	± 1.1
# 16	4.60E-05	5.08E-04	±	7.61E-04	-3.46E-01	±	4.52E-01	4.65E-03	±	1.59E-03	99.5	31.52	±	0.32	149.4	± 1.5
# 17	1.01E-04	6.70E-04	±	3.90E-04	2.45E-01	±	1.92E-01	3.95E-03	±	1.06E-03	99.4	32.20	±	0.17	152.5	± 0.8
# 18	2.28E-05	3.93E-03	±	1.72E-03	4.57E-01	±	8.22E-01	-7.10E-04	±	3.17E-03	96.4	31.38	±	0.58	148.8	± 2.7
Total	1.82E-03	6.37E-04	±	7.85E-05	6.57E-02	±	4.37E-02	4.09E-03	±	2.00E-04	99.4	32.95	±	0.04	155.9	± 1.3
N94.MS3		J = .2739E-02 ± .2404E-04														
# 1	1.01E-05	9.78E-03	±	4.88E-03	2.77E+00	±	1.70E+00	1.94E-03	±	3.59E-03	91.2	29.75	±	1.52	141.3	± 6.9

# 2	2.20E-05	4.20E-03	±	2.19E-03	-1.51E-01	±	8.74E-01	3.86E-03	±	2.12E-03	96.2	31.36	±	0.70	148.6	± 3.2
# 3	5.80E-05	2.40E-03	±	8.56E-04	-1.05E-01	±	3.23E-01	3.94E-03	±	1.20E-03	97.9	32.38	±	0.28	153.3	± 1.3
# 4	1.44E-04	2.32E-04	±	3.10E-04	1.83E-02	±	1.25E-01	3.73E-03	±	4.05E-04	99.8	32.79	±	0.12	155.2	± 0.5
# 5	1.19E-04	5.75E-04	±	4.09E-04	-1.29E-01	±	1.47E-01	5.13E-03	±	4.68E-04	99.5	32.41	±	0.16	153.4	± 0.7
# 6	1.29E-04	4.48E-04	±	3.56E-04	-1.04E-01	±	1.40E-01	3.92E-03	±	5.32E-04	99.6	32.55	±	0.15	154.1	± 0.7
# 7	6.93E-05	6.64E-04	±	7.05E-04	1.15E-02	±	2.72E-01	4.71E-03	±	7.96E-04	99.4	32.17	±	0.26	152.3	± 1.2
# 8	7.18E-05	5.73E-04	±	6.41E-04	5.27E-02	±	2.47E-01	4.49E-03	±	6.72E-04	99.5	33.15	±	0.27	156.8	± 1.2
# 9	9.33E-05	1.51E-03	±	5.05E-04	8.29E-02	±	2.00E-01	3.29E-03	±	6.42E-04	98.7	32.59	±	0.19	154.3	± 0.8
# 10	7.09E-05	1.83E-03	±	6.97E-04	5.80E-01	±	2.86E-01	3.38E-03	±	9.47E-04	98.3	31.96	±	0.25	151.4	± 1.1
# 11	1.07E-04	-1.64E-04	±	4.43E-04	-1.79E-02	±	1.90E-01	4.50E-03	±	6.59E-04	100.1	32.72	±	0.16	154.8	± 0.7
# 12	1.10E-04	1.68E-04	±	4.15E-04	-1.12E-01	±	1.89E-01	3.43E-03	±	5.46E-04	99.9	32.58	±	0.18	154.2	± 0.8
# 13	2.96E-05	7.97E-05	±	1.64E-03	-4.21E-01	±	6.12E-01	2.52E-03	±	1.48E-03	99.9	32.14	±	0.61	152.2	± 2.8
# 14	1.24E-04	-1.09E-05	±	3.81E-04	7.05E-02	±	1.50E-01	5.29E-03	±	4.68E-04	100.0	32.56	±	0.16	154.1	± 0.7
# 15	1.31E-05	2.92E-03	±	3.58E-03	-1.48E+00	±	1.64E+00	4.32E-03	±	3.64E-03	97.2	30.15	±	1.16	143.1	± 5.3
# 16	2.28E-05	-1.26E-03	±	2.12E-03	-8.86E-01	±	8.70E-01	5.85E-03	±	2.10E-03	101.2	32.31	±	0.73	153.0	± 3.3
Total	1.19E-03	7.20E-04	±	1.60E-04	-9.77E-03	±	6.37E-02	4.15E-03	±	1.90E-04	99.4	32.47	±	0.06	153.7	± 1.3
N95.MS3		J = .2738E-02 ± .2403E-04														
# 1	1.02E-05	4.78E-02	±	4.75E-03	1.85E+00	±	2.50E+00	2.08E-03	±	5.40E-03	66.7	28.23	±	1.46	134.4	± 6.7
# 2	4.08E-05	1.02E-02	±	9.41E-04	-6.49E-02	±	6.40E-01	3.96E-03	±	1.60E-03	91.5	32.61	±	0.34	154.3	± 1.5
# 3	1.16E-04	7.35E-04	±	3.18E-04	3.75E-02	±	2.28E-01	4.98E-03	±	7.97E-04	99.3	32.88	±	0.20	155.5	± 0.9
# 4	1.17E-04	-8.87E-05	±	3.75E-04	-1.82E-01	±	2.33E-01	4.43E-03	±	6.75E-04	100.1	33.17	±	0.17	156.8	± 0.8
# 5	1.76E-04	-1.76E-04	±	2.16E-04	3.82E-02	±	1.47E-01	3.93E-03	±	3.81E-04	100.2	32.74	±	0.13	154.9	± 0.6
# 6	1.86E-04	4.00E-05	±	2.09E-04	-8.81E-02	±	1.33E-01	3.12E-03	±	4.74E-04	100.0	33.03	±	0.17	156.2	± 0.8
# 7	1.32E-04	4.46E-04	±	2.89E-04	-4.58E-02	±	1.97E-01	4.53E-03	±	6.06E-04	99.6	32.99	±	0.19	156.0	± 0.8
# 8	1.49E-04	8.80E-04	±	2.72E-04	1.57E-01	±	1.76E-01	5.00E-03	±	5.53E-04	99.2	33.09	±	0.16	156.5	± 0.7
# 9	1.22E-04	1.36E-04	±	3.14E-04	2.58E-01	±	2.28E-01	3.39E-03	±	5.24E-04	99.9	32.94	±	0.16	155.8	± 0.7
# 10	1.62E-04	-2.63E-04	±	2.29E-04	8.06E-02	±	1.62E-01	3.25E-03	±	5.01E-04	100.2	32.95	±	0.13	155.8	± 0.6
# 11	1.75E-04	3.13E-05	±	2.05E-04	-5.20E-02	±	1.52E-01	4.36E-03	±	4.12E-04	100.0	32.67	±	0.11	154.6	± 0.5

# 12	1.68E-04	6.24E-05	±	2.00E-04	-1.80E-01	±	1.69E-01	3.36E-03	±	5.51E-04	99.9	32.53	±	0.09	153.9	±	0.4
# 13	1.55E-04	2.79E-04	±	2.25E-04	-1.13E-01	±	1.75E-01	4.06E-03	±	4.73E-04	99.8	32.60	±	0.11	154.3	±	0.5
# 14	7.35E-05	-1.05E-04	±	4.77E-04	1.40E-01	±	3.83E-01	3.76E-03	±	7.81E-04	100.1	32.10	±	0.19	152.0	±	0.9
# 15	1.88E-04	-1.29E-04	±	1.91E-04	-1.37E-01	±	1.45E-01	4.28E-03	±	4.27E-04	100.1	32.58	±	0.10	154.2	±	0.4
# 16	2.74E-05	-2.53E-03	±	1.22E-03	-4.10E-01	±	9.96E-01	1.59E-03	±	1.98E-03	102.3	33.21	±	0.41	157.0	±	1.9
# 17	6.68E-05	-1.24E-03	±	5.36E-04	5.11E-01	±	4.09E-01	7.90E-04	±	7.73E-04	101.1	33.19	±	0.20	156.9	±	0.9
Total	2.06E-03	4.82E-04	±	7.58E-05	1.14E-03	±	5.34E-02	3.86E-03	±	1.47E-04	99.6	32.79	±	0.04	155.1	±	1.3
N96.MS3		J = .2738E-02 ± .2403E-04															
# 1	3.63E-05	2.03E-02	±	1.04E-03	-1.09E-01	±	4.92E-01	2.78E-03	±	1.56E-03	78.2	21.47	±	0.33	103.1	±	1.5
# 2	2.14E-05	1.96E-03	±	1.59E-03	-1.25E+00	±	8.10E-01	4.10E-03	±	2.87E-03	98.2	32.22	±	0.55	152.6	±	2.5
# 3	1.08E-04	1.10E-03	±	3.06E-04	1.25E-01	±	1.79E-01	3.20E-03	±	5.87E-04	99.0	32.77	±	0.17	155.0	±	0.8
# 4	1.25E-04	6.79E-04	±	2.74E-04	1.08E-01	±	1.37E-01	3.51E-03	±	5.52E-04	99.4	32.42	±	0.12	153.4	±	0.6
# 5	1.15E-04	2.84E-04	±	3.00E-04	7.64E-02	±	1.60E-01	3.73E-03	±	6.94E-04	99.7	32.53	±	0.14	154.0	±	0.6
# 6	1.18E-04	3.77E-04	±	2.95E-04	5.46E-02	±	1.47E-01	4.53E-03	±	4.78E-04	99.7	32.39	±	0.14	153.3	±	0.6
# 7	1.52E-04	6.23E-04	±	2.38E-04	-3.47E-02	±	1.15E-01	3.63E-03	±	6.27E-04	99.4	32.85	±	0.13	155.4	±	0.6
# 8	6.34E-05	9.82E-04	±	5.97E-04	2.39E-01	±	2.84E-01	3.42E-03	±	1.10E-03	99.1	32.87	±	0.23	155.5	±	1.1
# 9	6.78E-05	1.24E-03	±	5.23E-04	-1.64E-01	±	2.40E-01	2.91E-03	±	9.92E-04	98.9	33.03	±	0.24	156.2	±	1.1
# 10	2.63E-04	4.80E-04	±	1.36E-04	1.97E-02	±	6.90E-02	3.64E-03	±	2.63E-04	99.6	32.88	±	0.11	155.5	±	0.5
# 11	1.23E-04	1.61E-03	±	2.76E-04	-5.73E-02	±	1.50E-01	3.30E-03	±	4.63E-04	98.5	32.11	±	0.15	152.0	±	0.7
# 12	1.41E-04	3.07E-04	±	2.83E-04	-2.70E-02	±	1.26E-01	3.25E-03	±	4.78E-04	99.7	32.37	±	0.17	153.2	±	0.8
# 13	6.46E-05	-1.74E-04	±	4.17E-04	1.38E-01	±	2.88E-01	1.65E-03	±	8.97E-04	100.2	32.51	±	0.18	153.9	±	0.8
# 14	2.96E-05	1.09E-04	±	7.63E-04	-7.56E-02	±	6.15E-01	3.99E-03	±	1.66E-03	99.9	32.33	±	0.31	153.0	±	1.4
# 15	2.93E-04	6.89E-05	±	9.79E-05	-2.06E-02	±	6.65E-02	3.26E-03	±	2.88E-04	99.9	32.53	±	0.11	153.9	±	0.5
# 16	1.25E-04	-1.31E-05	±	1.84E-04	7.81E-02	±	1.43E-01	3.15E-03	±	5.62E-04	100.0	32.51	±	0.13	153.9	±	0.6
# 17	1.51E-06	-2.36E-02	±	1.76E-02	1.79E+01	±	1.24E+01	-1.49E-03	±	3.27E-02	120.4	41.19	±	6.03	192.8	±	26.8
# 18	6.98E-06	-6.24E-03	±	3.90E-03	9.41E+00	±	2.54E+00	-1.88E-03	±	7.34E-03	105.7	34.26	±	1.42	161.8	±	6.4
Total	1.85E-03	8.62E-04	±	7.48E-05	5.80E-02	±	4.12E-02	3.39E-03	±	1.52E-04	99.2	32.38	±	0.04	153.3	±	1.3

N97.MS3		J = .2739E-02 ± .2405E-04														
# 1	1.48E-05	8.50E-02	±	3.52E-03	-3.83E+00	±	5.16E+00	6.97E-03	±	2.81E-03	29.2	10.36	±	1.18	50.5	± 5.7
# 2	1.12E-05	1.94E-02	±	3.77E-03	-2.53E+00	±	4.59E+00	4.50E-03	±	2.29E-03	79.8	22.63	±	1.17	108.5	± 5.4
# 3	1.54E-05	5.96E-03	±	2.44E-03	-1.59E+00	±	3.23E+00	7.06E-03	±	2.48E-03	94.5	29.98	±	0.77	142.4	± 3.5
# 4	4.90E-05	3.92E-03	±	7.43E-04	-2.44E-01	±	9.65E-01	7.82E-03	±	8.80E-04	96.5	31.71	±	0.28	150.3	± 1.3
# 5	1.70E-04	3.88E-04	±	2.15E-04	2.64E-01	±	2.86E-01	5.84E-03	±	3.18E-04	99.7	32.97	±	0.11	156.0	± 0.5
# 6	2.30E-04	6.16E-05	±	1.63E-04	-1.03E-01	±	2.07E-01	6.73E-03	±	2.64E-04	99.9	32.95	±	0.08	155.9	± 0.4
# 7	1.64E-04	1.18E-04	±	2.51E-04	-6.96E-02	±	2.86E-01	7.46E-03	±	4.23E-04	99.9	32.77	±	0.14	155.1	± 0.6
# 8	1.58E-04	7.17E-04	±	2.25E-04	2.83E-01	±	3.00E-01	6.90E-03	±	3.34E-04	99.4	32.83	±	0.14	155.4	± 0.6
# 9	1.68E-04	4.99E-04	±	2.32E-04	1.03E-01	±	2.95E-01	5.69E-03	±	4.33E-04	99.6	33.37	±	0.16	157.8	± 0.7
# 10	9.26E-05	1.69E-03	±	3.93E-04	-1.55E-01	±	4.98E-01	5.42E-03	±	4.14E-04	98.5	33.00	±	0.16	156.1	± 0.7
# 11	1.05E-04	2.22E-03	±	3.40E-04	-1.90E-01	±	4.53E-01	6.38E-03	±	5.02E-04	98.0	32.81	±	0.16	155.3	± 0.7
# 12	3.22E-04	1.49E-03	±	1.26E-04	-3.06E-02	±	1.50E-01	5.76E-03	±	2.42E-04	98.7	32.82	±	0.10	155.3	± 0.4
# 13	7.60E-05	2.51E-04	±	5.73E-04	3.25E-01	±	4.68E-01	4.80E-03	±	4.45E-04	99.8	32.78	±	0.23	155.2	± 1.1
# 14	1.28E-04	5.10E-04	±	3.21E-04	-1.50E-01	±	2.66E-01	6.30E-03	±	6.67E-04	99.5	32.64	±	0.15	154.5	± 0.7
# 15	1.02E-04	1.21E-02	±	4.10E-04	1.25E-01	±	3.46E-01	5.95E-03	±	7.04E-04	90.1	32.49	±	0.16	153.8	± 0.7
# 16	6.71E-05	1.33E-02	±	6.25E-04	-4.57E-01	±	4.92E-01	5.56E-03	±	6.39E-04	89.2	32.44	±	0.24	153.6	± 1.1
# 17	2.18E-04	3.54E-03	±	1.98E-04	-7.08E-02	±	1.47E-01	6.48E-03	±	3.48E-04	96.9	32.60	±	0.12	154.3	± 0.6
# 18	5.96E-05	1.89E-02	±	7.52E-04	4.44E-01	±	6.26E-01	6.78E-03	±	8.23E-04	85.3	32.58	±	0.30	154.2	± 1.3
# 19	5.42E-05	5.15E-02	±	8.90E-04	-4.14E-01	±	6.13E-01	2.88E-03	±	9.58E-04	67.7	31.91	±	0.32	151.2	± 1.4
# 20	2.20E-05	1.49E-02	±	2.11E-03	8.71E-01	±	1.72E+00	8.25E-04	±	1.40E-03	88.1	32.42	±	0.72	153.5	± 3.3
# 21	4.64E-06	2.84E-02	±	8.65E-03	9.61E-01	±	7.09E+00	-7.06E-03	±	6.99E-03	79.4	32.23	±	2.76	152.6	± 12.6
# 22	2.14E-07	-9.17E-02	±	2.02E-01	4.78E+02	±	3.11E+02	-1.08E-01	±	1.28E-01	131.4	113.30	±	84.12	487.7	± 317.2
Total	2.23E-03	4.60E-03	±	8.63E-05	3.70E-03	±	9.38E-02	6.08E-03	±	1.14E-04	96.0	32.56	±	0.04	154.1	± 1.3
N98.MS3		J = .2737E-02 ± .2401E-04														
# 1	5.81E-06	1.82E-01	±	7.05E-03	2.28E+00	±	5.13E+00	-7.81E-03	±	5.27E-03	16.5	10.65	±	1.89	51.8	± 9.1
# 2	2.12E-06	2.36E-02	±	1.76E-02	9.37E+00	±	1.53E+01	-1.11E-02	±	1.41E-02	78.7	25.69	±	5.38	122.6	± 24.8
# 3	3.01E-05	7.88E-03	±	1.27E-03	1.88E-01	±	1.10E+00	5.58E-03	±	1.30E-03	93.1	31.33	±	0.44	148.4	± 2.0

# 4	3.94E-05	6.23E-03	±	9.45E-04	-1.48E-01	±	8.12E-01	4.46E-03	±	1.07E-03	94.8	33.55	±	0.35	158.5	± 1.6
# 5	4.75E-05	1.40E-01	±	1.23E-03	5.29E-01	±	6.37E-01	8.00E-03	±	1.18E-03	44.2	32.79	±	0.36	155.0	± 1.6
# 6	9.04E-05	3.11E-03	±	4.53E-04	4.12E-01	±	3.71E-01	7.61E-03	±	4.22E-04	97.3	32.45	±	0.17	153.5	± 0.8
# 7	9.22E-05	1.26E-03	±	4.24E-04	2.85E-01	±	3.39E-01	7.64E-03	±	5.06E-04	98.9	32.40	±	0.22	153.3	± 1.0
# 8	8.28E-05	1.32E-03	±	4.63E-04	-4.63E-01	±	3.74E-01	6.36E-03	±	5.76E-04	98.9	33.65	±	0.28	158.9	± 1.3
# 9	9.81E-05	8.61E-03	±	4.53E-04	2.58E-03	±	3.25E-01	8.21E-03	±	5.95E-04	92.7	32.27	±	0.20	152.7	± 0.9
# 10	6.55E-05	1.58E-03	±	5.82E-04	5.03E-01	±	5.67E-01	6.83E-03	±	5.86E-04	98.6	32.45	±	0.21	153.5	± 0.9
# 11	4.24E-05	5.33E-03	±	8.98E-04	-2.12E-01	±	8.93E-01	7.31E-03	±	1.13E-03	95.4	32.34	±	0.28	153.0	± 1.3
# 12	1.38E-04	2.10E-03	±	2.91E-04	-2.36E-01	±	2.28E-01	7.61E-03	±	4.91E-04	98.1	32.08	±	0.14	151.8	± 0.6
# 13	1.52E-04	1.78E-03	±	2.66E-04	9.24E-02	±	2.21E-01	5.48E-03	±	5.56E-04	98.4	31.95	±	0.12	151.2	± 0.6
# 14	8.65E-05	2.17E-03	±	4.42E-04	-3.94E-01	±	4.07E-01	5.62E-03	±	6.32E-04	98.0	31.60	±	0.20	149.7	± 0.9
# 15	9.27E-05	1.34E-03	±	4.13E-04	1.76E-02	±	3.61E-01	6.04E-03	±	3.68E-04	98.8	31.89	±	0.15	151.0	± 0.7
# 16	2.15E-05	1.26E-03	±	1.79E-03	-2.96E-01	±	1.61E+00	6.30E-03	±	1.78E-03	98.8	31.19	±	0.62	147.8	± 2.8
# 17	8.67E-05	1.37E-04	±	4.60E-04	5.19E-01	±	3.66E-01	5.65E-03	±	5.34E-04	99.9	32.65	±	0.21	154.4	± 0.9
Total	1.17E-03	9.24E-03	±	1.40E-04	8.12E-02	±	1.16E-01	6.55E-03	±	1.72E-04	92.2	32.19	±	0.06	152.3	± 1.3
N99.MS3		J = .2737E-02 ± .2402E-04														
# 1	1.35E-05	5.70E-02	±	3.38E-03	-5.53E-01	±	3.44E+00	1.86E-02	±	3.82E-03	50.6	17.25	±	1.02	83.3	± 4.8
# 2	7.63E-06	6.75E-03	±	5.79E-03	8.82E+00	±	5.75E+00	1.37E-02	±	3.85E-03	94.3	32.77	±	1.80	155.0	± 8.1
# 3	8.51E-05	1.66E-03	±	5.29E-04	-2.85E-01	±	5.34E-01	5.54E-03	±	6.47E-04	98.5	32.44	±	0.19	153.5	± 0.9
# 4	1.75E-04	1.09E-03	±	2.52E-04	-4.29E-02	±	2.74E-01	5.09E-03	±	4.12E-04	99.0	32.56	±	0.12	154.0	± 0.5
# 5	1.12E-04	3.49E-04	±	4.07E-04	-3.58E-02	±	4.09E-01	3.61E-03	±	4.49E-04	99.7	32.38	±	0.14	153.2	± 0.6
# 6	1.69E-04	1.37E-03	±	2.66E-04	-3.59E-02	±	2.83E-01	5.19E-03	±	4.19E-04	98.8	32.67	±	0.14	154.5	± 0.6
# 7	6.82E-05	4.51E-03	±	6.83E-04	-3.98E-01	±	6.53E-01	2.47E-03	±	6.60E-04	96.0	32.32	±	0.23	152.9	± 1.1
# 8	9.69E-05	6.35E-03	±	4.90E-04	-2.16E-01	±	4.89E-01	3.56E-03	±	6.88E-04	94.6	32.84	±	0.17	155.3	± 0.8
# 9	1.18E-04	3.20E-03	±	3.82E-04	-2.41E-02	±	3.88E-01	4.78E-03	±	4.10E-04	97.2	32.26	±	0.17	152.7	± 0.8
# 10	1.08E-04	1.08E-03	±	4.26E-04	-4.95E-02	±	4.38E-01	4.57E-03	±	4.97E-04	99.0	32.04	±	0.15	151.7	± 0.7
# 11	8.05E-05	1.58E-03	±	5.60E-04	-5.34E-01	±	5.72E-01	4.80E-03	±	5.90E-04	98.6	32.19	±	0.19	152.3	± 0.9
# 12	2.56E-04	4.78E-04	±	1.75E-04	-9.56E-02	±	1.74E-01	5.01E-03	±	2.45E-04	99.6	32.41	±	0.13	153.4	± 0.6

# 13	1.03E-04	4.48E-04	±	4.34E-04	-2.63E-01	±	4.45E-01	4.22E-03	±	6.06E-04	99.6	32.25	±	0.17	152.6	±	0.8
# 14	8.16E-05	2.25E-03	±	5.50E-04	2.86E-01	±	5.97E-01	4.55E-03	±	5.49E-04	98.0	32.60	±	0.22	154.2	±	1.0
# 15	1.35E-05	5.79E-03	±	3.49E-03	1.82E+00	±	3.45E+00	3.49E-03	±	2.20E-03	95.0	32.26	±	1.09	152.7	±	4.9
# 16	1.21E-04	2.11E-03	±	3.69E-04	4.29E-01	±	3.69E-01	4.13E-03	±	4.13E-04	98.1	32.62	±	0.17	154.3	±	0.8
# 17	2.14E-06	-2.33E-03	±	2.08E-02	7.89E-01	±	2.08E+01	-1.69E-02	±	1.36E-02	102.0	34.44	±	6.36	162.5	±	28.7
Total	1.61E-03	2.26E-03	±	1.16E-04	-1.96E-02	±	1.18E-01	4.69E-03	±	1.35E-04	98.0	32.32	±	0.05	152.9	±	1.3

N100.MS3		J = .2736E-02 ± .2400E-04															
# 1	6.70E-06	1.19E-01	±	5.22E-03	5.01E+00	±	5.57E+00	1.24E-03	±	5.76E-03	30.6	15.49	±	1.54	74.9	±	7.3
# 2	3.87E-06	4.10E-02	±	8.87E-03	4.46E+00	±	1.01E+01	5.96E-03	±	9.79E-03	68.3	26.07	±	2.77	124.3	±	12.8
# 3	8.61E-05	2.26E-02	±	6.26E-04	4.27E-01	±	4.57E-01	4.78E-03	±	8.38E-04	81.3	29.07	±	0.23	138.1	±	1.1
# 4	3.58E-05	3.83E-03	±	1.04E-03	1.25E+00	±	1.18E+00	4.45E-03	±	1.22E-03	96.6	31.65	±	0.36	149.9	±	1.6
# 5	1.03E-04	3.26E-03	±	3.55E-04	3.29E-01	±	4.08E-01	6.06E-03	±	7.85E-04	97.1	32.48	±	0.15	153.6	±	0.7
# 6	2.01E-04	4.70E-04	±	1.70E-04	-8.78E-02	±	1.96E-01	5.66E-03	±	3.61E-04	99.6	32.90	±	0.10	155.5	±	0.5
# 7	1.08E-04	2.50E-03	±	3.15E-04	1.44E-02	±	4.07E-01	6.00E-03	±	4.86E-04	97.8	32.83	±	0.17	155.2	±	0.8
# 8	8.90E-05	5.85E-03	±	4.25E-04	-2.08E-01	±	4.45E-01	6.15E-03	±	7.56E-04	95.0	32.49	±	0.20	153.6	±	0.9
# 9	9.64E-05	6.67E-03	±	3.77E-04	3.99E-02	±	4.11E-01	6.90E-03	±	7.23E-04	94.4	32.95	±	0.20	155.7	±	0.9
# 10	7.38E-05	3.89E-03	±	4.86E-04	2.00E-01	±	5.63E-01	6.38E-03	±	7.92E-04	96.6	33.08	±	0.19	156.3	±	0.9
# 11	1.56E-04	4.34E-03	±	2.27E-04	1.21E-01	±	2.89E-01	6.90E-03	±	4.64E-04	96.2	32.80	±	0.16	155.1	±	0.7
# 12	1.03E-04	1.30E-02	±	4.38E-04	-3.81E-01	±	3.82E-01	5.65E-03	±	5.10E-04	89.4	32.38	±	0.18	153.2	±	0.8
# 13	1.14E-04	1.54E-03	±	3.17E-04	-9.29E-02	±	3.71E-01	6.65E-03	±	4.64E-04	98.6	32.24	±	0.15	152.5	±	0.7
# 14	1.14E-04	2.38E-03	±	3.09E-04	2.27E-01	±	3.50E-01	5.30E-03	±	5.20E-04	97.9	32.16	±	0.20	152.1	±	0.9
# 15	7.03E-05	2.44E-03	±	5.48E-04	-9.00E-02	±	6.07E-01	4.62E-03	±	7.82E-04	97.8	32.01	±	0.21	151.5	±	1.0
# 16	1.28E-04	3.65E-03	±	2.92E-04	2.60E-01	±	3.05E-01	6.35E-03	±	5.33E-04	96.8	32.20	±	0.12	152.4	±	0.5
# 17	4.38E-05	5.05E-03	±	8.59E-04	5.79E-01	±	9.83E-01	7.30E-03	±	1.23E-03	95.5	31.67	±	0.32	149.9	±	1.4
# 18	2.66E-05	1.99E-02	±	1.44E-03	2.27E+00	±	1.49E+00	3.03E-03	±	1.51E-03	83.5	29.69	±	0.48	140.9	±	2.2
# 19	4.85E-05	7.75E-03	±	7.15E-04	6.78E-02	±	7.74E-01	3.63E-03	±	8.72E-04	93.2	31.50	±	0.25	149.2	±	1.1
# 20	3.09E-06	-9.02E-03	±	1.11E-02	-9.55E+00	±	1.30E+01	-1.44E-02	±	1.25E-02	109.0	32.44	±	3.59	153.4	±	16.3
Total	1.61E-03	5.83E-03	±	1.04E-04	1.43E-01	±	1.13E-01	5.83E-03	±	1.61E-04	94.9	32.17	±	0.05	152.2	±	1.3

N101.MS3		J = .2740E-02 ± .2407E-04														
# 1	1.46E-05	1.19E-02	±	2.50E-03	1.96E+00	±	2.90E+00	2.98E-03	±	2.96E-03	65.7	6.71	±	0.76	32.9	± 3.7
# 2	3.95E-05	1.15E-02	±	9.34E-04	1.15E-01	±	1.03E+00	1.07E-03	±	1.31E-03	73.0	9.21	±	0.29	45.0	± 1.4
# 3	4.73E-05	1.01E-03	±	7.19E-04	-2.03E-01	±	7.45E-01	2.09E-04	±	8.84E-04	97.8	13.20	±	0.22	64.1	± 1.1
# 4	2.80E-05	8.01E-04	±	1.14E-03	-1.04E+00	±	1.33E+00	-4.80E-04	±	1.60E-03	98.7	17.38	±	0.39	84.0	± 1.8
# 5	2.25E-05	1.97E-03	±	1.59E-03	1.35E+00	±	1.61E+00	1.93E-03	±	1.93E-03	97.3	20.60	±	0.50	99.1	± 2.3
# 6	3.96E-05	-8.50E-04	±	8.59E-04	6.51E-02	±	8.45E-01	4.30E-03	±	1.06E-03	100.9	27.79	±	0.28	132.4	± 1.3
# 7	2.17E-05	-2.04E-03	±	1.45E-03	-2.52E-01	±	1.53E+00	5.05E-03	±	2.21E-03	102.1	29.62	±	0.50	140.8	± 2.3
# 8	2.41E-05	1.98E-04	±	1.37E-03	-2.53E-01	±	1.52E+00	5.75E-03	±	1.73E-03	99.8	30.99	±	0.46	147.1	± 2.1
# 9	2.14E-05	3.43E-03	±	1.53E-03	4.69E-01	±	1.62E+00	1.89E-03	±	1.89E-03	96.8	30.99	±	0.50	147.1	± 2.3
# 10	5.25E-05	3.11E-03	±	6.36E-04	-5.13E-01	±	6.28E-01	3.68E-03	±	1.10E-03	97.2	32.03	±	0.24	151.8	± 1.1
# 11	4.62E-06	7.60E-02	±	7.20E-03	-1.13E+01	±	7.62E+00	-2.46E-05	±	8.87E-03	50.0	22.42	±	2.19	107.6	± 10.2
# 12	1.10E-05	5.22E-03	±	3.12E-03	-7.54E+00	±	3.14E+00	4.29E-03	±	3.75E-03	91.7	17.05	±	0.96	82.4	± 4.5
Total	3.27E-04	4.02E-03	±	3.60E-04	-4.16E-01	±	3.83E-01	2.52E-03	±	4.77E-04	94.9	21.92	±	0.12	105.2	± 1.0

N102.MS3		J = .2740E-02 ± .2407E-04														
# 1	4.59E-06	8.25E-02	±	1.03E-02	1.03E+01	±	1.24E+01	-1.38E-02	±	8.24E-03	52.6	27.09	±	3.20	129.2	± 14.7
# 2	7.17E-06	1.25E-02	±	6.23E-03	-2.14E-02	±	7.58E+00	-1.94E-03	±	4.93E-03	89.9	32.88	±	2.05	155.6	± 9.3
# 3	1.55E-05	8.97E-03	±	2.91E-03	-5.03E+00	±	3.49E+00	-2.00E-03	±	2.26E-03	92.6	33.00	±	0.96	156.2	± 4.4
# 4	1.83E-05	-2.39E-03	±	2.48E-03	-3.91E-01	±	3.31E+00	5.16E-03	±	2.41E-03	102.1	33.81	±	0.84	159.9	± 3.8
# 5	1.58E-05	7.97E-04	±	2.98E-03	5.10E-01	±	3.61E+00	3.31E-03	±	2.37E-03	99.3	33.06	±	0.99	156.5	± 4.5
# 6	3.05E-05	4.35E-04	±	1.47E-03	-1.15E+00	±	1.82E+00	3.92E-03	±	1.35E-03	99.6	32.41	±	0.50	153.5	± 2.3
# 7	3.55E-05	6.40E-04	±	1.31E-03	-7.00E-01	±	1.63E+00	3.81E-03	±	1.22E-03	99.4	33.22	±	0.45	157.2	± 2.0
# 8	2.28E-05	6.24E-04	±	2.02E-03	1.48E+00	±	2.49E+00	2.11E-03	±	1.74E-03	99.5	34.13	±	0.65	161.3	± 3.0
# 9	3.59E-05	3.70E-04	±	1.27E-03	8.77E-01	±	1.71E+00	5.75E-03	±	1.22E-03	99.7	34.28	±	0.48	162.0	± 2.2
# 10	1.04E-04	3.55E-04	±	4.33E-04	4.21E-01	±	5.28E-01	2.22E-03	±	5.63E-04	99.7	32.76	±	0.17	155.1	± 0.8
# 11	4.81E-05	6.37E-04	±	9.45E-04	-2.48E-01	±	1.17E+00	4.32E-03	±	9.45E-04	99.4	32.50	±	0.37	153.9	± 1.7
# 12	7.83E-05	-7.38E-05	±	6.22E-04	1.24E+00	±	8.11E-01	2.70E-03	±	9.05E-04	100.1	32.67	±	0.23	154.7	± 1.1

# 13	4.78E-05	4.88E-07	±	9.59E-04	3.01E-01	±	1.21E+00	5.24E-03	±	8.94E-04	100.0	32.26	±	0.32	152.8	±	1.4
# 14	3.95E-06	2.90E-03	±	1.17E-02	1.14E+00	±	1.38E+01	-6.61E-03	±	8.86E-03	97.3	30.40	±	3.70	144.3	±	16.9
# 15	2.54E-05	1.54E-03	±	1.75E-03	8.15E-01	±	2.16E+00	3.51E-03	±	1.68E-03	98.6	31.70	±	0.59	150.3	±	2.7
Total	4.94E-04	1.52E-03	±	3.60E-04	2.92E-01	±	4.48E-01	3.06E-03	±	3.49E-04	98.7	32.79	±	0.12	155.2	±	1.4
N103.MS3		J = .2740E-02 ± .2407E-04															
# 1	1.33E-05	3.46E+00	±	3.72E-02	2.58E+00	±	2.96E+00	-4.96E-03	±	5.59E-03	5.4	58.59	±	4.23	268.6	±	18.0
# 2	1.02E-06	4.94E-02	±	4.71E-02	-5.36E+01	±	4.15E+01	1.96E-02	±	5.54E-02	21.3	3.95	±	14.12	19.4	±	69.1
# 3	2.30E-06	2.20E-02	±	2.12E-02	-1.89E+01	±	1.82E+01	-6.46E-03	±	2.44E-02	63.7	11.41	±	6.38	55.6	±	30.6
# 4	4.47E-06	3.71E-02	±	1.05E-02	-1.21E+01	±	1.01E+01	-6.66E-03	±	1.22E-02	61.6	17.57	±	3.18	84.8	±	15.0
# 5	4.95E-05	6.20E-03	±	9.72E-04	-6.56E-01	±	9.55E-01	1.25E-03	±	1.37E-03	93.9	28.21	±	0.31	134.3	±	1.4
# 6	5.19E-05	2.68E-03	±	9.57E-04	-5.04E-01	±	8.24E-01	4.61E-03	±	1.12E-03	97.6	32.36	±	0.34	153.3	±	1.5
# 7	7.07E-05	1.34E-03	±	6.67E-04	-3.45E-01	±	6.02E-01	4.38E-03	±	9.41E-04	98.8	32.86	±	0.24	155.5	±	1.1
# 8	7.04E-05	1.39E-03	±	6.92E-04	-4.52E-02	±	5.96E-01	5.79E-03	±	1.00E-03	98.8	33.04	±	0.22	156.3	±	1.0
# 9	1.69E-04	1.96E-03	±	2.97E-04	2.19E-01	±	2.81E-01	6.01E-03	±	5.51E-04	98.3	33.51	±	0.14	158.5	±	0.6
# 10	7.73E-05	2.00E-03	±	6.15E-04	3.68E-01	±	5.35E-01	4.54E-03	±	8.10E-04	98.3	33.50	±	0.23	158.4	±	1.0
# 11	7.04E-05	5.14E-03	±	6.70E-04	-3.89E-01	±	5.73E-01	3.12E-03	±	9.83E-04	95.6	32.76	±	0.26	155.1	±	1.2
# 12	9.37E-05	7.66E-03	±	5.56E-04	7.34E-01	±	4.53E-01	4.85E-03	±	9.22E-04	93.7	33.70	±	0.20	159.4	±	0.9
# 13	4.64E-05	9.90E-03	±	1.03E-03	-8.49E-01	±	9.28E-01	6.28E-03	±	1.42E-03	92.7	37.18	±	0.39	175.0	±	1.8
# 14	5.45E-05	7.33E-03	±	9.15E-04	1.48E-01	±	8.00E-01	4.59E-03	±	1.23E-03	94.0	33.82	±	0.32	159.9	±	1.5
# 15	8.80E-05	6.17E-03	±	5.59E-04	-3.69E-01	±	4.69E-01	5.37E-03	±	1.04E-03	94.9	33.54	±	0.21	158.6	±	0.9
# 16	7.95E-05	7.71E-03	±	6.22E-04	1.71E-01	±	5.52E-01	5.69E-03	±	9.60E-04	93.4	32.46	±	0.24	153.7	±	1.1
# 17	6.88E-05	8.75E-03	±	6.96E-04	1.68E-01	±	6.97E-01	4.68E-03	±	1.09E-03	92.4	31.61	±	0.25	149.9	±	1.1
# 18	1.08E-04	1.14E-03	±	4.39E-04	-1.25E-01	±	4.28E-01	4.96E-03	±	7.39E-04	99.0	31.99	±	0.23	151.6	±	1.1
# 19	1.35E-04	1.05E-03	±	3.61E-04	1.32E-01	±	3.51E-01	4.04E-03	±	5.49E-04	99.1	32.60	±	0.20	154.4	±	0.9
# 20	4.62E-05	3.22E-03	±	1.02E-03	-5.31E-01	±	9.51E-01	2.95E-03	±	1.25E-03	97.1	31.70	±	0.49	150.3	±	2.2
# 21	1.27E-04	2.66E-03	±	3.79E-04	-3.20E-01	±	3.24E-01	5.40E-03	±	5.21E-04	97.6	32.13	±	0.21	152.2	±	0.9
Total	1.43E-03	3.64E-02	±	1.94E-04	-1.38E-01	±	1.40E-01	4.67E-03	±	2.28E-04	75.4	32.93	±	0.07	155.9	±	1.4

N104.MS3		J = .2739E-02 ± .2404E-04															
# 1	5.84E-06	3.93E-01	±	1.13E-02	-1.16E+01	±	8.96E+00	-1.35E-03	±	8.01E-03	5.6	6.91	±	2.62	33.8	±	12.7
# 2	2.01E-06	2.76E-03	±	1.84E-02	-2.17E+01	±	2.63E+01	-3.42E-03	±	1.96E-02	97.4	30.42	±	6.05	144.4	±	27.6
# 3	7.18E-06	-4.57E-03	±	5.22E-03	1.73E+00	±	7.69E+00	-6.49E-03	±	5.75E-03	104.7	29.96	±	1.71	142.3	±	7.8
# 4	1.01E-05	-4.26E-03	±	3.71E-03	4.37E+00	±	5.32E+00	1.32E-03	±	4.00E-03	104.0	33.00	±	1.24	156.1	±	5.6
# 5	4.46E-05	5.59E-05	±	8.22E-04	3.44E-01	±	1.23E+00	2.50E-03	±	1.25E-03	100.0	32.78	±	0.29	155.1	±	1.3
# 6	5.07E-05	-7.70E-05	±	7.26E-04	3.44E-01	±	1.13E+00	2.56E-03	±	8.57E-04	100.1	32.84	±	0.30	155.4	±	1.4
# 7	4.43E-05	9.24E-04	±	8.35E-04	-8.49E-01	±	1.17E+00	2.48E-03	±	1.11E-03	99.2	33.20	±	0.36	157.0	±	1.6
# 8	2.99E-05	-1.19E-03	±	1.25E-03	-6.00E-01	±	1.83E+00	3.45E-03	±	1.35E-03	101.1	33.72	±	0.50	159.4	±	2.3
# 9	6.79E-05	-5.84E-04	±	5.43E-04	-1.59E-01	±	7.69E-01	4.87E-03	±	7.85E-04	100.5	33.06	±	0.25	156.4	±	1.1
# 10	2.81E-05	-6.86E-04	±	1.30E-03	1.08E+00	±	2.03E+00	4.05E-03	±	1.62E-03	100.6	33.29	±	0.50	157.4	±	2.3
# 11	2.04E-05	3.48E-03	±	1.84E-03	-2.39E+00	±	2.56E+00	3.82E-03	±	2.49E-03	96.8	31.28	±	0.63	148.3	±	2.9
# 12	1.17E-05	2.68E-04	±	3.23E-03	5.39E-01	±	4.54E+00	4.06E-03	±	4.04E-03	99.8	31.41	±	1.12	148.9	±	5.1
# 13	7.41E-06	-1.53E-03	±	4.86E-03	2.79E+00	±	7.23E+00	5.09E-03	±	6.16E-03	101.4	33.59	±	1.65	158.8	±	7.5
# 14	4.98E-05	9.86E-04	±	7.21E-04	-1.20E-01	±	1.07E+00	4.77E-03	±	9.84E-04	99.1	32.16	±	0.27	152.3	±	1.2
Total	3.80E-04	6.01E-03	±	3.74E-04	-2.27E-01	±	5.31E-01	3.29E-03	±	4.58E-04	94.8	32.35	±	0.14	153.2	±	1.4

Appendix table 8 Composition of the Qitianling granite and other plutonic and volcanic rocks

Samples	Qitianling						Watergums	Jamon	Wangrah		Lyngdal	Pinatubo
	QTL38C		QTL14A		QTL13		GIG-I	HBMzG	AB412	AB422	98N06	Dry glass
	Granite	Glass(20)	Granite	Glass(20)	Granite	Glass(20)	Granite	Granite	Granite	Granite	Granodiorite	Dacite
Exp-T(℃)	660-900		660-900		660-900		725-1000	700-900	700-900		775-1000	750-900
Exp-P (MPa)	100,200,300,360,400,700		100,200,300,360,400,700		100,200,300,360,400,700		100	300	200		200,400	220
Exp-fo_2	~NNO-1.3, ~NNO+3		~NNO-1.3, ~NNO+3		~NNO-1.3, ~NNO+2.5		QFM+0.3	NNO-1.5, NNO+2.5	~NNO		NNO-0.4 ~NNO+0.8	>NNO <NNO+2.7
wt.%												
SiO_2	65.72	64.78	68.07	68.17	70.92	71.11	73.60	70.62	70.45	72.53	65.20	64.60
TiO_2	1.04	1.06	0.73	0.67	0.38	0.33	0.34	0.68	0.54	0.37	1.11	0.53
Al_2O_3	13.58	13.91	14.35	14.35	13.79	13.92	12.44	12.92	13.26	13.08	14.40	16.50
Fe_2O_3	1.68		1.12		0.60		1.42	2.00				
FeO	4.22		2.98		1.97		1.49	2.37				
FeOT	5.74	5.51	3.99	3.96	2.51	2.46		4.17	4.06	2.50	5.80	4.37
MnO	0.10	0.11	0.07	0.07	0.04	0.06	0.08	0.07	0.08	0.05	0.10	
MgO	1.37	1.38	0.89	0.89	0.42	0.43	0.27	0.69	0.61	0.48	1.39	2.39
CaO	3.27	3.30	2.46	2.46	1.82	1.83	1.24	2.47	1.93	1.31	3.51	5.23
Na_2O	2.95	3.11	3.00	2.79	3.06	2.99	3.53	3.54	3.39	3.32	3.28	4.49
K_2O	3.91	4.21	5.17	5.31	5.38	5.58	4.23	3.52	3.98	4.88	4.32	1.54
P_2O_5	0.33	0.35	0.24	0.21	0.12	0.10	0.07	0.30	0.18	0.12	0.39	0.01
H_2O								0.57				
LOI	0.91		1.29		1.17			0.34	0.23	0.17		
F	0.20		0.19		0.15		0.12	0.12		0.10		
Total	98.91		100.24		99.62			99.32	98.71	98.81	99.50	99.66
A/CNK	0.90		0.96		0.97			0.91	0.99	1.00	0.87	0.89
X_{Fe}	0.81	0.80	0.82	0.82	0.86	0.85	0.91	0.86	0.87	0.84	0.81	0.65

Numbers in parentheses indicate the number of analyses; bulk rock or starting materials cited from: Watergums (Clemens et al.,1986), Jamon (Dall'Agnol et al.,1999), Wangrah (Klimm et al., 2008), Lyngdal (Bogaerts et al.,2003), Pinatubo (Prouteau and Scaillet, 2003)

Appendix table 9 Experimental results of 3 compositions (QTL-38C, QTL-14A and QTL-13)

Charge	XH_2O^{in}	$^{1}H_2O_{melt}$wt%	$^{2}H_2O_{melt}$wt%	△NNO[3]	△NNO[4]	Phase assemblage and phase proportions (wt%)	Σr^2
T: 660 ℃; P: 206MPa; run duration: 1337h							
38-01	1.00	6.45	—	-1.36	-1.36	Gl, Cpx, Bt, Ilm, Pl, Kfs, Qtz	—
38-02	0.91	6.02	—	-1.44		Cpx, Bt, Ilm, Pl, Kfs, Qtz	—
38-03	0.80	5.44	—	-1.55		Cpx, Bt, Ilm, Pl, Kfs, Qtz	—
T: 700 ℃; P: 202MPa; run duration: 689h							
38-04	1.00	6.39	6.91	-1.15	-1.15	Gl(59.9), Cpx(5.6), Bt(14.2), Ilm(0.1), Pl(19.9), Qtz(0.4)	0.32
38-05	0.87	5.87	—	-1.28		Cpx, Bt, Ilm, Pl, Kfs, Qtz	—
38-06	0.76	5.20	—	-1.40		Cpx, Bt, Ilm, Pl, Kfs, Qtz	—
T: 750 ℃; P: 194MPa; run duration: 471h							
38-07	0.93	5.80	6.84	-1.21	-1.27	Gl(62.1), Cpx(6.6), [Amp(0.5)], Bt(13.7), Ilm(0.7), Pl(16.5)	1.09
38-08	0.78	5.07	6.48	-1.36	-1.55	Gl(55.2), Cpx(8.7), Bt(12.1), Ilm(1.1), Pl(20.5), Kfs(<0.1), Qtz(2.5)	0.88
38-09	0.71	4.74	4.09	-1.44	-1.94	Gl, Cpx, Bt, Ilm, Pl, Kfs, Qtz	—
38-10	0.61	4.27	—	-1.57		(Gl), Cpx, Bt, Ilm, Pl, Kfs, Qtz	—
T:800 ℃; P: 203MPa; run duration: 351h							
38-11	1.00	6.26	7.84	-1.34	-1.34	Gl(74.8), Amp(7.6), Bt(10.1), Mag(-0.5), Ilm(1.2), Pl(6.9)	0.72
38-12	0.91	5.71	7.16	-1.42	-1.53	Gl(66.6), Lpx(-0.6), Cpx(7.0), Bt(12.4), Ilm(0.7), Pl(13.9)	0.08
38-13	0.78	5.07	6.00	-1.56	-1.78	Gl(61.4), Lpx(2.6), Cpx(5.3), Bt(9.1), Ilm(0.9), Pl(20.7)	0.06
38-14	0.71	4.75	5.58	-1.64	-1.96	Gl(56.7), Lpx(3.8), Cpx(6.0), Bt(8.2), Ilm(1.2), Pl(24.2)	0.02
38-15	0.61	4.27	—	-1.77		Gl, Lpx, Bt, Ilm, Pl, Qtz	—
38-16	0.51	3.78	—	-1.93		Gl, Lpx, Bt, Ilm, Pl, Kfs, Qtz	—
T: 850 ℃; P: 199MPa; run duration: 181h							
38-17	1.00	5.90	6.78	-0.96	-0.96	Gl(86.7), Lpx(-2.0), Cpx(2.9), Amp(4.1), Bt(5.9), Mag(2.1), Ilm(0.4)	0.23
38-18	0.90	5.47	7.12	-1.05	-1.20	Gl(83.5), Lpx(1.0), Cpx(trace), Amp(14.6), Bt(0), Ilm(1.3), Pl(-0.5)	1.34
38-19	0.79	4.95	4.67	-1.17	-1.40	Gl(74.2), Lpx(5.8), Cpx(4.5), Bt(2), Ilm(1.6), Pl(11.9)	0.22
38-20	0.69	4.50	5.23	-1.28	-1.74	Gl(69.9), Lpx(6.5), Cpx(4.4), Bt(1.6), Ilm(1.7), Pl(15.8)	0.22
38-21	0.61	4.13	4.85	-1.39	-2.21	Gl(70.6), Lpx(8.1), Cpx(2.7), Bt(1.9), Ilm(1.8), Pl(15.0)	0.34
38-22	0.53	3.76	4.10	-1.51		Gl(90.0), Lpx(6.1), Cpx(2.9), Bt(4.3), Ilm(1.1), Pl(-4.4)	0.63
38-23	0.38	3.02	3.14	-1.80		Gl(75.7), Lpx(8.9), Cpx(1.1), Bt(1.2), Ilm(0.9), Pl(12.1)	0.16
T: 900 ℃; P: 195MPa; run duration: 138h							
38-24	1.00	5.66	6.29	-0.91	-0.91	Gl(92.0), Lpx(3.9), Cpx(1.3), Bt(7.1), Ilm(0.2)	0.74
38-25	0.90	5.25	5.55	-1.00	-1.13	Gl(91.9), Lpx(4.2), Cpx(2.7), Ilm(1.2)	2.71
38-26	0.80	4.79	4.72	-1.10	-1.42	Gl(93.0), Lpx(5.7), Ilm(1.2)	1.82
38-27	0.71	4.36	5.41	-1.21	-2.00	Gl(91.4), Lpx(1.4), Cpx(4.59), Ilm(1.4)	0.41
38-28	0.62	3.93	3.98	-1.32	-2.34	Gl(85.6), Cpx(5.1), Lpx(2.6), Ilm(1.1)	0.56
38-29	0.53	3.47	3.70	-1.46	-2.63	Gl(79.9), Cpx(4.2), Lpx(4.2), Ilm(1.4)	0.71
38-30	0.38	3.00	—	-1.75		Gl(70.1), Cpx(-4.5), Lpx(15.4), Ilm(0.9)	0.48
T: 660 ℃; P: 298MPa; run duration: 1267h							
38-31	1.00	8.39	—	-1.39		Cpx, Bt, Ilm, Pl, Kfs, Qtz	—
38-31a	1.00	8.39	—			Cpx, Bt, Ilm, Pl, Kfs, Qtz, Amp, Ttn	—
T: 700 ℃; P: 316MPa; run duration: 570h							

38-32	1.00	8.63	10.87			Gl(66.1), Cpx(5.2), Amp(-1.1), Bt(16.4), Ilm(0.7), Pl(12.7)	0.78
T: 750 ℃; P: 300MPa; run duration: 571h							
38-33	1.00	8.20	9.17	-0.96	-0.96	Gl(72.9), Amp(9.4), Bt(9.6), Ilm(1.0), Pl(7.2), Mag(<0.1)	0.24
38-34	0.90	7.37	8.85	-1.05	-1.21	Gl(62.5), Amp(9.4), Bt(12.5), Ilm(0.8), Pl(16.2), Mag(-1.3)	0.2
38-35	0.80	6.76	7.67	-1.15	-1.55	Gl(60.2), Cpx(5.7), Amp(<0.1), Bt(14.5), Ilm(0.7), Pl(18.9)	0.04
38-37	0.60	5.44	—	-1.40		Gl, Cpx, Bt, Ilm, Pl, Kfs, Qtz	—
T: 800 ℃; P: 299MPa; run duration: 356h							
38-38	1.00	8.04	8.64	-0.90	-0.90	Gl(83.2), Amp(8.4), Bt(7.3), Ilm(1.1)	0.92
38-39	0.90	7.38	8.03	-0.99	-1.24	Gl(78.8), Amp(8.5), Ilm(0.9), Pl(5.2), Bt(6.5), Mag(0.2)	0.07
38-40	0.80	6.73	7.47	-1.10	-1.60	Gl(70.7), Amp(6.4), Lpx(2.5), Ilm(0.7), Pl(11.3), Bt(8.4)	0.2
38-41	0.70	6.03	6.29	-1.21	-2.05	Gl(67.4), Cpx(3.9), Lpx(4.0), Ilm(0.6), Pl(16.1), Bt(7.9)	0.13
38-42	0.60	5.41	5.95	-1.35	-1.96	Gl(50.7), Cpx(3.7), Lpx(5.9), Ilm(1.3), Pl(21.4), Bt(7.1)	0.58
T: 660 ℃; P: 362MPa; run duration: 648h							
38-43	1.00	9.66	9.72	-1.05		Gl(63.4), Cpx(6.6), Bt(16.9), Ilm(0.6), Pl(12.2), Qtz(<0.1), Ttn(0.2)	0.39
T: 700 ℃; P: 412MPa; run duration: 648h							
38-44	1.00	10.62	9.40	-1.38	-1.38	Gl(71.5), Cpx(6.4), Amp(-2.3), Bt(16.9), Ilm(0.8), Pl(6.7)	0.22
38-45	0.90	9.68	—	-1.48		Gl, Cpx, Bt, Ilm, Pl, Kfs, Qtz	—
38-46	0.80	8.82	—	-1.58		Gl, Cpx, Bt, Ilm, Pl, Kfs, Qtz	—
38-47	0.70	7.85	—	-1.69		Gl, Cpx, Amp, Bt, Ilm	—
T: 800 ℃; P: 360MPa; run duration: 263h							
38-48	1.00	9.33	9.74			Gl(81.2), Cpx(0.4), Amp(6.3), Bt(11.4), Mag(-0.1), Ilm(0.9)	2.49

Charge	**P(Mpa)**	**H_2O_{melt}wt%**	**H_2O^{melt}wt%**	**△NNO**	**Phase assemblage and phase proportions (wt%)**	**Σr^2**
T: 700 ℃; $XH2O^{in}$=1; run duration: 501h						
38-49	206	6.47	—	3.00	Gl, Cpx, Bt, Mag, Pl	—
T: 800 ℃; $XH2O^{in}$=1; run duration: 332h, 312h, 281h, 277h						
38-50	91	3.82	—	3.00	Gl, Cpx, Bt, Mag, Pl	—
38-51	205	6.17	—	3.00	Gl, Cpx, Amp, Bt, Mag, Pl	—
38-52	363	9.40	—	3.00	Gl, Cpx, Amp, Bt, Mag	—
38-53	673	—	—	3.00	Gl, Bt, Mag, Ttn	—
38-54	673	—	—	3.00	Gl, Cpx, Amp, Bt, Mag, Ttn	—

Charge	**XH_2O^{in}**	**[1]H_2O_{melt}wt%**	**[2]H_2O^{melt}wt%**	**△NNO[3]**	**△NNO[4]**	**Phase assemblage and proportions (wt%)**	**Σr^2**
T: 660 ℃; P: 200MPa; run duration: 1337h							
14-01	1.00	6.45	6.57	-1.36	-1.36	Gl, Cpx, Bt, Ilm, Pl, Kfs, Qtz	—
14-02	0.90	5.97	—	-1.45		Gl, Cpx, Bt, Ilm, Pl, Kfs, Qtz	—
14-03	0.80	5.44	—	-1.55		Gl, Cpx, Bt, Ilm, Pl, Kfs, Qtz	—
T: 700 ℃; P: 200MPa; run duration: 689h							
14-04	1.00	6.39	6.59	-1.15	-1.15	Gl(61.4), Cpx(2.8), Bt(10.4), Ilm(0.1), Pl(15.9), Kfs(9.4), Qtz(<0.1)	0.08
14-05	0.90	5.92	—	-1.25		Gl, Cpx, Bt, Ilm, Pl, Kfs, Qtz	—
14-06	0.76	5.20	—	-1.39		Gl, Cpx, Bt, Ilm, Pl, Kfs, Qtz	—
T: 750 ℃; P: 200MPa; run duration: 471h							
14-07	0.90	5.66	7.18	-1.23	-1.34	Gl(70.1), Cpx(2.3), Bt(13.9), Ilm(<0.1), Pl(13.8), Qtz(<0.1)	0.42
14-08	0.79	5.11	5.76	-1.35	-1.54	Gl(58.3), Cpx(4.3), Bt(9.0), Ilm(<0.1), Pl(17.4), Kfs(9.5), Qtz(1.5)	0.06
14-09	0.71	4.74	5.85	-1.44	-1.63	Gl(43.4), Cpx(3.8), Bt(9.9), Ilm(0.1), Pl(20.4), Kfs(13.5), Qtz(8.9)	0.06
14-10	0.61	4.27	—	-1.57		Gl, Cpx, Bt, Ilm, Pl, Kfs, Qtz	—
14-11	0.50	3.73	—	-1.75		Lpx, Bt, Ilm, Pl, Kfs, Qtz	—

T:800 ℃; P: 200MPa; run duration: 351h							
14-12	1.00	6.26	7.44	-1.34	-1.34	Gl(90.3), Cpx(<0.1), Bt(10.3), Ilm(<0.1)	1.51
14-13	0.93	5.80	5.56	-1.42	-1.54	Gl(80.4), Cpx(3.2), Bt(9.4), Ilm(<0.1), Pl(7.1)	1.47
14-14	0.78	5.07	5.77	-1.56	-1.89	Gl(76.4), Cpx(2.7), Bt(10.4), Ilm(<0.1), Pl(10.6)	0.55
14-15	0.69	4.65	5.15	-1.65	-2.15	Gl(71.2), Cpx(3.0), Lpx(0.5), Bt(9.0), Ilm(<0.1), Pl(14.6), Kfs(1.8)	0.3
14-16	0.61	4.27	—	-1.77		Gl, Lpx, Bt, Ilm, Pl, Kfs, Qtz	—
14-17	0.50	3.73	—	-1.94		Gl, Lpx, Cpx, Bt, Ilm, Pl, Kfs, Qtz	—
14-18	0.43	3.37	—	-2.08		Gl, Lpx, Cpx, Bt, Ilm, Pl, Kfs, Qtz	—
T: 850 ℃; P: 200MPa; run duration: 181h							
14-19	1.00	5.90	7.16	-0.96	-0.96	Gl(92), Cpx(0.4), Bt(7.3), Ilm(0.2)	0.61
14-20	0.89	5.43	5.84	-1.06	-1.22	Gl(92.1), Cpx(0.9), Bt(7.0), Ilm(0.1)	0.64
14-21	0.80	4.99	5.10	-1.16	-1.48	Gl(86.2), Lpx(<0.1), Cpx(3.1), Bt(7.2), Ilm(0.2), Pl(3.9)	0.49
14-22	0.71	4.59	4.22	-1.26	-1.72	Gl(79.5), Lpx(1.3), Cpx(3.2), Bt(4.8), Ilm(0.5), Pl(10.8)	0.13
14-23	0.61	4.13	3.93	-1.40	-2.14	Gl(75.4), Lpx(3.5), Cpx(1.6), Bt(3.7), Ilm(0.5), Pl(15.3)	0.05
14-24	0.49	3.56	3.50	-1.58	-2.65	Gl(70.0), Lpx(8.1), Bt(<0.1), Ilm(0.9), Pl(17.5), Kfs(3.2)	0.03
14-25	0.41	3.17	2.88	-1.74	-2.72	Gl(66.0), Lpx(7.2), Bt(<0.1), Ilm(0.9), Pl(21.3), Kfs(5.4)	0.3
T: 900 ℃; P: 200MPa; run duration: 138h							
14-26	1.00	5.66	5.80	-0.91	-0.91	Gl(>99), Ilm, (Lpx, Cpx)	—
14-27	0.91	5.29	4.93	-1.00	-1.12	Gl(99.6), Lpx(0.2), Ilm(0.2)	1.16
14-28	0.79	4.75	4.07	-1.12	-1.45	Gl(98.2), Lpx(1.4), Ilm(0.3)	0.32
14-29	0.70	4.36	3.73	-1.21	-1.88	Gl(97), Lpx(2.1), Cpx(0.4), Ilm(0.5)	0.65
14-30	0.62	4.01	3.45	-1.32	-2.66	Gl(96.8), Lpx(2.5), Cpx(0.4), Ilm(0.3)	0.5
14-31	0.49	3.43	2.89	-1.52	-3.41	Gl(89.1), Lpx(4.7), Cpx(<0.1), Ilm(0.5), Pl(5.7)	0.55
14-32	0.38	2.91	2.93	-1.75		Gl(86), Lpx(5.1), Cpx(<0.1), Ilm(0.6), Pl(8.3)	0.98
T: 660 ℃; P: 300MPa; run duration: 1267h							
14-33	1.00	8.39	6.83	-1.39	-1.39	Gl, Cpx, Bt, Ilm, Pl, Kfs, Qtz, Ttn	—
T: 700 ℃; P: 300MPa; run duration: 570h							
14-34	1.00	8.63	9.67			Gl(80.2), Cpx(0.1), Bt(12.9), Ilm(<0.1), Pl(6.8)	0.35
T: 750 ℃; P: 300MPa; run duration: 571h							
14-35	1.00	8.20	9.67	-0.96	-0.96	Gl(87), Cpx(1.2), Amp(-1.1), Bt(13), Ilm(-0.1)	0.31
14-36	0.90	7.57	7.46	-1.04	-1.21	Gl(77), Cpx(0.9), Bt(12), Ilm(<0.1), Pl(10.1)	0.14
14-37	0.80	6.76	7.57	-1.16	-1.25	Gl(30.2), Cpx(2.7), Bt(11.1), Ilm(<0.1), Pl(25.4), Kfs(16.7), Qtz(13.8)	0.05
14-38	0.70	6.27	5.59	-1.25	-1.48	Gl(46.4), Cpx(2.6), Bt(10.2), Ilm(<0.1), Pl(19.6), Kfs(13.1), Qtz(8.2)	0.09
14-39	0.60	5.54	7.48	-1.39		Gl, Cpx, Bt, Ilm, Pl, Kfs, Qtz	—
T: 800 ℃; P: 300MPa; run duration: 356h							
14-42	0.80	6.63	6.83	-1.11	-2.34	Gl(80.4), Cpx(1.1), Bt(10.7), Ilm(-0.2), Pl(8)	0.18
14-43	0.70	6.06	5.75	-1.21		Gl(75.6), Cpx(1.7), Lpx(0.2), Bt(8.8), Ilm(-0.2), Pl(13.9)	0.19
14-44	0.62	5.51	—	-1.32		Gl, Cpx, Lpx, Bt, Ilm, Pl	—
14-45	0.50	4.71	—	-1.51		Gl, Cpx, Lpx, Bt, Ilm, Pl, Kfs, Qtz	—
T: 660 ℃; P: 362MPa; run duration: 648h							
14-46	1.00	9.66	9.30	-1.05	-1.05	Gl(65.7), Cpx(3.6), Bt(10.4), Ilm(0.6), Pl(10.5), Qtz(<0.1), Ttn(<0.1)	0.14
T: 700 ℃; P: 400MPa; run duration: 648h							
14-47	1.00	10.62	9.90	-1.38	-1.38	Gl, Cpx, Bt, Ilm, Ttn, Pl	—
14-48	0.89	9.59	—	-1.49		Gl, Cpx, Bt, Ilm, Pl, Kfs	—
14-49	0.77	8.55	—	-1.62		Gl, Cpx, Bt, Ilm, Pl, Kfs, Qtz	—
14-50	0.69	7.77	—	-1.71		Gl, Cpx, Bt, Ilm, Pl, Kfs, Qtz	—
T: 800 ℃; P: 360MPa; run duration: 263h							
14-51	1.00	9.33	9.61			Gl(89.7), Cpx(-1.2), Bt(11.5), Ilm(0)	1.92

Charge	P(Mpa)	H_2O_{melt}wt%	H_2O^{melt}wt%	△NNO	Phase assemblage and phase proportions (wt%)	Σr^2
T: 700 ℃; $XH2O^{in}$=1; run duration: 501h						
14-52	200	6.47	—	3.00	Gl, Cpx, Bt, Mag, Ttn, Pl, Kfs	—
T: 800 ℃; $XH2O^{in}$=1; run duration: 332h, 312h, 281h, 277h						
14-53	90	3.82	—	3.00	Gl, Cpx, Bt, Mag, Pl	—
14-54	200	6.17	—	3.00	Gl, Cpx, Bt, Mag	—
14-55	360	9.40	—	3.00	Gl, Cpx, Bt, Mag	—
14-56	673	—	—	3.00	Gl, Bt, Mag, Ttn	—

Charge	XH_2O^{in}	$^1H_2O_{melt}$wt%	$^2H_2O^{melt}$wt%	$\triangle NNO^3$	$\triangle NNO^4$	Phase assemblage and phase proportions (wt%)	Σr^2
T: 660 ℃; P: 200MPa; run duration: 1137h							
13-01	1.00	6.45	6.49	-1.36	-1.36	Gl(27), Cpx(2.4), Bt(5.9), Ilm(0.2), Pl(18.8), Kfs(28.4), Qtz(17.3)	0.17
13-02	0.89	5.92	—	-1.46		Gl, Cpx, Bt, Ilm, Pl, Kfs, Qtz	—
13-03	0.76	5.24	—	-1.57		Gl, Cpx, Bt, Ilm, Pl, Kfs, Qtz	—
T: 700 ℃; P: 200MPa; run duration: 689h							
13-04	1.00	6.39	6.7	-1.15	-1.15	Gl(68.4), Cpx(2.5), Bt(3.9), Ilm(0.3), Pl(10.4), Kfs(14.4), Qtz(<0.1)	0.35
13-05	0.89	5.87	—	-1.25		Gl, Cpx, Bt, Ilm, Pl, Kfs, Qtz	—
13-06	0.78	5.29	—	-1.37		Gl, Cpx, Bt, Ilm, Pl, Kfs, Qtz	—
T: 750 ℃; P: 200MPa; run duration: 471h							
13-08	0.80	5.16	5.34	-1.34	-1.45	Gl(46.7), Cpx(2.5), Bt(5.2), Ilm(0.2), Pl(17.3), Kfs(17.5), Qtz(<0.1)	0.3
13-09	0.70	4.69	5.03	-1.45	-1.86	Gl(68.8), Lpx(3.1), Cpx(2.4), Bt(-3.8), Ilm(0.7), Pl(14.1), Kfs(14.8), Qtz(<0.1)	0.37
13-10	0.58	4.12	—	-1.57		Gl, Cpx, Bt, Ilm, Pl, Kfs, Qtz	—
13-11	0.51	3.78	—	-1.73		Gl, Cpx, Bt, Ilm, Pl, Kfs, Qtz	—
T:800 ℃; P: 200MPa; run duration: 351h							
13-12	1.00	6.26	4.06	-1.34	-1.34	Gl(85.3), Cpx(0.2), Bt(4.8), Ilm(0.1), Pl(9.6)	*
13-13	0.93	5.8	6.03	-1.41	-1.56	Gl(93.6), Cpx(1.0), Bt(2.5), Ilm(0.3), Pl(2.6)	0.4
13-14	0.81	5.21	5.04	-1.53	-1.88	Gl(86.1), Cpx(2.8), Bt(0.82), Ilm(0.5), Pl(6.6), Kfs(3.2)	1.87
13-15	0.70	4.7	4.12	-1.65	-2.02	Gl(69.1), Lpx(5.5), Cpx(3), Bt(-8), Ilm(1.3), Pl(11.4), Kfs(17.8), Qtz(<0.1)	1.07
13-16	0.62	4.32	4.16	-1.76	-2.38	Gl(67.9), Lpx(1.9), Cpx(5.4), Bt(-5.6), Ilm(0.9), Pl(9.2), Kfs(20.3), Qtz(<0.1)	0.45
13-17	0.51	3.78	—	-1.93		Gl, Lpx, Cpx, Bt, Ilm, Pl, Kfs, Qtz	—
13-18	0.38	3.11	—	-2.18		Gl, Lpx, Cpx, Bt, Ilm, Pl, Kfs, Qtz	—
T: 850 ℃; P: 200MPa; run duration: 181h							
13-19	1.00	5.9	6.86	-0.96	-0.96	Gl(99.9), Cpx(0.1), Bt(-0.3), Ilm(0.3)	1.96
13-20	0.91	5.52	6.73	-1.05	-1.27	Gl(98.6), Cpx(-0.2), Bt(1.4), Ilm(0.2)	1.42
13-21	0.80	4.99	5.3	-1.16	-1.69	Gl(99.6), Cpx(0.8), Bt(-0.2), Ilm(0.3), Pl(-0.4)	1.31
13-22	0.70	4.54	5.02	-1.27	-2.38	Gl(92.7), Cpx(2.2), Bt(0.1), Ilm(0.4), Pl(4.5)	1.39
13-23	0.61	4.13	4.04	-1.39	-2.47	Gl(84.5), Lpx(6.8), Cpx(-2.7), Bt(-0.9), Ilm(0.5), Pl(11.8), Qtz(<0.1)	0.51
13-24	0.51	3.66	3.38	-1.55	-4.03	Gl(82.5), Lpx(5.3), Cpx(-2.1), Ilm(0.4), Pl(14.9), Kfs(-0.7), Qtz(<0.1)	0.25
13-25	0.41	3.17	3.22	-1.74	-4.45	Gl(70.4), Lpx(11.4), Cpx(0.4), Bt(-6.4), Ilm(0.9), Pl(12.5), Kfs(10.9), Qtz(<0.1)	0.1
T: 900 ℃; P: 200MPa; run duration: 138h							
13-26	1.00	5.66	5.26	-0.91	-0.91	Gl(>99), Ilm	—
13-27	0.89	5.21	4.93	-1.01	-1.15	Gl(>99), Ilm	—
13-28	0.79	4.75	4.3	-1.12	-1.49	Gl(>99), Ilm	—
13-29	0.61	3.97	3.45	-1.33	-3.05	Gl(99.8), Cpx(<0.1), Ilm(0.2)	0.46
13-30	0.51	3.52	—	-1.50		Gl, Cpx, Ilm, Pl	—
13-31	0.40	3	—	-1.70		Gl, Cpx, Ilm, Pl	—
13-32	0.33	2.66	—	-1.88		Gl, Cpx, Ilm, Pl, Qtz	—

T: 660 ℃; P: 300MPa; run duration: 1267h							
13-33	1.00	8.39	7.85	-1.39	-1.39	Gl(13.6), Cpx(0.9), Bt(4.9), Ilm(0.2), Pl(23.3), Kfs(32.7), Qtz(24.5)	0.09
T: 700 ℃; P: 300MPa; run duration: 570h							
13-34	1.00	8.63	8.47			Gl(93.8), Cpx(-0.1), Bt(5.9), Ilm(0.1), Pl(0.3)	1.13
T: 750 ℃; P: 300MPa; run duration: 571h							
13-35	1.00	8.2	9.43	-0.96	-0.96	Gl(94.7), Cpx(0), Bt(5.2), Ilm(0.1)	0.5
13-36	0.90	7.5	7.81	-1.05	-1.54	Gl(85), Cpx(1.3), Bt(4.4), Ilm(0.2), Pl(5.1), Kfs(3.9)	0.24
13-37	0.80	6.7	6.23	-1.17	-1.56	Gl(67.5), Cpx(1.6), Bt(4.4), Ilm(0.1), Pl(14.5), Kfs(10.2), Qtz(1.7)	0.45
13-38	0.70	6.21	—	-1.26		Gl, Cpx, Bt, Ilm, Pl, Kfs, Qtz	—
13-39	0.60	5.44	—	-1.41		Gl, Cpx, Bt, Ilm, Pl, Kfs, Qtz	—
T: 800 ℃; P: 300MPa; run duration: 356h							
13-40	1.00	8.04	8.6	-0.90	-0.90	Gl(97.7), Cpx(-0.7), Bt(2.9), Ilm(0.2)	1.36
13-41	0.90	7.35	7.67	-1.00	-1.71	Gl(97.6), Cpx(0.2), Bt(1.9), Ilm(0.3)	0.87
13-42	0.80	6.63	6	-1.11	-2.24	Gl(92.4), Cpx(1.2), Bt(2.1), Ilm(0.3), Pl(4.0)	0.8
13-43	0.70	6.09	5.53	-1.21		Gl(87.7), Cpx(1.2), Bt(1.7), Ilm(0.4), Pl(9.0)	0.81
13-44	0.60	5.44	—	-1.34		Gl, (Lpx), Cpx, Bt, Ilm, Pl, Kfs, Qtz	—
13-45	0.50	4.74	—	-1.50		Gl, Lpx, Cpx, Bt, Ilm, Pl, Kfs, Qtz	—
T: 660 ℃; P: 362MPa; run duration: 648h							
14-46	1.00	9.66	9.61	-1.05	-1.05	Gl(58.2), Cpx(2.2), Bt(4.4), Ilm(0.3), Pl(8.2), Qtz(7.2), Ttn(<0.1)	0.14
T: 700 ℃; P: 400MPa; run duration: 648h							
13-47	1.00	10.62	8.16	-1.38	-1.38	Gl, Gl, Cpx, Bt, Ilm, Ttn	—
13-48	0.90	9.68	—	-1.48		Gl, Cpx, Bt, Ilm, Pl, Kfs, Qtz	—
13-49	0.80	8.82	—	-1.58		Gl, Cpx, Bt, Ilm, Pl, Kfs, Qtz	—
13-50	0.70	7.85	—	-1.69		Gl, Cpx, Bt, Ilm, Pl, Kfs, Qtz	—
T: 800 ℃; P: 360MPa; run duration: 263h							
13-51	1.00	9.33	8.88			Gl(96.2), Bt(3.8), Ilm(0)	3.96

Charge	**P(Mpa)**	**H_2O_{melt}wt%**	**H_2O^{melt}wt%**	**△NNO**	**Phase assemblage and phase proportions (wt%)**	**Σr^2**
T: 700 ℃; $XH2O^{in}$=1; run duration: 501h						
13-52	200	6.47	—	3.00	Gl, Cpx, Bt, Mag, Ttn, Pl, Kfs	—
T: 800 ℃; $XH2O^{in}$=1; run duration: 332h, 312h, 281h, 277h						
13-53	90	3.82	—	3.00	Gl, Cpx, Bt, Mag, Pl	—
13-54	200	6.17	—	3.00	Gl, Cpx, Bt, Mag	—
13-55	360	9.4	—	3.00	Gl, Bt, Mag	—
13-56	700	—	—	3.00	Gl, Bt, Mag	—

XH_2O_{in} : initial $H_2O/(H_2O/CO_2)$ loaded in each capsule (in moles)
H_2O_{melt}wt% : water content in the melt; [1]: determined by calculation of VolatileCalc; [2]: determined by by-difference method following Scaillet & Evans 1999
△NNO: logfO_2(experiment)-logfO_2(NNO; Chou, 1987); [3]: for H_2O- undersaturated charges, maximum fO_2 were estimated as logfO_2=logfO_2(XH_2O=1)+2*logXH_2O_{in}; [4]: fO_2 were calculated according to XH_2O_{fin}

Appendix table 10 The representative compositions of natural and experimental plagioclase

Sample	Natural						Experimental		
/Charge	QTL-38C	Range	QTL-14A	Range	QTL-13	Range	38-01(1)[1]	14-01(1)	13-01(1)
n:[2]	48		27		28		4	7	3
T/fO_2/P[3]								700 ℃/+3/200	
SiO_2	60.01(1.6)[4]	57.45–64.56	59.91(1.7)	56.98–63.44	63.29(2.6)	59.96–69.77	60.71(1.8)	60.67(1.3)	62.57(1.1)
Al_2O_3	24.33(1.1)	21.71–26.87	24.22(9)	22.63–25.90	22.75(1.5)	19.54–24.94	23.00(1.8)	23.55(1.1)	23.84(3)
FeO	0.21(9)	0.00–0.47	0.18(1)	0.00–0.34	0.13(1)	0.00–0.36	1.59(1.1)	1.01(6)	0.88(4)
CaO	6.70(1.1)	3.96–8.48	6.83(1.2)	4.66–9.03	5.01(1.9)	0.39–7.28	7.45(6)	7.37(8)	6.92(2)
Na_2O	7.69(6)	6.77–9.52	7.57(6)	6.35–8.70	8.09(1.1)	7.01–10.93	5.67(1.1)	5.81(2)	5.58(3)
K_2O	0.44(1)	0.23–0.99	0.41(1)	0.26–0.60	0.4(2)	0.00–0.62	1.15(2)	1.62	1.73(2)
Total	99.39		99.13		99.67		99.58	100.03	101.52
Ab	65.83	57.86–79.23	65.19	54.88–74.91	72.80	61.91–97.56	53.25	52.88	52.95
An	31.64	18.23–39.94	32.49	22.18–42.92	24.84	1.89–35.64	39.32	37.31	36.28
Or	2.49	1.27–5.61	2.33	1.46–3.32	2.36	0.00–3.73	7.43	9.80	10.77
Sample	Experimental								
/Charge	38-28(0.6)	14-31(0.5)	13-30(0.5)	38-12(0.9)	14-13(0.8)	13-13(0.8)	38-12(0.9)	14-13(0.9)	13-13(0.9)
n:	5	4	5	3	11	6	3	2	6
T/fO_2/P		900/-1.3/200			850/-1.3/200			800/-1.3/200	
SiO_2	56.06(2.0)	56.78(1.8)	58.73(7)	58.4(1.8)	57.79(1.5)	58.22(1.6)	58.93(1.0)	58.79(1.5)	58.37(7)
Al_2O_3	26.91(1.1)	27.86(7)	26.78(5)	27.04(7)	27.47(1.0)	26.89(7)	24.88(5)	24.56(1)	26.79(7)
FeO	0.67(4)	0.45(1)	0.38(2)	0.90(2)	0.57(1)	0.55(1)	0.85(2)	1.10(9)	0.35(1)
CaO	10.78(8)	10.05(9)	8.61(2)	8.92(1.1)	9.59(6)	9.07(4)	8.13(4)	7.90(1)	8.30(5)
Na_2O	4.54(1)	4.75(2)	5.19(2)	4.87(2)	5.43(3)	5.63(4)	6.18(4)	6.08(2)	6.58(3)
K_2O	0.81(3)	0.96(2)	1.11(1)	0.85(1)	0.91(2)	1.08(2)	0.72(1)	1.04(1)	0.85(1)
Total	99.78	100.84	100.80	100.99	101.75	101.44	99.70	99.47	101.24
Ab	41.19	43.47	48.58	46.94	47.93	49.58	55.41	54.62	56.09
An	53.94	50.72	44.57	47.66	46.77	44.16	40.32	39.24	39.12
Or	4.88	5.82	6.86	5.41	5.30	6.27	4.27	6.14	4.79
Sample	Experimental								
/Charge	38-39(0.9)	14-42(0.8)	13-42(0.8)	38-01(1)	14-01(1)	13-01(1)	38-12(1)	14-13(1)	13-13(1)
n:	5	9	9	4	7	3	3	2	6
T/fO_2/P		800/-1.3/300			700/-1.3/200			700/-1.3/300	
SiO_2	57.88(7)	58.72(7)	58.43(9)	59.65(8)	62.13(1.2)	63.37(7)	59.07(1.1)	58.97(8)	60.29(8)
Al_2O_3	25.23(9)	24.04(9)	23.99(6)	22.67(1)	22.64(5)	22.71(6)	23.77(6)	24.53(4)	24.32(3)
FeO	1.21(5)	0.59(3)	0.82(1.2)	0.6(1)	0.53(4)	0.30(1)	1.24(9)	0.24(0)	0.30(1)
CaO	9.27(5)	7.93(5)	7.57(7)	5.45(3)	5.92(4)	5.62(5)	8.02(6)	7.87(5)	8.06(4)
Na_2O	5.23(2)	5.28(2)	5.84(3)	7.75(3)	6.51(5)	6.50(5)	6.20(3)	6.69(2)	6.62(4)
K_2O	0.73(2)	1.10(2)	1.15(1)	0.96(1)	1.52(3)	2.0(9)	0.55(1)	0.69(1)	0.60(1)
Total	99.55	97.66	97.81	97.08	99.25	100.50	98.84	99.00	100.19
Ab	48.26	50.81	54.18	68.02	60.33	59.49	56.40	58.20	57.65
An	47.27	42.19	38.78	26.41	30.38	28.49	40.30	37.82	38.89
Or	4.48	7.00	7.04	5.57	9.29	12.02	3.30	3.98	3.46
Sample	Experimental								
/Charge	38-01(1)	14-01(1)	13-01(1)	38-12(1)	14-13(1)	13-13(1)	38-01(1)	14-01(1)	13-01(1)

n:	4	7	3	3	2	6	4	7	3
T/fO_2/P		660/-1.3/200			660/-1.3/300			660/-1.3/360	
SiO_2	61.84(1.4)	60.78(8)	60.46(5)	61.50(4)	59.88(6)	60.74(9)	59.66(9)	61.36(5)	62.03(8)
Al_2O_3	22.71(4)	23.42(6)	23.10(4)	22.82(4)	23.43(5)	22.59(5)	23.60(8)	23.30(5)	23.41(5)
FeO	0.71(8)	0.11(1)	0.24(1)	0.24(1)	0.66(6)	0.22(2)	0.88(1.1)	0.25(1)	0.29(1)
CaO	5.22(6)	5.65(5)	5.24(5)	5.19(4)	5.92(4)	4.72(5)	6.37(6)	5.20(5)	5.25(5)
Na_2O	7.11(6)	7.42(2)	7.34(5)	7.82(3)	7.73(2)	7.48(4)	7.15(4)	7.23(3)	7.42(3)
K_2O	1.05(1)	1.06(3)	1.50(9)	0.99(1)	0.97(2)	2.06(1.4)	0.91(2)	1.84(1.1)	1.59(8)
Total	98.64	98.45	97.88	98.56	98.58	97.81	98.57	99.18	99.99
Ab	66.50	66.03	65.35	68.97	66.40	65.43	63.46	63.97	65.30
An	27.03	27.75	25.79	25.30	28.08	22.87	31.20	25.44	25.53
Or	6.47	6.22	8.86	5.73	5.52	11.70	5.34	10.60	9.17

[1] The numbers in parentheses following in charge name indicate the XH_2O

[2] Number of analyses

[3] Temperature(℃)/△NNO/pressure(MPa)

[4] Numbers in parentheses indicate 1 s.d.in terms of the last one units cited

Appendix table 11 The representative compositions of experimental pyroxene

Charge	38-50(1)[1]	14-53(1)	13-54(1)	38-49(1)	14-52(1)	13-52(1)	38-24(1)	14-27(0.9)	13-29(0.6)
n:[2]	7	5	3	7	12	8	12	5	6
T/fO_2/P[3]		800/+3/200			700/+3/200			900/-1.3/200	
SiO_2	48.22(2.4)[4]	49.16(6)	49.9(9)	49.62(3.7)	46.37(1.9)	48.38(7)	52.1(8)	51.48(8)	50.87(9)
TiO_2	1.23(3)	0.76(1)	0.48(2)	1.35(7)	1.14(3)	0.85(2)	0.26(1)	0.26(1)	0.28(0)
Al_2O_3	5.69(1.3)	3.54(6)	1.95(4)	6.64(6)	5.14(1.1)	4.17(6)	0.83(5)	0.8(3)	0.91(4)
FeO	10.54(9)	9.14(7)	7.74(1.3)	11.1(2.3)	12.51(1.4)	9.98(1.6)	23.25(1.2)	22.87(1.5)	14.38(3.7)
MnO	0.48(1)	0.54(0)	0.49(0)	0.64(1)	0.7(1)	0.72(1)	0.56(1)	0.62(1)	0.54(1)
MgO	10.91(1.3)	12.84(6)	13.9(8)	8.34(4)	9.47(1.3)	11.4(9)	20.15(1.1)	20.84(2.0)	13.64(8)
CaO	22.27(2.7)	23.23(2)	25.31(5)	22.29(2.0)	24.62(5)	24.76(4)	1.85(1.4)	1.5(1.4)	17.78(2.6)
Na_2O	0.49(0)	0.54(0)	0.6(1)	0.63(1)	0.64(1)	0.76(1)	0.04(1)	0.03(0)	0.17(0)
K_2O	0.31(2)	0.09(0)	0.11(1)	0.45(1)	0.2(1)	0.19(1)	0.04(1)	0.04(0)	0.11(1)
Total	100.15	99.84	100.48	101.07	100.78	101.23	99.07	98.42	98.68
En	33	37	38	27	28	33	58	60	40
Fs	18	15	12	20	21	16	38	37	23
Wo	49	48	50	52	52	51	4	3	37
Charge	38-17(1)	14-19(1)	13-19(1)	38-12(0.9)	14-12(1)	13-12(1)	38-12(0.9)	14-15(0.7)	13-18(0.4)
n:	5	17	5	10	6	7	5	5	2
T/fO_2/P		850/-1.3/200			800/-1.3/200			800/-1.3/200	
SiO_2	46.57(6)	50.51(1.7)	51.52(2)	48.92(2.4)	49.68(9)	50.56(9)	50.18(1.6)	50.51(2.0)	49.79(5)
TiO_2	1.22(2)	0.59(3)	0.32(1)	1.12(8)	0.76(3)	0.35(0)	0.44(4)	0.18(1)	0.14(0)
Al_2O_3	5.22(5)	2(1.2)	0.74(3)	4.07(1.4)	2.44(9)	1.13(3)	1.77(1.0)	1.35(1.0)	1.7(3)
FeO	11.74(5)	15.78(2.5)	17.6(7)	18.37(4.1)	16.26(2.4)	24.3(2.7)	32.69(2.0)	32.32(3.1)	36.79(0)
MnO	0.53(0)	0.54(1)	0.55(0)	0.59(1)	0.54(1)	0.87(2)	0.98(1)	1.13(2)	1.5(0)
MgO	10.76(8)	10.7(1.2)	10.69(2)	8.4(9)	9.25(1.0)	7.65(3)	8.65(3)	8.33(7)	6.61(3)
CaO	21.41(5)	19.14(1.8)	19.07(8)	16.59(3.3)	21.58(1.2)	14.68(3.3)	4.59(1.9)	4.86(2.3)	4.02(2)
Na_2O	0.38(0)	0.31(1)	0.24(1)	0.35(1)	0.29(1)	0.21(1)	0.2(2)	0.14(1)	0.3(1)
K_2O	0.17(0)	0.18(2)	0.11(0)	0.29(2)	0.06(0)	0.22(1)	0.25(2)	0.4(4)	0.47(3)
Total	98.01	99.75	100.85	98.69	100.85	99.97	99.75	99.23	101.34
En	33	32	31	27	27	24	29	28	22
Fs	20	27	29	34	27	43	61	61	68
Wo	47	41	40	39	46	33	11	12	10
Charge	38-07(0.9)	14-07(0.9)	13-08(0.8)	38-35(0.8)	14-35(1)	13-36(0.9)	38-04(1)	14-04(1)	13-06(0.8)
n:	9	5	6	6	6	6	8	17	17
T/fO_2/P		750/-1.3/200			750/-1.3/300			700/-1.3/200	
SiO_2	46.34(1.7)	48.66(1.4)	50.27(1.7)	51.13(2.5)	47.36(4)	49.28(1.4)	45.86(1.7)	47.88(1.8)	48.19(1.3)
TiO_2	1.12(6)	1.15(2)	0.77(2)	0.99(3)	1.25(2)	0.89(1)	1.18(9)	0.99(2)	1.06(7)
Al_2O_3	5.42(2.0)	6.02(6)	5.62(1.0)	5.95(1.1)	3.96(3)	3.51(7)	3.97(2.0)	4.39(1.0)	3.53(8)
FeO	18.77(2.8)	18.77(6)	19.29(5)	16.91(1.5)	18.62(4)	19.61(4)	20.47(1.0)	19.32(7)	20.59(9)
MnO	0.72(2)	0.55(0)	0.63(1)	0.63(2)	0.54(1)	0.53(1)	0.76(1)	0.86(2)	0.92(2)
MgO	6.39(4)	5.35(3)	4.21(7)	5.9(1.1)	6.01(3)	5.39(5)	5.1(1.0)	4.8(5)	4.3(4)
CaO	19.74(2.4)	20.71(1.2)	19.23(1.5)	16.96(2.0)	21.09(3)	20.07(7)	20.43(8)	21.02(6)	20.68(5)
Na_2O	0.43(2)	0.6(2)	0.6(1)	0.5(2)	0.32(1)	0.31(1)	0.33(1)	0.36(0)	0.41(1)
K_2O	0.22(1)	0.34(3)	0.69(2)	0.7(4)	0.09(0)	0.31(1)	0.16(1)	0.16(1)	0.16(1)
Total	99.15	102.15	101.31	99.68	99.25	99.90	98.26	99.77	99.85

En	21	17	15	21	19	17	16	16	14
Fs	34	34	38	35	33	36	37	35	38
Wo	46	48	48	44	48	47	47	49	48
Charge	38-32(1)	14-34(1)	13-34(1)	38-01(1)	14-01(1)	13-01(1)	38-31(1)	14-33(1)	13-33(1)
n:	12	10	13	12	6	1	32	6	5
$T/fO_2/P$		700/-1.3/300			660/-1.3/200			660/-1.3/300	
SiO_2	51.51(1.7)	49.33(1.3)	49.2(1.3)	46.12(2.6)	46.15(9)	48.98(1)	47.76(2.3)	46.32(9)	47.39(1.4)
TiO_2	0.93(4)	0.99(3)	0.91(7)	0.73(6)	1.47(5)	0.9(3)	1.04(7)	1.01(3)	0.86(3)
Al_2O_3	4.1(1.0)	3.52(9)	3.21(8)	4.45(1.5)	4.12(8)	3.3(8)	5.57(1.8)	4.98(1.1)	3.65(5)
FeO	15.24(1.6)	18.44(2.4)	19.18(9)	21.34(1.2)	20.33(8)	19.33(2.3)	18.78(2.9)	19.69(6)	21.12(9)
MnO	0.92(1)	0.7(1)	0.85(2)	0.56(2)	0.8(2)	0.83(1)	0.68(2)	0.71(1)	0.83(1)
MgO	7.71(8)	5.88(1.6)	5.56(4)	4.11(4)	3.97(7)	5.46(1.4)	4.91(9)	4.05(3)	3.77(4)
CaO	19.62(1.3)	20.98(3)	20.96(5)	20.97(1.3)	21.19(3)	20.96(3)	20.3(3.0)	20.89(5)	20.14(1.0)
Na_2O	0.39(1)	0.46(1)	0.44(1)	0.44(1)	0.32(0)	0.44(1)	0.7(4)	0.45(1)	0.45(0)
K_2O	0.27(1)	0.09(0)	0.11(1)	0.19(8)	0.28(2)	0.12(0)	0.6(8)	0.25(2)	0.27(2)
Total	100.70	100.38	100.43	98.91	98.62	100.32	100.33	98.34	98.49
En	25	19	18	13	13	17	16	13	13
Fs	28	33	34	38	37	35	35	37	39
Wo	46	48	48	48	50	48	49	50	48

[1] The numbers in parentheses following in charge name indicate the XH_2O

[2] Number of analyses

[3] Temperature(℃)/△NNO/pressure(MPa)

[4] Numbers in parentheses indicate 1 s.d.in terms of the last one units cited

Appendix table 12 The representative compositions of natural and experimental amphibole

Sample	Natural						Experimental				
/Charge	QTL-38C	Range	QTL-14A	Range	QTL-13	Range	38-51(1)[1]	38-52(1)	38-54(1)	38-17(1)	38-18(0.9)
n:[2]	84		14		12		5	7	6	10	6
$T/fO_2/P$[3]							800/+3/200	800/+3/360	800/+3/700	850/-1.3/200	850/-1.3/200
SiO_2	42.50(6)[4]	41.11–44.11	42.64(9)	40.73–43.94	41.85(8)	40.51-42.99	46.67(8)	45.31(4)	46.53(4)	42.64(6)	41.98(2)
TiO_2	1.82(3)	0.75-2.21	1.65(4)	0.67-1.98	1.43(3)	1.11-1.95	0.92(1)	1.05(1)	1.04(1)	1.93(1)	2.27(1)
Al_2O_3	8.14(5)	7.18–9.41	7.76(5)	7.11-8.93	7.30(5)	6.78-8.27	8.78(7)	10.03(3)	9.85(1)	9.62(3)	10.42(3)
FeO	23.78(1.0)	20.97–25.60	24.42(1.7)	22.42-28.47	26.34(1.4)	23.46-28.13	8.2(5)	8.18(3)	7.10(4)	18.24(3)	18.95(3)
MnO	0.51(1)	0.18-0.72	0.45(2)	0.17-0.81	0.40(2)	0.28-1.00	0.37(2)	0.35(1)	0.36(1)	0.29(0)	0.26(0)
MgO	6.67(6)	4.78-8.80	6.68(1.0)	4.27-8.30	4.92(8)	3.91-6.46	17.36(4)	17.08(2)	17.77(0)	10.58(3)	9.73(2)
CaO	10.87(3)	9.94-11.59	10.60(2)	10.28-11.10	10.52(1)	10.36-10.67	12.17(2)	12.20(1)	12.76(4)	10.74(5)	10.73(1)
Na_2O	1.86(1)	1.58-2.09	1.92(1)	1.75-2.07	2.14(1)	2.02-2.39	1.44(1)	1.49(1)	1.47(0)	1.81(1)	1.94(1)
K_2O	1.24(1)	1.01-1.36	1.24(1)	1.09-1.60	1.25(1)	1.07-1.42	0.74(1)	0.89(1)	1.20(1)	0.80(1)	0.98(1)
F	0.32(2)	0.09-1.46	0.26(3)	0-0.63	0.89(4)	0.36-1.91	0.49(2)	0.34(1)	—	0.17(1)	0.21(0)
Cl	0.13(2)	0-0.80	0.35(4)	0.13-1.44	0.30(1)	0.14-0.51	—[8]	0.01(0)	—	0.01(0)	0.01(0)
Total	97.83		97.98		97.35		97.15	96.94	98.08	96.84	97.49
Al_{tot}	1.49		1.42		1.38		1.48	1.70	1.65	1.70	1.84
XFe[5]	0.66	0.58–0.74	0.67	0.60-0.79	0.75	0.68-0.80	0.21	0.21	0.18	0.49	0.52
P_{Cal}[6]	3.30		3.00		2.90						
T_{cal}[7]	776.00		768.00		737.00						

Sample	Experimental										
/Charge	38-11(1)	38-38(1)	38-39(0.9)	38-40(0.8)	38-33(1)	38-34(0.9)	38-35(0.8)	14-35(1)	38-32(1)	38-44(1)	38-40a(1)
n:	8	11	11	6	15	11	4	3	12	10	4
$T/fO_2/P$	800/-1.3/200	800/-1.3/300			750/-1.3/300			750/-1.3/300	700/-1.3/300	700/-1.3/400	660/-1.3/300
SiO_2	43.66(7)	43.21(5)	43.18(9)	44.02(7)	42.20(4)	43.00(6)	44.19(1.1)	42.37(1.4)	44.99(6)	42.36(8)	43.65(6)
TiO_2	1.67(1)	1.75(2)	1.84(1)	2.16(2)	1.57(2)	1.63(4)	1.64(1)	2.16(2)	1.27(2)	1.52(2)	1.46(1)
Al_2O_3	9.06(7)	9.21(4)	9.46(6)	9.48(2)	9.61(4)	8.29(5)	8.04(2)	10.80(6)	8.00(5)	9.73(8)	8.01(4)
FeO	21.56(6)	21.08(7)	21.68(6)	20.87(7)	22.69(7)	23.61(5)	22.95(4)	21.68(6)	24.11(3)	22.80(5)	25.54(3)
MnO	0.36(2)	0.32(1)	0.35(1)	0.21(1)	0.37(1)	0.44(1)	0.39(0)	0.29(1)	0.66(0)	0.34(1)	0.39(0)
MgO	8.77(3)	8.84(1)	8.46(4)	8.34(2)	6.78(2)	7.09(2)	7.28(1)	6.61(3)	6.54(3)	6.57(4)	4.97(1)
CaO	11.08(9)	10.48(2)	10.05(2)	10.28(3)	10.65(6)	10.14(3)	9.93(1)	11.11(3)	10.45(4)	11.01(2)	11.68(3)
Na_2O	1.58(1)	1.56(1)	1.62(1)	1.66(1)	1.49(1)	1.37(1)	1.35(0)	1.49(1)	1.35(1)	1.44(1)	1.12(2)
K_2O	0.73(1)	0.83(1)	0.76(1)	0.97(1)	0.90(1)	0.80(1)	0.97(1)	1.43(1)	0.76(1)	0.96(1)	1.18(2)
F	—	0.39(2)	0.43(2)	0.45(1)	0.29(2)	0.51(2)	0.53(2)	0.47(2)	0.02(0)	0.02(0)	0.43(1)
Cl	—	0.00(0)	0.01(0)	0.01(0)	0.01(0)	0.01(0)	0.02(0)	0.02(0)	0.01(0)	—	0.01(0)
Total	98.46	97.68	97.86	98.46	96.57	96.88	97.29	98.43	98.15	96.75	98.45
Al_{tot}	1.60	1.63	1.67	1.67	1.75	1.50	1.44	1.95	1.43	1.77	1.47
XFe	0.58	0.56	0.58	0.58	0.65	0.65	0.63	0.65	0.67	0.66	0.74

[1] The numbers in parentheses following in charge name indicate the XH_2O; [2] Number of analyses; [3] Temperature(℃)/△NNO/pressure(MPa);

[4] Numbers in parentheses indicate 1 s.d.in terms of the last one units cited; [5] XFe= Fe/(Fe+Mg) cationic ratio;

[6] Pressure calculation result are the average value following Hammarstrom and Zen, 1986; Hollister et al., 1987; Johnson and Rutherford, 1989; Schmidt, 1992; Anderson and Smith, 1995 (Temperature are using the T_{cal}) and Mutch 2016;

[7] Temperature calculation result are following Putirka and Keith, 2016; [8] Below detection limits.

Appendix table 13 The representative compositions of natural and experimental biotite

Sample	Natural						Experimental		
/Charge	QTL-38C	Range	QTL-14A	Range	QTL-13	Range	38-51(1)[1]	14-54(1)	13-54(1)
n:[2]	15		15		13		2	11	15
T/fO_2/P[3]								800/+3/200	
SiO_2	36.38(3)[4]	35.76–36.92	36.73(4)	36.03-37.59	36.29(5)	35.43-37.01	41.55(4)	40.78(8)	43.77(1.7)
TiO_2	4.31(3)	3.60-4.72	4.48(2)	3.86-4.94	3.90(3)	3.22-4.66	2.20(0)	2.16(1)	1.52(2)
Al_2O_3	11.54(2)	11.27-11.85	11.19(2)	10.79-11.41	12.26(1.0)	10.89-13.34	14.04(3)	14.99(4)	14.14(5)
FeO	26.96(3)	26.37–27.43	26.94(4)	26.27-27.81	28.26(1.1)	27.07-30.94	7.63(0)	8.31(4)	7.24(8)
MnO	0.13(0)	0.08-0.19	0.13(0)	0.09-0.17	0.16(0)	0.12-0.24	0.23(1)	0.16(1)	0.11(1)
MgO	7.43(3)	7.07-7.94	7.21(3)	6.39-7.58	5.88(2)	5.59-6.25	20.14(9)	20.03(4)	20.17(1.1)
CaO	0.003(0)	0.00-0.03	0.02(0)	0.00-0.08	0.03(1)	0.00-0.14	0.27(1)	0.2(1)	0.20(2)
Na_2O	0.14(0)	0.10-0.19	0.15(1)	0.07-0.25	0.14(0)	0.10-0.21	0.60(9)	0.39(0)	0.43(1)
K_2O	9.20(2)	8.87–9.43	8.96(2)	8.69-9.21	8.68(5)	7.44-9.19	8.40(3)	8.76(4)	8.22(6)
F	0.19(0)	0.18-0.21	0.42(1)	0.34-0.60	0.41(1)	0.31-0.52	0.01(0)	0.01(0)	0.01(0)
Cl	0.53(1)	0.28-0.72	0.50(1)	0.27-0.73	0.81(3)	0.44-1.31	0.68(2)	0.83(1)	0.91(2)
Total	96.81		96.73		96.82		95.65	96.28	96.57
XFe[5]	0.67	0.66-0.68	0.68	0.66–0.71	0.73	0.71–0.74	0.18	0.19	0.17
Sample	Experimental								
/Charge	38-53(1)	14-56(1)	13-56(1)	38-17(1)	14-19(1)	13-19(1)	38-11(1)	14-12(1)	13-12(1)
n:	5	4	5	6	11	5	6	1	5
T/fO_2/P	800/+3/700			850/-1.3/200			800/-1.3/200		
SiO_2	37.40(1.3)	37.21(5)	40.97(1.9)	37.40(1.3)	37.21(5)	40.97(1.9)	37.46(1.3)	37.29	40.38(1.9)
TiO_2	4.13(1)	4.61(1)	4.28(3)	4.13(1)	4.61(1)	4.28(3)	3.87(2)	4.40	5.87(2)

Al_2O_3	15.02(2)	14.86(2)	14.54(2)	15.02(2)	14.86(2)	14.54(2)	13.83(2)	13.86	14.83(2)
FeO	19.10(2)	17.69(6)	16.27(7)	19.10(2)	17.69(6)	16.27(7)	22.68(8)	21.42	20.66(1.2)
MnO	0.10(0)	0.12(0)	0.11(0)	0.10(0)	0.12(0)	0.11(0)	0.19(1)	0.00	0.18(0)
MgO	11.47(4)	12.63(4)	12.89(9)	11.47(4)	12.63(4)	12.89(9)	9.04(6)	9.33	8.07(4)
CaO	0.02(0)	0.04(0)	0.13(1)	0.02(0)	0.04(0)	0.13(1)	0.19(1)	0.18	0.14(1)
Na_2O	0.67(1)	0.56(0)	0.61(0)	0.67(1)	0.56(0)	0.61(0)	0.52(1)	0.46	0.60(1)
K_2O	8.73(1)	8.90(1)	8.53(5)	8.73(1)	8.90(1)	8.53(5)	8.51(2)	8.39	9.50(4)
F	0.01(0)	0.02(0)	0.01(0)	0.01(0)	0.02(0)	0.01(0)	0.02(0)	—[6]	—
Cl	0.34(0)	0.42(0)	0.54(0)	0.34(0)	0.42(0)	0.54(0)	0.05(0)	—	0.10(0)
Total	96.85	96.87	98.65	96.85	96.87	98.65	96.30	95.32	100.29
XFe	0.48	0.44	0.41	0.48	0.44	0.41	0.58	0.56	0.59
Sample	Experimental								
/Charge	38-38(1)	14-42(0.8)	13-42(1)	38-48(1)	14-51(1)	13-51(1)	38-33(1)	14-35(1)	13-35(1)
n:	17	1	8	4	6	3	6	2	6
T/fO_2/P	800/-1.3/300			800/-1.3/360			750/-1.3/300		
SiO_2	36.92(9)	39.26	37.68(9)	37.12(2.4)	36.62(6)	40.71(1.8)	38.20(1.1)	35.81(8)	38.92(1.8)
TiO_2	4.01(2)	5.24	4.38(2)	3.39(4)	4.06(1)	3.82(4)	4.13(2)	4.49(3)	4.26(4)
Al_2O_3	13.81(3)	14.11	13.29(3)	13.60(4)	13.52(2)	13.56(5)	14.62(4)	14.22(2)	13.65(5)
FeO	20.84(8)	20.81	18.47(4)	21.65(1.1)	21.01(9)	18.24(1.4)	22.16(1.3)	23.36(9)	22.05(1.7)
MnO	0.14(1)	0.20	0.08(1)	0.19(1)	0.11(1)	0.12(0)	0.19(0)	0.18(1)	0.13(1)
MgO	10.19(3)	8.13	11.36(5)	9.63(9)	10.12(3)	10.48(8)	7.69(3)	7.62(3)	6.99(5)
CaO	0.16(1)	0.29	0.08(0)	0.15(1)	0.04(1)	0.24(3)	0.33(2)	0.27(3)	0.23(1)
Na_2O	0.48(0)	0.59	0.38(0)	0.47(0)	0.37(1)	0.43(0)	0.56(2)	0.37(0)	0.38(1)
K_2O	8.54(5)	8.19	8.86(3)	8.43(5)	8.80(2)	8.46(3)	8.53(3)	8.79(3)	8.30(6)
F	0.02(0)	0.02	0.01(0)	—	—	—	0.02(0)	0.01(0)	0.02(0)

Cl	0.55(3)	0.74	0.85(4)	—	—	—	0.50(2)	0.46(3)	0.54(2)
Total	95.65	97.57	95.43	94.64	94.65	96.06	96.94	95.58	95.46
XFe	0.53	0.59	0.48	0.56	0.54	0.49	0.62	0.63	0.64
Sample	Experimental								
/Charge	38-32(1)	14-34(1)	13-34(1)	38-44(1)	14-33(1)	13-33(1)	38-43(1)	14-46(1)	13-46(1)
n:	8	14	7	3	2	6	5	9	9
T/fO_2/P	700/-1.3/300			700/-1.3/400	660/-1.3/300		660/-1.3/360		
SiO_2	42.15(1.0)	39.23(1.3)	37.51(1.1)	41.27(1.1)	42.74(5)	38.11(1.5)	42.52(6)	40.35(2.6)	39.40(2.0)
TiO_2	3.78(2)	4.47(2)	4.98(1)	3.71(3)	4.02(3)	4.08(1)	3.52(4)	3.89(3)	3.85(4)
Al_2O_3	12.83(3)	12.77(2)	12.96(2)	14.46(3)	13.96(4)	13.68(4)	13.65(4)	13.88(5)	13.75(4)
FeO	24.03(6)	24.27(5)	25.36(4)	23.12(2)	23.16(1.0)	27.47(7)	21.62(4)	23.47(2.1)	25.19(1.7)
MnO	0.28(0)	0.32(0)	0.30(0)	0.18(0)	0.37(1)	0.44(0)	0.26(0)	0.20(1)	0.23(1)
MgO	6.30(5)	6.47(2)	6.35(3)	6.34(4)	5.07(1)	4.67(2)	5.10(1)	5.56(5)	5.01(5)
CaO	0.38(1)	0.27(2)	0.11(2)	0.40(1)	0.48(0)	0.28(1)	0.61(0)	0.48(2)	0.33(1)
Na_2O	0.49(1)	0.39(1)	0.38(0)	0.52(1)	0.87(1)	0.57(1)	0.34(1)	0.38(1)	0.44(1)
K_2O	8.10(2)	8.60(2)	8.59(2)	8.37(4)	7.95(1)	8.46(2)	7.48(4)	8.11(5)	8.26(4)
F	0.01(0)	0.01(0)	0.01(0)	—	0.03(0)	0.02(0)	0.02(0)	0.01(0)	0.01(0)
Cl	0.10(0)	0.07(0)	0.12(0)	0.02(0)	0.64(1)	0.63(4)	0.54(0)	0.60(2)	0.51(3)
Total	98.41	96.85	96.63	98.41	99.29	98.41	95.65	96.94	96.99
XFe	0.68	0.68	0.69	0.67	0.72	0.77	0.70	0.70	0.74

[1] The numbers in parentheses following in charge name indicate the XH_2O;

[2] Number of analyses;

[3] Temperature(℃)/△NNO/pressure(MPa);

[4] Numbers in parentheses indicate 1 s.d.in terms of the last one units cited;

[5] XFe= Fe/(Fe+Mg) cationic ratio; [6] Below detection limits.

Appendix table 14 The representative compositions of natural and experimental Fe–Ti oxides

Sample	Natural						Experimental		
/Charge	QTL-38C		QTL-14A		QTL-13		38-51(1)[1]	14-54(1)	13-54(1)
n:[2]	9	19	5	18	5	8	10	10	15
T/fO_2/P[3]							800/+3/200		
TiO_2	0.89(3)[4]	49.8(4)	2.53(2.0)	50.56(8)	1.6(5)	50.6(7)	12.7(8)	9.38(1.5)	8.12(2.7)
Al_2O_3	0.17(1)	0.01(0)	0.09(1)	0.01(0)	0.08(1)	0.01(0)	0.69(0)	0.71(1)	0.67(2)
Fe_2O_3	66.42(8)	6.2(7)	62.66(4.0)	4.23(1.1)	65.08(1.0)	3.96(1.2)	42.02(1.1)	49.57(3.2)	51.36(6.1)
FeO	31.58(3)	41.71(6)	32.52(1.6)	41.64(1.1)	32.12(5)	40.9(9)	39.86(7)	38.03(1.1)	36.72(2.0)
MnO	0.03(0)	2.99(4)	0.26(2)	3.76(7)	0.09(0)	4.52(4)	0.25(0)	0.19(0)	0.16(0)
MgO	0(0)	0.03(0)	0.01(0)	0.02(0)	0.01(0)	0.02(0)	1.11(1)	0.82(1)	0.71(1)
Total	99.09	100.74	98.07	100.21	98.98	100.01	96.63	98.7	97.74
XIlm[5]		0.94		0.96		0.96			
Xusp[6]	0.03		0.07		0.05		0.37	0.27	0.24

Sample	Experimental								
/Charge	38-49(1)	14-52(1)	13-52(1)	38-24(1)	14-26(0.8)	38-17(1)		14-19(1)	13-19(1)
n:	8	7	3	4		5	8	12	3
T/fO_2/P	700/+3/200			900/-1.3/200		850/-1.3/200			
TiO_2	9.44(3.8)	10.28(2.5)	7.09(7)	47.91(3)	48.92	46.78(7)	17.31(3)	46.82(9)	47.16(1.4)
Al_2O_3	0.39(1)	0.42(1)	0.41(1)	0.22(1)	0.18	0.47(4)	2.64(1)	0.48(3)	0.72(3)
Fe_2O_3	48.18(7.1)	46.37(5.0)	52.43(1.5)	5.42(1.7)	5.91	7.19(8)	30.26(4)	8.52(1.1)	7.78(8)
FeO	37.43(3.2)	37.96(2.1)	35.35(6)	36.23(3)	36.98	38.76(6)	44.2(6)	37.68(8)	37.68(1.2)

MnO	0.37(1)	0.42(1)	0.32(0)	0.54(2)	0.57	0.57(0)	0.51(0)	0.71(0)	0.76(0)
MgO	0.55(2)	0.66(1)	0.53(1)	3.38(0)	3.54	1.47(1)	1.06(1)	2(2)	2.12(1)
Total	96.37	96.11	96.13	93.7	96.1	95.25	95.98	96.21	96.22
XIlm				0.94	0.94	0.93		0.91	0.92
Xusp	0.28	0.3	0.21				0.55		
Sample	Experimental								
/Charge	38-11(1)		14-12(0.6)	13-12(1)	38-48(1)	14-51(1)	13-51(1)	38-04(1)	14-04(1)
n:	5		3	5	5	3	2	4	
T/fO_2/P	800/-1.3/200				800/-1.3/360			700/-1.3/200	
TiO_2	45(1.3)	13.42	48.57(5)	50.13(6)	46.69(7)	46.88(1.2)	46(1.6)	37.29(1.7)	46.89
Al_2O_3	0.44(4)	3.51	0.19(2)	0.32(3)	0.78(5)	0.24(1)	0.49(4)	2.19(6)	0.98
Fe_2O_3	9.95(4)	36.6	4.7(1)	1(4)	9.68(2)	6.87(1.9)	6.61(3)	8.66(3)	7.08
FeO	37.46(1.3)	35.61	41.09(5)	41.44(4)	38.91(6)	38.92(1.2)	37.44(8)	31.14(1.7)	39.21
MnO	0.8(1)	0.74	0.65(1)	1.16(1)	0.8(0)	0.83(2)	0.89(4)	1.09(2)	1.44
MgO	1.03(0)	2.7	1.03(0)	1.35(1)	1.11(1)	1.17(1)	1.56(1)	0.37(0)	0.75
Total	94.68	92.58	96.24	95.41	97.98	94.9	92.98	80.74	96.35
XIlm	0.9		0.95	0.99	0.9	0.93	0.93	0.89	0.93
Xusp		0.41							

[1] The numbers in parentheses following in charge name indicate the XH_2O

[2] Number of analyses

[3] Temperature(℃)/△NNO/pressure(MPa)

[4] Numbers in parentheses indicate 1 s.d.in terms of the last one units cited

[5]% Ilmenite in rhombohedralhemoilmenite calculated following Stormer(1983)

[6]% ulvospinel in titanomagnetite calculated following Stormer(1983)

Appendix table 15 The representative compositions of experimental residual glass normalized to 100%

Sample-XH_2O(n)	Charge	SiO_2	TiO_2	Al_2O_3	FeO	MnO	MgO	CaO	Na_2O	K_2O	Total	Original total	A/CNK	XH_2O	n
T: 900 ℃; P: 195MPa; fO_2: NNO-1.3; run duration: 138h															
QTL38C-1.0(5)	38-24	70.61	0.65	14.97	2.74	0.08	0.20	3.24	3.31	4.20	100	91.83	0.94	1	5
sd		0.84	0.04	0.30	0.50	0.09	0.15	0.42	0.11	0.12					
QTL38C-0.9(5)	38-25	69.87	0.61	15.13	3.17	0.07	0.35	3.09	3.46	4.25	100	92.69	0.95	0.9	5
sd		0.66	0.12	0.15	0.48	0.06	0.14	0.34	0.15	0.19					
QTL38C-0.8(5)	38-26	69.36	0.55	15.16	3.53	0.09	0.55	2.69	3.30	4.77	100	93.66	0.98	0.8	5
sd		0.34	0.08	0.08	0.26	0.08	0.07	0.15	0.05	0.23					
QTL38C-0.7(4)	38-27	69.30	0.47	15.26	3.54	0.03	0.44	2.74	3.46	4.77	100	92.85	0.96	0.7	4
sd		0.35	0.12	0.07	0.20	0.03	0.03	0.10	0.10	0.21					
QTL38C-0.6(5)	38-28	70.01	0.69	14.70	3.44	0.04	0.43	2.48	3.34	4.86	100	94.51	0.96	0.6	5
sd		0.45	0.24	0.18	0.28	0.03	0.06	0.10	0.05	0.16					
QTL38C-0.5(5)	38-29	70.83	0.51	14.36	3.10	0.06	0.46	2.12	3.41	5.16	100	94.84	0.95	0.5	5
sd		0.22	0.10	0.17	0.28	0.08	0.04	0.03	0.12	0.07					
QTL38C-0.4(5)	38-30	72.46	0.74	13.62	2.33	0.04	0.35	1.91	2.96	5.59	100	95.09	0.95	0.4	5
sd		0.55	0.31	0.18	0.20	0.03	0.07	0.11	0.38	0.20					
QTL14A-1.0(7)	14-26	69.40	0.68	14.41	3.43	0.04	0.81	2.47	3.64	5.13	100	93.35	0.90	1	7
sd		0.41	0.11	0.16	0.38	0.03	0.06	0.05	0.32	0.11					
QTL14A-0.9(7)	14-27	69.27	0.65	14.22	3.54	0.08	0.83	2.39	3.84	5.19	100	93.67	0.87	0.9	7
sd		0.45	0.08	0.23	0.27	0.05	0.10	0.07	0.36	0.17					
QTL14A-0.8(6)	14-28	69.26	0.57	14.54	3.30	0.10	0.67	2.34	3.78	5.43	100	95.07	0.89	0.8	6
sd		0.28	0.09	0.18	0.16	0.09	0.07	0.12	0.14	0.15					

QTL14A-0.7(6)	14-29	69.80	0.50	14.62	2.84	0.04	0.63	2.29	3.73	5.56	100	95.41	0.90	0.7	6
sd		0.20	0.11	0.14	0.19	0.03	0.14	0.15	0.23	0.13					
QTL14A-0.6(6)	14-30	69.51	0.64	14.85	2.76	0.03	0.62	2.28	3.87	5.44	100	95.68	0.91	0.6	6
sd		0.20	0.09	0.22	0.21	0.05	0.04	0.10	0.13	0.14					
QTL14A-0.5(6)	14-31	71.09	0.54	14.24	2.37	0.07	0.39	1.91	3.51	5.89	100	96.26	0.91	0.5	6
sd		0.20	0.09	0.23	0.20	0.06	0.03	0.04	0.18	0.17					
QTL14A-0.4(10)	14-32	72.27	0.54	13.75	1.93	0.06	0.36	1.51	3.45	6.13	100	96.32	0.91	0.4	10
sd		0.53	0.09	0.21	0.28	0.06	0.12	0.19	0.20	0.27					
QTL13-1.0(7)	13-26	72.04	0.37	14.00	2.24	0.08	0.45	1.80	3.46	5.57	100	93.88	0.93	1	7
sd		0.41	0.07	0.21	0.16	0.07	0.07	0.05	0.28	0.25					
QTL13-0.9(6)	13-27	72.05	0.36	14.12	2.07	0.03	0.43	1.79	3.52	5.63	100	94.52	0.93	0.9	6
sd		0.28	0.07	0.20	0.24	0.05	0.02	0.07	0.18	0.12					
QTL13-0.8(6)	13-28	71.99	0.38	13.96	2.09	0.08	0.45	1.89	3.58	5.58	100	94.83	0.91	0.8	6
sd		0.27	0.04	0.10	0.20	0.11	0.05	0.12	0.19	0.07					
QTL13-0.6(6)	13-29	72.10	0.31	14.12	2.07	0.06	0.39	1.74	3.60	5.61	100	95.85	0.93	0.6	6
sd		0.26	0.06	0.23	0.12	0.05	0.04	0.07	0.20	0.07					
T: 850 ℃; P: 199MPa; fO_2: NNO-1.3; run duration: 181h															
QTL38C-1.0(4)	38-17	72.52	0.14	14.97	2.16	0.13	0.10	2.83	3.01	4.13	100	91.26	1.03	1	4
sd		0.60	0.08	0.02	0.59	0.02	0.05	0.10	0.14	0.25					
QTL38C-0.9(5)	38-18	71.88	0.32	14.92	2.73	0.04	0.19	2.34	3.00	4.58	100	90.86	1.05	0.9	5
sd		0.65	0.23	0.13	0.17	0.03	0.05	0.12	0.43	0.21					
QTL38C-0.8(5)	38-19	72.98	0.22	14.15	2.29	0.01	0.24	1.68	3.04	5.40	100	93.71	1.02	0.8	5
sd		0.30	0.08	0.16	0.13	0.01	0.04	0.03	0.20	0.13					
QTL38C-0.7(5)	38-20	73.53	0.20	13.99	1.96	0.02	0.20	1.52	2.94	5.64	100	93.06	1.02	0.7	5
sd		0.24	0.07	0.36	0.15	0.03	0.05	0.09	0.27	0.14					

QTL38C-0.6(6)	38-21	74.35	0.19	13.45	1.86	0.05	0.15	1.44	2.75	5.77	100	93.27	1.00	0.6	6
sd		0.54	0.12	0.26	0.18	0.05	0.02	0.17	0.21	0.17					
QTL38C-0.5(2)	38-22	72.78	0.47	13.76	2.60	0.02	0.38	1.93	2.95	5.12	100	92.93	0.99	0.5	2
sd		0.35	0.25	1.49	0.98	0.00	0.30	0.23	0.35	0.19					
QTL38C-0.4(5)	38-23	70.24	0.82	14.98	2.40	0.05	0.42	2.81	3.25	5.03	100	95.50	0.94	0.4	5
sd		0.40	0.25	0.77	1.17	0.08	0.28	0.11	0.33	0.03					
QTL14A-1.0(6)	14-19	71.63	0.31	14.52	2.25	0.10	0.23	2.39	3.61	4.96	100	92.01	0.93	1	6
sd		0.52	0.07	0.17	0.50	0.09	0.14	0.10	0.20	0.17					
QTL14A-0.9(6)	14-20	71.34	0.31	14.62	2.51	0.05	0.22	2.29	3.73	4.94	100	93.31	0.93	0.9	6
sd		0.63	0.05	0.22	0.25	0.04	0.07	0.10	0.27	0.25					
QTL14A-0.8(6)	14-21	72.39	0.30	14.21	2.07	0.03	0.20	1.77	3.78	5.24	100	92.69	0.94	0.8	6
sd		0.72	0.12	0.16	0.22	0.04	0.07	0.15	0.59	0.24					
QTL14A-0.7(5)	14-22	73.43	0.23	13.56	1.80	0.04	0.19	1.31	3.51	5.93	100	95.32	0.93	0.7	5
sd		0.30	0.11	0.21	0.08	0.04	0.04	0.03	0.14	0.25					
QTL14A-0.6(7)	14-23	73.54	0.27	13.34	1.79	0.02	0.14	1.28	3.32	6.29	100	94.90	0.91	0.6	7
sd		0.28	0.16	0.18	0.19	0.03	0.03	0.07	0.11	0.21					
QTL14A-0.5(6)	14-24	73.75	0.27	13.32	1.60	0.02	0.13	1.30	3.23	6.37	100	95.68	0.91	0.5	6
sd		0.57	0.04	0.47	0.25	0.04	0.05	0.30	0.29	0.30					
QTL14A-0.4(8)	14-25	74.97	0.30	12.54	1.60	0.04	0.16	1.10	2.92	6.37	100	96.45	0.92	0.4	8
sd		0.42	0.26	0.07	0.35	0.07	0.08	0.08	0.14	0.22					
QTL13-1.0(6)	13-19	72.49	0.26	14.19	2.14	0.06	0.30	1.74	3.45	5.38	100	92.29	0.97	1	6
sd		0.51	0.09	0.14	0.17	0.08	0.05	0.06	0.34	0.23					
QTL13-0.9(6)	13-20	72.88	0.23	14.12	1.92	0.05	0.23	1.67	3.50	5.40	100	92.42	0.97	0.9	6
sd		0.06	0.06	0.11	0.25	0.06	0.04	0.04	0.22	0.10					
QTL13-0.8(6)	13-21	72.33	0.26	14.24	1.99	0.07	0.23	1.68	3.55	5.64	100	93.84	0.95	0.8	6

sd		0.16	0.08	0.16	0.14	0.07	0.03	0.11	0.21	0.18					
QTL13-0.7(6)	13-22	73.89	0.23	13.71	1.39	0.06	0.16	1.21	3.39	5.96	100	93.44	0.96	0.7	6
sd		0.36	0.06	0.11	0.16	0.05	0.04	0.05	0.31	0.17					
QTL13-0.6(5)	13-23	74.66	0.29	13.28	1.11	0.05	0.16	0.97	3.26	6.21	100	95.11	0.96	0.6	5
sd		0.50	0.06	0.35	0.09	0.03	0.02	0.25	0.18	0.16					
QTL13-0.5(5)	13-24	74.93	0.21	13.04	1.32	0.02	0.12	0.93	3.00	6.44	100	95.80	0.96	0.5	5
sd		0.38	0.06	0.17	0.24	0.02	0.01	0.05	0.21	0.12					
QTL13-0.4(7)	13-25	76.10	0.25	12.31	1.15	0.01	0.12	0.81	2.96	6.30	100	95.96	0.94	0.4	7
sd		0.28	0.08	0.21	0.29	0.03	0.05	0.07	0.10	0.07					
T:800 ℃; P: 203MPa; fO_2: NNO-1.3; run duration: 351h															
QTL38C-1.0(6)	38-11	74.00	0.11	14.49	2.06	0.06	0.13	2.19	2.86	4.10	100	89.74	1.10	1	6
sd		0.65	0.04	0.18	0.39	0.10	0.04	0.15	0.17	0.11					
QTL38C-0.9(10)	38-12	75.23	0.24	13.01	1.60	0.06	0.09	1.62	3.54	4.62	100	92.05	0.95	0.9	10
sd		0.77	0.20	0.25	0.23	0.06	0.04	0.22	0.69	0.16					
QTL38C-0.8(5)	38-13	75.96	0.13	12.53	1.53	0.03	0.11	1.24	3.22	5.24	100	93.34	0.95	0.8	5
sd		0.52	0.04	0.30	0.31	0.04	0.08	0.11	0.39	0.22					
QTL38C-0.7(6)	38-14	76.85	0.14	12.05	1.32	0.07	0.15	1.01	2.78	5.63	100	93.64	0.96	0.7	6
sd		0.27	0.04	0.15	0.27	0.10	0.07	0.06	0.19	0.22					
QTL14A-1.0(6)	14-12	73.32	0.15	14.13	2.23	0.09	0.16	2.17	3.22	4.54	100	90.71	1.00	1	6
sd		0.34	0.08	0.06	0.14	0.10	0.05	0.07	0.23	0.21					
QTL14A-0.9(5)	14-13	73.25	0.21	13.91	1.43	0.08	0.14	1.49	4.08	5.41	100	91.36	0.91	0.9	5
sd		0.53	0.09	0.22	0.35	0.06	0.04	0.05	0.33	0.23					
QTL14A-0.8(4)	14-14	74.76	0.13	13.26	1.46	0.07	0.07	1.29	3.50	5.48	100	91.18	0.95	0.8	4
sd		0.95	0.10	0.11	0.16	0.08	0.03	0.06	0.67	0.45					
QTL14A-0.7(6)	14-15	75.31	0.26	12.68	1.45	0.09	0.11	1.01	3.15	5.95	100	91.71	0.94	0.7	6

sd		0.76	0.12	0.08	0.18	0.05	0.11	0.08	0.37	0.16					
QTL13-1.0(4)	13-12	76.28	0.11	12.54	1.11	0.02	0.09	0.98	2.98	5.89	100	94.29	0.96	1	4
sd		0.19	0.08	0.17	0.13	0.04	0.01	0.05	0.09	0.07					
QTL13-0.9(5)	13-13	74.52	0.13	13.90	1.45	0.07	0.09	1.43	2.74	5.69	100	92.12	1.05	0.9	5
sd		0.40	0.08	0.19	0.23	0.07	0.02	0.02	0.26	0.17					
QTL13-0.8(5)	13-14	74.55	0.06	13.30	1.12	0.05	0.07	1.04	3.81	6.00	100	91.80	0.91	0.8	5
sd		0.66	0.05	0.23	0.18	0.07	0.03	0.09	0.73	0.18					
QTL13-0.7(5)	13-15	75.94	0.08	12.71	1.03	0.04	0.06	0.74	3.56	5.84	100	92.59	0.94	0.7	5
sd		0.26	0.09	0.09	0.26	0.06	0.02	0.03	0.30	0.10					
QTL13-0.6(5)	13-16	76.32	0.15	12.40	1.34	0.04	0.09	0.86	3.13	5.67	100	92.56	0.96	0.6	5
sd		0.86	0.08	0.28	0.44	0.07	0.11	0.09	0.71	0.24					
T: 750 ℃; P: 194MPa; fO_2: NNO-1.3; run duration: 471h															
QTL38C-0.9(5)	38-07	77.65	0.14	12.52	1.27	0.05	0.10	1.34	2.29	4.65	100	91.18	1.12	0.9	5
sd		0.60	0.10	0.29	0.14	0.05	0.07	0.17	0.21	0.21					
QTL38C-0.8(4)	38-08	77.18	0.14	12.44	0.93	0.09	0.06	1.12	2.45	5.59	100	91.61	1.03	0.8	4
sd		0.71	0.13	0.36	0.10	0.09	0.02	0.31	0.09	0.08					
QTL14A-0.9(5)	14-07	76.72	0.13	12.64	1.04	0.05	0.10	1.10	2.73	5.49	100	92.06	1.02	0.9	5
sd		0.62	0.13	0.12	0.20	0.08	0.06	0.02	0.41	0.09					
QTL14A-0.8(5)	14-08	77.50	0.20	11.89	1.14	0.07	0.07	1.03	2.78	5.32	100	93.18	0.97	0.8	5
sd		0.36	0.27	0.18	0.12	0.05	0.04	0.06	0.15	0.12					
QTL13-0.8(6)	13-08	77.43	0.10	12.14	1.04	0.05	0.05	0.90	2.93	5.35	100	93.32	0.99	0.8	6
sd		0.21	0.08	0.29	0.13	0.04	0.03	0.06	0.19	0.19					
QTL13-0.7	13-09	77.25	0.15	11.93	1.41	0.08	0.07	0.85	2.71	5.56	100	93.34	0.99	0.7	1
T: 700 ℃; P: 202MPa; fO_2: NNO-1.3; run duration: 689h															
QTL38C-1.0(11)	38-04	77.09	0.15	12.33	0.98	0.03	0.08	1.38	3.35	4.60	100	90.37	0.95	1	11

sd		0.74	0.10	0.15	0.34	0.03	0.04	0.12	0.50	0.12					
QTL14A-1.0(9)	14-04	77.04	0.17	12.50	0.81	0.06	0.07	1.31	3.10	4.95	100	90.47	0.97	1	9
sd		0.71	0.20	0.16	0.29	0.07	0.04	0.10	0.50	0.17					
QTL13-1.0(5)	13-04	77.54	0.09	12.80	0.83	0.09	0.04	1.27	2.30	5.05	100	90.62	1.11	1	5
sd		0.48	0.06	0.22	0.14	0.09	0.03	0.15	0.16	0.22					
T: 660 ℃; P: 206MPa; fO_2: NNO-1.3; run duration: 1337h															
QTL14A-1.0(9)	14-01	77.32	0.12	12.75	0.73	0.06	0.10	1.18	3.17	4.58	100	90.49	1.03	1	9
sd		0.55	0.04	0.26	0.18	0.05	0.09	0.22	0.09	0.15					
QTL13-1.0(9)	13-01	77.23	0.05	13.04	0.66	0.05	0.02	0.91	3.49	4.57	100	91.51	1.06	1	9
sd		0.57	0.05	0.14	0.12	0.04	0.02	0.06	0.39	0.20					
T: 800 ℃; P: 299MPa; fO_2: NNO-1.3; run duration: 356h															
QTL38C-1(17)	38-38	72.99	0.17	14.57	1.81	0.09	0.10	2.77	3.25	4.24	100	89.58	0.97	1	17
sd		0.36	0.08	0.18	0.42	0.09	0.07	0.18	0.16	0.15					
QTL38C-0.9(23)	38-39	72.89	0.21	14.23	2.10	0.07	0.17	2.30	3.50	4.52	100	90.19	0.96	0.9	23
sd		0.63	0.11	0.21	0.43	0.07	0.12	0.14	0.20	0.20					
QTL38C-0.8(8)	38-40	74.39	0.29	13.60	1.73	0.04	0.14	2.02	3.14	4.65	100	90.75	0.98	0.8	8
sd		0.55	0.13	0.24	0.24	0.05	0.07	0.15	0.22	0.19					
QTL38C-0.7(3)	38-41	74.97	0.68	12.97	1.79	0.09	0.13	1.55	2.77	5.06	100	91.93	1.01	0.7	3
sd		0.64	0.62	0.23	0.51	0.02	0.02	0.11	0.12	0.01					
QTL38C-0.6(1)	38-42	76.28	0.11	12.95	1.57	0.00	0.10	1.26	2.11	5.60	100	92.27	1.09	0.6	1
sd		0.61	0.13	0.05	0.06	0.00	0.03	0.02	0.66	0.12					
QTL14A-0.8(14)	14-42	74.00	0.29	13.62	1.71	0.06	0.16	1.84	2.93	5.38	100	91.4	0.97	0.8	14
sd		0.29	0.13	0.20	0.16	0.05	0.10	0.17	0.19	0.16					
QTL14A-0.7(11)	14-43	74.80	0.29	13.13	1.86	0.04	0.20	1.60	2.58	5.52	100	92.47	1.00	0.7	11
sd		0.48	0.15	0.20	0.33	0.05	0.10	0.24	0.52	0.23					

QTL13-1.0(17)	13-40	74.22	0.21	13.99	1.54	0.03	0.13	1.86	2.64	5.38	100	89.62	1.03	1	17
sd		0.47	0.07	0.14	0.36	0.04	0.07	0.08	0.12	0.17					
QTL13-0.9(19)	13-41	73.80	0.19	13.94	1.50	0.05	0.14	1.73	3.06	5.59	100	90.56	0.98	0.9	19
sd		0.39	0.06	0.15	0.17	0.07	0.03	0.05	0.17	0.17					
QTL13-0.8(19)	13-42	74.39	0.23	13.75	1.15	0.04	0.13	1.46	3.05	5.80	100	92.22	0.99	0.8	19
sd		0.43	0.10	0.14	0.11	0.06	0.03	0.09	0.19	0.17					
QTL13-0.7(20)	13-43	74.96	0.16	13.27	1.26	0.08	0.12	1.27	2.90	5.99	100	92.69	0.98	0.7	20
sd		0.26	0.07	0.11	0.10	0.08	0.03	0.09	0.13	0.11					
T: 750 ℃; P: 300MPa; fO_2: NNO-1.3; run duration: 571h															
QTL38C-1(25)	38-33	74.78	0.09	14.15	1.24	0.07	0.08	2.26	2.99	4.33	100	89.06	1.03	1	25
sd		0.49	0.08	0.17	0.21	0.07	0.03	0.11	0.41	0.26					
QTL38C-0.9(16)	38-34	76.79	0.13	12.76	1.20	0.03	0.07	1.65	2.85	4.52	100	89.38	1.01	0.9	16
sd		0.67	0.10	0.21	0.16	0.04	0.03	0.07	0.63	0.26					
QTL38C-0.8(8)	38-35	77.40	0.05	12.38	1.14	0.07	0.06	1.45	2.73	4.73	100	90.56	1.01	0.8	8
sd		0.37	0.06	0.28	0.13	0.07	0.02	0.12	0.36	0.17					
QTL14A-1(30)	14-35	74.27	0.17	14.38	1.05	0.07	0.05	2.45	2.80	4.77	100	88.56	1.01	1	30
sd		0.56	0.19	0.20	0.21	0.05	0.03	0.19	0.43	0.19					
QTL14A-0.9(15)	14-36	75.01	0.19	13.24	1.40	0.09	0.17	1.79	2.73	5.38	100	90.76	0.98	0.9	15
sd		0.87	0.17	0.16	0.52	0.08	0.17	0.24	0.16	0.18					
QTL14A-0.8(7)	14-37	75.84	0.20	12.74	1.30	0.06	0.21	1.55	2.65	5.45	100	90.65	0.97	0.8	7
sd		0.74	0.11	0.53	0.49	0.04	0.14	0.30	0.35	0.32					
QTL14A-0.7(2)	14-38	75.39	0.27	12.77	1.64	0.08	0.26	1.45	2.57	5.59	100	92.63	0.99	0.7	2
sd		0.62	0.11	0.08	0.01	0.08	0.05	0.35	0.05	0.15					
QTL13-1.0(30)	13-35	74.61	0.11	13.94	1.01	0.04	0.07	1.80	2.99	5.43	100	88.79	0.99	1	30
sd		0.58	0.08	0.19	0.24	0.04	0.04	0.13	0.36	0.21					

QTL13-0.9(24)	13-36	75.55	0.08	13.45	0.91	0.05	0.05	1.47	2.84	5.59	100	90.41	1.00	0.9	24
sd		0.36	0.07	0.15	0.14	0.05	0.03	0.23	0.20	0.16					
QTL13-0.8(10)	13-37	76.73	0.15	12.50	0.96	0.07	0.08	1.21	2.94	5.35	100	91.99	0.97	0.8	10
sd		0.46	0.13	0.22	0.25	0.07	0.05	0.28	0.07	0.23					
T: 700 ℃; P: 316MPa; fO_2: NNO-1.3; run duration: 570h															
QTL38C-1.0(7)	38-32	77.31	0.12	13.57	1.08	0.07	0.05	2.19	1.85	3.75	100	87.71	1.22	1	7
sd		0.44	0.12	0.22	0.17	0.06	0.03	0.22	0.59	0.28					
QTL14A-1.0(5)	14-34	75.18	0.15	13.89	1.16	0.03	0.07	1.97	2.62	4.93	100	88.84	1.05	1	5
sd		0.30	0.07	0.19	0.20	0.03	0.02	0.04	0.17	0.15					
QTL13-1.0(5)	13-34	75.28	0.09	14.04	0.92	0.05	0.04	1.84	2.65	5.10	100	88.23	1.06	1	5
sd		0.22	0.07	0.20	0.14	0.06	0.02	0.17	0.23	0.21					
T: 660 ℃; P: 298MPa; fO_2: NNO-1.3; run duration: 1267h															
QTL13-1.0(21)	13-33	76.30	0.07	13.20	0.62	0.06	0.04	1.30	3.86	4.54	100	90.95	0.97	1	21
sd		0.64	0.06	0.23	0.25	0.07	0.05	0.08	0.55	0.24					
T: 800 ℃; P: 200MPa; fO_2: NNO+3; run duration: 312h															
QTL38C-1.0(10)	38-51	75.30	0.23	14.07	1.36	0.07	0.42	2.36	2.57	3.62	100	87.59	1.13	1	10
sd		0.47	0.11	0.15	0.13	0.07	0.20	0.13	0.30	0.12					
QTL14A-1.0(10)	14-54	74.52	0.24	14.33	1.10	0.03	0.34	2.54	2.72	4.19	100	87.75	1.05	1	10
sd		0.45	0.06	0.25	0.13	0.04	0.04	0.18	0.16	0.22					
QTL13-1.0(10)	13-54	75.63	0.14	13.74	1.12	0.06	0.31	1.84	2.73	4.43	100	87.68	1.09	1	10
sd		0.38	0.08	0.12	0.15	0.08	0.02	0.08	0.23	0.17					
T: 800 ℃; P:363MPa; fO_2: NNO+3; run duration: 281h															
QTL38C-1.0(5)	38-52	75.44	0.18	14.75	0.92	0.10	0.25	2.76	2.14	3.46	100	87.39	1.20	1	5
sd		0.27	0.06	0.18	0.07	0.09	0.05	0.09	0.18	0.10					
QTL14A-1.0(5)	14-55	74.72	0.20	14.47	1.16	0.06	0.36	2.51	2.23	4.28	100	86.76	1.12	1	5

sd		0.30	0.11	0.19	0.18	0.08	0.03	0.07	0.11	0.12					
QTL13-1.0(5)	13-55	76.29	0.12	13.79	1.07	0.05	0.31	1.82	2.13	4.43	100	86.82	1.19	1	5
sd		0.30	0.08	0.18	0.20	0.05	0.02	0.07	0.17	0.18					
T: 800 ℃; P: 673MPa; fO_2: NNO+3; run duration: 277h															
QTL38C-1.0(5)	38-53	74.73	0.19	14.82	0.90	0.14	0.21	3.14	2.36	3.51	100	87.09	1.11	1	5
sd		0.42	0.14	0.13	0.15	0.04	0.10	0.21	0.28	0.18					
QTL14A-1.0(5)	14-56	75.01	0.32	14.38	0.70	0.07	0.30	2.55	2.34	4.33	100	86.66	1.09	1	5
sd		0.47	0.15	0.12	0.12	0.07	0.11	0.18	0.23	0.09					
QTL13-1.0(5)	13-56	75.55	0.18	13.80	0.95	0.03	0.29	1.93	2.70	4.57	100	87.63	1.07	1	5
sd		0.40	0.08	0.20	0.15	0.04	0.08	0.14	0.21	0.15					
QTL38C-1.0a(5)	38-54	75.26	0.17	14.77	0.92	0.11	0.21	2.91	2.16	3.49	100	85.22	1.17	1	5
sd		0.36	0.11	0.20	0.13	0.03	0.05	0.13	0.19	0.11					
T: 700 ℃; P: 206MPa; fO_2: NNO+3; run duration: 312h															
QTL38C-1.0(5)	38-49	78.47	0.09	12.45	0.76	0.03	0.22	1.57	2.28	4.13	100	87.8	1.13	1	5
sd		0.95	0.10	0.19	0.18	0.05	0.26	0.31	0.13	0.11					
QTL14A-1.0(6)	14-52	78.43	0.10	12.49	0.66	0.05	0.09	1.38	2.21	4.58	100	85.57	1.12	1	6
sd		0.37	0.08	0.25	0.18	0.07	0.06	0.15	0.08	0.19					
QTL13-1.0(6)	13-52	78.91	0.05	12.66	0.50	0.04	0.08	1.26	2.14	4.36	100	85.41	1.20	1	6
sd		0.34	0.05	0.17	0.14	0.05	0.02	0.08	0.22	0.16					

Appendix table 16 Composition of the different starting materials for oxygen fugacity experiments

	QT38C	Qitianling QTL14A	QTL13	Santa maria	Pinatubo	Jamon HBMzG	Qitianling QT38C
	Granite	Granite	Granite	Dacite*	Dacite	Granite	Granite
	Glass(20)	Glass(20)	Glass(20)	Bulk rock	Glass	Bulk rock	Bulk rock
wt.%							
SiO_2	64.78	68.17	71.11	65.41	65.50	70.62	65.72
TiO_2	1.06	0.67	0.33	0.42	0.45	0.68	1.04
Al_2O_3	13.91	14.35	13.92	17.67	16.35	12.92	13.58
Fe_2O_3				4.84		2.00	1.68
FeO						2.37	4.22
FeO_{tot}	5.51	3.96	2.46	4.36	4.50	4.17	5.74
MnO	0.11	0.07	0.06	0.20	0.14	0.07	0.1
MgO	1.38	0.89	0.43	1.17	2.11	0.69	1.37
CaO	3.30	2.46	1.83	4.36	4.82	2.47	3.27
Na_2O	3.11	2.79	2.99	4.94	4.45	3.54	2.95
K_2O	4.21	5.31	5.58	1.90	1.67	3.52	3.91
P_2O_5	0.35	0.21	0.10	0.15		0.30	0.33
H_2O						0.57	
LOI						0.34	0.91
F						0.12	0.2
Total	97.72	98.88	98.81	100.58	99.99	98.98	98.01
A/CNK	0.89	0.97	0.97	0.97	0.91	0.91	0.90
X_{Fe}	0.80	0.82	0.85	0.79	0.68	0.86	0.81

Numbers in parentheses indicate the number of analyses; The compositions of bulk rock or glass are cited from: Santa maria (Rose,1987), Jamon (Dall'Agnol et al.,1999), Pinatubo (Scaillet and Evans, 1999); $X_{Fe}= FeO_{tot} / (FeO_{tot} + MgO)$

Appendix table 17 Oxygen fugacity experiments conditions and run product results

Charge	T (℃)	P (MPa)	[1]XH_2O^{in}	[2]H_2O_{melt} (wt%)	[3]△NNO	Phase assemblage	Duration (hours)
Crystallization experiment (dry glass as starting materials)							
38-51	800	205	1.00	6.17	2.37	Gl, Cpx, [4]**Amp**, **Bt**, Mag, Pl	312
38-52	800	363	1.00	9.40	2.37	Gl, Cpx, **Amp**, **Bt**, Mag	281
38-53	800	673	1.00	10.00*	2.37	Gl, Cpx, **Amp**, **Bt**, Mag, Ttn	277
38-54	800	673	1.00	15.00*	2.37	Gl, **Bt**, Mag, Ttn	277
38-55	800	320	1.00	8.48	0.15	Gl, **Amp**, **Bt**, Ilm, Mag	188
38-56	800	284	1.00	7.73	1.01	Gl, (Cpx), **Amp**, Bt, Ilm, Mag	284
14-54	800	205	1.00	6.17	2.37	Gl, Cpx, **Bt**, Mag	312
14-55	800	363	1.00	9.40	2.37	Gl, Cpx, **Bt**, Mag	281
14-56	800	673	1.00	15.00*	2.37	Gl, **Bt**, Mag, Ttn	277
14-57	800	320	1.00	8.48	0.15	Gl, Cpx, (Amp), Bt, Ilm, Mag	188
14-58	800	284	1.00	7.73	1.01	Gl, Cpx, **Bt**, Ilm, Mag	284
13-54	800	205	1.00	6.17	2.37	Gl, Cpx, Bt, Mag	312
13-55	800	363	1.00	9.40	2.37	Gl, **Bt**, Mag	281
13-56	800	673	1.00	15.00*	2.37	Gl, **Bt**, Mag	277
13-57	800	320	1.00	8.48	0.15	Gl, Cpx, (Amp), Bt, Ilm, Mag	188
13-58	800	284	1.00	7.73	1.01	Gl, Cpx, **Bt**, Ilm, Mag, Pl	284
SM-01	660	206	1.00	6.45	-1.36	— (crystals are too small)	1337
SM-02	700	202	1.00	6.39	-1.15	Gl, Amp, Ilm, (Bt), Pl	689
SM-03	700	412	1.00	10.62	-1.38	Gl, **Amp**, Ilm, Pl	648
SM-04	800	299	1.00	8.04	-0.90	Gl, **Amp**, Ilm, Pl	356
SM-05	800	320	1.00	8.48	0.15	Gl, **Amp**,Mag, Pl	188
SM-06	800	284	1.00	7.73	1.01	Gl, **Amp**,Mag, Pl	284
P-01	660	206	1.00	6.45	-1.36	— (crystals are too small)	1337
P-02	700	202	1.00	6.39	-1.15	Amp, (Ilm), (Bt), Pl, Qtz	689
P-03	700	412	1.00	10.62	-1.38	Gl, **Amp**, Ilm, (Bt), Pl	648
P-04	800	299	1.00	8.04	-0.90	Gl, **Amp**, Ilm, Pl	356
P-05	800	320	1.00	8.48	0.15	Gl, **Amp**, Ilm, (Mag), Pl	188
P-06	800	284	1.00	7.73	1.01	Gl, **Amp**, Ilm, Mag, Pl	284
Melting experiment (bulk rock powder as starting materials)							
M-J-01	660	206	1.00	10.00*	-1.36	— (powder)	1337
M-J-02	700	202	1.00	10.00*	-1.15	(Gl), **Amp**, Ilm, Mag, Bt, Pl, Kfs, Qtz	689
M-J-03	700	412	1.00	10.00*	-1.38	Gl, **Amp**, Ilm, Mag, Bt	648
M-J-05	800	320	1.00	10.00*	0.15	Gl, **Amp**, Ilm, Mag, (Bt)	188

M-J-06	800	284	1.00	10.00*	1.01	Gl, **Amp**, Ilm, Mag	284
M-38-01	660	206	1.00	10.00*	-1.36	— (powder)	1337
M-38-02	700	202	1.00	10.00*	-1.15	Gl, **Amp**, Ilm, Mag, Bt, Pl, Kfs, Qtz	689
M-38-03	700	412	1.00	10.00*	-1.38	Gl, **Amp**, Ilm, Mag, Bt, Pl, (Kfs)	648
M-38-04	750	300	1.00	10.00*	-0.96	Gl, **Amp**, Ilm, Mag, Bt, Pl, (Kfs)	571
M-38-05	800	320	1.00	10.00*	0.15	Gl, **Amp**, Ilm, Mag, Bt	188
M-38-06	800	284	1.00	10.00*	1.01	Gl, **Amp**, Ilm, Mag, Bt	284

[1]XH_2O_{in}: initial $H_2O/(H_2O+CO_2)$ loaded in each capsule (in moles)

[2]H_2O_{melt} wt%: water content in the melt; determined by calculation of VolatileCalc; Those water contents with * were loaded in the capsules.

[3]△NNO: $\log fO_2$(experiment)-$\log fO_2$(NNO; Chou, 1987); fO_2 were calculated according to XH_2O_{fin}

[4]All the phases in bold were successfully analysed by microprobe

Appendix table 18 The composition of amphibole of Oxygen fugacity experiments

Charge	38-55	SD	38-56	SD	P-03	SD	P-04	SD	P-05	SD
	n=15		n=15		n=4		n=14		n=21	
SiO_2	44.22	0.64	43.41	1.23	48.92	1.37	45.73	0.70	44.09	0.73
TiO_2	1.71	0.15	1.64	0.16	0.62	0.14	1.47	0.20	1.62	0.20
Al_2O_3	9.47	0.52	9.40	0.67	5.87	1.83	8.89	0.72	9.89	0.59
FeO	13.09	0.43	17.66	0.76	20.08	2.46	14.95	0.41	15.16	0.48
MnO	0.33	0.10	0.30	0.12	0.63	0.12	0.32	0.11	0.32	0.10
MgO	13.51	0.31	10.93	0.29	13.87	1.14	13.23	0.37	12.78	0.35
CaO	11.90	0.11	11.50	0.59	6.27	2.15	9.91	0.29	10.30	0.28
Na_2O	1.35	0.06	1.51	0.12	1.08	0.23	1.89	0.10	1.96	0.11
K_2O	0.97	0.09	0.95	0.10	0.11	0.05	0.20	0.06	0.27	0.06
F	0.54		0.38		0.02		0.08		0.09	
Cl	0.01		0.01		0.01		0.01		0.01	
O=F,Cl	0.23		0.16		0.01		0.04		0.04	
Total	96.85		97.53		97.47		96.62		96.46	
Si	6.530		6.480		7.094		6.620		6.443	
Al iv	1.470		1.520		0.894		1.376		1.557	
Al vi	0.178		0.135		0.103		0.140		0.147	
Ti	0.190		0.185		0.068		0.160		0.178	
Fe^{3+}	0.577		0.729		1.069		1.283		1.222	
Fe^{2+}	1.040		1.476		1.372		0.526		0.630	
Mn	0.041		0.038		0.077		0.039		0.040	
Mg	2.974		2.433		2.999		2.855		2.784	
Ca	1.882		1.839		0.968		1.537		1.613	
Na	0.387		0.437		0.303		0.530		0.557	
K	0.182		0.182		0.019		0.037		0.050	
Altot	1.648		1.654		0.997		1.516		1.704	
Fe#	0.35		0.48		0.45		0.39		0.40	
Charge	P-06	SD	SM-02	SD	SM-03	SD	SM-04	SD	SM-05	SD
	n=20		n=2		n=6		n=19		n=18	
SiO_2	45.45	0.79	51.63	0.49	48.24	1.90	45.56	1.56	45.08	0.95
TiO_2	1.50	0.15	1.07	0.13	0.91	0.20	1.37	0.23	1.16	0.28
Al_2O_3	8.99	0.52	6.41	0.70	8.09	1.13	10.07	0.68	10.08	0.94
FeO	12.10	0.36	18.22	0.86	21.15	3.44	17.27	1.13	16.45	0.77
MnO	0.38	0.13	1.31	0.10	0.97	0.15	0.58	0.10	0.57	0.12
MgO	14.90	0.44	10.28	0.14	10.35	1.12	10.82	0.84	11.40	0.71
CaO	11.05	0.26	8.07	0.76	7.43	2.02	9.07	0.66	9.73	0.41

Na_2O	1.52	0.10	1.27	0.14	1.52	0.32	2.08	0.12	2.01	0.15
K_2O	0.27	0.06	0.32	0.05	0.23	0.08	0.26	0.06	0.32	0.10
F	0.21		0.04		0.04		0.08		0.07	
Cl	0.02		0.01		0.01		0.01		0.01	
O=F,Cl	0.09		0.02		0.02		0.04		0.03	
Total	96.31		98.62		98.92		97.15		96.85	
Si	6.577		7.322		6.964		6.615		6.580	
Al iv	1.423		0.678		1.031		1.385		1.420	
Al vi	0.111		0.393		0.344		0.339		0.314	
Ti	0.163		0.114		0.098		0.150		0.127	
Fe^{3+}	1.083		1.196		1.047		1.287		1.180	
Fe^{2+}	0.382		0.965		1.511		0.810		0.828	
Mn	0.047		0.158		0.118		0.072		0.071	
Mg	3.215		2.174		2.230		2.342		2.480	
Ca	1.713		1.226		1.147		1.412		1.522	
Na	0.427		0.350		0.427		0.586		0.568	
K	0.050		0.058		0.042		0.049		0.060	
Altot	1.534		1.071		1.375		1.723		1.734	
Fe#	0.31		0.50		0.53		0.47		0.45	

Charge	SM-06 n=10	SD	M-J-02 n=3	SD	M-J-03 n=4	SD	M-J-05 n=11	SD	M-J-06 n=7	SD
SiO_2	48.68	1.54	43.48	0.65	44.24	0.47	47.75	1.07	47.53	1.57
TiO_2	1.03	0.15	1.32	0.12	1.15	0.05	0.95	0.19	1.15	0.16
Al_2O_3	9.95	0.73	6.31	0.55	8.12	0.18	6.06	0.69	6.73	0.95
FeO	12.72	0.63	29.43	0.62	26.67	0.95	16.70	0.46	11.73	0.30
MnO	0.70	0.09	0.72	0.01	0.39	0.02	0.35	0.13	0.37	0.04
MgO	12.41	0.73	3.88	0.47	5.82	0.60	13.01	0.68	15.40	0.51
CaO	9.53	0.48	9.65	0.08	10.23	0.21	10.15	0.34	11.49	0.18
Na_2O	1.79	0.24	1.63	0.13	1.48	0.06	1.35	0.11	1.21	0.15
K_2O	0.42	0.12	0.82	0.08	0.63	0.07	0.42	0.12	0.55	0.13
F	0.06		0.45		0.20		0.56		0.74	
Cl	0.01		0.03		0.01		0.01		0.01	
O=F,Cl	0.03		0.20		0.09		0.24		0.32	
Total	97.27		97.54		98.85		97.07		96.59	
Si	6.960		6.816		6.688		6.954		6.91	
Al iv	1.040		1.160		1.312		0.989		1.08	
Al vi	0.637		0.006		0.136		0.052		0.07	
Ti	0.111		0.156		0.131		0.105		0.13	
Fe^{3+}	0.690		0.987		1.043		1.214		0.75	
Fe^{2+}	0.831		2.872		2.329		0.820		0.68	
Mn	0.084		0.096		0.050		0.043		0.05	

Mg	2.647		0.907		1.311		2.823		3.34	
Ca	1.460		1.621		1.658		1.584		1.79	
Na	0.495		0.496		0.434		0.383		0.34	
K	0.076		0.164		0.121		0.077		0.10	
Altot	1.676		1.166		1.447		1.041		1.15	
Fe#	0.37		0.81		0.72		0.42		0.30	
Charge	M-38-02 n=10	SD	M-38-03 n=8	SD	M-38-04 n=6	SD	M-38-05 n=24	SD	M-38-06 n=	SD 4
SiO_2	41.97	0.52	42.12	0.52	42.63	0.84	44.11	0.39	44.22	1.01
TiO_2	1.68	0.36	1.82	0.23	1.74	0.12	1.65	0.04	1.61	0.13
Al_2O_3	8.09	0.47	8.09	0.29	10.07	0.74	9.32	0.43	9.59	0.58
FeO	24.27	0.80	24.24	0.85	22.73	1.15	17.47	0.18	13.53	0.49
MnO	0.64	0.12	0.63	0.12	0.50	0.09	0.37	0.02	0.40	0.10
MgO	6.63	0.62	6.44	0.51	6.87	0.44	11.76	0.30	13.42	0.49
CaO	10.56	0.29	10.66	0.19	10.85	0.45	11.27	0.09	11.82	0.22
Na_2O	1.79	0.18	1.78	0.11	1.65	0.17	1.58	0.07	1.43	0.16
K_2O	1.27	0.09	1.33	0.04	1.14	0.08	1.02	0.07	1.13	0.13
F	0.15		0.15		0.32		0.31		0.63	
Cl	0.00		0.00		0.04		0.01		0.01	
O=F,Cl	0.07		0.06		0.14		0.13		0.27	
Total	96.99		97.21		98.40		98.74		97.54	
Si	6.54		6.56		6.48		6.46		6.50	
Si	1.44		1.43		1.52		1.54		1.50	
Al iv	0.04		0.05		0.29		0.07		0.16	
Al vi	0.20		0.21		0.20		0.18		0.18	
Ti	0.73		0.60		0.59		0.94		0.63	
Fe^{3+}	2.43		2.56		2.31		1.20		1.03	
Fe^{2+}	0.08		0.08		0.06		0.05		0.05	
Mn	1.54		1.50		1.56		2.57		2.94	
Mg	1.76		1.78		1.77		1.77		1.86	
Ca	0.54		0.54		0.49		0.45		0.41	
Na	0.25		0.26		0.22		0.19		0.21	
K	1.48		1.49		1.81		1.61		1.66	
Fe#	0.67		0.68		0.65		0.45		0.36	

Appendix table 19 The composition of biotite of Oxygen fugacity experiments

Charge	38-55	SD	38-56	SD	14-58	SD	14-57	SD	13-58	SD	13-57
	n=6		n=19		n=6		n=2		n=5		1
SiO_2	37.98	0.52	39.41	1.21	39.71	0.76	39.64	1.33	39.51	1.65	37.08
TiO_2	2.97	0.19	3.61	0.21	3.93	0.23	3.46	0.51	4.43	0.23	3.77
Al_2O_3	13.52	0.14	14.05	0.34	13.98	0.34	14.01	0.18	13.73	0.55	13.69
FeO	19.61	0.33	13.68	1.05	14.36	1.03	18.69	0.85	15.50	0.26	19.59
MnO	0.12	0.09	0.16	0.08	0.18	0.07	0.13	0.00	0.16	0.04	0.14
MgO	11.74	0.21	14.92	0.34	14.40	0.46	10.59	0.52	13.29	0.38	11.53
CaO	0.17	0.08	0.22	0.14	0.18	0.05	0.47	0.20	0.24	0.31	0.16
Na_2O	0.51	0.06	0.45	0.06	0.43	0.03	0.41	0.06	0.41	0.06	0.39
K_2O	6.97	0.15	8.78	0.22	8.93	0.35	7.78	0.40	8.63	0.56	8.52
F	0.70	0.19	0.88	0.25	0.90	0.27	0.28	0.09	1.06	0.45	0.28
Cl	0.01	0.01	0.01	0.01	0.01	0.01	0.01	0.00	0.01	0.01	0.00
O=F,Cl	0.30	0.08	0.37	0.10	0.38	0.11	0.12	0.04	0.45	0.19	0.12
TOTAL	93.36	0.56	95.15	1.08	95.99	1.65	94.70	1.05	95.87	1.63	94.38
Based on 22 Oxygen											
Si	5.400	0.074	5.603	0.172	5.623	0.107	5.612	0.189	5.474	0.229	5.138
Al	2.406	0.034	2.327	0.093	2.336	0.071	2.368	0.161	2.301	0.022	2.455
Al	0.000	0.000	0.070	0.086	0.035	0.056	0.095	0.134	0.034	0.074	0.000
Ti	0.338	0.019	0.394	0.024	0.426	0.023	0.388	0.057	0.482	0.033	0.432
Fe(ii)	2.477	0.055	1.657	0.142	1.728	0.111	2.331	0.102	1.872	0.036	2.493
Mn	0.015	0.012	0.019	0.010	0.022	0.009	0.016	0.001	0.020	0.005	0.018
Mg	2.644	0.053	3.220	0.082	3.090	0.089	2.355	0.111	2.863	0.143	2.616
Ca	0.028	0.013	0.034	0.021	0.027	0.008	0.076	0.032	0.037	0.046	0.025
Na	0.150	0.016	0.125	0.015	0.119	0.009	0.117	0.018	0.115	0.017	0.114
K	1.343	0.034	1.622	0.030	1.639	0.060	1.480	0.072	1.591	0.130	1.653
Cl	0.003		0.002		0.410		0.130		0.483		0.134
F	0.333		0.403		0.003		0.002		0.003		0.000
TOTAL	14.80		15.07		15.05		14.84		14.79		14.94
Fe#	0.48		0.34		0.36		0.50		0.40		0.49

Appendix table 20 The information of experimental amphibole from literatures

	Charge	Amp-Fe#	T（℃）	△NNO	W-Fe#	P（MPa）
Jamon	15	0.20	848	3.12	0.858	310
	1	0.30	801	2.37	0.858	313
	7	0.35	707	2.79	0.858	314
	46	0.57	801	-1.15	0.858	304
	23	0.71	706	-1.35	0.858	299
Wangrah	1	0.43	800	0	0.869	200
	25	0.48	800	-0.09	0.869	200
	7	0.57	800	-0.19	0.869	200
	13	0.50	750	0	0.869	200
	23	0.60	750	-0.19	0.869	200
	15	0.60	700	0	0.869	200
Pinatubo	8	0.27	785	2.7	0.681	221
	16	0.44	776	-0.01	0.681	224
	18	0.39	776	1.04	0.681	224
	20	0.34	776	1.71	0.681	225
	22	0.31	834	2.01	0.681	230
	23	0.29	834	1.93	0.681	230
	24	0.29	834	1.82	0.681	230
	33	0.35	866	1	0.681	209
	34	0.36	866	0.91	0.681	209
	35	0.37	866	0.81	0.681	209
	42	0.33	899	1.2	0.681	225
	43	0.35	899	1.1	0.681	225
	44	0.36	899	1.01	0.681	225
	51	0.31	781	2.3	0.681	224
	65	0.34	780	2.6	0.681	389
	66	0.33	780	2.5	0.681	389
	67	0.36	780	2.4	0.681	389
	900	0.19	900	4	0.646	400
	900	0.19	900	3.8	0.646	400
	900	0.19	900	3.6	0.646	400
	900	0.17	900	3.4	0.646	400
	950	0.22	950	3.5	0.646	400
	750	0.25	750	4.6	0.646	940
	750	0.19	750	4.7	0.646	940
	750	0.16	750	4.8	0.646	940
	841	0.40	841	2.1	0.646	960
	841	0.24	841	2.3	0.646	960
	841	0.30	841	2.6	0.646	960
	841	0.31	841	2.7	0.646	960
	841	0.25	841	2.9	0.646	960

	892	0.23	892	2	0.646	830
	892	0.29	892	2.4	0.646	830
	892	0.26	892	2.4	0.646	830
	892	0.20	892	2.6	0.646	830
	892	0.24	892	2.7	0.646	830
	892	0.17	892	3	0.646	830
	943	0.22	943	3	0.646	960
	943	0.19	943	3.4	0.646	960
Lyngdal	50-9	0.46	850	0.59	0.812	404
	50-10	0.46	850	0.5	0.812	404
	50-25	0.55	830	-0.01	0.812	399
	50-26	0.56	830	-0.11	0.812	399
	06-10	0.51	850	0.5	0.807	404
	06-9	0.51	850	0.58	0.807	404
	06-25	0.55	830	0.01	0.807	399
	50-17	0.38	880	0.41	0.812	404
	50-18	0.42	880	0.29	0.812	404
	50-19	0.48	880	0.17	0.812	404
	50-20	0.45	880	0.03	0.812	404
	50-7	0.43	850	0.79	0.812	404
	50-8	0.43	850	0.69	0.812	404
	50-11	0.49	850	0.34	0.812	404
	50-23	0.48	830	0.2	0.812	399
	50-24	0.51	830	0.05	0.812	399
	50-27	0.62	830	-0.28	0.812	399
	50-13	0.57	800	0.07	0.812	390
	50-14	0.59	800	-0.05	0.812	390
	50-15	0.62	800	-0.15	0.812	390
	50-16	0.62	800	-0.23	0.812	390
	50-29	0.55	775	-0.031	0.812	414
	50-30	0.56	775	-0.094	0.812	414
	50-31	0.58	775	-0.304	0.812	414
	06-20	0.49	880	0.01	0.807	404
	06-21	0.49	880	-0.09	0.807	404
	06-10	0.51	850	0.5	0.807	404
	06-09	0.47	850	0.58	0.807	404
	06-25	0.55	830	0.01	0.807	399
	06-13	0.56	800	0.07	0.807	390
	06-14	0.63	800	-0.05	0.807	390
	06-15	0.65	800	-0.15	0.807	390
	06-29	0.58	775	-0.03	0.807	414
	06-30	0.61	775	-0.13	0.807	414

Data are from Dall'Agnol et al. (1999); Bogaerts et al. (2003); Klimm et al. (2003); Scaillet and Evans, (1999) and Prouteau and Scaillet, (2003)

Appendix table 21 The information of experimental biotite from literatures

Point#		Bt-Fe#	T（℃）	△NNO	W-Fe#	P（kbar）
Jamon	RD5	0.38	801	1.64	0.858	313
	RD8	0.42	707	2.78	0.858	314
	RD20	0.24	848	2.47	0.858	310
	RD23	0.72	706	-1.35	0.858	299
	RD51	0.57	801	-1.75	0.858	304
Lvngdal	50-11	0.53	850	0.34	0.812	404
	50-12	0.51	850	0.19	0.812	404
	50-25	0.58	830	-0.01	0.812	399
	50-26	0.58	830	-0.01	0.812	399
	50-27	0.62	830	-0.28	0.812	399
	50-28	0.62	830	-0.42	0.812	399
	50-14	0.64	800	-0.05	0.812	390
	50-15	0.64	800	-0.15	0.812	390
	50-16	0.63	800	-0.23	0.812	390
	06-21	0.55	880	-0.09	0.807	404
	06-20	0.52	880	0.01	0.807	404
	06-19	0.48	880	0.17	0.807	404
	06-18	0.44	880	0.28	0.807	404
	06-17	0.39	880	0.41	0.807	404
	06-11	0.52	850	0.35	0.807	404
	06-10	0.49	850	0.50	0.807	404
	06-09	0.47	850	0.58	0.807	404
	06-08	0.44	850	0.67	0.807	404
	06-07	0.40	850	0.79	0.807	404
	06-23	0.49	830	0.20	0.807	399
	06-24	0.53	830	0.09	0.807	399
	06-25	0.56	830	0.01	0.807	399
	06-26	0.59	830	-0.12	0.807	399
	06-13	0.56	800	0.07	0.807	390
	06-14	0.62	800	-0.05	0.807	390
	06-15	0.66	800	-0.15	0.807	390
	06-16	0.66	800	-0.23	0.807	390
	06-29	0.60	775	-0.03	0.807	414
	06-30	0.62	775	-0.13	0.807	414
	06-45	0.33	850	1.50	0.807	191
Kenva	002-33	0.90	693	-1.80	0.963	156
	575-47	0.97	661	-1.70	0.990	151
	49-44	0.97	661	-1.70	1.000	151
Himalavan	DK31	0.48	803	-1.27	0.817	407
	DK15	0.48	749	-0.72	0.817	405
	DK19*	0.58	720	-1.17	0.817	398
	DK34*	0.59	682	-1.08	0.817	408
	DK41*	0.67	682	-1.00	0.817	408
	DK44"	0.63	663	-1.33	0.817	416

Data are from Dall'Agnol et al.,1999; Bogaerts et al., 2003; Klimm et al., 2003; Prouteau and Scaillet, 2003; and Scaillet, 1995; Scaillet and Macdonald, 2003

Appendix table 22 The test for our oxybarometer using other data from literatures

Literature	3	5	5	2	1	1	1	1	4	4	4
	11	MC1314R10	MC1314RB02	94A5-3	3	48	46	42	MD	MD	MD
T（℃）	775	705	700	710	800	800	800	800	800	800	775
Fe#Bt	0.460	0.480	0.460	0.590	0.390	0.410	0.400	0.390	0.355	0.359	0.363
Fe#Amp*Fe#w	0.470	0.460	0.430	0.590	0.350	0.370	0.360	0.370	0.348	0.379	0.312
Fe#w	0.660	0.702	0.702	0.832	0.750	0.800	0.760	0.760	0.710	0.710	0.710
P（MPa）	300	200	250	260	850	850	850	850	200	200	200
Fe#Bt*Fe#w	0.30	0.34	0.32	0.49	0.29	0.33	0.30	0.30	0.25	0.26	0.26
Fe#amp*Fe#w	0.31	0.32	0.30	0.49	0.26	0.30	0.27	0.28	0.25	0.27	0.22
wTiO2	0.70	1.15	1.15	0.18	0.55	0.55	0.56	0.56	1.54	1.54	1.54
wAl2O3/SiO2	0.25	0.25	0.25	0.17	0.24	0.24	0.24	0.24	0.24	0.24	0.24
wNa2O/K2O	1.44	1.29	1.29	0.56	0.99	0.84	0.81	0.83	0.71	0.71	0.71
Exp-NNO	0.00	0.60	0.70	0.22	1.88	1.88	1.88	1.88	0.00	-0.09	-0.09
(1)Cal-NNO	-0.11	0.23	0.60	-0.77	1.83	1.72	1.71	1.64	1.04	0.74	1.44
(3)Cal-NNO	-0.55	-0.78	-0.50	-0.76	1.74	1.78	1.71	1.78	0.10	0.08	0.06

Data are from [1]Whitney and Stormer, 1985; [2]Chesner, 1998; [3]Holtz et al., 2005; [4]Pietranik et al., 2009 and [5]Mutch et al., 2016.

Appendix table 23. Major elements and trace elements compositions of the Xianghualing No. 431 dike

Rock type	Ongonite I					Ongonite II				Topazite			
Sample No.	ZK840–					XXL–		XHL–		XXL–			
	10*	11*	12*	14*	20*	33	34	310	73	08	10	11	12
SiO_2 (wt. %)	65.83	70.21	69.67	70.76	71.74	67.23	67.51	67.14	67.20	57.77	59.60	63.08	56.57
TiO_2						0.01	0.01	0.01	0.01	0.03	0.03	0.02	0.03
Al_2O_3	19.63	16.08	17.11	16.93	17.23	19.91	19.49	19.78	20.05	27.77	23.94	23.08	25.78
Fe_2O_3	0.44	0.40	0.29	0.10	0.42	0.17	0.02	0.02	0.02	0.44	1.07	0.36	1.68
FeO	2.63	2.66	1.73	0.79	0.55	0.14	0.26	0.15	0.22	0.92	2.14	1.15	2.08
MnO	0.06	0.06	0.04	0.03	0.02	0.03	0.08	0.09	0.08	0.83	0.47	0.36	0.49
MgO	0.16	0.30	0.14	0.12	0.62	0.01	0.01	0.02	0.01	0.11	0.08	0.04	0.05
CaO	0.49	0.57	0.71	0.70	1.00	0.03	0.02	0.02	0.05	0.04	0.03	0.01	0.03
Na_2O	4.00	3.80	6.88	5.70	4.52	4.54	4.54	4.80	4.13	0.08	0.07	0.06	0.07
K_2O	4.32	3.80	2.04	3.30	1.05	4.59	4.23	4.26	4.26	3.56	5.57	5.18	3.62
P_2O_5	0.00	0.00	0.01	0.00	0.00	0.01	0.03	0.02	0.02	0.01	0.01	0.02	0.01
Li_2O	0.21		0.18	0.13	0.05	0.31	0.45	0.48	0.54	1.47	1.67	1.38	1.49
H_2O	0.85	1.11	1.06	1.16	1.82								
LOI						2.13	2.74	2.49	3.06	5.99	4.73	4.61	7.34
F	3.30	2.32	1.20	1.16	2.06	1.11	1.19	1.42	1.34	4.99	5.18	5.36	6.22
Total	100.53	100.34	100.56	100.39	100.21	99.10	99.37	99.26	99.65	99.01	99.41	99.35	99.25
A/CNK	1.62	1.41	1.15	1.19	1.66	1.59	1.61	1.58	1.74	6.86	3.87	4.03	6.29
FeO_t	3.03	3.02	1.99	0.88	0.93	0.29	0.28	0.17	0.24	1.32	3.10	1.47	3.59

FeO_t/MnO	50.43	50.33	49.78	29.33	46.40	9.77	3.48	1.87	2.98	1.59	6.60	4.09	7.33
Li (ppm)		1230		886		765	958	1130	1450	6061	6110	5608	6252
Be		8.5		7.7		179	30	13	11	249	34	34	30
Sc		6.5		7.3		8.5	8.7	8.6	8.6	7.1	6.8	5.4	4.9
V		4.7		2.4		1.3	1.2	0.85	1.5	2.5	2.0	1.4	4.2
Cr		9.7		7.9		4.2	11	4.2	11	1.6	2.4	3.5	7.4
Cs		52		39		28	49	60	51	67	74	61	93
Rb		1418		1073		3880	4310	4670	4780	4918	5087	4440	4640
Ba		63		51		14	14	19	17	11	12	7.3	5.4
Th		6.6		6.3		20	11	15	10.0	39	27	30	23
U		25		15		9.5	4.9	7.4	6.9	18	6.9	20	11
Nb		149		248		97	99	133	105	223	105	193	163
Ta		57		175		114	65	97	69	207	100	175	161
Pb		42		30		140	106	52	40	180	139	193	58
Sr		59		78		11	14	15	8.2	16	13	32	12
Zr		71		18		46	30	32	35	77	4.2	86	70
Hf		16		3.2		7.7	3.9	5.7	5.1	22	0.69	24	19
Y		1.7		1.4		0.34	0.35	0.30	0.44	0.54	0.18	0.33	0.57
Ga		59		66		57	55	53	59	25	41	24	33
Sn		35		13		18	38	63	29	142	438	247	802
W		4.6		5.5		39	25	69	24	114	60	758	771
La		1.5		4.5		1.9	2.5	2.5	1.4	2.1	1.0	1.9	1.5
Ce		5.5		17		5.2	6.9	6.2	4.0	5.2	3.8	5.8	3.9
Pr		0.73		1.7		0.52	0.70	0.65	0.40	0.70	0.44	0.67	0.53

Nd	1.8	3.4	0.97	1.3	1.2	0.85	1.6	0.86	1.1	1.2
Sm	0.55	0.88	0.26	0.34	0.29	0.31	0.34	0.16	0.19	0.23
Eu	0.03	0.02	0.02	0.02	0.02	0.02	0.05	0.02	0.01	0.02
Gd	0.32	0.47	0.12	0.14	0.12	0.16	0.13	0.06	0.09	0.15
Tb	0.09	0.08	0.04	0.04	0.03	0.05	0.04	0.02	0.02	0.02
Dy	0.60	0.56	0.27	0.21	0.21	0.34	0.22	0.06	0.10	0.15
Ho	0.11	0.11	0.05	0.04	0.04	0.06	0.05	0.02	0.02	0.03
Er	0.36	0.39	0.21	0.15	0.16	0.25	0.12	0.03	0.10	0.09
Tm	0.08	0.09	0.07	0.05	0.05	0.08	0.05	0.02	0.04	0.04
Yb	0.95	1.2	0.95	0.59	0.69	0.98	0.58	0.13	0.55	0.59
Lu	0.14	0.17	0.15	0.09	0.11	0.16	0.09	0.02	0.07	0.06
Nb/Ta	2.62	1.42	0.85	1.52	1.37	1.53	1.08	1.04	1.10	1.01
Zr/Hf	4.41	5.73	5.97	7.70	5.64	6.76	3.54	6.12	3.63	3.63
Rb/Sr	24.11	13.84	352.73	314.60	313.42	585.07	314.42	406.42	137.17	389.96
Total REE	12.76	30.06	10.72	13.01	12.24	9.07	11.26	6.67	10.68	8.61
LREE/HREE	3.80	8.90	4.77	8.96	7.66	3.36	7.92	17.38	9.71	6.52
δEu	0.06	0.03	0.09	0.07	0.08	0.07	0.21	0.16	0.07	0.12

Note: Major element of the samples with* are cited from Zhu et al., 1993; $FeO_t = FeO+Fe_2O_3*0.9$

Appendix table 24. Representative electron–microprobe results of feldspars and topaz in the Xianghualing No. 431 dike

Rock type	Ongonite						Topazite	
Samples	K–feldspar		Albite		Topaz (matrix)		Topaz	
	Phenocryst	Phenocryst	Phenocryst	Matrix	Columnar	Acicular	Matrix	Phenocryst
SiO_2 (wt. %)	62.80	63.55	69.08	68.79	31.47	31.38	32.30	32.40
TiO_2	–	–	–	–	–	–	–	0.01
Al_2O_3	18.40	18.38	20.51	20.17	57.76	56.30	55.92	55.50
MgO	0.02	–	–	–	–	0.03	–	–
CaO	–	0.00	0.13	0.01				
MnO	0.02	0.04	0.04	–	–	0.02	–	0.02
FeO	–	–	0.04	0.03	–	0.11	–	0.03
Na_2O	0.29	0.30	10.72	10.82				
K_2O	17.42	16.32	0.16	0.20	–	0.02	0.029	0.04
F					19.91	20.17	20.42	20.23
F=O					8.36	8.47	8.58	8.50
Total	98.94	98.60	100.68	100.01	100.76	99.55	100.07	99.76
Si (apfu)					0.948	0.963	0.987	0.994
Al					2.052	2.037	2.013	2.006
F					1.898	1.958	1.973	1.963
An	0.00	0.01	0.64	0.04				
Or	97.57	97.24	0.99	1.21				
Ab	2.43	2.75	98.37	98.75				

Note: –: Below detection limits; structural formulae of topaz were calculated on the basis of (Al+ Si= 3).

Appendix table 25. Representative electron–microprobe results of micas in the Xianghualing No. 431 dike

Rock type	Ongonite I			Ongonite II			Topazite		
Samples	1	2	3	4	5	6	7	8	9
SiO_2 (wt. %)	42.51	42.76	42.06	52.62	52.83	52.55	52.08	53.35	49.35
TiO_2	0.08	0.12	0.15	0.04	0.01	0.07	–	0.03	–
Al_2O_3	21.97	21.81	22.16	22.51	20.59	19.79	19.99	19.54	20.61
FeO	13.32	14.16	15.66	5.34	5.70	4.34	7.71	7.05	9.19
MnO	0.68	0.62	0.83	1.10	0.88	2.00	1.69	1.37	1.74
MgO	0.12	0.05	0.09	–	0.07	0.14	0.09	0.10	0.05
CaO	0.01	0.01	0.04	–	–	–	–	0.02	0.01
Na_2O	0.32	0.40	0.25	0.27	0.11	0.26	0.15	0.17	0.09
K_2O	10.00	10.09	9.28	10.82	9.22	11.03	10.41	9.67	10.28
Rb_2O	0.91	0.85	0.81	–	–	1.42	–	–	–
Cs_2O	0.04	0.02	0.04	–	–	0.04	0.02	–	0.01
F	6.35	7.85	6.14	8.58	8.36	8.45	8.04	8.28	7.92
F= O	2.67	3.31	2.58	3.61	3.52	3.56	3.39	3.49	3.33
Li_2O*	2.65	2.72	2.52	2.60	2.53	2.56	2.43	2.50	2.39
H_2O*	1.03	0.35	1.15	0.37	0.36	0.32	0.53	0.43	0.49
Total	97.30	98.48	98.58	100.63	97.13	99.40	99.75	99.02	98.80
Si	6.311	6.302	6.211	7.107	7.320	7.288	7.197	7.341	6.967
Al^{IV}	1.689	1.698	1.789	0.893	0.680	0.712	0.803	0.659	1.033
Al^{VI}	2.155	2.092	2.068	2.692	2.684	2.524	2.454	2.511	2.396
Ti	0.009	0.013	0.016	0.004	0.001	0.007	0.000	0.003	0.000

Fe	1.654	1.745	1.934	0.604	0.660	0.503	0.891	0.812	1.085
Mn	0.085	0.077	0.103	0.126	0.103	0.235	0.198	0.159	0.209
Mg	0.026	0.010	0.020	0.000	0.015	0.029	0.019	0.021	0.009
Li*	1.581	1.612	1.497	1.410	1.408	1.426	1.350	1.385	1.356
Sum Oct	5.509	5.549	5.638	4.835	4.871	4.724	4.911	4.891	5.056
Ca	0.002	0.001	0.006	0.000	0.000	0.000	0.000	0.002	0.002
Na	0.093	0.114	0.071	0.070	0.031	0.070	0.040	0.045	0.025
K	1.893	1.897	1.747	1.864	1.629	1.951	1.836	1.696	1.852
Rb	0.087	0.080	0.077	0.000	0.000	0.126	0.000	0.000	0.000
Cs	0.002	0.001	0.002	0.000	0.000	0.003	0.001	0.000	0.001
Sum Int	2.078	2.094	1.903	1.934	1.660	2.150	1.877	1.744	1.879
OH*	1.018	0.340	1.135	0.335	0.337	0.292	0.485	0.396	0.466
F	2.982	3.660	2.865	3.665	3.663	3.708	3.515	3.604	3.534
Al total	3.844	3.790	3.857	3.585	3.364	3.236	3.256	3.170	3.429
Fe/(Fe+Mg)	0.985	0.994	0.990	1.000	0.978	0.946	0.980	0.975	0.991

Note: –: Below detection limits. Structural formula calculated based on O= 23. *: LiO_2 and H_2O calculation of Fe-rich mica (ongonite I) and Fe-poor mica (ongonite II and topazite) are after Tindle and Webb (1990) and Monier and Robert (1986), respectively.

Appendix table 26. Representative compositions of columbite-group minerals and tapiolite in the Xianghualing No. 431 dike

Rock type	Ongonite I											
Samples	Columbite–group minerals									Tapiolite		
	1	2	Range	3	4	Range	5	6	Range	7	8	Range
WO_3 (wt.%)	0.36	0.48	0.00–2.33	1.58	1.73	1.18–19.83	10.21	3.62	0.70–5.68	0.91	0.80	0.00–1.24
Nb_2O_5	62.54	67.64	38.40–74.55	28.59	35.02	20.73–45.93	23.34	25.09	22.83–28.05	5.54	8.42	4.82–12.62
Ta_2O_5	16.70	10.51	5.38–39.89	51.04	45.89	32.48–54.14	48.53	51.94	48.53–55.32	79.79	73.65	67.93–79.79
TiO_2	1.74	0.48	0.23–3.34	1.09	0.80	0.32–2.89	1.04	0.48	0.48–2.04	0.74	2.31	0.40–2.32
SnO_2	0.07	0.01	0.00–0.15	0.01	0.01	0.00–0.96	0.16	0.19	0.07–0.20	0.13	0.17	0.05–0.23
Sc_2O_3	0.67	0.16	0.12–2.27	0.59	0.09	0.01–0.80	–	0.29	0.00–0.29	–	–	0.00–0.20
MnO	11.13	13.13	8.09–14.55	5.74	4.77	3.01–10.67	3.72	3.99	3.28–7.99	0.51	0.55	0.41–0.59
FeO	5.80	8.37	6.43–10.87	12.11	12.67	6.57–15.58	13.36	14.83	11.16–14.83	14.02	14.18	13.83–16.48
Total	99.01	100.78		100.74	100.97		100.36	100.43		101.63	100.08	
W	0.006	0.007		0.029	0.030		0.191	0.067		0.019	0.016	
Nb	1.694	1.781		0.905	1.078		0.760	0.815		0.202	0.300	
Ta	0.272	0.166		0.973	0.850		0.950	1.015		1.746	1.578	
Ti	0.078	0.021		0.057	0.041		0.056	0.026		0.044	0.137	
Sn	0.002	0.000		0.000	0.000		0.005	0.005		0.004	0.005	
Sc	0.035	0.008		0.036	0.006		0.000	0.018		0.000	0.000	
Mn	0.565	0.648		0.341	0.275		0.227	0.242		0.035	0.037	
Fe	0.291	0.408		0.710	0.722		0.804	0.891		0.943	0.934	
Mn/(Fe+Mn)	0.66	0.61	0.46–0.70	0.32	0.28	0.17–0.62	0.22	0.21	0.20–0.42	0.04	0.04	0.03–0.04
Ta/(Nb+Ta)	0.14	0.09	0.04–0.38	0.52	0.44	0.30–0.58	0.56	0.55	0.52–0.58	0.90	0.84	0.76–0.90

Appendix table 26. Continued

Rock type	Ongonite II					Topazite			
Samples	Columbite-group minerals					Columbite-group minerals			
	9	10	11	12	Range	13	14	15	Range
WO_3 (wt.%)	1.44	0.09	8.82	4.05	0.00–14.34	4.67	2.02	13.07	1.13–17.46
Nb_2O_5	65.41	41.93	32.55	47.82	28.20–65.49	37.96	40.38	33.89	33.89–44.83
Ta_2O_5	10.19	38.11	35.46	25.32	9.97–38.51	35.68	34.08	31.03	24.22–37.47
TiO_2	1.19	1.56	3.85	3.20	0.51–4.14	3.99	3.13	3.68	1.54–5.09
SnO_2	0.01	0.29	0.67	0.08	0.00–1.24	0.87	0.48	1.32	0.09–11.72
Sc_2O_3	0.27	1.24	1.14	0.82	0.22–1.26	0.68	1.26	1.07	0.30–2.56
MnO	12.00	15.44	16.53	18.02	10.95–18.85	15.97	16.76	14.45	13.23–17.48
FeO	9.62	1.38	0.96	1.39	0.67–9.62	0.49	1.33	1.93	0.40–6.51
Total	100.12	100.03	99.97	100.68		100.30	99.43	100.44	
W	0.022	0.001	0.152	0.065		0.079	0.034	0.222	
Nb	1.734	1.239	0.977	1.340		1.116	1.185	1.006	
Ta	0.163	0.677	0.640	0.427		0.631	0.602	0.554	
Ti	0.053	0.077	0.192	0.149		0.195	0.153	0.182	
Sn	0.000	0.008	0.018	0.002		0.023	0.012	0.034	
Sc	0.014	0.071	0.066	0.044		0.038	0.071	0.061	
Mn	0.596	0.855	0.930	0.946		0.879	0.922	0.804	
Fe	0.472	0.075	0.053	0.072		0.027	0.072	0.106	
Mn/(Fe+Mn)	0.56	0.92	0.95	0.93	0.55–0.96	0.97	0.93	0.88	0.68–0.98
Ta/(Nb+Ta)	0.09	0.35	0.40	0.24	0.09–0.41	0.36	0.34	0.36	0.25–0.39

Note: –: Below detection limits. 1, 2 are the representative results of the columbite-(Mn) core; 3, 4 are the representative results of the columbite-(Fe) or tantalite-(Fe) rim; 5, 6 are the representative results of the tantalite-(Fe) associated with tapiolite.

Appendix table 27 Representative electron-microprobe results of microlite in Xianghualing No. 431 dike

Rock type	Ongonite I			Ongonite II			Topazite		
Samples	1	2	3	4	5	6	7	8	9
Nb_2O_5 (wt.%)	10.41	16.21	3.93	5.64	7.63	7.25	7.38	7.62	13.06
Ta_2O_5	62.25	53.14	73.30	66.81	63.23	57.80	60.48	59.34	56.06
TiO_2	0.73	0.61	0.27	1.26	1.33	1.18	1.07	1.62	3.45
Na_2O	7.70	9.22	8.50	0.20	0.28	0.11	7.41	7.62	13.06
CaO	6.23	5.28	5.62	3.28	2.18	1.54	3.50	3.96	3.22
MnO	–	–	0.01	0.20	0.57	0.38	0.18	0.13	0.46
FeO	0.03	0.09	0.05	0.25	0.38	0.81	0.23	0.41	0.09
UO_2	6.97	6.91	4.26	12.71	13.61	13.22	12.48	12.50	17.46
PbO	0.39	0.48	0.26	0.33	0.66	6.56	0.39	0.38	0.56
WO_3	–	1.43	0.30	0.75	1.24	1.62	1.09	0.65	0.73
SnO_2	0.26	0.18	0.15	0.32	0.25	0.34	0.33	0.28	0.34
Sc_2O_3	1.09	0.96	1.09	1.25	0.91	1.03	1.01	1.06	0.50
F	3.15	3.35	3.96	2.70	1.81	1.01	2.24	2.40	1.50
F=O	1.33	1.41	1.67	1.14	0.76	0.42	0.94	1.01	0.63
Total	97.89	96.43	100.02	94.55	93.31	92.42	96.84	95.26	97.55
B site									
Nb	0.424	0.648	0.162	0.233	0.314	0.323	0.320	0.329	0.493
Ta	1.526	1.279	1.813	1.662	1.566	1.548	1.576	1.539	1.274
W	0.000	0.033	0.007	0.018	0.029	0.041	0.027	0.016	0.016
Ti	0.050	0.041	0.018	0.087	0.091	0.087	0.077	0.116	0.217
A site									
Na	1.346	1.581	1.498	0.036	0.049	0.021	1.376	1.409	2.116
Ca	0.602	0.501	0.547	0.322	0.212	0.163	0.359	0.404	0.288
U	0.140	0.136	0.086	0.259	0.276	0.290	0.266	0.265	0.325
Pb	0.010	0.011	0.006	0.008	0.016	0.174	0.010	0.010	0.013
Mn	0.000	0.000	0.000	0.005	0.015	0.010	0.005	0.003	0.011
Fe	0.003	0.007	0.004	0.019	0.029	0.067	0.019	0.033	0.007
Sc	0.086	0.074	0.086	0.099	0.072	0.088	0.084	0.088	0.036
Sn	0.009	0.006	0.006	0.012	0.009	0.014	0.012	0.011	0.011
F	0.897	0.937	1.140	0.781	0.521	0.314	0.679	0.724	0.395

Note: –: Below detection limits. Structural formulae based on Nb+Ta+W+Ti=2.

Appendix table 28 Representative electron-microprobe results of cassiterites in the Xianghualing No. 431 dike

Rock type	Ongonite II				Topazite							
	Cassiterite				Cassiterite I				Cassiterite II			
Samples	1	2	Average	SD	3	4	Average	SD	5	6	Average	SD
			n=20				n=41				n=32	
WO_3 (wt.%)	0.83	0.11	0.22	0.39	–	1.82	0.88	1.04	0.18	0.04	0.21	0.47
Nb_2O_5	0.37	0.04	0.14	0.18	0.20	2.63	1.26	1.08	0.07	0.01	0.11	0.18
Ta_2O_5	0.04	–	0.34	0.48	2.33	5.83	3.04	1.75	0.51	0.03	0.17	0.30
TiO_2	0.19	–	0.22	0.36	0.18	0.62	0.31	0.36	0.09	–	0.16	0.28
SnO_2	98.35	99.73	98.32	1.42	97.44	87.37	92.42	4.16	98.12	99.23	98.13	1.24
Sc_2O_3	–	–	0.01	0.02	–	0.08	0.03	0.04	0.02	–	0.01	0.03
MnO	0.09	0.01	0.03	0.04	0.04	0.70	0.24	0.29	–	–	0.05	0.08
FeO	0.38	0.08	0.20	0.15	0.18	1.87	1.42	1.01	0.11	0.05	0.22	0.26
Total	100.24	99.97	99.48		100.38	100.93	99.60		99.09	99.37	99.07	
W	0.005	0.001	0.001		0.000	0.012	0.006		0.001	0.000	0.001	
Nb	0.002	0.000	0.001		0.001	0.015	0.007		0.000	0.000	0.001	
Ta	0.000	0.000	0.001		0.008	0.020	0.011		0.002	0.000	0.001	
Ti	0.004	0.000	0.004		0.003	0.012	0.006		0.002	0.000	0.003	
Sn	0.981	0.998	0.987		0.973	0.877	0.934		0.990	0.999	0.990	
Sc	0.000	0.000	0.000		0.000	0.001	0.000		0.000	0.000	0.000	
Mn	0.002	0.000	0.001		0.001	0.015	0.005		0.000	0.000	0.001	
Fe	0.004	0.001	0.002		0.002	0.017	0.013		0.001	0.000	0.002	

Note: –: Below detection limits. The number of cations is calculated on the basis of 2 atoms of oxygen.

Appendix table 29 Summary of distribution of ore minerals in different rock types in the Xianghualing No. 431 dike

	Sample No.	Columbite-group minerals	Tapiolite	Microlite	Cassiterite
Ongonite I	ZK840–11	+ + +	+ +	+ +	−
	ZK840–12	+ + +	+ +	+ +	−
	ZK840–14	+ +	−	+	−
	ZK840–15	+ +	−	−	−
	ZK840–16	+ + +	−	−	−
	ZK840–20	+ +	−	−	−
Ongonite II	XXL–33	+ +	−	+ +	+
	XXL–34	+ +	−	−	+
	XHL–310	+	−	−	+
	XHL–73	+	−	−	−
Topazite	XXL–08	+	−	+	+ +
	XXL–10	+ +	−	+	+ + +
	XXL–11	+	−	−	+ + +
	XXL–12	+	−	−	+ + +

Note: +++: most frequent; ++: more abundant; +: relatively abundant; − : rare or absent.

References

.

Aigner-Torres, M., Blundy, J., Ulmer, P., & Pettke, T. (2007). Laser ablation ICPMS study of trace element partitioning between plagioclase and basaltic melts: an experimental approach. Contributions to Mineralogy and Petrology, 153(6), 647-667.

Aigner-Torres, M., Blundy, J., Ulmer, P., & Pettke, T. (2007). Laser ablation ICPMS study of trace element partitioning between plagioclase and basaltic melts: an experimental approach. Contributions to Mineralogy and Petrology, 153(6), 647-667.

Anders, E., Grevesse, N. 1989. Abundances of the elements: Meteoritic and solar. Geochimica et Cosmochimica Acta 53, 197-214.

Andersen, D. J. (1985). New (and final!) models for the Ti-magnetite/ilmenite geothermometer and oxygen barometer. In Abstracts of American Geophysical Union 1985 Spring Meeting. American Geophysical Union.

Anderson, A. T. (1968). Oxidation of the LaBlache Lake titaniferous magnetite deposit, Quebec. The Journal of Geology, 76(5), 528-547.

Anderson, J. L., and Smith, D. R. (1995). The effects of temperature and fo_2 on the al-in-hornblende barometer. American Mineralogist, 80(5-6), 549-559.

Anderson, J.L. (1996) Status of thermobarometry in granitic batholiths. Transactions of the Royal Society of Edinburgh: Earth Sciences, 87, 125–138.

Anderson, J.L., Barth, A.P., Wooden, J.L., and Mazdab, F. (2008) Thermometers and thermobarometers in granitic systems. Reviews in Mineralogy and Geochemistry, 69, 121–142.

Annen, C., Scaillet, B., & Sparks, R. S. J. (2005). Thermal constraints on the emplacement rate of a large intrusive complex: the Manaslu Leucogranite, Nepal Himalaya. Journal of Petrology, 47(1), 71-95.

Badanina, E.V., Veksler, I.V., Thomas, R., Syritso, L.F., Trumbull, R.B., 2004. Magmatic evolution of Li –F, rare-metal granites: a case study of melt inclusions in the Khangilay complex, Eastern Transbaikalia (Russia). Chemical Geology 210, 113– 133.

Bai, D. Y., Chen, J. C., Ma, T. Q., & Wang, X. H. (2005). Geochemical characteristics and tectonic setting of A -type granitic pluton Qitianling in southeast Hunan. Acta Petrologica et Mineralogica., 24(4), 255-272. (in Chinese with English abstract)

Bai, D. Y., Liu, Y. R., Wang, X. H., Tie-Qiu, M. A., & Chen, B. H. (2005). ^{40}Ar-^{39}Ar dating of the biotite monzogranite in northeast Qitianling granite body and its geological significance. Volcanology & Mineral Resources.

Bai, X. J., Wang, M., Jiang, Y. D., & Qiu, H. N. (2013). Direct dating of tin–tungsten mineralization of the piaotang tungsten deposit, south china, by 40 ar/ 39 ar progressive crushing. Geochimica Et Cosmochimica Acta, 114(4), 1-12.

Ballard, J. R., Palin, M. J., & Campbell, I. H. (2002). Relative oxidation states of magmas inferred from Ce (IV)/Ce (III) in zircon: application to porphyry copper deposits of northern Chile. Contributions to Mineralogy and Petrology, 144(3), 347-364.

Barsukov, V. L., Durasova, N. A., Ryabchikov, I. D., Khramov, D. A., & Kravtsova, R. P. (1983). Peculiarities of the behaviour of tin during the liquid immiscibility of alumosilicate melts. Geokhimiya, 2, 189-192.

BAS, M. L., Maitre, R. L., Streckeisen, A., Zanettin, B., & IUGS Subcommission on the Systematics of Igneous Rocks. (1986). A chemical classification of volcanic rocks based on the total alkali-silica diagram. Journal of petrology, 27(3), 745-750.

Beard, J. S., & Lofgren, G. E. (1991). Dehydration melting and water-saturated melting of basaltic and andesitic greenstones and amphibolites at 1, 3, and 6. 9 kb. Journal of Petrology, 32(2), 365-401.

Belkasmi, M., Cuney, M., Pollard, P.J., Bastoul, A., 2000. Chemistry of the Ta-Nb-Sn-W oxide minerals from the Yichun rare metal granite (SE China): genetic

implications and comparison with Moroccan and French Hercynian examples. Mineralogical Magazine 64, 507-523.

Berndt, J., Koepke, J., & Holtz, F. (2004). An experimental investigation of the influence of water and oxygen fugacity on differentiation of MORB at 200 MPa. Journal of Petrology, 46(1), 135-167.

Berndt, J., Liebske, C., Holtz, F., Freise, M., Nowak, M., Ziegenbein, D., ... & Koepke, J. (2002). A combined rapid-quench and H2-membrane setup for internally heated pressure vessels: Description and application for water solubility in basaltic melts. American Mineralogist, 87(11-12), 1717-1726.

Beurlen, H., Da Silva, M.R., Thomas, R., Soares, D.R., Olivier, P., 2008. Nb–Ta–(Ti–Sn) oxide mineral chemistry as tracer of rare-element granitic pegmatite fractionation in the Borborema Province, Northeastern Brazil. Mineralium Deposita 43, 207-228.

Bhalla, P., Holtz, F., Linnen, R. L., & Behrens, H. (2005). Solubility of cassiterite in evolved granitic melts: effect of T, fO2, and additional volatiles. Lithos, 80(1-4), 387-400.

Bindeman, I. N., Davis, A. M., & Drake, M. J. (1998). Ion microprobe study of plagioclase-basalt partition experiments at natural concentration levels of trace elements. Geochimica et Cosmochimica Acta, 62(7), 1175-1193.

Black, L. P. (1978). The age of the mud tank carbonatite, strangways range, northern territory. J. Aust. Geol. Geophys., 3, 227-232.

Blevin, P. L. (2004). Redox and compositional parameters for interpreting the granitoid metallogeny of eastern Australia: Implications for gold‐rich ore systems. Resource Geology, 54(3), 241-252.

Blevin, P. L., & Chappell, B. W. (1992). The role of magma sources, oxidation states and fractionation in determining the granite metallogeny of eastern Australia. Earth and Environmental Science Transactions of the Royal Society of Edinburgh, 83(1-2), 305-316.

Blevin, P. L., & Chappell, B. W. (1995). Chemistry, origin, and evolution of mineralized granites in the Lachlan fold belt, Australia; the metallogeny of I-and S-type granites. Economic Geology, 90(6), 1604-1619.

Bogaerts, M. (2003). Pétrologie expérimentale, géochimie et dynamique de mise en place du massif de Lyngdal (Norvège): implications pour le magmatisme AMCG. Ph.D. thesis, Université de Liège.

Bogaerts, M., Scaillet, B., & Auwera, J. V. (2006). Phase equilibria of the Lyngdal granodiorite (Norway): implications for the origin of metaluminous ferroan granitoids. Journal of Petrology, 47(12), 2405-2431.

Boldyrev, V. V. (2002). Thermal decomposition of silver oxalate. Thermochimica acta, 388(1-2), 63-90.

Bonin, B. (2007). A-type granites and related rocks: evolution of a concept, problems and prospects. Lithos, 97(1-2), 1-29.

Bowen, N. L. (1956). The evolution of the igneous rocks. Dover Publications.

Braun, J., Van Der Beek, P., & Batt, G. (2006). Quantitative thermochronology: numerical methods for the interpretation of thermochronological data. Cambridge University Press.

Breiter, K., 2012. Nearly contemporaneous evolution of the A-and S-type fractionated granites in the Krušné hory/Erzgebirge Mts., Central Europe. Lithos 151, 105-121.

Breiter, K., Müller, A., Leichmann, J., Gabašová, A., 2005. Textural and chemical evolution of a fractionated granitic system: the Podlesí stock, Czech Republic. Lithos 80, 323–345.

Breiter, K., Škoda, R., Uher, P., 2007. Nb-Ta-Ti-W-Sn-oxide minerals as indicators of a peraluminous P-and F-rich granitic system evolution: Podlesí, Czech Republic. Mineralogy and Petrology 91, 225-248.

Buddington, A. F., & Lindsley, D. H. (1964). Iron-titanium oxide minerals and synthetic equivalents. Journal of petrology, 5(2), 310-357.

Burnham, A. D., & Berry, A. J. (2012). An experimental study of trace element

partitioning between zircon and melt as a function of oxygen fugacity. Geochimica et Cosmochimica Acta, 95, 196-212.

Burnham, C. W., Holloway, J. R., Davis, N. F. (1969). Thermodynamic Properties of Water to 1,000 deg C and 10,000 Bars, 1969, The Geological Society of America, GSA Special Paper, 132, 1-96.

Burt, D.M., 1992. Lunar mining of oxygen using fluorine. In The Sencond Conf. on Lunar Bases and Space Activities of the 21st Century 1, 423-428.

Cadoux, A., Scaillet, B., Druitt, T. H., and Deloule, E. (2014). Magma storage conditions of large Plinian eruptions of Santorini Volcano (Greece). Journal of Petrology, 55(6), 1129-1171.

Cai J.H., MaoX.D., Cai M.H., et a1. (2002). Geological characteristics of Bailashui tin deposit in Qitianling orefield, eouthem Hunan Province[J].Geology and Mineral Resources of South China,10 (2):55-59 (in Chinese with English abstract)

Cai, D. W., Tang, Y., Zhang, H., Lv, Z. H., Liu, Y. L. (2016). Petrogenesis and tectonic setting of the devonian xiqin a-type granite in the northeastern cathaysia block, se china. Journal of Asian Earth Sciences.

Cai, X.L., Zhu, J.S., Cao, J.M., Yan, Z.Q., Yang, Z.X., and Hong, X.H. Structure and dynamics of lithosphere and asthenosphere in the gigantic East AsianWest Pacific rift system. Geology in China, 2002, 29(3): 234-245 (in Chinese with English abstract).

Carmichael, I. S. (1966). The iron-titanium oxides of salic volcanic rocks and their associated ferromagnesian silicates. Contributions to mineralogy and petrology, 14(1), 36-64.

Carter, A., Roques, D., Bristow, C., & Kinny, P. (2001). Understanding Mesozoic accretion in Southeast Asia: significance of Triassic thermotectonism (Indosinian orogeny) in Vietnam. Geology, 29(3), 211-214.

Černý, P., 1989. Characteristics of pegmatite deposits of tantalum. In Lanthanides, tantalum and niobium (Möller P., Černý P., Saupé F., Eds.). Special Publication

No. 7 of the Society for Geology Applied to Mineral Deposits 195-239.

Černý, P., Chapman, R., Chackowsky, L.E., Ercit, T.S., 1989a. A ferrotantalite-ferrotapiolite intergrowth from Spittal ad Drau, Carinthia, Austria. Mineralogy and Petrology 41, 53-63.

Černý, P., Ercit, T.S., 1989b. Mineralogy of niobium and tantalum: crystal chemical relationships, paragenetic aspects and their economic implications. In Lanthanides, tantalum and niobium (Möller P., Černý P., Saup é F., Eds.). Special Publication No. 7 of the Society for Geology Applied to Mineral Deposits, 27-79.

Černý, P., Ercit, T.S., Wise, M.A., 1992. The tantalite-tapiolite gap: natural assemblages versus experimental data. The Canadian Mineralogist 30, 587-596.

Černý, P., Ucakuwun, E. K., Chapman, R., 1989b. A ferrotantalite-ferrotapiolite exsolution from Uganda: Neues Jahrbuch fur Mineralogie Monatshefte 3,109-120.

Chappell, B. W., and White, A. J. R. (1974). Two contrasting granite types. Pacific Geology 8, 173–174

Chappell, B. W., and White, A. J. R. (2001). Two contrasting granite types: 25 years later. Journal of the Geological Society of Australia, 48(4), 489-499.

Charvet, J. (2013). The neoproterozoic–early paleozoic tectonic evolution of the South China Block: an overview. Journal of Asian Earth Sciences, 74, 198-209.

Charvet, J., Lapierre, H. and Yu, Y.W. Geodynamic significance of the Mesozoic volcanism of southeastern China. J. Southeast Asian Earth Sci., 1994,9(4): 387-396.

Charvet, J., Shu, L., Shi, Y., Guo, L., & Faure, M. (1996). The building of south China: collision of Yangzi and Cathaysia blocks, problems and tentative answers. Journal of Southeast Asian Earth Sciences, 13(3-5), 223-235.

Chaussard, E., and Amelung, F. (2014). Regional controls on magma ascent and storage in volcanic arcs. Geochemistry, Geophysics, Geosystems, 15(4), 1407-1418.

Che, X. D., Wu, F. Y., Wang, R. C., Gerdes, A., Ji, W. Q., Zhao, Z. H., ... & Zhu, Z. Y. (2015). In situ U–Pb isotopic dating of columbite–tantalite by LA–ICP–MS. Ore

Geology Reviews, 65, 979-989.

Chelle-Michou, C., Chiaradia, M., Ovtcharova, M., Ulianov, A., & Wotzlaw, J. F. (2014). Zircon petrochronology reveals the temporal link between porphyry systems and the magmatic evolution of their hidden plutonic roots (the Eocene Coroccohuayco deposit, Peru). Lithos, 198, 129-140.

Chen, D.Q., 1984. On the characteristics and genesis of topaz-felsite porphyry. Acta Petrologica et Mineralogica 1, 9-17 (in Chinese with English abstract).

Chen, J., and B.-m. Jahn (1998). Crustal evolution of southeastern China: Nd and Sr isotopic evidence, Tectonophysics, 284(1), 101-133, doi: http://dx.doi.org/10.1016/S0040-1951(97)00186-8.

Chen, J., Wang, R. C., Zhu, J. C., Jianjun, L. U., and Dongsheng, M. A. (2013). Multiple-aged granitoids and related tungsten-tin mineralization in the nanling range, south china. Science China Earth Sciences, 56(12), 2045-2055. (in Chinese with English abstract).

Chen, P.R., Hua, R.M., Zhang, B.T., Lu, J.J., Fan, C.F., 2002a. Early Yanshanian postorogenic granitoids in the Nanling Range region–petrological constraints and geodynamic settings. Science in China (Series D) 48 (8), 755–768.

Chen, X., Zhang, Y.D., Fan, J.X., Cheng, J.F., Li, Q.J., 2010. Ordovician graptolite-bearing strata in southern Jiangxi with a special reference to the Kwangsian Orogeny. Science in China (Earth Sciences) 53 (1), 1602–1610.

Cherniak, D. J., & Watson, E. B. (2001). Pb diffusion in zircon. Chemical Geology, 172(1-2), 5-24.

Chesner, C. A. (1998). Petrogenesis of the toba tuffs, sumatra, indonesia. Journal of Petrology, 39(3), 397-438.

Chu, Y., Faure M., Lin W, Wang Q. (2012). Tectonic evolution of the Early Mesozoic intracontinental Xuefengshan belt (Hunan, South China), J. Asian Earth Sciences, 61, 199-220.

Chudik, P., Uher, P., Kohut, M., Bačík, P., 2008. Accessory columbite to tantalite,

tapiolite and zircon: products of extreme fractionation in highly peraluminous pegmatitic granite from the Povžaský Inovec Mountains, Western Carpathians, Slovakia. Journal of Geosciences 53, 323-334.

Clarke, D.B., Henry, A.S., White, M.A., 1998. Exploding xenoliths and the absence of 'elephants' graveyards in granite batholiths. Journal of Structural Geology 20, 1325-1343.

Clemens, J. D., and Wall, V. J. (1981). Origin and crystallization of some peraluminous (s-type) granitic magmas. Canadian Mineralogist, 19(1), 111-131.

Clemens, J. D., Holloway, J. R. and White, A. J. R. (1986). Origin of an A-type granite: experimental constraints. American Mineralogist 71, 317–324.

Clemens, J., & Watkins, J. (2001). The fluid regime of high-temperature metamorphism during granitoid magma genesis. Contributions to Mineralogy & Petrology, 140(5), 600-606.

Cobbing, E.J., Mallick, D.I.J., Pitfield, P.E.J., Teoh, L.H., 1986. The granites of the Southeast Asian tin belt. Journal of the Geological Society 143, 537-550.

Collins, W. J., Beams, S. D., White, A. J. R., & Chappell, B. W. (1982). Nature and origin of A-type granites with particular reference to southeastern Australia. Contributions to mineralogy and petrology, 80(2), 189-200.

Collins, W. J., Huang, H. Q., and Jiang, X. (2016). Water-fluxed crustal melting produces cordilleran batholiths. Geology, 44, G37398.1.

Cuney, M., Marignac, C., Weisbrod, A., 1992. The Beauvoir topaz-lepidolite albite granite (Massif Central, France); the disseminated magmatic Sn-Li-Ta-Nb-Be mineralization. Economic Geology 87, 1766-1794.

Dall'Agnol R, Scaillet B, Pichavant M. An Experimental Study of a Lower Proterozoic A-type Granite from theEastern Amazonian Craton, Brazil[J]. Journal of Petrology, 1999, 40(11): 1673-1698.

Dall'Agnol, R., Pichavant, M., & Champenois, M. (1997). Iron-titanium oxide minerals of the Jamon Granite, eastern Amazonian region, Brazil: implications for the

oxygen fugacity in Proterozoic, A-type granites. ANAIS-ACADEMIA BRASILEIRA DE CIENCIAS, 69, 325-348.

Deng, P., Shen, W. Z., Ling, H. F., Ye, H. M., Wang, X. C., Pu, W., et al. (2003). Uranium mineralization related to mantle fluid: a case study of the xianshi deposit in the xiazhuang uranium orefield. Geochimica, 32(6), 520-528.

Deng, X. G., Li, X. H., Liu, Y. M., Huang, G. F., & Hou, M. S. (2005). Geochemical characteristics of Qitianling granites and their implications for mineralization. Yanshi Kuangwuxue Zazhi(Acta Petrol. Mineralog.), 24(2), 93-102. (in Chinese with English abstract)

Dodson, M. H. (1973). Closure temperature in cooling geochronological and petrological systems. Contributions to Mineralogy and Petrology, 40(3), 259-274.

Dong, S.B., Shen, Q.H., Sun, D.Z., Lu, L.Z. (1986). Metamorphic Map of China (1:4000000). Geol. Publ. House, Beijing, pp. 1–40.

Drummond, M. S., & Defant, M. J. (1990). A model for trondhjemite‐tonalite‐dacite genesis and crustal growth via slab melting: Archean to modern comparisons. Journal of Geophysical Research: Solid Earth, 95(B13), 21503-21521.

Du, S.H., Huang, Y.H., 1984. Investigation on Xianghualingite. Science in China (Series B) 11, 1039-1047 (in Chinese with English abstract).

Duc-Tin, Q., Audétat, A., & Keppler, H. (2007). Solubility of tin in (Cl, F)-bearing aqueous fluids at 700 C, 140 MPa: a LA-ICP-MS study on synthetic fluid inclusions. Geochimica et Cosmochimica Acta, 71(13), 3323-3335.

Eadington, P.J., Nashar, B., 1978. Evidence for the magmatic origin of quartz-topaz rocks from the New England Batholith, Australia. Contributions to Mineralogy and Petrology 67, 433-438.

Eby, G. N. (1990). The A-type granitoids: a review of their occurrence and chemical characteristics and speculations on their petrogenesis. Lithos, 26(1-2), 115-134.

Eby, G. N. (1992). Chemical subdivision of the A-type granitoids: petrogenetic and tectonic implications. Geology, 20(7), 641-644.

Faure M., Lin, W. Chu, Y., C. Lepvrier. (2016). Triassic tectonics of the Southern margin of the South China Block. CR Geoscience, 348, 5-14.

Faure, M., Chen, Y., Feng, Z., Shu, L., Xu, Z. (2017). Tectonics and geodynamics of South China: An introductory note. Journal of Asian Earth Sciences, 141, 1-6.

Faure, M., Lepvrier, C., Van Nguyen, V., Van Vu, T., Lin, W., & Chen, Z. (2014). The South China Block-Indochina collision: where, when, and how?. Journal of Asian Earth Sciences, 79, 260-274.

Faure, M., Lin, W., Shu, L., Sun, Y., & Scha Èrer, U. (1999). Tectonics of the Dabieshan (eastern China) and possible exhumation mechanism of ultra high - pressure rocks. Terra Nova, 11(6), 251-258.

Faure, M., Shu, L., Wang, B., Charvet, J., Choulet, F., & Moni é, P. (2009). Intracontinental subduction: a possible mechanism for the Early Palaeozoic Orogen of SE China. Terra Nova, 21(5), 360-368.

Feng, S. J., Zhao, K. D., Ling, H. F., Chen, P. R., Chen, W. F., Sun, T. (2014). Geochronology, elemental and nd–hf isotopic geochemistry of devonian a-type granites in central jiangxi, south china: constraints on petrogenesis and post-collisional extension of the wuyi–yunkai orogeny. Lithos, 206-207(1), 1-18.

Feng, Z., Wang, C., Zhang, M., and Liang, J. (2012). Unusually dumbbell-shaped guposhan–huashan twin granite plutons in nanling range of south china: discussion on their incremental emplacement and growth mechanism. Journal of Asian Earth Sciences, 48(6), 9-23.

Fenn, P.M., 1977. The nucleation and growth of alkali feldspars from hydrous melts. The Canadian Mineralogist 15,135-161.

Finch, R. J., & Hanchar, J. M. (2003). Structure and chemistry of zircon and zircon-group minerals. Reviews in mineralogy and geochemistry, 53(1), 1-25.

Foster, M.D., 1960a. Interpretation of the composition of trioctahedral micas. United States Geological Survey Professional Paper 354-B, 11-49.

Foster, M.D., 1960b. Interpretation of the composition of lithium micas. United States

Geological Survey Professional Paper 354-E, 115-147.

France, L., Ildefonse, B., Koepke, J., & Bech, F. (2010). A new method to estimate the oxidation state of basaltic series from microprobe analyses. Journal of Volcanology and Geothermal Research, 189(3-4), 340-346.

Frost, B. R. (1991). Introduction to oxygen fugacity and its petrologic importance. Reviews in Mineralogy and Geochemistry, 25(1), 1-9.

Fu, J. (2004). SHRIMP U-Pb zircon dating of the Jiuyishan composite granite in Hunan and its geological significance. Geotectonica Et Metallogenia, 28(4), 370-378.

Fu, J. M. (2004). Zircon SHRIMP dating of the Cailing granite on the eastern margin of the Qitianling granite, Hunan, South China, and its significance. Geol. China, 31, 96-100. (in Chinese with English abstract).

Fu, J. M., Ma, C. Q., Xie, C. F., Zhang, Y. M., and Peng, S. B. (2004). Geochemistry and tectonic setting of xishan aluminous a-type granitic volcanic-intrusive complex, southern hunan. Journal of Earth Science and Enivronmental, 26(4), 15-23.

Fu, J. M., Xie, C. F., Peng, S. B., Yang, X. J., & Mei, Y. P. (2006). Geochemistry and Crust-Mantle Magmatic Mixing of the Qitianling Granitesand Their Dark Microgranular Enclaves in Hunan Province. ACTA GEOSCIENTIA SINICA, 27(6), 557. (in Chinese with English abstract)

Gaillard, F., Scaillet, B., & Arndt, N. T. (2011). Atmospheric oxygenation caused by a change in volcanic degassing pressure. Nature, 478(7368), 229.

Gan, C., Wang, Y., Zhang, Y., & Zhang, J. (2017). The earliest Jurassic A-type granite in the Nanling Range of southeastern South China: petrogenesis and geological implications. International Geology Review, 59(3), 274-292.

Gao, J. F., Zhou, M. F., Lightfoot, P. C., Wang, C. Y., Qi, L., & Sun, M. (2013). Sulfide saturation and magma emplacement in the formation of the Permian Huangshandong Ni-Cu sulfide deposit, Xinjiang, northwestern China. Economic Geology, 108(8), 1833-1848.

Gao, P., Zheng, Y. F., & Zhao, Z. F. (2017). Triassic granites in South China: A geochemical perspective on their characteristics, petrogenesis, and tectonic significance. Earth-Science Reviews, 173, 266-294.

Gao, S., J. Yang, L. Zhou, M. Li, Z. Hu, J. Guo, H. Yuan, H. Gong, G. Xiao, and J. Wei (2011). Age and growth of the Archean Kongling terrain, South China, with emphasis on 3.3 Ga granitoid gneisses, Am. J. Sci., 311(2), 153-182.

Gilder, S.A., Keller, G.R., Luo, M., and Goodell, P.C. Timing and spatial distribution of rifting in China. Tectonophysics, 1991, 197: 225-243.

Gioncada, A., Orlandi, P., Vezzoli, L., Omarini, R.H., Mazzuoli, R., Lopez-Azarevich, V., Ruch, J., 2014. Topaz magmatic crystallization in rhyolites of the Central Andes (Chivinar volcanic complex, NW Argentina): constraints from texture, mineralogy and rock chemistry. Lithos 184, 62-73.

Gladney, E.S., and Roelandts, I. (1988). 1987 compilation of elemental concentration data for USGS BIR-1, DNC-1, and W-2: Geostandards Newsletter, 12:63-118.

Griffin, W. L. (2008). GLITTER: data reduction software for laser ablation ICP-MS. Laser Ablation ICP-MS in the Earth Sciences: Current practices and outstanding issues, 308-311.

Grove, T. L., & Baker, M. B. (1984). Phase equilibrium controls on the tholeiitic versus calc‐alkaline differentiation trends. Journal of Geophysical Research: Solid Earth, 89(B5), 3253-3274.

Guan, Y., Chao, Y., Long, X., Wang, Y., Zhang Y., Huang, Z. (2013). Early paleozoic intracontinental orogeny of the eastern south china block: evidence from i-type granitic plutons in the se yangtze block. Geotectonica Et Metallogenia, 37(4), 698-720.

Guo, C., Zeng, L., Li, Q., Fu, J., Ding, T. (2016). Hybrid genesis of jurassic fayalite-bearing felsic subvolcanic rocks in south china: inspired by petrography, geochronology, and sr–nd–o–hf isotopes. Lithos, 264, 175-188.

Guo, F., Fan, W. M., Lin, G., & Wu, Y. L. (1997). Petrological characteristics and

dating on gneiss xenoliths in mesozoic basalts in huziyan, daoxian region, hunan province. (in Chinese with English abstract).

Guo, L.Z., Shi, Y.S., and Ma, R.S. The geotectonic framework and crustal evolution of South China, in Guo, L.Z., ed, 2001, The plate tectonics of South China: Beijing, Geological Publishing House, 1980, 1-264 (in Chinese with English abstract).

Hacker, B. R., Ratschbacher, L., & Liou, J. G. (2004). Subduction, collision and exhumation in the ultrahigh-pressure Qinling-Dabie orogen. Geological Society, London, Special Publications, 226(1), 157-175.

Hammarstrom, J. M., & Zen, E. A. (1986). Aluminum in hornblende: an empirical igneous geobarometer. American Mineralogist, 71(11-12), 1297-1313.

Hanchar, J. M., & Watson, E. B. (2003). Zircon saturation thermometry. Reviews in mineralogy and geochemistry, 53(1), 89-112.

Harrison, T. M., & McDougall, I. (1982). The thermal significance of potassium feldspar K-Ar ages inferred from 40Ar39Ar age spectrum results. Geochimica et Cosmochimica Acta, 46(10), 1811-1820.

Harrison, T. M., & Watson, E. B. (1983). Kinetics of zircon dissolution and zirconium diffusion in granitic melts of variable water content. Contributions to Mineralogy and Petrology, 84(1), 66-72.

He, Z.Y., Xu, X.S., Niu, Y.L., (2010). Petrogenesis and tectonic significance of a Mesozoic granite–syenite–gabbro association from inland South China. Lithos 119, 621-641.

Helba, H., Trumbull, R.B., Morteani, G., Khalil, S.O., Arslan, A., 1997. Geochemical and petrographic studies of Ta mineralization in the Nuweibi albite granite complex, Eastern Desert, Egypt. Mineralium Deposita 32, 164-179.

Hersum T.G., Marsh B.D., 2007. Igneous textures: on the kinetics behind the words. Elements 3:247–252.

Hogarth, D.D., 1977. Classification and nomenclature of the pyrochlore group. American Mineralogist 62, 403-410.

Holland, T., & Blundy, J. (1994). Non-ideal interactions in calcic amphiboles and their bearing on amphibole-plagioclase thermometry. Contributions to mineralogy and petrology, 116(4), 433-447.

Hollister, L. S. (1987). Confirmation of the empirical correlation of Al in hornblende with pressure of solidification of calc-alkaline plutons. Am. Mineral., 72, 231-239.

Hollister, L. S., Grissom, G. C., Peters, E. K., Stowell, H. H., and Sisson, V. B. (1987). Confirmation of the empirical correlation of al in hornblende with pressure of solidification of calc-alkaline plutons. American Mineralogist, 72(3), 231–239.

Holtz, F., Johannes, W., Tamic, N., and Behrens, H. (2001). Maximum and minimum water contents of granitic melts generated in the crust: a reevaluation and implications. Lithos, 56(1), 1-14.

Hong, D.W., Xie, X.L., Zhang, J.S., (1998). Isotope geochemistry of granitoids in South China and their metallogeny. Resource Geology 48, 251-263.

Hoskin, P. W., & Schaltegger, U. (2003). The composition of zircon and igneous and metamorphic petrogenesis. Reviews in mineralogy and geochemistry, 53(1), 27-62.

Hsieh, P. S., Chen, C. H., Yang, H. J., & Lee, C. Y. (2008). Petrogenesis of the Nanling Mountains granites from South China: constraints from systematic apatite geochemistry and whole-rock geochemical and Sr–Nd isotope compositions. Journal of Asian Earth Sciences, 33(5-6), 428-451.

Hu, M. Y., Fan, X. T., Stoll, B., Kuzmin, D., Liu, Y., Liu, Y., ... & Jochum, K. P. (2011). Preliminary characterisation of new reference materials for microanalysis: Chinese Geological Standard Glasses CGSG‐1, CGSG‐2, CGSG‐4 and CGSG‐5. Geostandards and Geoanalytical Research, 35(2), 235-251.

Hu, R. Z., Burnard, P. G., Bi, X. W., Zhou, M. F., Peng, J. T., Su, W. C., et al. (2009). Mantle-derived gaseous components in ore-forming fluids of the xiangshan uranium deposit, jiangxi province, china: evidence from he, ar and c isotopes. Chemical Geology, 266(1), 86-95.

Hu, X., Bi, X., Hu, R., Cai, G., & Chen, Y. (2016). Tin partition behavior and implications for the Furong tin ore formation associated with peralkaline intrusive granite in Hunan Province, China. Acta Geochimica, 35(2), 138-147.

Huang, F. F., Wang, R. C., Xie, L., Zhu, J. C., Erdmann, S., and Che, X. D., et al. (2015). Differentiated rare-element mineralization in an ongonite–topazite composite dike at the xianghualing tin district, southern china: an electron-microprobe study on the evolution from niobium–tantalum-oxides to cassiterite. Ore Geology Reviews, 65(3), 761-778.

Huang, G.F., Zeng, Q.W., Wei, S.L., Xu, Y.M., Hou, M.S., Kang, W.Q. (2001). Geological characteristics and ore-controlling factors of the Furong orefield, Qitianling, Hunan Geol. China, 28, pp. 30-34 (in Chinese with English abstract)

Huang, H. Q., X. H. Li, W. X. Li, and Z. X. Li (2011), Formation of high 18O fayalite-bearing A-type granite by high-temperature melting of granulitic metasedimentary rocks, southern China, Geology, 39(10), 903-906, doi:10.1130/g32080.1.

Huang, W.H., Tu, S.H., Wang, K.H, Chao, C.L., Yu, C.C., 1958. Hsiang-hua-shih, a new beryllium mineral. Ti-Chih-yueh-K'an 7, 35 (in Chinese). New mineral name introduced in American Mineralogist 1959, 44, 1327-1328.

Huang, X. L., Yu, Y., Li, J., Tong, L. X., Chen, L. L. (2013). Geochronology and petrogenesis of the early Paleozoic I-type granite in the Taishan area, South China: middle-lower crustal melting during orogenic collapse. Lithos, 177, 268-284.

Huang, X., Lu, J., Sizaret, S., Wang, R., Ma, D., Zhang, R., ... & Wu, J. (2017). Petrogenetic differences between the Middle-Late Jurassic Cu-Pb-Zn-bearing and W-bearing granites in the Nanling Range, South China: A case study of the Tongshanling and Weijia deposits in southern Hunan Province. Science China Earth Sciences, 60(7), 1220-1236.

Huang, X.L., Wang, R.C., Chen, X.M., Hu, H., Liu, C.S., 2002. Vertical variations in the mineralogy of the Yichun topaz–lepidolite granite, Jiangxi Province, southern China. The Canadian Mineralogist 40, 1047-1068.

Huang, Y.H., Du S.H., Zhou, X.Z., 1988. Xianghualing rocks, mineral deposits and minerals. Beijing: Science and Technology Press. pp. 1-255 (in Chinese with English abstract).

Ishihara, S., Sawata, H., Arpornsuwan, S., Busaracome, P., & Bungbrakearti, N. (1979). The magnetite-series and ilmenite-series granitoids and their bearing on tin mineralization, particularly of the Malay Peninsula region.

Jackson, S. E., Pearson, N. J., Griffin, W. L., & Belousova, E. A. (2004). The application of laser ablation-inductively coupled plasma-mass spectrometry to in situ U–Pb zircon geochronology. Chemical Geology, 211(1-2), 47-69.

Jahn, B.M., Chen, P.Y., and Yen, T.P. Rb-Sr ages of the granitic rocks in southeastern China and their tectonic significance. Geological Society of America Bulletin, 1976, 87: 763-776.

Jahn, B.M., Zhou, X.H., and Li, J.L. Formation and tectonic evolution of southeastern China and Taiwan: isotopic and geochemical constraints. Tectonophysics, 1990, (183):145-160.

James, R. S., & Hamilton, D. L. (1969). Phase relations in the system $NaAlSi_3O_8$-$KAlSi_3O_8$-$CaAl_2Si_2O_8$-SiO_2 at 1 kilo bar water vapour pressure. Contributions to Mineralogy and Petrology, 21(2), 111-141.

Jeff, R., & Mark, I. P. (1992). The calibration and application of accurate redox sensors. American Mineralogist, 77, 284-295.

Jiang, S. Y., Zhao, K. D., Jiang, Y. H., and Dai, B. Z. (2008). Characteristics and genesis of mesozoic a-type granites and associated mineral deposits in the southern hunan and northern guangxi provinces along the shi-hang belt,south china. Geological Journal of China Universities, 14(4), 496-509. (in Chinese with English abstract).

Johnson, M. C., & Rutherford, M. J. (1989). Experimental calibration of the aluminum-in-hornblende geobarometer with application to Long Valley caldera (California) volcanic rocks. Geology, 17(9), 837-841.

Johnston, C., Chappell, B.W., 1992. Topaz-bearing rocks from Mount Gibson, North

Queensland, Australia. American Mineralogist 77, 303-313.

Joseph B. Whalen, Kenneth L. Currie, and Bruce W. Chappell. (1987). A-type granites: geochemical characteristics, discrimination and petrogenesis. Contributions to Mineralogy and Petrology, 95(4), 407-419.

Kamenetsky, V.S., Kamenetsky, M.B., 2010. Magmatic fluids immiscible with silicate melts: examples from inclusions in phenocrysts and glasses, and implications for magma evolution and metal transport. Geofluids 10, 293-311.

King, P. L., White, A. J. R., Chappell, B. W., & Allen, C. M. (1997). Characterization and origin of aluminous A-type granites from the Lachlan Fold Belt, southeastern Australia. Journal of petrology, 38(3), 371-391.

KKlimm, K., Holtz, F., and King, P. L. (2008). Fractionation vs. magma mixing in the wangrah suite a-type granites, lachlan fold belt, australia: experimental constraints. Lithos, 102(3–4), 415-434.

Klimm, K., Holtz, F., Johannes, W., & King, P. L. (2003). Fractionation of metaluminous A-type granites: an experimental study of the Wangrah Suite, Lachlan Fold Belt, Australia. Precambrian Research, 124(2-4), 327-341.

Kortemeier, W.T., Burt, D.M. 1988. Ongonite and topazite dikes in the Flying W ranch area, Tonto basin, Arizona. American Mineralogist 73, 507-523.

Kovalenko, V.I., Grebennikov, A.M., Antipin, V.S. 1975. Ongonite of the Arybulak stock, Transbaikal: The first find of a subvolcanic analog of rare metal-bearing lithium-fluorine granite (apogranite) in the USSR. Doklady of the Academy of Sciences of the USSR, Earth Science Sections, 220, 158-160 (translated from Doklady Akademii Nauk SSSR, 220, No.5, 1169-1171.

Kovalenko, V.I., Kovalenko, N.I., 1976. Ongonite (topaz-bearing quartz Keratophyre)-subvolcanic analogure of rare-metal Li–F granite. Nauka Press, Moscow (128 pp. (in Russian)).

Kovalenko, V.I., Kuzmin, M.I., Antipin, V.S., Petrov, L.L., 1971. Topaz-bearing quartz keratophyre (ongonite), a new variety of subvolcanic igneous vein rock. Acad Sci

USSR Doklady Earth Sci Sec, 199, 132-134.

Kuidong, Z., Shaoyong, J., Yaohui, J., & Dunyi, L. (2006). SHRIMP U-Pb dating of the Furong unit of Qitangling granite from southeast Hunan province and their geological implications. Acta Petrologica Sinica, 22(10), 2611-2616. (in Chinese with English abstract).

Lapierre, H., Jahn, B. M., Charvet, J. and Yu, Y.W. (1997). Mesozoic felsic arc magmatism and continental olivine tholeiites in Zhejiang Province and their relationship with tectonic activities in SE China. Tectonophysics., 274, 321-338.

Leake, B. E., Wooley, A. R., Arps, C. E. S., Birch, W. D., Gilbert, M. C., and Grice, J. D., et al. (1997). Nomenclature of amphiboles; report of the subcommittee on amphiboles of the international mineralogical association commission on new minerals and mineral names. American Mineralogist, 82(9), 1019-1037.

Leake, B. E., Wooley, A. R., Arps, C. E. S., Birch, W. D., Gilbert, M. C., and Grice, J. D., et al. (1997). Nomenclature of amphiboles; report of the subcommittee on amphiboles of the international mineralogical association commission on new minerals and mineral names. American Mineralogist, 82(9), 1019-1037.

Leake, B. E., Woolley, A. R., Arps, C. E., Birch, W. D., Gilbert, M. C., Grice, J. D., ... & Linthout, K. (1997). Report. Nomenclature of amphiboles: report of the subcommittee on amphiboles of the international mineralogical association commission on new minerals and mineral names. Mineralogical magazine, 61(2), 295-321.

Leake, B. E., Woolley, A. R., Birch, W. D., Burke, E. A., Ferraris, G., Grice, J. D., ... and Stephenson, N. C. (2003). Nomenclature of amphiboles: additions and revisions to the International Mineralogical Association's 1997 recommendations. The Canadian Mineralogist, 41(6), 1355-1362.

Leake, B. E., Woolley, A. R., Birch, W. D., Burke, E. A., Ferraris, G., Grice, J. D., ... & Stephenson, N. C. (2003). Nomenclature of amphiboles: additions and revisions to the International Mineralogical Association's 1997 recommendations. The

Canadian Mineralogist, 41(6), 1355-1362.

Lehmann, B. (1990). Large-scale tin depletion in the Tanjungpandan tin granite, Belitung Island, Indonesia. Economic Geology, 85(1), 99-111.

Lepage, L. D. (2003). ILMAT: an excel worksheet for ilmenite--magnetite geothermometry and geobarometry. Computers & Geosciences, 29(5), 673-678.

Lepvrier, C., Maluski, H., Van Tich, V., Leyreloup, A., Thi, P. T., & Van Vuong, N. (2004). The early Triassic Indosinian orogeny in Vietnam (Truong Son Belt and Kontum Massif); implications for the geodynamic evolution of Indochina. Tectonophysics, 393(1-4), 87-118.

Li, C. N., Zhong, C. S., and Wang, F. Z. (2001). Geochemistry and petrogenesis of mesozoic basaltic rocks and their deep-source enclaves in northern guangxi-southern hunan. Acta Petrologica Et Mineralogica. (in Chinese with English abstract).

Li, H. L. (2007). Mineral chemistry of biotite from the Qitianling granite associated with Furong tin deposit: tracing Sn-metallogeny signatures. Acta Petrol. Sin., 23, 2605-2614. (in Chinese with English abstract).

Li, H. Q., Lu, Y. F., Wang, D. H., Chen, Y. C., Yang, H. M., Guo, J., ... & Ma, L. Y. (2006). Dating of the rock-forming and ore-forming ages and their geological significances in the Furong ore-field, Qitian Mountain, Hunan. Geological Review, 52(1), 113-121. (in Chinese with English abstract).

Li, J. D., Bai, D. Y., Wu, G. Y., Che, Q. L., Liu, Y. R., & Ma, T. Q. (2005). Zircon SHRIMP dating of the Qitianling granite, Chenzhou, southern Hunan, and its geological significance. Geological Bulletin of China, 24(5), 411-414. (in Chinese with English abstract).

Li, J., Zhang, Y., Zhao, G., Johnston, S. T., Dong, S., Koppers, A., ... & Xin, Y. (2017). New insights into Phanerozoic tectonics of South China: Early Paleozoic sinistral and Triassic dextral transpression in the east Wuyishan and Chencai domains, NE Cathaysia. Tectonics, 36(5), 819-853.

Li, X. H. (1994). SHRIMP ion microprobe zircon U-Pb age of the NE Jiangxi ophiolite and its tectonic implications. Geochemica, 23, 125-131. (in Chinese with English abstract)

Li, X. H. (1997). Timing of the Cathaysia Block formation: Constraints from SHRIMP U-Pb zircon geochronology. Episode, 20, 188-192.

Li, X. H. (2000). Cretaceous magmatism and lithospheric extension in southeast china. Journal of Asian Earth Sciences, 18(3), 293-305.

Li, X. H., Li, W. X., Li, Z. X., Lo, C. H., Wang, J., Ye, M. F., & Yang, Y. H. (2009). Amalgamation between the Yangtze and Cathaysia Blocks in South China: constraints from SHRIMP U–Pb zircon ages, geochemistry and Nd–Hf isotopes of the Shuangxiwu volcanic rocks. Precambrian Research, 174(1-2), 117-128.

Li, X. H., Li, Z. X., Li, W. X., Liu, Y., Yuan, C., and Wei, G., et al. (2007). U–pb zircon, geochemical and sr–nd–hf isotopic constraints on age and origin of jurassic i- and a-type granites from central guangdong, se china: a major igneous event in response to foundering of a subducted flat-slab?. Lithos, 96(1–2), 186-204.

Li, X. H., Li, Z. X., Zhou, H., Liu, Y., & Kinny, P. D. (2002). U–Pb zircon geochronology, geochemistry and Nd isotopic study of Neoproterozoic bimodal volcanic rocks in the Kangdian Rift of South China: implications for the initial rifting of Rodinia. Precambrian Research, 113(1-2), 135-154.

Li, X.H. (2000) Cretaceous magmatism and lithosphere extension in Southeast China. Journal of Asian Earth Science, 18: 293-305.

Li, X.H., Zhou, H.W., Liu, Y., Lee, C.Y., Chen, C.H., Yu, J.S., and Gui, X.T. Mesozoic shoshonitic intrusives in the Yangchun Basin, western Guangdong, and the tectonic significance: II. Trace elements and Sr-Nd isotopes. Geochinica, 2001, 30: 57-65 (in Chinese with English abstract).

Li, Z. L., Hu, R. Z., Peng, J. T., Bi, X. W., and Li, X. M. (2006). Helium isotope geochemistry of ore‐forming fluids from furong tin orefield in hunan province, china. Resource Geology, 56(1), 9-15.

Li, Z. L., Hu, R. Z., Yang, J. S., Peng, J. T., Li, X. M., & Bi, X. W. (2007a). He, pb and s isotopic constraints on the relationship between the a-type qitianling granite and the furong tin deposit, hunan province, china. Lithos, 97(1), 161-173.

Li, Z. X., Li, X. H., Kinny, P. D., Wang, J., Zhang, S., & Zhou, H. (2003). Geochronology of Neoproterozoic syn-rift magmatism in the Yangtze Craton, South China and correlations with other continents: evidence for a mantle superplume that broke up Rodinia. Precambrian Research, 122(1-4), 85-109.

Li, Z. X., Wartho, J. A., Occhipinti, S., Zhang, C. L., Li, X. H., Wang, J., & Bao, C. (2007b). Early history of the eastern Sibao Orogen (South China) during the assembly of Rodinia: new mica 40Ar/39Ar dating and SHRIMP U–Pb detrital zircon provenance constraints. Precambrian Research, 159(1-2), 79-94.

Li, Z.-X., Li, X.-H., (2007c). Formation of the 1300-km-wide intracontinental orogen and postorogenic magmatic province in Mesozoic South China: A flat-slab subduction model. Geology 35, 179-182.

Lindsley, D. H., & Spencer, K. J. (1982). Fe-Ti oxide geothermometry: Reducing analyses of coexisting Ti-magnetite (Mt) and ilmenite (Ilm). EOS Transactions, American Geophysical Union, 63(18), 471.

Linnen R L, Pichavant M, Holtz F. The combined effects of f O2 and melt composition on SnO_2 solubility and tin diffusivity in haplogranitic melts[J]. Geochimica et Cosmochimica Acta, 1996, 60(24): 4965-4976.

Linnen, R. L., Pichavant, M., Holtz, F., & Burgess, S. (1995). The effect of fO2 on the solubility, diffusion, and speciation of tin in haplogranitic melt at 850 C and 2 kbar. Geochimica et Cosmochimica Acta, 59(8), 1579-1588.

Linnen, R.L., 1998. The solubility of Nb-Ta-Zr-Hf-W in granitic melts with Li and Li+F; constraints for mineralization in rare metal granites and pegmatites. Economic Geology 93, 1013-1025.

Linnen, R.L., 2004. Ferrocolumbite–manganotantalite trends in granites and pegmatites: experimental and natural constraints. Geological Society of American Abstracts

with Programs, 36(5), 115.

Linnen, R.L., Keppler, H., 1997. Columbite solubility in granitic melts: consequences for the enrichment and fractionation of Nb and Ta in the Earth's crust. Contributions to Mineralogy and Petrology 128, 213-227.

Liu, C.S., Shen, W.Z., Wang D.Z., 1996. The characteristics and genetic mechanism of igneous topazites in South China. Acta Geologica Sinica 9, 33-45.

Liu, H.S., Martelet, G., Wang, B., Erdmann, S., Chen, Y., Faure, M., Huang, F.F., Scaillet, B., le-Breton, N., Wang, R.C., & Zhu, J.C. (2018). Incremental emplacement of a mid-crustal, lopolith-like intrusion revealed by AMS and Bouguer gravity data: a case study from the late Jurassic Qitianling pluton, South China. (Under review)

Liu, Y. P., Zhengxiang, L. I., Huimin, L. I., Guo, L. G., Wei, X. U., Lin, Y. E., et al. (2007). U-pb geochronology of cassiterite and zircon from the dulong sn-zn deposit:evidence for cretaceous large-scale granitic magmatism and mineralization events in southeastern yunnan province,china. Acta Petrologica Sinica, 23(5), 967-976.

Liu, Y., Hu, Z., Gao, S., Günther, D., Xu, J., Gao, C., & Chen, H. (2008). In situ analysis of major and trace elements of anhydrous minerals by LA-ICP-MS without applying an internal standard. Chemical Geology, 257(1-2), 34-43.

Liu, Y., Xu, J., Dai, T., Li, X., Deng, X., and Wang, Q. (2003). 40 Ar/ 39Ar isotopic ages of qitianling granite and their geologic implications. Science China Earth Sciences, 46(s2), 50-59.

Loiselle, M.C., and Wones, D.R., 1979, Characteristics and origin of anorogenic granites: Geological Society of America Abstracts with Programs, v. 11, p. 468.

London, D., Morgan, G.B., 2012. The pegmatite puzzle. Elements 8, 263-268.

lshihara S. (1981) The granitoid series and mineralization. Econ.Geol. 75th Anniv. Vol. pp. 458-484.

Lu, H. Z. (2003). Mineralization and fluid inclusion study of the shizhuyuan w-sn-bi-

mo-f skarn deposit, hunan province, china. Economic Geology, 98(5), 955-974.

Lu, J. J. (2005). Re-Os age for molybdenite from the Dexing porphyry Cu-Au deposit of Jiangxi Province, China. Geochim. Cosmochim. Acta, 69, A882. (in Chinese with English abstract).

Luth, W. C. (1967). Studies in the System $KAlSiO_4$-Mg_2SiO_4-SiO_2-H_2O: I, Inferred Phase Relations and Petrologic Applications. Journal of Petrology, 8(3), 372-416.

Luth, W. C. (1969). The systems $NaAlSi_3O_8$-SiO_2 and $KAlSi_3O_8$-SiO_2 to 20 kb and the relationship between H_2O content, P_{H2O}) and P_{total} granitic magmas. American Journal of Science, 267, 325-341.

Mahood, G. A. (1984). Pyroclastic rocks and calderas associated with strongly peralkaline magmatism. Journal of Geophysical Research: Solid Earth, 89(B10), 8540-8552.

Maitre, L. (1989). A classification of igneous rocks and glossary of terms. Recommendations of the international union of geological sciences subcommission on the systematics of igneous rocks, 193.

Mao Jingwen, Li, Hongyan, Hidehiko, Shimazaki, Louis, Raimbault, Bernard, Guy. (1996). Geology and metallogeny of the shizhuyuan skarn-greisen deposit, hunan province, china. International Geology Review, 38(11), 1020-1039.

Mao, J. (2004). ^{40}Ar-^{39}Ar dating of tin ores and related granite in furong tin orefield, hunan province, and its geodynamic significance. Mineral Deposits, 23.

Mao, J. W. (2004). ^{40}Ar-^{39}Ar dating of tin ores and related granite in Furong Tin orefield, Hunan Province, and its geodynanmic significance. Mineral. Deposits, 23, 164-175. (in Chinese with English abstract).

Mao, J. W., Xie, G. Q., Li, X. F., Zhang, C. Q., and Mei, Y. X. (2004a). Mesozoic large scale mineralization and multiple lithospheric extension in south china. Earth Science Frontiers, 11(1), 45-55. (in Chinese with English abstract).

Mao, J. W., Xie, G. Q., Li, X. F., Zhang, C. Q., Mei, Y. X. (2004). Mesozoic large scale mineralization and multiple lithospheric extension in south china. Earth Science

Frontiers, 1, 44-55. (in Chinese with English abstract)

Mao, J., Li, X., Lehmann, B., Chen, W., Lan, X., and Wei, S. (2004b). ~(^{40})Ar-~(^{39})Ar dating of tin ores and related granite in furong tin orefield, hunan province, and its geodynamic significance. Mineral Deposits. 23(2), 164-175. (in Chinese with English abstract).

Mao, J., Pirajno, F., & Cook, N. (2011). Mesozoic metallogeny in East China and corresponding geodynamic settings—an introduction to the special issue.

Mao, J.W., Y.B. Cheng, M.H. Chen, F. Pirajno. (2013). Major types and time–space distribution of Mesozoic ore deposits in South China and their geodynamic settings. Mineralium Deposita, 48(3), 267-294.

Martin, R. F. (2006). A-type granites of crustal origin ultimately result from open-system fenitization-type reactions in an extensional environment. Lithos, 91(1-4), 125-136.

Mattauer, M., Matte, P., Malavieille, J., Tapponnier, P., Maluski, H., Qin, X. Z., ... & Qin, T. Y. (1985). Tectonics of the Qinling belt: build-up and evolution of eastern Asia. Nature, 317(6037), 496.

McDougall, I., & Harrison, T. M. (1999). Geochronology and Thermochronology by the 40Ar/39Ar Method. Oxford University Press, Oxford, 252 pp.

Meert, J. G., Nédélec, A., Hall, C., Wingate, M. T., & Rakotondrazafy, M. (2001). Paleomagnetism, geochronology and tectonic implications of the Cambrian-age Carion granite, Central Madagascar. Tectonophysics, 340(1), 1-21.

Miles, A. J., Graham, C. M., Hawkesworth, C. J., Gillespie, M. R., Hinton, R. W., & Bromiley, G. D. (2014). Apatite: A new redox proxy for silicic magmas?. Geochimica et Cosmochimica Acta, 132, 101-119.

Mo Z.S. A discussion on the classification of Nanling granites according to geological environment. Geotectonica Et Metallogenia, 1985, 9(1): 17-27 (in Chinese with English abstract).

Mo, S.Z., Ye B.D., Pang W.Z., Wan S.N., 1980. Granitoid geology in the Nanling

Region. Geological Publishing House, Beijing, pp. 115–180.

Monier, G., Robert, J.L., 1986. Evolution of the miscibility gap between muscovite and biotite solid solutions with increasing lithium content: an experimental study in the system K_2O− Li_2O− MgO− FeO− Al_2O_3− SiO_2− H_2O− HF. Mineralogical Magazine 50, 641-651.

Moretti, R. (2005). Polymerisation, basicity, oxidation state and their role in ionic modelling of silicate melts. Annals of Geophysics, 48(4-5).

Morimoto, N. (1988). Nomenclature of pyroxenes. Mineralogy and Petrology, 39(1), 55-76.

Mutch, E. J. F., Blundy, J. D., Tattitch, B. C., Cooper, F. J., & Brooker, R. A. (2016). An experimental study of amphibole stability in low-pressure granitic magmas and a revised Al-in-hornblende geobarometer. Contributions to Mineralogy and Petrology, 171(10), 85.

Nabelek, P. I., Hofmeister, A. M., & Whittington, A. G. (2012). The influence of temperature-dependent thermal diffusivity on the conductive cooling rates of plutons and temperature-time paths in contact aureoles. Earth and Planetary Science Letters, 317, 157-164.

Naney, M. T. (1983). Phase equilibria of rock-forming ferromagnesian silicates in granitic systems. American Journal of Science, 283(10), 993-1033.

Neiva, M.R., 1996. Geochemistry of cassiterite and its inclusion and exsolution products from tin and tungsten deposits in Portugal. Canadian Mineralogist 34, 745 -768.

Nekrasov, I. Y. (1984). Olovo v magmaticheskikh i postmag maticheskikh protsessakh (Tin in Magmatic and Post Magmatic Processes).

Newman, S., and Lowenstern, J. B. (2002). VolatileCalc: a silicate melt–H_2O–CO_2 solution model written in Visual Basic for excel. Computers and Geosciences, 28(5), 597-604.

Niu, Y.L. Generation and evolution of basaltic magmas: Some basic concepts and new

views on the origin of Mesozoic-Cenozoic basaltic volcanism in eastern China. Geological Journal of China Universities, 2005, 11: 9-46.

Novák, M., Černý, P., Uher, P., 2003. Extreme variation and apparent reversal of Nb-Ta fractionation in columbite-group minerals from the Scheibengraben beryl-columbite granitic pegmatite, Maršíkov, Czech Republic. European Journal of Mineralogy 15, 565-574.

Nyman, H. A. R. R. Y., Hyde, B. G., & Andersson, S. (1984). Zircon, anhydrite, scheelite and some related structures containing bisdisphenoids. Acta Crystallographica Section B, 40(5), 441-447.

Ottonello, G., Moretti, R., Marini, L., & Zuccolini, M. V. (2001). Oxidation state of iron in silicate glasses and melts: a thermochemical model. Chemical geology, 174(1-3), 157-179.

Pang, B. C., Yang, D. S., Zhou, Z., Liu, Y. M., Liu, P. C., Liu, Y. D. (2011). Trace elements in pyrites and their implication for hydrothermal ore-forming process in longshan gold-antimony deposits,hunan,china. Geoscience, 25(5), 832-845.

Patiño Douce, A. E., and Beard, J. S. (1995). Dehydration-melting of biotite gneiss and quartz amphibolite from 3 to 15 kbar. Journal of Petrology, 36(3), 707-738.

Pearce, J. A., Harris, N. B., & Tindle, A. G. (1984). Trace element discrimination diagrams for the tectonic interpretation of granitic rocks. Journal of petrology, 25(4), 956-983.

Pearce, N. J., Perkins, W. T., Westgate, J. A., Gorton, M. P., Jackson, S. E., Neal, C. R., & Chenery, S. P. (1997). A compilation of new and published major and trace element data for NIST SRM 610 and NIST SRM 612 glass reference materials. Geostandards Newsletter, 21(1), 115-144.

Pearce, N. J., Perkins, W. T., Westgate, J. A., Gorton, M. P., Jackson, S. E., Neal, C. R., & Chenery, S. P. (1997). A compilation of new and published major and trace element data for NIST SRM 610 and NIST SRM 612 glass reference materials. Geostandards Newsletter, 21(1), 115-144.

Peng, B., Frei, R. (2004). Nd-sr-pb isotopic constraints on metal and fluid sources in w-sb-au mineralization at woxi and liaojiaping (western hunan, china). Mineralium Deposita, 39(3), 313-327.

Peng, J. T. (2001). Strontium isotope geochemistry of the xikuangshan antimony deposit, central hunan. Geochimica, 30.

Peng, T., Fan, W., Zhao, G., Peng, B., Xia, X., Mao, Y. (2015). Petrogenesis of the early paleozoic strongly peraluminous granites in the western south china block and its tectonic implications. Journal of Asian Earth Sciences, 98(98), 399-420.

Peretyazhko, I.S., 2010. Genesis of Mineralized Cavities (Miaroles) in Granitic Pegmatites and Granites. Petrology 18, 183–208.

Peretyazhko, I.S., Zagorsky, V.Y., Tsareva, E.A., Sapozhnikov, A.N., 2007. Immiscibility of calcium fluoride and aluminosilicate melts in ongonite from the Ary-Bulak intrusion, Eastern Transbaikal region. Doklady Earth Sciences 413, 315-320.

Pichavant, M. (1987). Effects of B and H_2O on liquidus phase relations in the haplogranite system at l kbar. American Mineralogist, 72(11-12), 1056-1070.

Pichavant, M., Costa, F., Burgisser, A., Scaillet, B., Martel, C., and Poussineau, S. (2007). Equilibration scales in silicic to intermediate magmas—implications for experimental studies. Journal of Petrology, 48(10), 1955-1972.

Pichavant, M., Herrera, J.V., Boulmier, S., Briqueu, L., Joron, J.L., Juteau, M., Vernet, M., 1987. The Macusani glasses, SE Peru: evidence of chemical fractionation in peraluminous magmas. In Magmatic Processes: Physicochemical Principles, (Mysen, B.O., editor), 359-373.

Pietranik, A., Holtz, F., Koepke, J., & Puziewicz, J. (2009). Crystallization of quartz dioritic magmas at 2 and 1 kbar: experimental results. Mineralogy and Petrology, 97(1-2), 1.

Pietro, A., 2008. Decryption of igneous rock textures: crystal size distribution. Reviews in Mineralogy & Geochemistry 69, 623–649.

Pitcher, W. S. (1997). The Nature and Origin of Granite. Springer Netherlands.

Pollard, P.J., 1989. Geologic characteristics and genetic problems associated with the development of granite-hosted deposits of tantalum and niobium. In Lanthanides, tantalum and niobium (Möller P., Černý P., Saupé F., Eds. Springer Berlin Heidelberg.). Special Publication No. 7 of the Society for Geology Applied to Mineral Deposits In Lanthanides, Tantalum and Niobium (pp. 240-256).

Powell, R., & Powell, M. (1977). Geothermometry and oxygen barometry using coexisting iron-titanium oxides: a reappraisal. Mineralogical Magazine, 41(318), 257-263.

Pownceby, M. I., & O'Neill, H. S. C. (1994). Thermodynamic data from redox reactions at high temperatures. iii. activity-composition relations in ni-pd alloys from emf measurements at 850–1250 k, and calibration of the nio+ni-pd assemblage as a redox sensor. Contributions to Mineralogy & Petrology, 116(3), 327-339.

Prouteau, G., & Scaillet, B. (2003). Experimental constraints on the origin of the 1991 Pinatubo dacite. Journal of Petrology, 44(12), 2203-2241.

Putirka, and Keith. (2016). Special collection: rates and depths of magma ascent on earth: amphibole thermometers and barometers for igneous systems and some implications for eruption mechanisms of felsic magmas at arc volcanoes. American Mineralogist, 101(4), 841-858.

Putirka, K. (2016). Amphibole thermometers and barometers for igneous systems and some implications for eruption mechanisms of felsic magmas at arc volcanoes. American Mineralogist, 101(4), 841-858.

Qi, L., Hu, J., and Gregoire, D. C. (2000). Determination of trace elements in granites by inductively coupled plasma mass spectrometry. Talanta, 51(3), 507-513.

Qiu, Y.M., Gao, S., McNaughton, N.J., Groves, D.I., Ling, W.L., (2000). First evidence of > 3.2 Ga continental crust in the Yangtze craton of south China and its implications for Archean crustal evolution and Phanerozoic tectonics. Geology 28, 11–14.

Raimbault, L., Burnol, L., 1998. The Richemont rhyolite dike, Massif Central, France; a subvolcanic equivalent of rare-metal granites. The Canadian Mineralogist, 36, 265-282.

Rajesh, H. M. (2000). Characterization and origin of a compositionally zoned aluminous A-type granite from South India. Geological Magazine, 137(3), 291-318.

Rao, C., Wang, R.C., Hu, H., Zhang, W.L., 2009. Complex internal textures in oxide minerals from the Nanping No. 31 dike of granitic pegmatite, Fujian province, southeastern China. The Canadian Mineralogist 47, 1195-1212.

Rapp, R. P., & Watson, E. B. (1995). Dehydration melting of metabasalt at 8–32 kbar: implications for continental growth and crust-mantle recycling. Journal of Petrology, 36(4), 891-931.

Reiners, P. W., Ehlers, T. A., & Zeitler, P. K. (2005). Past, present, and future of thermochronology. Reviews in Mineralogy and Geochemistry, 58(1), 1-18.

Renne, P. R., Swisher, C. C., Deino, A. L., Karner, D. B., Owens, T. L., & DePaolo, D. J. (1998). Intercalibration of standards, absolute ages and uncertainties in 40Ar/39Ar dating. Chemical Geology, 145(1-2), 117-152.

Rieder, M., Cavazzini, G., D'yakonov, Y. S., Frank-Kamenetskii, V. A., Gottardi, G., Guggenheim, S., ... and Robert, J. L. (1998). Nomenclature of the micas. Clays and clay minerals, 46(5), 586-595.

Robinson K, Gibbs GV, Ribbe PH. (1971). The structure of zircon: a comparison with garnet. Am Mineral 56:782-790.

Roedder, E., 1992. Fluid inclusion evidence for immiscibility in magmatic differentiation. Geochimica et Cosmochimica Acta 56, 5-20.

Roedder, E., Coombs, D.S., 1967. Immiscibility in Granitic Melts, Indicated by Fluid Inclusions in Ejected Granitic Blocks from Ascension Island. Journal of Petrology 8, 417-451.

Rollinson, H. R. (2014). Using geochemical data: evaluation, presentation,

interpretation. Routledge.

Rose, W. I. (1987). Santa María, Guatemala: bimodal soda-rich calc-alkalic stratovolcano. Journal of Volcanology and Geothermal Research, 33(1-3), 109-129.

Rubin, A.M., 1993. Tensile fracture of rock at high confining pressure: implications for dike propagation. Journal of Geophysical Research 98, 15919-15935.

Ryabchikov, I.D., Durasova, N.A., Barsukov, V.L., Eflmov, A.S. (1978b). Oxidation-reduction potential as factor of an ore-bearing capacity of acid magmas. Geokhimiya 6, 832-834. (in Russian)

Ryabchikov, I.D., Durasova, N.A., Barsukov, V.L., Laputina, I.P., Efimov, A.S. (1978 a). Role of volatiles for the mobilization of tin from granitic magmas. Metallization Associated with Acid Magmatism 3 (M. Stemprok, L. Burnol, G. Tischendorf ed., Geol.Survey, Prague).

S. Scaillet (2000) Numerical error analysis in $^{40}Ar/^{39}Ar$ dating, Chem. Geol. (Isot. Geosci. Sec.) 162, 269-298.

Sato, H., Holtz, F., Behrens, H., Botcharnikov, R., & Nakada, S. (2004). Experimental petrology of the 1991–1995 Unzen dacite, Japan. Part II: Cl/OH partitioning between hornblende and melt and its implications for the origin of oscillatory zoning of hornblende phenocrysts. Journal of Petrology, 46(2), 339-354.

Scaillet, B., & Evans, B. W. (1999). The 15 June 1991 eruption of Mount Pinatubo. I. Phase equilibria and pre-eruption P–T–fO_2–$f\,H_2O$ conditions of the dacite magma. Journal of Petrology, 40(3), 381-411.

Scaillet, B., & Macdonald, R. (2003). Experimental constraints on the relationships between peralkaline rhyolites of the Kenya Rift Valley. Journal of Petrology, 44(10), 1867-1894.

Scaillet, B., & Macdonald, R. A. Y. (2001). Phase relations of peralkaline silicic magmas and petrogenetic implications. Journal of Petrology, 42(4), 825-845.

Scaillet, B., and Evans, B. W. (1999). The 15 june 1991 eruption of mount pinatubo. i.

phase equilibria and pre-eruption P–T–fO_2–fH_2O conditions of the dacite magma. Journal of Petrology, 40(3), 381-411(31).

Scaillet, B., and Macdonald, R. A. Y. (2001). Phase relations of peralkaline silicic magmas and petrogenetic implications. Journal of Petrology, 42(4), 825-845.

Scaillet, B., Holtz, F., & Pichavant, M. (1998). Phase equilibrium constraints on the viscosity of silicic magmas: 1. Volcanic - plutonic comparison. Journal of Geophysical Research: Solid Earth, 103(B11), 27257-27266.

Scaillet, B., Holtz, F., and Pichavant, M. (2016). Experimental constraints on the formation of silicic magmas. Elements, 12(2), 109-114.

Scaillet, B., Pichavant, M., & Roux, J. (1995). Experimental crystallization of leucogranite magmas. Journal of Petrology, 36(3), 663-705.

Scaillet, B., Pichavant, M., Roux, J., Humbert, G., and Lefevre, A. (1992). Improvements of the shaw membrane technique for measurement and control of fh_2 at high-temperatures and pressures. American Mineralogist, 77(5), 647-655.

Schmidt, M. W. (1992). Amphibole composition in tonalite as a function of pressure: an experimental calibration of the Al-in-hornblende barometer. Contributions to mineralogy and petrology, 110(2-3), 304-310.

Shannon, R. D. (1976). Revised effective ionic radii and systematic studies of interatomic distances in halides and chalcogenides. Acta crystallographica section A: crystal physics, diffraction, theoretical and general crystallography, 32(5), 751-767.

Shchekina, T.I., Gramenitskiy, E.N., Alferyeva, Y.O., 2013. Leucocratic magmatic melts with the maximum fluorine concentrations: Experiment and relations in nature. Petrology 21, 457-470.

Shu L.S., Faure M., Jiang S.Y., Yang Q., & Wang Y.J. (2006). SHRIMP zircon U-Pb age, litho- and biostratigraphic analyses of the Huaiyu Domain in South China—Evidence for a Neoproterozoic orogen, not Late Paleozoic-Early Mesozoic collision. Episodes, 29(4): 244-252. (in Chinese with English abstract)

Shu L.S., Zhou G.Q., Shi Y.S. & Yin J. (1994). Study of the high pressure metamorphic blueschist and its Late Proterozoic age in the Eastern Jiangnan belt. Chinese Science Bulletin, 39(14): 1200-1204.

Shu, L. S. (2012). An analysis of principal features of tectonic evolution in South China Block. Geol. Bull. China, 31, 1035-1053. (in Chinese with English abstract).

Shu, L. S., Faure, M., Yu, J. H., & Jahn, B. M. (2011). Geochronological and geochemical features of the Cathaysia block (South China): new evidence for the Neoproterozoic breakup of Rodinia. Precambrian Research, 187(3-4), 263-276.

Shu, L., & Charvet, J. (1996). Kinematics and geochronology of the Proterozoic Dongxiang-Shexian ductile shear zone: With HP metamorphism and ophiolitic melange (Jiangnan region, south China). Tectonophysics, 267(1-4), 291-302.

Shu, L., Wang, B., Cawood, P. A., Santosh, M., & Xu, Z. (2015). Early Paleozoic and Early Mesozoic intraplate tectonic and magmatic events in the Cathaysia Block, South China. Tectonics, 34(8), 1600-1621.

Shu, L., Zhou, X., Ping, D., University, N., Nanjing, and Beijing, et al. (2006). Principal geological features of nanling tectonic belt, south china. Geological Review, 52(2), 251-265. (in Chinese with English abstract).

Shu, X. J., Wang, X. L., Sun, T., Chen, W. F., and Shen, W. Z. (2013). Crustal formation in the nanling range, south china block: hf isotope evidence of zircons from phanerozoic granitoids. Journal of Asian Earth Sciences, 74(18), 210-224.

Smythe, D. J., & Brenan, J. M. (2016). Magmatic oxygen fugacity estimated using zircon-melt partitioning of cerium. Earth and Planetary Science Letters, 453, 260-266.

So, C. S., Zhang, D., Yun, S. T., Li, D. (1998). Alteration-mineralization zoning and fluid inclusions of the high sulfidation epithermal cu-au mineralization at zijinshan, fujian province, china. International Journal of Safety & Security in Tourism/hospitality, 93(7), 961-980.

Spencer, K. J., & Lindsley, D. H. (1981). A solution model for coexisting iron-titanium

oxides. American mineralogist, 66(11-12), 1189-1201.

Štemprok, M. (1982). Tin-fluorine relationship in ore-bearing assemblage. Metallization associated with acid magmatism, Edited by A.M. Evans. John Wiley & Sons: 321-338.

Štemprok, M. (1990). Solubility of tin, tungsten and molybdenum oxides in felsic magmas. Mineralium Deposita, 25(3), 205-212.

Štemprok, M., (1991). Ongonite from Ongon Khairkhan, Mongolia. Mineralogy and Petrology 43, 255-273.

Štemprok, M., Dolejš, D., Müller, A., Seltmann, R., (2008). Textural evidence of magma decompression, devolatilization and disequilibrium quenching: an example from the Western Krušné hory/Erzgebirge granite pluton. Contributions to Mineralogy and Petrology 155, 93-109.

Štemprok, M., Voldfin, J. : Solubility of tin dioxide in dry sodium rich granite melts. Proceedings of the XI. General Meeting of IMA:125-133 Novosibirsk 4-10. Sept. 1970. Izd. Nauka, Leningrad (1978).

Stormer, J. C. (1983). The effects of recalculation on estimates of temperature and oxygen fugacity from analyses of multicomponent iron-titanium oxides. American Mineralogist, 68(5-6), 586-594.

Sun, T., and Zhou, X.M. Late Mesozoie Extension in Southeast China: Petrologic Symbols. Journal of Nanjing University (Natural Science), 2002, 38(6): 737-746 (in Chinese with English abstract).

Sun, T., Zhou, X.M., Chen, P.R., Li, H.M., Zhou, H.Y., Wang, Z.C., Shen, W.Z., 2003. Petrogenesis and geotectonic significance of Mesozoic strongly peraluminous granites in eastern Nanling. Science in China (Series D) 33, 1209–1218 (in Chinese with English abstract).

Sun, Y., Ma, C., Liu, Y., & She, Z. (2011). Geochronological and geochemical constraints on the petrogenesis of late Triassic aluminous A-type granites in southeast China. Journal of Asian Earth Sciences, 42(6), 1117-1131.

Sun. T. (2006). A new map showing the distribution of granites in South China and its explanatory notes. Geologcal Bulletin of China, 25(3), 332-335.

Swanson, S. E. (1979). The effect of CO2 on phase equilibria and crystal growth in the system $KAlSi_3O_8$-$NaAlSi_3O_8$-$CaAl_2Si_2O_8$-SiO_2-H_2O-CO_2 to 8000 bars. American Journal of Science, 279(6), 703-720.

Swanson, S.E., 1977. Relation of nucleation and crystal-growth rate to the development of granitic textures. American Mineralogist 62, 966-978.

Takahashi, Y., Yoshida, H., Sato, N., Hama, K., Yusa, Y., Shimizu, H., 2002. W-and M-type tetrad effects in REE patterns for water–rock systems in the Tono uranium deposit, central Japan. Chemical geology 184, 311-335.

Tang, Y., Li, X., Zhang, X., Yang, J., Xie, Y., Huang, Y., ... & Yin, R. (2015). Some new data on the genesis of the Linghou Cu–Pb–Zn polymetallic deposit—based on the study of fluid inclusions and C–H–O–S–Pb isotopes. Ore Geology Reviews, 71, 248-262.

Taylor, J. R., & Wall, V. J. (1992a). The behavior of tin in granitoid magmas. Economic Geology, 87(2), 403-420.

Taylor, J. R., Wall, V. J., and Pownceby, M. I. (1992b). The calibration and application of accurate redox sensors. American Mineralogist, 77(3), 284-295.

Taylor, R.P., (1992c). Petrological and geochemical characteristics of the Pleasant Ridge zinnwaldite-topaz granite, southern New Brunswick, and comparisons with other topaz-bearing felsic rocks. The Canadian Mineralogist 30, 895-921.

Tindle, A.G., Breaks, F.W., 1998. Oxide minerals of the Separation Rapids rare-element granitic pegmatite group, northwestern Ontario. The Canadian Mineralogist 36, 609-635.

Tindle, A.G., Webb, P.C., 1990. Estimation of lithium contents in trioctahedral micas using microprobe data: application to micas from granitic rocks. European Journal of Mineralogy 2, 595-610.

Trail, D., Thomas, J. B., & Watson, E. B. (2011). The incorporation of hydroxyl into

zircon. American Mineralogist, 96(1), 60-67.

Trail, D., Watson, E. B., & Tailby, N. D. (2012). Ce and Eu anomalies in zircon as proxies for the oxidation state of magmas. Geochimica et Cosmochimica Acta, 97, 70-87.

Tuttle, O. F., & Bowen, N. L. (1958). Origin of granite in the light of experimental studies in the system: $NaAlSi_3O_8$ (Vol. 74). Geological Society of America.

Veksler, I.V., 2004. Liquid immiscibility and its role at the magmatic-hydrothermal transition: a summary of experimental studies. Chemical Geology 210, 7-31.

Veksler, I.V., Dorfman, A.M., Dulski, P., Kamenetsky, V.S., Danyushevsky, L.V., Jeffries, T., Dingwell, D.B., 2012. Partitioning of elements between silicate melt and immiscible fluoride, chloride, carbonate, phosphate and sulfate melts, with implications to the origin of natrocarbonatite. Geochimica et Cosmochimica Acta 79, 20-40.

Veksler, I.V., Thomas, R., 2002. An experimental study of B-, P- and F-rich synthetic granite pegmatite at 0.1 and 0.2 GPa. Contributions to Mineralogy and Petrology 143, 673- 683.

Wang, D.Z. The Study of Granitic Rocks in South China: Looking Back and Forward. Geological Journal of China Universities, 2004, 10(3): 305-314 (in Chinese with English abstract).

Wang, L., Zhu, W., & Zhang, S. (1984). The evolution of two petrogenesis-mineralization series of granites in southern China. Geochemistry, 3(1), 1-13.

Wang, QY., Hu, RZ., Peng, JT., Bi, XW., Wu, LY., Liu, H., Su, BX. (2007). Characteristics and significances of the fluid inclusion from Yaogangxian Tungsten deposit in south of Hunan. Acta Petrologica Sinica, 23(9): 2263-2273 (in Chinese with English abstract).

Wang, R. C., Xie, L., Chen, J., Yu, A., Wang, L., & Lu, J., et al. (2013). Tin-carrier minerals in metaluminous granites of the western nanling range (southern china): constraints on processes of tin mineralization in oxidized granites. Journal of

Asian Earth Sciences, 74(18), 361-372.

Wang, R. C., Xie, L., Lu, J. J., Zhu, J. C., and Chen, J. (2017). Diversity of mesozoic tin-bearing granites in the nanling and adjacent regions, south china: distinctive mineralogical patterns. Science China Earth Sciences, 60(11), 1-11.

Wang, R.C., Fontan, F., Monchoux, P., 1992. Mineraux dissemines comme indicateurs du caractere pegmatitique du granite de Beauvoir, Massif d'Echassieres, allier, France. The Canadian. Mineralogist 30, 763-770.

Wang, R.C., Fontan, F., Xu, S.J., Chen, X.M., Monchoux, P., 1997. The association of columbite, tantalite and tapiolite in the Suzhou granite, China. The Canadian Mineralogist 35, 699-706.

Wang, R.C., Xie, L., Chen, J., Yu, A.P., Wang, L.B., Lu, J.J., Zhu, J.C. (2013). Tin-carrier minerals in metaluminous granites of the western Nanling Range (southern China): constraints on processes of tin mineralization in oxidized granites. J. Asian Earth Sci., 74, 361–372.

Wang, R.C., Yu, A.P., Chen, J., Xie, L., Lu, J.J., Zhu, J.C., (2012). Cassiterite exsolution with ilmenite lamellae in magnetite from the Huashan met aluminous tin granite in southern China. Mineralogy and Petrology 105, 71–84.

Wang, X. L., Zhao, G., Zhou, J. C., Liu, Y., & Hu, J. (2008). Geochronology and Hf isotopes of zircon from volcanic rocks of the Shuangqiaoshan Group, South China: implications for the Neoproterozoic tectonic evolution of the eastern Jiangnan orogen. Gondwana Research, 14(3), 355-367.

Wang, X. L., Zhou, J. C., Griffin, W. A., Wang, R. C., Qiu, J. S., O'reilly, S. Y., ... & Zhang, G. L. (2007a). Detrital zircon geochronology of Precambrian basement sequences in the Jiangnan orogen: dating the assembly of the Yangtze and Cathaysia Blocks. Precambrian Research, 159(1-2), 117-131.

Wang, X. L., Zhou, J. C., Qiu, J. S., Zhang, W. L., Liu, X. M., & Zhang, G. L. (2006). LA-ICP-MS U-Pb zircon geochronology of the Neoproterozoic igneous rocks from Northern Guangxi, South China: Implications for tectonic evolution.

Precambrian Research, 145(1-2), 111-130.

Wang, X. L., Zhou, J. C., Wan, Y. S., Kitajima, K., Wang, D., Bonamici, C., ... & Sun, T. (2013). Magmatic evolution and crustal recycling for Neoproterozoic strongly peraluminous granitoids from southern China: Hf and O isotopes in zircon. Earth and Planetary Science Letters, 366, 71-82.

Wang, X., Zhou, J., Qiu, J., & Gao, J. (2004a). Geochemistry of the Meso-to Neoproterozoic basic–acid rocks from Hunan Province, South China: implications for the evolution of the western Jiangnan orogen. Precambrian Research, 135(1), 79-103.

Wang, X.W., Wang, X.D., Liu, J.Q., &Chang, H.L. (2004b). Relationship of qitianling granite to sn mineralization in Hunan province. Geological Science & Technology Information, 23(2), 1-12. (in Chinese with English abstract).

Wang, Y. J., Fan, W. M., Guo, F., Peng, T. P.,and Li, C. W. (2003). Geochemistry of mesozoic mafic rocks adjacent to the chenzhou-linwu fault, south china: implications for the lithospheric boundary between the yangtze and cathaysia blocks. International Geology Review, 45(3), 263-286.

Wang, Y., Fan, W., Sun, M., Liang, X., Zhang, Y., & Peng, T. (2007b). Geochronological, geochemical and geothermal constraints on petrogenesis of the Indosinian peraluminous granites in the South China Block: a case study in the Hunan Province. Lithos, 96(3-4), 475-502.

Wang, Y., Fan, W., Zhang, G., Zhang, Y. (2013). Phanerozoic tectonics of the South China Block: key observations and controversies. Gondwana Research, 23(4), 1273-1305.

Wang, Z., Chen, B., & Ma, X. (2014). Petrogenesis of the late Mesozoic Guposhan composite plutons from the Nanling range, South China: Implications for W-Sn mineralization. American Journal of Science, 314(1), 235-277.

Watson, E. B., & Harrison, T. M. (1984). Accessory minerals and the geochemical evolution of crustal magmatic systems: a summary and prospectus of experimental

approaches. Physics of the Earth and Planetary Interiors, 35(1-3), 19-30.

Webster, J. D. (1997). Exsolution of magmatic volatile phases from Cl-enriched mineralizing granitic magmas and implications for ore metal transport. Geochimica et Cosmochimica Acta, 61(5), 1017-1029.

Webster, J. D., Burt, D. M., & Aguillon, R. A. (1996). Volatile and lithophile trace-element geochemistry of Mexican tin rhyolite magmas deduced from melt inclusions. Geochimica et Cosmochimica Acta, 60(17), 3267-3283.

Wei, S. L., Zeng, Q. W., Yi-Ming, X. U., Lan, X. M., Kang, W. Q., and Liao, X. Y. (2002a). Characteristics and ore prospects of tin deposits in the qitianling area,hunan. Chinese Geology, 29(1), 67-75. (in Chinese with English abstract).

Wei, S.L., Zeng, Q.W., Xu, Y.M., et al. (2002): Characteristics and ore prospects of tin deposits in the Qitianling area, Hunan.Chinese Geology, 29, 67-75.

Whalen, J. B., Currie, K. L., & Chappell, B. W. (1987b). A-type granites: geochemical characteristics, discrimination and petrogenesis. Contributions to mineralogy and petrology, 95(4), 407-419.

White, A. J. R., and Chappell, B. W. (1977) Ultrametamorphism and granitoild genesis. Tectonophysics 43 : 7-22.

Whitney, J. A. (1972). History of granodioritic and related magma systems: an experimental study. Dept. of Geology.

Whitney, J. A. (1975). The effects of pressure, temperature, and on phase assemblage in four synthetic rock compositions. The Journal of Geology, 83(1), 1-31.

Whitney, J. A., & Stormer JR, J. C. (1985). Mineralogy, petrology, and magmatic conditions from the Fish Canyon Tuff, central San Juan volcanic field, Colorado. Journal of Petrology, 26(3), 726-762.

Witney, D.L. and Evans, B.W. (2010) Abbreviations for Names of Rock-Forming Minerals. American Mineralogist, 95, 185-187.

Wolf, M. B., & London, D. (1994). Apatite dissolution into peraluminous haplogranitic melts: an experimental study of solubilities and mechanisms. Geochimica et

Cosmochimica Acta, 58(19), 4127-4145.

Wolf, M. B., & Wyllie, P. J. (1994). Dehydration-melting of amphibolite at 10 kbar: the effects of temperature and time. Contributions to Mineralogy and Petrology, 115(4), 369-383.

Wones, D. R., and Eugster, H. P. (1965). Stability of biotite: experiment, theory, and application. American Mineralogist: Journal of Earth and Planetary Materials 50(9), 1228-1272.

Wu, F. Y., Sun, D. Y., Li, H., Jahn, B. M., & Wilde, S. (2002). A-type granites in northeastern China: age and geochemical constraints on their petrogenesis. Chemical Geology, 187(1-2), 143-173.

Xiaomin, L., Ruizhong, H., Xianwu, B., & Jiantang, P. (2010). Geochemistry and tin metallogenic potential for Qitianling granite mass in southern Hunan. Journal of Jilin University (Earth Science Edition), 40(1), 80-92. (in Chinese with English abstract).

Xie, D.K., Ma, R.S., Zhang Y.S., Zhao, X.X., and Coe, R.S. The crust growth and mantle plume tectonics of South China Continent: Beijing, Geological Publishing House, 1996, 1-257 (in Chinese with English abstract).

Xie, G.Q., Hu, R.Z., Zhao, J.H., Jiang, G.H. Mantle plume and the relationship between it and Mesozoic large-scale metallogenesis in southeastern China: A preliminary discussion. Geotectonica et Metallogenia, 2001, 25(2):179-186 (in Chinese with English abstract).

Xie, L., Wang, R. C., Chen, J., & Zhu, J. C. (2010). Mineralogical evidence for magmatic and hydrothermal processes in the Qitianling oxidized tin-bearing granite (Hunan, South China): EMP and (MC)-LA-ICPMS investigations of three types of titanite. Chemical Geology, 276(1-2), 53-68.

Xie, L., Wang, R., Chen, J., Zhu, J., Zhang, W., Lu, J., & Zhang, R. (2013). A tin-mineralized topaz rhyolite dike with coeval topaz granite enclaves at Qiguling in the Qitianling tin district, southern China. Lithos, 170, 252-268.

Xiong, X., Zhao, Z., Zhu, J., Rao, B., & Lai, M. (1998a). Phase equilibria in the granite-H_2O-HFsystem and effect of fluorine on granitic melt structure. Chinese Journal of Geochemistry, 17(2), 114-122. (in Chinese with English abstract)

Xiong, X., Zhao, Z., Zhu, J., Rao, B., & Lai, M. (1998b). Partitioning of f between aqueous fluids and albite granite melt and its petrogenetic and metallogenetic significance. Chinese Journal of Geochemistry, 17(4), 303-310. (in Chinese with English abstract)

Xirouchakis, D., and Lindsley, D. H. (1998). Equilibria among titanite, hedenbergite, fayalite, quartz, ilmenite, and magnetite: experiments and internally consistent thermodynamic data for titanite. American Mineralogist, 83(7-8), 712-725.

Xu X.S., O'Reilly, S.Y., Griffin W.L., Deng P., Pearson, N.J., (2005). Relict Proterozoic basement in the Nanling Mountains (SE China) and its tectonothermal overprinting. Tectonics 24.

Xu, K.Q., Sun, N., Wang, D.Z., Hu, S.X. (1963). Investigation on the polycyclic granite intrusions of southern china, with special notice on their ages of intrusions, distribution, characteristics, and their genetic relations to mineral deposits. Acta Geological Sinica, 43(2): 141-155 (in Chinese with English abstract).

Xu, X. S., & Zhou, X. M., (1992). Precambrian S-type granitoids in south china and their geological signigicance. Journal of Nanjing University, 3, 423-430. (in Chinese with English abstract)

Yan, D. P., Zhou, M. F., Li, S. B., & Wei, G. Q. (2011). Structural and geochronological constraints on the Mesozoic - Cenozoic tectonic evolution of the Longmen Shan thrust belt, eastern Tibetan Plateau. Tectonics, 30(6).

Yan, S., XianWu, B., RuiZhong, H., JianTang, P., WenChao, S., & ChangSheng, Z. (2009). Study on the ore-forming fluid geochemistry of the Furong tin polymetallic deposit, Hunan province, China. ACTA PETROLOGICA SINICA, 25(10), 2588-2600. (in Chinese with English abstract)

Yao, J. M., Hua, R. M., Wenjun, Q. U., Huawen, Q. I., Lin, J. F., Andao, D. U. (2007).

Re-os isotope dating of molybdenites in the huangshaping pb-zn-w-mo polymetallic deposit,hunan province,south china and its geological significance. Science in China, 50(4), 519-526.

Ye, M. F., Li, X. H., Li, W. X., Liu, Y., & Li, Z. X. (2007). SHRIMP zircon U–Pb geochronological and whole-rock geochemical evidence for an early Neoproterozoic Sibaoan magmatic arc along the southeastern margin of the Yangtze Block. Gondwana Research, 12(1-2), 144-156.

Yu, J. H., O'Reilly, S. Y., Wang, L., Griffin, W. L., Zhou, M. F., Zhang, M., Shu, L. (2010). Components and episodic growth of Precambrian crust in the Cathaysia Block, South China: evidence from U–Pb ages and Hf isotopes of zircons in Neoproterozoic sediments. Precambrian Research, 181(1), 97-114.

Yu, J. H., Wang, L., O'reilly, S. Y., Griffin, W. L., Zhang, M., Li, C., & Shu, L. (2009). A Paleoproterozoic orogeny recorded in a long-lived cratonic remnant (Wuyishan terrane), eastern Cathaysia Block, China. Precambrian Research, 174(3-4), 347-363.

Yu, J., O Reilly, Y.S., Wang, L., Griffin, W.L., Jiang, S., Wang, Y., Xu, X., (2007). Finding of ancient materials in Cathaysia and implication for the formation of Precambrian crust. Chinese Science Bulletin 52, 11–18.

Yu, J.H., O'Reilly, S.Y., Zhou, M.F., Griffin, W.L., Wang, L.J., (2012). U–Pb geochronology and Hf–Nd isotopic geochemistry of the Badu Complex, Southeastern China: Implications for the Precambrian crustal evolution and paleogeography of the Cathaysia Block. Precambrian Research, 222-223, 424-449.

Yuan, S., Mao, J., Zhao, P., Yuan, Y. (2018). Geochronology and petrogenesis of the qibaoshan cu-polymetallic deposit, northeastern hunan province: implications for the metal source and metallogenic evolution of the intracontinental qinhang cu-polymetallic belt, south china. Lithos, 302.

Yuan, S., Peng, J., Hao, S., Li, H., Geng, J., & Zhang, D. (2011). In situ LA-MC-ICP-MS and ID-TIMS U–Pb geochronology of cassiterite in the giant Furong tin

deposit, Hunan Province, South China: New constraints on the timing of tin–polymetallic mineralization. Ore Geology Reviews, 43(1), 235-242.

Yuan, S.D., Peng, J.T., Hu, R.Z., Li, H.M., Shen, N.P., Zhang, D.L., 2008. A precise U–Pb age on cassiterite from the Xianghualing tin-polymetallic deposit (Hunan, South China). Mineralium Deposita 43, 375-382.

Yuan, S.D., Peng, J.T., Shen, N.P., Hu, R.Z., Dai, T.M., 2007. ^{40}Ar-^{39} Ar isotopic dating of the Xianghualing Sn-polymetallic orefield in Southern Hunan, China and its geological implications. Acta Geologica Sinica (English Edition) 81, 278-286.

Zhang, A.C., Wang, R.C., Hu, H., Zhang, H., Zhu, J.C., Chen, X.M., 2004. Chemical evolution of Nb-Ta oxides and zircon from the Koktokay No. 3 granitic pegmatite, Altai, northwestern China. Mineralogical Magazine 68, 739-756.

Zhang, R., Lehmann, B., Seltmann, R., Sun, W., & Li, C. (2017). Cassiterite U-Pb geochronology constrains magmatic-hydrothermal evolution in complex evolved granite systems: The classic Erzgebirge tin province (Saxony and Bohemia). Geology, 45(12), 1095-1098.

Zhang, R., Lu, J., Wang, R., Hu, J., Zhang, H. (2015). Redox state of the granitic rocks and formation of the scheelite skarn in the xintianling deposit, nanling range, south china. Acta Geologica Sinica, 88(s2), 64-65.

Zhang, W., Hua, R., Wang, R., Chen, P., Li, H. (2007). New dating of dajishan granite and related tungsten mineralization, south jiangxi province, china. Frontiers of Earth Science in China, 1(2), 218-225.

Zhang, Y., Shu, L. S., Chen, X. Y. (2011). Geochemistry, geochronology, and petro-genesis of the early paleozoic granitic plutons in the central-southern jiangxi province, china. Science China Earth Sciences, 54(10), 1492.

Zhao, D., Essene, E. J., & Zhang, Y. (1999). An oxygen barometer for rutile–ilmenite assemblages: oxidation state of metasomatic agents in the mantle. Earth and Planetary Science Letters, 166(3-4), 127-137.

Zhao, G., Guo, J. (2012). Precambrian geology of China: preface. Precambrian

Research, 222, 1-12.

Zhao, K. D., Jiang, S. Y., Jiang, Y. H., and Wang, R. C. (2005). Mineral chemistry of the qitianling granitoid and the furong tin oredeposit in hunan province, south china. European Journal of Mineralogy, 17(4), 635-648.

Zhao, K. D., Jiang, S. Y., Nakamura, E., Moriguti, T., Palmer, M. R., Yang, S. Y., ... & Jiang, Y. H. (2011). Fluid–rock interaction in the Qitianling granite and associated tin deposits, South China: evidence from boron and oxygen isotopes. Ore Geology Reviews, 43(1), 243-248.

Zhao, K. D., Jiang, S. Y., Yang, S. Y., Dai, B. Z., & Lu, J. J. (2012). Mineral chemistry, trace elements and Sr–Nd–Hf isotope geochemistry and petrogenesis of Cailing and Furong granites and mafic enclaves from the Qitianling batholith in the Shi-Hang zone, South China. Gondwana Research, 22(1), 310-324.

Zhao, K.D., Jiang, S.Y., Jiang, Y.H., Wang, R.C. Mineral chemistry of the Qitianling granitoid and the Furong tin ore deposit in Hunan Province, South China: implication for the genesis of granite and related tin mineralization. European Journal of Mineralogy, 2005, 17(4), 635–648.

Zhao, K.-D., S.-Y. Jiang, Y.-H. Jiang, and R.-C. Wang (2005). Mineral chemistry of the Qitianling granitoid and the Furong tin oredeposit in Hunan Province, South China, European Journal of Mineralogy, 17(4), 635.

Zheng, Y. F., Xiao, W. J., & Zhao, G. (2013). Introduction to tectonics of China.

Zhong, J., Chen, Y. J., Pirajno, F., Chen, J., Li, J., Qi, J. P., et al. (2014). Geology, geochronology, fluid inclusion and h–o isotope geochemistry of the luoboling porphyry cu–mo deposit, zijinshan orefield, fujian province, china. Ore Geology Reviews, 57(1), 61-77.

Zhong, Y., Wang, L., Zhao, J., Liu, L., Ma, C., Zheng, J., et al. (2016). Partial melting of an ancient sub-continental lithospheric mantle in the early paleozoic intracontinental regime and its contribution to petrogenesis of the coeval peraluminous granites in south china. Lithos, 264, 224-238.

Zhou X, Sun T, Shen W, et al. Petrogenesis of Mesozoic granitoids and volcanic rocks in South China: a response to tectonic evolution. Episodes, 2006, 29(1): 26-33.

Zhou, B. X., Sun, T., Shen, W., Shu, L., and Niu, Y. (2006). Petrogenesis of Mesozoic granitoids and volcanic rocks in South China: a response to tectonic evolution. Episodes, 29(1), 26.

Zhou, X. M., Li, W. X. (2000). Origin of Late Mesozoic igneous rocks in Southeastern China: implications for lithosphere subduction and underplating of mafic magmas. Tectonophysics, 326(3), 269-287.

Zhou, X., Sun, T., Shen, W., Shu, L., Niu, Y. (2006). Petrogenesis of Mesozoic granitoids and volcanic rocks in South China: a response to tectonic evolution. Episodes, 29(1), 26.

Zhou, X.M., and Li, W.X. Origin of Late Mesozoic igneous rocks of southeastern China: implications for lithosphere subduction and underplating of mafic magma. Tectonophysics, 2000, 326: 269-287.

Zhu J.C., Zhang P.H., Xie C.F., Zhang H.,Yang C. (2006). Zircon U-Pb age framework of Huashan-Guposhan intrusive belt, western part of Nanling Range, and its geological significance． Acta Petrologica Sinica, 22 (9), 2270-2278 (in Chinese with English abstract).

Zhu, J. (2006). Zircon u-pb age framework of huashan-guposhan intrusive belt, western part of nanling range, and its geological significance. Acta Petrologica Sinica, 22.

Zhu, J. C. (2003). On the emplacement age and material sources for the granites of Cailing superunit, Qitianling pluton, South Hunan Province. Geol. Rev., 49, 245-252. (in Chinese with English abstract)

Zhu, J. C., Chen, J., Wang, R. C., Lu, J. J., Xie, L. (2008). Early yanshanian ne trending sn/w-bearing a-type granites in the western-middle part of the nanling mts region. Geological Journal of China Universities, 14(4), 474-484. (in Chinese with English abstract).

Zhu, J. C., Wang, R. C., Zhang, P. H., Xie, C. F., Zhang, W. L., and Zhao, K. D., et al.

(2009), Zircon U-Pb geochronological framework of Qitianling granite batholith, middle part of Nanling Range, South China, Science in China Series D: Earth Sciences, 52(9), 1279-1294, doi:10.1007/s11430-009-0154-4.

Zhu, J. C., Zhang, H., Xie, C. F., Zhang, P. H., & Yang, C. (2005). Zircon SHRIMP U-Pb geochronology, petrology and geochemistry of the Zhujianshui granite, Qitianling pluton, southern Hunan Province. Geological Journal of China Universities, 11(3), 335-342. (in Chinese with English abstract).

Zhu, J.C., Li, R.K., Li, F.C., Xiong, X.L., Zhou, F.Y., Huang, X.L. 2001. Topaz–albite granites and rare-metal mineralization in the Limu district, Guangxi Province, southeast China. Mineralium Deposita 36, 393-405.

Zhu, J.C., Liu, W.X., 1990. Topazite-ongonite relationship and its bearing on vertical zonation in rare-metal granites: evidence from Xianghualing District, Hunan Province, China. Proceedings of the Eighth Quadrennial IAGOD Symposium, VI, 303-313.

Zhu, J.C., Liu, W.X., Zhou, F.Y., 1993. Ongonite and topazite in dike No. 431 of Xianghualing district and their spatial zonation and genetic relationship. Acta Petrologica Sinica 9, 158-166 (in Chinese with English abstract).

Zhu, J.C., Wang, R.C., Liu, J.J., Zhang, H., Zhang, W.L., Xie, L., Zhang, R.Q., 2011. Fractionation, Evolution, Petrogenesis and Mineralization of Laiziling Granite Pluton, Southern Hunan Province. Geological Journal of China Universities 17, 381-392 (in Chinese with English abstract).

Zhu, J.S., Cao, J.M., Li, X.G., and Zhou, B. 1997.A preliminary three-dimensional Earth's model of China and adjacent regions and its implications. Chinese Journal of Geophysics, 40 (4):499-518.

Zimmer, M. M., Plank, T., Hauri, E. H., Yogodzinski, G. M., Stelling, P., Larsen, J., ... & Nye, C. J. (2010). The role of water in generating the calc-alkaline trend: new volatile data for Aleutian magmas and a new tholeiitic index. Journal of Petrology, 51(12), 2411-244.

Fangfang HUANG

Contribution de la pétrologie expérimentale sur les processus de formation de roches et de minéralisation de granites du Jurassique en Chine du Sud

En tant que laboratoire naturel, les énormes quantités de granites mésozoïques du sud de la Chine fournissent une occasion unique de comprendre la formation et l'évolution de la croûte mésozoïque et de guider les efforts d'exploration minière dans cette région. Quelles sont les conditions de mise en place de ces granites mésozoïques en Chine du Sud ? Quelle est la relation entre les conditions de mise en place et la minéralisation associée à ces granites mésozoïques?

Nous avons établi expérimentalement les relations de phase du granite Jurassique de Qitianling en Chine du Sud. Trois échantillons représentatifs de granites métalumineux contenant des amphiboles ont été choisis pour définir les conditions de cristallisation de ce pluton. Des expériences de cristallisation ont été réalisées à 100-700 MPa, mais principalement à 200 MPa ou 300 MPa, à une fO_2 de ~ NNO-1,3 (1,3 log sous le tampon Ni-NiO) ou ~ NNO + 2,4, à 660 ° C à 900 ° C, et à des teneurs variables en eau (~ 3-8% en poids). Le champ de stabilité des amphiboles et les données de barométrie montrent tous deux que la pression de mise en place du magma se situait autour de 300-350 MPa. Les rapports Fe / Mg amphiboles et biotites suggèrent en outre que la fO_2 magmatique se situait autour de NNO-1 ± 0,5 près du solidus, alors que les oxydes de Fe-Ti enregistrent une augmentation de fO_2 jusqu'à NNO + 1 en conditions sub-solidus. La cristallisation de l'amphibole est limitée aux conditions proches de la saturation en H_2O, nécessitant au moins 5,5% en poids de H_2O dissout à 200 MPa, ou 6 à 8% en poids à> 300 MPa. La présence d'amphibole dans des magmas siliceux métalumineux riches en K_2O indique donc des teneurs en eau significativement supérieures à la valeur canonique de 4% en poids. Les compositions de liquides expérimentaux obtenus à 200-300 MPa reproduisent la tendance géochimique définie par le pluton, ce qui suggère qu'une différenciation dans le réservoir de la croûte supérieure a pu se produire. L'ensemble de ces résultats indique que la fugacité relativement faible en oxygène, la température élevée du magma lors de sa mise en place et sa richesse en eau constituent un environnement favorable à la concentration d'éléments minéralisés au stade magmatique précoce.

Mots clés: *Chine du Sud, granite Jurassique, conditions de mise en place, équilibre de phase, amphibole, oxybaromètre*

Contribution of experimental petrology on the rock-forming and mineralization processes of Jurassic granites in South China

As a natural laboratory, the huge amounts of Mesozoic granite distributing in South China provided a unique opportunity to unravel the Mesozoic crust formation and evolution in southern China as well as for guiding mining exploration efforts in this area. What are the emplacement conditions of those Mesozoic granite in South China? What are the relationship between the emplacement conditions and the mineralization among those Mesozoic granites?

We have experimentally established the phase relationships for the tin-bearing Jurassic Qitianling granite in South China. Three representative amphibole-bearing, metaluminous granitic samples were chosen for constraining crystallization conditions of the Qitianling pluton. Crystallization experiments were performed at 100-700 MPa, albeit mainly at 200 MPa or 300 MPa, at an fO_2 of ~NNO-1.3 (1.3 log unit below the Ni-NiO buffer) or ~NNO+2.4, at 660°C to 900°C, and at variable melt water contents (~3-8 wt%). Amphibole stability field and barometry both show that the pressure of magma emplacement was around 300-350 MPa. Amphibole and biotite Fe/Mg ratios further suggest that magmatic fO_2 was around NNO-1±0.5 near solidus, while Fe-Ti oxides record an fO_2 increase up to NNO+1 below solidus. Amphibole crystallization is restricted to near H_2O-saturation conditions, requiring at least 5.5 wt% H_2Omelt at 200 MPa, or 6-8 wt % at ≥ 300 MPa. Amphibole occurrence in K_2O-rich metaluminous silicic magmas thus indicates water contents significantly higher than the canonical value of 4 wt%. The experimental liquid line of descent obtained at 200-300 MPa mimic the geochemical trend expressed by the pluton suggesting that fractionation in the upper crustal reservoir could happen. We deduced that the relatively low oxygen fugacity, high liquidus temperature and melt water rich condition may be an enabling environment for concentrating the ore elements in the early magmatic stage.

Key words: *South China, Jurassic granite, emplacement conditions, phase equilibrium, amphibole, oxybarometer*

Institut des Sciences de la Terre d'Orléans-CNRS/Université d'Orléans

1A, rue de la Férollerie – 45071 Orléans Cedex 2, France

School of Earth Sciences and Engineering, Nanjing University

163, Xianlin Avenue – 210046 Nanjing, Chine